Conference Proceedings of the Society for Experimental Mechanics Series

Shamim Pakzad · Caicedo Juan *Editors*

Dynamics of Civil Structures, Volume 2

Proceedings of the 34th IMAC, A Conference and Exposition on Structural Dynamics 2016

SEM

Springer

Conference Proceedings of the Society for Experimental Mechanics Series

Shamim Pakzad • Caicedo Juan
Editors

Dynamics of Civil Structures, Volume 2

Proceedings of the 34th IMAC, A Conference and Exposition on Structural Dynamics 2016

Springer

Editors
Shamim Pakzad
Department of Civil & Environment Engineering
Lehigh University
Bethlehem, PA, USA

Caicedo Juan
University of South Carolina
Columbia, SC, USA

ISSN 2191-5644 ISSN 2191-5652 (electronic)
Conference Proceedings of the Society for Experimental Mechanics Series
ISBN 978-3-319-29750-7 ISBN 978-3-319-29751-4 (eBook)
DOI 10.1007/978-3-319-29751-4

Library of Congress Control Number: 2016937011

Printed on acid-free paper

This Springer imprint is published by Springer Nature
The registered company is Springer International Publishing AG Switzerland

Preface

Dynamics of Civil Structures represents one of ten volumes of technical papers presented at the 34th IMAC, A Conference and Exposition on Structural Dynamics, organized by the Society for Experimental Mechanics, and held in Orlando, Florida, in January 25–28, 2016. The full proceedings also include volumes on *Nonlinear Dynamics*; *Model Validation and Uncertainty Quantification*; *Dynamics of Coupled Structures*; *Sensors and Instrumentation*; *Special Topics in Structural Dynamics*; *Structural Health Monitoring, Damage Detection & Mechatronics*; *Rotating Machinery, Hybrid Test Methods, Vibro-Acoustics & Laser Vibrometry*; *Shock & Vibration, Aircraft/Aerospace, Energy Harvesting, Acoustics & Optics*; and *Topics in Modal Analysis & Testing*.

Each collection presents early findings from analytical, experimental, and computational investigations on an important area within structural dynamics. *Dynamics of Civil Structures* is one of these areas which cover topics of interest of several disciplines in engineering and science.

The Dynamics of Civil Structures Technical Division serves as a primary focal point within the SEM umbrella for technical activities devoted to civil structures analysis, testing, monitoring, and assessment. This volume covers a variety of topics including damage identification, human-structure interaction, hybrid testing, vibration control, model updating, modal analysis of in-service structures, sensing and measurements of structural systems, and bridge dynamics. Papers cover testing and analysis of all kinds of civil engineering structures such as buildings, bridges, stadiums, dams, and others.

The organizers would like to thank the authors, presenters, session organizers, and session chairs for their participation in this track.

Bethlehem, PA — Shamim Pakzad
Columbia, SC — Caicedo Juan

Contents

Chapter 1
Damage Assessment of Steel Structures Using Multi-Autoregressive Model

Chin-Hsiung Loh and Chun-Kai Chan

Abstract For application in operational modal analysis considering simultaneously the temporal and spatial response data of multi-channel measurements, the multivariate-autoregressive (MV-AR) model was used. The parameters of MV-AR model are estimated by using the least squares method via the implementation of the QR factorization as an essential numerical tool and are used to extract the structural damage sensitive features. These parameters are used to develop the Vectors of autoregressive model and Mahalanobis distance, and then to identify the damage features and damage locations. Verification of the proposed method using a series of white noise response data of a steel structure is demonstrated. This method is thus very effective for damage detection in case of ambient vibrations dealing with output-only modal analysis. In addition, comparisons and discussions on the proposed method with other methods, such as stochastic subspace identification and wavelet-based energy index, are also presented.

Keywords Damage detection • Multi-autoregressive model • Damage sensitive feature • SSI-COV • Wavelet-based energy index

1.1 Introduction

Structural system identification and damage detection have received more and more attention in the field of civil engineering. Through monitoring data on structures a quantity of information can be obtained. A well known classification for damage identification methods can be defined four levels: (Level-1) Determination or detection that damage is present in the structure, (Level-2) Determination of the geometric location of the damage, (Level-3) Quantification of the severity of the damage, (Level-4) Prediction of the remaining service life of the structure. Generally, detection is performed by pattern recognition methods or Novelty detection [16], and the key issue for inverse methods is the damage location identification. Once the damage is located, it may be parameterized with a limited set of parameters and quantification.

One of the efficiently and accurately monitoring techniques to all types of structural systems is the vibration-based damage detection. It is based on the principal that damage in a structure will alter the dynamic response of that structure and the selection of damage-sensitive features such as natural frequencies [12], displacement mode shapes [5], wavelet analysis of dynamic signals [7] will be concerned. In the viewpoint of global monitoring, system identification techniques extract natural frequencies, damping ratios, and mode shapes of a structure using acceleration data [3, 8]. But these dynamic features are not sensitive to damage. Fundamentally, feature extraction can also be based on fitting some model, either physics-based [Moaveni et al., 2008] or data-driven [13], to the measured system response data. Time-series analysis based on the use of autoregressive (AR) models have been extensively used in the SHM process as a feature extraction technique and also applied to damage detection [10, 11]. The algorithm is based on the premise that structural damage will change the vibration response of the structure.

In this study, damage identification on the seismic response of two steel structures is examined. By using the response data of the two structures from white noise excitation between a series of earthquake excitations back to back from the shaking table tests, the multivariate signal processing techniques are used to extract the dynamic features directly from response measurements. The state of damage severity as well as the damage location through the developed novel damage detection algorithms is proposed.

C.-H. Loh (✉) • C.-K. Chan
Department of Civil Engineering, National Taiwan University, Taipei 10617, Taiwan
e-mail: lohc0220@ccms.ntu.edu.tw; r98521205@ntu.edu.tw

S. Pakzad, C. Juan (eds.), *Dynamics of Civil Structures, Volume 2*, Conference Proceedings of the Society for Experimental Mechanics Series, DOI 10.1007/978-3-319-29751-4_1

1.2 Structural Model and Instrumentation

The major research objective of this study is to examine the applicability of the proposed damage features to detect the structural damage and to identify the damage location using the output-only measurement. The structural models used for this study are two 3-story (Specimen 1 and Specimen 2) with 350 cm in height steel structures and the floor area is 1.5 m × 1.1 m, respectively. The two steel structures are constructed with the same member size except Specimen 2 in which one column in the first floor (i.e. column at the north-west corner designed with smaller web thickness). Therefore, specimen 1 is a symmetric structure while specimen 2 is an anti-symmetric structure. The total weight of each structure is 2.94 t (include additional 0.5 t on each floor). Three different types of instrumentation were installed to collect the vibration response of the structure: accelerometer, LVDT and NDI optical tracker. The distribution of accelerometer and the LVDT is shown in Fig. 1.1. The two specimens are tested on NCREE shaking table. The spectrum compatible acceleration record (from Ch-Chi earthquake station TCU071) is used as the desired base excitation of the shaking table.

The base excitation is arranged back to back with different input intensity level. In between the earthquake excitation white noise excitation (with peak acceleration of 50 gal) was also applied to serve as the reference state of the structure before and after each earthquake excitation, as shown in Table 1.1. In these experiments all the response measurement is with 200 Hz sampling frequency.

1.3 Methods on Damage Identification

Two methods on structural damage identification were applied by using output-only measurement of structure: the multivariate autoregressive model (parametric MV-AR model) and the time-frequency analysis of response signal.

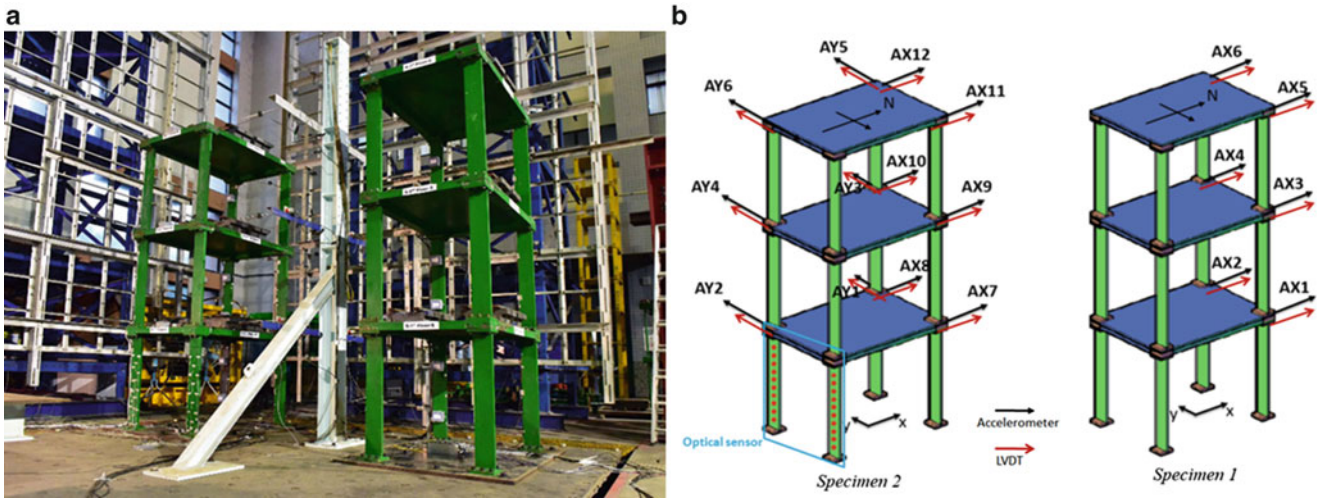

Fig. 1.1 (**a**) Photo of the two structures on shaking table. (**b**) Instrumentation of accelerometer

Table 1.1 Test protocol for the two steel structures

CASE	**WN1**	**WN2**	**EQ1**	**WN3**	**EQ2**	**WN4**	**EQ3**	**WN5**	**EQ4**	**WN6**	**EQ5**
PGA(gal)	50	50	95	50	269	50	400	50	572	50	674
CASE	**WN7**	**EQ6**	**WN8**	**EQ7**	**WN9**	**EQ8**	**WN10**	**EQ9**	**WN11**	**EQ10**	**WN12**
PGA(gal)	50	858	50	994	50	1090	50	1329	50	1440	50

1.3.1 Damage Detection Using Migration of Autoregressive Model Coefficients

Consider the multiple measurement in the experiments, a multivariate autoregressive model (MV-AR model) was used. First, a vector autoregressive model with d sensors can be expressed as follows [4, 14]:

$$\{y(t)\} + [\alpha_1]\{y(t-1)\} + [\alpha_2]\{y(t-2)\} + \cdots [\alpha_p]\{y(t-p)\} = \{e(t)\} \tag{1.1}$$

Or

$$\{y(t)\}_{d\times 1} = [A]_{d\times dp}\{\phi(t)\}_{dp\times 1} + \{e(t)\}_{d\times 1}$$

Where

$$[A]_{d\times dp} = \left[-[\alpha_1] - [\alpha_2]\cdots - [\alpha_i]\cdots - [\alpha_p]\right] \tag{1.2}$$

is the model parameter matrix and p is the order of the AR model, $[\alpha_i]_{d\times d}$ is the matrix of autoregressive parameters relating the output {y(t−i)} to {y(t)}, i = 1:p. And

$$\{\phi(t)\}_{dp\times 1} = \begin{Bmatrix} \{y(t-1)\}_{d\times 1} \\ \{y(t-2)\}_{d\times 1} \\ \vdots \\ \{y(t-p)\}_{d\times 1} \end{Bmatrix} \tag{1.3}$$

is the regressor for the output vector {y(t)}, $\{y(t-i)\}_{d\times 1}$ (i−1:p) is the output vector with delay time i × Ts, T is the sampling period (s), and $\{e(t)\}_{d\times 1}$ is the residual vector of all output channels, which is considered as the error of the model. If (N ≥ dp + d) consecutive output vectors of the responses from {y(k)} to {y(k + N − 1)} are taken into account, the model parameters can obviously be estimated with the least squares method by minimizing a norm of error sequences. The data matrix is first constructed from N successive sample:

$$[K]_{N\times(dp+d)} = \begin{bmatrix} \{\phi(t)\}^T_{dp\times 1} & \{y(t)\}^T_{d\times 1} \\ \{\phi(t+1)\}^T_{dp\times 1} & \{y(t+1)\}^T_{d\times 1} \\ \vdots & \vdots \\ \{\phi(t+N-1)\}^T_{dp\times 1} & \{y(t+N-1)\}^T_{d\times 1} \end{bmatrix} \tag{1.4}$$

The QR factorization of the data matrix $[K]_{N\times(dp+d)} = [Q]_{N\times N}\ [R]_{N\times(dp+d)}$ can be computed by the Householder method or Givens rotation. It gives $[Q]_{N\times N}$ which is an orthogonal matrix ($QQ^T = I$) and $[R]_{N\times(dp+d)}$ is an upper triangular matrix. Through detail derivation, the model parameters matrix $[A]_{d\times dp}$ can be calculated. Once the model parameters are estimated, the state matrix of the system can be established in the form of autoregressive parameters [2]:

$$[\Phi]_{dp\times dp} = \begin{bmatrix} -[\alpha_1]_{d\times d} & -[\alpha_2]_{d\times d} & -[\alpha_i]_{d\times d} & \cdots & -[\alpha_p]_{d\times d} \\ I & 0 & 0 & \cdots & 0 \\ 0 & I & 0 & \cdots & 0 \\ \vdots & \vdots & \ddots & \ddots & \vdots \\ 0 & 0 & 0 & I & 0 \end{bmatrix} \tag{1.5}$$

The identified model parameters can also be used for damage detection. It is assumed the matrix coefficients for obtained MV-AR models, in particular diagonal elements in matrix $[\alpha_1]$ and $[\alpha_2]$ are used to extract the damage features in sensor location *j* at different events of the system. By applying MVAR model to the ambient vibration data the system natural frequencies of specimen 1 and specimen 2 can be identified, as shown in Fig. 1.2. It is observed that for the symmetric structure (Specimen 1) the lowest five modes can be identified while for the torsion-coupling structure (Specimen 2) nine modes can be identified. Besides, the identified modal frequencies of the two structures did not change with respect to different test even though the structure was subjected to severe earthquake excitation.

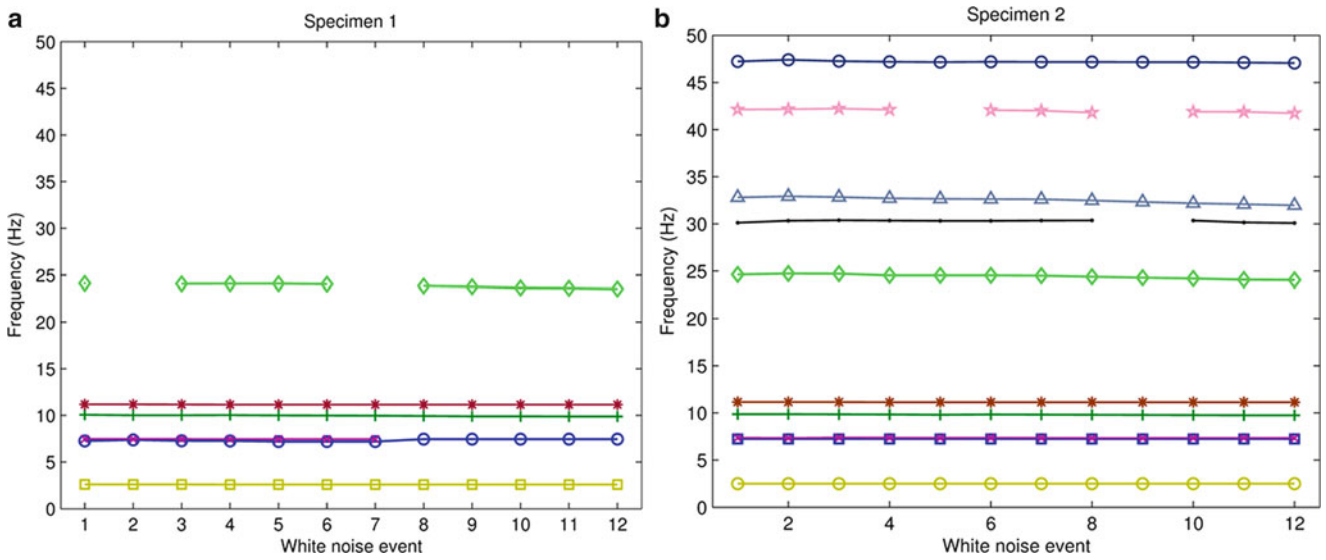

Fig. 1.2 Comparison on the identified dominant frequencies from two test specimen; (**a**) Specimen 1, (**b**) Specimen 2

Since the coefficients for recent time lags of AR model are most informative about different modes of vibration [14], therefore, the damage feature is defined as

$$[DF_i]_{2\times \mathrm{M}} = \begin{bmatrix} \phi^1_{ii,1} & \phi^2_{ii,1} & \cdots & \phi^k_{ii,1} & \cdots & \phi^M_{ii,1} \\ \phi^1_{ii,2} & \phi^2_{ii,2} & \cdots & \phi^k_{ii,2} & \cdots & \phi^M_{ii,2} \end{bmatrix} \tag{1.6}$$

The reason for selecting the previous two step of AR model coefficients is because that other coefficient in the parameter matrix contains mixed information about sensor locations so that they do not capture vibration changes at a single location, where '*m*' is the *m-th* dataset collected from sensor node '*i*' and a total of *M* data set is collected from a particular test case. Each column vector in $[DF_m]_{2\times \mathrm{M}}$ represents the two coefficients identified from a specific time window data using MV-AR model. Data from $[DF_m]_{2\times \mathrm{M}}$ matrix can be plotted into a Cartesian coordinate system with $\phi^k_{ii,1}$ and $\phi^k_{ii,2}$ as two perpendicular coordinates. The distribution of each coefficient pair represents the variation of the identified coefficients from a specific sensing node with dataset from '*k-th*' time window of the specific test. Combine all the distribution of each coefficient pair from a specific test data indicated the uncertainty of the subsystem system near the sensing node. This approach can be applied to all the recorded sensing nodes and extended to all the test cases.

Based on the calculated damage feature matrix, $[DF_i]_{2\times \mathrm{M}}$, a covariance matrix can be defined:

$$[C_i]_{2\times 2} = [DF_i]\ [DF_i]^T \tag{1.7}$$

Through eigen-value analysis on the covariance matrix $[C_i]_{2\times 2}$, two eigen-vectors and the corresponding eigen-values can be calculated. As a result, the error ellipse by considering two eigen-values as major and minor axes and two eigen-vectors as the orientation of the ellipse is developed to get a clearer result for observation. One can observe the migration of the ellipse error among all the test cases to see the change of feature. If the migration of ellipse calculated from each test case becomes diverse, it indicated the structural properties near the sensing node are changed from event to event. Through such an observation one can detect the damage location.

Based on the white noise test data the damage feature matrix of each sensing node for each test case can be constructed using MV-AR coefficients. From which the error ellipse at each sensing node for all test cases can be generated. Significant migration of error ellipse at any particular sensing node through all the test cases indicated the dynamic characteristics of local structure near that sensing node were changed. From the observation of the migration of error ellipse of all sensing nodes one can identify the damage location. Consider the test case of specimen 2 the migration of AR-coefficient ellipse error from each sensing node is calculated. The ellipse error index calculated from the top floor and the first floor was shown in Fig. 1.2. The three identified fundamental modes of specimen 2 is also shown in this figure. To detect the damage location of the specimen 2, the migration of elliptic error index in cooperated with the identified mode shapes of specimen 2 are used. The following observation were pointed out:

1. Location of sensing node with significant migration of elliptic error index shows good correlation with the large nodal modal response of the identified torsion mode (i.e. AX11 node and AY6 node). Besides, location of sensing node with

significant migration of elliptic error of AX11 node is also caused by first and second transverse modes while the elliptic error of AY6 node is cause by second transverse mode and the torsion mode. Besides, small migration error index was observed from AX12 node and AY5 node. These results indicated the floor rotation center is at the location of North-West column (Large migration of the elliptic error index can be observed at the two corner of the roof floor).

2. Large migration of elliptic error index can also be observed from AX7 node and AX8 node of the first floor. This effect is due to the translational and torsion modes of columns at the first floor (also shown in Fig. 1.3). Other nodes, such as AX9, AX10, AX 12, AY1, AY2, AY3, AY4 and AY5, the migration of error elliptic index is very small.

Based on these two analysis, it can be confirmed that the location of stiffness reduction is located in the first floor of north-west column.

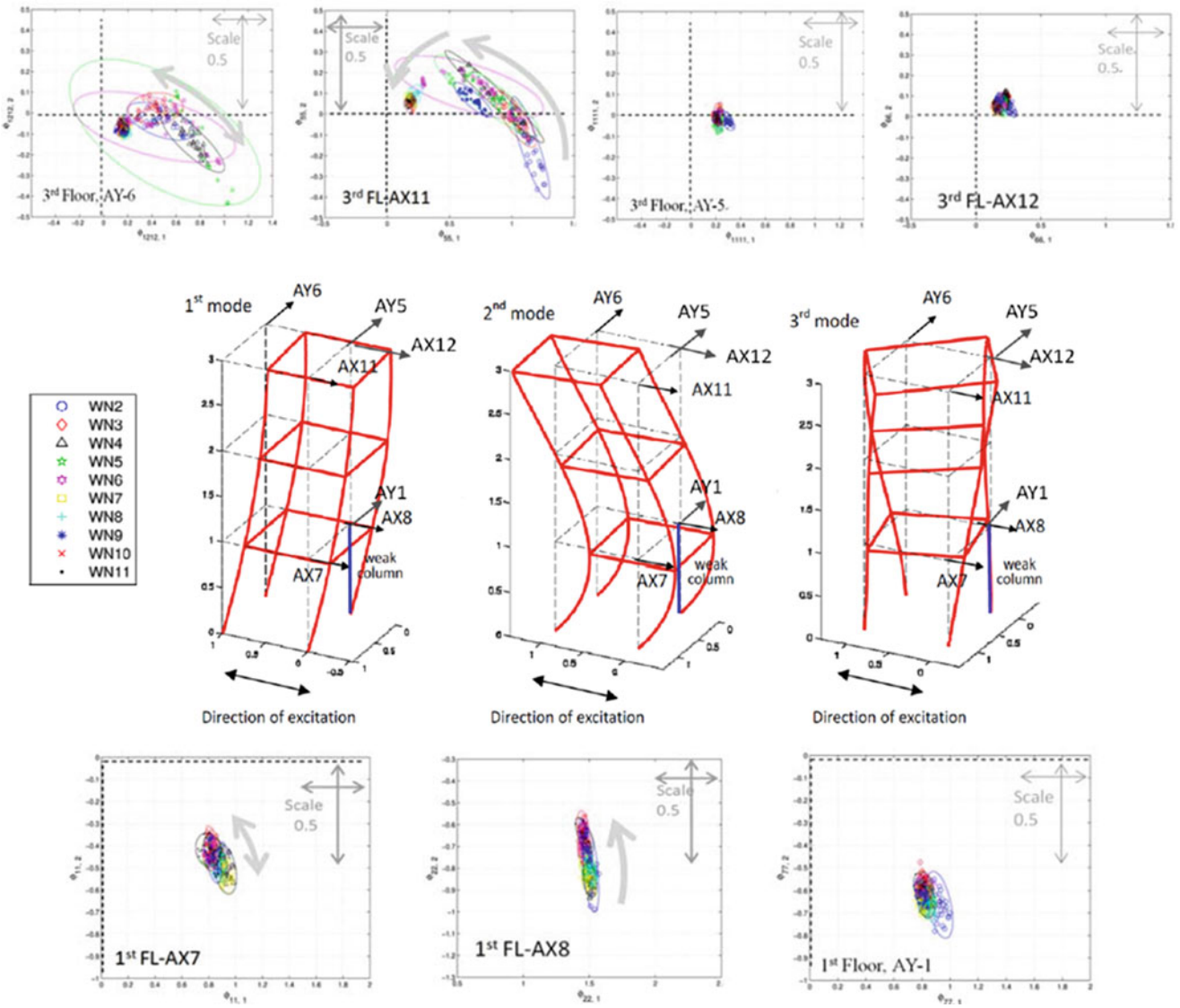

Fig. 1.3 Plot the migration of AR-coefficient elliptic error from sensing nodes on top floor and the first floor. Besides, the identified three fundamental modes of specimen 2 is also shown

1.3.2 Enhanced Time-Frequency Analysis for Damage Location Identification

Based on WPT, the absolute acceleration response data can be decomposed into several components that each component corresponds to a central frequency. Thus, one can generate a time-frequency matrix $W(t,f)$ by the decomposed components $f_j^i(t)$, and the value of each element in the matrix is calculated by the absolute value of the Hilbert transform of the value itself. Since the time-frequency representation $W(t,f)$ may be greatly affected due to the presence of noise and may cause poor resolution. An SVD-based technique is proposed [6] to enhance the spectrogram of the signal.

$$W(t,f) = [U][S][V]^T \tag{1.8}$$

To reduce the noise effect, Savitzky-Golay smooth filter is employed on the singular vectors (SVs) $[U]$ and $[V]$. The Savitzky-Golay filter is a low-pass filter which has the advantage of no shift effect in the time series after filtering [1]. With pre-assigned polynomial P and degree k, the SVs, the smoothed SVs, $[U']$ and $[V']$, can be obtained. Then the enhanced time-frequency representation is represented as;

$$W'(t,f) = [U'][S][V']^T \tag{1.9}$$

If a structure is in a damage state, the response of the damage state will be different from the healthy state. As a result, a damage index is proposed based on WPT and Hilbert transform of the recorded response is proposed. First, the WPT is applied to each of the recorded response data, i.e. $x_i^k(t)$, where i and k indicate the sensor location and the test event. First, the Hilbert amplitude of the reconstructed data set is calculated:

$$A_i^k(t) = \sqrt{\left[x_i^k(t)\right]^2 + \left[\tilde{x}_i^k(t)\right]^2} \tag{1.10}$$

where $\tilde{x}_i^k(t)$ represents the Hilbert transform of $x_i^k(t)$. Second, define the total energy time history of the Hilbert amplitude of *i-th* sensor and *k-th* event as

$$IDE_i^k = \int E_i^k(t)dt \quad \text{where} \quad E_i^k(t) = \frac{1}{2} \times A_i^k(t)^2 \tag{1.11}$$

Therefore, the cross energy matrix in *k-th* event is defined as:

$$[M]_k = \begin{bmatrix} \sqrt{IDE_1^k IDE_1^k} & \sqrt{IDE_1^k IDE_2^k} & \cdots & \sqrt{IDE_1^k IDE_N^k} \\ \sqrt{IDE_2^k IDE_1^k} & \sqrt{IDE_2^k IDE_2^k} & \cdots & \sqrt{IDE_2^k IDE_N^k} \\ \vdots & \vdots & \ddots & \vdots \\ \sqrt{IDE_N^k IDE_1^k} & \sqrt{IDE_N^k IDE_2^k} & \cdots & \sqrt{IDE_N^k IDE_N^k} \end{bmatrix} \tag{1.12}$$

By comparing the cross energy matrix of different state of a structure, the damaged location will have larger difference than the others. The damage matrix is defined as:

$$[D]_k = \frac{[M]_{ref} - [M]_k}{[M]_{ref}} \tag{1.13}$$

where *ref* represents the referenced event. The larger value in the damage matrix indicates larger difference at the sensor location.

Based on the enhanced WPT-based Hilbert amplitude spectrum the damage index matrix was calculated using data from specimen 1 and 2. It is observed that a relative larger index value was calculated between WN3 and WN2 in the first floor, while in the second and third floors much less index value are observed. This larger index value in the first story can be explained as the influence of earthquake loading. For specimen 1 larger index value will concentrate in the first floor and then propagate to the second floor due to the impact of larger earthquake excitation. The off-diagonal index value is relative small as compare to the diagonal element as shown in Fig. 1.4a. On the contrary, for specimen 2 the damage index propagated to the upper floor and to the off-diagonal terms of index matrix. This phenomenon becomes significant starting

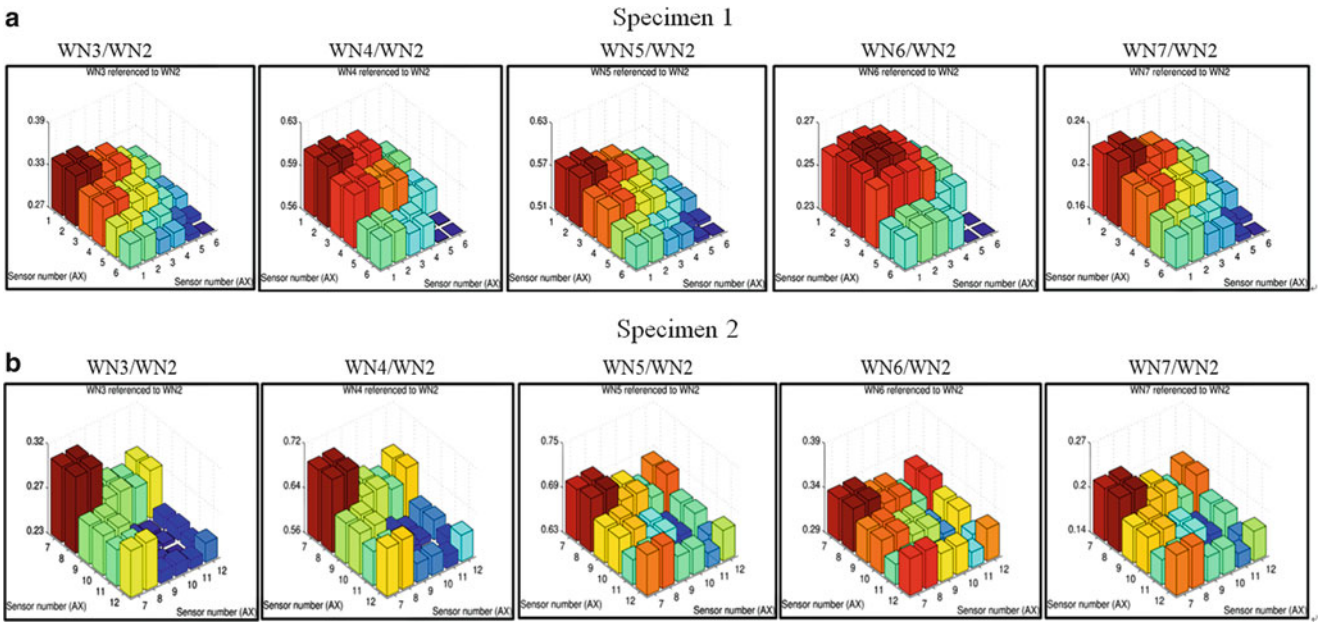

Fig. 1.4 Damage index matrix between test cases WN2 and WN3, WN2 and WN4, WN2 and WN5, WN2 and WN6, WN2 and WN7 of specimen 2

from the test case of WN6/WN2. It demonstrated that after the earthquake excitation of Run-03 (Earthquake excitation with PGA = 95 gal), the response of the first floor is different from the original response (reference case) for both test cases. The calculated damage matrix between WN6 test case (after EQ 4 earthquake excitation) and WN2 test case for specimen 2 is not just concentrated on the first floor, but also distributed to other floors including the off-diagonal term of damage matrix, as shown in Fig. 1.4b. This indicated that for specimen 2 the stronger base excitation which may induce the torsion-coupling effect that may cause the distribution of damage index more diverse.

From the damage detection point of view, the migration of AR coefficients elliptic error index and the wavelet-based energy damage index were proposed. The wavelet-based energy damage index can detect the abnormal condition of structural response with respect to the reference state. Through the comparison on wavelet-based energy damage index from different state, the abnormal condition can be identified. Through the observation of migration of AR coefficient elliptic error on a series of test, the damage location can be identified. Both damage detection methods need reference state (undamaged test case) as a base case for comparison.

1.4 Conclusions

In this research signal processing techniques and damage evaluation methods were proposed and applied to the ambient vibration response measurements (white noise excitation) of two steel structures after a series of seismic base excitation. Both modal-based and signal-based system identification and feature extraction techniques were studied to examine the damage severity of the two steel structures from output-only measurement. The system identification using both parametric MV-AR model and non-parametric SOBI method are used. Through MV-AR model the mode shapes and system natural frequencies can be identified. This method can provide a more clear stability diagram to estimate the dynamic characteristics of the structure. The SOBI method provided a fast computation on the estimation of modal contribution function (or source function) for structure with well-separated modes. The modal contributions for each test case were also identified using SOBI. The signal-based damage identification methods, which included the proposed wavelet-based energy index and the migration of AR coefficients elliptic error, can provide feature for detecting damage location. To quantify the damage local deformation measurement from dense optical tractor was used to quantify the damage of the test structure. From the data analyses the following conclusions are drawn:

1. In this study the MU-AR algorithm provided a straight forward method through selecting a suitable model order in advance to construct the stability diagram from which the system modal parameters can be identified. Besides, use SOBI it is assumed that the sources have different autocorrelation function and are mutually uncorrelated. For the analysis of

building structural system this assumption is acceptable. The identified sources are the modal response functions which can be used to estimate modal contribution.
2. Based on the identified modal frequencies and mode shapes from the white noise test data after each earthquake input excitation, the identified modal frequencies from each test case almost no change at all even for input PGA = 1300 gal. Different from the reinforced concrete structure, almost no severe stiffness degradation and stiffness deterioration were observed from the test of these two structures.
3. Combine the enhanced time-frequency analysis on response measurement (WPT-based signal analysis) and the wavelet-based damage index matrix; the damage severity can be identified. A further study of damage location identification using the migration of AR-coefficient elliptic error, damage location can be identified.
4. The optical tracker provided good ability for recording the local behavior of a structure. Analysis through PCA technique, physical local feature could be extracted. PCA could be used to reduce the noise effect as well as the rigid body motion; therefore, the precise time history of member displacement could be extracted which can be used to estimate the stress distribution of the element.

This approach can only be applied where the light target of optical tracker were installed.

Acknowledgements The authors wish to express their thanks to National Center for Research on Earthquake Engineering, NARL, for developing the two test specimens and conduct the shaking table tests. The support from Ministry of Science & Technology (Taiwan) under grant No. MOST 103-2625-M-002-006 is acknowledged.

References

1. Biydreaux-Bartels, G.F., Parks, T.W.: Time-varying filtering and signal estimation using Wigner distribution synthesis techniques. IEEE Trans. Acoust. Speech Signal Process. **ASSP-34**(3), 442–451 (1996)
2. Bjorck, A.: Numerical Methods for Least Squares Problems. Society for Industrial and Applied Mathematics, Philadelphia (1996)
3. Ceravolo, R.: Use of instantaneous estimators for the evaluation of structural damping. J. Sound Vib. **274**(1–2), 385–401 (2004)
4. Chatfield, C.: The Analysis of Time Series. Chapman & Hall, London (1989)
5. Doebling, S.W., Farrar, C.R., Prime, M.B., Shevitz, D.W.: Damage identification and health monitoring of structural and mechanical systems from changes in their vibration characteristics: a literature review. Research Report, LA-13070-MS, ESA-EA, Los Alamos National Laboratory, Los Alamos, NM (1996)
6. Hassanpour, H.: Improved SVD-based technique for enhancing time–frequency representation of signals. In: IEEE International Symposium on Circuits and Systems (ISCAS), pp. 1819–1822, New Orleans, LA (2007)
7. Kim, H., Melhelm, H.: Damage detection of structures by wavelet analysis. Eng. Struct. **26**, 347–362 (2004)
8. Loh, C.H., Mao, C.H., Huang, J.R., Pan, T.C.: System identification of degrading hysteresis of reinforced concrete frames. Earthq. Eng. Struct. Dyn. **40**, 623–640 (2011)
9. Mosavi, A.A., Dickey, D., Seracino, R., Rizkalla, S.: Identifying damage locations under ambient vibrations utilizing vector autoregressive models and Mahalanobis distances. Mech. Syst. Signal Process. **26**(1), 254–267 (2012)
10. Nair, K.K., et al.: Time series-based damage detection and localization algorithm with application to the ASCE benchmark structure. J. Sound Vib. **291**(2), 349–368 (2006)
11. Naira, K.K., Kiremidjian, A.S.: Damage diagnosis algorithms for wireless structural health monitoring. Stanford University, Technical report (2007)
12. Salawu, O.S.: Detection of structural damage through changes in frequency: a review. Eng. Struct. **19**, 718–723 (1997)
13. Sohn, H., et al.: Reference-free damage classification based on cluster analysis. Comput. Aided Civ. Infrastruct. Eng. **23**(5), 324–338 (2008)
14. Vu, V.H., Thomas, M., Lakis, A.A., Marcouiller, L.: Operational modal analysis of non-stationary mechanics systems by short-time autoregressive (STAR) modeling. In: Proceedings of the 3rd International Conference on Integrity, Reliability and Failure (2009)
15. Vu, V.H., Thomas, M., Lakis, A.A., Marcouiller, L.: Operational modal analysis by updating autoregressive model. Mech. Syst. Signal Process. **25**(3), 1028–1044 (2011)
16. Worden, K., Manson, G., Fieller, N.R.J.: Damage detection using outlier analysis. J. Sound Vib. **229**, 647–667 (2000)

Chapter 2
Damage Detection with Symplectic Geometry Spectrum Analysis in Changing Environment

Dong-Sheng Li and Xiao-Hai Li

Abstract Time-varying environmental and operational conditions such as temperature and external loading may often mask subtle structural changes caused by damage and have to be removed for successful structural damage identification. In the paper, a symplectic geometry spectrum analysis method is employed to decompose a time series into the sum of a small number of independent and interpretable components, in which one can determine which components are caused by external influences. The symplectic geometry spectrum analysis method is performed in four steps: embedding, symplectic QR decomposition, grouping and diagonal averaging. One excellent advantage of the method is that it can deal with nonlinear time series which is inherently rooted in structural damage due to crack opening and closing. Numerical simulation shows that the method is promising to detect structural damage in the presence of environmental and operational variations.

Keywords Structural health monitoring • Environment variable • Damage identification • Symplectic geometry spectrum analysis

2.1 Introduction

Nowadays, Damage identification method based on vibration characteristics in structural health monitoring has been widely researched and applied [1, 2]. The main idea is that the structure characteristics will change after structure damage, thus through the analysis of the real-time on-line monitoring data (acceleration, velocity, etc.) of a structure, one can infer if damage is present or not to the structure. While, in fact, varying environmental and operational conditions also have a great influence on structure characteristics [3] and may mask changes in the system's vibration signal caused by damage, so that one may make a wrong judgment to the structure damage. For instance, temperature affects the Young's modulus of many materials, thus the stiffness distribution of a structure is changed with temperature. Moreover, thermal expansion and contraction render joint connections and boundary conditions of a structure varied [4]. Therefore, how to separate environmental effect in the structural damage identification has drew more and more attention to researchers and practitioners. Damage identification algorithms can only be feasible and possible to be applied to the actual structure when the environmental factors are taken into account.

Many structure damage identification algorithms have been proposed considering the effects of environmental factors, According to the necessity to measure environmental variables or not, they can be divided into two categories. One category is to first measure the environmental parameters, and then to establish the relationship between environmental parameters and damage feature. While, in reality, measuring environmental variables have many shortcomings and limitations [4]. Totally different with the first category, the other one does not need to directly measure the environmental parameters. It separates the external influences from the measured signals with complex algorithms. Compared with the former category, this one detects structure damage based on the structure response signals, and therefore is becoming a promising approach. Liang et al. [5] put forward a damage identification method based on the combination of the structure continuous displacement curvature, and the linear combination of the structure displacement curvature of adjacent three-node under static force is used as the damage feature. The new damage feature is not sensitive to the changes of environment temperature and is verified in identifying and locating damage with a simulated example of a simply supported beam. Moreover, the concept of cointegration in econometrics is introduced into the structural damage identification to eliminate the influence of ambient temperature [6] and frequency cointegration is proposed as a simple online damage feature, which is based on the theory that changes of the structural frequency caused by environmental factors is different from real structural damage for linear systems. To eliminate

D.-S. Li (✉) • X.-H. Li
Dalian University of Technology, School of Civil Engineering, Linggong Road 2, Dalian 116023, China
e-mail: dsli@dlut.edu.cn

S. Pakzad, C. Juan (eds.), *Dynamics of Civil Structures, Volume 2*, Conference Proceedings of the Society for Experimental Mechanics Series, DOI 10.1007/978-3-319-29751-4_2

these environmental and operational influences, data normalization methods such as the factor analysis [7], statistical means [8], co-integration, outlier analysis and principal component analysis [9] and recent state-space reconstruction [10] may be employed. In fact, such non-stationary changes in the structural state requires a corresponding time-varying structural model based on the consistent load–effect relationship.

In this paper, a symplectic geometry spectrum analysis method is introduced as a time series analysis method. It can decompose the structural response signals into the sum of a small number of independent and interpretable components. Certain component may reflect the effects of changing environmental and operational changes and can thus be eliminated. This paper first introduce the theoretical basis and implementation process of the symplectic geometry spectrum analysis method, then a computer-simulated example is used to demonstrate the effectiveness of the method in structural damage identification considering temperature effect.

2.2 Theoretical Basis and Procedure of the SGSA

The SGSA is based on symplectic QR decomposition. Its implementation procedure is similar to the principal component analysis method and can be summarized as following four steps: embedding, symplectic QR decomposition, grouping and diagonal averaging [11].

2.2.1 Embedding

This step can also be named as phase space reconstruction, let the original time series signal as $x_1, x_2, \cdots, x_n$, and

$$X = \begin{bmatrix} x_1 & x_{1+\tau} & \cdots & x_{1+(d-1)\tau} \\ x_2 & x_{2+\tau} & \cdots & x_{2+(d-1)\tau} \\ \vdots & \vdots & \cdots & \vdots \\ x_m & x_{m+\tau} & \cdots & x_{m+(d-1)\tau} \end{bmatrix}$$

d is called embedding dimension, τ is delay time. In this step, choosing a proper embedding dimension d is the most important factor.

2.2.2 Orthogonal Symplectic QR Decomposition

This step is the core of SGSA. First, a Hamilton matrix M is constructed. Let $A = X^T X, M = \begin{bmatrix} A^T & 0 \\ 0 & -A \end{bmatrix}, \quad N = M^2$, then according to the definition above one knows that matrix M and N are all Hamilton matrix, construct an orthogonal symplectic matrix Q, making

$$Q^T N Q = \begin{bmatrix} H & R \\ 0 & H^T \end{bmatrix} \tag{2.1}$$

According to the introduction in Sect. 2.2, the upper triangular matrix H in Eq. (2.1) can be calculated through the transformation of N by the two kinds of orthogonal symplectic matrix. Decomposing matrix H by QR decomposition to get its eigenvalues $\lambda_1, \lambda_2, \cdots \lambda_d$. According to the properties of the Hamilton matrix, $\sigma_i = \sqrt{\lambda_i}\,(i = 1, \cdots d)$ is the eigenvalues of matrix A, $Q_i\,(i = 1, \cdots d)$ is the eigenvector of A corresponding to the eigenvalues σ_i. Let $S_i = Q_i^T X^T, \quad Y = Yi\ \ (i = 1, \cdots d)$, then the restructured matrix is, $Y = Yi$ and the original phase space reconstruction matrix can be represented as $X = X_1 + X_2 \cdots X_d$.

2.2.3 Components Grouping

After orthogonal symplectic QR decomposition, one obtains $X_1, X_2 \cdots X_d$, totally d components. Although these components are not totally independent with each other, some of them do have the same periods. Therefore, d components are grouped into p independent components as follows,

$$X = X_1 + X_2 \cdots X_{\mathrm{p}} \tag{2.2}$$

2.2.4 Diagonal Averaging

$X_i\ (i = 1, \cdots p)$ in Eq. (2.2) is transformed into a time series with the length n by this step, the procedure of this step is as follows: let $(X_i)_{m\times d}$ with the elements y_{ij}, $1 \le i \le m,\ 1 \le j \le d$, and $d^* = \min\ (m, d), m^* = \max\ (m, d), n = m+(d-1)\,\tau$, then the matrix $(X_i)_{m\times d}$ can be transferred to a series $y_1, y_2 \cdots y_n$ according to Eq. (2.3):

$$y_k = \begin{cases} \dfrac{1}{k}\displaystyle\sum_{p=1}^{k} y^*_{p,\,k-p+1} & \\ \dfrac{1}{d^*}\displaystyle\sum_{p=1}^{d^*} y^*_{p,\,k-p+1} & \begin{matrix} 1 \le k < d^* \\ d^* \le k \le m^* \\ m^* < k \le n \end{matrix} \\ \dfrac{1}{n-k+1}\displaystyle\sum_{p=k-m^*+1}^{n-m^*+1} y^*_{p,\,k-p+1} & \end{cases} \tag{2.3}$$

After the four steps, the original time series is decomposed into p independent superimposed components with different trend and frequency band. The trend in certain scale can be employed to eliminate the effects of changing environmental and operational changes

2.3 Application of the SGSA to a Simply Supported Beam

In this section, temperature variation in a yearly cycle will be introduced to a beam along with damage and the beam frequency change induced by the damage is totally masked by the temperature change. SGSA method is then used to decompose the frequency change into five components. The first component is employed to eliminate the variation of temperature change and damage is identified.

2.3.1 Brief Introduction of the Model

The length of the simply supported beam is 6 m (L = 6 m), rectangular section with the size of 0.2 m × 0.3 m. The density of the material is 2500 kg/m^3. The simply supported beam is divided into 40 elements with equal length, Consistent mass matrix are used. The relationship between temperature and the elastic modulus of the material is shown in Fig. 2.1.

2.3.2 Temperature Variation and the First Natural Frequency of the Beam

The temperature in Beijing from Jan 1, 2011 to Jan 31, 2012 is selected in our simulation. The sampling period T is set as 2 h and there are totally 4752 sampling points as shown in Fig. 2.2a. Per unit length on the horizontal axis is set to represent 2 h long for analysis convenience. At 6000 h after Jan 1, 2011 (the 3000th point on the horizontal axis), the stiffness of the eighth element is reduced to 60 % to simulate the structure damage. The vibration frequency of the beam is influenced

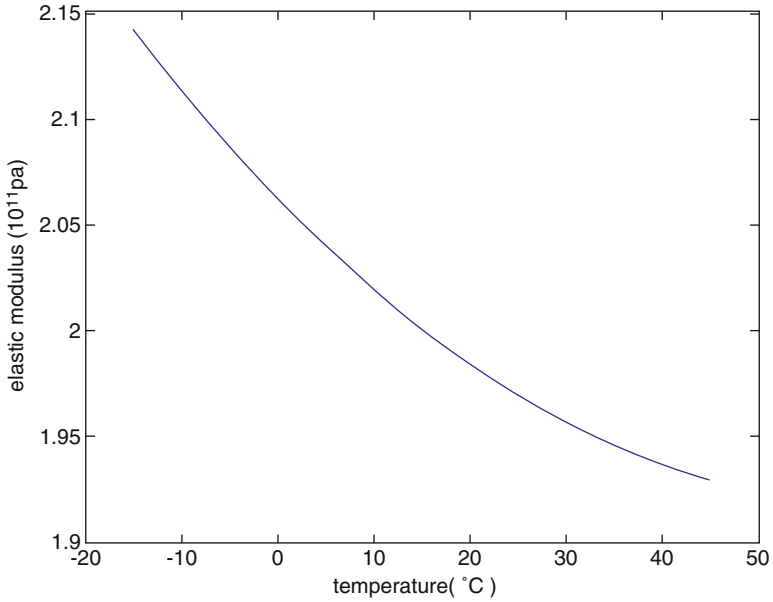

Fig. 2.1 Elastic modulus variation with temperature. (**a**) Temperature variation with time. (**b**) First natural frequency of the beam

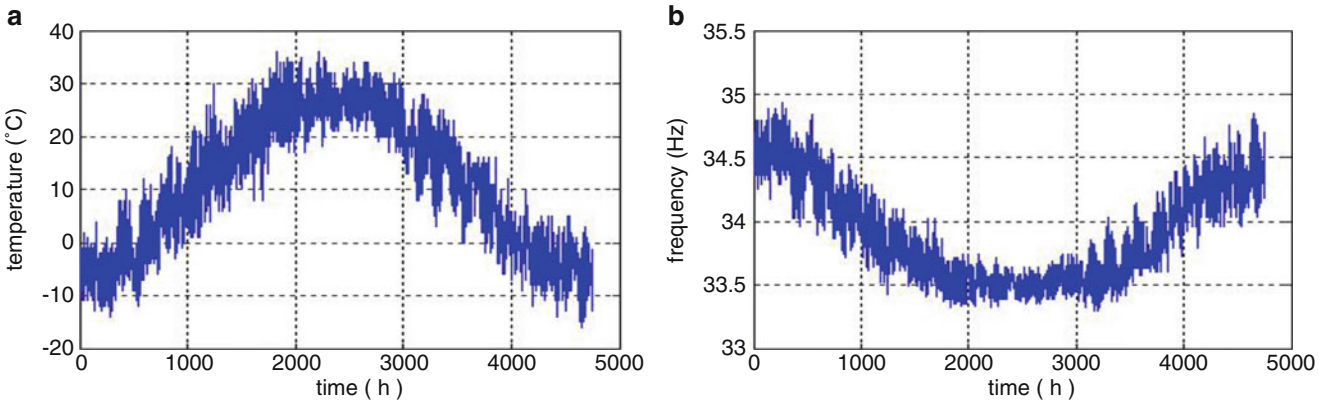

Fig. 2.2 Temperature variation and the first natural frequency of the beam

both by environmental temperature and damage. The frequency variation with time is shown in Fig. 2.2b. Compared with Fig. 2.2a, it is found that in Fig. 2.2b there is a strong correlation between the frequency and the temperature, and that the structural damage is completely submerged in the temperature's influence.

2.3.3 Damage Identification of the Simply Supported Beam

First, the temperature data is decomposed by SGSA with the embedding dimension set to five. The decomposed five components are shown in Fig. 2.3. Figure 2.3a shows the original temperature signal, whereas Fig. 2.3b–f shows the five components of the original temperature decomposed by the SGSA. As illustrated in Fig. 2.3, the first component shown in Fig. 2.3b represents temperature seasonal trend, whereas the second component shown in Fig. 2.3c is the daily temperature fluctuation which is an approximately simple harmonic signal as shown in the enlarged picture of Fig. 2.4. The daily temperature fluctuates within around 10°. The amplitude of the components shown in Fig. 2.3d–f are very small compared with the first two components and they can be neglected as noise.

Second, decomposing the first natural frequency of the beam by SGSA and the embedding dimension also set to five. The decomposed five components are shown in Fig. 2.5. Figure 2.5a shows the original frequency, whereas Fig. 2.5b–f

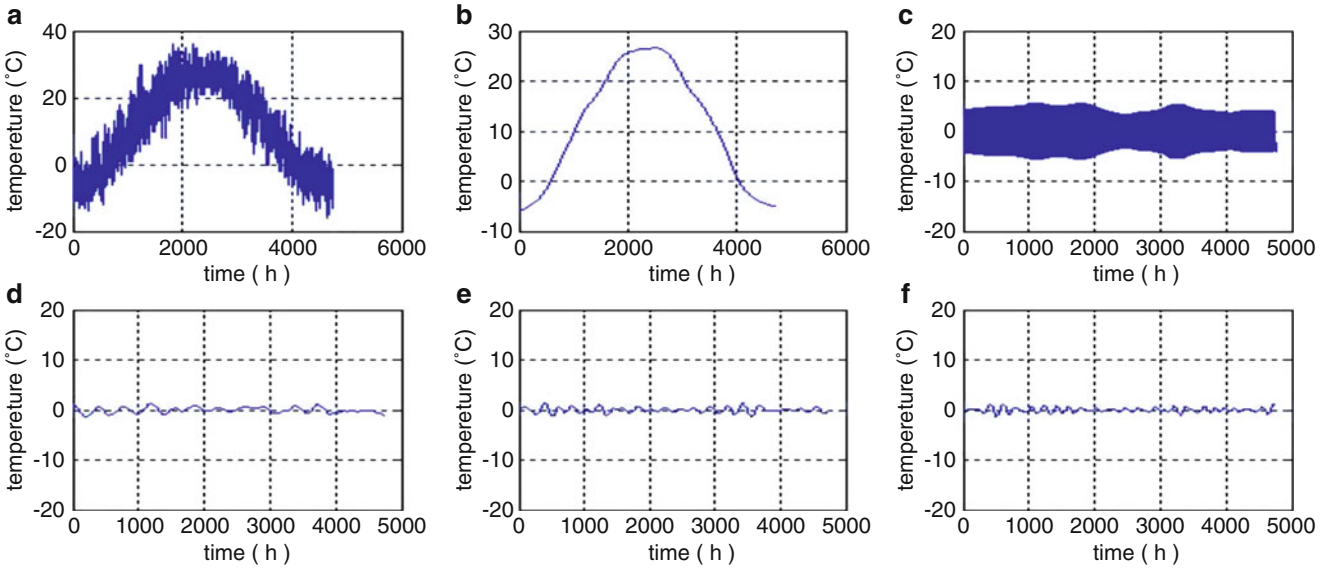

Fig. 2.3 Temperature decomposed by SGSA

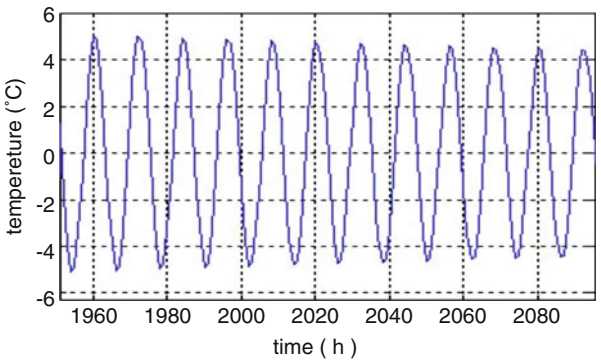

Fig. 2.4 Partially enlarged picture of the Fig. 2.3c

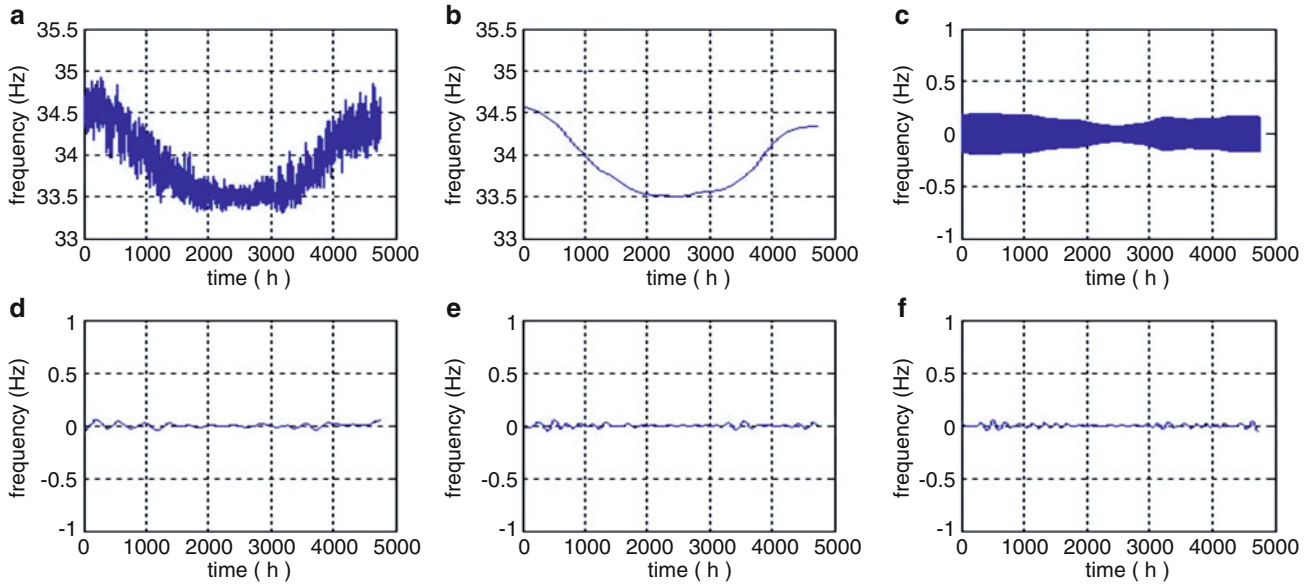

Fig. 2.5 First natural frequency of the beam decomposed by SGSA

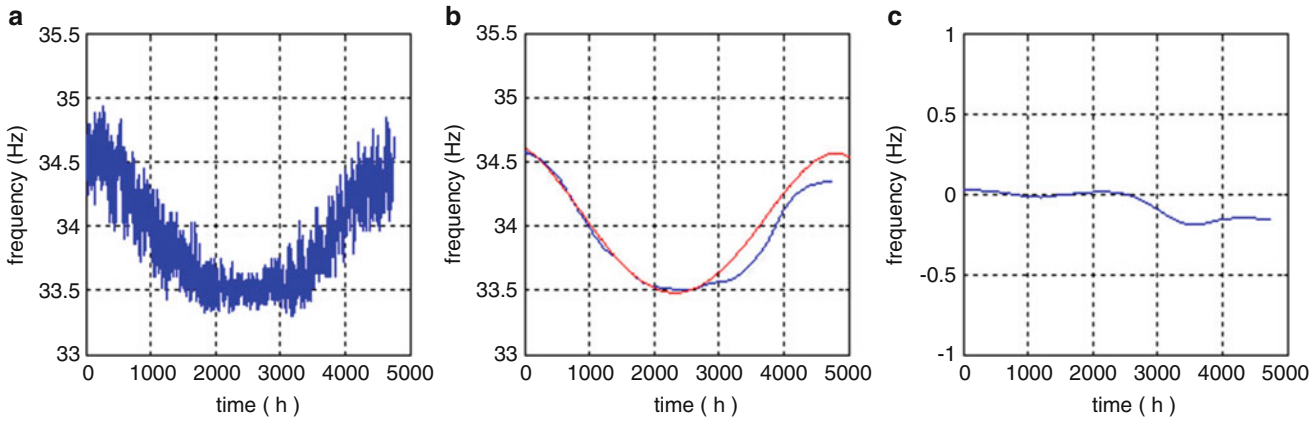

Fig. 2.6 Filter of frequency changes induced by temperature and damage identification

shows the five components of the first nature frequency decomposed by the SGSA. Similar to the analysis of the temperature decomposition, the first two components shown in Fig. 2.5b and c represent the main trend and fluctuation amplitude of the original frequency signal. Compared with the first two components of the temperature in Fig. 2.3, it can be concluded that the first frequency component shown in Fig. 2.5b reflects the frequency variation influenced by the seasonal trend of temperature and structural damage whereas the second component in Fig. 2.5c represents the frequency variation induced by the daily temperature fluctuation. The other frequency components shown in Fig. 2.5d–f can be neglected as noise due to their tiny amplitude.

To finally identify structural damage, the first component shown in Fig. 2.5b that includes both temperature and damage influences are further analyzed. If the frequency variation induced by the temperature trend can be filtered out from this component, the remaining part of the frequency changes can be inferred as induced from structural damage. To filter out the frequency change induced by seasonal temperature trend, a cross validation approach is adopted to fit the frequency variation induced only by temperature. The temperature data in Fig. 2.5b are divided into ten segments. The length of first nine segments is set to 500 and the last segment 250. Nine segments of data are then sequentially taken as fitting data and the remaining segment for validation data in turn. A quartic curve is then obtained as shown in red in Fig. 2.6b. The red curve in Fig. 2.6b represents the frequency change induced by temperature and the blue curve shows the frequency change induced both by temperature and damage, which is the same curve as that in Fig. 2.5b.

Figure 2.6b shows that the frequency change by temperature trend can be eliminated. Subtracting the blue cure from the red curve in Fig. 2.6b, the blue curve in Fig. 2.5c is obtained, which is the frequency of the beam induced only by the damage. It is easily observed that there is a relatively large change at about the 3000th point (6000 h after Jan 1, 2011). Therefore, it can be deduced that at the 3000th moment, damage occurs in the beam.

2.4 Conclusions

A symplectic geometric spectral analysis method is applied to structural damage identification considering the influences of environmental influences. The frequency change induced by seasonal temperature is filtered out through SGSA and damage is identified. It shows that the SGSA method can detect structural damage in the presence of environmental and operational variations successfully. The advantage of this method is that it does not need to directly measure the environment parameters and if feasible to practical damage identification.

Acknowledgement The authors appreciate the support by the National Natural Science Foundation of China (Grant No. 51121005, 51578107) and 973 Project (2015CB057704).

References

1. Sohn, H., Farrar, C.L., Hemez, F.M., Shunk, D.D., Stinemates, D.W., Nadler, B.R., Czarnecki, J.J.: A review of structural health monitoring literature: 1996–2001. Los Alamos National Laboratory Report, LA-13976-MS (2004)
2. Carden, E.P., Fanning, P.: Vibration based condition monitoring: a review. Struct. Health Monit. **34**(3), 355–377 (2004)
3. Sohn, H.: Effects of environmental and operational variability on structural health monitoring. Philos. Trans. R. Soc. A: Math. Phys. Eng. Sci. **365**(1851), 539–560 (2007)
4. Zhou, C., Li, H.N., Li, D.S., Lin, Y.X.: Online damage detection using pair cointegration of time-varying displacement time series. Smart Struct. Syst. **12**(3–4), 309–325 (2013)
5. Deraemaeker, A., Reynders, E., De Roeck, G., Kullaa, J.: Vibration based structural health monitoring using output-only measurements under changing environment. Mech. Syst. Signal Process. **22**(1), 34–56 (2008)
6. Liang, Y.B., Li, D.S., Li, H.N.: Damage detection method based on the combination of successive displacement curvature under the influence of environmental temperature. J. Shenyang Jianzhu Univ. **30**(3), 399–407 (2014)
7. Liang, Y.B., Li, D.S., Li, H.N.: Online damage detection based on cointegration of frequencies under influence of environmental temperature. J. Dalian Univ. Technol. **54**(3), 307–314 (2014)
8. Yan, A.-M., Kerschen, G., De Boe, P., Golinval, J.-C.: Structural damage diagnosis under varying environmental conditions—Part I: a linear analysis. Mech. Syst. Signal Process. **19**(2005), 847–864 (2005)
9. Cross, E., Manson, G., Worden, K., Pierce, S.: Features for damage detection with insensitivity to environmental and operational variations. Proc. R. Soc. A: Math. Phys. Eng. Sci. **468**(2148), 4098–4122 (2012)
10. Figueiredo, E., Todd, M., Farrar, C., Flynn, E.: Autoregressive modeling with state-space embedding vectors for damage detection under operational variability. Int. J. Eng. Sci. **48**(10), 822–834 (2010)
11. Xie, H.B., Guo, T.R., Sivakumar, B., Liew, A.W.L., Dokos, S.: Symplectic geometry spectrum analysis of nonlinear time series. Proc. R. Soc. A **470**, 20140409 (2014)

Chapter 3
Compressive Sensing Strategies for Multiple Damage Detection and Localization

S. Golnaz Shahidi, Nur Sila Gulgec, and Shamim N. Pakzad

Abstract Structural health monitoring (SHM) techniques have been studied over the past few decades to detect the deficiencies affecting the performance of the structures. Detecting and localizing these deficiencies require long-term data collection from dense sensor networks which creates a challenging task for data transmission and processing. To address this problem, a comparative study of two image-based compressive sensing approaches for multiple damage localization is presented in this paper. The first methodology consists of compressive sampling from the sensor network in global and local formats. Then through statistical change point analysis on the sampled datasets, and Bayesian probability estimation, the study estimates the location of damage. The second algorithm implements compressive sensing to the subset of samples obtained from the sensor network space divided into blocks. The damage existence and location are determined by statistical hypothesis testing of Discrete Cosine Transformation (DCT) coefficients avoiding the original signal recovery. In order to evaluate the performance of both algorithms, multiple damage scenarios are simulated in steel gusset plate model. The comparison results are presented in terms of compression ratios and successful detection rates.

Keywords Structural health monitoring • Big data • Damage detection and localization • Compressive sensing • Digital image correlation

3.1 Introduction

Multiple damage localization has been one of the most challenging problems in structural damage identification. While implementing dense sensor networks has shown to improve the damage localization accuracy [1], collecting and processing data from such networks can become a challenge in itself [2]. This paper aims to address this issue by proposing damage localization algorithms based on Compressive Sensing (CS).

CS [3, 4] was introduced to the research community for the promise of its potential to reduce the volume of data transmitted, stored and processed. The framework of CS achieves this goal by compressing the signal at the time of sampling by exploiting the sparsity [5]. As an emerging field, the SHM research community has also begun to apply CS techniques in recent years.

This framework has been applied to SHM datasets by using the sparsity of Fourier and wavelet orthogonal bases [6, 7], stiffness damage parameters [8] and the difference between a measured and predicted signal [9]. In such studies, the original signal was reconstructed with fewer measurements exploiting CS techniques. In addition to these studies, collecting the data in a compressed form by integrating CS and Analog-to-Information (AIC) architecture was offered [10]. A digital prototype of compressed sensor which can collect compressed coefficients was implemented to detect damage [11]. Furthermore, compressed sensors were installed on the Telegraph Road Bridge located in Michigan to reconstruct the signal by collected sub-Nyquist Fourier coefficients [12]. This study showed that CS is promising in terms of energy savings, battery levels and communication reliability. The theory of CS has many benefits for data recovery and reconstruction, however, it was also proposed for use without the need for signal recovery. A compressed classification technique called "smashed filter" was suggested by Davenport et al. [13] and used for damage detection purposes [11]. An iterative spatial compressive sensing for damage identification and localization was also proposed by using Ant Colony optimization [14].

Shahidi and Pakzad (2015) introduced a hierarchal sampling framework for damage localization based on change point analysis and Bayesian probability estimation [15]. Moreover, Gulgec et al. (2016) proposed block-wise sampling by exploiting the sparsity of DCT [16]. This paper compares the performance of these two previously proposed algorithms for

S.G. Shahidi • N.S. Gulgec (✉) • S.N. Pakzad
Department of Civil and Environmental Engineering, Lehigh University, 117 ATLSS Drive, Imbt Labs, Bethlehem, PA 18015, USA
e-mail: nsg214@lehigh.edu

S. Pakzad, C. Juan (eds.), *Dynamics of Civil Structures, Volume 2*, Conference Proceedings of the Society for Experimental Mechanics Series, DOI 10.1007/978-3-319-29751-4_3

multiple damage scenarios of a gusset plate connection. In the following sections of the paper, a brief explanation about two compressive damage diagnosis techniques is given. Then, the "healthy" and "multi-damaged" cases of the structural steel gusset plate model is described. Finally, the results are compared in terms of compression ratios and successful detection rates.

3.2 Multiple Damage Detection Using Hierarchical Compressive Sampling

This CS-based damage localization was previously introduced by the authors [15] for single damage localization. In this paper, this algorithm is extended to address multiple damage localization scenarios. The algorithm works based on compressive sampling from the entire area under consideration. Data from the globally sampled locations are used to extract damage sensitive features. Such features are then processed through statistical change detection tests to assess significance of any potential change. Several change point tests can be used for this purpose. Previous works of the authors show successful applications of such change detection tests for data-driven structural damage identification [17–20]. A Matlab-based toolsuite was also developed by the authors that facilitates implementation of these change point analyses [21], and can be downloaded from dit.atlss.lehigh.edu.

With the assumption of single damage, the maximum change statistics would define a local sampling window for a finer damage localization. For multiple damage detection, a partitioning step is added to transition from global sampling to local sampling. The partitioning algorithm is used following the change point analysis of the globally sampled data, in order to set different boundaries for local search. In this paper, the k-mean algorithm [22] is adopted which partitions the change points into k mutually exclusive clusters. After randomly selecting k initial points as the mean of the clusters, the algorithm proceeds by alternating between two steps until convergence. The first step consists of assigning each observation to the cluster mean shows the least distance measure inside that cluster (e.g. sum of Euclidean distance). In the second step, the clusters' means are updated based on the new centroid of clusters.

After global samples are partitioned, a search window is centered on the maximum change statistics within each cluster, and data are sampled inside these windows. This moving window is recentered when a change point shows higher statistics than that of the current center point's statistics. As local sampling proceeds, the posterior probability of damage location is estimated using a Gaussian likelihood model shown in Eq. (3.1) [23].

$$L\left(H_{x,y}\middle|\, D_k\right) = \frac{1}{\sqrt{(2\pi)^2\,|\Sigma|}}\,\exp\left(\frac{-\left(D_k-[x\;y]\right)\Sigma^{-1}\left(D_k-[x\;y]\right)^T}{2}\right) \tag{3.1}$$

Then the recursive Bayesian probability estimation shown in Eq. (3.2) is performed [23].

$$Po_k\left(H_{x,y}\right) = \frac{\Pr_k\left(H_{x,y}\right) L\left(H_{x,y}\middle|\, D_k\right)}{\sum_x \sum_y \Pr_k\left(H_{x,y}\right) L\left(H_{x,y}\middle|\, D_k\right)} \tag{3.2}$$

In this equation $\Pr_k$ and Po_k respectively indicate prior and posterior probability of damage for the kth iteration. When $k = 1$, a uniform prior is used; however, when $k > 1$, the posterior probability estimated in the previous step (i.e. $Po_{k-1}\left(H_{x,y}\right)$) is recursively used as the prior probability of the damage location.

3.3 Multiple Damage Detection Using Block-Wise Compressive Sampling

Block-wise CS was introduced in a previous work by the authors for single damage detection and localization [16]. In this paper, the same methodology is applied for the diagnosis of multiple damage localization scenarios. The block-wise damage detection algorithm is comprised of two main parts as compressed sensing using sparsity of DCT and statistical hypothesis testing. In this section, these parts will be discussed briefly. More detailed information about the algorithm and CS theory can also be found in the references [3–5, 16].

In the setting, a densely located sensor network (i.e. two-dimensional image) is divided into the square blocks of R × R probing points, each presented in terms of the discrete cosine basis. The 2-D DCT coefficients of $(i,j)th$ term of the block g are expressed in Eq. (3.3).

$$s(u,v) = \alpha(u)\beta(v)\sum_{i=0}^{R-1}\sum_{j=0}^{R-1} g(i,j)\ \cos\ \frac{\pi\,(2i+1)\,(u)}{2R}\ \cos\ \frac{\pi\,(2j+1)\,(v)}{2R} \tag{3.3}$$

where

$$\alpha(u),\beta(v) = \begin{cases} \sqrt{1/R}, & u,v = 0 \\ \sqrt{2/R}, & u,v = 1,\ldots,R-1 \end{cases} \tag{3.4}$$

Suppose the vectorized version of each sample block consisting of x terms in $\Re^N$ has k nonzero coefficients. Then, the signal $x = \Psi s$ can be reconstructed from $M < N$ inner products between x and the collection of vectors $\{\phi_j\}_{j=1}^{M}$ as shown in Eq. (3.5).

$$y_j = \langle x, \phi_j \rangle \quad \text{or} \quad y = \Phi x = \Phi\Psi s = \Theta s \tag{3.5}$$

where Φ is the submeasurement matrix which does not depend on the signal x and $\Theta = \Phi\Psi$ is an M×N matrix. The approach for reconstruction can be defined as searching the sparsest vector of s that minimizes the ℓ_2 norm between the original and reconstructed signal. The approach called Orthogonal Matching pursuit (OMP) [24] is used for the regularization of the samples obtained from each block. The OMP algorithm selects a column of the measurement matrix Φ in a greedy manner, and observes the contribution to the measurement vector y. In each iteration, the highest correlation between the picked column and the remaining part of y is computed. Then, the index set is updated with the index belonging to the highest correlation. These steps are repeated until the algorithm yields to find the best approximated set of columns.

After obtaining the approximated coefficients for each block, the damage is detected through the hypothesis testing on the statistics of DCT coefficients. The Laplacian distribution is used to model the distribution of DCT coefficients which is the dominant preference among previous research [25]. Based on the properties of Laplace distribution, the difference between the absolute values of "healthy" and "multi-damaged" DCT coefficients also follows the Laplace distribution. This property is exploited to observe the change of the statistics for the damaged regions. Based on the experiments, the computed values fluctuate more in damage areas which can be an indicator of damage. Therefore, the sum of the difference between the absolute values of DCT coefficients which can be defined by closed form distribution, is utilized to diagnose damage. The threshold is obtained from the 50 "healthy" cases and the possible damage locations are determined when the computed values exceed the threshold.

3.4 Numerical Validation

In order to assess the effectiveness of the proposed methodologies, a gusset plate connection is simulated in ABAQUS [26] by using shell elements. The structural connection in a truss bridge is designed based on load rating evaluation suggested by the Federal Highway Administration (FHWA) manual [27]. The connection consists of five rectangular sections connected to gusset plates in both sides as can be seen from Fig. 3.1. The element size of 0.5 in. is selected to obtain the strain field of the surface of the gusset plate. Figure 3.2 shows the finite element (FE) model of the "multi-damaged" connection having two 2-in. long cracks. The maximum in-plane strain field measured on the surface of steel plate is considered in the evaluation of the proposed CS damage localization algorithms. The next section presents the results of compressed damage detection on this gusset plate connection using the two proposed methods.

3.5 Results and Discussion

The results of hierarchical and block-wise compressed sensing for multiple damage detection are presented in this section. The maximum in-plane strain field is collected for "healthy" and "damaged" simulated models. The measurement error is introduced to the system by adding 5 % Gaussian noise to strain values. These analyses are repeated 50 times to determine success rate of both methodologies where successful detection is defined as successfully localizing both of the cracks.

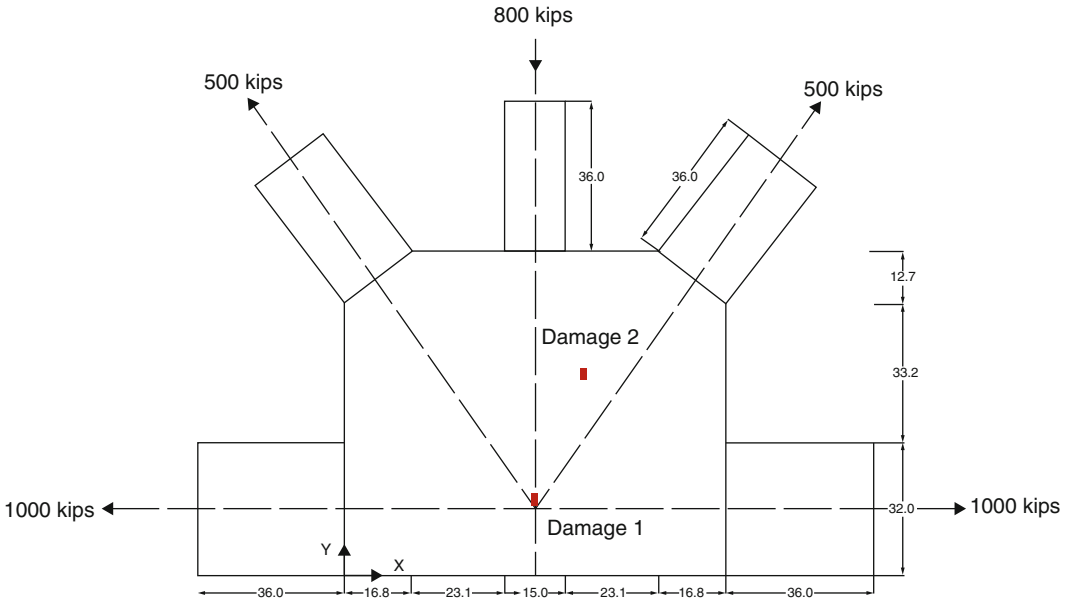

Fig. 3.1 Sketch of the designed gusset plate connection

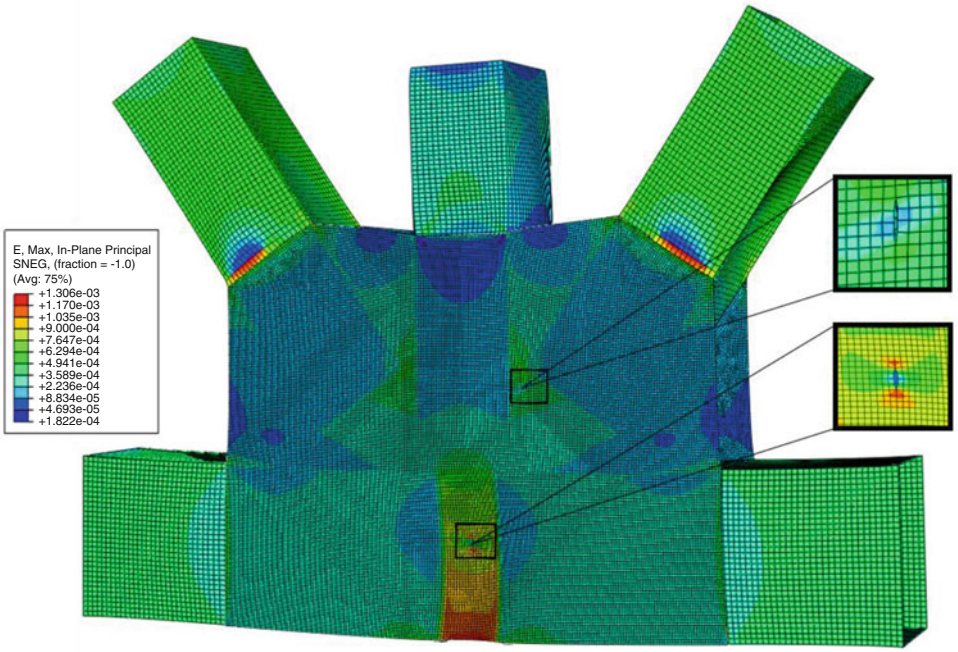

Fig. 3.2 Simulated gusset plate connection with multiple damages

A block size of 8×8 is selected for the block-wise sampling method as suggested in previous research [16] and compression ratios are controlled by choosing the number of samples regularized in each block. In the hierarchical sampling method, width and height of the local window are set to ¼ of those of the gusset plate, respectively. Figure 3.3 summarizes the results of multiple damage localization for block-wise and hierarchical sampling. The figure shows that the hierarchical sampling achieves approximately 80 % of success rate for different compression ratios which are in effect controlled by the global sampling ratios set at the beginning of the analysis (4, 8, 16, 32, and 64 %). This shows that sampling more data points in the global step would not significantly improve the success rate. On the other hand, block-wise sampling achieves higher

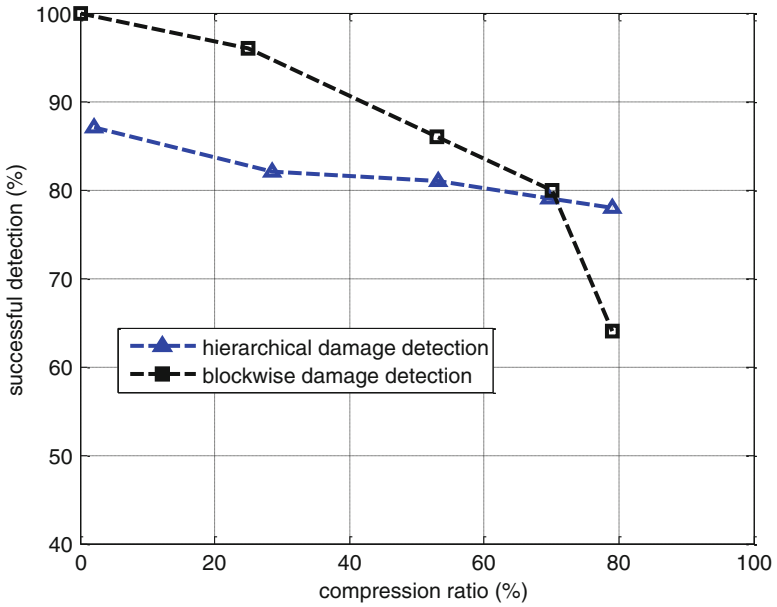

Fig. 3.3 Results of compressive sampling approaches for damage localization

successful localization rates when the compression ratio is low. This rate reduces with the increase in compression ratio and falls below the 80 % success rate after 70 % of compression. Furthermore, block-wise sampling determines the candidate damage areas (i.e. blocks exceeding the threshold value) that creates false positives around 4 %.

3.6 Conclusion

This paper presents two CS-based multi-damage localization algorithms. The first methodology consists of compressive sampling from the sensor network in global and local formats. Then through statistical change point analysis on the sampled datasets, and Bayesian probability estimation, location of damage is estimated. The second algorithm implements compressive sensing to the subset of samples obtained from the sensor network space divided into blocks. The damage existence and location are determined by statistical hypothesis testing of DCT coefficients avoiding the original signal recovery. Performance of these algorithms is verified through a numerical case study of a gusset plate. The findings show that the hierarchical sampling method is more stable in terms of success rate while detecting the multiple damages. However, in order to achieve higher a success rate (i.e. more than 95 %), block-wise sampling with a lower compression ratio might be more desirable. Moreover, it is important to consider several other factors for this comparative analysis. For instance, prior information required by the algorithms differs for the two approaches. The number of local sampling windows is a parameter that plays an important role in transmission from global to local sampling steps in hierarchical sampling. In the block-wise sampling process, no prior assumption is needed, since data from all the sensor blocks are sampled. Moreover, the hierarchical sampling method requires the repetitive measurements from the “baseline” and “unknown” state of the structure to estimate statistics for change point analysis. Nevertheless, the block-wise method requires repetitive measurements from only the “baseline” state to find the threshold value. Finally, block-wise sampling estimates the damage area instead of the exact damage coordinates (i.e. detecting a 2-in. crack in a 4 square-in. area) and produces some false positives. However, hierarchical sampling detects the damage location in terms of coordinates without any false positives.

Acknowledgement The authors would like to thank Jamie Hudson who created the FE model used in the simulation study. Research funding is partially provided by the National Science Foundation through Grant No. CMMI-1351537 by Hazard Mitigation and Structural Engineering program, and by a grant from the Commonwealth of Pennsylvania, Department of Community and Economic Development, through the Pennsylvania Infrastructure Technology Alliance (PITA).

References

1. Matarazzo, T.J., Shahidi, S.G., Pakzad, S.N.: Exploring the efficiency of BIGDATA analyses in SHM. In: Proceedings of the 10th International Workshop on Structural Health Monitoring, Stanford, CA, vol. 2, pp. 2981–2989 (2015)
2. Matarazzo, T.J., Shahidi, G., Chang, M., Pakzad, S.N.: Are today's SHM procedures suitable for tomorrow's data? In: Proceedings of the Society of Experimental Mechanics IMAC XXXIII, Orlando, FL (2015)
3. Candès, E.J., Romberg, J., Tao, T.: Robust uncertainty principles: exact signal reconstruction from highly incomplete frequency information. IEEE Trans. Inform. Theory **52**(2), 489–509 (2006)
4. Donoho, D.L.: Compressed sensing. IEEE Trans. Inform. Theory **52**(4), 1289–1306 (2006)
5. Candès, E.J., Wakin, M.B.: An introduction to compressive sampling. IEEE Signal Process. Mag. **25**(2), 21–30 (2008)
6. Bao, Y., Beck, J.L., Li, H.: Compressive sampling for accelerometer signals in structural health monitoring. Struct. Health Monit. **10**(3), 235–246 (2010)
7. Haile, M., Ghoshal, A.: Application of compressed sensing in full-field structural health monitoring. In: Proceedings of the SPIE 8346, Smart Sensor Phenomena, Technology, Networks and Systems Integration, San Diego, CA (2012)
8. Zhou, S., Bao, Y., Li, H.: Structural damage identification based on substructure sensitivity and l1 sparse regularization. In: SPIE Smart Structures and Materials + Nondestructive Evaluation and Health Monitoring, pp. 86923N–86923N. International Society for Optics and Photonics (2013)
9. Cortial, J., Farhat, C., Guibas, L.J., Rajashekhar, M.: Compressed sensing and time-parallel reduced-order modeling for structural health monitoring using a DDDAS. In: Computational Science–ICCS 2007, pp. 1171–1179. Springer, Heidelberg (2007)
10. Kirolos, S., Laska, J., Wakin, M., Duarte, M., Baron, D., Ragheb, T., Massoud, Y., Baraniuk, R.: Analog-to-information conversion via random demodulation. In: Design, Applications, Integration and Software, 2006 IEEE Dallas/CAS Workshop on, pp. 71–74. IEEE (2006)
11. Mascareñas, D., Cattaneo, A., Theiler, J., Farrar, C.: Compressed sensing techniques for detecting damage in structures. Struct. Health Monit. **12**(4), 325–338 (2013)
12. O'Connor, S.M., Lynch, J.P., Gilbert, A.C.: Compressed sensing embedded in an operational wireless sensor network to achieve energy efficiency in long-term monitoring applications. Smart Mater. Struct. **23**(8), 085014 (2014)
13. Davenport, M.A., Duarte, M.F., Wakin, M.B., Laska, J.N., Takhar, D., Kelly, K.F., Baraniuk, R.G.: The smashed filter for compressive classification and target recognition. In: Electronic Imaging 2007, pp. 64980H–64980H. International Society for Optics and Photonics (2007)
14. Yao, R., Pakzad, S.N., Venkitasubramaniam, P., Hudson, J.M.: Iterative spatial compressive sensing strategy for structural damage diagnosis as a BIG DATA problem. In: Proceedings of the Society of Experimental Mechanics IMAC XXXIII, vol. 2, pp. 185–190. Springer International Publishing (2015)
15. Shahidi, S.G., Pakzad, S.N.: A compressed sensing approach in structural damage identification. In: Proceedings of the 10th International Workshop on Structural Health Monitoring, Stanford, CA, vol. 2, pp. 2245–2252 (2015)
16. Gulgec, N.S., Shahidi, S.G., Pakzad S.N.: A comparative study of compressive sensing approaches for structural damage diagnosis. In: Proceedings of GeoStructures Congress, Phoenix, AZ (2016)
17. Nigro, M.B., Pakzad, S.N., Dorvash, S.: Localized structural damage detection: a change point analysis, (Blackwell Publishing). Comput. Aided Civ. Infrastruct. Eng. **29**(6), 416–432 (2014). doi:10.1111/mice.12059
18. Shahidi, S.G., Nigro, M.B., Pakzad, S.N., Pan, Y.: Structural damage detection and localization using multivariate regression models and two-sample control statistics. Struct. Infrastruct. Eng. **11**(10), 1277–1293 (2015)
19. Dorvash, S., Pakzad, S.N., Labuz, E.L.: Statistics based localized damage detection using vibration response. Smart Struct. Syst., Int. J. **14**(2), 85–104 (2014). doi:10.12989/sss.2014.14.2.085, 2014
20. Dorvash, S., Pakzad, S.N., Labuz, E.L., Ricles, J.M., Hodgson, I.C.: Localized damage detection algorithm and implementation on a large-scale steel beam-to-column moment connection. Earthq. Spectra **31**(3), 1543–1566 (2014). doi:10.1193/031613EQS069M
21. Shahidi, G., Yao, R., Pakzad, S.N., Chamberlain, M., Nigro, M.B.: Data-driven structural damage identification using DIT. In: Proceedings of the Society of Experimental Mechanics IMAC XXXIII, Orlando, FL (2015)
22. Lloyd, S.P.: Least squares quantization in PCM. IEEE Trans. Inform. Theory **28**(2), 129–137 (1982)
23. Thrun, S., Burgard, W., Fox, D.: Probabilistic Robotics. MIT Press, Cambridge (2005)
24. Tropp, J.A., Gilbert, A.C.: Signal recovery from random measurements via orthogonal matching pursuit. IEEE Trans. Inform. Theory **53**(12), 4655 (2007)
25. Lam, E.Y., Goodman, J.W.: A mathematical analysis of the DCT coefficient distributions for images. IEEE Trans. Image Process. **9**(10), 1661–1666 (2000)
26. ABAQUS. Version "6.13," Dassault systemes. Pawtucket, Rhode Island (2013)
27. Ibrahim, F.I.S.: Load Rating Evaluation of Gusset Plates in Truss Bridges, FHWA Design Guidance No. 1. (2008)

Chapter 4
Structural Damage Detection Through Vibrational Feature Analysis with Missing Data

Matthew Horner and Shamim N. Pakzad

Abstract To mitigate the expensive and time-consuming nature of visual structural inspections, vibration-based structural damage detection methods have been proposed that rely on different damage-sensitive features. These features are derived from data collected by sensor networks implemented on the structure. Damage detection through vibration-based feature analysis thus far has relied on simulation or the responses of fixed sensor networks for feature creation. Another type of monitoring scheme, called mobile sensing, has the ability to eliminate the limited spatial information constraint of fixed sensor networks. However, regardless of the monitoring approach of a real-world structure, data sets can incur cases of missing data, either due to such situations like sensor malfunction or loss of communication connectivity, or in the case of mobile sensing due to the nature of the approach itself. In this paper, a fixed sensor network is implemented on a scale laboratory frame structure, and observations are removed from the resulting complete datasets to simulate data missingness. Damage is simulated through interchangeable, variable stiffness elements that make up the frame. Damage detection is conducted by fitting a numerical model to the data and assessing the significance of the change in the model parameters when damage is introduced.

Keywords Structural damage detection • Missing data • ARX model • Big data • Mobile sensing

4.1 Introduction

Accurate damage detection in a structure is vital for assuring its safe operation. Furthermore, properly locating damage and identifying the time at which it occurs is essential for expediting maintenance and repair. Visual inspections of civil structures are expensive, time-consuming, and unreliable, as they rely on the individual expertise of inspectors and can therefore be subject to inconsistent characterization over time [1]. Furthermore, only visible damage is detectable with this type of monitoring strategy [2], so structural health monitoring in recent years has focused more on extraction of useful information from a sensor network implemented on a structure. These efforts have focused on identifying dynamic properties of structures, for example as in [3–5], or features that more closely relate to structural damage, for example in [6]. Particularly comprehensive reviews of structural identification and damage detection methodologies are presented in [7, 8]. If the data collected from such a network contains missing observations, one or both of these important characteristics of damage detection schemes could suffer. If damage-sensitive features are extracted from vibration data, their estimates may be biased if they are not based on an analysis capable of incorporating data with missing observations.

There are many potential sources of missing observations in datasets collected from sensors on civil structures. Sensors may malfunction for reasons including inadequate power, operating temperatures, or hardware issues. These types of issues may plague any sensor networks, but a relatively new class of monitoring scheme referred to here as "mobile sensing" inherently contains missing observations [9]. A vehicle fitted with accelerometers, for example, may traverse the entire length of a bridge, but can only collect one observation at one location at a given time, resulting in "missing data" at all other desired monitoring locations for that instance of time.

The efficiency of any sensor network is diminished with increasing sensor and setup costs, setup and collection times, network reliability, and power requirements [10]. For these reasons, the number of fixed sensors in a monitoring scheme

M. Horner (✉) • S.N. Pakzad
Lehigh University, 117 ATLSS Drive, Bethlehem, PA 18015, USA
e-mail: mph214@lehigh.edu

S. Pakzad, C. Juan (eds.), *Dynamics of Civil Structures, Volume 2*, Conference Proceedings of the Society for Experimental Mechanics Series, DOI 10.1007/978-3-319-29751-4_4

allowed by cost should be placed in optimal locations on a structure to avoid collection of more redundant data. However, to this end, optimal sensor locations may be inaccessible based on bridge geometries. Studies on finding optimal sensor placements exist, e.g. in [11, 12], but this tradeoff between spatial density and network size practicality is the primary flaw of fixed sensor networks.

Mobile sensor networks, then, inherently eliminate the limited spatial capacity of practical fixed sensor networks. An individual sensor continually traversing a structure, however, then results in the missing data case mentioned above. Alternatively, an individual mobile sensor may be used by periodically stopping and moving along a bridge, collecting vast temporal information at a variety of locations.

An important point must be made in regard to missing data analyses in association with mobile sensor networks. Extracting useful structural information from a mobile sensor network is possible without a missing data analysis. A review of other approaches to the mobile sensing problem, also referred to as "indirect" monitoring, is provided in [13]. For particularly recent examples of damage detection with mobile sensing schemes, but again not in the context of a missing data problem, the reader is referred to [14, 15]. However, the formulation of the problem here inherently makes the responses of a mobile sensor network the input to a missing data problem. Furthermore, we pose the missing data view as an analysis methodology not specific to mobile sensing, but also beneficial to fixed sensing schemes with unexpected missing observations, as many current damage detection methodologies do not formally accept missing data.

In this paper, acceleration response signals are collected from fixed sensors on a laboratory scale frame with interchangeable stiffness elements. A portion of the sensor data is then removed, which may correspond to either malfunctioning fixed sensors, or alternatively mobile acceleration sensors traversing other portions of the structure at the times of the missing observations. The presented methodology below shows how a missing data analysis may be used to reconstruct the maximum likelihood missing observations for the dataset, facilitating then extraction of damage-sensitive features from the completed datasets. Evaluation of the significance of the changes in these damage features when frame sections with reduced stiffness are substituted into the frame can then indicate the presence of this simulated "damage."

4.2 Missing Data Analysis

Dependent on actual or simulated mobile sensing paths on a structure, certain locations will be missing observations at times when other locations include them. If statistical models are fit to the structural responses at individual locations in the presence of missing observations, biased estimates may occur for the model parameters. Therefore, the purpose of a missing data analysis is to extract useful information about the underlying statistical model governing an incomplete dataset.

The appropriate formulation of a missing data analysis is governed by the goals of the monitoring scheme. For example, Matarazzo and Pakzad use the expectation maximization (EM) algorithm in conjunction with the Kalman filter for system identification of bridges [16]. In the context of damage detection, a missing data analysis can be tuned to estimate certain dataset characteristics based on the desired damage-sensitive features. As elaborated upon in Sect. 4.3, the damage-sensitive features used in this paper are a function of the coefficients of an autoregressive-exogenous (ARX) model fit to the responses at a pair of locations on a structure. These coefficients are estimated through the use of a separate formulation of the EM algorithm from that in [16], which is largely based on that provided in [17]. The nth-order ARX model with mth-order exogenous portion is described in Eq. (4.1), below.

$$y(k) = \mu_y + a_1 y(k-1) + \cdots + a_n y(k-n) + b_1 u(k-1) + \cdots + b_m u(k-m) + v(k) \tag{4.1}$$

In Eq. (4.1), y(k) is the output, u(k) the input, v(k) a white noise process independent of the input with variance λ_1, and μ_y, a_k, and b_k the parameters to be estimated. In the context of the presented damage detection algorithm, the 'output' in the model is the structural acceleration response signal at one location, while the 'input' is the response at another. In this way, locations are coupled together by the ARX model for analysis. A model must also be assumed for the 'input,' which in this case will be an assumed autoregression, as in Eq. (4.2).

$$u(k) = \mu_u + c_1 u(k\text{–}1) + \cdots + c_n u(k\text{–}n) + w(k) \tag{4.2}$$

Here, μ_u and c_k represent another set of parameters to identify, and w(k) another white noise process. For the remainder of this derivation, the order of the exogenous portion will be considered the same as that of the autoregression as this is used in the analysis to follow, and allows for simpler notation, though this is not required. The first step of the formulation is to define a new variable $z(k) = \left[\, y(k)\ u(k) \,\right]^T$, followed by the following vectors:

$$\varphi_1^T(k) = \left[z^T(k-1) \cdots z^T(k-n) \right] \qquad \theta_1 = \left[a_1\ b_1 \cdots a_n\ b_n \right]^T$$
$$\varphi_2^T(k) = \left[u(k-1) \cdots u(k-n) \right] \qquad \theta_2 = \left[c_1 \cdots c_n \right]^T$$

So, Eqs. (4.1) and (4.2) may be written as below.

$$\begin{aligned} y(k) &= \mu_y + \varphi_1^T(k)\theta_1 + v(k) \\ u(k) &= \mu_u + \varphi_2^T(k)\theta_2 + w(k) \end{aligned} \tag{4.3}$$

The complete data loglikelihood criterion is derived from the joint density of the N observations, given in Eq. (4.4).

$$f = \prod_{k=1}^{N} \left\{ \frac{1}{\sqrt{2\pi\lambda_1}} \exp\left[\frac{-\left(y(k) - \varphi_1^T(k)\theta_1 - \mu_y\right)^2}{2\lambda_1} \right] \right\} \left\{ \frac{1}{\sqrt{2\pi\lambda_2}} \exp\left[\frac{-\left(u(k) - \varphi_2^T(k)\theta_2 - \mu_u\right)^2}{2\lambda_2} \right] \right\} \tag{4.4}$$

The loglikelihood criterion is then derived by taking the natural logarithm of this density:

$$L(\theta, \Lambda) = C - \frac{N}{2}\log\ (\lambda_1) - \frac{N}{2}\log\ (\lambda_2) - \frac{1}{2\lambda_1}\sum_{k=1}^{N}\left(y(k) - \varphi_1^T(k)\theta_1 - \mu_y\right)^2 - \frac{1}{2\lambda_2}\sum_{k=1}^{N}\left(u(k) - \varphi_2^T(k)\theta_2 - \mu_u\right)^2 \tag{4.5}$$

Differentiating with respect to Λ yields the following criteria to maximize the likelihood with respect to the variances:

$$\lambda_1 = \frac{1}{N}\sum_{k=1}^{N} E\left[\left(y(k) - \varphi_1^T(k)\theta_1 - \mu_y\right)^2\right] \tag{4.6}$$

$$\lambda_2 = \frac{1}{N}\sum_{k=1}^{N} E\left[\left(u(k) - \varphi_2^T(k)\theta_2 - \mu_u\right)^2\right] \tag{4.7}$$

To define the other unknown parameters μ_y and μ_u and parameter vectors θ_1 and θ_2, it is simplest to back substitute Eqs. (4.6) and (4.7) into Eq. (4.5):

$$L(\theta, \Lambda) = C - \frac{N}{2}\log\left(\frac{1}{N}\sum_{k=1}^{N} E\left[\left(y(k) - \varphi_1^T(k)\theta_1 - \mu_y\right)^2\right]\right) - \frac{N}{2}\log\left(\frac{1}{N}\sum_{k=1}^{N} E\left[\left(u(k) - \varphi_2^T(k)\theta_2 - \mu_u\right)^2\right]\right) \tag{4.8}$$

Maximizing this likelihood is equivalent to minimizing the terms within the logarithms, so differentiating those terms with respect to the unknown parameters and parameter vectors yields:

$$\theta_1 = \left(\sum_{k=1}^{N} E\left[\varphi_1(k)\varphi_1^T(k)\right]\right)^{-1} \sum_{k=1}^{N} E\left[\varphi_1(k)y(k)\right] \tag{4.9}$$

$$\theta_2 = \left(\sum_{k=1}^{N} E\left[\varphi_2(k)\varphi_2^T(k)\right]\right)^{-1} \sum_{k=1}^{N} E\left[\varphi_2(k)u(k)\right] \tag{4.10}$$

$$\mu_y = \frac{1}{N}\sum_{k=1}^{N}\left(y(k) - \varphi_1^T(k)\theta_1\right) \tag{4.11}$$

$$\mu_u = \frac{1}{N}\sum_{k=1}^{N}\left(u(k) - \varphi_2^T(k)\theta_2\right) \tag{4.12}$$

In Eqs. (4.6) through (4.12), the expectations are now included as the data may be incomplete. Given a current iteration's guess at the two parameter vectors, the kth missing observation is estimated for the output y(k) and input u(k), respectively, with Eq. (4.10) below:

$$\begin{aligned} y(k) &= \varphi_1^T(k)\theta_1 \\ u(k) &= \varphi_2^T(k)\theta_2 \end{aligned} \tag{4.13}$$

The above equations define the EM algorithm for the ARX model. The process involves defining initial unknown parameter guesses, completing the datasets based on those guesses, computing the maximum likelihood parameter values based on those completed datasets, and iterating until convergence. The differentiations in Eqs. (4.6), (4.7), and (4.9) through (4.12) mean the algorithm may converge to a local maximum rather than global, a characteristic of the EM algorithm in general. Therefore, the closer the initial guesses to the actual parameter values, the more likely the convergence to the global maximum parameters. As of this analysis, several randomly-generated initial guesses were used in multiple runs of the algorithm with the intention of selecting the converged parameter estimates that appear most often.

4.3 Damage-Sensitive Features

The success of a damage detection methodology depends on the sensitivity of the selected dataset features to changes in structural behavior due to damage. These features must be able to distinguish changes due to damage from environmental changes typical in real-world applications. A missing data analysis for structural identification, like that presented in [16] could in theory use the identified frequencies, mode shapes, or damping ratios as damage-sensitive features. However, there is conflicting evidence in the literature on the effectiveness of these features for damage detection. Fundamental frequency shifts have been used for damage identification in [18], but these shifts are not able to localize damage, and may not be as sensitive as other features, such as damping. Damping, however, is well-known as harder to accurately predict than other structural characteristics, and often is associated with larger error [19]. Finally, mode shapes have some benefit in local damage sensitivity, but are as of yet not experimentally validated for this use [13].

Damage-sensitive features associated with regression model parameters have not yet been used in mobile sensing applications, but their computational and damage identification benefits over modal property shifts are discussed in [20]. Autoregressive (AR), ARX, and autoregressive-moving-average (ARMA) models are mentioned. A sensitivity analysis associated with these regression model parameters is provided in [21]. AR models are not considered in this paper, but for a similar derivation of the EM algorithm for their estimation, the reader is referred to [22]. Along with collinear regression (CR), and single-variate regression (SVR) models, AR and ARX models are used for damage detection with complete fixed sensor network data taken from the same laboratory frame as in this paper in [23].

One such feature will be considered in this paper, deemed the *Angle Coefficient* Γ in [23], which measures the angle between regressed lines from two different system states. It is computed as in Eq. (4.14), where v and v′ are vectors for undamaged and unknown system states, respectively, and are of the form $\begin{bmatrix} -1 & a_1 & \cdots & a_n & b_1 & \cdots & b_n \end{bmatrix}^T$ for the ARX model presented in Sect. 4.2.

$$\Gamma = \cos^{-1}\left|\frac{v \times v'}{\|v\|\,\|v'\|}\right| \tag{4.14}$$

Once damage-sensitive features are extracted, it is important to distinguish whether or not a change indicated by these features is due to random variations of the measurements over time, or if a damaging event has occurred to alter the measurements. In [23], several healthy and damaged test runs are conducted from which damage-sensitive features are extracted, then change point analysis is conducted with a normalized likelihood ratio test (NLRT) [24] or two-sample *t*-test [25] to detect the test number where damage was first simulated. In this paper, angle coefficient means are determined for a series of undamaged structural scenarios, and for a set of damaged structural scenarios. The shifts in these means are explored for different locations on the structure, elaborated upon in Sect. 4.5.

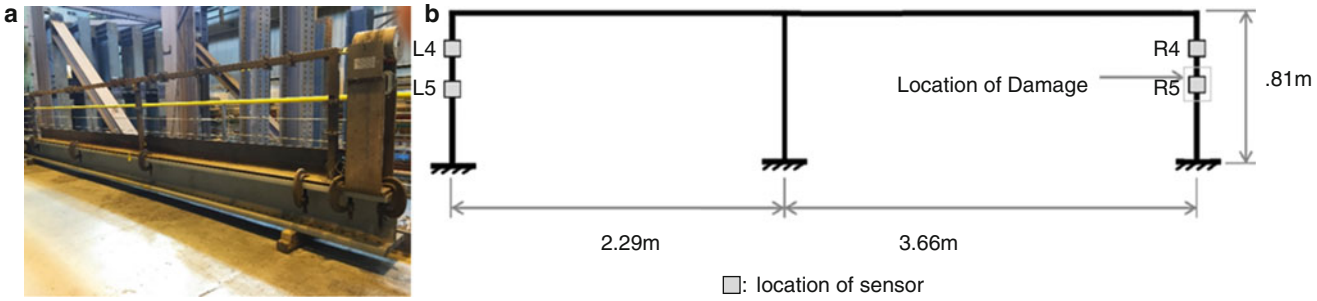

Fig. 4.1 (**a**) Steel tubular testing frame. (**b**) Sensor designations and locations, with pertinent dimensions and damage location (acceleration data is collected in the horizontal direction)

4.4 Experimental Setup

The laboratory scale frame of interest is two-bay and comprised of interchangeable steel tube sections. The section introduced into the frame to simulate damage corresponds to a 20 % reduction in the individual member's stiffness in reference to a baseline healthy tube member. This translates to less than a 1 % change in lateral stiffness of the frame, thereby creating a negligible change in global behavior. Figure 4.1a shows the setup itself, followed by an elevation view of the frame with the locations of the sensors of interest in this study in Fig. 4.1b.

The same sensor designations are used here as in [23] so as not to cause confusion when cross-referencing these works. The 39 datasets used here were also previously used in [26] in their complete sense with regression features and change point analysis for damage detection. For each run, the sensors sampled for 2 s at 500 Hz.

It is assumed that the structure behaves linearly during specific sets of data collection. The excitation must therefore be limited in amplitude to assure this assumption. An impact loading was selected for the tests, due to its similarities to ambient vibration in not imposing any specific excitation frequencies to the frame. This similarity to ambient vibration is desirable in a laboratory setup, as this is perhaps the most common scenario under which monitoring would occur on real-world structures.

To evaluate the proposed missing data approach, the middle one third of each dataset is assumed to be lost. We reiterate that this type of situation may arise in real-world applications with faulty sensors, or depending on prescribed mobile sensing paths across a structure. The EM algorithm presented in Sect. 4.2 is used to estimate ML regression parameters of these incomplete, as well as the original complete, datasets. In this way, the effectiveness of the proposed algorithm for extraction of damage-sensitive features may be explored, as well as its effectiveness in obtaining the same regression parameter estimates had there been no missing data.

The presented sensor pairings are selected to explore the behavior of the angle coefficients at locations both near and far from where the damage is introduced, with the idea that a larger change in damage-sensitive features for a particular location than another signifies that that location is nearer to the damage.

4.5 Results and Discussion

Figure 4.2 displays the computed angle coefficients for each test, derived from datasets with one third of the observations missing. Test 1 was used as a reference healthy structural baseline condition for computation of the angle coefficients for all other tests (i.e., v in Eq. (4.14), for computation of all other test angle coefficients, is a vector of the regression parameters derived for test 1). Damage was introduced just before the 21st test via an interchangeable stiffness element at the location specified in Fig. 4.1b. In theory, since no structural change was implemented from test 1 to test 20, the regression parameters should not change from the baseline state, and the angle coefficient for each of these tests would be zero; however, due to the inherent noisy nature of real-world data, some measurement fluctuation occurs, and the angle coefficient is non-zero. However, the introduction of damage and subsequent angle coefficient evaluations shows that the angle coefficients associated with random measurement fluctuation are significantly less than those coming about from the addition of damage, thus providing a means by which to distinguish the two, and thus indicate damage. The sensor grouping schemes are provided in the Fig. 4.2 legend, with the first sensor listed corresponding to that considered the 'output' in the ARX model of Eq. (4.1).

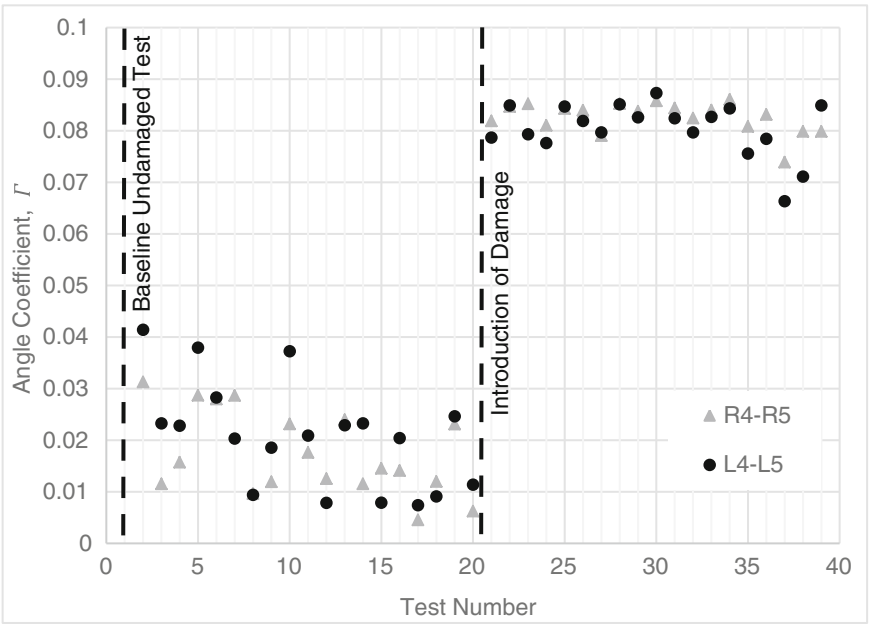

Fig. 4.2 Angle coefficient features for each test and sensing group, with test 1 undamaged baseline, and damage introduced before test 21

Table 4.1 Angle coefficient means for damaged and undamaged cases at each sensor grouping location

	Mean undamaged angle coefficient, $\overline{\Gamma_U}$	Mean damaged angle coefficient, $\overline{\Gamma_D}$	Absolute difference, $\lvert\overline{\Gamma_D} - \overline{\Gamma_U}\rvert$
R4–R5	0.017306	0.082608	0.065302
L4–L5	0.020784	0.080389	0.059605

To evaluate the effectiveness of the proposed approach for damage localization, Table 4.1 is referenced, below. Looking at the means of the angle coefficients at each location for the damaged cases, the mean of the damaged R4–R5 (near damage) coefficients is higher than that of the L4–L5 (away from damage) coefficients, implying a larger difference from the baseline case nearer to the actual damage location. Furthermore, the undamaged mean table column indicates that on average, the effect of measurement fluctuation was lower in the case of the R4–R5 sensor group than for the L4–L5 group. Thus, if the influence of random measurement fluctuation could be removed from the calculation of the damaged case angle coefficients, this implies there would be even more of a discrepancy between the means at different distances from the actual damage location. An attempt at this visualization is made through the final table column, representing the difference in angle coefficient means for damaged and undamaged cases. In this way, the greater angle coefficient mean at locations closer to that of actual structural damage implies that finding the locations on a structure of the greatest damage features effectively gives some idea of the relative location of damage on the structure.

Finally, Fig. 4.3 explores the closeness of regression parameters estimated from complete datasets to those estimated from those same datasets with the introduction of missing observations as above. In this case, angle coefficients are utilized not as "damage-sensitive" features, but as a measure of the difference between two regression parameter vectors. For each angle coefficient calculation, the complete data regression coefficient estimate vector is used as the baseline v, with the incomplete data parameter estimates the v′, as per Eq. (4.14). The important notion here is that while the non-zero angle coefficient values indicate some error in determining the same parameter estimates as from a complete dataset, the coefficients are on average a full order of magnitude lower than those resulting from even measurement fluctuation, as in Fig. 4.2. This implies that, at least for the missing data pattern of interest in this paper, the missingness has a negligible influence on the effectiveness of the damage detection algorithm when handled with the proposed approach.

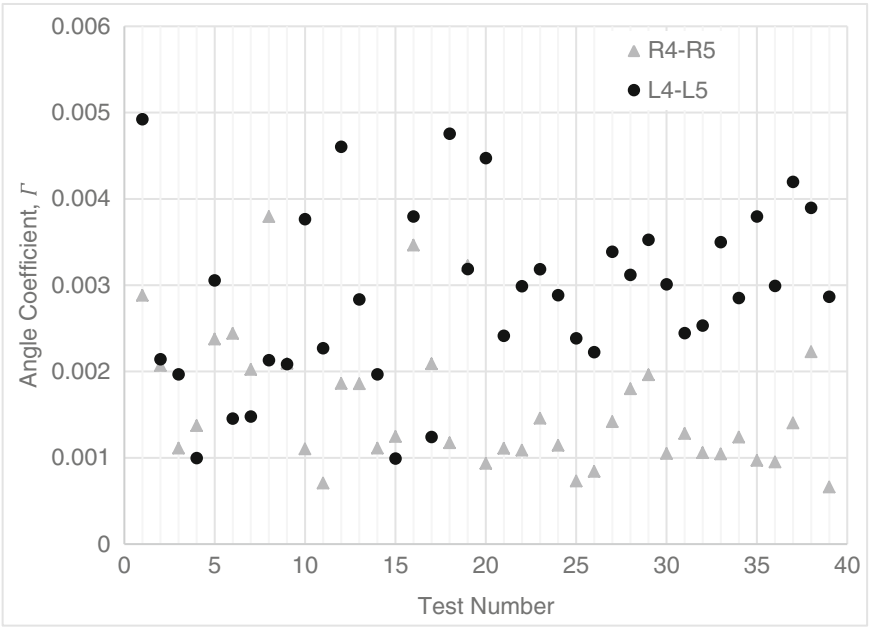

Fig. 4.3 Angle coefficients between complete data regression vector baselines and corresponding test datasets with missing observations

4.6 Conclusions

In this paper, the formulation of the EM algorithm for identification of ARX model parameters was derived based on the likelihood function of two sets of time series data. The purpose of this formulation is to make accurate parameter estimates when the time series datasets have missing observations. ARX parameters are of particular interest for their use in conjunction with certain structural damage-sensitive features, one of which, the angle coefficient, is explored in this paper. The significance of a change in these damage-sensitive features can indicate that a change has occurred in the structural system.

Preliminary results presented in this paper indicate that the effect of the considered missing data pattern has a negligible influence on the accuracy of regression parameter estimates when compared to the effect of measurement fluctuation or structural damage. Furthermore, the results here seem to indicate that a change in the presented damage-sensitive features due to damage is in fact significantly larger than that typical of random measurement fluctuation between different tests. Finally, the change in damage-sensitive features appears larger the closer a sensor group is to the location of induced local structural damage, indicating the propensity of the presented damage features for damage localization.

There are many extensions to this work that will be explored in future publications. Different patterns of missing data will be explored for analysis of the influence on these patterns to the accuracy of the regression parameter estimates. These analyses will be conducted with the eventual goal of moving toward more likely paths that would be traversed by real-world mobile sensors as they cross structures. The influence of more sensing locations should be explored, as well as the influence of other forms of excitation that more accurately simulate ambient structural vibration. Finally, the influence of environmental factors should be considered on the accuracy of the missing data analysis.

Acknowledgement Research funding is partially provided by the National Science Foundation through Grant No. CMMI-1351537 by Hazard Mitigation and Structural Engineering program, and by a grant from the Commonwealth of Pennsylvania, Department of Community and Economic Development, through the Pennsylvania Infrastructure Technology Alliance (PITA).

References

1. Giraldo, D.F., Dyke, S.J., Caicedo, J.M.: Damage detection accommodating varying environmental conditions. Struct. Health Monit. **5**(2), 155–172 (2006)
2. Zhu, D., Yi, X., Wang, Y., Lee, K.-M., Guo, J.: A mobile sensing system for structural health monitoring: design and validation. Smart Mater. Struct. **19**(5), 055011 (2010)

3. Pakzad, S.N., Rocha, G.V., Yu, B.: Distributed modal identification using restricted auto regressive models. Int. J. Syst. Sci. **42**(9), 1473–1489 (2011)
4. Dorvash, S., Pakzad, S.N.: Stochastic iterative modal identification algorithm and application in wireless sensor networks. Struct. Control Health Monit. **20**(8), 1121–1137 (2013)
5. Yang, Y.-B., Lin, C.W., Yau, J.D.: Extracting bridge frequencies from the dynamic response of a passing vehicle. J. Sound Vib. **272**(3–5), 471–493 (2004)
6. Lynch, J.P., Sundararajan, A., Law, K.H., Kiremidjian, A.S., Carryer, E.: Embedding damage detection algorithms in a wireless sensing unit for operational power efficiency. Smart Mater. Struct. **13**(4), 800–810 (2004)
7. Doebling, S.W., Farrar, C.R., Prime, M.B., Shevitz, D.W.: Damage identification and health monitoring of structural and mechanical systems from changes in their vibration characteristics: a literature review. Los Alamos National Laboratory Report LA-13070-MS (1996)
8. Sohn, H., Farrar, C.R., Hemez, F.M., Shunk, D.D., Stinemates, D.W., Nadler, B.R., Czarnecki, J.J.: A review of structural health monitoring literature: 1996–2001. Los Alamos National Laboratory Report LA-13976-MS (2004)
9. Matarazzo, T.J., Pakzad, S.N.: Mobile sensors in bridge health monitoring. In: Proceedings of the 9th International Workshop on Structural Health Monitoring, Stanford, CA, vol. 2, pp. 1881–1888 (2013)
10. Horner, M., Koser, K., Korneva, K., Matarazzo, T.J., Pakzad, S.N.: A wireless mobile sensor platform for structural health monitoring. Presented at Joint 6th International Conference on Advances in Experimental Structural Engineering and 11th International Workshop on Advanced Smart Materials and Smart Structures Technology, University of Illinois, Urbana-Champaign, 2015
11. Chang, M., Pakzad, S.N.: Optimal sensor placement for modal identification of bridge systems considering number of sensing nodes. J. Bridge Eng. **19**(6), 04014019 (2014)
12. Chang, M., Pakzad, S.N.: Optimal sensor configuration for flexible structures with multi-dimensional mode shapes. Smart Mater. Struct. **24**(5), 055012 (2015)
13. Malekjafarian, A., McGetrick, P.J., OBrien, E.J.: A review of indirect bridge monitoring using passing vehicles. Shock Vib. **2015**, 1–16 (2015)
14. Cerda, F., Chen, S., Bielak, J., Garrett, J.H., Rizzo, P., Kovacevic, J.: Indirect structural health monitoring of a simplified laboratory-scale bridge model. Smart Struct. Syst. **13**(5), 849–868 (2014)
15. OBrien, E.J., Keenahan, J.: Drive-by damage detection in bridges using the apparent profile. Struct. Control Health Monit. **22**(5), 813–825 (2015)
16. Matarazzo, T.J.., Pakzad, S.N.: Modal identification of golden gate bridge using pseudo mobile sensing data with STRIDE. In: Proceedings of the Society for Experimental Mechanics IMAC XXXII, Orlando, FL, vol. 4, pp. 293–298 (2014)
17. Isaksson, A.J.: Identification of ARX-models subject to missing data. IEEE Trans. Autom. Control **38**(5), 813–819 (1993)
18. Cerda, F., Garrett, J., Bielak, J., Rizzo, P., Barrera, J.A., Zhang, Z., Chen, S., McCann, M.T., Kovacevic, J.: Indirect structural health monitoring in bridges: scale experiments. In: Proceedings of the Seventh International Conference on Bridge Maintenance, Safety and Management, Lago Como, pp. 346–353 (2012)
19. Chang, M., Pakzad, S.N.: Modified natural excitation technique for stochastic modal identification. J. Struct. Eng. **139**(10), 1753–1762 (2013)
20. Yao, R., Pakzad, S.N.: Autoregressive statistical pattern recognition algorithms for damage detection in civil structures. Mech. Syst. Signal Process. **31**, 355–368 (2012)
21. Yao, R., Pakzad, S.N.: Damage and noise sensitivity evaluation of autoregressive features extracted from structure vibration. Smart Mater. Struct. **23**(2), 025007 (2014)
22. Little, R.J.A., Rubin, D.B.: Statistical Analysis with Missing Data, 2nd edn. Wiley, Hoboken, NJ (2002)
23. Shahidi, S.G., Nigro, M.B., Pakzad, S.N., Pan, Y.: Structural damage detection and localisation using multivariate regression models and two-sample control statistics. Struct. Infrastruct. Eng. **11**(10), 1277–1293 (2015)
24. Sullivan, J.H., Woodall, W.H.: A control chart for preliminary analysis of individual observations. J. Qual. Technol. **28**(3), 265–278 (1996)
25. Montgomery, R.H., Loftis, J.C.: Applicability of the t-test for detecting trends in water quality variables. J. Am. Water Resour. Assoc. **23**(4), 653–662 (1987)
26. Nigro, M.B., Pakzad, S.N., Dorvash, S.: Localized structural damage detection: a change point analysis. Comput. Aided Civ. Infrastruct. Eng. **29**(6), 416–432 (2014)

Chapter 5
Structural Assessment of a School Building in Sankhu, Nepal Damaged Due to Torsional Response During the 2015 Gorkha Earthquake

Supratik Bose, Amin Nozari, Mohammad Ebrahim Mohammadi, Andreas Stavridis, Moaveni Babak, Richard Wood, Dan Gillins, and Andre Barbosa

Abstract This paper discusses the structural assessment of a red-tagged four-story school building in Sankhu, Nepal. The building had a masonry-infilled reinforced concrete frame which was severely damaged during the 2015 Gorkha Earthquake. The concentration of damage in the west end of the first story indicates that the frame exhibited torsional response to the ground excitation. The authors visited the structure 2 months after the earthquake, collected LiDAR scans, and recorded the ambient vibrations of the damaged structure. The LiDAR data has been used to create a three-dimensional point cloud of the building which has allowed the identification of the locations and geometry of the major cracks but also the measurement of the permanent deformations of the building. The structure was also instrumented with four unidirectional accelerometers on every floor; two at opposite corners, to capture the translational and torsional motion. The translational and torsional modes have been identified with an operational modal analysis method and have been used to validate a finite element model of the structure. The comparison indicates that the model can capture the modal properties of the structure utilizing the strut modeling approach for the infill panels.

Keywords Infilled RC frame • 2015 Nepal Earthquake • LiDAR scan • Stochastic subspace identification method • Finite element model

5.1 Introduction

On April 25, 2015, a devastating, 7.8 M_w, shallow earthquake with a focal depth of 15 km [1] struck Nepal. In Kathmandu, which is at a distance of 82 km from the epicenter, the ground motion shown in Fig. 5.1 was recorded at the KATNP station (27.7 N, 85.3 E). As it can be seen in the figure, the horizontal peak ground acceleration (PGA) in the North–South direction, during the main-shock was equal to 0.164 g. The response spectra of the three components of the recorded ground motion are illustrated in Fig. 5.2a, where it can be observed that in the short-period range which is typical for low-rise infilled reinforced concrete (RC) frames, the spectral acceleration exceeded 0.6 g, while unusually large spectral amplification was observed in the long-period range (3–6 s). The isoseismal map presented in Fig. 5.2b indicates widespread damage with a maximum magnitude of IX in Mercalli scale. The earthquake was followed by 400 after-shocks of magnitudes larger than 4.0 M_w, including two of magnitudes of 6.6 M_w and 7.3 M_w and epicenters in the districts of Gorkha and Dolakha, respectively. The seismic sequence caused more than 9000 fatalities, almost 25,000 injuries and damaged beyond repair over 500,000 buildings [1, 4].

Between June 5 and July 8, 2015 the authors, along with other researchers from the US, Italy, Portugal and Nepal visited the affected regions to conduct rapid and detailed damage assessment of buildings. Part of the goal of this visit was to obtain

S. Bose • A. Stavridis (✉)
Department of Civil, Structural and Environmental Engineering, University at Buffalo, Buffalo, NY, USA
e-mail: astavrid@buffalo.edu

A. Nozari • M. Babak
Department of Civil and Environmental Engineering, Tufts University, Medford, MA, USA

M.E. Mohammadi • R. Wood
Department of Civil Engineering, University of Nebraska Lincoln, Lincoln, NE, USA

D. Gillins • A. Barbosa
Department of Civil and Construction Engineering, Oregon State University, Corvallis, OR, USA

S. Pakzad, C. Juan (eds.), *Dynamics of Civil Structures, Volume 2*, Conference Proceedings of the Society for Experimental Mechanics Series, DOI 10.1007/978-3-319-29751-4_5

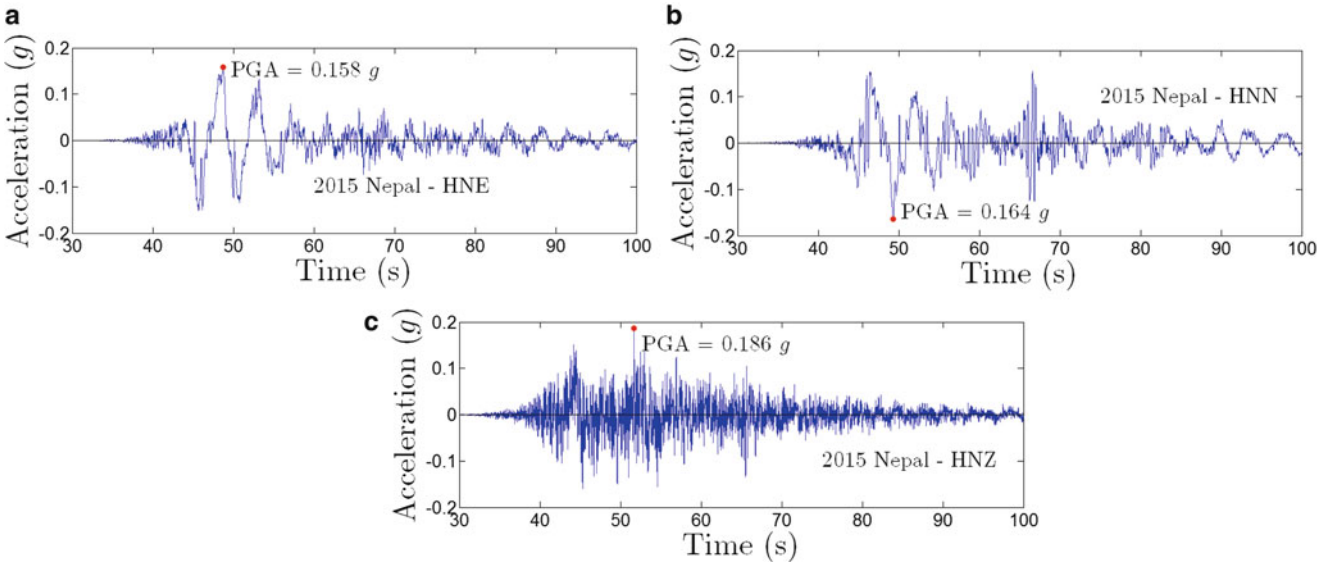

Fig. 5.1 Acceleration time histories of the main-shock [2]. (**a**) East–West component, (**b**) North–South component, (**c**) Vertical component

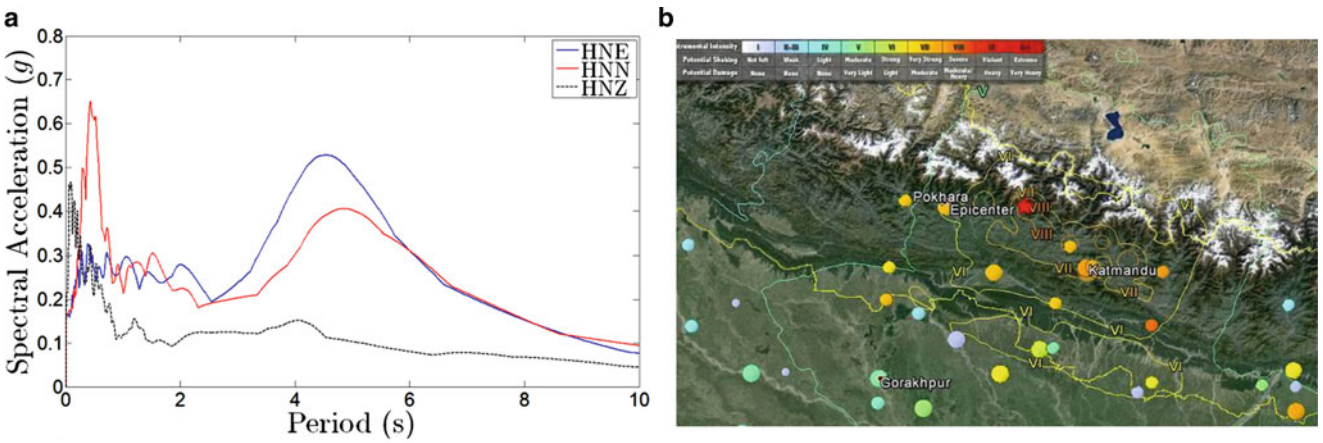

Fig. 5.2 Response spectra and iso-seismal map of the recorded ground motion. (**a**) 5% damped acceleration response spectra, (**b**) 2015 Gorkha isoseismal (Mercalli scale) map [3]

data from advanced laser sensing technologies (LiDAR) and ambient vibration recordings which can be used for damage assessment, system identification, and validation of numerical models. The team acquired dimensions of structures along with design details and material properties.

The focal point of this paper is a four-story school building in Sankhu, a town north of Kathmandu. The building had a masonry-infilled reinforced concrete frame which was severely damaged on the west end of the ground story. The structure was instrumented with accelerometers to measure the ambient vibrations, while light detection and ranging (LiDAR) data was obtained to identify the locations and geometry of the major cracks. A finite element (FE) model of the damaged school building has been calibrated using typical values of material properties from Nepal [5, 6], and it has been validated though the comparison of the modal frequencies of the model with the identified frequencies obtained from the Natural Excitation Technique combined with Eigensystem Realization Algorithm (NExT-ERA), an operational modal analysis method. The primary objectives of this paper is to the discuss the benefits of utilizing advanced sensing technologies and to investigate the accuracy of the numerical model in the predicting the periods of the damaged structure identified from the ambient-vibration recordings.

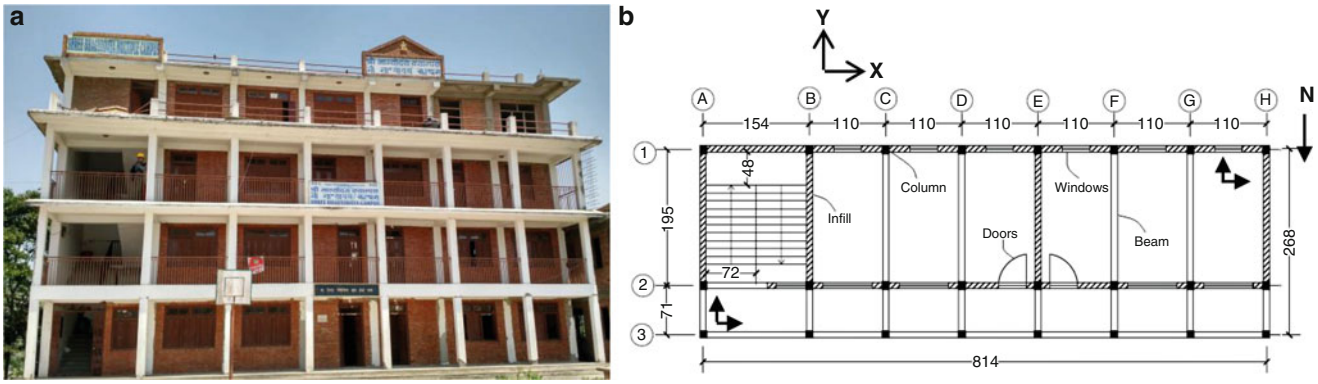

Fig. 5.3 School building at Sankhu. (**a**) North elevation of the building, (**b**) Plan view

5.2 Structural Details, Seismic Damage and Instrumentation Layout

5.2.1 4-Story Infilled RC School Building

The four-story school building located in Sankhu, Nepal (27.7 N, 85.5 E) at 20 km from the recording station is shown in Fig. 5.3a. The plan view of the structure is shown in Fig. 5.3b. As it can be seen in the figures, the building has a relatively simple structural system consisting of a reinforced concrete frame of seven bays on the east–west direction and two bays in the north south direction. On the façade of the building in the north side, a balcony, serving as corridor, is supported by bare RC columns and is exposed to the weather. On the contrary, the bays in the south side are infilled and have a wide but relatively short window, while in the bays along line 2 of Fig. 5.3b have larger windows and/or doors. As it can be observed, the stair cases are located towards the east end, thus inducing torsional irregularity in the structure.

5.2.2 Observed Damage

After the seismic sequence, shear failure in the columns and extensive damage in the beam-column joints in the west end of the ground story was observed, as shown in Fig. 5.4a–d. This can be attributed to the torsion induced by the irregularity due to the staircases. The damaged columns revealed inadequate reinforcement detailing and spacing of stirrups, in addition to poor construction. Damage in the infill panels including dominant diagonal and horizontal cracks as shown in Fig. 5.4e, f was also observed and it was mostly concentrated in the lower story. The infill panels were also found to be separated from the bounding RC elements.

5.3 Damage Assessment Using Laser Scanning

Laser scanners can capture and document the geometry and sometimes textural information of visible surfaces of objects. Hence, they can be used to non-destructively assess surface defects [7–10]. These systems emit laser pulses in defined, horizontal and vertical angular increments to rapidly measure the range, or distance, to objects within the line-of-sight of the scanner. A scan results in a quantitative three-dimensional digital representation of objects, known as a 3D point cloud, with x, y, z distances of each point referenced from the location of the scanner. The resulting 3D point cloud is highly detailed, and can be explored and analyzed virtually. The points in a terrestrial laser scan are typically spaced every mm to cm along objects and structural members in the field-of-view of the scanner. Such detailed data allows rapid, high-accuracy measurement of structures, including complex geometries, rotations and deflections of individual members, vertical and horizontal displacements, and the width and orientation of cracks larger than a few mm. A major advantage of laser scanning is that it provides high-resolution data in three dimensions, enabling the measurement of both the magnitude and direction of the deformations of the structure.

Fig. 5.4 Damages observed in the first-story of the school building at Sankhu during the earthquake. (**a**) Column G1, (**b**) Column G2, (**c**) Column H1, (**d**) Column H2, (**e**) Infill panel H12, (**f**) Infill panel E12

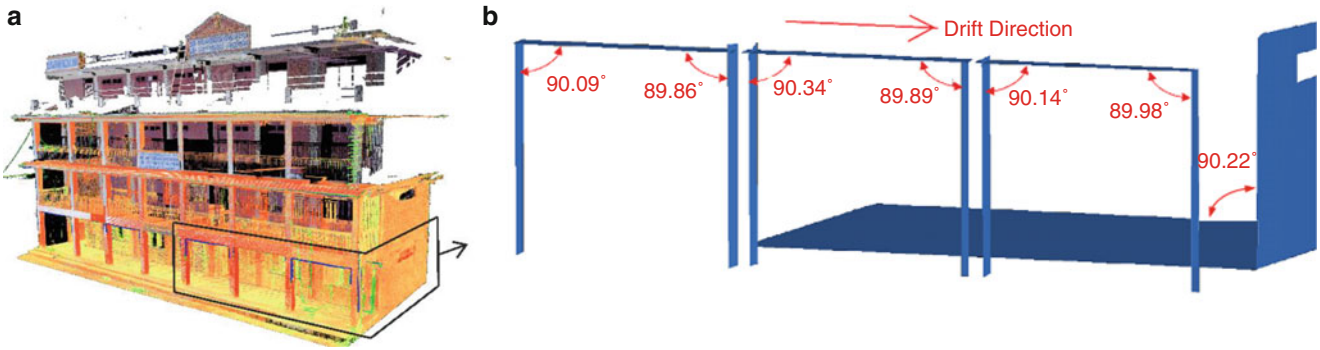

Fig. 5.5 Selected bays and west wall analyzed for global deformations. (**a**) aligned and registered LiDAR point cloud, (**b**) drift of structure estimated from planes fitted to the selected wall and columns

While visiting the building, the team collected 32 terrestrial laser scans of the school building. Two laser scanners were used: a Riegl® VZ®-400 [11] and a Faro Focus3D × 130 [12]. The Riegl scanner uses a near-infrared laser to acquire range data with an estimated accuracy of 5 mm at one standard deviation [11] throughout a 360° horizontal and 100° (+60°/−40°) vertical view, while its angular resolution can be up to 0.0005°. Twenty scans were collected with the Riegl scanner in high-speed mode, which typically measures 122,000 points per second at distances up to 350 m. The Faro scanner has a 1550 nm wavelength laser with a maximum range of 130 m [12]. It captures up to 976,000 points per second with a ranging error of ±2 mm at one standard deviation. The Faro scanner collects ranging data throughout a 360° horizontal and 300° vertical view at an angular resolution up to 0.009°. Twelve scans were collected with the Faro scanner. In both cases, paper targets were set on the school to assist with the data collection and registration. The point clouds from the 32 scanning positions were aligned and registered into the same coordinate system using Leica Cyclone software [13]. Cyclone also aligned the overlapping areas of point clouds without targets. The final point cloud of the school is presented in Fig. 5.5a.

5.3.1 Estimation of Global Deformation from Laser Scans

As discussed in a previous section, the damage was more severe in the west end of the first story. The aligned point cloud allows the estimation of the global deformations near this end of the structure. Using Cyclone, planes were fitted to the front three bays as well as the inner western wall and floor, as illustrated in Fig. 5.5a. The angles subtended by these planes per Fig. 5.5b indicate that the structure permanently drifted towards the west. As it can be seen, the angles at the top of the columns are just slightly greater than 90° for the left side of each bay, and slightly less than 90° for the right side of each bay. Assuming that the west wall was initially vertical, the data indicates it rotated approximately 0.22° out of plumb, with respect to the vertical plane.

5.3.2 Identification of Significant Surface Defects

The 12 scans conducted by the Faro scanner have been used to detect and quantify the structural damage. To this end, scans were collected from the façade and one of the interior rooms that sustained significant damage during the earthquake. Figure 5.6 presents the location of the severely cracked infill walls and columns on the west side whose damage is quantified in this section. This has been achieved through the exploration of the surface geometry variation from the collected point cloud set. Once the point cloud data is organized, the normal vectors for each of the vertices are computed, based on the selected number of neighboring points. Once the surface normal is generated for each vertex, the dot product is computed with respect to the best-fit reference plane for the entire cloud and it is binned to indicate local surface perturbations. The likelihood for surface defects and/or architectural details increases, as the dot product deviates from unity.

Figures 5.7 and 5.8 illustrate the location and geometry of surface defects for the selected walls which are indicated in Fig. 5.6. The light color lines in Figs. 5.7a and 5.8a indicate various surface defects, such as loss of concrete cover or cracks. For the regions of interest, the detected defects are mapped on the actual point cloud as illustrated in Figs. 5.7b and 5.8b. The quantified surface defects on the exterior wall are presented in Table 5.1. As shown in the table, the right column sustained significant spalling of the concrete cover (47.8 %) which exposed the shear and flexural reinforcement. On the other hand, the left column experienced only moderate spalling equivalent to 10 % loss of cover; however, a 37-cm (length) by 2-cm (width) crack developed.

Fig. 5.6 Front view of the point cloud (the two -*red* and *blue- rectangles* indicate location of the exterior and interior walls, respectively)

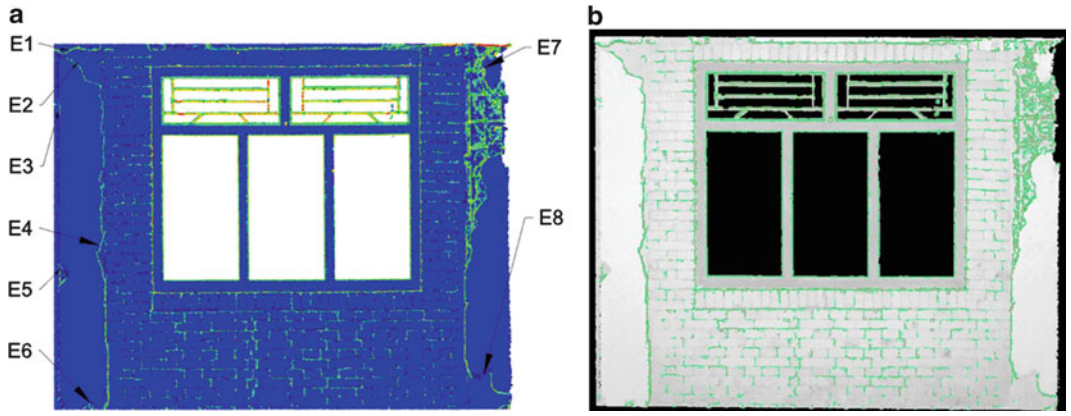

Fig. 5.7 Detected surface defects on exterior wall (bay 2GH in Fig. 5.3b). (**a**) Color coded point cloud of defects and cracks, (**b**) image of superimposed detected defects

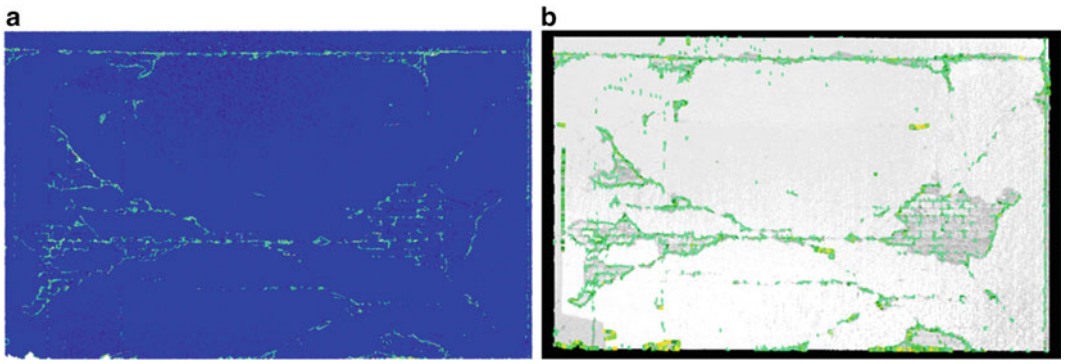

Fig. 5.8 Detected surface defects on the interior wall (bay E12 in Fig. 5.3b). (**a**) Color coded point cloud of defects and cracks, (**b**) image of superimposed detected defects

Table 5.1 Details of detected surface defects from the exterior wall

Location	Identifier	Classification	Quantified damage	Percent loss (%)
Left column	E1	Shear crack at column top	0.37 m (L) by 0.02 m (W)	–
Left column	E2–E6	Loss of concrete cover	0.09 (m^2)	9.3
Right column	E7 and E8	Loss of concrete cover	0.33 (m^2)	47.8

5.3.3 Instrumentation Layout for Ambient Vibration Recordings

The ambient vibration recordings were obtained using 12 accelerometers in two different setups as shown in Fig. 5.9. Initially, for Setup A, the accelerometers were installed on the roof, as well as the 4th- and 3rd-story slabs. For Setup B, the instruments from the top two slabs were moved to the 2nd story and the ground floor with the instruments on the 3rd floor kept intact to provide reference measurements between the two setups. A sampling rate of 2048 Hz was used for acceleration measurements. In all floor levels, four accelerometers were installed at two opposite corners of the building, namely the North–East and the South–West corners as shown in Fig. 5.3b, to measure the acceleration response at two perpendicular directions, defined as X and Y directions. A total of 54 and 45 min of ambient vibrations were recorded in 18 and 15 3-min data sets for Setup A and B, respectively.

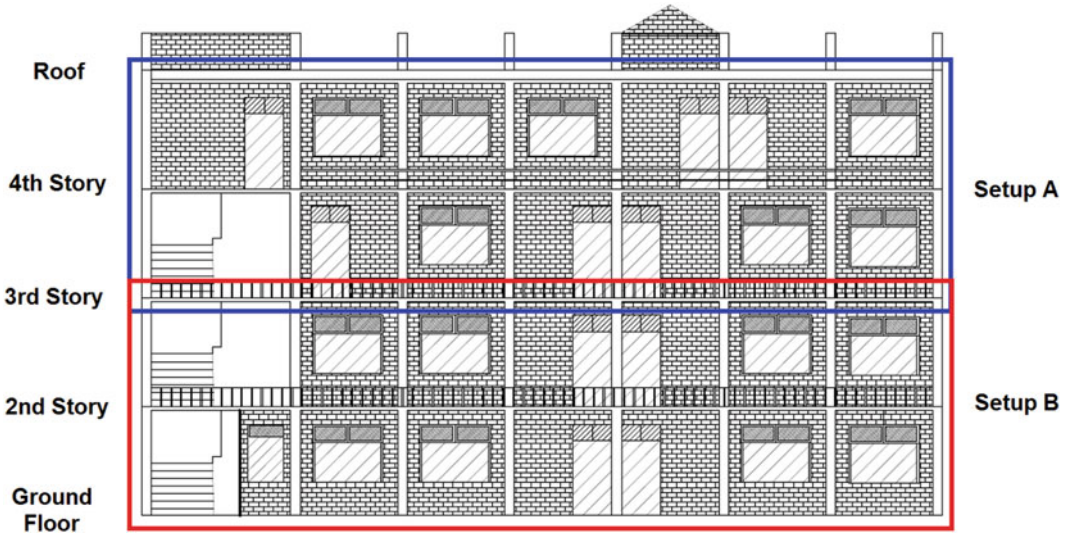

Fig. 5.9 Elevation plan view of the four-story school building at Sankhu

5.4 System Identification

In the application of system identification, every three consecutive sets of measurements of ambient vibration recordings are combined to form a 9-min set, resulting in 6 sets of modal parameters for Setup A and 5 sets for Setup B. The acceleration time histories of each data set are filtered in the frequency range between 1.0 and 8.0 Hz using a Finite Impulse Response (FIR) filter of order 4096. The filtered response is then down-sampled from the actual sampling rate of 2048 to 256 Hz to increase the computational efficiency. Figure 5.10 shows samples of the filtered time-histories which have been measured at the third floor through Setup A, while Fig. 5.11 displays the corresponding Fourier amplitude spectra.

The Natural Excitation Technique combined with the Eigensystem Realization Algorithm (NExT-ERA) is employed to identify the natural frequencies of the structure from the ambient vibration measurements. The NExT-ERA method is an output-only parametric system identification approach which estimates the modal parameters of a linear dynamic system from its measured response to a broadband excitation [14]. This method provides a framework for system identification of civil structures when the input excitation is not known [15, 16] but can be assumed to be adequately close to white noise.

In order to employ the NExT-ERA method for the identification of the vibration modes of the building, the auto-correlation and cross-correlation of the filtered ambient data are estimated as the inverse Fourier transformation of power spectral density and cross spectral density functions of the data. The spectral density functions are computed using equal length Hanning windows with 50 % overlap based on the Welch method [17]. Two reference channels are used in the system identification to account for excitations in both X and Y directions. In the Setup A, the acceleration measurements in the X-direction of the fourth floor and in the Y-direction of the third floor, both at South–West corner, are used as reference channels. In Setup B, the acceleration measurements in the X-direction of the second floor and Y-direction of the third floor, both at South–West corner, are considered as the reference channels. The estimated auto correlation and cross correlation are then used to establish a block Hankel matrix of size $(12 \times 400) \times (400 \times 2)$ for Eigensystem Realization Algorithm. This algorithm uses the Hankel matrix to estimate the underlying state-space matrices which can be used to identify the modal parameters of the system which include the natural frequencies, mode shapes, and damping ratios. However, only the natural frequencies and the damping ratios are reported in this study. A stabilization diagram [18] is used to select an appropriate system order for the identification of the stable modes. In the stabilization diagram, the identified natural frequencies of stable modes do not vary at increasing system orders. A sample stabilization diagram is illustrated in Fig. 5.12.

The framework is applied to all data: the 6 sets of identified modal parameters are obtained from Setup A and 5 sets from Setup B. Considering the stabilization diagrams obtained from the recorded data sets, the first three stable vibration modes are reported in Table 5.2, which includes the average of identified natural frequencies and damping ratios, along with the corresponding coefficients of variation (CoV). It can be observed that the natural frequencies are consistently identified as indicated by the low CoV values at each setup, and they are also consistent between the two setups. However, the identified damping ratios demonstrate a much higher level of variability even for the same setup.

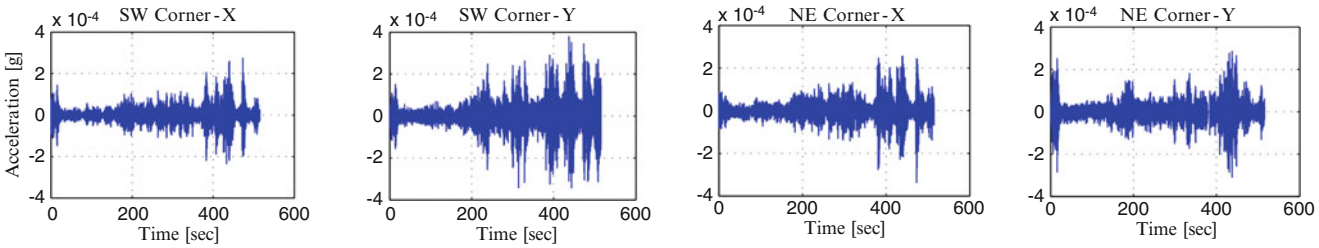

Fig. 5.10 Filtered acceleration response of the third floor through experiment Setup A

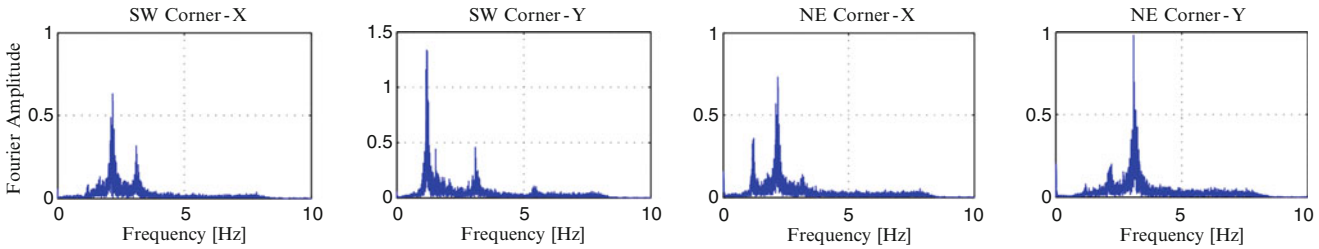

Fig. 5.11 Frequency content of filtered acceleration data of the third floor

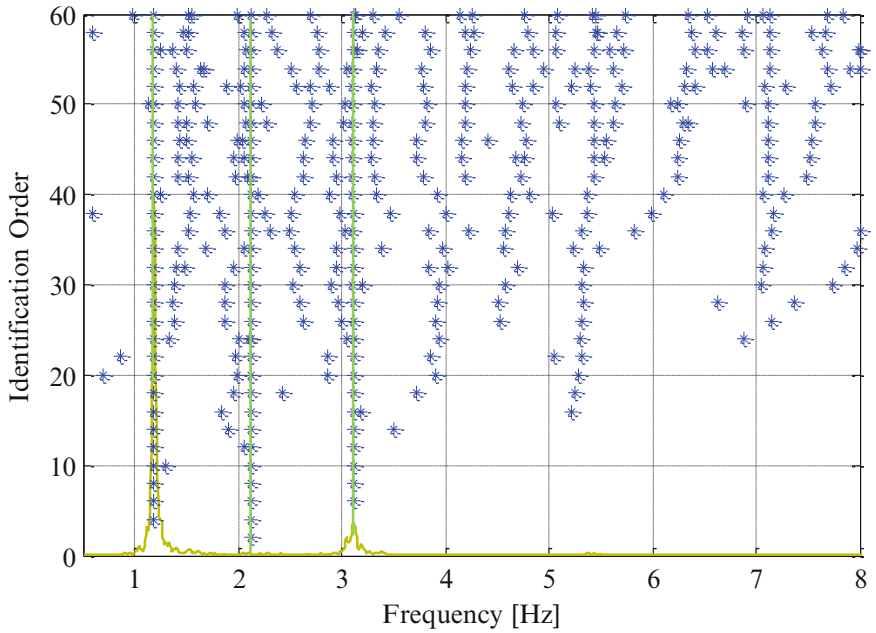

Fig. 5.12 Sample stabilization diagram for identification of natural frequencies

Table 5.2 Statistical properties of identified modal parameters of the building

Test Setup	Mode	Natural frequency [Hz]		Damping ratio [%]	
		Mean	CoV [%]	Mean	CoV [%]
A	1	1.18	0.7	2.2	15.3
	2	2.16	1.1	2.2	17.6
	3	3.15	1.1	3.0	36.2
B	1	1.19	0.5	1.8	32.5
	2	2.14	2.0	1.5	42.0
	3	3.19	0.6	2.4	18.4

5.5 Numerical Model

A simplified finite element model of the four-story school building has been developed in the structural analysis software Opensees [19]. In lack of engineering drawings and material properties, the geometry of the model is based on in-situ measurements of the geometry of the structure, while the material properties are based on the commonly measured properties of RC and masonry structures in Nepal [5, 6]. The numerical model employs strut elements for the infill panels and the staircases, and beam-column elements for the RC members (Fig. 5.13a). The simplified modeling approach adopted here cannot capture in detail the failure mechanism. It can however, simulate the lateral force-vs.-lateral drift relation of infilled frames accurately [20].

The infilled bays of the building have been grouped in seven types based on the aspect ratio and opening geometry. A simplified curve (Fig. 5.13d) is developed for every infilled bay of the frame in the building as illustrated in Fig. 5.13, based on the guidelines [20] developed based in the results of a parametric study using a detailed FE modeling scheme combining smeared crack and interface elements [21]. These envelop curves are then used to calibrate strut models simulating the behavior of the infill panel in every bay using Opensees. The thickness of the diagonal struts is kept equal to the infill thickness (9 in.), while the strut width, the strains at peak strength and at the onset of residual strength are selected so that the calibrated lateral force-vs.-drift response of the corresponding infilled frames match the simplified curves (Fig. 5.14). The calibrated material parameters are summarized in Table 5.3. Once the diagonal struts are calibrated, the 3D model of the entire building is assembled as shown in Fig. 5.13a.

5.5.1 *Comparison of Modal Parameters*

The modal frequencies are identified for the damaged structure as the ambient vibration recordings were obtained from the school building after the earthquake. In order to simulate the condition of the structure after the earthquake with a relatively simple model, the infill panels and the RC columns that were severely damaged have been removed from the numerical

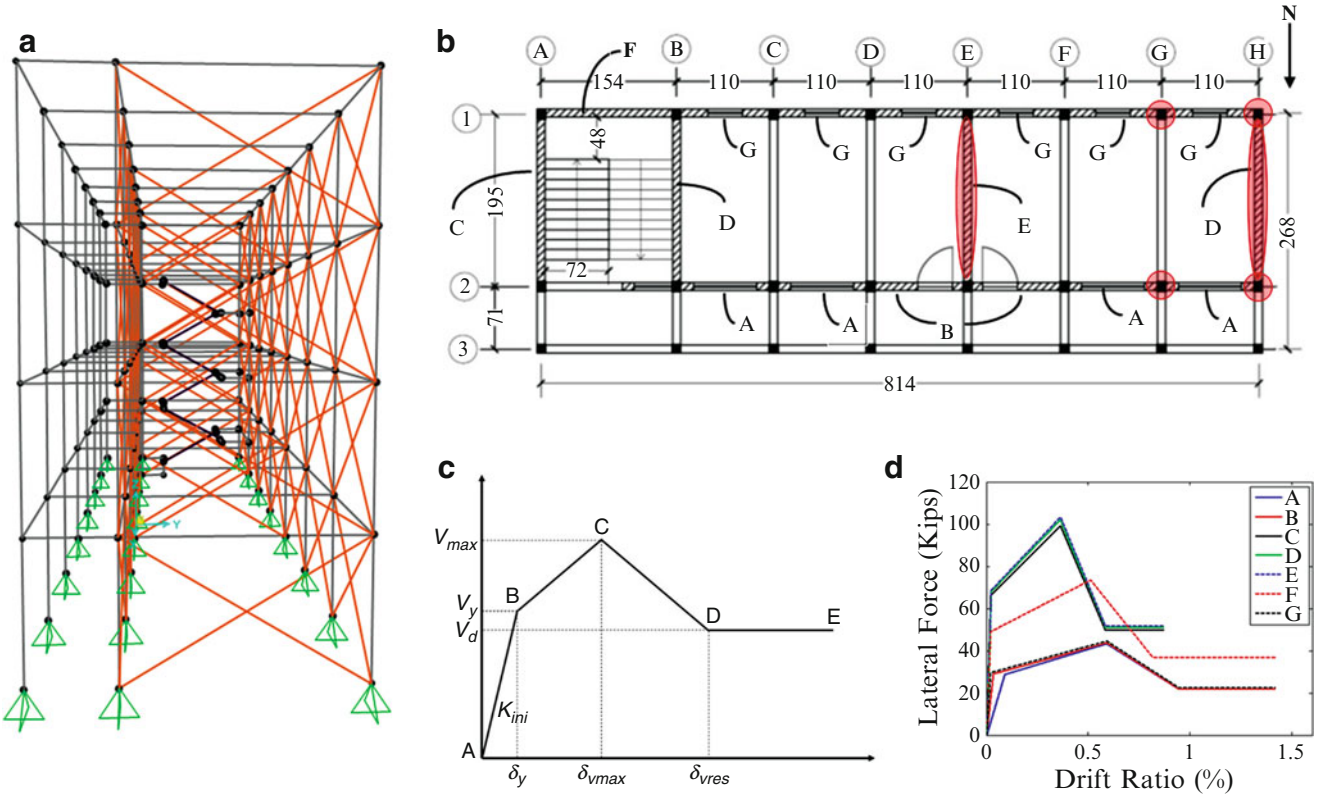

Fig. 5.13 (**a**) Diagonal strut model and estimation of simplified curves for single-story single-bay frames, (**b**) Different types of infill panel, (**c**) Force vs. displacement curves, (**d**) Estimation of simplified curve

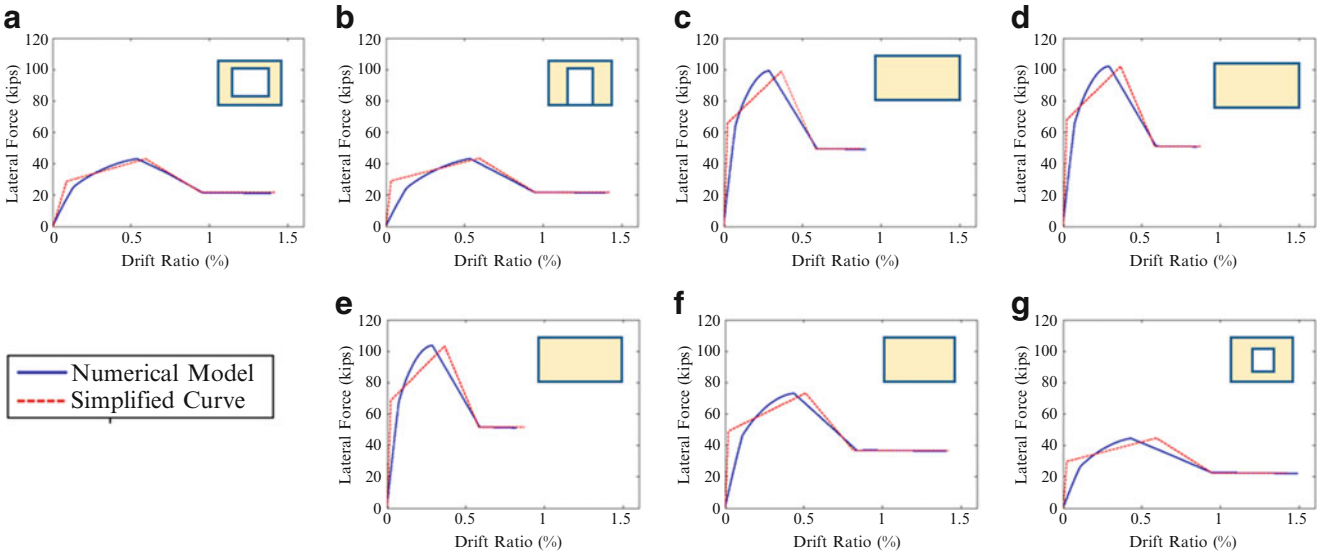

Fig. 5.14 Calibrated response of single-story single-bay frames. (**a**) Frame A, (**b**) Frame B, (**c**) Frame C, (**d**) Frame D, (**e**) Frame E, (**f**) Frame F, (**g**) Frame G

Table 5.3 Assumed material properties of concrete and masonry

	Assumed material properties	
Parameters	Concrete	Masonry
Compressive strength (ksi)	3.0	0.50
Strain at peak strength	0.003	0.004
Strain at onset of residual strength	0.006	0.008
Residual strength (ksi)	0.30	0.05
Tensile strength (ksi)	0.30	0.25
Maximum tensile strain	0.008	0.008

Table 5.4 Comparison of frequencies obtained from ambient vibration data and finite element model

		Natural frequency after earthquake		
Mode	Natural frequency (s)	Ambient vibration (s)	Finite element (s)	Error (%)
1	1.460	1.185	1.178	0.6
2	3.534	2.150	2.471	14.9
3	3.953	3.170	3.115	1.7

model to simulate the damage. Therefore, the RC columns H1, H2, G1, G2 and Infill Panels: H12 and E12 of the first story are removed from the model as indicated in Fig. 5.13b. The modal periods obtained are compared to those identified from the ambient vibration recordings in Table 5.4. It can be observed that the natural frequencies of the structure obtained from the finite element model for the first three modes are very close to those estimated from the ambient vibration data. The error is actually less than 2 % for modes 1 and 3, while it is close to 15 % for the second mode. Given the simplicity of the model this is a very good agreement considering the complexity involved with modeling a damaged actual structure.

5.6 Conclusions

The damage assessment, system identification, and modeling of a four-story masonry-infilled reinforced concrete frame building in Sankhu, Nepal, which was severely damaged during the 2015 Gorkha Earthquake is presented in this paper. The damage in the school building was concentrated towards the west end in the first story indicating that the structure exhibited torsional response to the ground excitation. The detailed damage assessment was conducted using advanced

sensing technologies (LiDAR). In this study, 32 terrestrial laser scans obtained from two scanners are used to create a three-dimensional point cloud of the building with the locations and geometry of the major cracks identified. The scan data is used to estimate the global deformations and quantify the damage in the infill panels and RC columns towards the west end of the building. Based on the analyses of the scans, the west wall appears to have rotated out of vertical, while the RC columns sustained significant spalling of concrete cover and exposed reinforcement.

The structure was also instrumented with four unidirectional accelerometers on each floor, two at opposite corners, to capture the translational and torsional modes. The system identification of the school building is conducted in this study by analyzing different subsets of the ambient vibration data. The modal parameters of the structure are identified using the NExT-ERA identification method. It is observed that the natural frequencies are consistently identified in all data sets. A simplified finite element model of the structure is developed adopting the strut method. In order to simulate the condition of the damaged structure after the earthquake, the infill panels and the RC columns that were severely damaged are removed from the numerical model. The natural frequencies of the first three modes estimated from the system identification are in good agreement with those from the finite element model indicating the ability of the model to capture the basic dynamic properties of the structure.

Acknowledgements The researchers from the University at Buffalo and Oregon State University were supported by NSF Awards #1545595 and #1545632, respectively. The authors would also like to acknowledge the support of National Society of Earthquake Technology (NSET) in Nepal, through the support of Ramesh Guragain and Dev Kumar Maharjan. The collaboration of other researchers including Patrick Burns, Matt Gillins, Michael Olsen, Giuseppe Brando, Davide Rapone, Enrico Spacone, Rajendra Soti, Humberto Varum, António Arêde, Nelson Vila-Pouca, André Furtado, João Oliveira, Hugo Rodrigues, Marco Faggella and Rosario Gigliotti during the reconnaissance trip and in the collection of data is greatly appreciated as well. However, the opinions expressed in this paper are those of the authors and do not necessarily represent those of the sponsor or the collaborators.

References

1. Rai, D.C., Singhal, V., Raj, B.S., Sagar, L.: Reconnaissance of the effects of the M7.8 Gorkha (Nepal) earthquake of April 25, 2015. J. Geomatics Nat. Hazards Risk **7**(1), 1–17 (2015). Taylor and Francis
2. United State Geological Survey. http://earthquake.usgs.gov/earthquakes/eventpage/us20002926#scientific_waveforms USGS (2015)
3. United State Geological Survey (USGS). http://earthquake.usgs.gov/hazard/apps/vs30 (2015)
4. Brando, G., Rapone, D., Spacone, E., Barbosa, A., Olsen, M., Gillins, D., Soti, R., Varum, H., Arede, A., Vila-Pouca, N., Furtado, A., Oliveira, J., Rodriges, H., Stavridis, A., Bose, S., Faggella, M., Gigliotti, R., Wood, R.L.: Reconnaissance report on the 2015 Gorkha earthquake effects in Nepal. XVI Congegno ANIDIS, L'AQUILA (2015)
5. Chaulagain, H., Rodrigues, H., Spacone, E., Varum, H.: Seismic assessment of RC structures with infill masonry panels in Nepal—Sensitivity analysis. In: Second European Conference on Earthquake Engineering and Seismology, Istanbul, Aug 2014
6. Pradhan, P.L.: Composite actions of brick infill wall in RC frame under in-plane lateral load. Ph.D. Dissertation, Tribhuvan University, Pulchowk Campus (2009)
7. Guldur, B., Hajjar, J.F.: Laser-based structural sensing and surface damage detection, Report No. NEU-CEE-2014-03, Department of Civil and Environmental Engineering, Northeastern University, Boston (2014)
8. Wood, R.L.: Methods of structural damage characterization for infrastructure. 34th Annual Structural Congress, Structural Engineer (2014)
9. Olsen, M.J., Kuester, F., Chang, B., Hutchinson, T.: Terrestrial laser scanning based structural damage assessment. J. Comput. Civ. Eng. **24**(3), 264–272 (2010)
10. Olsen, M.J., Cheung, K.F., Yamazaki, Y., Butcher, S., Garlock, M., Yim, S., Piaskowy, S., Robertson, I., Burgos, L., Young, Y.L.: Damage assessment of the 2010 Chile earthquake and tsunami using terrestrial laser scanning. Earthq. Spectra **28**(S1), S179–S197 (2012)
11. Riegl, Riegl VZ-400 Datasheet, Riegl Laser Measuring Systems GmbH, Austria (2014)
12. Trimble, Faro Focus3D × 130 high-speed 3d laser scanner datasheet. Trimble Navigation Limited, Westminster (2015)
13. Leica, Leica Cyclone SURVEY 9.1, Processing laser scans into civil/survey deliverables. Leica Geosystems AG, Heerbrugg (2014)
14. Junag, J.N., Pappa, R.S.: An eigensystem realization algorithm for modal parameter identification and model reduction. J. Guid. Control. Dyn. **8**(5), 620–627 (1985)
15. Farrar, C., James III, G.: System identification from ambient vibration measurements on a bridge. J. Sound Vib. **205**(1), 1–18 (1997)
16. Moaveni, B., He, X., Conte, J.P., Restrepo, J.I., Panagiotou, M.: System identification study of a 7-story full-scale building slice tested on the UCSD-NEES shake table. J. Struct. Eng. **137**(6), 705–717 (2010)
17. Welch, P.D.: The use of fast Fourier transform for the estimation of power spectra: a method based on time averaging over short, modified period programs. IEEE Trans. Audio Electroacoust. **15**(2), 70–73 (1967)
18. Verboven, P., Parloo, E., Guillaume, P., Van Overmeire, M.: Autonomous structural health monitoring—part I: modal parameter estimation and tracking. J. Mech. Syst. Signal Process. **16**(4), 637–657 (2002)
19. McKenna, F., Fenves, G.L., Scott, M.H., Jeremic, B.: Open system for earthquake engineering simulation (opensees). Pacific Earthquake Engineering Research Center, University of California, Berkeley (2000)
20. Stavridis, A.: Analytical and experimental study of seismic performance of reinforced concrete frames infilled with masonry walls. Ph.D. Dissertation, University of California, San Diego (2009)
21. Stavridis, A., Shing, P.B.: Finite element modeling of nonlinear behavior of masonry-infilled RC frames. J. Struct. Eng. **136**(3), 285–296 (2010)

Chapter 6
Damage Detection Optimization Using Wavelet Multiresolution Analysis and Genetic Algorithm

S.A. Ravanfar, H. Abdul Razak, Z. Ismail, and S.J.S. Hakim

Abstract In this study, an optimized damage detection using genetic algorithm (GA) in beam-like structures without using baseline data. For this purpose, a vibration-based damage detection algorithm using a damage indicator called 'Relative Wavelet Packet Entropy' (RWPE) was applied to determine the location and severity of damage. To improve the algorithm, GA was utilized to optimize the algorithm so as to identify the best choice of wavelet parameters. To examine the robustness and accuracy of the proposed method, numerical examples and experimental cases with different damage depths were considered and conducted.

Keywords Relative wavelet packet entropy • Genetic algorithm • Damage detection • Beam-like structures

6.1 Introduction

Structural monitoring and damage detection are areas of current interest in civil, mechanical and aerospace engineering. Most damage detection methods are visual or localized experimental procedures such as acoustic or ultrasonic methods, magnetic field methods, radiographs, eddy-current and thermal field methods. All these experimental techniques require that the location of damage be known a priori and that the portion of the structure under inspection be easily accessible. These limitations led to the development of global monitoring techniques based on changes in the vibration characteristics of the structure. Structural identification made on the basis of vibration data is an important research topic that has wide application for structural health monitoring, structural control, and response prediction [1, 2].

Most of the vibration-based damage detection methods are often formulated as given changes of structural dynamic characteristics between the baseline and the current state to identify the location and severity of damage. However, due to absence of baseline data from undamaged states for most of the existing structures, these methods cannot be applied. To avoid this limitation, researchers have proposed several approaches for detecting structural damage without prior knowledge of the undamaged state. Ratcliffe [3] employed a modified Laplacian operator to propose a damage identification method for discretely measuring the mode shape of a beam. This method operates only on data exploited from the damaged structure to locate variations in the structural stiffness. Yoon et al. [4] extended the 1-D gapped-smoothing method to the 2-D gapped-smoothing method to locate regions in a structure where the stiffness varies, in which baseline data and theoretical models of the presumably undamaged structure are not applied during the analysis. The procedure was conducted with a finite element model of a plate, and experiments on composite plates with deliberately induced multiple delaminations. Most of the proposed techniques for damage identification without the baseline modal parameters require the use of finite element models of the test structure to replace the baseline data from the intact structure. Therefore, an inaccurate finite element model may lead to large model errors which will consequently yield incorrect results in damage detection.

Recently, wavelet analysis has become a widely used signal processing tool in the field of vibration-based damage detection due to its potential characteristics such as singularity detection, good handling of noisy data and being very informative about damage location/time. Consequently, many studies on damage detection have focused on the wavelet transform scheme [5–7]. Zhong and Oyadiji [8] developed an approach based on the difference between two sets of detailed coefficients by using stationary wavelet transform (SWT) for crack detection in beam-like structures. The main limitation of the method is its applicability in symmetric beams. A new approach to measure acceleration response of a damaged beam

S.A. Ravanfar (✉) • H.A. Razak • S.J.S. Hakim
StrucHMRS Group, Department of Civil Engineering, University of Malaya, Kuala Lumpur, Malaysia
e-mail: r.ravanfar@gmail.com

Z. Ismail
Department of Civil Engineering, Faculty of Engineering, University of Malaya, Kuala Lumpur, Malaysia

S. Pakzad, C. Juan (eds.), *Dynamics of Civil Structures, Volume 2*, Conference Proceedings of the Society for Experimental Mechanics Series, DOI 10.1007/978-3-319-29751-4_6

was proposed by Mikami et al. [9]. This method was based on the variation between two sets of power spectrum density magnitudes calculated by means of wavelet packet decomposition (WPD) components of two sets of dynamic data of the damaged beam.

In the last two decades, genetic algorithms (GAs) [10] have been recognized as promising intelligent search techniques for difficult optimization problems. Vakil-Baghmisheh et al. [11] successfully applied the genetic algorithm to predict the size and location of a crack in a cantilever beam.

In this study, a new approach for optimized damage detection in beam-like structures is investigated and applied to a damaged steel beam. This new approach is based on wavelet packet transform (WPT) combined with entropy analysis to determine an effective damage indicator, RWPE, for investigating the location and severity of damage. To improve the algorithm, GA was used to optimize the algorithm so as to identify the best choice of wavelet parameters. The proposed approach is verified through the numerical and experimental examples on damaged beam with different damage scenarios. It is shown that the present algorithm is able to identify the location and severity of damage precisely.

6.2 Wavelet Packet

6.2.1 Wavelet Packet Decomposition

Wavelet transform (WT) is a relatively new signal processing method efficient for multi-resolution analysis and local features of non-stationary signals. It can be considered as an extension of the traditional Fourier transform with modifiable window size and location [12]. The wavelet packet function is defined as

$$\psi_{\mathrm{j,k}}^{\mathrm{i}}(\mathrm{t}) = 2^{j/2}\psi^{i}\left(2^{j}t-k\right) \quad i=0,1,2,\ldots,2^{j}-1 \tag{6.1}$$

where a wavelet packet $\psi_{\mathrm{j,k}}^{\mathrm{i}}(\mathrm{t})$ is a function of three indices with integers i, j and k, denoting the modulation, the scale and the translation parameter, respectively. Moreover, $\psi^{0}(t) = \varphi(t)$ for $i=0$ and $\psi^{1}(t) = \psi(t)$ for $\mathrm{i}=1$. The wavelet $\varphi(t)$ is called the scaling function and $\psi(t)$ is called the mother wavelet function. The wavelets ψ^{i} for $\mathrm{i}>1$ are obtained from the scaling function and the mother wavelet function as:

$$\psi^{2i} = \sqrt{2}\sum_{k} h(k)\psi^{i}(2t-k) \tag{6.2}$$

$$\psi^{2i+1} = \sqrt{2}\sum_{k} g(k)\psi^{i}(2t-k) \tag{6.3}$$

where g(k) and h(k) are quadrature mirror filters associated with the mother wavelet function and the scaling function. The original signal can be expressed as a summation of WPD components as,

$$f(t) = \sum_{i=1}^{2^{j}} f_{j}^{i}(t) \tag{6.4}$$

where t is time lag; $f_{j}^{i}(t)$ is the WPD component signal that can be represented by a linear combination of wavelet packet functions as follows:

$$f_{j}^{i}(t) = \sum_{k=-\infty}^{\infty} C_{j,k}^{i}\psi_{j,k}^{i}(t) \tag{6.5}$$

WPT offers good time resolution in the high-frequency range of a signal and good frequency resolution in the low-frequency range of the signal.

6.3 Damage Identification Procedure

The wavelet packet component energy is a suitable tool to identify and characterize a specific phenomenon of signal in the time-frequency domain. The wavelet packet energy E_f of a signal is defined as

$$E_f = \int_{-\infty}^{\infty} f^2(t)dt = \sum_{m_1=1}^{2^j} \sum_{m_2=1}^{2^j} \int_{-\infty}^{\infty} f_j^{m_1}(t) f_j^{m_2}(t)dt \tag{6.6}$$

where $f_j^{m_1}$ and $f_j^{m_2}$ stand for decomposed wavelet components. The total signal energy can be expressed as the summation of wavelet packet component energies when the mother wavelet is orthogonal.

The damage detection problem can be formulated through the changes in the wavelet packet entropy of damaged structures to detect the location and severity of damage. To identify the change of vibration signals of a structure, the fundamental fitness function at a location "α" has been considered as:

$$S_{RWPE}^k \left(p^\alpha \middle| p^\beta\right) = \sum_j \sum_i \left| p_{ij}^{\alpha k} \ln \left(\frac{p_{ij}^\alpha}{p_{ij}^\beta} \right) \right| \tag{6.7}$$

where p_{ij} is the energy ratio of each wavelet coefficient, α and β denote locations where the data is measured. It is notable that accelerations measured in the same direction should be used in computations of RWPE.

6.4 Numerical Investigation

6.4.1 Finite Element Method Analysis

To verify the suitability of the proposed method in subsea pipeline free span identification, numerical simulations of pipeline responses with different assumed damage conditions subjected to ambient wave force are carried out.

To verify the suitability of the proposed method in beam-like structures, numerical simulations were conducted on I-section steel beam with a span length of 3 m and simulated damage elements, as shown in Fig. 6.1. Damage was simulated in the form of a notch with a 3 mm width located at point 5. Damage depth for all beams was increased gradually from 3 mm up to 75 mm as depicted in Fig. 6.1a. The mass density and modulus of elasticity of the beam material were 7850 kg/m^3 and 2.1 GPa, respectively, and the Poisson's ratio was 0.33.

To identify to identify the characteristics of damage in the beam, the node acceleration responses of the beam under the impulse load were obtained from 16 locations on the top flange as shown in Fig. 6.1b at a sampling frequency of 2000 Hz. To simulate an impulse load, the force-time history was applied at location 14 on the beam.

GA was employed to search for the optimal Daubechies order and decomposition level of the signals by maximizing the fitness function. The parameters of GA are: probability of crossover Pc is 0.7, probability of mutation Pm is 0.2, the selection function is Tournament, the maximum number of generation is 200, the fitness normalization is Rank and the population size pop is 30. In addition, Table 6.1 indicates the variables of the GA used in the research.

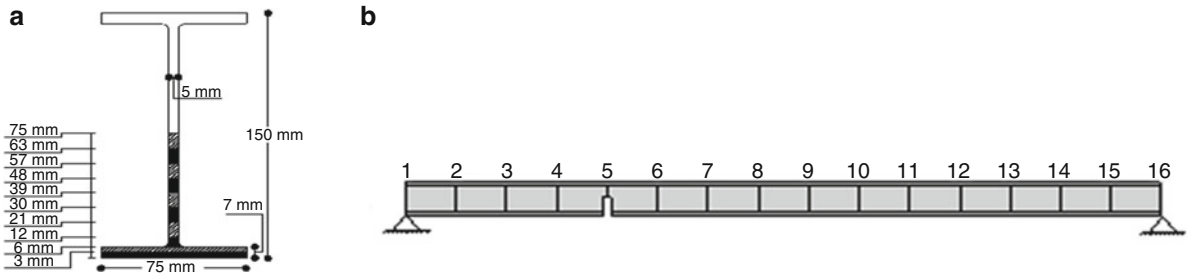

Fig. 6.1 Numerical model of tested beam: (**a**) Cross section; (**b**) Damage location

Table 6.1 GA variables

Variable name	Range	Optimized value in tested beam
Daubechies order	DB1–DB31	DB2
Decomposition level	2–7	5

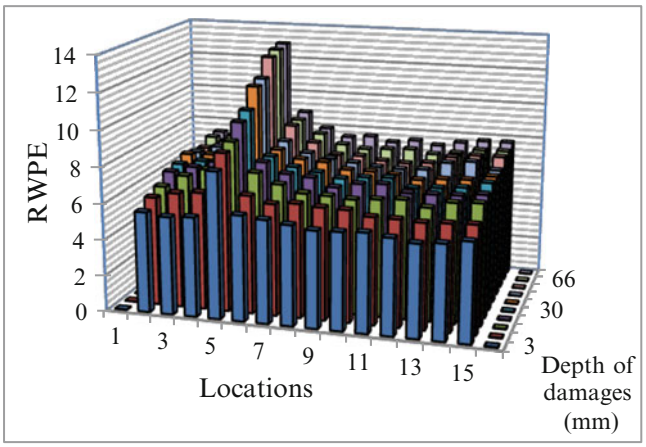

Fig. 6.2 Histograms of damage indictors in beam 3 with DB2

6.4.2 Results and Discussion

To validate the proposed damage detection method, the simulated simply-supported beams with damage elements were considered. Fig. 6.2 shows the values of damage indicators calculated according to Eq. (6.7). By running the GA, DB2 and level 5 were selected as the best values for the Daubechies order and decomposition level, respectively.

Results have illustrated that the damage locations can be accurately determined from the measured time history acceleration responses through variation of damage indicators. In addition, the respective amplitude levels of the histograms can be used as a criterion to identify severity of damage, although not quantitatively.

6.5 Experimental Verification

Most modal-based damage features such as natural frequencies, mode shapes, modal strain energy and modal flexibility are sensitive to noise and measurement errors, which results in difficulties for practical applications. Therefore, the proposed damage detection method should be verified with real measurement data from dynamic tests on structures where noise and measurement errors are present. To illustrate the proposed algorithm, the vibration tests were performed on the steel beam with a span length and different damage scenarios, as shown in Fig. 6.3. Sixteen accelerometers were mounted on the top flange along the beam to measure the acceleration response with a sampling frequency of 2000 Hz for all signals.

6.5.1 Experimental Results

From the results, the following observations can be made based on the structural response signal of damaged beam. By running the GA, Daubechies order 2 and decomposition level 6 were chosen as the best parameters for the adjustment of the algorithm for differentiating the damages, as shown in Fig. 6.4. The damage location at position 5 could be precisely identified with the significant change in values of damage indicators.

The results have demonstrated that for different wavelet-based methods, the choice of the mother wavelet function is of paramount importance to improve the performance of the algorithm.

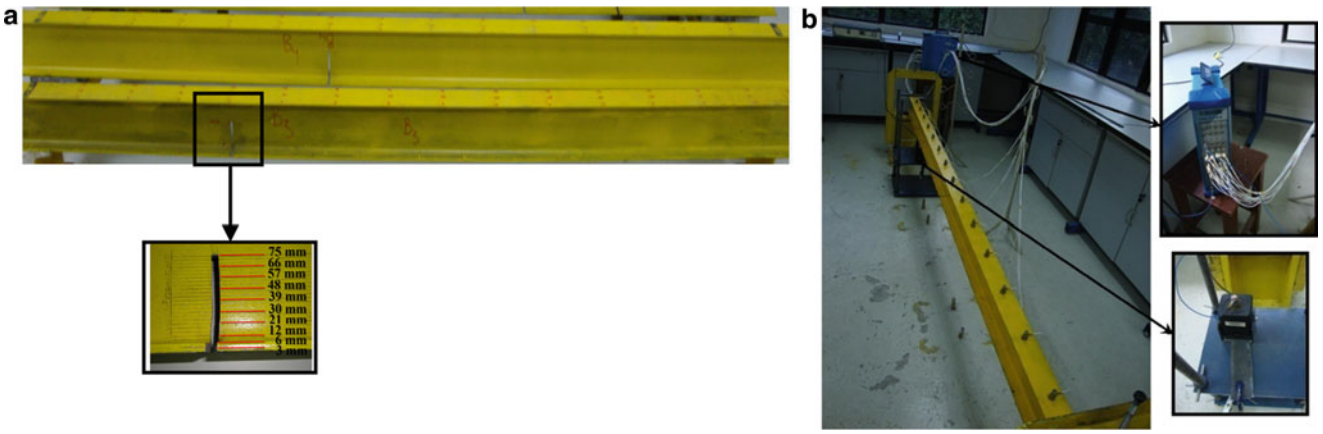

Fig. 6.3 Beam tested in the laboratory: (**a**) Damage locations of tested beams; (**b**) data acquisition system

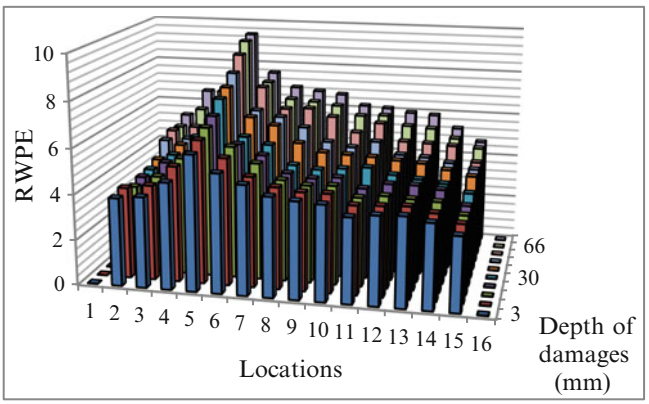

Fig. 6.4 Histograms of RWPE

6.6 Conclusions

An intelligent damage identification algorithm to detect damage in beam-like structures using vibration signal was developed and implemented. To verify the efficiency and practicability of the method proposed in the current research, both numerical simulation and experimental tests were carried out. The damage indicator was obtained from an optimized wavelet packet transform which was combined with the information entropy to gain the advantages of both techniques. Also, all the results show that the optimal damage indicator can be successfully used to identify the damage locations as well as damage severity from the response data of the damaged beam using an effective comparative approach.

Acknowledgement The authors would like to express their sincere thanks to the Ministry of Education, Malaysia for the support given through research grants PG222-2014B and FP027/2012A.

References

1. Fan, W., Qiao, P.: Vibration-based damage identification methods: a review and comparative study. Struct. Health Monit. **10**(1), 83–111 (2011)
2. Farrar, C.R., Doebling, S.W., Nix, D.A.: Vibration–based structural damage identification. Philos. Trans. R. Soc. Lond. Ser. A: Math. Phys. Eng. Sci. **359**(1778), 131–149 (2001)
3. Ratcliffe, C.P.: Damage detection using a modified Laplacian operator on mode shape data. J. Sound Vib. **204**(3), 505–517 (1997)
4. Yoon, M., Heider, D., Gillespie Jr., J., Ratcliffe, C., Crane, R.: Local damage detection using the two-dimensional gapped smoothing method. J. Sound Vib. **279**(1), 119–139 (2005)
5. Ovanesova, A., Suarez, L.: Applications of wavelet transforms to damage detection in frame structures. Eng. Struct. **26**(1), 39–49 (2004)
6. Kim, H., Melhem, H.: Damage detection of structures by wavelet analysis. Eng. Struct. **26**(3), 347–362 (2004)

7. Umesha, P., Ravichandran, R., Sivasubramanian, K.: Crack detection and quantification in beams using wavelets. Comput. Aided Civ. Infrastruct. Eng. **24**(8), 593–607 (2009)
8. Zhong, S., Oyadiji, S.O.: Crack detection in simply supported beams without baseline modal parameters by stationary wavelet transform. Mech. Syst. Signal Process. **21**(4), 1853–1884 (2007)
9. Mikami, S., Beskhyroun, S., Oshima, T.: Wavelet packet based damage detection in beam-like structures without baseline modal parameters. Struct. Infrastruct. Eng. **7**(3), 211–227 (2011)
10. Haupt, R.L., Haupt, S.E.: Practical Genetic Algorithms. Wiley, Upper Saddle River (2004)
11. Vakil-Baghmisheh, M.-T., Peimani, M., Sadeghi, M.H., Ettefagh, M.M.: Crack detection in beam-like structures using genetic algorithms. Appl. Soft Comput. **8**(2), 1150–1160 (2008)
12. Neild, S., McFadden, P., Williams, M.: A review of time-frequency methods for structural vibration analysis. Eng. Struct. **25**(6), 713–728 (2003)

Chapter 7
A Novel Acoustoelastic-Based Technique for Stress Measurement in Structural Components

Mohammad I. Albakri and Pablo A. Tarazaga

Abstract The acoustoelastic theory has been widely utilized for nondestructive stress measurement in structural components. Most of the currently available techniques operate at the high-frequency, weakly-dispersive portions of the dispersion curves, and rely on time-of-flight measurements to quantify the effects of stress state on wave speed. This adversely affects the sensitivity and accuracy of such techniques, and renders their accuracy limited by the precision within which time-of-flight can be determined.

In this work, a novel acoustoelastic-based stress measurement technique is developed by combining dispersion compensation algorithms and numerical optimization schemes. Dispersion compensation allows the use of highly-stress-sensitive, low-frequency flexural waves for stress measurement, which in turn enhances the sensitivity of the developed technique. The need for accurate time-of-flight measurements is eliminated in this work by analyzing the entire propagated waveform to reconstruct the dispersion curve over the frequency range of interest. The fact that an entire section of the dispersion curve, as opposed to a single wave speed measurement, is used to calculate the state of stress in the structure enhances the technique's accuracy and robustness. A criterion for optimal selection of excitation waveform is developed in this work. The effects of material properties uncertainties on the accuracy of stress measurements are also investigated.

Keywords Acoustoelasticity • Dispersion compensation • Stress measurement • Reflections • Optimization

7.1 Introduction

All structural elements and mechanical components are subjected to internal stresses. Such stresses arise from external loads acting upon the structure, or induced by changes in operation and environmental conditions such as temperature and humidity. Manufacturing processes, such as casting, rolling, and forming, also result in non-uniformly distributed residual stresses in the manufactured parts [1]. Nondestructive, nonintrusive, and accurate solution for measuring the state of stress in structural and mechanical components is of significant importance for structural health monitoring and remaining life predictions.

Several theories and techniques have been developed over the last few decades to tackle the problem of stress state measurement, many of them are destructive in nature. Nondestructive techniques, on the other hand, exploit the dependence of mechanical, acoustic, electrical, and magnetic characteristics of the material on the state of stress [2–4]. One particular theory that attracted most of the attention is the acoustoelastic theory; the dependence of propagating waves characteristics on the state of stress [5–9]. Acoustoelastic-based methods involve introducing a low energy, high frequency stress wave in the material and analyzing its propagation and reflections to evaluate the state of stress in the structure. It has been established that dispersion relations depend on the initial state of stress in the structure. For a plane wave propagating in a plate under biaxial stress, in a direction that makes an angle θ with the 11 direction, the change in ultrasonic plane wave velocity with the application of stress can be expressed as [1]:

$$\frac{\Delta C_p(\theta)}{C_p^0(\theta)} = (K_1\sigma_{11} + K_2\sigma_{22})\cos^2(\theta) + (K_3\sigma_{11} + K_4\sigma_{22})\sin^2(\theta), \tag{7.1}$$

where ΔC_p is the change in phase velocity due to the application of stress, C_p^0 is the stress-free phase velocity, θ is the direction of wave propagation in the principal coordinate system, σ_{11} and σ_{22} are the principal stresses, and the constants

M.I. Albakri (✉) • P.A. Tarazaga
Vibration, Adaptive Structures and Testing Laboratory, Virginia Tech, 635 Prices Fork Road, Blacksburg, VA 24061, USA
e-mail: malbakri@vt.edu

S. Pakzad, C. Juan (eds.), *Dynamics of Civil Structures, Volume 2*, Conference Proceedings of the Society for Experimental Mechanics Series, DOI 10.1007/978-3-319-29751-4_7

$K_1, \ldots, K_4$, are the acoustoelastic constants for the particular wave mode. Changes in phase velocity are typically determined based on Time-of-Flight (T.O.F) measurements. Successful implementation of T.O.F-based wave speed measurements requires dispersion effects to be minimal. Therefore, high frequency excitations are normally utilized. At such frequency ranges, changes in ultrasonic wave speed are in the order of 10^{-6} per MPa [1]. Hence, T.O.F has to be measured with a nanosecond accuracy, requiring an extremely high sampling rate. Furthermore, uncertainties associated with noise contamination, ultrasonic attenuation, along with dispersion effects adversely affect the accuracy with which T.O.F can be determined, which in turn results in high uncertainty in the measured stress state.

In this work, a novel acoustoelastic-based stress measurement technique is developed by combining dispersion compensation algorithms and numerical optimization schemes. Dispersion compensation allows the use of highly-stress-sensitive, low-frequency flexural waves for stress measurement, which in turn enhances the sensitivity of the developed technique. The need for accurate T.O.F measurements is eliminated in this work by analyzing the entire propagated waveform to reconstruct the dispersion curve over the frequency range of interest. A criterion for optimal selection of excitation waveform is also developed in this work. The effects of material properties uncertainties on the accuracy of stress measurements are investigated through a number of numerical experiments.

7.2 Model Development

An Euler-Bernoulli beam subjected to an axial load is shown in Fig. 7.1. Considering a segment in the deformed configuration, which is shown in the magnified part of the figure, the axial load appears as an additional moment term in the equation of motion [10]:

$$\rho A \frac{\partial^2 v}{\partial t^2} + EI \frac{\partial^4 v}{\partial x^4} - F_x \frac{\partial^2 v}{\partial x^2} = 0, \tag{7.2}$$

where $v = v(x,t)$, is the lateral deflection of the beam, F_x is a constant axial force acting on the beam, ρ, A, and EI are the beam's density, cross sectional area, and flexural rigidity, respectively. In frequency domain, a general solution of the following form can be assumed for the lateral displacement:

$$v(x,t) = \frac{1}{N} \sum_{n=0}^{N-1} \sum_{m} A_m \; e^{-ik_{mn}x} \, e^{i\omega_n t}, \tag{7.3}$$

where k_{mn} is the wave number corresponding to the m^{th} mode at the n^{th} angular frequency ω_n, $\boldsymbol{A} \in \mathbb{R}^{1\times m}$ is the amplitude vector for the Fourier coefficients in frequency domain, and N is the number of spectral components considered in the discrete Fourier transform, with $N/2$ being the Nyquist frequency. Substituting in the equation of motion yields the following characteristic equation:

$$EIk^4 + F_x k^2 - \rho A \omega^2 = 0, \tag{7.4}$$

which is the dispersion relation describing the dependence of wavenumbers on frequency. The subscripts m and n are dropped for brevity. Based on this relation, group velocity, denoted by C_{gr}, for each mode can be calculated at different levels of axial

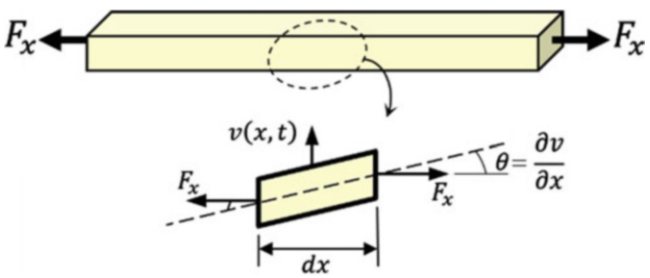

Fig. 7.1 Schematic of Euler-Bernoulli beam with axial loading. A differential element for equation of motion derivation is also shown

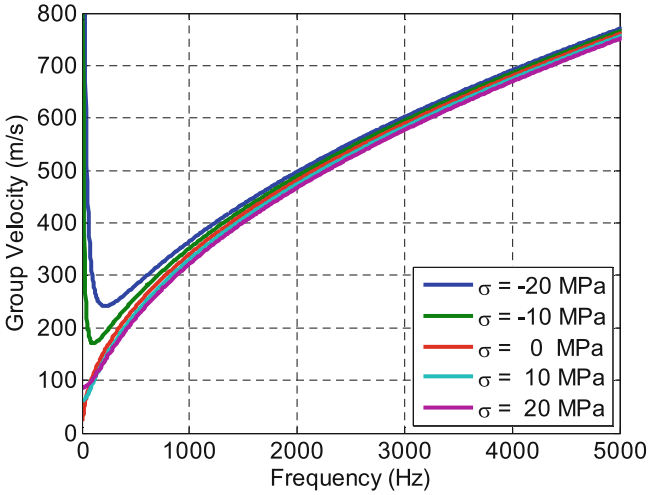

Fig. 7.2 Group velocity of flexural waves at different levels of axial loading

loading as:

$$C_{gr} = \frac{\partial \omega}{\partial k} = \left(\frac{2EI}{\rho A} k^2 + \frac{\sigma_{xx}}{\rho} \right) \frac{k}{\omega}. \tag{7.5}$$

Figure 7.2 shows the dependence of group velocity on both frequency and loading state. These curves are calculated for a 2 in. wide, 1/8 in. thick aluminum beam, with 69 GPa modulus of elasticity, and 2750 kg/m^3 density. The results suggest that the low frequency range is the most sensitive to axial loading, however, dispersion effects are most profound there, which renders T.O.F-based measurements impractical.

To tackle the problem of wave propagation in dispersive media, an optimization-based algorithm is developed. This algorithm back calculates the loading state by minimizing the discrepancy between a compensated waveform and the original excitation. In this study, the distance between excitation and measurement locations are assumed to be known a priori. This assumption will be relaxed in later studies to account for the variations in excitation and measurement locations resulting from the finite deformations induced by the applied state of stress. In its simplest form, the algorithm starts with an initial guess of the external loading state acting on the structure under consideration. Based on the acoustoelastic theory, dispersion curves are calculated for the assumed loading state and compared to that calculated from the propagating waveform. An error function is then evaluated, and loading state is updated along the directions minimizing this error function. Once converged, the algorithm provides an estimate of the loading state acting on the structure.

7.3 Results and Discussion

In this section, the effects of excitation waveform on the stress measurements are investigated, and a criterion for selecting optimal excitation waveform and frequency is developed. The effects of material properties uncertainties on the accuracy of stress measurements are then briefly investigated.

7.3.1 Excitation Signal Selection

The fundamental principle of all acoustoelastic methods is to introduce a low energy stress wave in the material and analyze its propagation and reflections to evaluate the state of stress in the structure. Therefore, excitation signal type and frequency content play a key role in such methods. Besides determining the frequency range over which the structure is interrogated and information is retrieved, the type of the excitation signal, along with the structure's material and geometric characteristics, determines how reflections interfere with the measured response. Successful implementation of acoustoelastic methods

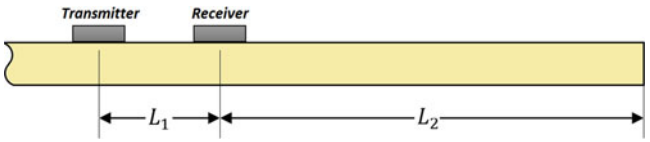

Fig. 7.3 Schematic of a beam with a transmitter–receiver pair showing the separation distance between the transducers and the boundaries

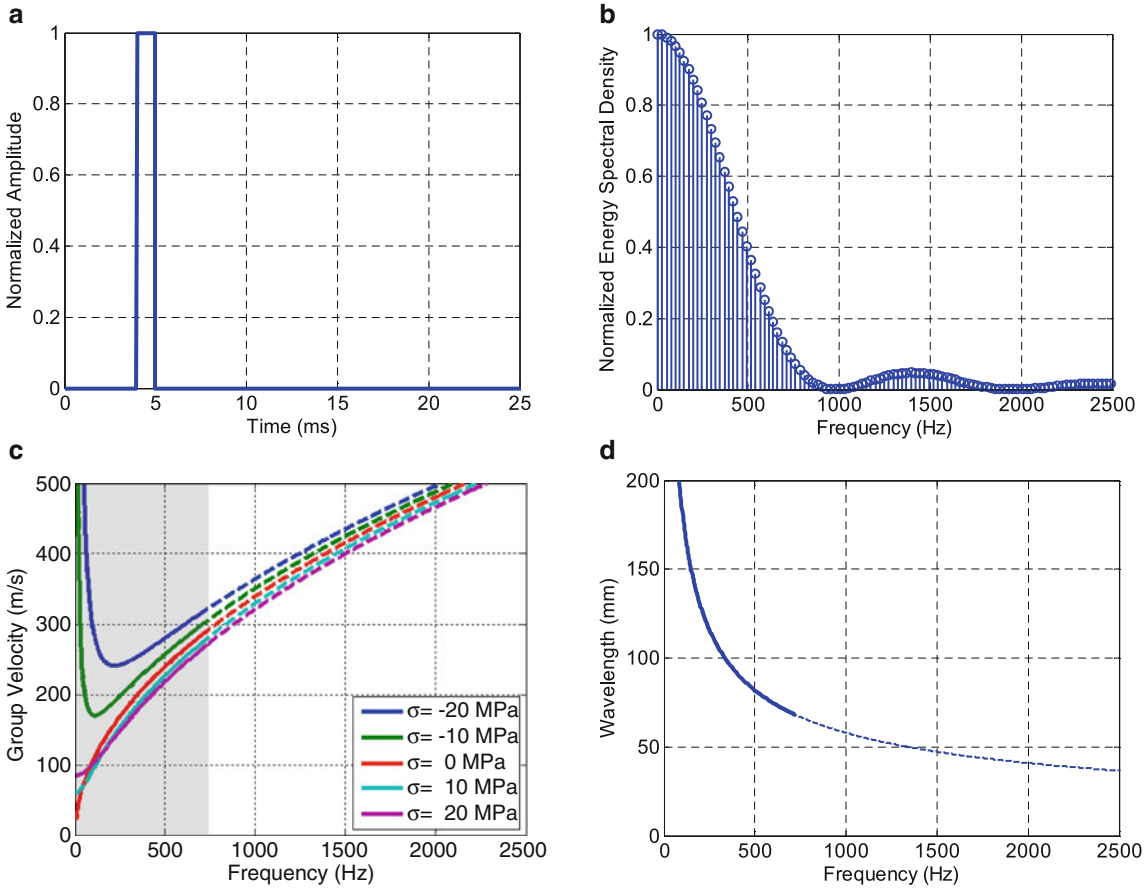

Fig. 7.4 A 1 ms duration pulse. (**a**) Waveform, (**b**) energy spectral density, (**c**) dispersion curves, and (**d**) wavelength. The shaded area in (**c**) and the solid thick line in (**d**) highlight the range over which information are carried by this waveform

requires a reflections-free measurement of the propagating wave. Let a transmitter/receiver pair be placed L_1 meters from each other, and the boundaries of the structure under consideration are L_2 meters form the receiver, as shown in Fig. 7.3. In order to obtain a reflections-free response at the receiver, the following simple relation needs to be satisfied:

$$\frac{L_1 + 2L_2}{v_{max}} > \frac{L_1 + n\lambda_{max}}{v_{min}}, \tag{7.6}$$

where v_{max} and v_{min} are respectively the maximum and minimum wave speeds in the frequency range of interest, λ_{max} is the maximum wavelength in the frequency range, which is normally associated with v_{min}, and n is the number of cycles of the excitation signal.

Several excitation signal types are investigated in this section, including a square pulse, a 2-cycle tone burst, and a 2-cycle tone burst with a Hanning window. Figure 7.4 shows the waveform of a 1 ms duration square pulse, along with its energy spectral density, group velocity and wavelength. Impulse excitations, such as hammer impacts, are known to have a low frequency content, as shown in Fig. 7.4b. This low frequency content makes it difficult to get a reflections-free response in a finite structures with low damping, as the high frequency components propagate much faster than the low frequency components, as shown in Fig. 7.4c. Therefore, pulses and impacts are unsuitable for the problem at hand, as the measured

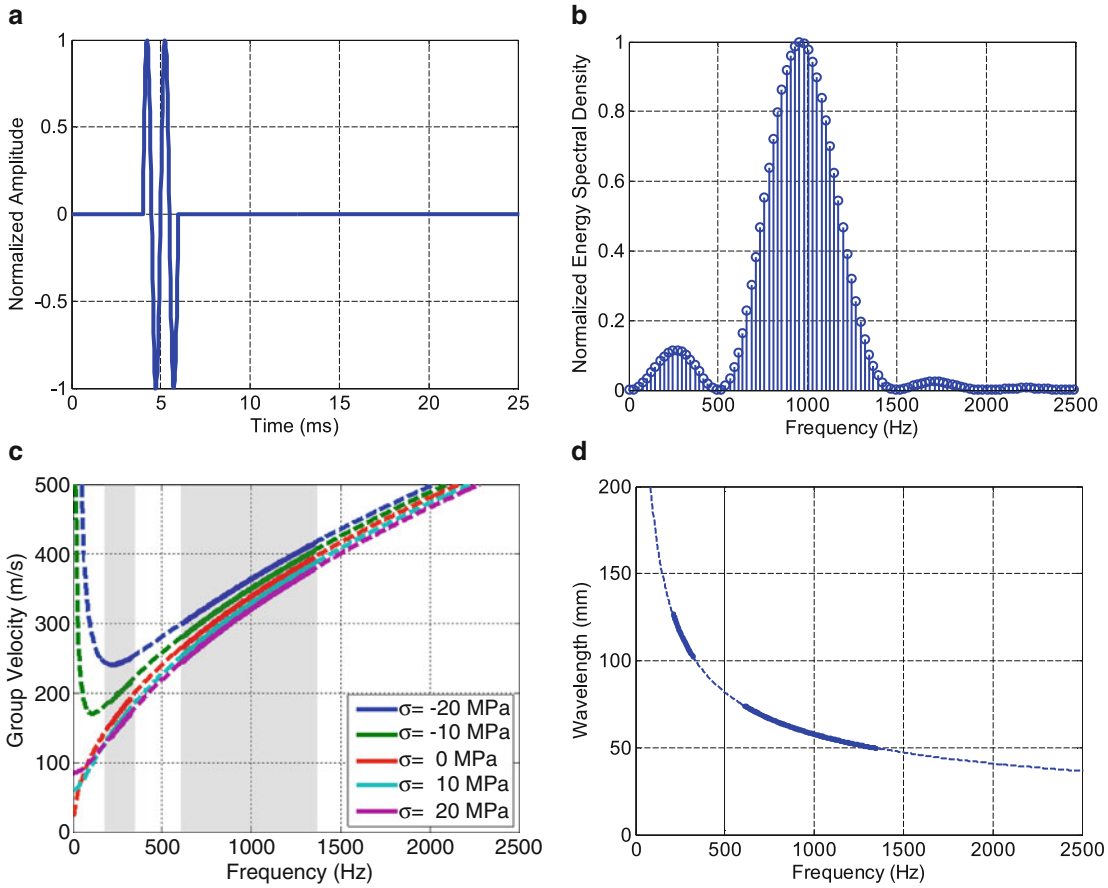

Fig. 7.5 A 1 kHz sinewave tone burst of two cycles. (**a**) Waveform, (**b**) energy spectral density, (**c**) dispersion curves, and (**d**) wavelength. The shaded area in (**c**) and the solid thick line in (**d**) highlight the range over which information are carried by this waveform

response will be always contaminated with reflections, or missing some low frequency components, which adversely affects the accuracy of the stress measurement algorithm.

For the two-cycle, 1 kHz sinewave excitation signal, shown in Fig. 7.5a, energy is mostly contained in a relatively narrow band centered at the excitation main frequency. However, there is a small fraction of the energy carried by significantly lower frequencies, as shown in Fig. 7.5b. Dispersion information carried by such signals are highlighted by the shaded area in Fig. 7.5c. As shown in the figure, this excitation signal provides information about dispersion relations around the main frequency, the 1 kHz in this case, as well as a narrow band of lower frequency content. This discontinuity in energy spectrum and the carried dispersion information increases the minimum length for reflections-free response, L_2 in Eq. (7.6), since λ_{max} and v_{min} are those coming from the low frequency band. Furthermore, since signal energy is spread over several frequency bands, noise contamination is expected to be significant, which adversely affects stress measurements.

A more confined energy spectrum can be achieved by adding a Hanning window to the previous signal, as shown in Fig. 7.6a, b. This eliminates the small, low-frequency energy band noticed in the previous case, and hence, information carried by this signal is limited to a single band centered at the main excitation frequency, as shown in Fig. 7.6c. Assuming the distance between the transmitter and the receiver, L_1, is 0.1 m, the minimum length for reflections-free response, L_2, is found to be 0.174 m. This distance is calculated for the unloaded case, where v_{min} and v_{max} are found to be 242.9 m/s and 415.4 m/s, respectively, and $\lambda_{max} = 0.081\ m$, as shown in Fig. 7.6c, d.

For a given configuration, L_1 and L_2, an optimal excitation signal for stress measurement can be determined. Using an n-cycle tone burst with a Hanning window, the design space includes two main parameters: the center frequency (f_c), and the number of cycles (n). Engineering judgment suggests that 2 is the optimal value for n, as it yields the broadest continuous frequency band, and minimizes the constraints on L_2. The former enhances the accuracy of the stress measurement algorithm, as it provides more information about dispersion relations, while the later allows for a wider reflections-free window. For optimal sensitivity to stress state, f_c is selected to be the lowest frequency for which the constraints defined by Eq. (7.6) are satisfied.

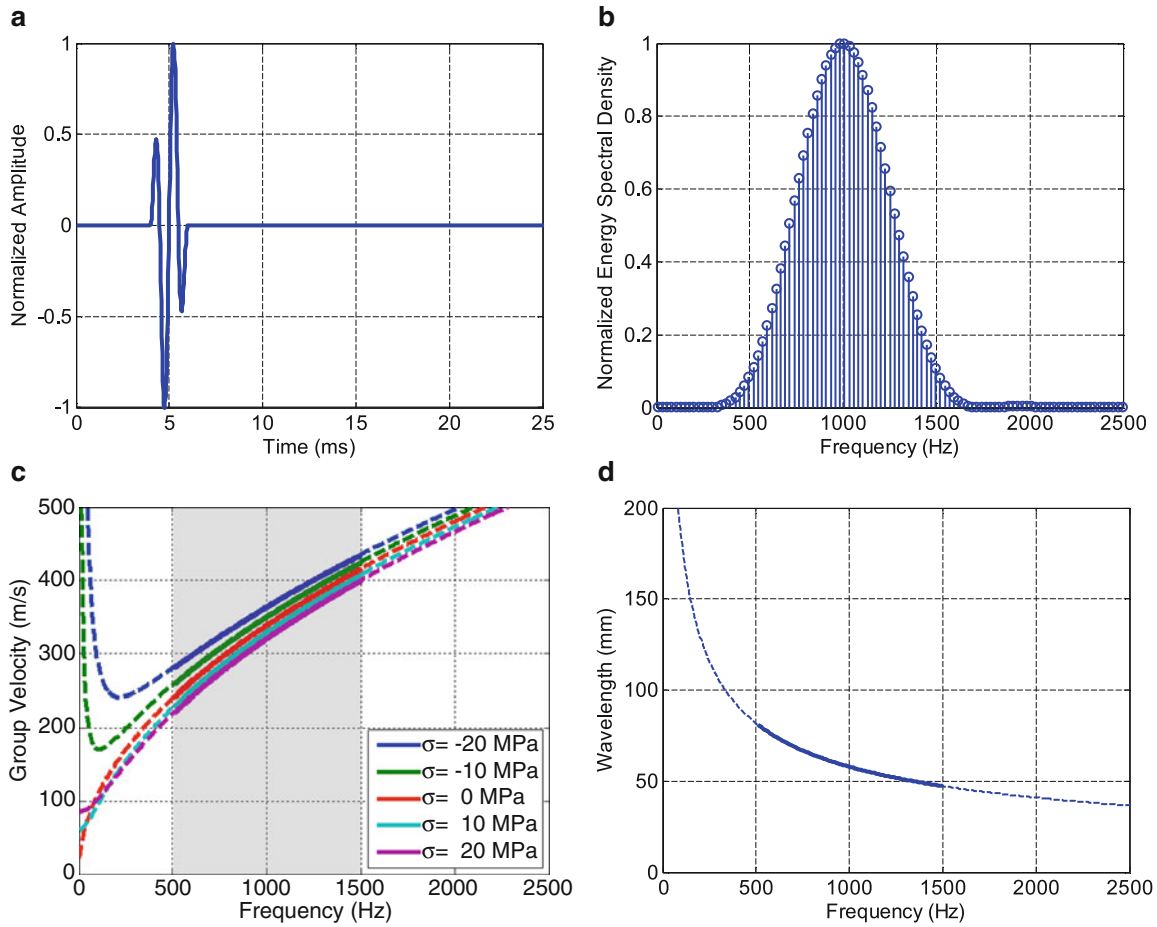

Fig. 7.6 An amplitude-modulated, 1 kHz, sinewave tone burst of two cycles. (**a**) Waveform, (**b**) energy spectral density, (**c**) dispersion curves, and (**d**) wavelength. The shaded area in (**c**) and the solid thick line in (**d**) highlight the range over which information are carried by this waveform

7.3.2 Effects of Uncertainties in Material Properties

Acoustoelastic-based stress monitoring techniques are in general model based. Hence, a prior knowledge of the structure under consideration, in terms of geometry and material characteristics, is necessary to accurately correlate changes in wave speed to the state of stress. In this section, the effects of uncertainties in material properties, namely the Young's modulus of elasticity, on stress measurement accuracy are investigated. The developed technique calculates the loading state by minimizing an error function that quantifies the discrepancy between theoretically derived dispersion curves and that calculated using the propagating waveform. Based on the results presented in Sect. 7.3.1, a 2-cycle sinewave tone burst with a Hanning window is used to excite the structure. Three center frequencies are investigated: 100, 500, and 1000 Hz. For each case, the energy spectral density of the excitation signal is calculated, and an active frequency band is defined by selecting those frequencies with a normalized energy density of 0.05 or greater. For all three cases, the initial state of stress in the structure is assumed to be 15 MPa. The state of stress is then calculated utilizing the developed technique with several levels of Young's modulus uncertainty. The results are shown in Fig. 7.7. With the exact value of Young's modulus, the stress state measurement optimization algorithm is found to converge to the actual value, i.e. 15 MPa, regardless of the excitation frequency. As Young's modulus deviates from its exact value, errors in the calculated stress state increases, with error bounds being very dependent on the frequency content of the excitation signal.

For a relatively low excitation frequency, $f_c = 100$ Hz, the technique is of good robustness against material uncertainties, as suggested by Fig. 7.7a. Upon convergence, the predicted state of stress is within 9 % of the actual value, even with uncertainty levels as high as 20 % in Young's modulus. As the excitation frequency increases, the robustness of stress-state calculations degrades, and small uncertainties in Young's modulus value results in a significant error in the calculated state of stress, as shown in Fig. 7.7b, c. Alternative objective function formulations to enhance technique's robustness will be investigated in later studies.

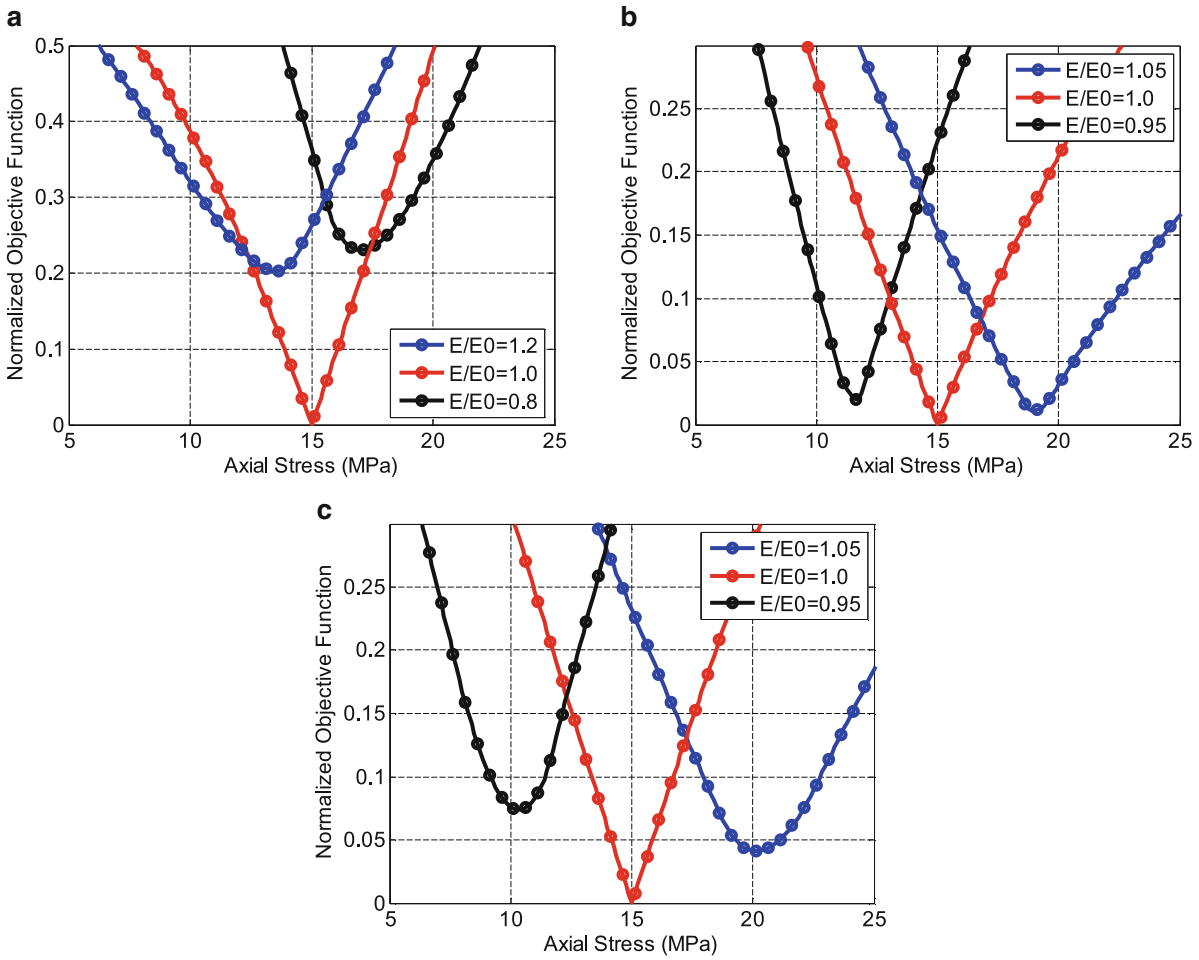

Fig. 7.7 Normalized error function values as a function of loading state and uncertainty in Young's modulus for (**a**) 100 Hz, (**b**) 500 Hz, and (**c**) 1 kHz excitation frequencies

The minimum length for reflections-free response, L_2, is calculated for the three center frequencies considered in this study by solving Eq. (7.6) with $L_1 = 0.1$ m and $n = 2$. Minimum length values are found to be 0.643 m, 0.265 m, and 0.174 m for the 100 Hz, 500 Hz and 1000 Hz cases, respectively. This indicates that the gained robustness at low frequency ranges comes at the cost of increased separation requirements between the transducers and the structure's boundaries. Several techniques for reflections suppression will be investigated in later studies to facilitate the use of low frequency excitations in geometrically constrained structures.

7.4 Conclusions

In this work, a novel acoustoelastic-based stress measurement technique is developed by combining dispersion compensation algorithms and numerical optimization schemes. The technique utilizes the highly-stress-sensitive, low-frequency, guided waves for stress measurement. Several excitation signals are investigated in this paper, and a criterion for optimal selection of excitation waveform is developed taking into consideration sensitivity to the state of stress and reflections contamination. The effects of uncertainties in material properties on the accuracy of stress measurements are also investigated. It has been found that the technique is very robust when low frequency excitations are utilized. However, this gained robustness comes at the cost of increased separation requirements between the transducers and structure's boundaries.

Acknowledgments The authors are grateful for the support of the Association of American Railroads.

References

1. Hauk, V.: Structural and Residual Stress Analysis by Nondestructive Methods: Evaluation-Application-Assessment. Elsevier, Amsterdam (1997)
2. Schneider, E., Altpeter, I., Theiner, W.: Nondestructive determination of residual and applied stress by micro-magnetic and ultrasonic methods. In: Nondestructive Methods for Material Property Determination, pp. 115–122. Springer, Berlin (1984)
3. Sanderson, R.M., Shen, Y.C.: Measurement of residual stress using laser-generated ultrasound. Int. J. Pres. Ves. Pip. **87**(12), 762–765 (2010)
4. Rossini, N.S., Dassisti, M., Benyounis, K.Y., Olabi, A.G.: Methods of measuring residual stresses in components. Mater. Des. **35**, 572–588 (2012)
5. Hayes, M.: Wave propagation and uniqueness in prestressed elastic solids. Proc. R. Soc. Lond. Math. Phys. Eng. Sci. **274**(1359), 500–506 (1963)
6. Guz, A.N.: On foundations of the ultrasonic nondestructive method for determination of stresses in near-surface layers of solid bodies. Int. Appl. Mech. **41**(8), 944–955 (2005)
7. Chaki, S., Bourse, G.: Guided ultrasonic waves for non-destructive monitoring of the stress levels in prestressed steel strands. Ultrasonics **49**(2), 162–171 (2009)
8. Shi, F., Michaels, J.E., Lee, S.J.: In situ estimation of applied biaxial loads with Lamb waves. J. Acoust. Soc. Am. **133**(2), 677–687 (2013)
9. Szelążek, J.: Sets of piezoelectric probeheads for stress evaluation with subsurface waves. J. Nondestruct. Eval. **32**(2), 188–199 (2013)
10. Doyle, J.F.: Wave Propagation in Structures: Spectral Analysis Using Fast Discrete Fourier Transforms, 2nd edn. Springer, New York (1997)

Chapter 8
A Machine Learning Framework for Automated Functionality Monitoring of Movable Bridges

Masoud Malekzadeh and F. Necati Catbas

Abstract Functionality of movable bridge highly depends on the performance of the mechanical components including gearbox and motor. Therefore, on-going maintenance of these components are extremely important for uninterrupted operation of movable bridges. Unfortunately, there have been only a few studies on monitoring of mechanical components of movable bridges. As a result, in this study, a statistical framework is proposed for continuous maintenance monitoring of the mechanical components. The efficiency of this framework is verified using long-term data that has been collected from both gearbox and motor of a movable bridge. In the first step, critical features are extracted from massive amount of Structural Health Monitoring (SHM) data. Next, these critical features are analyzed using Moving Principal Component Analysis (MPCA) and a condition-sensitive index is calculated. In order to study the efficiency of this framework, critical maintenance issues have been extracted from the maintenance reports prepared by the maintenance personnel and compared against the calculated condition index. It has been shown that there is a strong correlation between the critical maintenance actions, reported individually by maintenance personnel, and the condition index calculated by proposed framework and SHM data. The framework is tested for the gearbox.

Keywords Structural health monitoring • Machine learning • Big data • Movable bridge • Automated condition monitoring

8.1 Introduction

Obtaining reliable and timely assessments of bridge condition, performance and safety throughout increasingly longer service lives represents a considerable challenge for bridge owners, engineers and the Federal Highway Administration (FHWA). The ability to quantitatively characterize existing bridges may lead to more cost-effective and efficient maintenance management decisions, and more robust evaluations of structural safety. Presently, the long-term performance and condition of most bridges are evaluated on the basis of biennial visual inspection data. Visual inspection data are inherently qualitative and are subject to other important limitations that can hamper their effectiveness for assessing bridge performance and safety.

A study by the FHWA on the reliability of visual inspection [1] revealed many of the uncertainties associated with this assessment approach. Structural Health Monitoring (SHM) is an emerging approach that has gained significant attention because it promises to enable more quantitative, reliable and timely assessments of bridge condition and performance than are possible using only visual inspection data [2, 3].

The health status of structures is under threat from several sources including environmental effects, overload, design and construction issues. Proximity to waterways, mechanical system failure and fatigue due to the stress fluctuations during the operation make the situation even worse for movable bridges. As a consequence, there is an unavoidable progressively demand for monitoring the behavior of such a structures over time [2] . Operational monitoring of the most critical machinery components of movable bridges will provide information about any possible issues associated with mechanical and electrical parts of these structures. Subsequently, the maintenance plan can be rescheduled and maximized in light of such information to enhance the service life of the structure. Furthermore, the design code for movable bridges can be revised and promoted based upon the data captured from the monitoring system.

M. Malekzadeh
Metal Fatigue Solutions, 7251 West Lake Mead Boulevard Suite 300, Las Vegas, NV 89128, USA
e-mail: m.malekzadeh@knights.ucf.edu

F.N. Catbas (✉)
Department of Civil, Environmental and Construction Engineering, University of Central Florida, Orlando, FL 32816, USA
e-mail: catbas@ucf.edu

S. Pakzad, C. Juan (eds.), *Dynamics of Civil Structures, Volume 2*, Conference Proceedings of the Society for Experimental Mechanics Series, DOI 10.1007/978-3-319-29751-4_8

In this study, an analysis of the maintenance reports is conducted in order to compare and correlate the monitoring data with the maintenance records. The objective of this paper is to propose and evaluate a framework for long-term condition assessment of the machinery components including the gearbox.

8.2 Structural Health Monitoring System for Sunrise Bridge

8.2.1 Mechanical Monitoring System

A total of 160 sensors (adding up to more than 200 channels) were deployed to the bridge for monitoring the electrical, mechanical and structural components as well as collecting environmental data. The electrical and mechanical components were monitored with accelerometers, strain rosettes, tiltmeters, microphones, infrared temperature sensors, ampmeters, video cameras, and pressure gages [2]. Structural components were mainly monitored with accelerometers, high speed strain gages and slow speed vibrating wire strain gages. A video camera detecting the traffic to correlate it with other measurements was also installed. Finally, a weather station was installed to measure wind speed, wind direction, humidity, temperature, barometric pressure, and rain. The data acquisition system (DAQ) was controlled by two computers, which were synchronized by using a GPS and wireless Internet communication. Data collection and processing on each leaf of the bridge were handled by the two DAQs. All the dynamic sensors were connected to one of the two National Instruments SCXI 1001 chassis with its corresponding modules. In this study the focus is on mechanical component and in particular gearbox component.

8.2.1.1 Gearbox

The gearbox, also called the transmission, uses gears to provide speed and torque conversion from a rotating power source to another device. The gearbox is equipped to serve the necessary amount of oil to the various gear meshes and bearings, thereby resulting in smooth and trouble-free operation, Fig. 8.1. The gearbox should be regularly checked for any leaks to see if it has enough oil. In this research, the gearbox has been instrumented with six accelerometers in order to monitor the vibration level (Fig. 8.1).

8.3 A Machine Learning Framework for Long-Term Assessment of Machinery Components

8.3.1 Moving Principal Component Analysis (MCA)

Principal component analysis (PCA) is a multivariate statistical process for transferring a number of possibly correlated variables into a smaller number of uncorrelated variables, called principal components. In fact, by transferring the data into the lower dimension (uncorrelated variable) space, the redundancy in the data is reduced. In other words, in order to reduce the redundancy in the collected data and extract the valuable information, the data has to be converted into the space in which the variables are not correlated.

In order to make PCA more feasible for processing large amount of data, MPCA has been developed [4–6]. In order to conduct MPCA, principal component analysis is conducted for each of the fixed-size moving window and the corresponding covariance matrix is computed. After computing the covariance matrix, the corresponding eigenvalues and eigenvectors are extracted. The derived damage indices that are considered for this study are based on the time history of the first eigenvector and the corresponding coefficient between original and principal variables. As results, the number of damage indices is equal to the number of original variables (sensors). Thus, in the first step, the time history of the raw data captured from each sensor is assigned to individual columns of a matrix called matrix of data. Afterward, a fixed-size moving window is defined based on the characteristics of the available data (for instance, periodicity). Then, the covariance matrices are computed for individual windows. Subsequently, eigenvectors and eigenvalues are extracted for the corresponding covariance matrix. Lastly, the damage indices are calculated based on the time history of the first eigenvector. These damage indices are then studied in order to monitor the performance of the machinery component of the movable bridge.

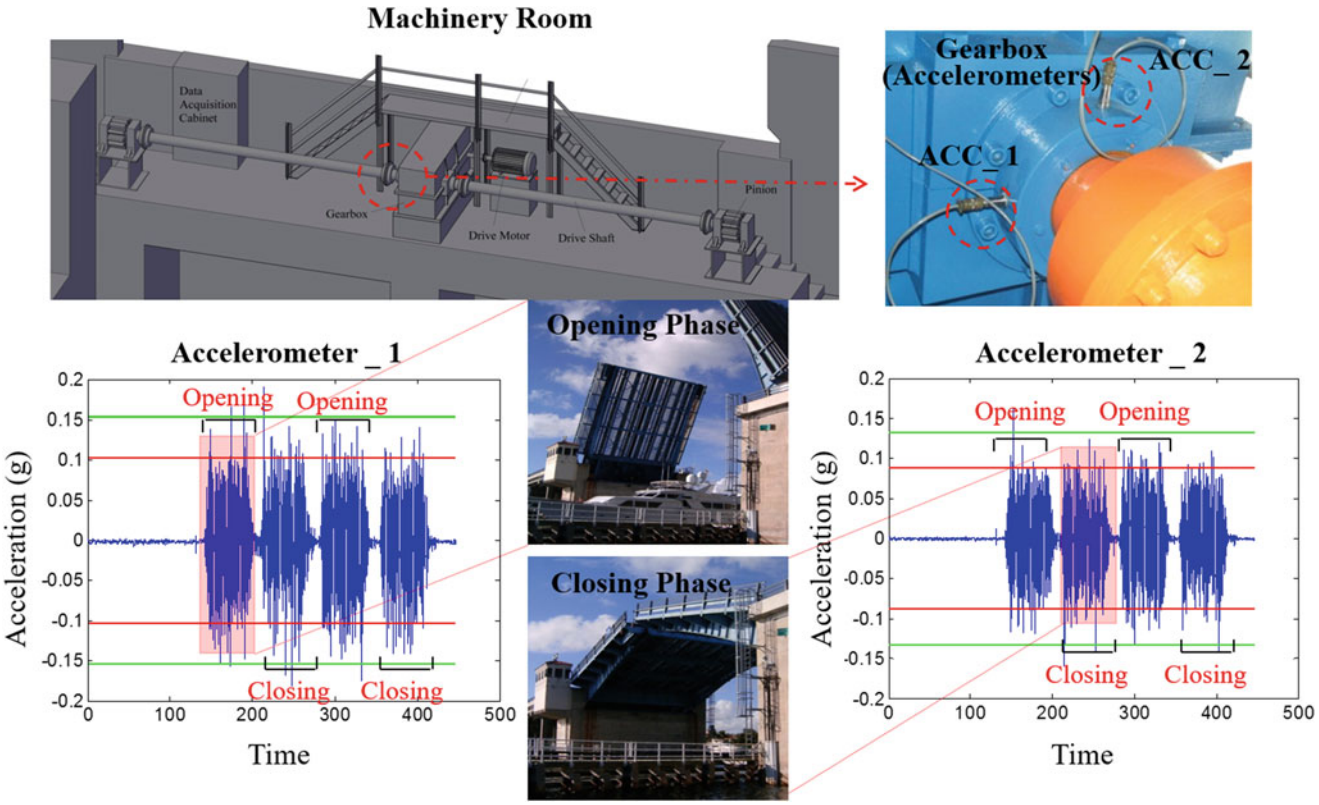

Fig. 8.1 Overview of the Bridge, Monitoring System and the Data

8.3.2 The Proposed Framework for Long-Term Monitoring

When it comes to long-term condition monitoring of machinery components, compiling the raw data from all openings over years results in a very large data matrix, massive amount of SHM data, which is quite time consuming to analyze. In fact, it is not practical to continuously monitor the gearbox or rack and pinion systems with traditional principal component analysis. Therefore, the MPCA algorithm requires some modification to render it practical for continuous monitoring. A new approach is proposed in order to make the existing algorithm more appropriate for long-term monitoring applications. The steps described in the following sections are proposed to generate the main data matrix. It should be noted that after the main data matrix is formed, the rest of the procedure is the same as explained in Sect. 8.3.1.

Four individual statistical features including maximum vibration (average of the ten largest values to avoid outliers) and minimum vibration (average of the ten minimum values to avoid outliers), standard deviation of opening data sets, and finally root mean square of signals are extracted from raw acceleration data. These features can be expressed as follows:

$$Feature1\ (Max) = \frac{\sum_{i=1}^{10} Sort\ (\text{Opening data}, 'descend')(i)}{10} \tag{8.1}$$

$$Feature2\ (Min) = \frac{\sum_{i=1}^{10} Sort\ (\text{Opening data}, 'ascend')(i)}{10} \tag{8.2}$$

$$Feature3\ (Stdev) = \sqrt{\frac{1}{N}\sum_{i=1}^{N}(x_i - \bar{x})^2} \tag{8.3}$$

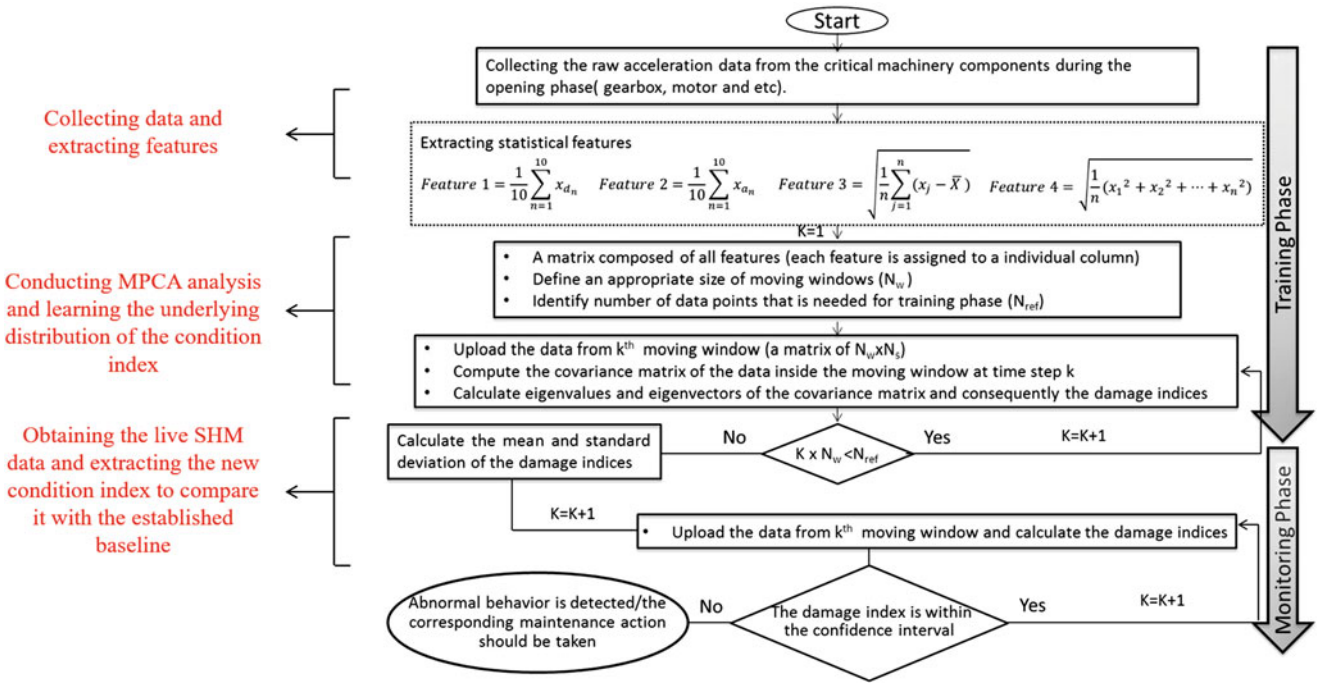

Fig. 8.2 Flowchart for Data Analysis

$$Feature4\ (Rms) = \sqrt{\frac{1}{N}\left(x^2{}_1 + x^2{}_2 + \cdots + x^2{}_n\right)} \tag{8.4}$$

The main data matrix is assembled by a continuous statistical analysis of opening data sets collected from the machinery components. Subsequently, the MPCA algorithm is applied to this matrix to extract the damage index. This process is illustrated in Fig. 8.2, which divides the algorithm into two distinct stages: the training phase and the monitoring phase. Throughout the training phase, the algorithm develops a confidence interval for the baseline condition. In other words, a threshold is established based on the data (eigenvector values) from the healthy state. In the first step, the raw acceleration data was collected from opening phase of movable bridge. Afterward, four of the aforementioned statistical features were extracted and stored over a long period of time.

The main matrix is generated by assigning the time series of each individual feature to a column. The next step is to define the size of appropriate window, which is supposed to move forward along the time dimension. The PCA analysis is performed for each window of data during the training phase and subsequently the eigenvalues and eigenvectors are stored. The next critical step is to establish a confidence interval or a threshold for healthy state based on the eigenvector values from training period. Any variations to the threshold or the confidence interval observed in the monitoring phase are considered to indicate changes or damage. These steps are illustrated by the flowchart shown in Fig. 8.3.

8.3.3 Long-Term Condition Monitoring of Gearbox

8.3.3.1 Analysis of the Maintenance Report

In order to compare and correlate monitoring data and maintenance records, it is important to develop a numerical scheme for the maintenance actions. A preliminary study is conducted by evaluating the available maintenance and inspection reports from September 2009 to May 2013 that were obtained from the engineers and the maintenance personnel of the Sunrise Bridge. A total of 17 reports spanning over almost 4 years were analyzed to have a good understanding of the maintenance schedule and procedures at the Sunrise Blvd. bridge. The most critical actions were identified and categorized through inspection of the maintenance reports for each of the machinery components. In the following sections, the results of principal component analysis for the gearbox are discussed in more detail. The eigenvectors (for gearbox) are also correlated with maintenance actions.

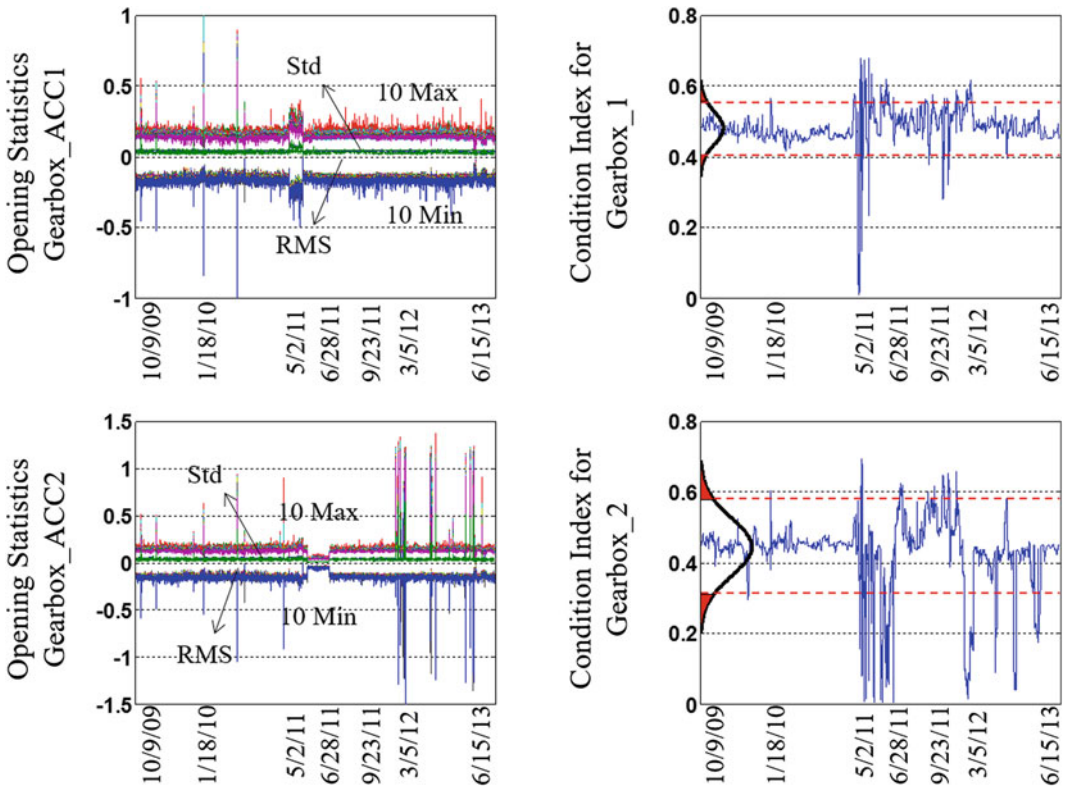

Fig. 8.3 Long term Raw Data and the PCA Results

8.3.3.2 Correlation of Eigenvector and Gearbox Maintenance Actions

Time series of eigenvector values is calculated according to the procedure explained in Sect. 8.3.2. The results for the gearbox are shown in Fig. 8.3 in which the time series of statistical features are plotted against the time history of eigenvectors for each individual gearbox accelerometer. As observed from Fig. 8.3, all the calculated eigenvectors demonstrate the abnormal behavior between May 2, 2011 and March 5, 2012. In other words, all eigenvectors are consistent with each other in terms of normal conditions and abnormal behavior. As a result, the eigenvector correspondent to the third accelerometer (Acc3) was selected as the most informative one and subsequently was studied in more detail along with maintenance reports. The results are demonstrated in Fig. 8.4.

The idea was to investigate the correlation of eigenvector values and the maintenance actions extracted from maintenance reports. It is concluded that the variations in eigenvector values show good consistency with the major maintenance actions applied to the gearbox component over the past 4 years. In effect, it is shown that time series of eigenvectors is an appropriate index for the purpose of gearbox (in general, machinery components) condition assessment. Any variations in the values of this index can be correlated to a major action occurring to the gearbox.

In order to automate the process of machinery condition assessment for the movable bridge, a confidence interval was established based on the value of index during the period of October 9, 2009 and January 5, 2010 (training phase). The values of the index are confined within the confidence interval between October 9, 2009 and May 1, 2011 except for a few points, which were due to the issues with the gearbox component during this timeframe.

It is obvious from Fig. 8.4 that the index values exceeded the confidence interval on January 13, 2010. The abnormal behavior continued until January 18, 2010 when the index values shifted back to the normal condition. This anomaly in behavior was further investigated through the maintenance report where it was realized that on January 18, 2010 the gear reducer break was replaced by FDOT maintenance personnel. The ID that is assigned to this action is A, and it is shown in Fig. 8.4.

It should be noted that the bridge maintenance personnel were not able to detect this issue until January 18, 2010, which was almost 5 days after the abnormal gearbox behavior began. The SHM system was able to identify and detect this malfunction immediately after it occurred. Indeed, this malfunction could result in a major problem and the timely detection of this kind of gearbox issue is very critical for the continuous operation of the entire movable bridge.

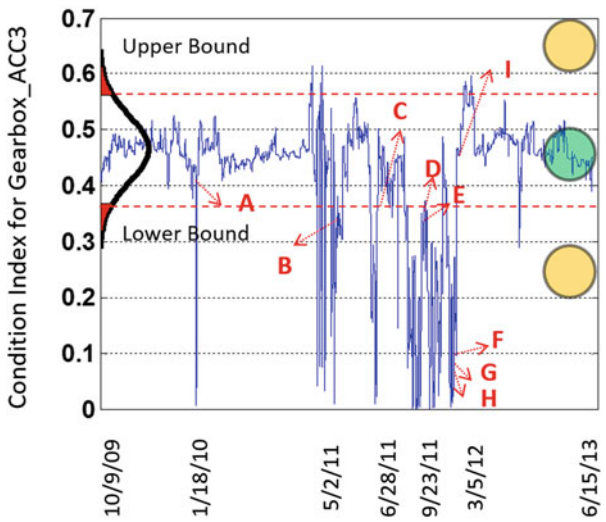

Point ID	Date	Maintenance Action
A	1/18/2010	Replace Gear Reducer Break as Needed
B	5/2/2011	Replace West Span Gear Box Input Shaft Seal
C	6/28/2011	Replace output shaft seal on West Gearbox
D	9/21/2011	Check F.A. Span Motor for Motor Replacement
E	9/23/2011	Check F.A. Span Motor for Motor Replacement
F	9/26/2011	Removed Brake on F.A. Span Motor
G	9/27/2011	F.A. Span Motor Bearing trouble shoot
H	9/28/2011	The Motor was Repaired
I	3/5/2012	Replace Gearboxes Breaks

94

Fig. 8.4 PCA Results Compared with Maintenance Report and Inspections

After the gear reducer brake was replaced, the gearbox operated in a normal range until April 24, 2010 at which time the index started fluctuating again. Inspection of the maintenance reports indicated that on May 2, 2011 the input shaft seal had been replaced for the gearbox. The input shaft seal for the west gearbox had a major issues that began around April 24, 2010 and because of that the index exceeded the confidence interval. However, similar to the first issue, it was detected almost 1 year after the occurrence, which could result in a major problem as well.

After replacing the input shaft seal for the west gearbox, the index changed back again to the normal range for a short period of time. However, on June 17, 2011 (6 weeks) the index again went beyond the developed confidence interval.

Analysis of maintenance reports for the Sunrise Blvd. Bridge indicated that on June 28, 2011 the output shaft seal was replaced for the west gearbox. After changing the input shaft seal on May 2, 2011, this time (June 28, 2011) the output shaft seal had a major issue and accordingly it was replaced by a new one. The SHM system was able to detect this issue on June 17, 2011, which is almost 10 days ahead of maintenance personnel. This timely detection highlights the advantage of implementing the SHM system for condition assessment of critical components. Having output shaft seal replaced, the index changed back to the normal condition again. However, after a short period of normal operation, the gearbox experienced another major issue, which caused a dramatic alteration in the value of the condition index. This time the problem was not due to the gearbox, but instead the motor which is connected directly to it had an operational issue. There are several notes in the report from September 21, 2011 until September 27, 2011 related to the motor's abnormal behavior. There were some serious problem associated with the motor including bearing and brake issues. As it is clearly noticed from Fig. 8.4, these functionality issues in the motor resulted in operational abnormality in the gearbox during that period.

Finally on March 5, 2012 the gearbox brakes were replaced by new ones allowing the condition index to change back to the normal range. After this point the gearbox operated in normal condition for more than 1 year (until June 15, 2013) and the index continued bounded within the confidence interval, meaning that there were not any critical issues related to the gearbox.

8.4 Conclusion

The machinery components are critical elements for the functionality of the movable bridges. As a consequence, the continuous condition assessment of these components is necessary. In this study the efficiency of implementing SHM system for tracking the condition of the components including gearbox has been explored. For the purpose, the Sunrise Blvd. Bridge has been selected and heavily instrumented with various types of sensors. Accordingly the data has been collected over the past 4 years from all the mechanical and structural components of the bridge. The proposed data interpretation methodology has been evaluated along with the maintenance actions that were extracted from the maintenance reports (logs). The reports have been prepared and documented by the FDOT maintenance personnel for more than 4 years. The maintenance reports have been investigated and the critical maintenance action have been extracted and classified for the corresponding mechanical components. The condition indices were interpreted through the critical maintenance actions in order to test the reliability of the indices. The condition indices were found very meaningful in terms of being consistent with the extracted maintenance actions for gearbox.

References

1. Phares, B.M., Washer, G.A., Rolander, D.D., Graybeal, B.A., Moore, M.: Routine highway bridge inspection condition documentation accuracy and reliability. J. Bridge Eng. **9**(4), 403–413 (2004)
2. Catbas, F.N., Malekzadeh, M., Khuc, T.: Movable Bridge Maintenance Monitoring. Florida Department of Transportation, Tallahassee (2013)
3. Malekzadeh, M., Atia, G., Catbas, F.N.: Performance-based structural health monitoring through an innovative hybrid data interpretation framework. J. Civ. Struct. Heal. Monit. **5**(3), 287–305 (2015)
4. Catbas, N., Malekzadeh, M., Gul, M., Kwon, I.B.: An integrated approach for structural health monitoring using an in-house built fiber optic system and non-parametric data analysis. Smart Struct. Syst. **14**(5), 917 (2014)
5. Malekzadeh, M., Catbas, F.N.: A comparative evaluation of two statistical analysis methods for damage detection using fibre optic sensor data. Int. J. Reliab. Saf. **8**(2–4), 135–155 (2014)
6. Laory, I., Trinh, T.N., Smith, I.F.: Evaluating two model-free data interpretation methods for measurements that are influenced by temperature. Adv. Eng. Inf. **25**(3), 495–506 (2011)

Chapter 9
Non-Model-Based Damage Identification of Plates Using Curvature Mode Shapes

Y.F. Xu and W.D. Zhu

Abstract Mode shapes (MSs) have been extensively used to identify structural damage. This paper presents a new non-model-based method that uses principal, mean and Gaussian curvature MSs (CMSs) to identify damage in plates. A multi-scale discrete differential-geometry scheme is proposed to calculate principal, mean and Gaussian CMSs associated with a MS of a plate, which can alleviate adverse effects of measurement noise on calculating the CMSs. Principal, mean and Gaussian CMSs of a damaged plate and those of an undamaged one are used to yield four curvature damage indices (CDIs), including Maximum-CDIs, Minimum-CDIs, Mean-CDIs and Gaussian-CDIs. Damage can be identified near regions with consistently higher values of the CDIs. It is shown that a MS of an undamaged plate can be well approximated using a polynomial with a properly determined order that fits a MS of a damaged one. New fitting and convergence indices are proposed to quantify the level of approximation of a MS from a polynomial fit to that of a damaged plate and to determine the proper order of the polynomial fit, respectively. The proposed method is numerically applied to MSs of an aluminum plate with damage in the form of a thickness reduction area to investigate its effectiveness; the damage on the plate is successfully identified.

Keywords Damage identification • Plate • Curvature mode shape • Mode shape approximation • Damage index

9.1 Introduction

Vibration-based damage detection has been a major research topic of structural dynamics in the past few decades. Measured modal characteristics, such as natural frequencies and mode shapes (MSs), are processed in various methods for detecting, locating and characterizing damage in structures, since modal characteristics are related to physical properties of structures, such as mass, stiffness and damping, which can change due to damage. A method can be categorized as a model-based or non-model-based method; the difference between them is that the former requires use of a precise model of a structure and the latter does not. A method that only requires a minimum amount of measured natural frequencies was developed to accurately detect locations and extent of damage in such structures as lightening masts [1, 2], space frames [3] and pipelines [4]. It is model-based and requires a precise physics-based model of a structure, and results of the method highly depend on the accuracy of the model of the structure. However, it can be difficult to construct models of most structures that can accurately predict their natural frequencies before and after occurrence of damage.

Methods that use measured MSs to identify damage in a structure can be good alternatives. While effects of damage on natural frequencies are global, those on MSs are local; abrupt changes in MSs in the neighborhood of damage can be observed. A two-dimensional gapped smoothing method was developed based on the one-dimensional gapped smoothing method [5]. CMSs and curvatures of operating deflection shapes (ODSs) were used in the two-dimensional method to identify damage in plates [6], where MSs of an undamaged plate were not needed. However, a gapped polynomial fitting the curvatures was used to eliminate global trends of CMSs and curvatures of ODSs at each measurement point; it was a local method and could be computationally inefficient, especially for a dense measurement grid. A method that used curvatures of frequency-shift surfaces of plates to identify damage was proposed in [7]; curvatures of frequency-shift surfaces of associated undamaged plates could be obtained using a technique of locally weighted regression. It was shown to be better than the two-dimensional gapped smoothing method, since a frequency-shift surface contained information of a squared MS. A CMS-based method was proposed in [8], where a CMS of a plate was processed using a wavelet transform and a Teager energy operator to eliminate adverse effects of measurement noise on calculating a CMS and global trends of the transformed CMS,

Y.F. Xu • W.D. Zhu (✉)
Department of Mechanical Engineering, University of Maryland, Baltimore County, Baltimore, MD 21250, USA
e-mail: wzhu@umbc.edu

S. Pakzad, C. Juan (eds.), *Dynamics of Civil Structures, Volume 2*, Conference Proceedings of the Society for Experimental Mechanics Series, DOI 10.1007/978-3-319-29751-4_9

respectively. Changes in curvatures of uniform-load surfaces were used to identify damage in plates; the curvatures were shown to be sensitive to presence of local damage, even with truncated, incomplete and noisy measurements [9]. The method used frequencies and MSs of the first few modes of the damaged and undamaged plates. A simplified gapped smoothing method, a generalized fractal dimension method and a strain energy method were used to process CMSs and curvatures of uniform-load surfaces to detect delamination in a composite plate [10]. Besides curvature-based methods, wavelet transform-based methods have been widely studied to identify damage in plates [11–13]. Gabor wavelets were used to identify damage in a rectangular plate [11]; effects of various wavelets on identifying damage, such as Haar, Daubechies, Gaussian and Coiflet wavelets, were studied and compared in [12]. Depths of cracks in plates could be detected using a wavelet transform-based method with the aid of models of undamaged plates [13]. However, whether damage can be identified using a wavelet transform-based method depends on the type and parameters of an applied wavelet. Changes in the strain energy of a structure have been used to identify damage; the method was extended from the one for beams [14]. It requires MSs of damaged and undamaged structures. A two-dimensional polynomial annihilation edge detection method was proposed for detection and localization of damage in plates [15]; it was extended from the one for beams, which can detect discontinuities in piecewise smooth functions and their derivatives [16].

A non-model-based method based on principal, mean and Gaussian CMSs is proposed in this work to identify damage in plates. Theoretical bases of principal CMSs of a plate are shown. A multi-scale discrete differential-geometry scheme is proposed to calculate principal, mean and Gaussian CMSs associated with a MS of a plate, which can alleviate adverse effects of measurement noise on calculating the CMSs. Differences between principal, mean and Gaussian CMSs of a damaged plate and those of the associated undamaged one are used to yield four curvature damage indices (CDIs), including Maximum-CDI, Minimum-CDI, Mean-CDI and Gaussian-CDI. A MS from a polynomial with a properly determined order that fits a MS of a damaged plate can be used to approximate the corresponding MS of the associated undamaged one, provided that the undamaged plate has a smooth geometry and is made of material that has no stiffness and mass discontinuities. New fitting and convergence indices are proposed to assist determination of the proper order of the polynomial. MSs of a damaged plate are used to investigate the effectiveness of the proposed method.

9.2 Methodology

A finite element (FE) model of a damaged rectangular steel plate that has a length of 0.3 m, a width of 0.4 m and a thickness of 0.002 m is constructed. The damage is in the form of a thickness reduction area, and its position and dimensions are shown in Fig. 9.1a; the depth of the thickness reduction area is 0.0002 m. The mass density, elastic modulus and Poisson's ratio of the plate are 7850 $\mathrm{kg/m^3}$, 200 GPa and 0.3, respectively. A FE model of an undamaged plate of the same dimensions and material properties is constructed. Undamped MSs of the damaged and undamaged plates associated with their 30-th modes are calculated and denoted by $\mathbf{Z}^{d,30}$ and $\mathbf{Z}^{u,30}$, respectively; $\mathbf{Z}^{d,30}$ and $\mathbf{Z}^{u,30}$ are in the same phase, and they are normalized so that their maximum absolute values are equal to one. MSs $\mathbf{Z}^{d,30}$ and $\mathbf{Z}^{u,30}$ are shown in Figs. 9.1b and c, respectively.

9.2.1 Principal CMSs of Plates

While the curvature at a point on a MS of a one-dimensional structure, such as a beam, is defined along the length of the structure, that on a MS of a plate is defined on a unit vector tangent to the MS at the point, and its value depends on the unit vector. The curvature at a point $\mathbf{p}$ on a MS $\mathbf{Z}$ shown in Fig. 9.2 with respect to a unit vector $\mathbf{v}$ tangent to $\mathbf{Z}$ at $\mathbf{p}$ is defined by O'neill [17]

$$\kappa_{\mathbf{Z},\mathbf{p}}(\mathbf{v}) = -(\nabla_{\mathbf{v}}\mathbf{n}) \cdot \mathbf{v} \tag{9.1}$$

where $\mathbf{n}$ is a unit normal vector field in the neighborhood of $\mathbf{p}$ on $\mathbf{Z}$, and $\nabla_{\mathbf{v}}\mathbf{n}$ is the covariant derivative of $\mathbf{n}$ with respect to $\mathbf{v}$, defined by

$$\nabla_{\mathbf{v}}\mathbf{n} = \frac{\mathrm{d}}{\mathrm{d}t}\mathbf{n}(\mathbf{p} + t\mathbf{v}) \tag{9.2}$$

The geometric meaning of the curvature is that it quantifies the bending rate of a curve $\boldsymbol{\sigma}$ on $\mathbf{Z}$ with respect to $\mathbf{n}$; $\boldsymbol{\sigma}$ is obtained by intersecting $\mathbf{Z}$ with a plane that is determined by $\mathbf{n}$ and $\mathbf{v}$, as shown in Fig. 9.2. When $\mathbf{p}$ is an umbilic point, $\kappa_{\mathbf{Z},\mathbf{p}}$ are equal

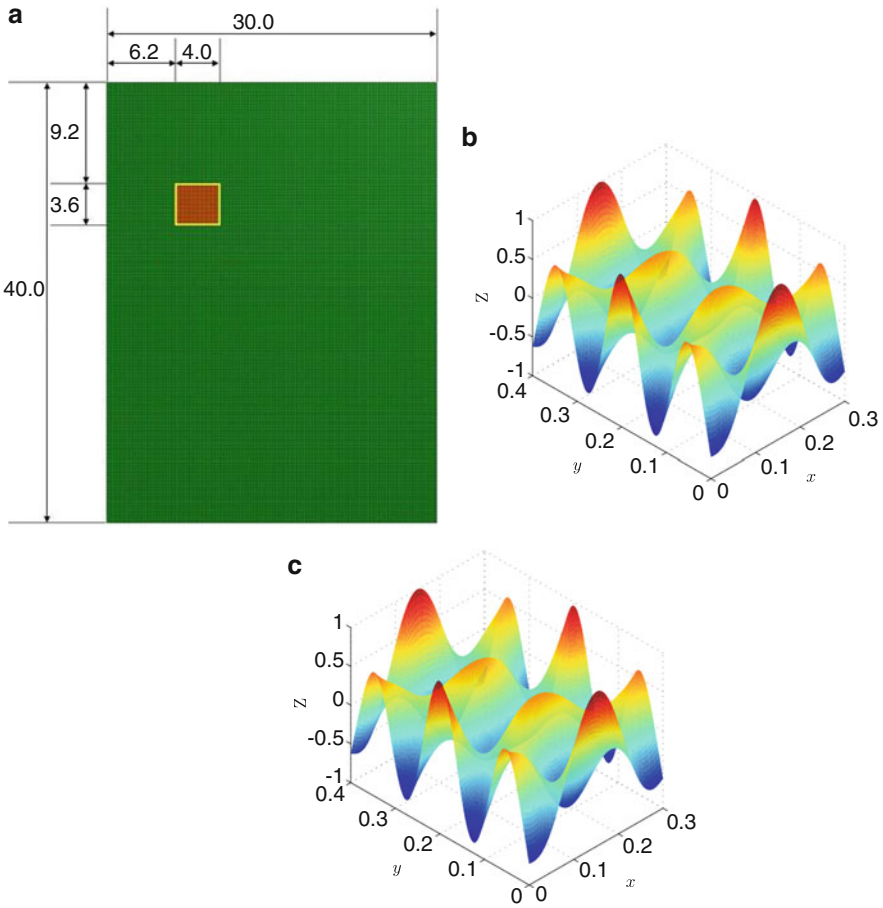

Fig. 9.1 (**a**) FE model of a plate with damage in the form of a thickness reduction area, (**b**) the 30-th MS of the damaged plate and (**c**) the 30-th MS of an undamaged plate of the same dimensions and material properties as the damaged one

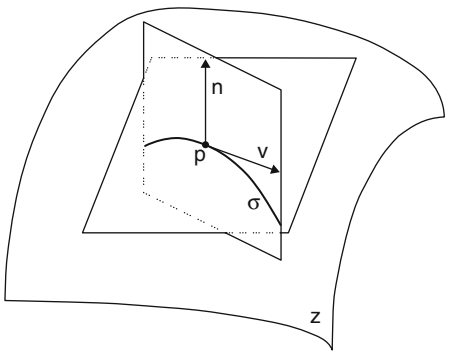

Fig. 9.2 Point **p** on a MS **Z**, a unit normal vector **n** and a unit tangent vector **v** associated with **p**, and a curve σ obtained by intersecting **Z** with the plane determined by **n** and **v**

to one value with any **v**. Examples of surfaces that consist of umbilic points are planes and spheres. More commonly for a MS, when **p** is a nonumbilic point, there are two orthogonal principal directions, along which $\kappa_{\mathbf{Z},\mathbf{p}}$ attains its maximum and minimum values, denoted by $\kappa_{\mathbf{Z},\mathbf{p}}^{\max}$ and $\kappa_{\mathbf{Z},\mathbf{p}}^{\min}$, respectively; the two curvatures, i.e., the maximum and minimum curvatures, are termed as principal curvatures. Shapes that are formed by maximum and minimum curvatures associated with a MS are termed as maximum and minimum CMSs, respectively, and they are principal CMSs.

For a constant-thickness plate made of homogeneous material, one has

$$\begin{bmatrix} M_{xx} \\ M_{yy} \\ M_{xy} \end{bmatrix} = \frac{Eh^3}{12\left(\nu^2-1\right)} \begin{bmatrix} 1 & \nu & 0 \\ \nu & 1 & 0 \\ 0 & 0 & \nu-1 \end{bmatrix} \begin{bmatrix} \kappa_{xx} \\ \kappa_{yy} \\ \kappa_{xy} \end{bmatrix} \tag{9.3}$$

where M_{xx} and M_{yy} are bending moments per unit length acting on edges of a differential element parallel to y- and x- axes of a global three-dimensional Cartesian coordinate $O-xyz$, respectively; M_{xy} is the twisting moment with respect to x- and y- axes; E, h and υ are the thickness, Young's modulus and Poisson's ratio of the plate, respectively; κ_{xx} and κ_{yy} are curvatures with respect to x- and y- axes, respectively; and κ_{xy} is the twist with respect to x- and y- axes. For a point $\mathbf{p}$ on the plate, a local Cartesian coordinate $\mathbf{p}-x'y'z'$ can be defined, where x'- and y'- axes are along principal directions associated with the maximum and minimum curvatures of $\mathbf{p}$ on $\mathbf{Z}$, respectively. In this case, associated $M_{x'y'}$ and $\kappa_{x'y'}$ vanish, and one has

$$\begin{cases} \kappa_{\mathbf{Z},\mathbf{p}}^{\mathrm{Max}} = -\frac{12}{Eh^3}\left(M_{x'x'} - \upsilon M_{y'y'}\right) \\ \kappa_{\mathbf{Z},\mathbf{p}}^{\mathrm{Min}} = -\frac{12}{Eh^3}\left(M_{y'y'} - \upsilon M_{x'x'}\right) \end{cases} \tag{9.4}$$

Principal curvatures can be used to construct a quadratic approximation of $\mathbf{Z}$ near $\mathbf{p}$. When υ in Eq. (9.1) is not on a principal direction, $\kappa_{\mathbf{Z},\mathbf{p}}$ can be expressed by

$$\kappa_{\mathbf{Z},\mathbf{p}}(\mathbf{v}) = \kappa_{\mathbf{Z},\mathbf{p}}^{\mathrm{Max}} \cos\vartheta_1 + \kappa_{\mathbf{Z},\mathbf{p}}^{\mathrm{Min}} \cos\vartheta_2 \tag{9.5}$$

where ϑ_1 and ϑ_2 are angles between $\mathbf{v}$ and principal directions associated with the maximum and minimum curvatures, respectively. Hence, principal curvatures can be considered to be properties of $\mathbf{Z}$ at $\mathbf{p}$ that are independent of $\mathbf{v}$.

9.2.2 Multi-Scale Discrete Differential-Geometry Scheme

When $\mathbf{Z}$ can be analytically expressed, principal CMSs can be calculated using a well-established analytical method [17]. When $\mathbf{Z}$ cannot be analytically expressed and is presented in a discrete form, a numerical scheme is needed to calculate discrete principal CMSs associated with $\mathbf{Z}$. For a one-dimensional structure, a discrete CMS can be accurately calculated using a finite difference scheme. Discrete principal CMSs associated with $\mathbf{Z}$ cannot be easily calculated in that $\kappa_{\mathbf{Z},\mathbf{p}}$ depends on $\mathbf{v}$ in Eq. (9.1) and there are an infinite number of $\mathbf{v}$ at $\mathbf{p}$. One can perform a one-dimensional finite difference scheme at the point along different $\mathbf{v}$ to calculate curvatures and find principal curvatures as the maximum and minimum values among resulting curvatures, but it can be computationally inefficient.

To efficiently and accurately calculate principal CMSs associated with $\mathbf{Z}$, a numerical scheme in [18] for shapes with a triangulated mesh is introduced. The scheme includes two operators that can be used to calculate mean and Gaussian curvatures of a point $\mathbf{p}$, denoted by $H_{\mathbf{Z},\mathbf{p}}$ and $G_{\mathbf{Z},\mathbf{p}}$, respectively. Mean and Gaussian curvatures of $\mathbf{Z}$ at $\mathbf{p}$ are the average and product of two principal curvatures of $\mathbf{Z}$ at $\mathbf{p}$, respectively, which can be expressed by

$$H_{\mathbf{Z},\mathbf{p}} = \frac{\kappa_{\mathbf{Z},\mathbf{p}}^{\mathrm{Max}} + \kappa_{\mathbf{Z},\mathbf{p}}^{\mathrm{Min}}}{2} \tag{9.6}$$

and

$$G_{\mathbf{Z},\mathbf{p}} = \kappa_{\mathbf{Z},\mathbf{p}}^{\mathrm{Max}} \times \kappa_{\mathbf{Z},\mathbf{p}}^{\mathrm{Min}} \tag{9.7}$$

Shapes that are formed by mean and Gaussian curvatures associated with a MS are termed as mean and Gaussian CMSs, respectively. In the operators for mean and Gaussian curvatures of $\mathbf{p}$ on $\mathbf{Z}$ with a triangulated mesh, a new surface area $A_{\mathbf{P}}$ is calculated for a one-ring neighborhood associated with $\mathbf{p}$, which is formed by all triangulated elements of the mesh consisting of $\mathbf{p}$, as shown in Fig. 9.3a. The pseudo-code for calculating $A_{\mathbf{P}}$ is shown in Fig. 9.4, where the Voronoi area of an acute triangle $\triangle\mathbf{pqr}$ shown in Fig. 9.3b can be expressed by

$$A_{\mathrm{Voronoi}} = \frac{1}{8}\left(|\mathbf{pr}|^2 \cot\angle\mathbf{q} + |\mathbf{pq}|^2 \cot\angle\mathbf{r}\right) \tag{9.8}$$

and A is the area of a triangle in the one-ring neighborhood. Mean and Gaussian curvatures of $\mathbf{p}$ on $\mathbf{Z}$ can be calculated by

$$H_{\mathbf{Z},\mathbf{p}} = \frac{1}{4A_{\mathbf{P}}}\left[\sum_{i\in N_1(\mathbf{p})}\left(\cot\alpha_i + \cot\beta_i\right)\left(\mathbf{p}-\mathbf{r}_i\right)\right]\cdot\mathbf{n}(\mathbf{p}) \tag{9.9}$$

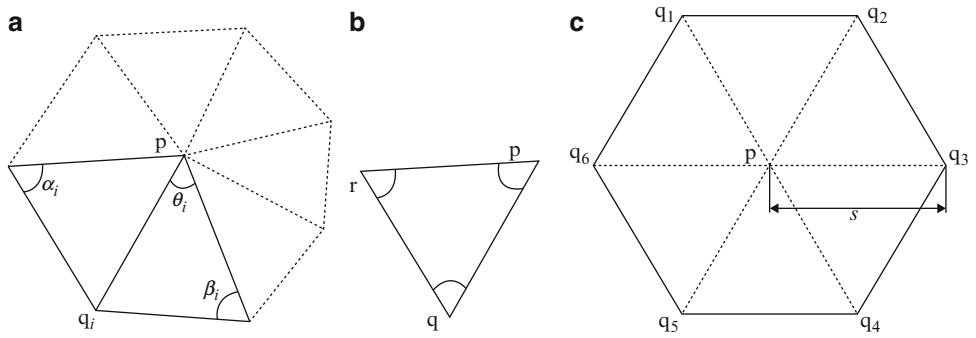

Fig. 9.3 (**a**) One-ring neighborhood of a triangulated mesh associated with **p**, (**b**) an acute triangle $\triangle$**pqr** and (**c**) a hexagon one-ring neighborhood with a side length of s

$A_{\mathbf{P}} = 0$
For each triangle in the one-ring neighborhood of $\mathbf{p}$
  If the triangle is acute,
    $A_{\mathbf{P}} = A_{\mathbf{P}} + A_{\text{Voronoi}}$
  Else
    If $\angle\mathbf{p}$ is obtuse
      $A_{\mathbf{P}} = A_{\mathbf{P}} + \frac{A}{2}$
    Else
      $A_{\mathbf{P}} = A_{\mathbf{P}} + \frac{A}{4}$

Fig. 9.4 Pseudo-code for calculating the new surface area $A_{\mathbf{p}}$ associated with **p**

and

$$G_{\mathbf{Z},\mathbf{p}} = \frac{2\pi - \sum_{i\in N_1(\mathbf{p})} \theta_i}{A_{\mathbf{P}}} \tag{9.10}$$

where $N_1(\mathbf{p})$ is the number of points that are connected with **p** in the one-ring neighborhood, and θ_i is the angle associated with $\mathbf{q}_i$, as shown in Fig. 9.3a. With calculated $H_{\mathbf{Z},\mathbf{p}}$ and $G_{\mathbf{Z},\mathbf{p}}$, principal curvatures at **p** can be calculated by

$$\kappa^{\text{Max}}_{\mathbf{Z},\mathbf{p}} = H_{\mathbf{Z},\mathbf{p}} + \sqrt{G_{\mathbf{Z},\mathbf{p}} - H_{\mathbf{Z},\mathbf{p}}} \tag{9.11}$$

and

$$\kappa^{\text{Min}}_{\mathbf{Z},\mathbf{p}} = H_{\mathbf{Z},\mathbf{p}} - \sqrt{G_{\mathbf{Z},\mathbf{p}} - H_{\mathbf{Z},\mathbf{p}}} \tag{9.12}$$

Similar to calculating curvatures of a one-dimensional structure, that of a MS of a plate can be jeopardized by measurement noise. To alleviate adverse effects of measurement noise on the operators introduced above, a hexagon one-ring neighborhood that has a side length of s associated with each measurement point is constructed for the operators. The hexagon one-ring neighborhood associated with **p** projected onto the undeformed plate is equilateral, as shown in Fig. 9.3c. Coordinates of $\mathbf{q}_i$ of the hexagon one-ring neighborhood, where $i = 1, 2, \ldots, 6$, are obtained from interpolation based on **Z**. For a measured MS with an unknown noise level, one needs to progressively test different values of s from smaller to larger ones. A proper value of s is the one with which the resulting CMS becomes smooth and has a clear global trend.

To illustrate adverse effects of measurement noise and the effectiveness of the scheme, white noise is added to $\mathbf{Z}^{d,30}$ with a signal-to-noise ratio (SNR) of 60 db to simulate measurement noise. Maximum CMSs associated with $\mathbf{Z}^{d,30}$ from the scheme with $s = 0.002$, 0.005 and 0.015 are shown in Fig. 9.5a through c, respectively; the maximum CMS associated with noise-free $\mathbf{Z}^{d,30}$ is shown in Fig. 9.5d. It can be seen that measurement noise is amplified and becomes dominant in the resulting maximum CMS from the scheme with $s = 0.002$, since differences between the value of a noise-free $\mathbf{Z}^{d,30}$ at a point and those in the hexagon one-ring neighborhood with a side length of s are small compared with those associated with a noisy $\mathbf{Z}^{d,30}$. Figures 9.5b and c show that maximum CMSs can be obtained with a lower noise level with a larger value of s. Though

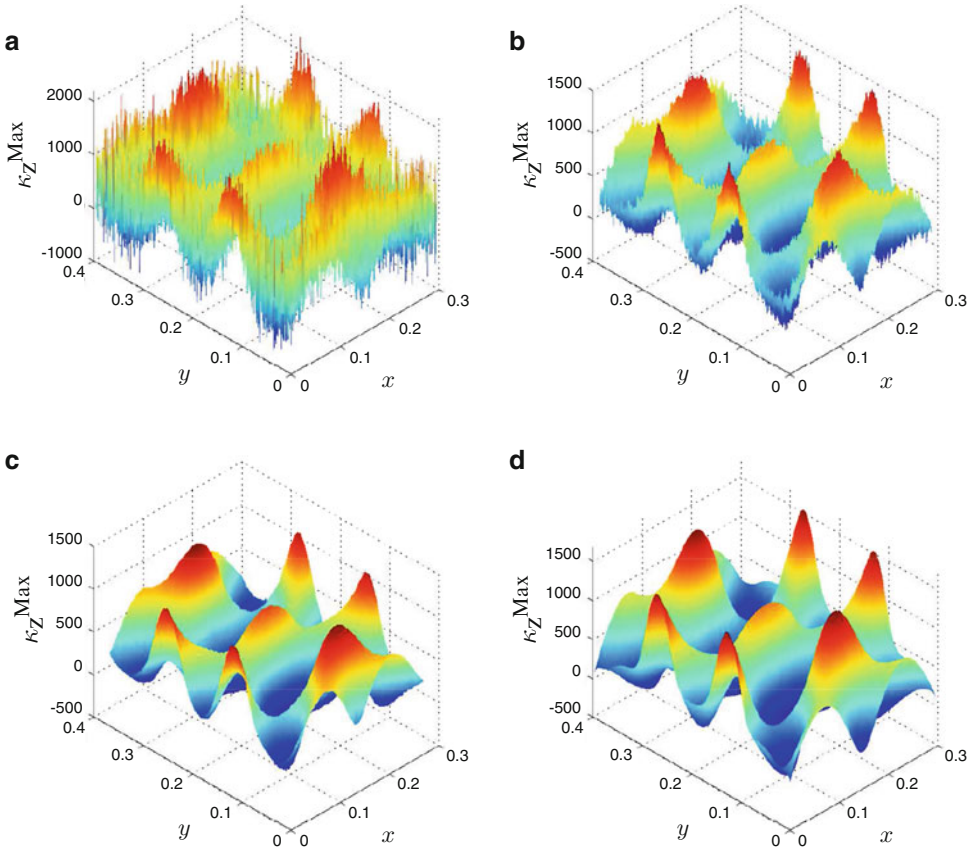

Fig. 9.5 Maximum CMSs associated with $\mathbf{Z}^{d,30}$ with measurement noise from the scheme with (**a**) $s = 0.002$, (**b**) $s = 0.005$ and (**c**) $s = 0.015$; (**d**) the maximum CMS associated with noise-free $\mathbf{Z}^{d,30}$ from the scheme with $s = 0.002$

maximum curvatures of $\mathbf{Z}^{d,30}$ at a point from the scheme with different values of s are different from those associated with noise-free $\mathbf{Z}^{d,30}$ at the point from the scheme with $s = 0.002$, global trends of the maximum CMSs are retained; the larger the value of s, the lower the noise level in the resulting maximum CMS, which is also the case for minimum, mean and Gaussian CMSs.

9.2.3 CMS-Based Damage Indices

CMSs have been widely used to identify damage in beams, since the curvature at a point on a beam can be expressed by

$$v'' = \frac{M}{EI} \tag{9.13}$$

where v'' is the curvature at the point, M is the bending moment applied at the point, and EI is the bending stiffness of the cross-section at the point. Since damage can introduce reduction in EI in its neighborhood, the magnitude of v'' increases in the neighborhood of the damage compared with that of the undamaged beam. Differences between v" associated with the damaged and undamaged beams can be used for identifying the damage. When E in Eq. (9.4) changes in the neighborhood of damage in a plate, magnitudes of principal curvatures in the neighborhood of the damage would change, and so would those of mean and Gaussian curvatures. Hence, differences between principal, mean and Gaussian CMSs associated with the damaged and undamaged plates can be used for identifying damage in a plate. Four CDIs associated with a MS of a plate are proposed to identify damage; for each point on the plate, the CDIs are listed below:

1. **Maximum-CDI.** A Maximum-CDI denoted by $\delta^{\text{Max}}(\mathbf{p})$ is defined by

$$\delta^{\text{Max}}(\mathbf{p}) = \left(\kappa^{\text{Max}}_{\mathbf{Z}^d,\mathbf{p}} - \kappa^{\text{Max}}_{\mathbf{Z}^u,\mathbf{p}}\right)^2 \tag{9.14}$$

2. **Minimum-CDI.** A Minimum-CDI denoted by $\delta^{\text{Min}}(\mathbf{p})$ is defined by

$$\delta^{\text{Min}}(\mathbf{p}) = \left(\kappa^{\text{Min}}_{\mathbf{Z}^d,\mathbf{p}} - \kappa^{\text{Min}}_{\mathbf{Z}^u,\mathbf{p}}\right)^2 \tag{9.15}$$

3. **Mean-CDI.** A Mean-CDI denoted by $\delta^{\text{Mean}}(\mathbf{p})$ is defined by

$$\delta^{\text{Mean}}(\mathbf{p}) = \left(H_{\mathbf{Z}^d,\mathbf{p}} - H_{\mathbf{Z}^u,\mathbf{p}}\right)^2 \tag{9.16}$$

4. **Gaussian-CDI.** A Gaussian-CDI denoted by $\delta^{\text{Gaussian}}(\mathbf{p})$ is defined by

$$\delta^{\text{Gaussian}}(\mathbf{p}) = \left(G_{\mathbf{Z}^d,\mathbf{p}} - G_{\mathbf{Z}^u,\mathbf{p}}\right)^2 \tag{9.17}$$

Maximum-CDIs, Minimum-CDIs, Mean-CDIs and Gaussian-CDIs associated with noise-free $\mathbf{Z}^{d,30}$ and $\mathbf{Z}^{u,30}$ from the scheme with $s = 0.002$ are shown in Fig. 9.6a through d, respectively. It can be seen that the damage can be identified near regions with high values of the CDIs.

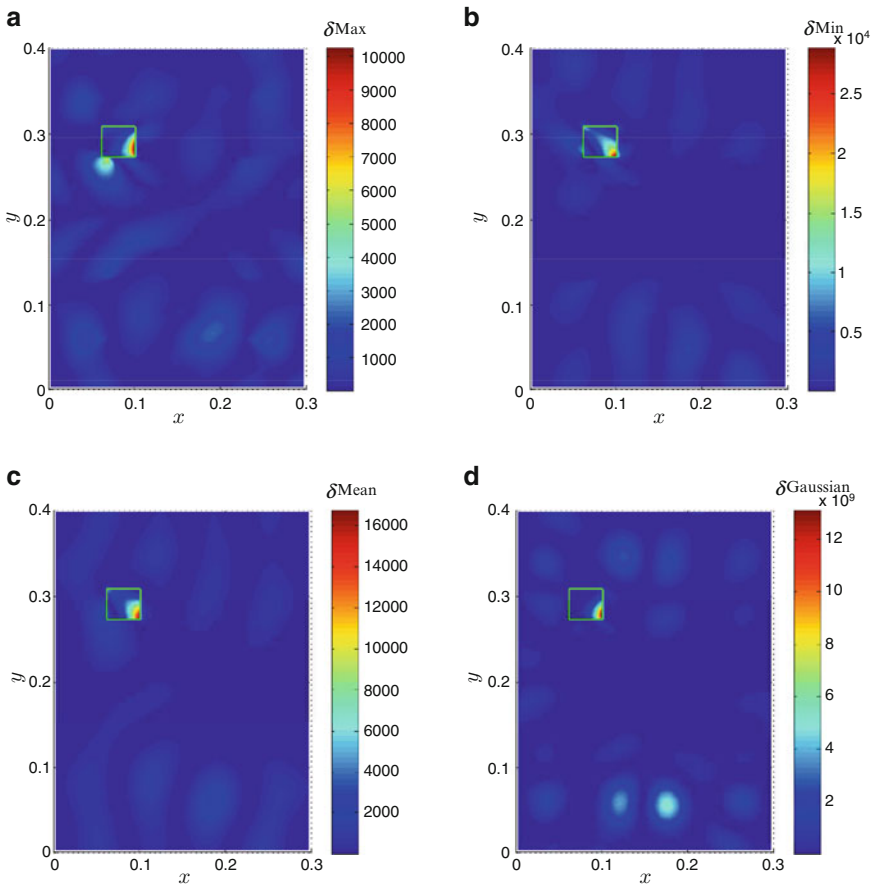

Fig. 9.6 (**a**) Maximum-CDIs, (**b**) Minimum-CDIs, (**c**) Mean-CDIs, and (**d**) Gaussian-CDIs associated with noise-free $\mathbf{Z}^{d,30}$ and $\mathbf{Z}^{u,30}$ from the scheme with $s = 0.002$

9.2.4 Approximation of MSs of an Undamaged Plate

While the CDIs proposed above can be used to identify damage in a plate, they require use of MSs of an undamaged plate, which are usually unavailable in practice. Assuming that existence of relatively small damage in a plate does not cause prominent changes in its MSs in the neighborhood of the damage, one can approximate MSs of the associated undamaged plate using polynomials that fit the corresponding MSs of the damaged plate, provided that the undamaged plate is geometrically smooth and made of materials that have no stiffness and mass discontinuities. The modal assurance criterion (MAC) value in percent between $\mathbf{Z}^{d,30}$ and $\mathbf{Z}^{u,30}$ is 99.85 %, which indicates that they are almost identical to each other and validates the assumption on the existence of relatively small damage. A similar technique has been proposed in [19] to approximate MSs of an undamaged beam using polynomials that fit the corresponding MSs of the damaged one. MSs of an undamaged plate corresponding to those of a damaged one are not measured in this work, and it is proposed that a MS of the undamaged plate be obtained from a polynomial of a properly determined order that fits the corresponding MS of the damaged plate:

$$z^p(x,y) = \sum_{k=0}^{n}\sum_{i=0}^{k} a_{i,k-i}x^i y^{k-i} \tag{9.18}$$

where n is the order of the polynomial, which controls the level of approximation of the polynomial fit to the MS of the damaged plate, (x, y) are coordinates of a point on an undeformed plate, and $a_{i,k-i}$ are coefficients of the polynomial that can be obtained by solving a linear equation

$$\mathbf{Va} = \mathbf{z} \tag{9.19}$$

in which $\mathbf{V}$ is the $N \times \left(\sum_{p=1}^{n+1} p\right)$-dimensional bivariate Vandermonde matrix with N being the dimension of $\mathbf{z}$, the Vandermonde matrix can be expressed by

$$\mathbf{V} = \begin{bmatrix} 1 & x_1 & y_1 & \dots & x_1^n & \dots & x_1^i y_1^{n-i} & \dots & y_1^n \\ 1 & x_2 & y_2 & \dots & x_2^n & \dots & x_2^i y_2^{n-i} & \dots & y_2^n \\ \vdots & \vdots & \vdots & \ddots & \vdots & \ddots & \vdots & \ddots & \vdots \\ 1 & x_N & y_N & \dots & x_N^n & \dots & x_N^i y_N^{n-i} & \dots & y_N^n \end{bmatrix} \tag{9.20}$$

$\mathbf{a} = \begin{bmatrix} a_{0,0} & a_{1,0} & a_{0,1} & \dots & a_{n,0} & \dots & a_{i,n-i} & \dots & a_{0,n} \end{bmatrix}^{\mathrm{T}}$ is the $\left(\sum_{p=1}^{n+1} p\right)$-dimensional coefficient vector, and $\mathbf{z}$ is the MS vector of the damaged plate to be fit. Solving Eq. (9.19) for the coefficient vector is equivalent to solving an unconstrained least-squares problem $\min \frac{1}{2}\|\mathbf{Va}^* - \mathbf{z}\|^2$ for an optimum minimizer $\mathbf{a}^*$ [20], which is usually an over-determined problem, i.e., $N > \sum_{p=1}^{n+1} p$. A solution can be obtained using the singular-value decomposition (SVD) of $\mathbf{V}$ [20], which gives

$$\mathbf{V} = \mathbf{U}\begin{bmatrix} S \\ 0 \end{bmatrix}\mathbf{W}^{\mathrm{T}} \tag{9.21}$$

where $\mathbf{U}$ and $\mathbf{W}$ are $N \times N$ and $\left(\sum_{p=1}^{n+1} p\right) \times \left(\sum_{p=1}^{n+1} p\right)$ orthogonal matrices, respectively, and $\mathbf{S}$ is a $\left(\sum_{p=1}^{n+1} p\right) \times \left(\sum_{p=1}^{n+1} p\right)$ diagonal matrix. An optimum minimizer $\mathbf{a}^*$ based on the SVD of $\mathbf{V}$ can be obtained by

$$\mathbf{a}^* = \mathbf{WS}^{-1}\mathbf{U}_1^{\mathrm{T}}\mathbf{z} \tag{9.22}$$

where $\mathbf{U}_1$ is the first $\sum_{p=1}^{n+1} p$ columns of $\mathbf{U}$. When n in Eq. (9.18) becomes a large value, $\mathbf{S}$ can be ill-conditioned, which can result in a low level of approximation of the associated polynomial fit. To avoid ill-conditioning of $\mathbf{S}$, it is proposed that x

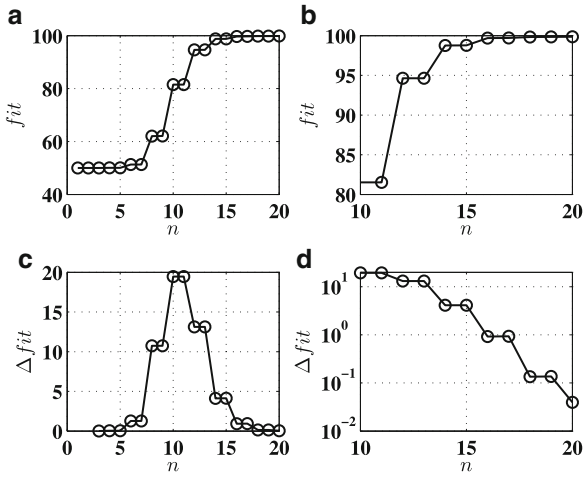

Fig. 9.7 (**a**) Fitting index *fit* associated with $\mathbf{Z}^{d,30}$, (**b**) an enlarged view of *fit*, (**c**) *con* associated with $\mathbf{Z}^{d,30}$ and (**d**) an enlarged view of *con*

and y in Eq. (9.18) be normalized using the "center and scale" technique [21] before formulation of the linear equation in Eq. (9.19). Normalized coordinates $\tilde{x}$ and $\tilde{y}$ can be expressed by

$$\begin{cases} \tilde{x} = \frac{2x - l_1}{l_1} \\ \tilde{y} = \frac{2y - l_2}{l_2} \end{cases} \tag{9.23}$$

where l_1 and l_2 are lengths of the plate along the x- and y-axes, respectively.

An increase of n in the polynomial fit in Eq. (9.18) can improve its level of approximation of the resulting MS to that to be fit. To quantify the level of approximation, a fitting index *fit* in percent, defined by

$$\mathit{fit}\,(n) = \frac{\mathrm{RMS}\,(\mathbf{z})}{\mathrm{RMS}\,(\mathbf{z}) + \mathrm{RMS}\,(\mathbf{e})} \times 100\,\% \tag{9.24}$$

is proposed, where RMS $(\cdot)$ denotes the root-mean-square (RMS) value of a vector and $\mathbf{e}$ is the error vector between the MS to be fit and the corresponding one from the current polynomial fit, i.e., $\mathbf{e} = \mathbf{V}\mathbf{a}^* - \mathbf{z}$. When the fitting index is close to 100 %, the MS from the current polynomial fit is almost completely identical to $\mathbf{z}$; the lower the fitting index, the lower the level of approximation of the MS from the current polynomial fit. Fitting indices *fit* associated with $\mathbf{Z}^{d,30}$ for different n are shown in Fig. 9.7a. It can be seen in Fig. 9.7b that *fit* converges to a certain value as n increases. To determine the proper order of a polynomial fit, a convergence index *con* for the polynomial fit with $n \geqslant 3$ is defined based on *fit*, which can be expressed by

$$\mathit{con}\,(n) = \mathit{fit}\,(n) - \mathit{fit}\,(n-2) \tag{9.25}$$

Fitting indices *con* associated with $\mathbf{Z}^{d,30}$ for different n are shown in Fig. 9.7c. It can be seen that when n is larger than a certain value, *con* starts to decrease. When *con* is sufficiently small after its start of decrease, there is no significant improvement in the level of approximation of the polynomial fit. To determine a proper value of n, it is proposed that the value be the smallest one with which *con* is smaller than a prescribed threshold value. In this work, the prescribed threshold value for *con* is 0.50 %. Hence, the proper value of n associated with $\mathbf{Z}^{d,30}$ is determined to be 18, with which $\mathit{con} = 0.14\,\%$, as shown in Fig. 9.7d. Maximum-CDIs, Minimum-CDIs, Mean-CDIs and Gaussian-CDIs associated with noise-free $\mathbf{Z}^{d,30}$ and the corresponding MS from the polynomial fit with $n = 18$ are shown in Fig. 9.8a through d, respectively. Similar to the CDIs associated with noise-free $\mathbf{Z}^{d,30}$ and $\mathbf{Z}^{u,30}$ in Fig. 9.6, the damage can be identified near regions with high values of CDIs.

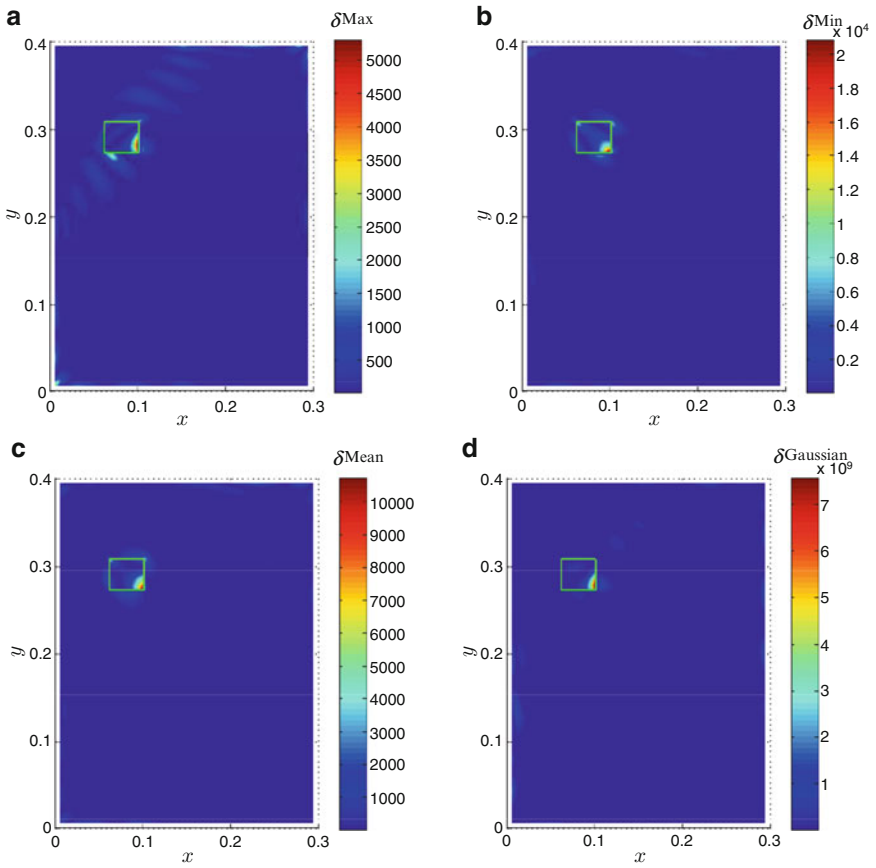

Fig. 9.8 (**a**) Maximum-CDIs, (**b**) Minimum-CDIs, (**c**) Mean-CDIs and (**d**) Gaussian-CDIs associated with noise-free $\mathbf{Z}^{d,30}$ and the corresponding MS from the polynomial fit with $n = 18$ from the scheme with $s = 0.002$

9.3 Numerical Investigation

The damage identification method proposed in Sect. 9.2 is numerically applied to the plate in Fig. 9.1a to identify the damage using MSs of its 27th and 28th elastic modes, denoted by $\mathbf{Z}^{d,27}$ and $\mathbf{Z}^{d,28}$, as shown in Figs. 9.9a and b, respectively. White noise is added to the two MSs with a SNR of 60 db to simulate measurement noise. Maximum, minimum, mean and Gaussian CMSs associated with $\mathbf{Z}^{d,27}$ from the scheme with $s = 0.002$, $s = 0.010$ and $s = 0.015$ are shown in Figs. 9.10, 9.11, and 9.12, respectively; those associated with $\mathbf{Z}^{d,28}$ from the scheme with $s = 0.002$, 0.010 and 0.015 are shown in Figs. 9.13, 9.14, and 9.15, respectively. In Figs. 9.10 and 9.13, global trends of the CMSs associated with $\mathbf{Z}^{d,27}$ and $\mathbf{Z}^{d,28}$ from the scheme with $s = 0.002$ could be observed with severe noise caused by measurement noise. When $s = 0.010$, the scheme yields CMSs with much lower noise levels and their global trends become clearer than those from the scheme with $s = 0.002$, as shown in Figs. 9.11 and 9.14. When $s = 0.015$, associated CMSs were of the best qualities compared with those from the scheme with $s = 0.002$ and 0.010, as shown in Figs. 9.12 and 9.15. Adverse effects of measurement noise are mostly eliminated with a larger value of s.

Fitting indices *fit* and convergence indices *con* associated with $\mathbf{Z}^{d,27}$ and $\mathbf{Z}^{d,28}$ for different n are shown in Figs. 9.16 and 9.17, respectively. Proper orders for polynomial fits associated with $Z^{d,27}$ and $Z^{d,28}$ are determined to be 17 and 18, respectively. Maximum-CDIs, Minimum-CDIs, Mean-CDIs and Gaussian-CDIs associated with $\mathbf{Z}^{d,27}$ from the scheme with $s = 0.002$, 0.010 and 0.015 are shown in Figs. 9.18, 9.19, and 9.20, respectively; those associated with $\mathbf{Z}^{d,28}$ from the scheme with $s = 0.002$, 0.010 and 0.015 are shown in Figs. 9.21, 9.22, and 9.23, respectively. In Figs. 9.18 and 9.21, the damage

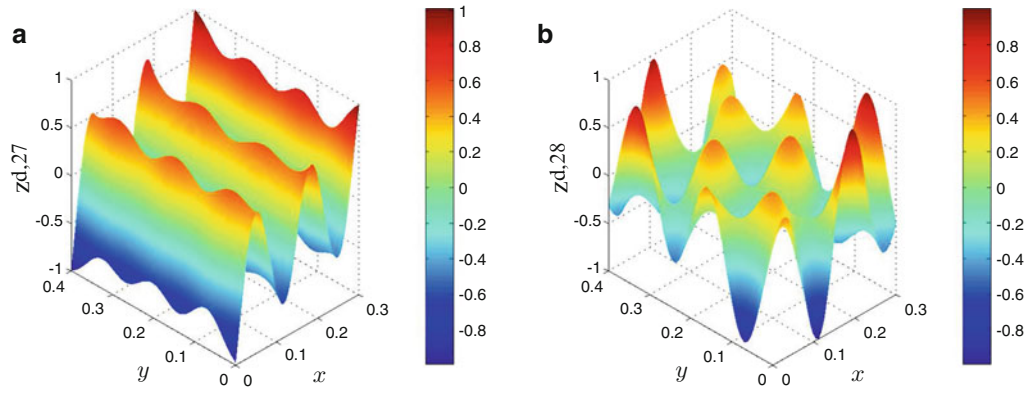

Fig. 9.9 (**a**) The 27th and (**b**) 28th MSs of the damaged plate in Fig. 9.1

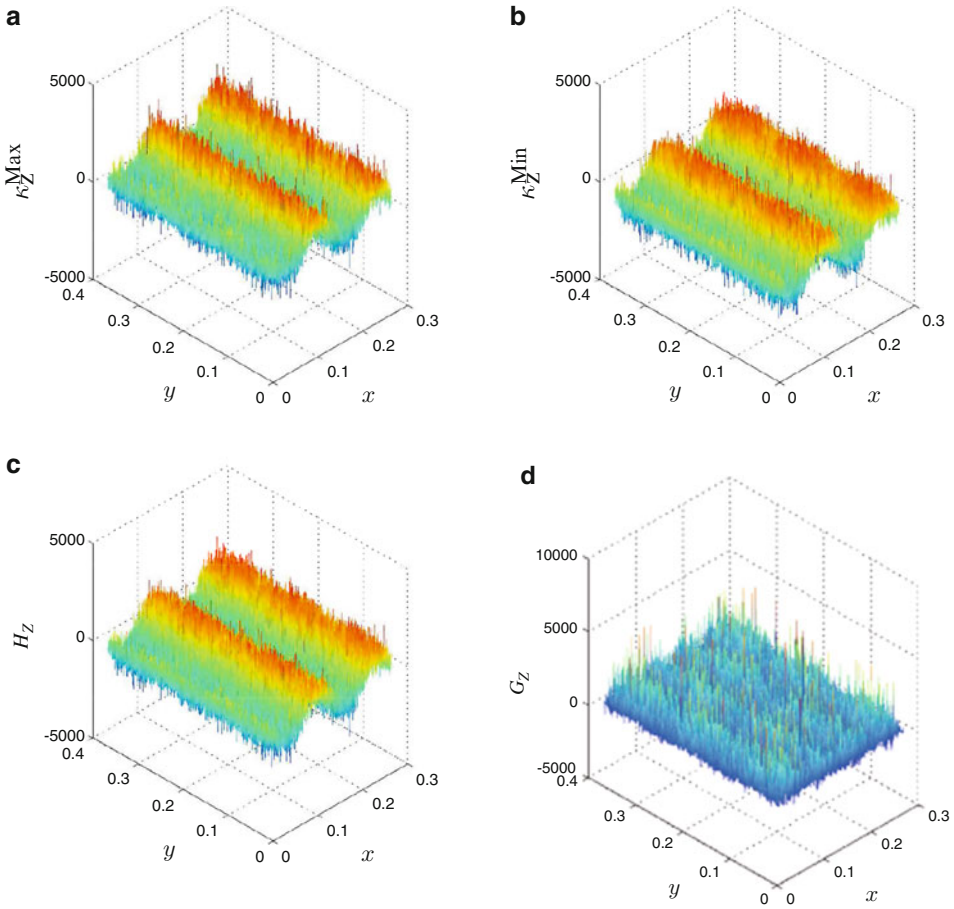

Fig. 9.10 (**a**) Maximum, (**b**) minimum, (**c**) mean and (**d**) Gaussian CMSs associated with $\mathbf{Z}^{d,27}$ from the scheme with $s = 0.002$

cannot be identified from the CDIs. The reason is that their associated CMSs are noisy since effects of measurement noise are amplified, and the existence of the damage on the CMSs are fussed. When s is increased to 0.010 in the scheme, regions that are formed by relatively high values of the CDIs in the neighborhood of and beyond the damage can be observed, as shown in Figs. 9.19 and 9.22, and one still cannot clearly identify the damage based on the CDIs. When $s = 0.015$, regions similar to those in Figs. 9.19 and 9.22 can still be observed in the CDIs, as shown in Figs. 9.20 and 9.23, respectively. The difference is that higher values of the CDIs can be observed in the neighborhood of the damage when $s = 0.015$, compared with those beyond the damage. By use of the CDIs in Figs. 9.20 and 9.23, one can identify the damage in regions with consistently higher values of the CDIs.

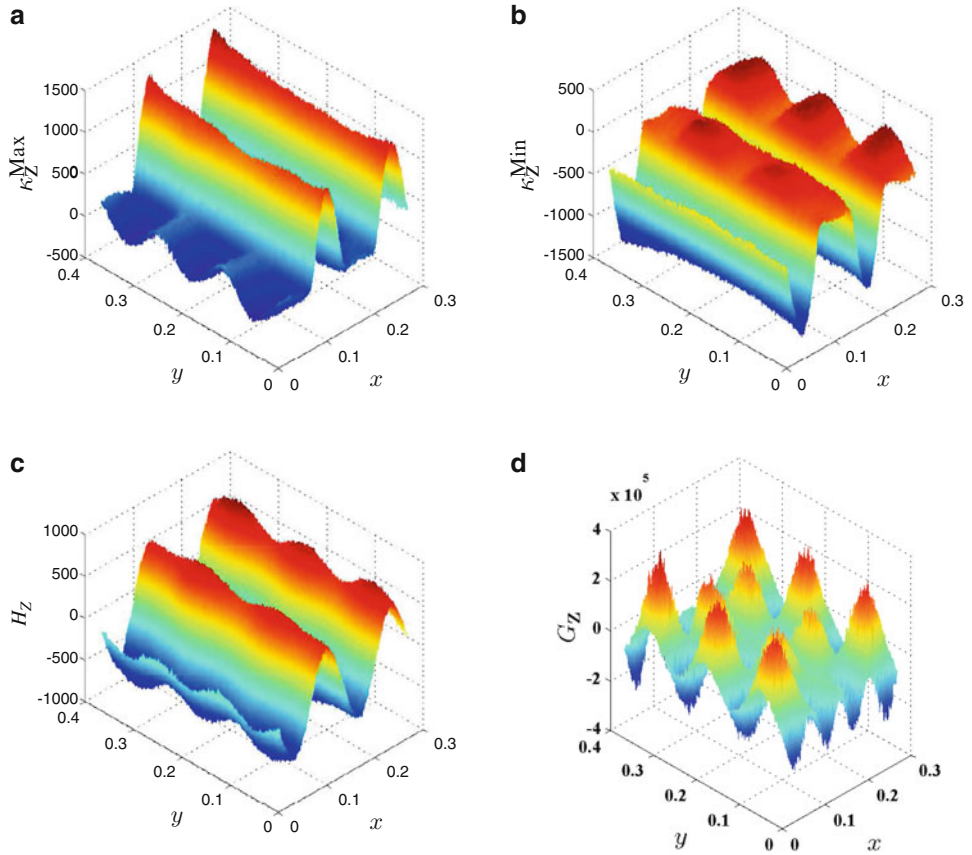

Fig. 9.11 (**a**) Maximum, (**b**) minimum, (**c**) mean and (**d**) Gaussian CMSs associated with $\mathbf{Z}^{d,27}$ from the scheme with $s = 0.010$

9.4 Conclusion

A new non-model-based plate damage identification method based on principal, mean and Gaussian CMSs is proposed. It can be applied to a damaged plate without use of any a priori information of the associated undamaged one, if the undamaged plate is geometrically smooth and made of materials that have no stiffness and mass discontinuities. A multi-scale differential-geometry scheme is proposed to calculate the CMSs associated with a MS. The advantage of the scheme is that adverse effects of measurement noise can be alleviated with use of a larger scale parameter. Differences between the aforementioned CMSs of a damaged plate and those associated with a MS from a polynomial that fits the corresponding MS of the damaged plate are processed to yield four CDIs. Based on the proposed fitting index, a MS from a polynomial that fits the corresponding MS of a damaged plate would have a higher level of approximation as the order of the polynomial increases. A threshold value is proposed for the convergence index, based on which the order of the polynomial can be properly determined. CMSs associated with a MS from a polynomial of a properly determined order can be used to eliminate global trends of CMSs associated with the corresponding MS of a damaged plate. The proposed method is numerically applied to a plate with damage in the form of a thickness reduction area. The damage can be successfully identified by locating consistently higher values of the CDIs. A larger value of the scale parameter in the scheme can manifest existence of damage in the CDIs.

Acknowledgements The authors are grateful for the financial support from the National Science Foundation under Grant Number CMMI-1335024.

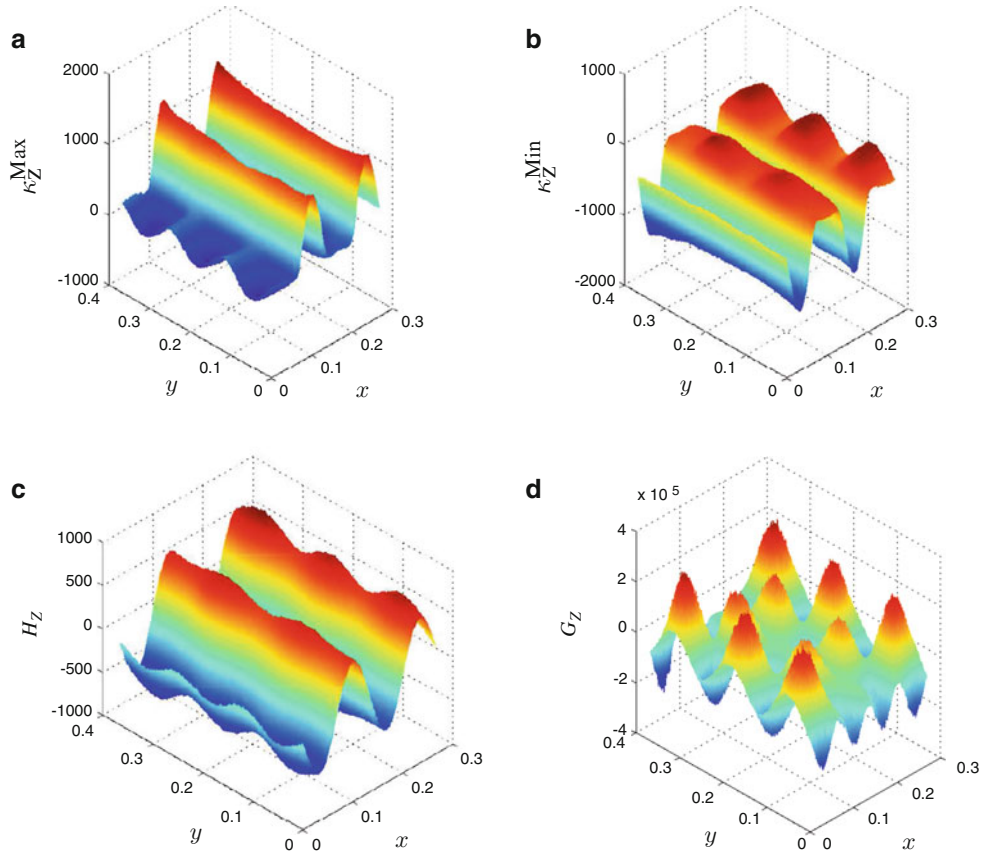

Fig. 9.12 (**a**) Maximum, (**b**) minimum, (**c**) mean and (**d**) Gaussian CMSs associated with $\mathbf{Z}^{d,27}$ from the scheme with $s = 0.015$

References

1. He, K., Zhu, W.D.: Detection of damage and loosening of bolted connections in structures using changes in natural frequencies. ASNT Mater. Eval. **68**(6), 721–732 (2010)
2. He, K., Zhu, W.D.: Vibration-based structural damage detection method and its applications to engineering structures. Int. J. Smart Nano Mater. **2**(3), 194–218 (2011)
3. Zhu, W.D., He, K., Detection of damage in space frame structures with L-shaped beams and bolted joints using changes in natural frequencies. J. Vib. Acoust. **135**(5), 051001 (2013)
4. He, K., Zhu, W.D.: Detecting loosening of bolted connections in a pipeline using changes in natural frequencies. J. Vib. Acoust. **136**(3), 034503 (2014)
5. Ratcliffe, C.P.: A frequency and curvature based experimental method for locating damage in structures. J. Vib. Acoust. **122**(3), 324–329 (2000)
6. Yoon, M.K., Heider, D., Gillespie, J.W., Ratcliffe, C.P., Crane, R.M.: Local damage detection using the two-dimensional gapped smoothing method. J. Sound Vib. **279**(1), 119–139 (2005)
7. Zhang, Y., Wang, L., Lie, S.T., Xiang, Z.: Damage detection in plates structures based on frequency shift surface curvature. J. Sound Vib. **332**(25), 6665–6684 (2013)
8. Xu, W., Cao, M., Ostachowicz, W., Radzieński, M. , Xia, N.: Two-dimensional curvature mode shape method based on wavelets and Teager energy for damage detection in plates. J. Sound Vib. **347**, 266–278 (2015)
9. Wu, D., Law, S.S.: Damage localization in plate structures from uniform load surface curvature. J. Sound Vib. **276**(1), 227–244 (2004)
10. Qiao, P., Lu, K., Lestari, W., Wang, J.: Curvature mode shape-based damage detection in composite laminated plates. Compos. Struct. **80**(3), 409–428 (2007)
11. Chang, C.-C., Chen, L.-W.: Damage detection of a rectangular plate by spatial wavelet based approach. Appl. Acoust. **65**(8), 819–832 (2004)
12. Rucka, M., Wilde, K.: Application of continuous wavelet transform in vibration based damage detection method for beams and plates. J. Sound Vib. **297**(3), 536–550 (2006)
13. Douka, E., Loutridis, S., Trochidis A.: Crack identification in plates using wavelet analysis. J. Sound Vib. **270**(1), 279–295 (2004)
14. Cornwell, P., Doebling, S.W., Farrar, C.R.: Application of the strain energy damage detection method to plate-like structures. J. Sound Vib. **224**(2), 359–374 (1999)
15. Surace, C., Saxena, R., Gherlone, M., Darwich, H.: Damage localisation in plate like-structures using the two-dimensional polynomial annihilation edge detection method. J. Sound Vib. **333**(21), 5412–5426 (2014)

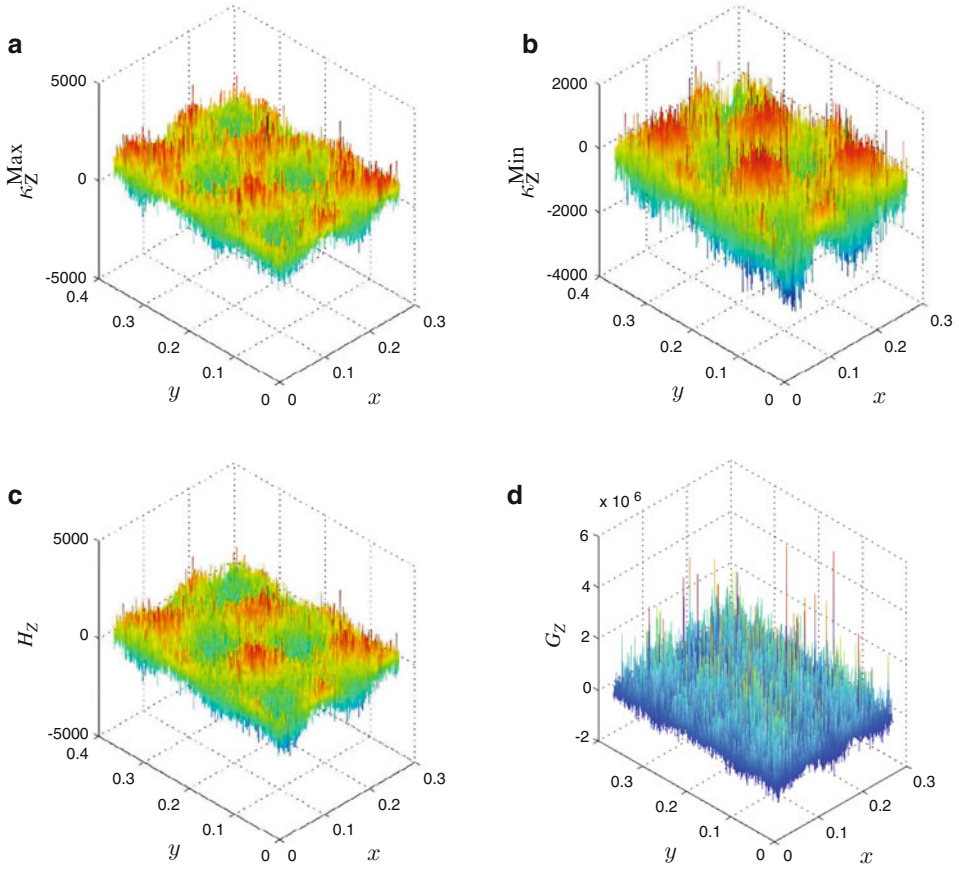

Fig. 9.13 (**a**) Maximum, (**b**) minimum, (**c**) mean and (**d**) Gaussian CMSs associated with $\mathbf{Z}^{d,28}$ from the scheme with $s = 0.002$

16. Surace, C., Archibald, R., Saxena, R.: On the use of the polynomial annihilation edge detection for locating cracks in beam-like structures. Comput. Struct. **114**, 72–83 (2013)
17. O'neill, B.: Elementary Differential Geometry, 2nd edn. Academic, New York (2006)
18. Meyer, M., Desbrun, M., Schröder, P., Barr, A.H.: Discrete differential geometry operators for triangulated 2-manifolds. Visualization and Mathematics III, pp. 35–57. Springer, Berlin (2003)
19. Xu, Y.F., Zhu, W.D., Liu, J., Shao, Y.M.: Identification of embedded horizontal cracks in beams using measured mode shapes. J. Sound Vib. **333**(23), 6273–6294 (2014)
20. Nocedal, J., Wright, S.: Numerical Optimization. Springer Science & Business Media, New York (2006)
21. Cox, I., Gaudard, M.: Discovering Partial Least Squares with JMP. SAS Institute, Cary (2013)

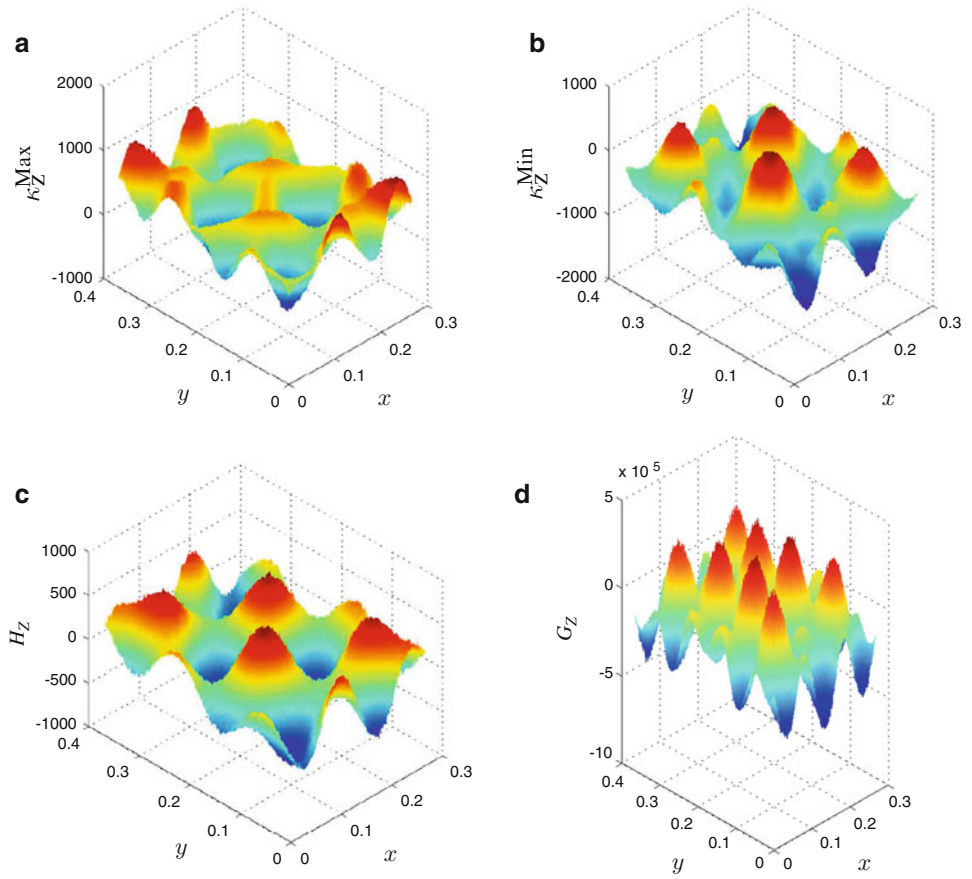

Fig. 9.14 (**a**) Maximum, (**b**) minimum, (**c**) mean and (**d**) Gaussian CMSs associated with $\mathbf{Z}^{d,28}$ from the scheme with $s = 0.010$

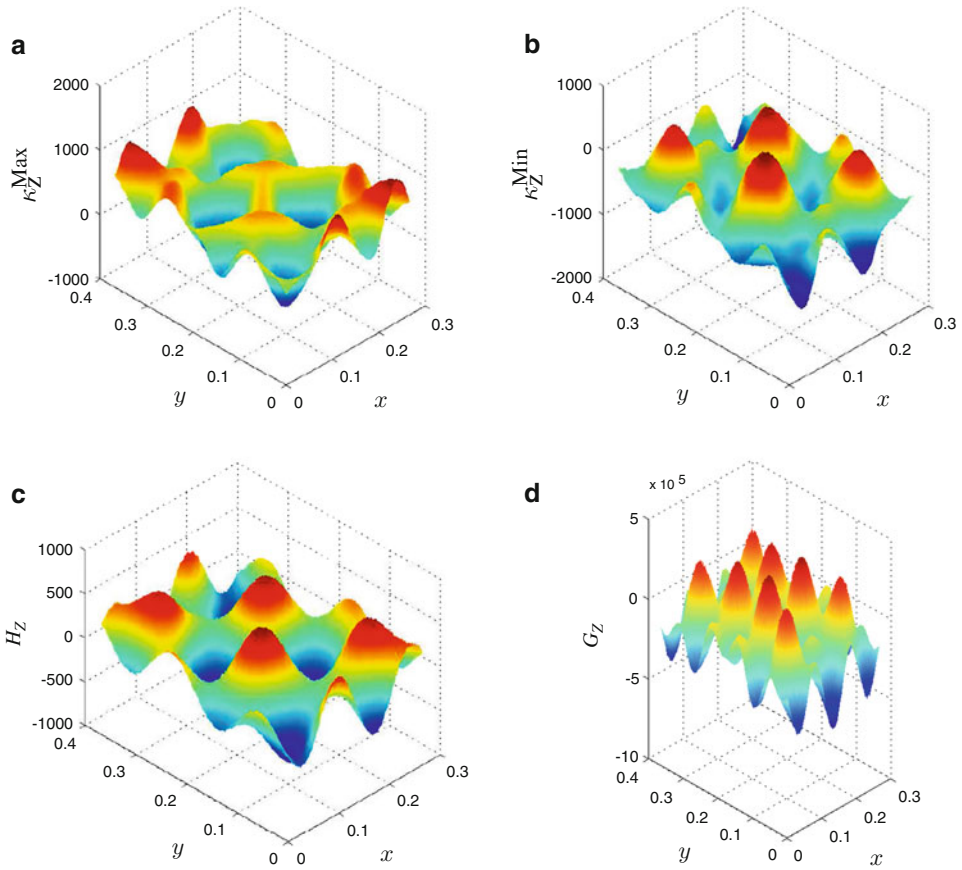

Fig. 9.15 (**a**) Maximum, (**b**) minimum, (**c**) mean and (**d**) Gaussian CMSs associated with $\mathbf{Z}^{d,28}$ from the scheme with $s = 0.015$

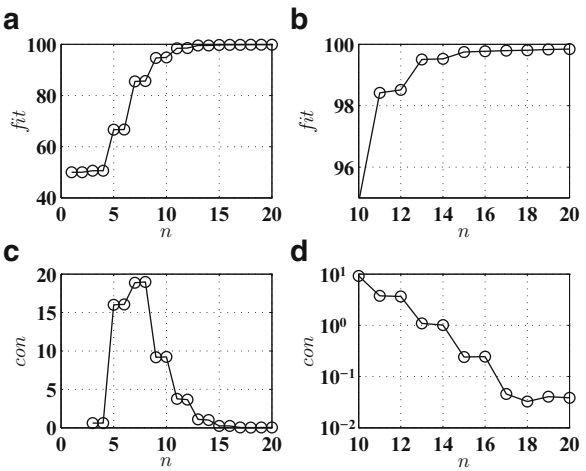

Fig. 9.16 (**a**) Fitting index *fit* associated with $\mathbf{Z}^{d,27}$, (**b**) an enlarged view of *fit*, (**c**) *con* associated with $\mathbf{Z}^{d,27}$ and (**d**) an enlarged view of *con*

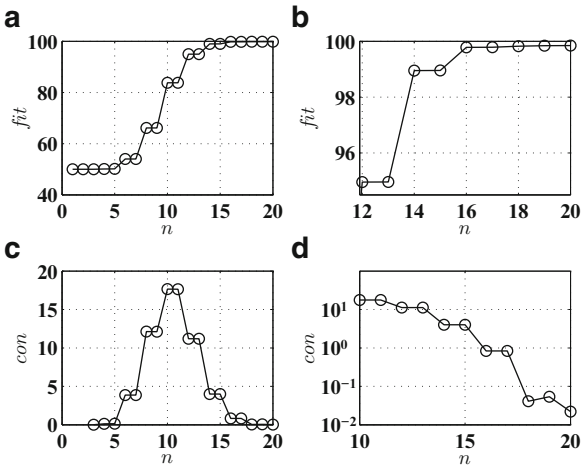

Fig. 9.17 (**a**) Fitting index *fit* associated with $\mathbf{Z}^{d,28}$, (**b**) an enlarged view of *fit*, (**c**) *con* associated with $\mathbf{Z}^{d,28}$ and (**d**) an enlarged view of *con*

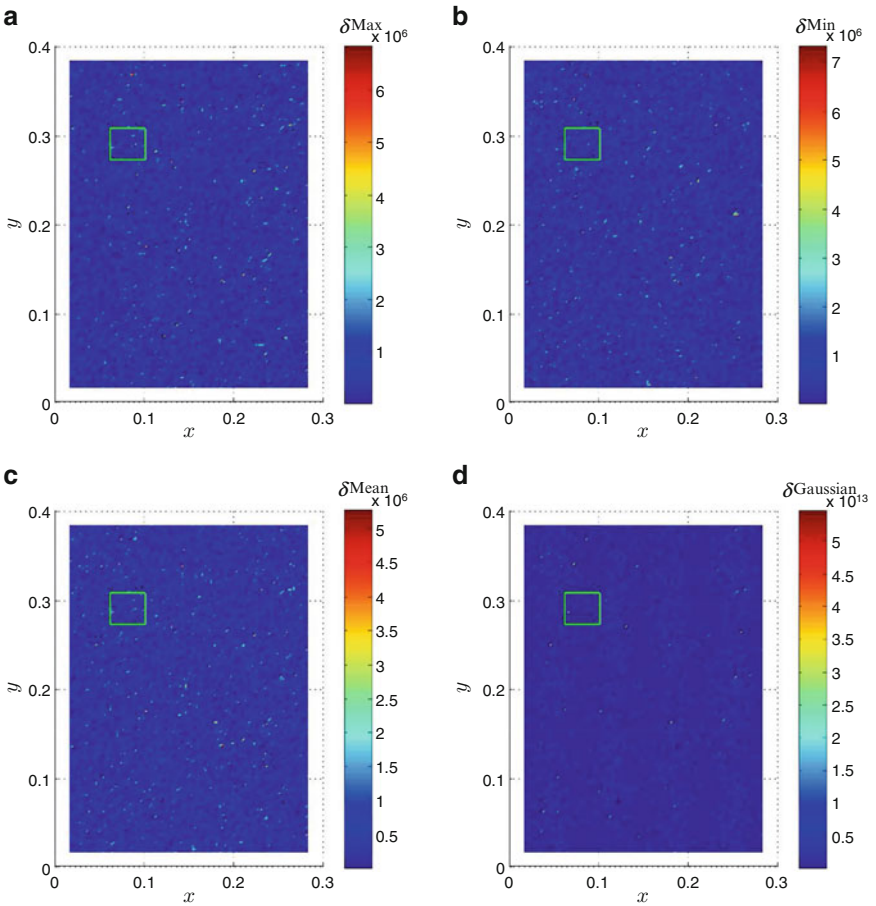

Fig. 9.18 (**a**) Maximum-CDIs, (**b**) Minimum-CDIs, (**c**) Mean-CDIs and (**d**) Gaussian- CDIs associated with $Z^{d,27}$; $s = 0.002$ in the scheme

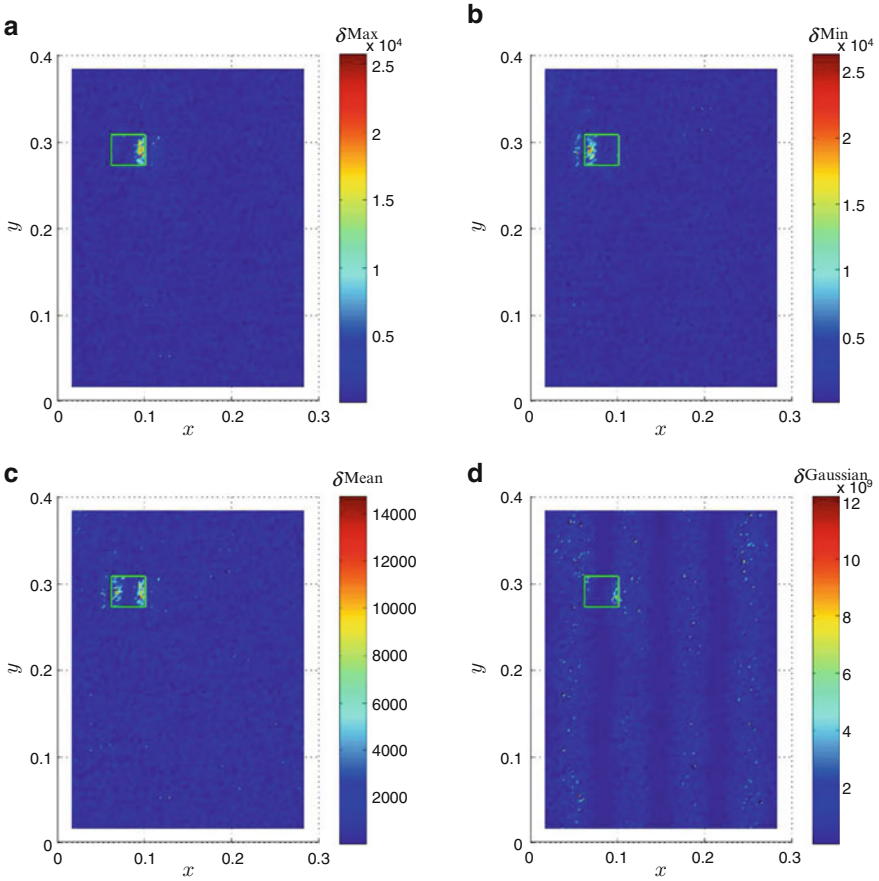

Fig. 9.19 (**a**) Maximum-CDIs, (**b**) Minimum-CDIs, (**c**) Mean-CDIs and (**d**) Gaussian-CDIs associated with $Z^{d,27}$; $s = 0.010$ in the scheme

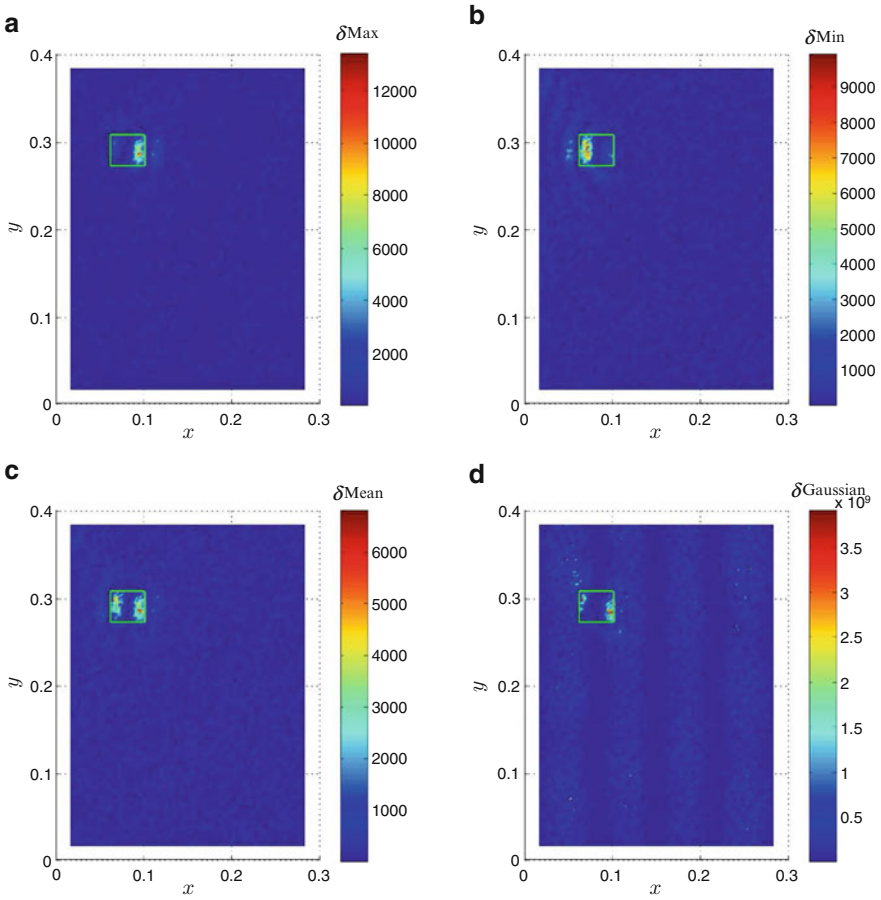

Fig. 9.20 (**a**) Maximum, (**b**) Minimum, (**c**) Mean and (**d**) Gaussian CMSs associated with $\mathbf{Z}^{d,27}$ from the scheme with $s = 0.015$

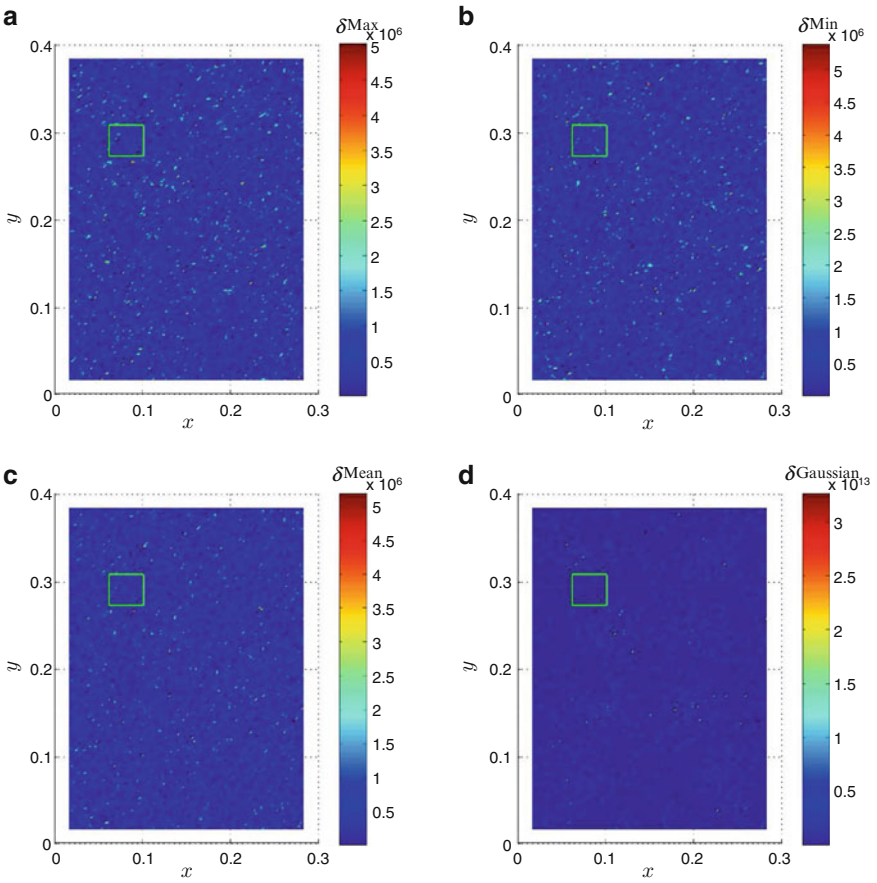

Fig. 9.21 (**a**) Maximum-CDIs, (**b**) Minimum-CDIs, (**c**) Mean-CDIs and (**d**) Gaussian-CDIs associated with $Z^{d,28}$; $s = 0.002$ in the scheme

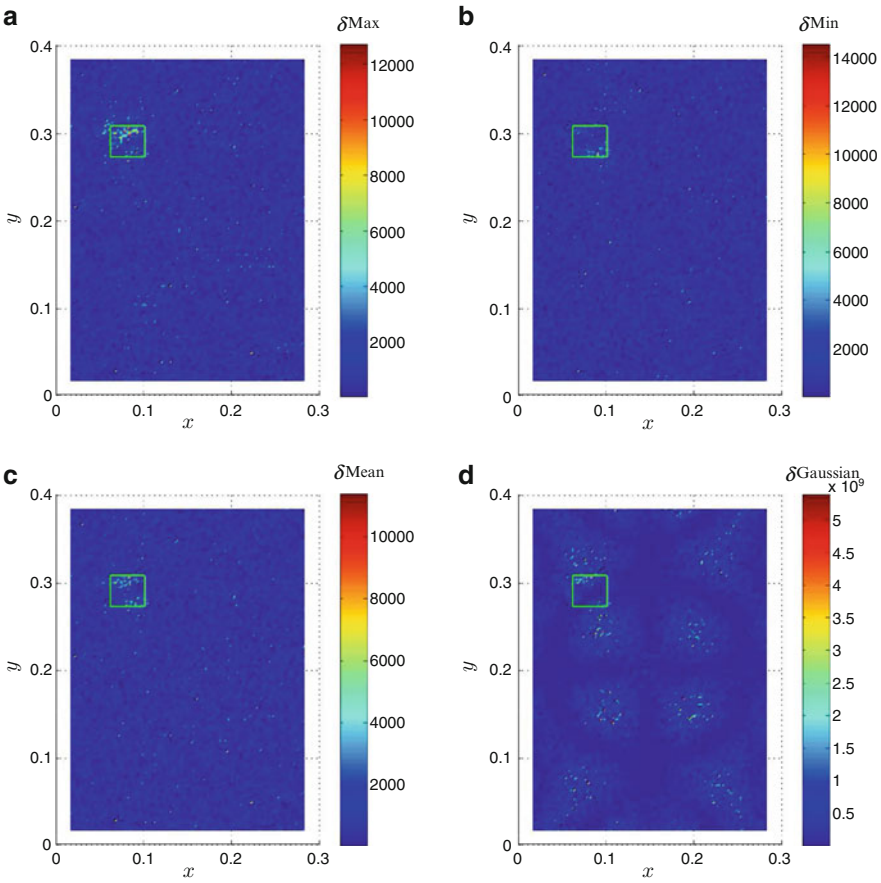

Fig. 9.22 (**a**) Maximum, (**b**) minimum, (**c**) mean and (**d**) Gaussian CMSs associated with $\mathbf{Z}^{d,28}$ from the scheme with $s = 0.010$

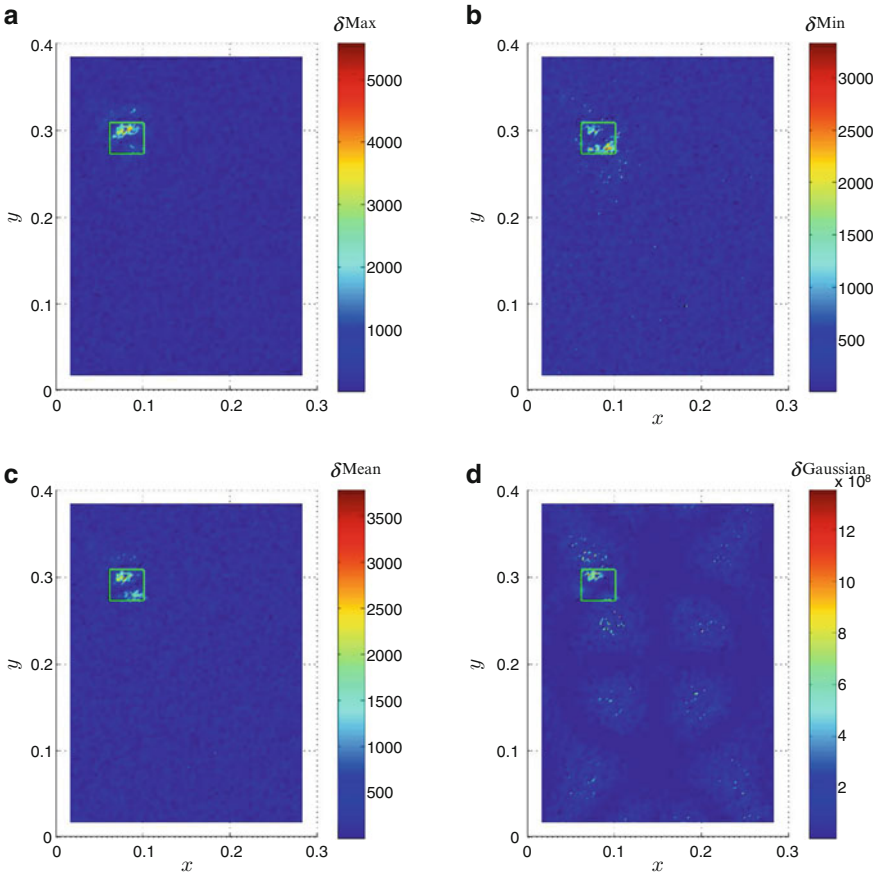

Fig. 9.23 (**a**) Maximum-CDIs, (**b**) Minimum-CDIs, (**c**) Mean-CDIs and (**d**) Gaussian-CDIs associated with $Z^{d,28}$; $s = 0.015$ in the scheme

Chapter 10
Ambient Vibration Testing of Two Highly Irregular Tall Buildings in Shanghai

Xiang Li, Carlos E. Ventura, Yu Feng, Yuxin Pan, Yavuz Kaya, Haibei Xiong, Fengliang Zhang, Jixing Cao, and Minghui Zhou

Abstract This paper presents the detailed experiment setups and data analysis results of the ambient vibration testing of two irregular high-rise buildings done by a joint research team from the University of British Columbia and Tongji University. Two full-scale tests were conducted in May 2015 at the Siping Campus of Tongji University, Shanghai, China. The first Multi-Functional Building (MFB) has 21 stories with a typical floor height of 4 m. The structure shows significant irregularity in both plane and vertical direction, where every three floors combine into one L-shaped unit and the L-shape floor rotates 90° along the height of the building. The second building tested is the Shanghai International Design Center (SIDC). SIDC is an h-shape asymmetry double tower structure consists of main tower (25 story) and secondary tower (12 story). The two towers are rigidly connected with steel truss system between the 11th and 12th floors. Considering the complexities and irregularities of the two buildings, it is essential to study their dynamic properties and the associated principal modes of vibration. Several modal analysis techniques were adopted to determine the modal parameters of two buildings.

Keywords Operational modal analysis • Ambient vibration test • Frequency domain decomposition • System identification • Highly irregular building

10.1 Introduction

The intent of this paper is to present the overall description of experimental and data analysis of the Ambient Vibration (AV) testing of the Tongji Multi-functional Building (MFB) and Shanghai International Design Center (SIDC) done by joint research team from the University of British Columbia (Canada) and Tongji University (China). Both buildings are very unique in structure layout which brings many uncertain and interesting dynamic properties that hard to be understood by conventional dynamic estimation. In order to study the dynamic characteristic of this building, ambient vibration tests were conducted by researchers and graduate students from both institutes during the 5th Tongji-UBC earthquake engineering symposium in May 2015. This study introduced the background information of the tested structure, testing plan, the data collection and process and system identification. Final test results are presented and discussed at the end of this paper.

10.2 Descriptions of the Buildings

10.2.1 The Multi-Function Building (MFB)

The MFB is located at the northeast corner of Tongji University (Siping Campus), Shanghai, China, as seen in Fig. 10.1. The building has 21 stories in total (which represent "the twenty-first century") above ground and one level of basement. The total height is approximately 100 m (which represent "the 100th Anniversary of Tongji University") with a typical floor height of 4 m, floor plan is square shape with dimension of 48.6×48.6 m. The structure is made of 9×9 steel frame supported by

X. Li • C.E. Ventura • Y. Feng • Y. Pan (✉) • Y. Kaya
Department of Civil Engineering, The University of British Columbia, 6250 Applied Science Lane, Vancouver, BC, Canada V6T 1Z4
e-mail: ypan@civil.ubc.ca

H. Xiong • F. Zhang • J. Cao • M. Zhou
State Key Laboratory of Disaster Reduction in Civil Engineering, Tongji University, Shanghai 200092, China

S. Pakzad, C. Juan (eds.), *Dynamics of Civil Structures, Volume 2*, Conference Proceedings of the Society for Experimental Mechanics Series, DOI 10.1007/978-3-319-29751-4_10

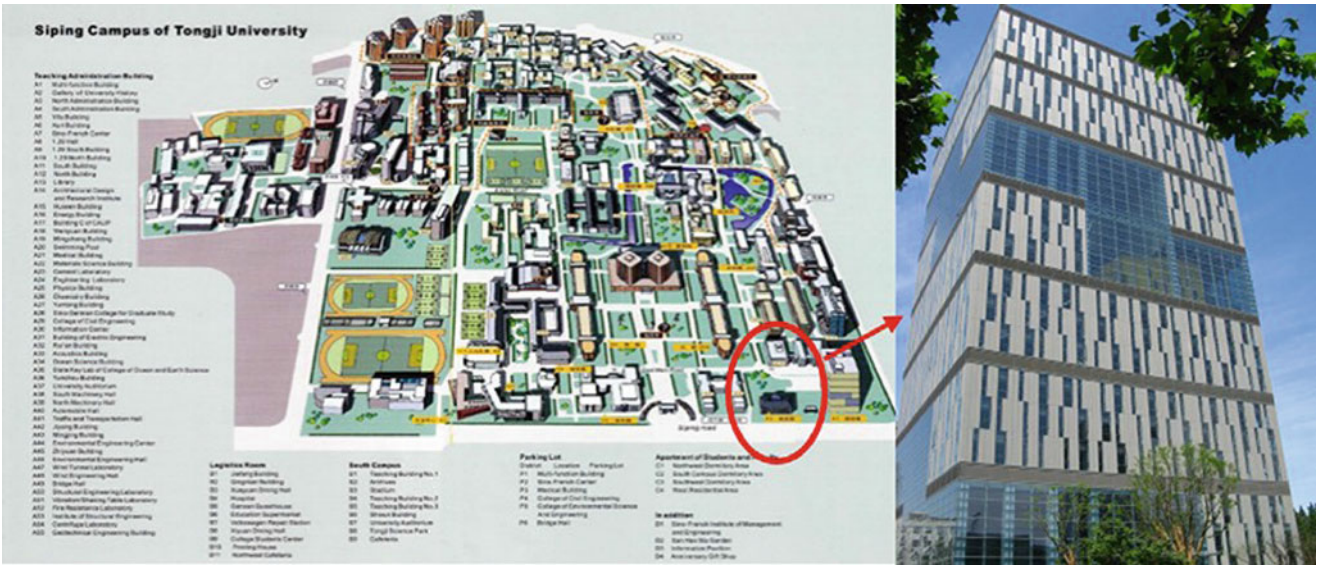

Fig. 10.1 Location of the MFB in Tongji University and building elevation view

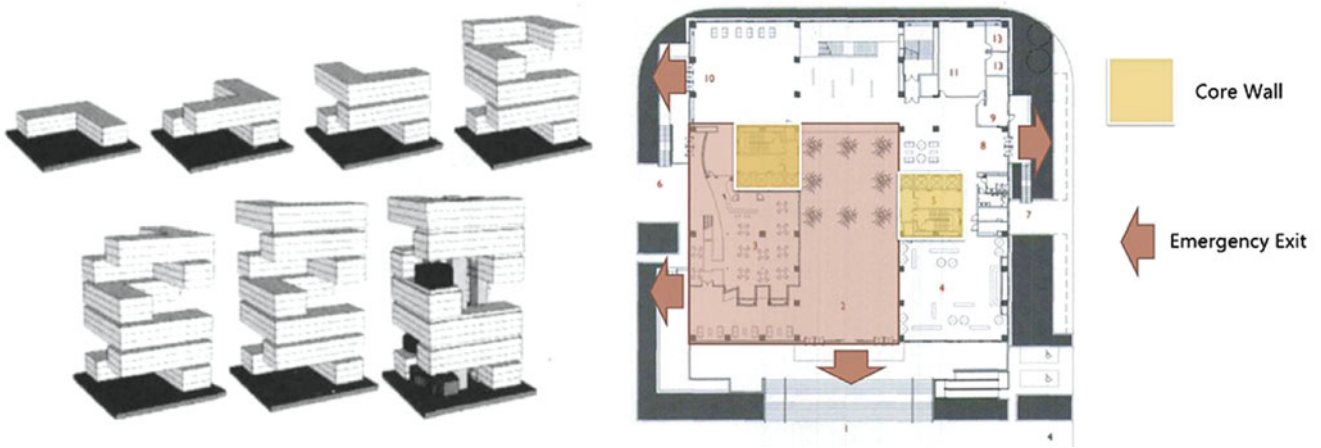

Fig. 10.2 Spiral vertical layout of the "L" shape units and plan view of the lobby

inconsistent layout of diagonal steel brace and viscous damping brace. The structure of the building shows plane and vertical irregularity: every three floors combine into one L-shaped function unit with long side of 48.6 m and short side of 16.2 m, figure of the L-shape floor rotates 90° clockwise every unit from the bottom to the top, this spiral layout forms a center atrium with a dimension of 16.2 × 16.2 m, two stair well core walls are formed by gravity columns surrounding the wells [1, 2], as shown in Fig. 10.2.

10.2.2 The Shanghai International Design Center (SIDC)

Located in National Science and Technology Park of Tongji University, Shanghai, the Shanghai International Design Center (SIDC) was jointly designed by Milanese office AM Progetti and Tongji Architectural Design Institute, as shown in Fig. 10.3.

SIDC is an "h-shape" asymmetry double-tower structure consists of main tower, secondary tower and connecting structure. The main tower is a 25-story concrete core wall-steel frame structure with story height of 4 m. The secondary tower is located in 17.5 m east of main tower with a 12-story in height. The two towers are connected between 11th and 12th story with steel truss system. There is significant difference in mass and stiffness between the two towers and the connecting system is rigid, which leads to a highly irregular dynamic response of the whole structural system. Therefore,

Fig. 10.3 Location and view of Shanghai international design center

seismic response of the building is expected to be highly complicated and uncertain. Many researchers have carried out either finite element analysis or small-scale shake table test to study its complex dynamic properties, however, great difference and errors could be found among various analysis techniques. And so far, limit field tests have been conducted to obtain its natural frequency and mode shape. In order to evaluate the reliability of the building under earthquake, and provide accurate information for theoretical analysis and validation for computational models, an ambient vibration test was performed in the building [3, 4].

10.3 Ambient Vibration Testing of the Buildings

10.3.1 Introduction

Ambient Vibration (AV) testing is a non-destructive test whereby the external forces applied are not controlled. In AV testing, the structure is assumed to be excited through primarily wind and possible human activity. Data collected from AVT could be processed to obtain modal information of tested structure, which is crucial in many research areas including seismic rehabilitation of existing structures and finite element model updating, etc.

Structural vibration sensor called TROMINO® is used to carry out the AVT of two buildings. TROMINO® sensor is widely used by researchers to study dynamic characteristics of existing structures. The sensors are set to record signal in 10 channels including high sensitivity velocities, low sensitivity velocities channels and accelerometer channels in all three directions X, Y and Z, plus one GPS time stamp channel that used for synchronization of recorded signal. Configuration and main technical specifications of TROMINO® are shown Fig. 10.4 [5].

For both tests, both GPS and Radio are not applicable since the signal is blocked within the building. Therefore, data synchronization was performed manually afterwards based on internal clocks of the sensors. The internal clocks of the sensors need to be synchronized every time before the test where satellite signal could be received. In order to synchronize all sensors participated for both tests and make sure there is no any time delay, the "pre-setups" which includes "Setup X" and "Setup Y" are conducted before both tests. First, a 30-min measurement using satellite signal (refer to Setup X), all sensors are placed close to each other in an open field with no shield above and the internal GPS is set for time synchronization, the sampling rate is set to 512 Hz, as seen in Fig. 10.4 (right). Secondly, to make sure there is no time delay during test setup, a 20-min measurement based on internal clock (called Setup Y) is conducted with all sensors at same location. During Setup Y a set of impact load (heel drops on the ground next to the sensor) is applied at 5, 10 and 15 min. The purpose is to create a set of clear peaks in the time history signal of all sensors, thereby to verify no time delay is observed and provide solutions once the delay exists.

Weight	1kg
Size	10*14*8cm
Power	2 AA batteries
Channel	12
Operating Range	0.1-1024Hz
Built-in GPS receiver	
Built-in radio receiver	

Fig. 10.4 Trominos® used in ambient vibration (*left*) and the pre-setup layout (*right*)

Table 10.1 Start and end time of each setup

	Pre-setup		Main test		
Setup no.	X	Y	1	2	3
Start time	12:14	12:51	13:09	14:14	15:16
End time	12:44	13:11	14:00	15:06	16:08
Length (minutes)	30	20	51	51	51

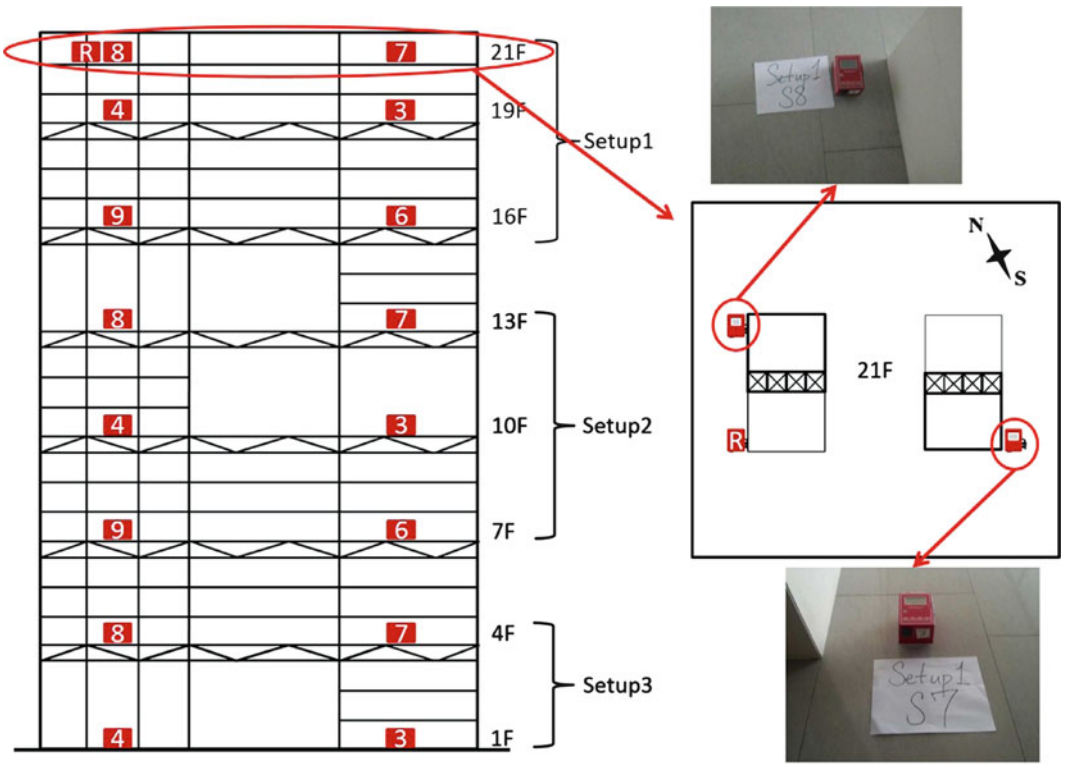

Fig. 10.5 Setup plan from south elevation view (*left*) and plan view of 21th floor (*right*)

10.3.2 AV Testing of MFB

On May 3rd, 2015, the AV testing was conducted at 3:15 pm and ended at 8:08 pm within 1 day. The whole test includes two pre-setups (Setup X and Y) and three test setups (Setup 1–3). Table 10.1 lists the start and end time of each setup, notice that all time mentioned in this report is local China Standard Time (CST).

In total seven sensors were utilized in all three setups of the test. Sensor No.1 was selected as reference sensor and placed at the top floor of the building, its location will remain unchanged throughout the entire test. During each setup, all sensors were placed parallel to the stair well core wall next to the corner and face to the north side of the building. Fig. 10.5 shows

the comprehensive layout of all setups. The acquisition length of each setup is 1 h with a sampling rate of 512 Hz, and all sensors are leveled and photographically recorded before every measurement. It should be noticed that due to the limitation of memory of each partition, only 51 min length of data were recorded by using sampling rate of 512 Hz.

10.3.3 AV Testing of SIDC

AV Testing of SIDC was carried out on Thursday, May 7th, 2015. Due to the security control, the testing personnel were only allowed to access the elevator and the surrounding areas. Therefore, for both the main and the secondary towers, sensors were placed at same locations of each tested floor around the elevator corridor.

Before the main setups, two pre-setups were carried out to synchronize the internal clock as previous experiment. In total eight sensors were utilized in all three setups of the test. Considering the unique structural system, sensor No.1 and No. 9 were selected as reference sensors and placed at the top floor of both main and secondary buildings, its location will remain unchanged throughout the entire test. During each setup, all sensors were placed parallel to the stair well core wall next to the corner and face to the north side of the building. Fig. 10.6 shows the comprehensive layout of all setups. A more detailed illustration can be found in Fig. 10.7 from top view of the building. For the main tower, the sensors were strictly put around the right elevator corridor, while for the secondary tower, a larger area was captured.

Two sensors were placed on the top floor of the two towers as reference points and kept recording for the duration of test. Reference sensor of the main tower was placed on 24th floor at the location highlighted in Fig. 10.8 left. For secondary tower, reference sensor was placed in the stairwell between 11th and 12th floor, as shown in Fig. 10.8 right.

A total of 6 setups were tested on the testing day, with 3 setups for main tower, 2 setups for secondary tower and 1 setup for basement. The test last from 11:37 pm to 17:34 pm, with acquisition length of 30 min for each setup and a sampling rate of 512 Hz. Table 10.2 summarizes the start and stop time as well as tested floors for each setup.

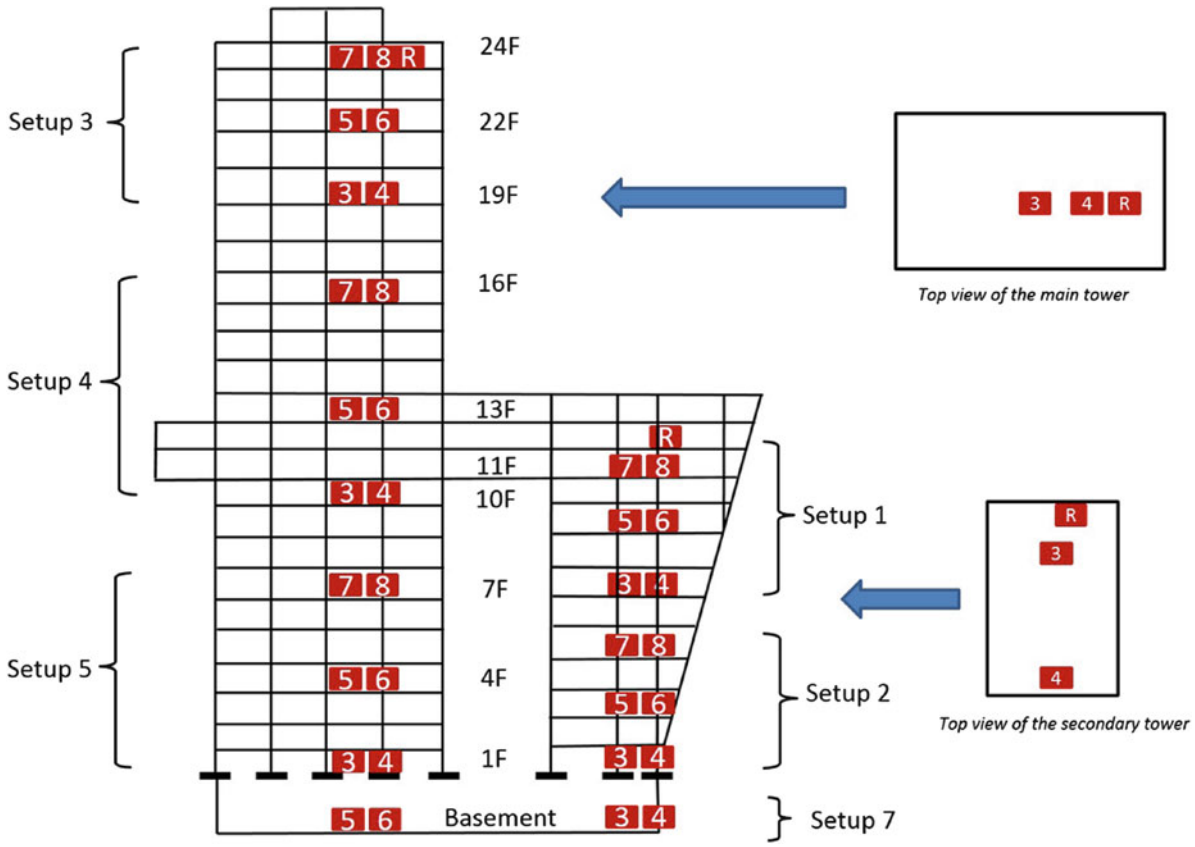

Fig. 10.6 Setup plan from south elevation view and top view of two towers

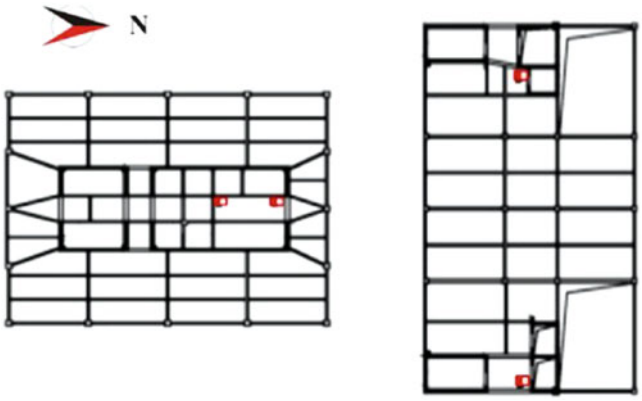

Fig. 10.7 Top view of sensor locations for the main (*left*) and the secondary tower (*right*)

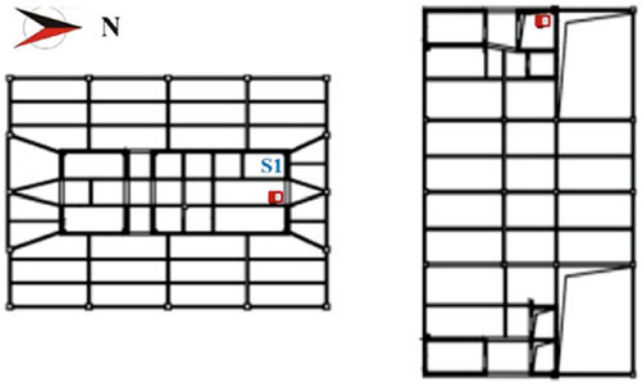

Fig. 10.8 Reference sensor locations for main (*left*) and secondary (*right*) tower

Table 10.2 Start and stop time for each test setup

Setup no.	Start time	Stop time	Description
1	12:37	13:07	7 F, 9 F, 11 F Secondary
2	13:19	13:49	1 F, 3 F, 5 F Secondary
3	14:34	15:04	19 F, 22 F, 24 F Main
4	15:14	15:44	10 F, 13 F, 16 F Main
5	15:49	16:19	1 F, 4 F, 7 F Main
6	16:40	17:10	Basement

10.4 System Identification and Results

After the test, further data processing, filtering and modal identification are done using ARTeMIS Modal Pro® (SVIBS) [6]. The data was decimated and filtered in different ways to zoom into specific frequency bands so the effect of noise can be minimized. The inbuilt Frequency Domain Decomposition (FDD) techniques is used to identify the possible natural frequencies and mode shapes, all mode shapes are manually selected by peak-picking method. An example of the SIDC building is presented in Fig. 10.9 to show the picked values of the natural frequencies.

The results of the identified natural frequencies of two buildings are summarized in Table 10.3 and 10.4. For comparison purpose, results from previous study of the MFB done by Liu [7] and the SIDC done by Wang [8] are also listed.

Totally five and six modes are recognized for MFB and SIDC respectively, it can be observed from the modal frequencies acquired from the AV testing have a fairly good match with the previous study results. However, although the possible natural frequencies of both buildings are estimated by ARTeMIS®, the ideal corresponding mode shapes were not acquired as expected, instead the mode shapes calculated from both test data were irregular and can hardly be recognized therefore they will not be presented in this report. After reflection of the entire test process, there are two reasons that might cause the failure of extracting the mode shapes: (1) Although the pre-setups were carried out before each test to prevent time stamp

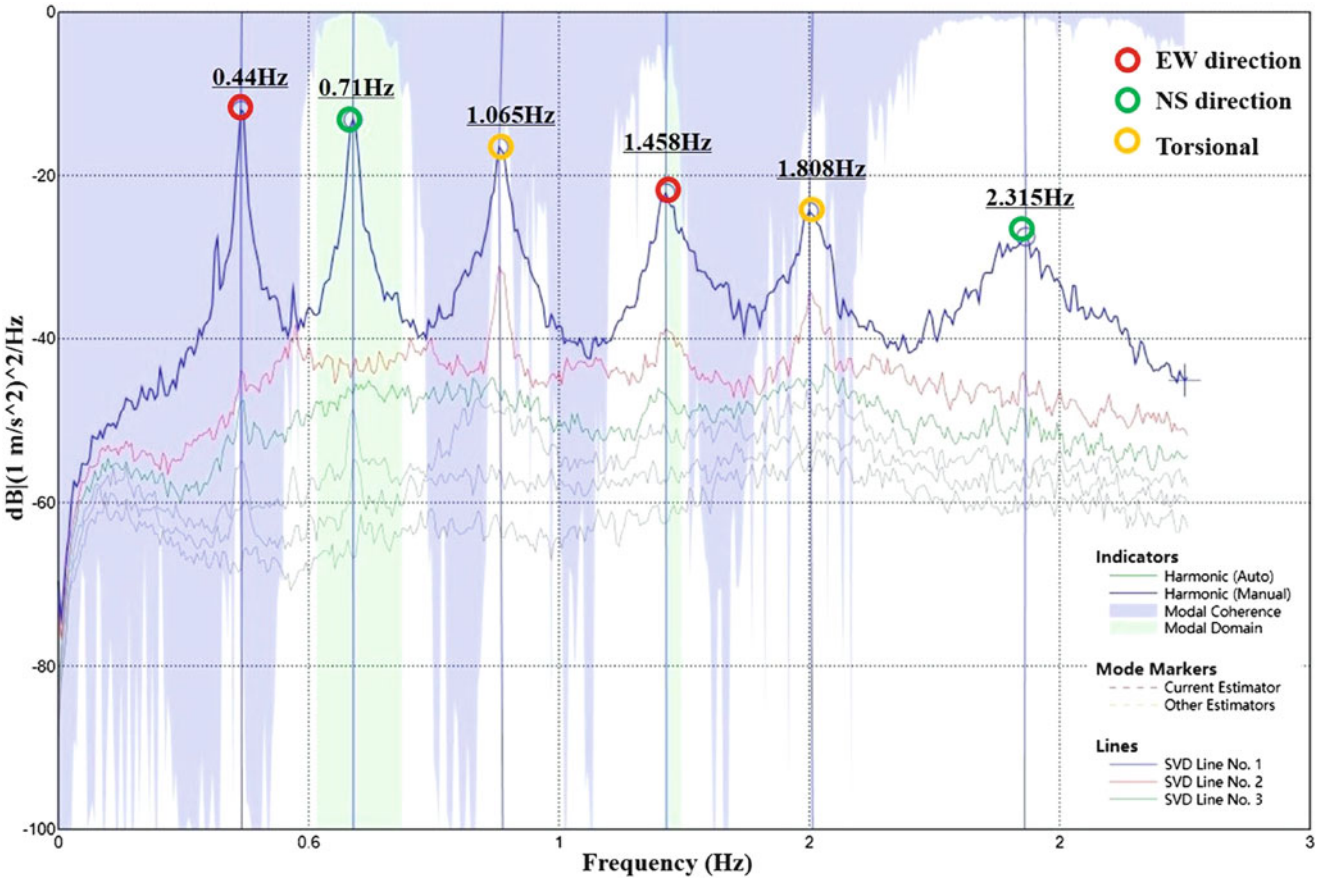

Fig. 10.9 Peak-picking of singular values of spectral densities of the SIDC

Table 10.3 AV testing results of MFB

Mode	Mode shape description	Frequency/Hz [7]	Frequency/Hz
1	1st EW	0.45	0.442
2	1st NS	0.51	0.492
3	2nd EW	1.54	1.483
4	2nd NS	1.72	1.752
5	3rd NS	2.68	–
6	3rd EW	2.87	2.619

Table 10.4 AV testing results of SIDC

Mode	Mode shape description	Frequency/Hz [8]	Frequency/Hz
1	1st EW dir.	0.45	0.44
2	1st NS dir.	0.73	0.71
3	1st torsional	1.124	1.065
4	2nd EW dir.	1.563	1.458
5	2nd torsional	1.923	1.808
6	2nd NS dir.	2.439	2.315

drifting between sensors, it still happened sometime during the test. It is probably due to the inherent problem with the sensor that the internal clock time drift occurs when synchronization is not done before every setup. (2) For the SIDC building, since very limited area can be reached in the main tower (as shown in Fig. 10.7), the torsional responses of the structure cannot be fully recorded.

10.5 Conclusions

In this paper, modal frequencies of two highly irregular buildings located in Tongji University were studied by performing Ambient Vibration tests using TROMINO® transducers. Data processing including data decimation and filtering are done in program ARTeMIS®, FDD technique was utilized to identify the natural frequencies of the buildings. And finally the results are compared with previous studies. However the corresponding mode shapes of both buildings cannot be extracted, one possible main reason is that the time stamps of each sensor fail to synchronize without the GPS signal. Therefore it is recommended to perform synchronization using GPS before every setup, so the time drift problem can be efficiently prevented.

Acknowledgements The authors wish to thank the State Key Laboratory of Disaster Reduction in Civil Engineering from Tong University for their interest and support in this study. The assistance and permission to access to the building of the owner of Shanghai Tower is greatly appreciated. The authors would like to acknowledge all the graduate students from Tongji University for assisting the test, Zhi Yu, Hongsheng Xu, Lu Ouyang, Hao Fu, Chengyou Wang, Kangli Wang, Weiwen Lai, Gan Luo and Guiquang Yang, their cooperation and enthusiasm is acknowledged with thanks. The technical support from Mr. Felix Yao from UBC EERF is also well appreciated. The authors would like to acknowledge Ms. Sharlie Huffman of the BC Ministry of Transportation for use of the sensors. Special thanks are given to Dr. Palle Andersen of SVS for providing license of ARTeMIS Modal 3.6 for analysis. This work is partially funded by Natural Nature Science Foundation of China (Grant Nos.: 51508407, 51508413), Shanghai Pujiang Program (Grant No.: 15PJ1408600) and the Grant from the Fundamental Research Funds for the Central Universities, China (Grant No. 2014KJ040). The financial support is gratefully acknowledged

References

1. Ding, J., He, Z.: Structural analysis and design of the complex highrise structure of Teaching and Research Complex of Tongji University. J. Build. Struct. (2008)
2. Wang, H., Ding, J: Study on column and brace system of Teaching and Research Complex of Tongji University. J. Build. Struct. (2008)
3. He, Z., Ding, J.: Design of asymmetry double-tower connected structure of Shanghai International Design Center. J. Build. Struct. (2008)
4. Zhang, M., Yuan, Z.: Elasto-plastic time history analysis of Shanghai International Design Center. J. Build. Struct. (2012)
5. Micromed, Tromino User's manual (2012)
6. Solutions Vibration Structural, ARTeMIS Extractor Pro 1999–2015 Version 3.6 (2015)
7. Liu, J.: Dynamic characteristics testing of the Muti-functional Building in Tongji University (Chinese). http://blog.163.com/art_strucutre/blog/static/190785230201162501359479/ (2011)
8. Wang, F., Shi, W.: Ambient vibration test study of Shanghai International Design Center. (2013)

Chapter 11
Development of an Acoustic Sensing Based SHM Technique for Wind Turbine Blades

Rukiye Canturk and Murat Inalpolat

Abstract Wind turbine blades are exposed to continuously-varying aerodynamic forces, gravitational loads, lightning strikes, and weather conditions that lead the blade damage such as leading and trailing edge splits, cracks and holes. In this study, actively-controlled acoustic sources were utilized in order to excite the blade's cavity structure from internal. The blade damage manifests itself in changes to the acoustic cavity frequency response functions and to the blade acoustic transmission loss. Proposed research examines the use of wireless sensing approach for detecting surface damage of the blades, while they are rotating when wind turbine is operational. A subscale wind turbine was built and used for carrying out preliminary experimental studies. Sensing system and strategy was benchmarked both using computational (FEM) model of the blades as well as the experimental results in the lab.

Keywords Acoustics • Surface damage • Wireless sensing • Blades • Wind turbine

11.1 Introduction

There has been a persistent increase in the demands for clean energy generation, supply, and storage around the world. As the reliability of the clean energy sources such as wind turbines increase, this trend will be prevalent. Wind turbines are currently supplying a considerable amount of the clean energy at a 66 Gigawatt (5 % of the energy need) overall capacity in US and significantly more in Europe [1]. The biggest roadblock for an even faster increase of the use of this technology has been the reliability problems and thus the cost of operability and maintenance (O&M). Blades of a wind turbine are the most vulnerable components as they are in direct interaction with wind as well as other environmental factors, such as temperature variations, humidity, erosion etc. The time-varying loads such as aerodynamic forces, gravitational loads, lightning strikes, and weather conditions, will cause all blades to experience edge splits, delamination, cracks, or holes.

There are several methods, which are currently available for the inspection of the blades for detecting blade faults such as holes, cracks, and delamination. Vibration-based, acoustic emission and wave propagation based methods are frequently used in order to evaluate the structural integrity of the blades [2–4]. Photogrammetry-based optical techniques have recently been used to detect defects from the wind turbine blades [5–11]. Ultrasound-based inspection is one of the most widely used blade inspection techniques in industry and has been successful demonstrated in the literature [12–15]. Acoustic beamforming is a versatile but costly technique that has been demonstrated to succeed under certain conditions [16–20]. Acoustic signature taken from the structure, before and after the defect, will allow us to differentiate the fault existence and can also be used as a blade inspection method. Aizawa et al. [13] investigated damage detection of wind turbine blades by installing an audio speaker inside of a stationary wind turbine blade and qualitatively characterized the sound radiation using a microphone array. Their observation in the end was that the faults would change the radiated sound energy from the object. One other potentially viable damage detection method, vibroacoustic modal analysis, could also be used for damage detection. Arora et al. [2] showed that vibroacoustically-coupled mode shapes would change due to damage on the structure by exciting the structure using a loudspeaker from inside a box. Other studies that utilize vibroacoustic modal analysis for damage detection from composite structures are rather sparse and only limited to a few papers [21–24].

In this paper, a wind turbine blade inspection and potential health monitoring methodology that relies on determination of the changes to the acoustic response and perturbations to the perceived source directivity of wind turbine blades is proposed. This new technique has a completely different approach compared to the existing methods and it is solely based upon the audio-range acoustic sensing techniques. A commercially available finite element (FE) based acoustic analysis tool

R. Canturk • M. Inalpolat (✉)
University of Massachusetts Lowell, Lowell, MA 01854, USA
e-mail: Rukiye_Canturk@student.uml.edu; Murat_Inalpolat@uml.edu

S. Pakzad, C. Juan (eds.), *Dynamics of Civil Structures, Volume 2*, Conference Proceedings of the Society for Experimental Mechanics Series, DOI 10.1007/978-3-319-29751-4_11

was used for the subsequent computational analysis required for the initial development of this new methodology. These subsequent analyses include a FE model of a "healthy" blade with no defect/damage and also a "damaged blade" with an intentionally created opening (circular hole) with varying location and size. An acoustic-solid interaction model was developed to investigate the sensitivity of acoustic modal properties (eigenvalues and eigenvectors) to the changes on the severity (size) and location of the damage on the wind turbine blade. Then, a subscale wind turbine test rig was built in order to test some of the hypotheses about the proposed technique for inspection and health monitoring of the wind turbine blades. Some of the preliminary results of the computational and the experimental investigations are presented in this paper.

11.2 Problem Definition

The wind turbine blades constitute closed cavities which interact with stochastic aerodynamic excitations (wind) and mostly deterministic mechanical excitations (gravitational loads) during the operation of a wind turbine. Consequently, they are exposed to aerodynamic wind noise, blade pass noise (a deterministic, speed dependent but still wind-related noise), turbine rotating machinery tonal noise (gears, bearings, generator, etc.), and background noise, when the blades are healthy (no structural damage) and operating in their baseline situation. The hypothesis here is that the noise spectrum measured both inside and the outside of the operational blades will change when blades get damaged. In this paper, we are presenting the preliminary results of our computational and experimental test campaign designed to test our hypothesis. The first step of this test program involves laboratory-scale tests and corresponding experimental verification. At this stage, all of the tests intentionally exclude the wind flow noise. However, our planned test matrix includes measurements where the flow noise will be induced by an industrial size fan located at a certain distance away from the laboratory scale test rig. Next sections of the paper present both the computational and the experimental investigations and their corresponding results obtained at this stage of the test campaign.

11.3 Computational Investigation of the Cavity Acoustics

The acoustic modal analysis is required in order to understand the cavity acoustics for the blade. In the proposed inspection/health monitoring technique, a sound sensor (microphone) and an acoustic speaker is placed inside a blade to excite the cavity from within. Consequently, it is vital to do the modal analysis and extract the acoustic modal properties. In this study, a FE package is utilized to do the acoustic modal analysis. The FE analysis of composite blades with damage requires a multi-domain modeling approach. In the subsequent analyses, the blade is treated as a solid body made up of a composite material with averaged material properties of density at 1064 kg/m^3 and modulus of elasticity at 4.85 GPa [25]. The internal cavity of the subscale blade is modeled as air and the damage is modeled as a separate air column coupled with the internal (in the blade cavity) and external air (outside the blade) regions. This turns the overall problem into a fluid-structure interaction problem and to solve the fluid-structure problem, acoustic-solid interaction interface of the tool is utilized. Specifically, the following parameters for both healthy and damaged blade were obtained to create a basis for the continuation to pursue this new technique: (i) acoustic natural frequencies, (ii) acoustic mode shapes, and acoustic directivity (SPL at the far field $\sim$1.5 m away from the source). The solid model that is required for the FE analysis of the subscale wind turbine blade was created in a solid modeling tool and imported into the FEM package for the analysis part.

The peripheral view of the subscale blade model that exhibits the simple nomenclature used in the paper and the finite element model of the subscale turbine blade are shown in Fig. 11.1a and b, respectively. Tetrahedral elements with a minimum element size of 0.03 m are used in modeling the structure for the healthy blade and reduced when the damage was introduced.

11.3.1 Acoustic Modal Analysis

The wind turbine blades have geometrically sophisticated internal cavities in general. To gage the potential of success in ensonifying the cavity of a wind turbine blade using an internal or external sound source, modal properties and frequency response functions (FRF) of that cavity should be determined first. Here, modal analysis of the much simpler cavity of the subscale wind turbine is carried out. The output of this analysis enables us to determine the ideal location of a sound speaker

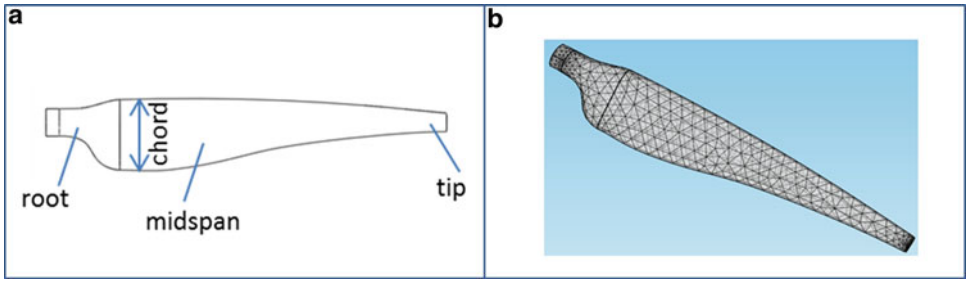

Fig. 11.1 (**a**) The nomenclature, (**b**) the FEM mesh used for the subscale wind turbine blade model

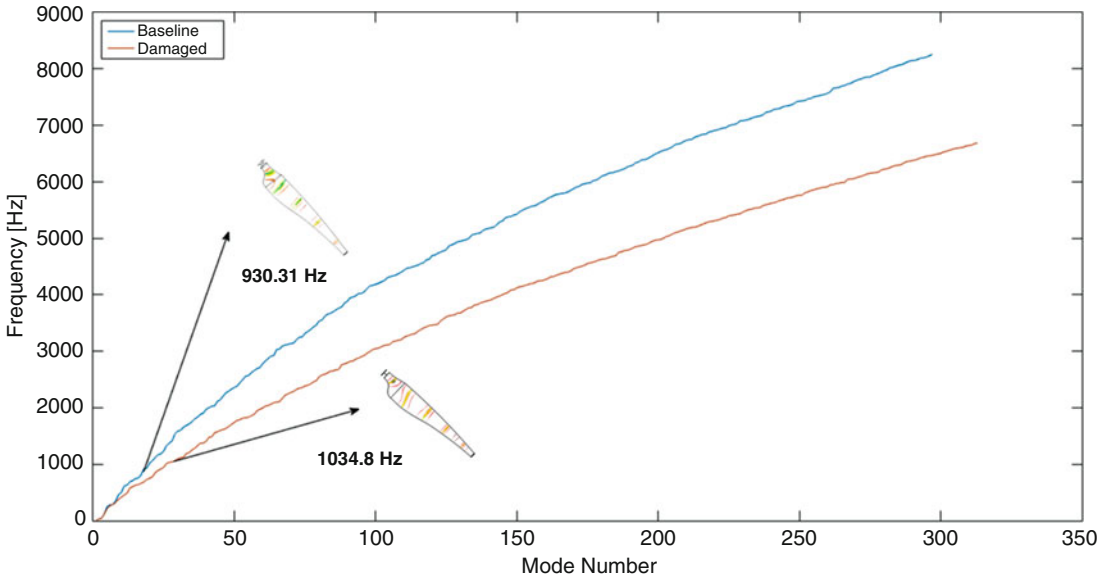

Fig. 11.2 Comparison of the general trends in the natural frequencies of a healthy blade and a damaged blade with a 3 mm root hole

that excites the blade cavity with relatively high efficiency for the frequency range of interest. The main idea is that if the blade has damage, it will manifest itself by changes in natural frequencies and transmission loss of the blade. Furthermore, these changes are affected by severity and location of damage. The natural frequencies of a baseline subscale blade and a representative damaged blade with a root hole (D = 3 mm) are determined from the computational acoustic modal analysis and results are compared in Fig. 11.2.

The first impression on the predictions as obtained from Fig. 11.2 is that the natural frequencies of the damaged blade are lower in general when compared to a baseline healthy blade. However, the natural frequencies should not be compared for the same mode number for these two analyses. In other words, mode number shifts occur for a certain mode when damage occurs. For example, a mode number 19 ($f_{19} = 930.31$ Hz) from the healthy blade should be compared to a mode number 27 ($f_{27} = 1034.8$ Hz) from the damaged blade as these two modes carry the same mode shapes indeed. Nevertheless, when the blade has a root hole, the general trend of damaged blades having higher natural frequencies stays persistent. This result depends on the mode shapes of the cavity and the relative location of the hole on the blade and may not be generalized for all wind turbine blades. The same blade structure was reported to have consistently decreased natural frequencies when the damage was a hole on the midspan region [26].

11.3.2 Far-Field Directivity Analysis

The computational model is leveraged to understand the influence of the damage on the far field sound pressure distribution around the blade. The results of this analysis are helpful in order to understand the best position of a measurement microphone to be located outside of the blade in the far field. It is also required to determine a best position for the acoustic speaker inside

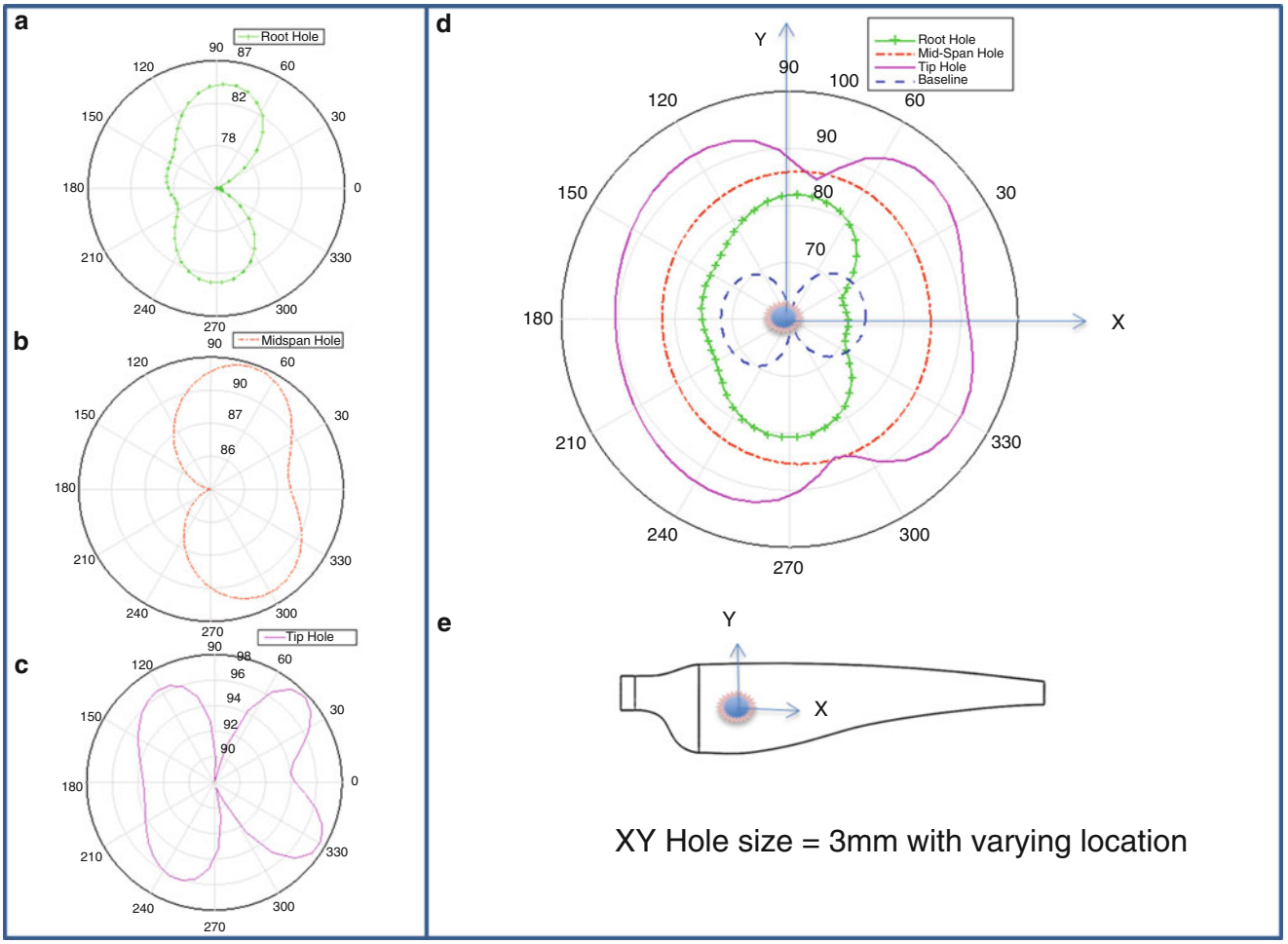

Fig. 11.3 The far-field directivity plots on the X-Y plane for the blade with the same size (D = 3 mm) (**a**) root hole, (**b**) mid span hole, and (**c**) tip hole, (**d**) results superimposed, and (**e**) the plane of analysis

the blade. The subscale turbine blade's cavity is rather small and thus the significance of finding the optimal sound source location is relatively less. However, it will be critical when the same analysis routine was repeated with a full-scale turbine blade with a significantly larger and complicated internal cavity.

In this investigation, far field directivity plots, such as Fig. 11.3a–d, were employed to exhibit the difference between several different analyses steps. A virtual sound source is located inside the blade towards the root as schematically shown in Fig. 11.3e to excite the acoustic cavity of the blade and the corresponding far-field directivity evaluation is performed 1.5 m away from the source, outside the blade. The sound source operates at a pure tone of 500 Hz in this specific computational test. The directivity plots in Fig. 11.3a–c illustrate the directivity information for the damaged blade with a D = 3 mm diameter hole located at various locations (root, midspan, and tip, respectively) and the same results are compared against the baseline directivity in Fig. 11.3d. It is important to note that the center of the directivity plots is always coinciding with the location of the virtual sound source. The directivity plots in Fig. 11.3 indicate that a tip hole has a dominant angular directivity and sound pressure level distribution compared to a midspan and a root hole of the same size. Although these analyses excluded the aerodynamic interactions (wind flow induced noise), they suggest an external microphone located on the turbine and relatively close to the tip of the blades will potentially receive the highest signal-to-noise ratio.

The influence of damage location on the sound directivity and level is investigated for the three separate regions on the blade, root, midspan and the tip as projected on the Y-Z plane. All of these results are presented in Fig. 11.4 and they indicate a tip hole will result in a higher pressure distribution with a directivity indicating an optimal microphone location to be on the trailing-edge side.

In order to gage the sensitivity of the directivity patterns and sound pressure distribution to the severity (size) of the damage, three different size holes are utilized at three different axial locations and the corresponding results are shown in

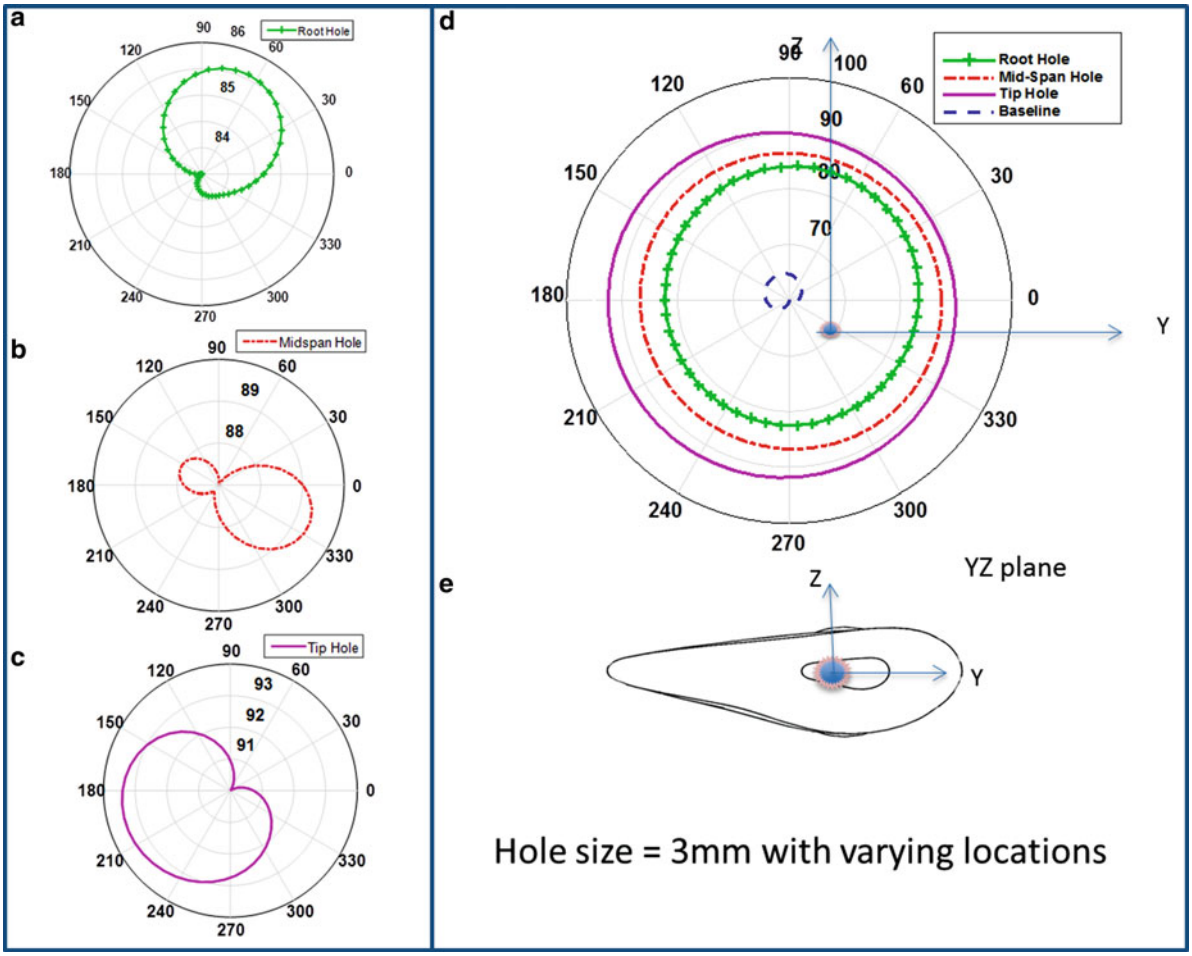

Fig. 11.4 The directivity information given on the Y-Z plane for the blade with different size (**a**) root holes, (**b**) mid-span holes, and (**c**) tip holes, (**d**) results superimposed, and (**e**) the plane of analysis

Fig. 11.5. The blue dots on the blade sketches denote the location of the holes for that experiment. The results shown in Fig. 11.5a follow the common intuition and as such the sound pressure values at all angular location around the blade (on the X-Y plane) increase as the size of the damage grows. The results from the second test with the blade with a midspan hole are exhibited in Fig. 11.5b and counter-intuitive as the size of the damage do not change neither the directivity nor the sound pressure level distribution. However, the damaged case still has a higher pressure level distribution compared to the healthy baseline case. For the cases including the blade with different sizes of a tip hole, it is seen that as the hole diameter increases, sound pressure level distribution decreases. These results are counter-intuitive as well. All of the results are exhibiting the fact that the cavity acoustics, specifically the mode shapes and the corresponding pressure amplitude distribution inside the cavity, significantly impacts the test results.

The results from a similar analysis, but for a different plane are shown in Fig. 11.6. These results exhibit the directivity information on the Y-Z plane that passes through the sound source and are in-line with the results on the X-Y plane.

11.4 Experimental Investigation

The proposed technique is based on an understanding of the influence of structural damage on the acoustic transfer functions for blades exposed to internal and external acoustic excitations. It utilizes **(1)** low-cost, low-maintenance microphones for passive monitoring of natural aerodynamically-driven, flow-induced noise that couples with the structural damage and **(2)** acoustic sources to excite the dynamic cavity structure from within. The blade damage will manifest itself in changes to the acoustic cavity frequency response functions and to the blade acoustic transmission loss. A number of optimally-located

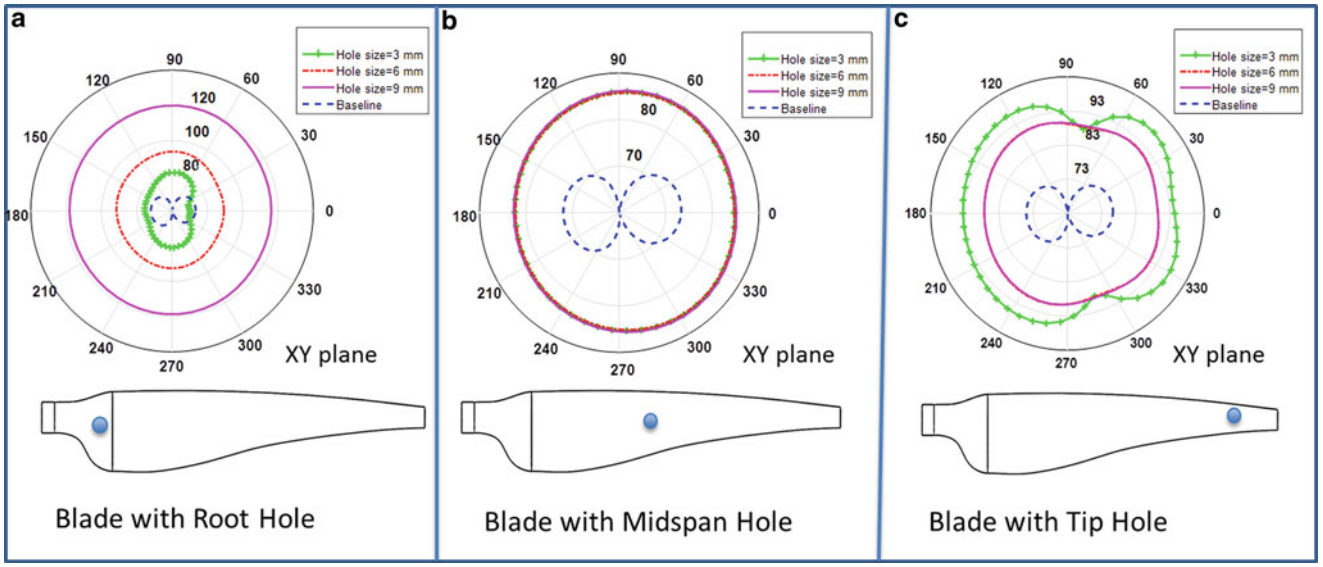

Fig. 11.5 The directivity information on the X-Y plane given for the blade with different size (D = 3 mm, 6 mm or 9 mm) (**a**) root holes, (**b**) mid-span holes, and (**c**) tip holes

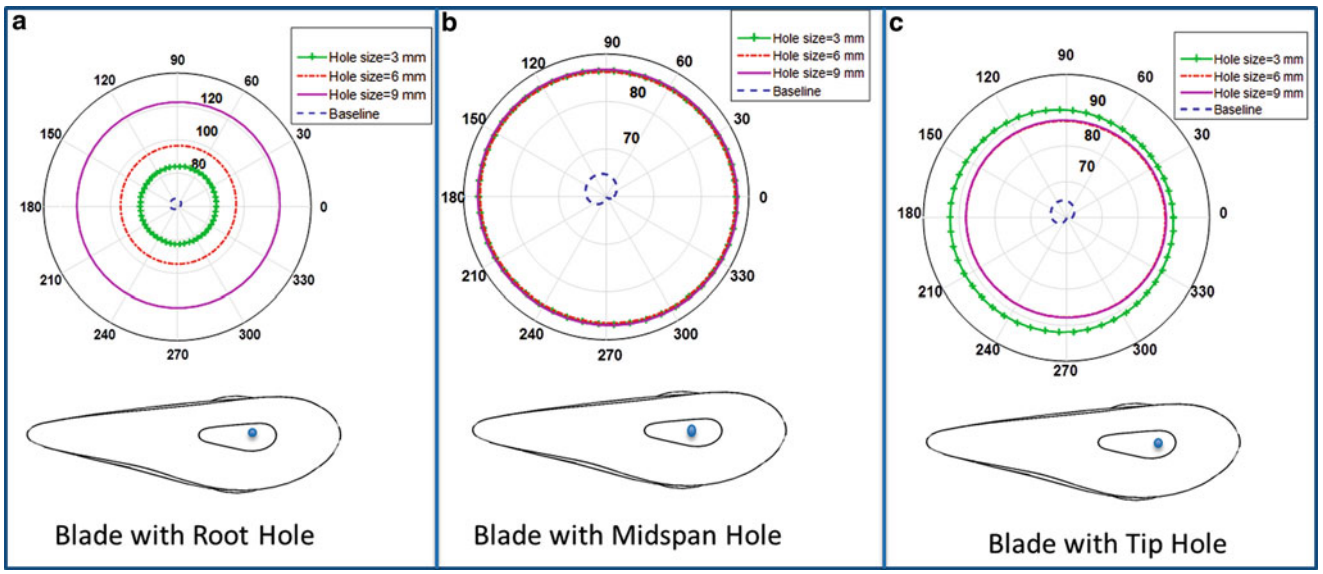

Fig. 11.6 The directivity information on the Y-Z plane given for the blade with different size (D = 3 mm, 6 mm or 9 mm) (**a**) root holes, (**b**) mid-span holes, and (**c**) tip holes

wireless microphones can be used for the (1) ***internal passive detection*** and a single microphone located outside but nearby the blades will be used for the (2) ***external active detection*** of damage. The first approach leverages the energy caused by the wind/flow-induced noise, exterior to the cavity. The blade can be continuously monitored and when damage is originated, the internal acoustic signature will change due to the changes in the transmission loss (caused by the hole or crack) and/or the distorted acoustic pressure field. A laboratory-scale wind turbine is designed and built by the team and shown in Fig. 11.8. This wind turbine has composite blades with internal cavities specifically designed to accommodate wireless sensors as well as wireless speakers. A total number of six composite blades were molded, three of which will be healthy blades with no damage, and the other three contain different types (hole, edge split, cracks, delamination) and severity (smaller to larger sizes) of intentionally-induced damage. The blades are held by a hub that allows access to the sensors and the speaker systems inside the blades (i.e., for battery replacements and fine-tuning of the speakers etc.). There is one wireless microphone inside each blade accompanied by a wireless, battery-operated speaker that can ensonify the internal cavity of each blade for the internal passive detection. An additional microphone is placed outside the blades, under the nacelle for the external active detection of the damage to the blades. Sensing scheme is also shown in Fig. 11.7 for one of the blades.

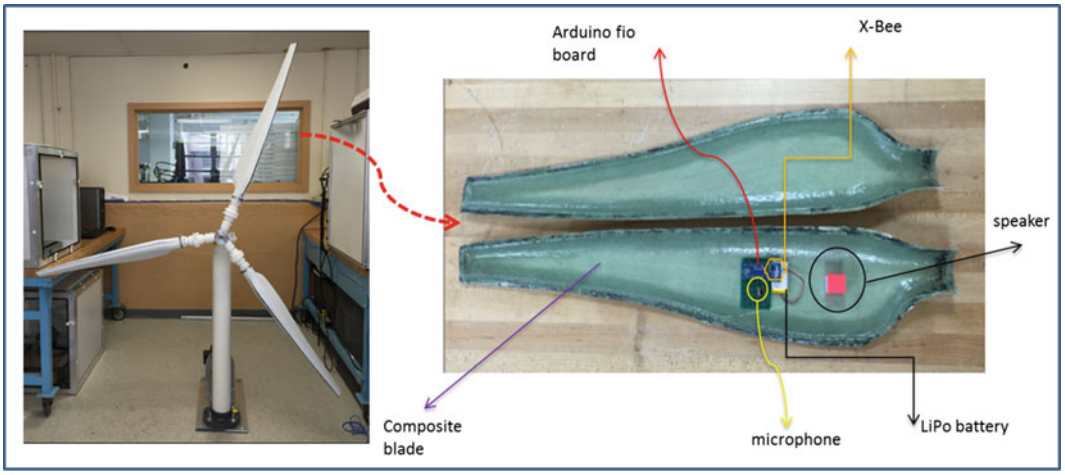

Fig. 11.7 The subscale wind turbine and a close-up view of the micro-controller and the associated connections for a wireless acoustic sensing circuitry

11.4.1 Test Results from a Non-rotating Blade

Frequency response functions (FRFs) are obtained in order to establish a baseline FRF between the source and the sensing element within the blade cavity. The main idea is that the FRF will deviate from this baseline FRF when damage occurs. One of the difficulties in establishing any baseline data, including the FRFs, is that the baseline itself changes due to changes in environmental conditions (temperature, humidity, dust, etc.). The team is in the process of advanced machine learning algorithms in order to accommodate the changes to the baseline and to differentiate the changes due to environmental conditions and the changes due to damage. However, the machine learning piece of this study is beyond the scope of this paper and will be disseminated with the future publications.

One of the non-rotating (stationary) composite blades (shown in Fig. 11.7) is utilized in its healthy (undamaged) state in preliminary tests in order to establish baseline FRFs between the speaker and the microphone inside the blade cavity. The cavity of the composite blade is expected to be in complete isolation to the outside when there is no damage. Broadband random noise is used to acoustically excite the cavity from inside and National Instruments PXI 64 channel data acquisition system powered by M + P data acquisition software was utilized in order to collect the signals from a microphone inside the blade and another microphone located outside the blade but located on the tower of the subscale turbine. All signals were transmitted wirelessly using an XBee data transfer platform to the outside node, which is connected to the PXI DAQ system. The sound pressure spectra obtained from the stationary and healthy blade and when the same blade has an intentionally created 3 mm tip hole are compared in Fig. 11.8.

The preliminary data obtained from these preliminary experiments turned out to have low signal-to-noise ratio because of the insufficient number of averaging used during the data collection process. The team has used only five linear averages, to be increased in the later experiments. The peaks exhibited in Fig. 11.8 are expected to be the cavity modes of the blade. Consequently, any changes due to the damage should be reflected as shifts to these peaks. Most of the changes have occurred for the relatively high frequency modes for a 3 mm tip hole. This is intuitive as the lower frequency modes and their pressure distribution in the form of harmonic pressure waves with larger wavelengths are not imacted by the small holes. Some of the variations in these peaks were quantified on the peaks and anti-peaks in Fig. 11.8.

In the meanwhile the data obtained from the external microphone located on the blade for the same two cases are compared in Fig. 11.9. However, this set of data was taken all three blades were ensonified by their internal speakers generating three different tones at 500 Hz, 550 Hz, and 600 Hz, respectively. Although the speakers generated pure tones at discrete frequencies, the signals get distorted by the cavity acoustics and thus the corresponding spectra have multiple harmonics $\left(f_i = i.500,\ f_j = j.550,\ f_k = k.600\ \text{Hz},\ \textit{where } i, j \textit{ and } k \textit{ are the harmonic \#}\right)$ of the intended pure tone signals. The comparison presented in Fig. 11.10 not only indicate a SPL increase at 500 Hz (first blade with a damage), but also indicate the existence of other peaks, for instance the peaks located at 698 Hz, 908 Hz, 1397 Hz *etc*.

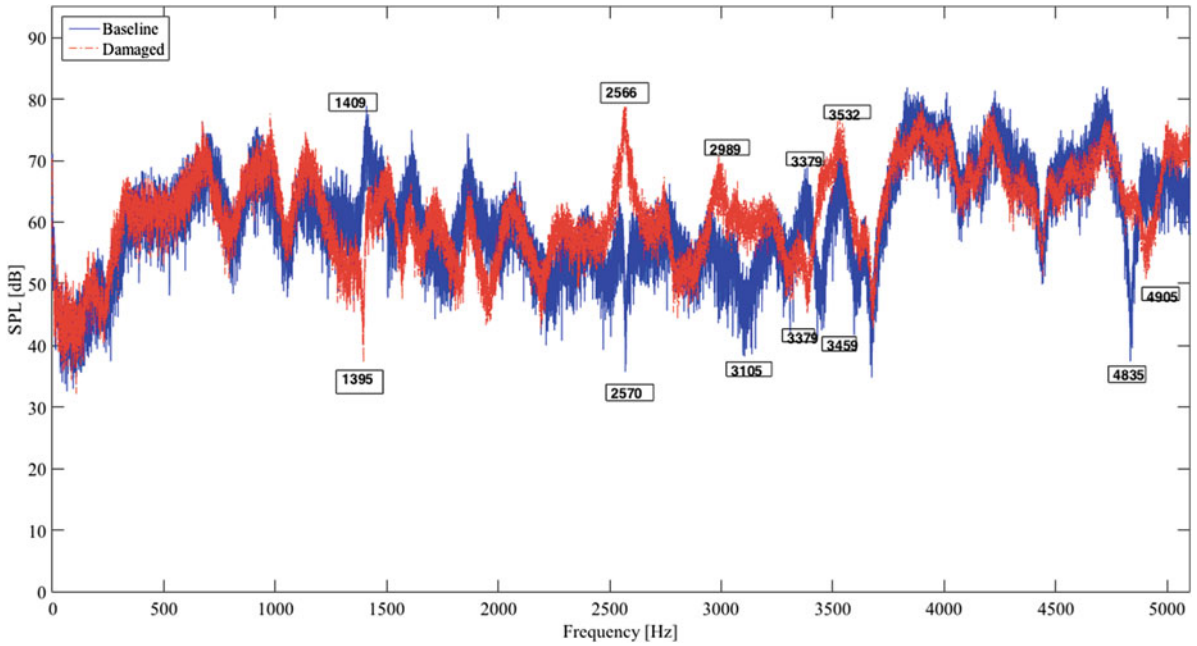

Fig. 11.8 Comparison of the SPL spectra obtained by a blade internal microphone located in a non-rotating baseline blade and it's damaged version with a tip hole

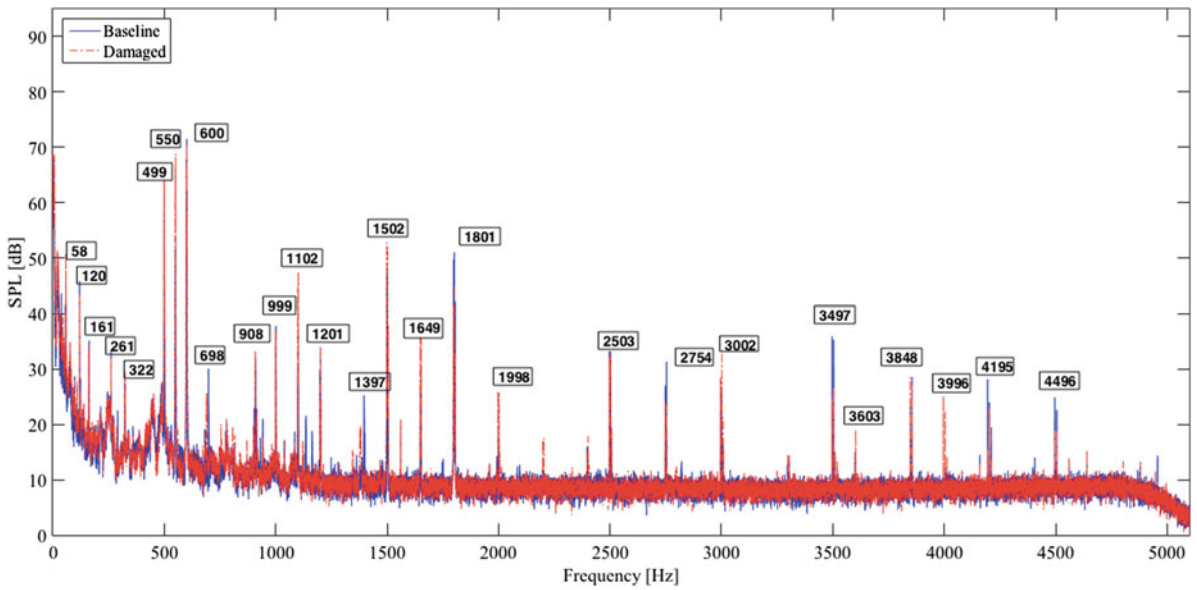

Fig. 11.9 Comparison of the SPL spectra obtained by a blade external microphone located on the subscale wind turbine with non-rotating baseline blades and when one of the blades had a tip hole (D = 3 mm)

11.4.2 Results from a Rotating Blades

The subscale wind turbine test rig has a speed controlled DC motor to control the rotational speed of the blades. A set of experiments at a constant rotational rotor speed of 43 rpm was done in order to understand the influence of rotations of the blade on the sound signal received by the external microphone. A subsequent set of spectra are compared for a completely health blade and a damaged blade #1 scenario and the results are exhibited in Fig. 11.10. A first comparison between Figs. 11.9 and 11.10 reflect a 1 *to* 3 dB reduction in SPL throughout the whole frequency range, when the blades were rotating. The influence of rotations and thus the changes to the directivity orientation of each blade with respect to the

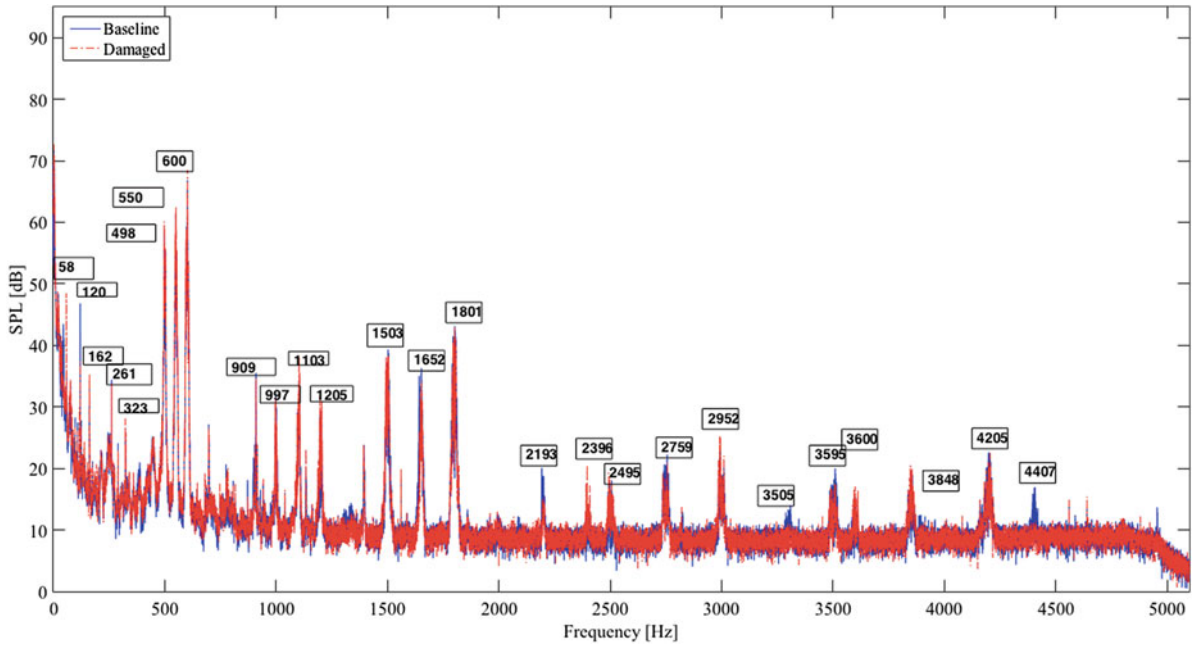

Fig. 11.10 Comparison of the SPL spectra obtained by a blade external microphone located on the subscale wind turbine with rotating baseline blades and when one of the blades had a tip hole (D = 3 mm)

fixed microphone position causes the microphone to receive the half of the sound pressure (on a linear scale). Additionally, there are shifts occurring at the higher frequency range of the spectrum. For instance the peak at 3497 Hz (∼ 7.500 Hz), shifts up to 3505 Hz. This may have been caused by a layer of modulations due to rotating blades. These shift in the frequencies and amplitudes of some of the peaks observed are essentially expected to be instrumental in the damage detection stage. However, it is beyond the scope of this paper and will be disseminated in later studies.

11.5 Conclusions

In this paper, a new approach for both inspection (for stationary blades) and for structural health monitoring of wind turbine blades is proposed. This new approach is based upon a periodic acoustic interrogation idea. The blades are actively ensonified from internal by low-cost wireless acoustic speakers, while a wireless, battery-operated, low-cost microphone (one microphone per blade cavity) located internal to each blade and a single microphone outside the blades on the wind turbine tower continuously interrogates the sensed acoustic variations based upon a machine learning algorithm. This paper presents the preliminary results from a computational investigation of the blade's cavity acoustics and of the laboratory scale experiments to test the fundamental hypothesis behind the idea. Preliminary results indicate that the proposed approach is meritorious but the signal processing and the machine learning algorithms that will continuously be interrogating the blades will be critical in order to interpret the results and need to be adaptable to different environmental conditions and background noise.

Acknowledgements The authors would like to acknowledge the help from Elizabeth Slavkovsky and Patrick Logan of The Structural Dynamics and Acoustic Systems Laboratory at University of Massachusetts Lowell, during some of the experimental stages of this study.

References

1. U.S. Wind Industry Market Reports, AWEA (2015)
2. Arora, V., Wijnant, Y.H., de Boer, A.: Acoustic-based damage detection method. Appl. Acoust. **80**, 23–27 (2014)
3. Yang, W.: Testing and Condition Monitoring of Composite Wind Turbine Blades. Recent Advances in Composite Materials for Wind Turbine Blade, pp. 147–169. World Academic, Hong Kong (2013)

4. Hyers, R.W., McGowan, J.G., Sullivan, K.L., Manwell, J.F., Syrett, B.C.: Condition monitoring and prognosis of utility scale wind turbines. Energ. Mater. **1**(3), 187–203 (2006)
5. Kahn-Jetter, Z.L., Chu, T.C.: Three-dimensional displacement measurements using digital image correlation and photogrammic analysis. Exp. Mech. **30**(1), 10–16 (1990)
6. Ozbek, M., Rixen, D.J.: Optical measurements and operational modal analysis on a large wind turbine: lessons learned. Shock Vib. **5**, 257–276 (2011)
7. Ozbek, M., Rixen, D.J., Erne, O., Sanow, G.: Feasibility of monitoring large wind turbines using photogrammetry. Third Int. Conf. Sustainable Energy Environ. Protect SEEP 2009 **35**(12), 4802–4811 (2010)
8. Ozbek, M., Mengt, F., Rixen, D.J., Van Tooren, M.J.L.: Identification of the dynamics of large wind turbines by using photogrammetry. Struct. Dyn. Renew. Energy **1**, 351–359 (2011)
9. Ozbek, M., Rixen, D.J.: Operational modal analysis of a 2.5 mw wind turbine using optical measurement techniques and strain gauges. Wind Energ. **16**, 367–381 (2013)
10. Carr, J., Baqersad, J., Niezrecki, C., Avitabile, P.: Dynamic stress-strain on turbine blade using digital image correlation techniques, Part 1—static calibration. Proceedings of the Thirtieth International Modal Analysis Conference, Jacksonville (Feb 2012)
11. Carr, J., Baqersad, J., Niezrecki, C., Avitabile, P.: Dynamic stress-strain on turbine blade using digital image correlation techniques, Part 2—dynamic measurements. Proceedings of the Thirtieth International Modal Analysis Conference, Jacksonville (Feb 2012)
12. Niezrecki, C., Avitable, P., Chen, J., Sherwood, J., Lundstorm, T., LeBlanc, B., Hughes, S., Desmond, M., Beattie, A., Rumsey, M., Klute, S.M., Pedrazzani, R., Werlink, R., Newman, J.: Inspection and monitoring of wind turbine blade-embedded wave defects during fatigue testing. Struct. Heal. Monit. **13**, 629–643 (2014)
13. Aizawa, K., Poozesh, P., Niezrecki, C., Baqersad, J., Inalpolat, M., Heilmann, G.: An acoustic-array based structural health monitoring technique for wind turbine blades. Struct. Heal. Monit. Inspect. Adv. Mater. Aerospace Civil Infrastruct. SPIE **9437**, 1–17 (2015)
14. Tipperman, J., Lanza di Scalea, F.: Experiments on a wind turbine blade testing an indication for damage using the casual and anti-casual Green's function reconstructed from a diffuse field. SPIE **9064**, 1–1 (2014)
15. Boukabache, H., Escriba, C., Zedek, S., Fourniols, J.: Wavelet decomposition based diagnostic for structural health monitoring on metallic aircrafts: case of crack triangulation and corrosion detection. Int. J. Prognostics Health Manag., ISSN 2153-2648 (2013)
16. Aizawa, K., Niezrecki, C.: Wind turbine blade health monitoring using acoustic beamforming techniques. J. Acoust. Soc. Am. **135**(4), 2392–2393 (2014)
17. Pierro, E., Mucchi, E., Soria, L., Vecchio, A.: On the vibro-acoustical operational modal analysis of a helicopter cabin. Mech. Syst. Signal Process. **23**, 1205–1217 (2009)
18. Farshidi, R., Trieu, D., Park, S.S., Freiheit, T.: Non-contact experimental modal analysis using air excitation and a microphone array. Measurement **43**, 755–765 (2010)
19. Rumsey, M.A., Paquette, J.A.: Structural health monitoring of wind turbine blades. Proceedings of the SPIE Smart Sensor Phenomena, Technology, Networks, and System (2008)
20. Sundaresan, M.J., Schulz, M.J., Ghoshal, A.: Structural health monitoring static test of a wind turbine blade. National Renewable Energy Laboratory Report (1999)
21. Fazenda, B.M.: Acoustic based condition monitoring of turbine blades. ICSV 18, Rio de Janeiro, Brazil, pp. 1–8 (2011)
22. Fazenda, B.M., Comboni, D.: Acoustic condition monitoring of wind turbines: tip faults. The 9th International Conference on Condition Monitoring and Machinery Failure Prevention Technologies, London (2012)
23. Stearman, R.O., Schulz, G.H., Rohre, S.M.: Aircraft damage detection from acoustic and noise impressed signals found by a cockpit voice recorder. J. Acoust. Soc. Am. **101**, 3085 (1997)
24. Lam, H.F., Ng, C.T., Lee, Y.Y., Sun, H.Y.: System identification of an enclosure with leakages using a probabilistic approach. J. Sound Vibr. **322**, 756–771 (2009)
25. Kim, S., Adams, D.E., Sohn, H., Rodriguez-Rivera, G., Myrent, N., Bond, R., Vitek, J., Carr, S., Grama, A., Meyer, J.J.: Crack detection technique for operating wind turbine blades using vibro-acoustic modulation. Struct. Heal. Monit. **13**(6), 660–670 (2014)
26. Canturk, R., Inalpolat, M.: A computational acoustic interrogation of wind turbine blades with damage. Comsol Conference, Boston (2015)

Chapter 12
Damage Location by Maximum Entropy Method on a Civil Structure

Pastor Villalpando, Viviana Meruane, Rubén Boroschek, and Marcos Orchard

Abstract This article presents the application of a new damage assessment method based on a supervised learning algorithm that uses the principle of maximum entropy. The proposed algorithm employs, as reference information, the natural frequencies and mode shapes obtained with a numerical model of the structure in an undamaged condition and under different damage scenarios. The algorithm is validated with experimental tests on a laboratory six-levels-structure that is 2 m tall. The structure was anchored to a horizontal vibrating shaker table and it was excited at the support level by different seismic records and colored noise. The change in the structure from a normal condition to a damaged one is made by three consecutive reductions in the cross-section of a column. Additionally, a perturbation is introduced as a 0.5 % increase in the total mass of the structure. The experimental modal properties are identified by the Stochastic Subspace and Multivariable Output Error State sPace (MOESP) methods and they are compared with those obtained with a numerical model. The identification, location and quantification of damage that has been obtained with the proposed algorithm in the different test conditions, agrees well with the experimental damage, even for the conditions were few sensors are located in the structure.

Keywords Structural damage assessment • Supervised learning algorithms • Maximum entropy principle • Linear approximation • Subspace based system identification

12.1 Introduction

The application of structural health monitoring for detection, localization and quantification of damage to civilian structures is an area that in recent years has become very important. This arises in order to ensure the safety of occupants and to provide continuity of operations in the industry. Traditionally, the structures are subjected to inspections due to aging elements, material degradation and to seismic events, among others. Most of the conditions during inspections often fail to be evaluated effectively in inaccessible areas, or areas with architectural covers that hide the true extent of the damage to the structure. In these cases, the detection of damage using vibration-based methods becomes relevant [1]. The fundamental idea is based on the observation of the structure under different excitations (colored noise, seismic records), so that they can determine the changes in dynamic properties of the structure (frequencies, damping and mode shapes) due to damage. Therefore, any abrupt or cumulative change, measured from a certain threshold, can be observable in the modal properties of the structure. Here, it is considered that the structure remains in a linear range between states of change.

Subspace identification methods have made great progress in recent years, in both theoretical and practical levels, as they can estimate directly the system matrices from sensor measurements. The core of the identification process is the QR factorization and singular value decomposition, applied to the Hankel matrix built from observations [2]. Two methods are presented in this article, which are based on the response of the system; MOESP (Multivariable Output Error State Space) from both the seismic input and output data [3] and SSI-COV (Stochastic Subspace Identification-based Covariance) [4] for the Operational Modal Analysis where excitation forces are not measure, such as environmental or operational excitations.

P. Villalpando • R. Boroschek, Ph.D. (✉)
Department of Civil Engineering, University of Chile, Santiago, Chile
e-mail: pvillalpando@ing.uchile.com; rborosch@ing.uchile.cl

V. Meruane, Ph.D.
Department of Mechanical Engineering, University of Chile, Santiago, Chile
e-mail: vmeruane@ing.uchile.cl

M. Orchard, Ph.D.
Department of Electrical Engineering, University of Chile, Santiago, Chile
e-mail: morchard@ing.uchile.cl

S. Pakzad, C. Juan (eds.), *Dynamics of Civil Structures, Volume 2*, Conference Proceedings of the Society for Experimental Mechanics Series, DOI 10.1007/978-3-319-29751-4_12

The results obtained with these algorithms need to be evaluated under multiple system orders. For this purpose, we have used the methodology of Fast multi-order [5], which reduces the computational complexity with mathematical reformulation reducing considerably the calculation time. A stability diagram [6] helps in determining representative modal parameters of the structure from the defined orders. Stable modal parameters of identifications (MOESP or SSI-COV) under different test conditions should give similar modal parameters within a limited range of variability.

Model-based damage assessment requires solving a nonlinear inverse problem that can be solved with supervised learning algorithms [7, 8]. The most traditional methods are based on artificial neural networks, but its application stumbles on the time needed to train the model and the need to have a lot of parameters to be selected. Alternatively Gupta [9], presented a nonparametric method of supervised learning, which generalizes the linear approximation by using the principle of maximum entropy [10], by means of statistical inference. The first investigations using maximum entropy to the detection, location and quantification of damage have been applied to one-dimensional structural elements such as a cantilever beam [11], an eight-DOF spring-mass system, an experimental beam and a car exhaust system [8], in addition this algorithm has been applied to a two-dimensional plate structure to assess debonding in honeycomb aluminum panels [7]. Experimental results have shown to be successful in identifying the assigned damages, moreover calculation time was similar to a neural network, but with the precision of a model updating algorithm based on global optimization, making their use attractive to damage detection in complex structures.

This paper presents the identification of damage in a three-dimensional structure, by means of a supervised learning algorithm based on a linear approximation using the principle of maximum entropy in conjunction with the structure's modal properties (frequencies and modal shapes). The performance of the proposed algorithm is validated with experimental tests in a laboratory structure. The structure has six levels, and it is 2 m tall. The structure was attached to a horizontal shaking table and it was tested with different seismic records (Valparaiso, Chile 1985, Maule, Chile 2010, Loma Prieta, USA 1989 Northridge, USA 1994) and colored noise (filtered from 0 to 15 Hz). Modifying the structure from the undamaged condition to a condition with damage is done by introducing a progressive reduction in the cross-section of a column located in the second level. Additionally a condition of disturbance in the structure was induced with the addition of 0.50 % of the total mass of the structure at the fourth level. The purpose of this, is to observe the behavior of the structure and of the damage identification algorithm to anomalous conditions which do not correspond to damage or accumulation to damage in the structure.

12.2 Linear Approximation to Maximum Entropy Principle

Let the observation vector $\boldsymbol{Y}^j = \left\{Y_1^j, Y_2^j, \ldots, Y_m^j\right\} \in \mathbb{R}^m$ represent the *j-th* damage state of the structure, where m is the number of structural elements and Y_m^j is percentage of damage of element m for structural state j. Notice that it does not represent a single damage scenario but to an element global change. Let the feature vector $\boldsymbol{X}^j = \left\{X_1^j, X_2^j, \ldots, X_n^j\right\} \in \mathbb{R}^n$, represents a set of vibration characteristics of the structure associated with a state of damage $\boldsymbol{Y}^j$. The variables $\boldsymbol{X}$ and $\boldsymbol{Y}$ have joint probability distribution $P_{X,Y}$. Let a set of k independent and identically distributed samples are drawn from $P_{X,Y}$; these samples represent the database $(\boldsymbol{X}^1, \boldsymbol{Y}^1), (\boldsymbol{X}^2, \boldsymbol{Y}^2), \ldots, (\boldsymbol{X}^k, \boldsymbol{Y}^k)$. The main problem in supervised learning algorithms is the best estimate $P_{Y\left|X\right.}$, i.e., given a feature vector $\boldsymbol{X}$, estimate the corresponding observation $\boldsymbol{Y}$. Let $\hat{\boldsymbol{Y}}$ denotes the estimated value of $\boldsymbol{Y}$. Linear approximation takes the N nearest neighbors to a test point X and uses a linear combination of them to represent X as:

$$\boldsymbol{X} = \sum_{j=1}^{N} \omega_j(\boldsymbol{X}) \cdot \boldsymbol{X}^j(\boldsymbol{X}), \quad \sum_{j=1}^{N} \omega_j(\boldsymbol{X}) = 1, \tag{12.1}$$

where $\omega_1, \omega_2, \ldots, \omega_N$ are weighting functions, and $\boldsymbol{X}^1(\boldsymbol{X}), \boldsymbol{X}^2(\boldsymbol{X}), \ldots, \boldsymbol{X}^N(\boldsymbol{X})$ are the N nearest neighbors to a test point $\boldsymbol{X}$, out of database set. The equations given in (12.1) can be expressed as the following system of linear system:

$$\boldsymbol{A} \cdot \boldsymbol{w} = b, \ \boldsymbol{w} \geq 0 \tag{12.2}$$

with

$$\boldsymbol{A} = \begin{bmatrix} X_1^1 & X_1^2 & \cdots & X_n^N \\ X_2^1 & X_2^2 & \cdots & X_n^N \\ \vdots & \vdots & \ddots & \vdots \\ X_n^1 & X_n^2 & \cdots & X_n^N \\ 1 & 1 & \cdots & 1 \end{bmatrix}_{(n+1)\times N}, \quad b = \begin{bmatrix} X_1 \\ X_2 \\ \vdots \\ X_n \\ 1 \end{bmatrix}_{(n+1)\times 1}, \quad \boldsymbol{w} = \begin{bmatrix} \omega_1 \\ \omega_2 \\ \vdots \\ \omega_N \end{bmatrix}_{N\times 1}$$

After $\boldsymbol{w}$ is obtained from (12.2), $\hat{\boldsymbol{Y}}$ is estimated as

$$\widehat{\boldsymbol{Y}} = \sum_{j=1}^{N} \omega_j(\boldsymbol{X}) \cdot \boldsymbol{Y}^j(\boldsymbol{X}), \tag{12.3}$$

where $\boldsymbol{Y}^1(\boldsymbol{X}), \boldsymbol{Y}^2(\boldsymbol{X}), \ldots, \boldsymbol{Y}^N(\boldsymbol{X})$ are the corresponding observations to the N selected neighbors. Typically, the system of equations (12.2) is undetermined, and its solution is tackled via a constrained optimization technique of the family of least-squares. However, these methods produce some negative weights, which lacks physical meaning. An alternative that generates positive weights is obtained via the maximum-entropy principle [10], which can be written as:

$$\max_{p\in\mathbb{R}_+^N} \left[H(\omega) = -\sum_{j=1}^{N} \omega_j(\boldsymbol{X}) \ln\left(\frac{\omega_j(\boldsymbol{X})}{m_j(\boldsymbol{X})}\right) \right] \tag{12.4a}$$

Subject to the restrictions:

$$\sum_{j=1}^{N} \omega_j(\boldsymbol{X}) \cdot \tilde{\boldsymbol{X}}^j = 0, \ \sum_{j=1}^{N} \omega_j(\boldsymbol{X}) = 1, \tag{12.4b}$$

where $m_j(\boldsymbol{X})$ is a prior distribution that acts as a 'first estimation' for $\omega_j(\boldsymbol{X})$ and $\tilde{\boldsymbol{X}}^j = \boldsymbol{X}^j - \boldsymbol{X}$ has been introduced as a shifted measure for stability purposes. A typical prior distribution is the smooth Gaussian [12], defined as

$$m_j(\boldsymbol{X}) = exp\left(-\beta_j \left|\left|\tilde{\boldsymbol{X}}^j\right|\right|^2\right), \tag{12.5}$$

where: $\beta_j = \gamma/h_j^2$; γ is a parameter that controls the radius of the Gaussian prior at $\boldsymbol{X}^j$, and therefore its associated weight function; and h_j is a n-dimensional Euclidean distance between neighbors that can be distinct for each $\boldsymbol{X}^j$. In view of the optimization problem posed in (12.4a) for supervised learning, maximizing the entropy chooses the weight solution that commits the least to anyone in the databases samples [13]. The solution of the maximum entropy optimization problem is handled by using the procedure of Lagrange multipliers, which yields

$$\omega_j(\boldsymbol{X}) = \frac{Z_j(\boldsymbol{X};\boldsymbol{\lambda}^*)}{Z(\boldsymbol{X};\boldsymbol{\lambda}^*)}, \ Z_j(\boldsymbol{X};\boldsymbol{\lambda}^*) = m_j(\boldsymbol{X}) \cdot exp\left(-\boldsymbol{\lambda}^* \cdot \widetilde{\boldsymbol{X}}^i\right), \tag{12.6}$$

where: $Z(\boldsymbol{X};\boldsymbol{\lambda}^*) = \Sigma_j Z_j(\boldsymbol{X};\boldsymbol{\lambda}^*)$, $\widetilde{\boldsymbol{X}}^i = \left[\widetilde{X}_1^i \ldots \widetilde{X}_N^i\right]^T$ y $\boldsymbol{\lambda}^* = \left[\lambda_1^* \ldots \lambda_N^*\right]^T$

In (12.6) the vector of Lagrange multiplier, $\boldsymbol{\lambda}^*$, is the minimizer of the double optimization problem proposed in (12.4b)

$$\boldsymbol{\lambda}^* = \arg\min_{\lambda\in\mathbb{R}^N} \ln Z(\boldsymbol{X};\lambda) \tag{12.7}$$

Which leads to the following system of nonlinear equations

$$f(\boldsymbol{\lambda}) = \nabla_\lambda \ln Z(\boldsymbol{\lambda}) = -\sum_{j=1}^{N} \omega_j(\boldsymbol{X}) \cdot \widetilde{\boldsymbol{X}}^i = 0, \tag{12.8}$$

where ∇_λ represents the gradient with respect to $\boldsymbol{\lambda}$. Once convergence $\boldsymbol{\lambda}^*$ is found, the weighting functions are calculated in (12.6).

12.3 Case Study

12.3.1 Numerical Model

The numerical model has been built based on finite element considering: cross-sections, masses and the boundary condition with the shaking table. Each of the beam-column elements (frames) that make up the elements of the structure were divided into eight segments to get a good representation of masses distributed in the structure and to ensure proper frequency response and modal characteristics. Figure 12.1 shows the structure modeled with numbered columns.

The structure has been adjusted to initial test conditions, modifying only the elasticity modulus. The mechanical properties of the steel used in the numerical model are shown in Table 12.1.

12.3.2 Experimental Model

The structure to be tested is a metal structure shown in Fig. 12.2a; its height is 1.99 m, which is distributed in six levels with varying heights, Fig. 12.2b. The structure has been attached to the shaking table by means of bolts. Levels behave as rigid diaphragms, and their elements are rectangular tube profiles with a cross-section of $30 \times 50 \times 3$ mm in all levels, whereas the columns are steel flat bars with a cross-section of 50×3 mm. The attachment between columns and diaphragm elements beams is performed by means of a bolted joint.

The structure's response to different excitations has been registered by a central recording and nine uniaxial accelerometers as shown in Fig. 12.2c. The accelerometers are arranged to measure bending and torsional motions with three sensors at level six and one sensor in each of the remaining levels; in addition one sensor is place on the shaking table to measure the forcing function.

The different conditions under which the structure was tested, from the normal condition to slight and severe damage, including the addition of mass to the structure is detailed in Table 12.2.

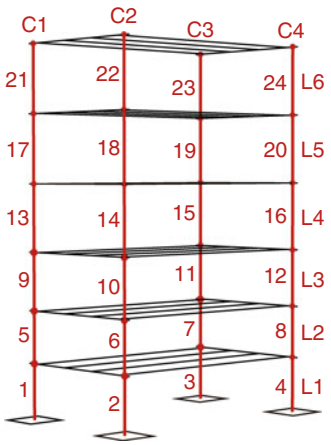

Fig. 12.1 Model of the structure with numbered elements. Columns are designated as 'C' and levels as 'L'

Table 12.1 Structural steel mechanical properties ASTM A36

Property	Unit	Value
Elasticity modulus, E	GPa	200
Shear modulus, G	GPa	76.9
Poisson's ratio	0.3	0.3
Coefficient of thermal expansion, δ	mm/mm °C	1.17e-05

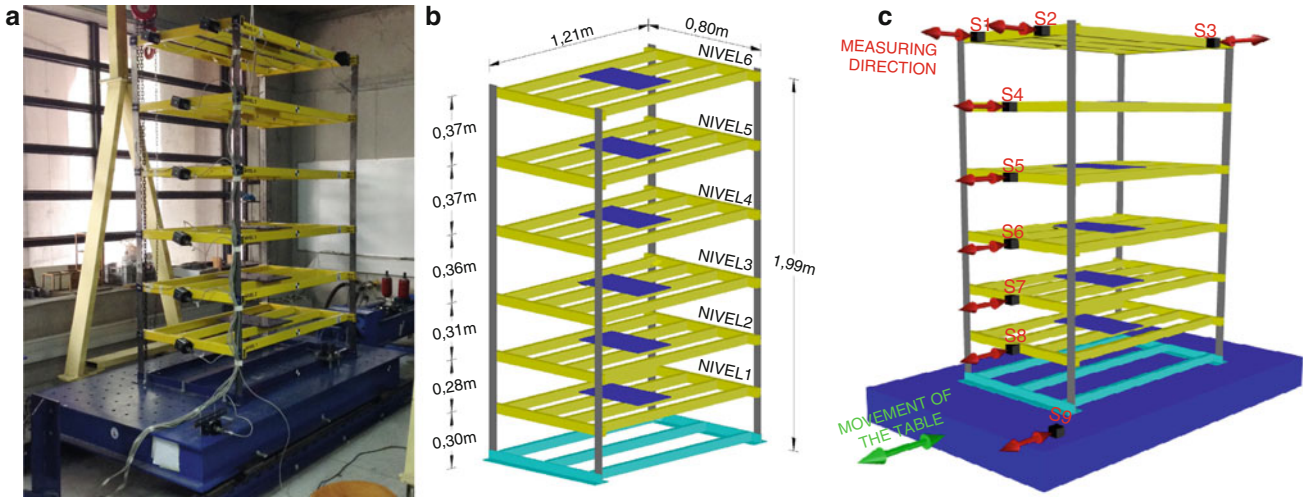

Fig. 12.2 Experimental structure. (**a**) Laboratory image, (**b**) Geometry, (**c**) Configuration, eight sensors and measuring direction

Table 12.2 Tests conducted

Test	Condition	Legend
Normal	Normal	Norm
Normal	Normal + added 0.50 % mass	NR + M
Slight damage	Reduction of 20 % in element 5	RE20
Slight damage	Reduction of 20 % in element 5 + added 0.50 % mass	R20M
Slight damage	Reduction of 35 % in element 5	RE35
Slight damage	Reduction of 35 % in element 5 + added 0.50 % mass	R35M
Slight damage	Reduction of 50 % in element 5	RE50
Slight damage	Reduction of 50 % in element 5 + added 0.50 % mass	R50M
Severe damage	Reduction of 35 %, all columns in level 2	RT35
Severe damage	Reduction of 50 %, all columns in level 2	RT50

Table 12.3 Records tested in the structure

Identification	Scale	Symbol
Earthquake Valparaiso 1985, Llolleo, 100°	0.12	○
Earthquake Valparaiso 1985, Melipilla, EW	0.16	○
Earthquake Maule 2010, Constitucion, V	0.16	○
Earthquake Loma Prieta 1989, Gilroy, N3 UP	1.00	△
Earthquake Northridge 1994, Arleta, UP	0.30	△
Colored noise 1	1.00	□
Colored noise 2	1.00	□
Colored noise 3	1.00	□

For each of the conditions presented in Table 12.2, eight input records are used. These records are derived from seismic events in Chile and in the United States, in addition to colored noise; as shown in Table 12.3. The records were scaled so that the structure maintains in a linear range of observations during testing, while avoiding additional damage.

Eight modes are identified in most of the tests, they are shown in Fig. 12.3. Figure 12.3a shows the reduction in the frequency as the damage increase for each of the different tests. The corresponding modal shapes 1, 2, 3, 4, 5 and 7 are modes in the direction of shaking table, the modal shape 6 is orthogonal to the direction of shaking table and the modal shape 8 is a torsional mode.

The comparison between measured modal shapes is performed with the Modal Assurance Criteria (MAC), defined according to the expression (12.9) and the scale factor between numerical and experimental modes is computed using the Modal Scale Factor (MSF) expressed in Eq. (12.10):

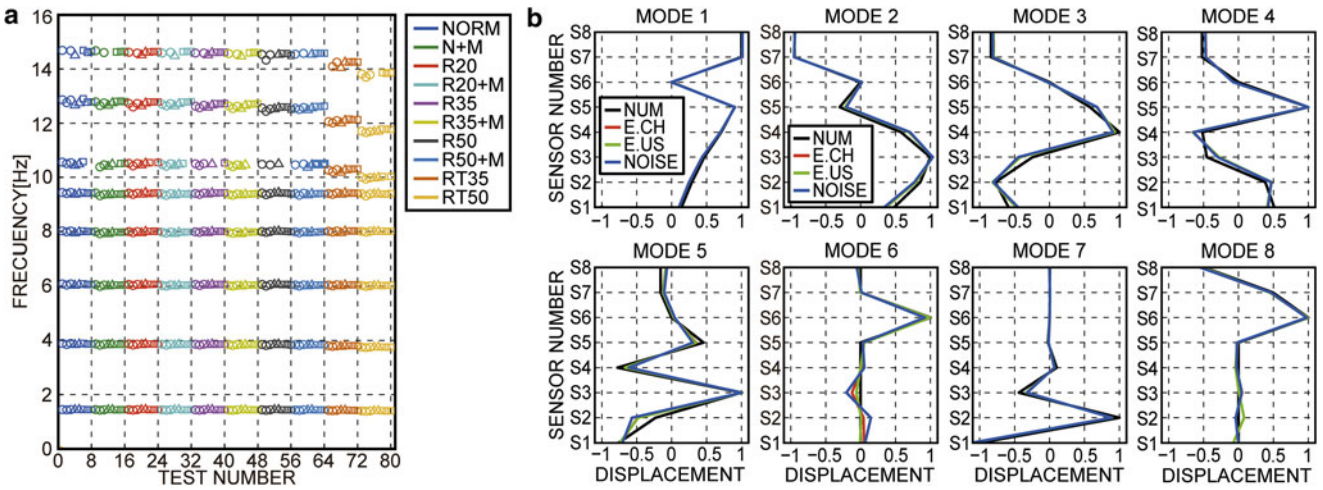

Fig. 12.3 Identification of modal properties in the structure. (**a**) Modal frequencies, (**b**) Modal shapes (NUM: Numerical model, E.CH: Earthquake Chile, E.US: Earthquake United States, NOISE: Colored Noise)

$$MAC = \frac{\left(\phi_{N,i}^{T} \cdot \phi_{E,i}\right)^{2}}{\left(\phi_{N,i}^{T} \cdot \phi_{N,i}\right)\left(\phi_{E,i}^{T} \cdot \phi_{E,i}\right)} \tag{12.9}$$

$$MSF = \frac{\phi_{N,i}^{T} \cdot \phi_{E,i}}{\phi_{E,i}^{T} \cdot \phi_{E,i}}, \tag{12.10}$$

where ϕ_i is the ith modal shape, and the superscripts N, E refer to responses obtained numerically and experimentally respectively, a value $MAC = 0$ indicates no correlation between modal shapes, while a $MAC = 1$ shows a complete correlation. The comparison between numerical and experimental modal shapes are shown in Fig. 12.3b. The MAC found for all modal shapes is above 95 % except for modes 5 and 6 identified using noise records.

12.4 Construction of the Database

12.4.1 Characteristic Vector

The characteristic vector is formed from the modal properties of the structure (frequency and modal shape) and compares the normal condition versus the damage one, as shown in the expression (12.11).

$$X^{j} = \begin{Bmatrix} \sum_{j} \left(\phi_{j}^{D} - \phi_{j}^{U}\right)^{2} \\ \left(\dfrac{\omega^{D} - \omega^{U}}{\omega^{U}}\right)^{2} \end{Bmatrix} \tag{12.11}$$

where: ϕ_j is the *j-th* modal shape as a column vector; and ω represents the natural frequency. Superscripts D and U, refer to the damaged conditions and undamaged conditions to the structure, respectively. The characteristic vector of the numerical model is formed with information from the theoretical modal properties of the structure. The characteristic vector of the tested structure is determined from an identification process that considers the different types of record evaluated.

12.4.2 Observation Vector

Training observation vector are constructed by considering damage applied to each column element in the structure, reducing their elasticity modulus. Therefore, 24 columns are evaluated, in the six levels and four corners presented in Fig. 12.1; the observation matrix is described as: $Y^j = \left[Y_1^j, Y_2^j, \ldots, Y_{24}^j\right]^T$, where a value of: $Y_i^j = 0$, represents a undamaged condition to the element; $Y_i^j > 0$, represent a damaged element; and $Y_i^j = 1$, represents the full damage of the element. For every elements it has been considered ten damage scenarios by reduction of the elastic modulus distributed as 10, 20, 30, 40, 50, 60, 70, 80, 90, 99 %.

12.5 Damage Assessment Results

Experimental damage to the structure is applied in two conditions; The first condition is called slight damage, it is the consecutive reduction of the cross section at the ends of only one of the columns of the second level: 10 mm (20 %), 17.5 mm (35 %) and 25 mm (50 %); while the second one is called severe damage, which reduces the cross section of the remaining three columns on the second level, with cuts in the same places, the reductions are 17.5 mm (35 %) and 25 mm (50 %). The reduction sequence is shown in Fig. 12.4.

The additional mass was applied on the fourth level in the tests described in Table 12.2; this mass is 0.50 % of the total mass of the structure, equivalent to 0.80 [Kgf·s^2/m], the arrangement is shown in Fig. 12.5.

To evaluate the performance of the algorithm, we consider three sensor configurations. The configuration 2 and 3 are defined from a reduced number of sensors in the structure, as shown in Fig. 12.6.

Identified frequencies and mode shapes for configurations 2 and 3 are presented in Figs. 12.7 and 12.8. It is possible to see that the amount of observable modes in the structure are sensitive the location of the sensors.

In all three sensor configurations, the solution is obtained by using the closest 10 neighbor vectors by the linear approximation algorithm. Two results of the evaluation of damage for the sensor configuration 1 are shown in Fig. 12.9. It is observed that under the conditions for the structure and the sensor localization, the assigned damage has a similar magnitude for every column elements in the same level. Similar results are obtained in other configuration, therefore the results shown in Figs. 12.10, 12.11, and 12.12 show the level, and not the column, in which the damage is located; it is differentiated by type of record, test condition and quantification of damage. The damage location is performed considering two procedures, the first considers the formation of the feature vector for all modes identified and the second considers only the modes in the direction of the shaking table.

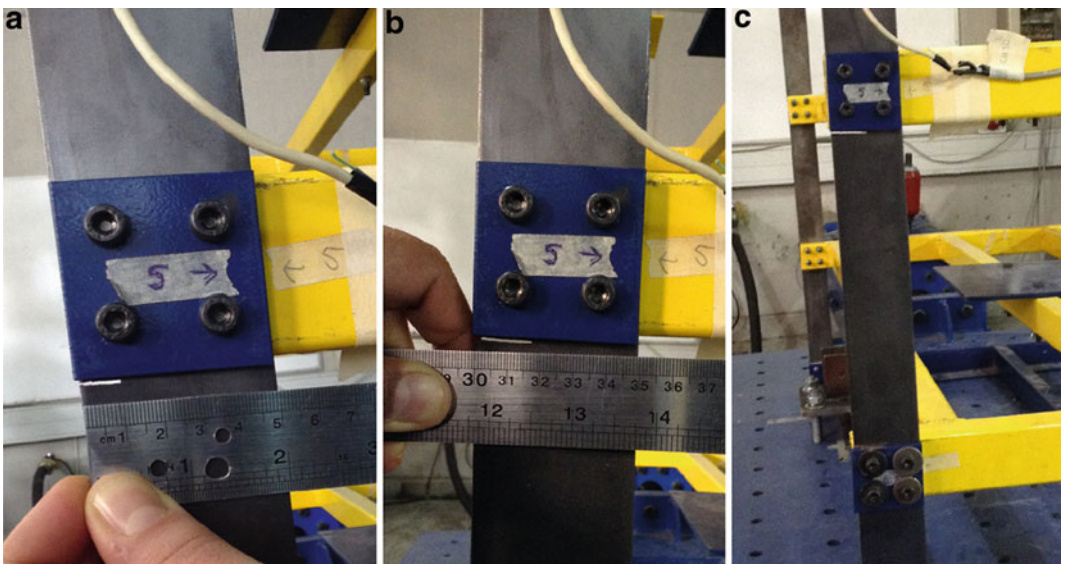

Fig. 12.4 Slight damage and severe damage in the structure (**a**) Cut: 10 mm, (**b**) Cut: 17.5 mm, (**c**) Cut: 25 mm

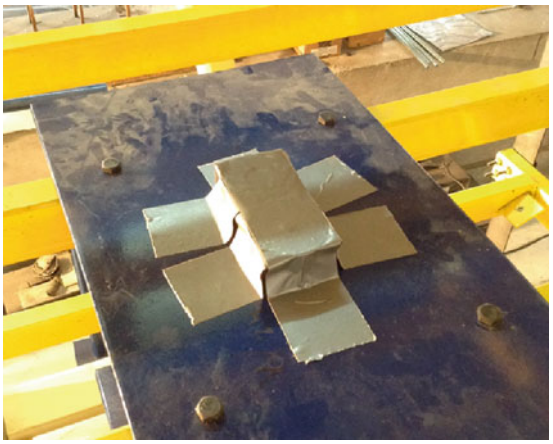

Fig. 12.5 Application of mass in the structure

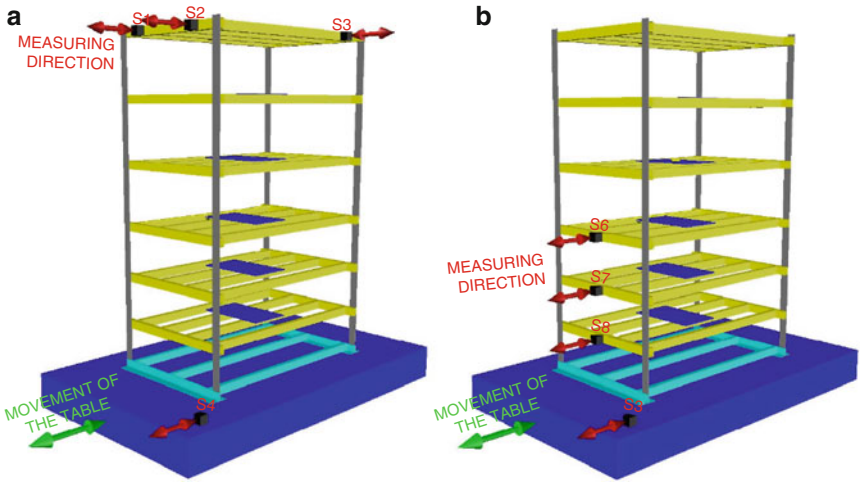

Fig. 12.6 Additional configuration sensors in the structure. (**a**) Configuration 2. Sensors: 1, 2 and 3, (**b**) Configuration 3. Sensors: 6, 7 and 8

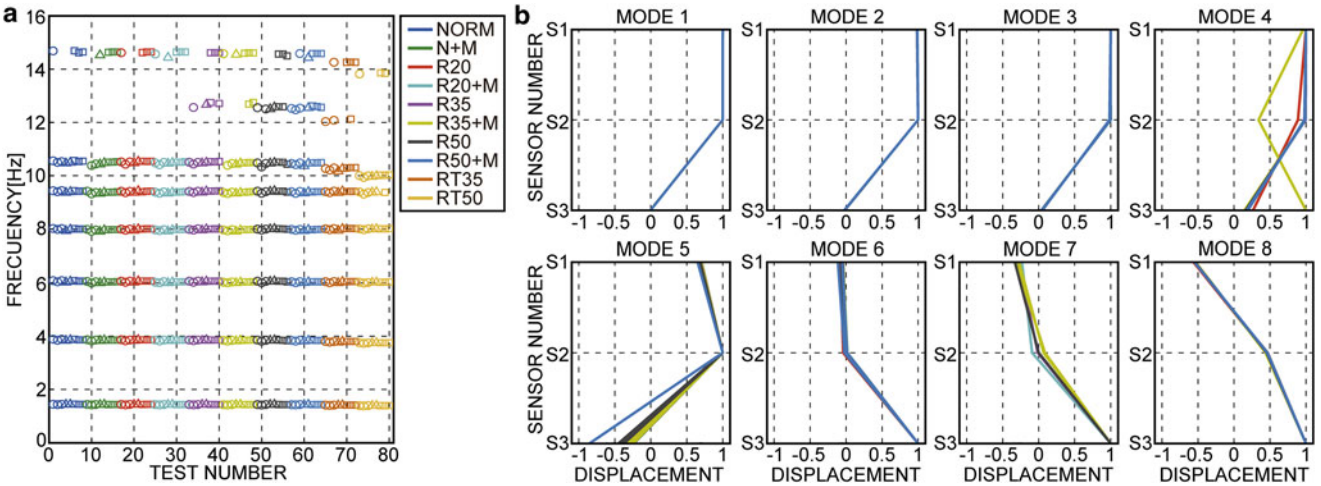

Fig. 12.7 Configuration 2. (**a**) Frequencies, (**b**) Identified mode shapes

Figures 12.10, 12.11, and 12.12 left coordinate axis shows different damage location levels in the structure; symbols used there correspond to: ∘ earthquake in Chile, △ earthquake in United States and □ colored noise. Different colors inside every symbol indicate the condition of applied test detailed in its legend and in Table 12.2. Right ordered axis indicates damage magnitude in percent for an element; gray solid line shows magnitude quantified by the algorithm for every tests performed

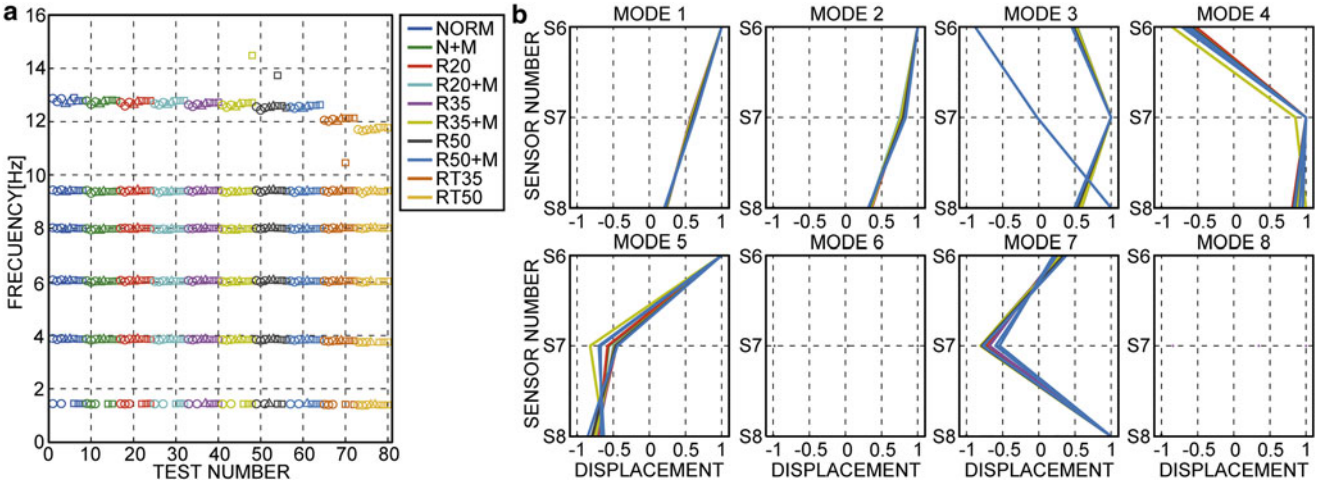

Fig. 12.8 Configuration 3. (**a**) Frequencies, (**b**) Identified mode shapes

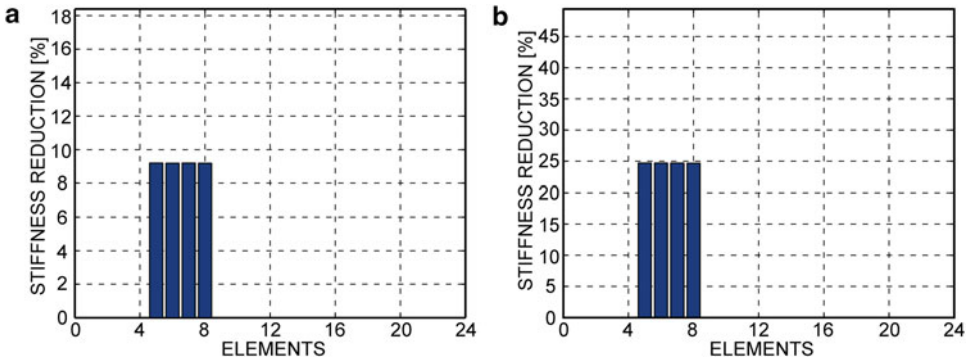

Fig. 12.9 Damage detection elements column. (**a**) Assignments of slight damage 35 %, (**b**) Assignments of severe damage 50 %

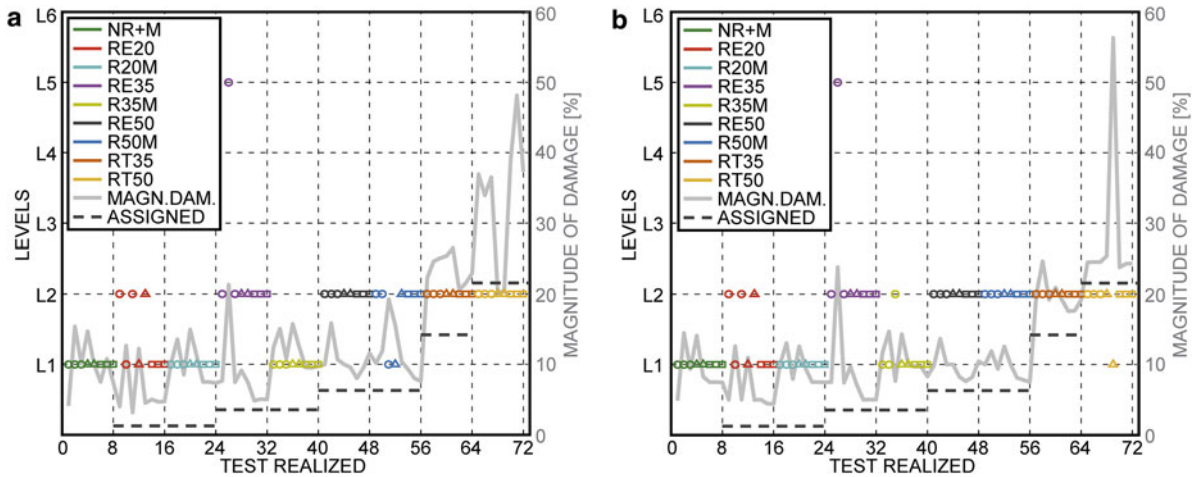

Fig. 12.10 Configuration 1. (eight sensors). Identification of damage to the structure. (**a**) All modes identified, (**b**) Only modes in the direction of the shaking table

and gray dashed line indicates assigned damage magnitude in a theoretical manner. In the Figs. 12.10, 12.11, and 12.12 show a tendency to locate the damage at level 1 for the conditions of slight damage. This location changes to level 2 with increasing magnitude of the assigned damage; in conditions of severe damage, the location is accurate in all records tested. The location of the damage with mass perturbation, is only significant with a reduction of 50 % of the section, in the status of slight damage with the configurations 1 and 3.

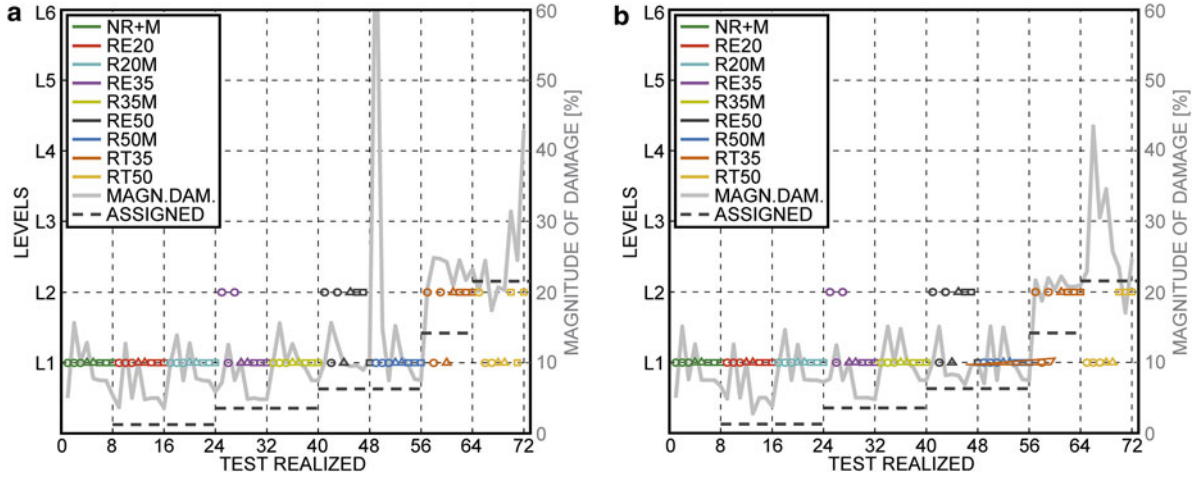

Fig. 12.11 Configuration 2 (three sensor located at level six). Identification of damage to the structure. (**a**) All modes identified, (**b**) Only modes in the direction of the shaking table

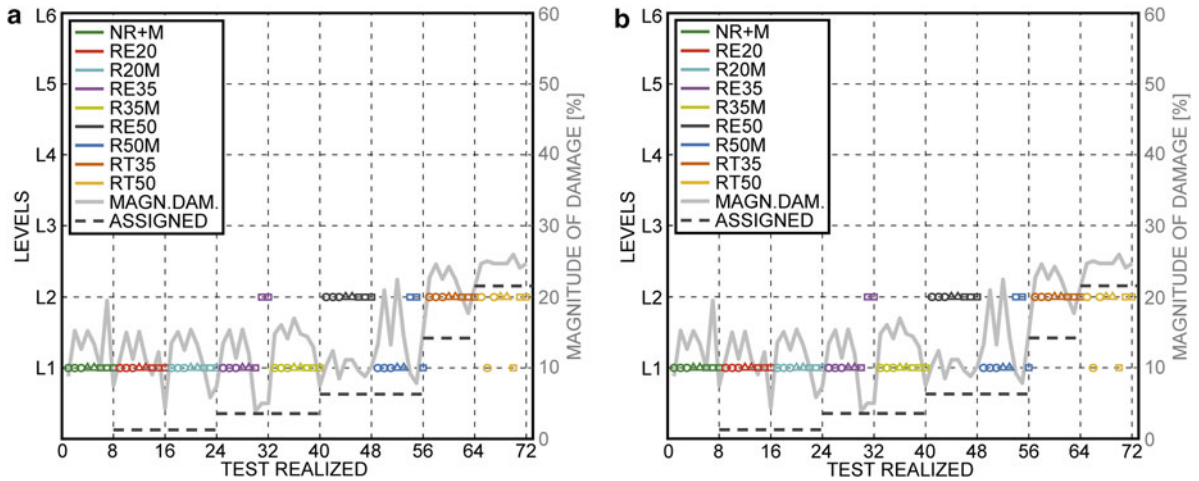

Fig. 12.12 Configuration 3 (three sensor at levels one, two and three in the direction of motion). Identification of damage to the structure. (**a**) All modes identified, (**b**) Only modes in the direction of the shaking table

The identified magnitude of damage (MAGN.DAM.) compared with the assigned damage (ASSIGNED) is not accurate; this difficulty is seen mainly in conditions of slight damage where high variability of results are present in seismic records. The quantification of the magnitude improves in conditions of severe damage. In Figs. 12.10b and 12.11b the variation of the magnitude is more gradual and consistent than in Figs. 12.10a and 12.11a, this may be due to the fact that modal shapes six and eight provide noise due to a low MAC value. Both in Fig. 12.12a and in 12.12b one have the same damage location and damage quantification assigned because the configuration 3, only identifies the modes in the direction of the shaking table, see Fig. 12.8a.

The best results for the localization and quantification of damage are observed with colored noise records for all tests and configurations in which the use of identified modes are defined; this is achieved because noise excites the structure in a wide range of frequencies, and the energy applied is considered to be constant throughout the entire record.

12.6 Conclusions

The present article introduces a new methodology to identify damage in a three-dimensional structure using a linear approximation method with statistical inference based on the principle of maximum entropy. The validation is performed with experimental tests on a six-level metal structure subjected to seismic records and colored noise, which are generated with a shaking table of horizontal movement.

Depending on the configuration of sensors, eight modes have been identified in the structure, six in the direction of shaking table, one orthogonal to the direction of shaking table, and one torsional. The eight identified modes are well correlated with the modes of a numerical model calibrated to the undamaged structure.

The methodology shows that the detected damage is assigned to all of the column elements of a same level. This is due to the lack of local damage information, therefore the method assigns a magnitude to elements having similar characteristics in the same level. The location of damage for the first reductions in the cross-section of the column is assigned to level 1, this may be because the amplitude of the accelerations recorded by the sensors, therefore the sensor that is closest to the base is less representative than the rest of sensors in the others levels. This could be solved with a normalization of amplitudes in the sensors.

Damage location with perturbation due to an additional mass is visible only under conditions of slight damage with a reduction of 50 %, and when observation is made with eight sensors (configuration 1), it shows that changes caused by a perturbation can alter the location of the damage. This is because modal properties of the structure are most affected by the perturbation than an assigned damage to the structure.

The localization of the damage is achieved successfully, from a section reduction of 35 % for the configuration 1, and from a section reduction of 50 % for the configurations 2 and 3. The magnitude of damage is determined in better shape when only translational modes of the structure are considered, showing that orthogonal and rotational mode far from providing information provide perturbation to quantification, which may be due to the low MAC value of these modes. The best results in damage quantification correspond to noise records for all sensor configurations, demonstrating its application to an analysis of online monitoring.

Under different observation and damage conditions, the tested structure has successfully validated the proposed methodology, since it was possible to identify damage and to quantify their magnitude. The low capability to detect damage in the first tests is because the local damage in the column element is not represented in the measured global modal parameters. Future research should be carried out considering different conditions of asymmetry in the structure, testing a wider set of damage scenarios with different noise records.

References

1. Carden, E.P., Fanning, P.: Vibration based condition monitoring: a review. Struct. Heal. Monit. **3**(4), 355–377 (2004)
2. Jamaludin, I.W., Wahab, N.A., Khalid, N.S., Sahlan, S., Ibrahim, Z., Rahmat, M.F.: N4SID and MOESP subspace identification methods. IEEE 9th International Colloquium on Signal Processing and its Applications, Kuala Lumpur (2013)
3. Verhaegen, M., Dewilde, P.: Subspace model identification. Part 1. The output-error stat-space model identification class of algorithms. Int. J. Control **56**(5), 1187–1210 (1992)
4. Peeters, B., De Roeck, G.: Reference-based stochastic subspace identification for output-only modal analysis. Mech. Syst. Signal Process. **1249**, 855–878 (1999)
5. Döhler, M., Mevel, L.: Fast multi-order computation of system matrices in subspace-based system identification. Control Eng. Pract. **20**, 882–894 (2012)
6. Bakir, P.G.: Automation of the stabilization diagrams for subspace based system identification. Expert Syst. Appl. **38**, 14390–14397 (2011)
7. Meruane, V., Ortiz-Bernardin, A.: Structural damage assessment using linear approximation with maximum entropy and transmissibility data. Mech. Syst. Signal Process. **54–55**, 210–223 (2015)
8. Meruane, V., Del Fierro, V., Ortiz-Bernardin, A.: A maximum entropy approach to assess debonding in honeycomb aluminum plates. Entropy **16**, 2869–2889 (2014)
9. Gupta, M.R., Gray, R.M., Olshen, R.A.: Nonparametric supervised learning by linear interpolation with maximum entropy. IEEE Trans. Pattern Anal. Mach. Intell. **28**(5), 766–781 (2006)
10. Jaynes, E.T.: Information theory and statistical mechanics. Phys. Rev. **106**(4), 620–630 (1957)
11. Mares, C., Kyprianou, A.: Minimum relative entropy criterion for damage detection and location. Proceedings of the IMAC-XXVII (2009)
12. Arroyo, M., Ortiz, M.: Local maximum-entropy approximation schemes: a seamless bridge between finite elements and meshfree methods. Int. J. Numer. Meth. Eng. **65**, 2167–2202 (2006)
13. Gupta, M.R.: An information theory approach to supervised learning. PhD Thesis, Stanford University (2003)

Chapter 13
Making Structural Condition Diagnostics Robust to Environmental Variability

Harry Edwards, Kyle Neal, Jack Reilly, Kendra Van Buren, and François Hemez

Abstract Advances in sensor deployment and computational modeling have allowed significant strides to be made recently in the field of Structural Health Monitoring (SHM). One widely used SHM technique is to perform a vibration analysis where a model of the structure's pristine (undamaged) condition is compared with vibration response data collected from the physical structure. Discrepancies between model predictions and monitoring data can be interpreted as structural damage. Unfortunately, multiple sources of uncertainty must also be considered in the analysis, including environmental variability and unknown values for model parameters. Not accounting for uncertainty in the analysis can lead to false-positives or false-negatives in the assessment of the structural condition. To manage the aforementioned uncertainty, we propose a robust-SHM methodology that combines three technologies. A time series algorithm is trained using "baseline" data to predict the vibration response, compare predictions to actual measurements collected on a potentially damaged structure, and calculate a user-defined damage indicator. The second technology handles the uncertainty present in the problem. An analysis of robustness is performed to propagate this uncertainty through the time series algorithm and obtain the corresponding bounds of variation of the damage indicator. The uncertainty description and robustness analysis are both inspired by the theory of info-gap decision-making. Lastly, an appropriate "size" of the uncertainty space is determined through physical experiments performed in laboratory conditions. Our hypothesis is that examining how the uncertainty space changes in time might lead to superior diagnostics of structural damage as compared to only monitoring the damage indicator. This methodology is applied to a portal frame structure to assess if the strategy holds promise for robust SHM.

Keywords Structural health monitoring • Uncertainty • Time series modeling • Robustness

13.1 Introduction

In the discipline of Structural Health Monitoring (SHM), the condition of a structure is often assessed using a combination of measurements and numerical models that attempt to infer the structural condition through changes in the vibration signature response. A structure inevitably degrades as it ages, through cycles of thermal loading, structural loading, and other conditions that affect structural health. At some point the structure may no longer be able to meet its performance requirements. This work contributes to the vast body of literature that develops diagnostics to detect such changes before they become safety or mission critical [1, 2].

H. Edwards
Atomic Weapons Establishment, Environment and Test Group, Reading, UK
e-mail: Harry.Edwards@awe.co.uk

K. Neal
Department of Civil and Environmental Engineering, Vanderbilt University, Box 1831-B, Nashville, TN 37235, USA
e-mail: kyle.d.neal@vanderbilt.edu

J. Reilly
Department of Civil and Environmental Engineering, Princeton University, Princeton, NJ 08544, USA
e-mail: jpr2@princeton.edu

K. Van Buren (✉)
Los Alamos National Laboratory, XCP-8, Mail Stop F644, Los Alamos, NM 87545, USA
e-mail: klvan@lanl.gov

F. Hemez
Los Alamos National Laboratory, XTD-IDA, Mail Stop T087, Los Alamos, NM 87545, USA
e-mail: hemez@lanl.gov

S. Pakzad, C. Juan (eds.), *Dynamics of Civil Structures, Volume 2*, Conference Proceedings of the Society for Experimental Mechanics Series, DOI 10.1007/978-3-319-29751-4_13

To detect the onset of structural changes that can adversely affect structural integrity, sensors are attached to the structure to measure its response from external excitation. Commonly, accelerometers and strain gauges are used to measure the structure's response. For in-service structures, ambient excitations such as cars on a bridge, wind over a building, or ground vibrations are typically used to elicit vibration response. In contrast, it is typical to perform deliberate and controlled excitation such as a modal hammer impact strike or modal shaker for laboratory tests. It is common practice to analyze the measurements through changes to the Frequency Response Function (FRF) data, which is appropriate for dynamics that remain mostly linear and stationary [3]. Another approach is to train a time series model on the pristine condition of the structure, and then use the model to predict the structure's response and assess if its condition remains unchanged. Shifts in natural frequencies observed from the FRF data, or deviations from predictions of the time series model, could indicate structural damage. It is emphasized that this process is only effective if measurements of the structure in its current state can be compared to measurements obtained from the pristine structure, which form a known "baseline." In the absence of baseline test data, mathematical modeling can be substituted to create theoretical "data" of the pristine condition.

In this study, a time series model from the family of Auto Regressive (AR) representations [4] is used to analyze the acceleration response data (measurements) from an aluminum frame structure tested in controlled laboratory settings. The AR model is trained using multiple sets of measured vibration response collected while the structure is in a "pristine," or undamaged, condition. The hypothesis is that the occurrence of damage manifests itself as a significant difference between what is measured on the (now damaged) structure and what the trained model predicts. The difference in structural state is diagnosed by the large prediction residuals that occur when the time series model is fit to damaged data that start to differ from the pristine data. A damage indicator is proposed that derives from statistics of the prediction residuals.

While the aforementioned strategy is relatively well accepted within the SHM community, one challenge, which remains for the most part unresolved, is the ***management of uncertainty***. A change in vibration signature does not necessarily indicate that the structure is damaged. Instead, it might be due to environmental variability, such as a change in input excitation. To avoid the possibility of generating false-positives or false-negatives, it is highly desirable to "separate" the effects of environmental variability from those of structural damage.

Another unavoidable source of uncertainty is lack-of-knowledge that originates from the model used to predict vibration response. For example, when using the AR representation, the choice of the order of the model has been shown to affect the assessment of structural health [5]. Further, when training a model of arbitrary mathematical form, the model parameters might be non-unique whereby multiple sets of parameter values are able to replicate the training data with comparable fidelity. It is highly desirable to "isolate" the effects of model-form uncertainty from those of structural damage. We quantify the effects of environmental uncertainty by replicating the vibration tests as the input excitations are varied within reasonable bounds. Likewise, we quantify the effects of modeling uncertainty by analyzing, not a single best-fitted time series model, but a family of models that includes all representations that fit the measurements with a similar level of accuracy. The effects of these two main sources of uncertainty (environmental variability and model-form uncertainty) are quantified such that the detection of structural damage can be rendered ***robust*** to their unavoidable occurrence.

The description of environmental variability and modeling lack-of-knowledge is inspired by the theory of information-gap (or info-gap) for decision-making [6]. The magnitude, or "size," of the uncertainty, which the decision (*"is the structural state pristine or damaged?"*) must be robust to, is controlled by a horizon-of-uncertainty parameter denoted "α." A larger value of α increases the uncertainty considered in the analysis and, therefore, allows for greater potential deviation between reality and the numerical model used to predict the structural state.

This study aims to assess the structural state by examining the value of α needed to make the nominal AR time series model, which is developed to characterize the pristine state, predict a set of measurements obtained on a potentially damaged structure. The preliminary results indicate the success of this strategy. Damage states can be reliably diagnosed from observing the "growth" of the uncertainty space, that is, the extent to which α increases, while offering robustness to the environmental variability and modeling lack-of-knowledge.

13.2 Experimental Procedure

The test structure considered is a two-story portal frame made of aluminum bars and steel brackets with bolted connections as shown in Fig. 13.1a (left). The structure is clamped to the support table with four C-clamps. A modal shaker is bolted to one of the columns at 40.7 cm above the base plate. The structure is excited with a chirp sine wave whose frequency varies from 1000 Hz down to 2 Hz, and to which uniform white noise is added. It is verified that the applied chirp signal excites most of the lower resonant frequencies of the structure, which helps to capture a more descriptive response envelope. White noise added to the input shaker signal adds a variability of known magnitude to the excitation. It introduces one of the sources of environmental variability considered in the problem; the other sources are described later.

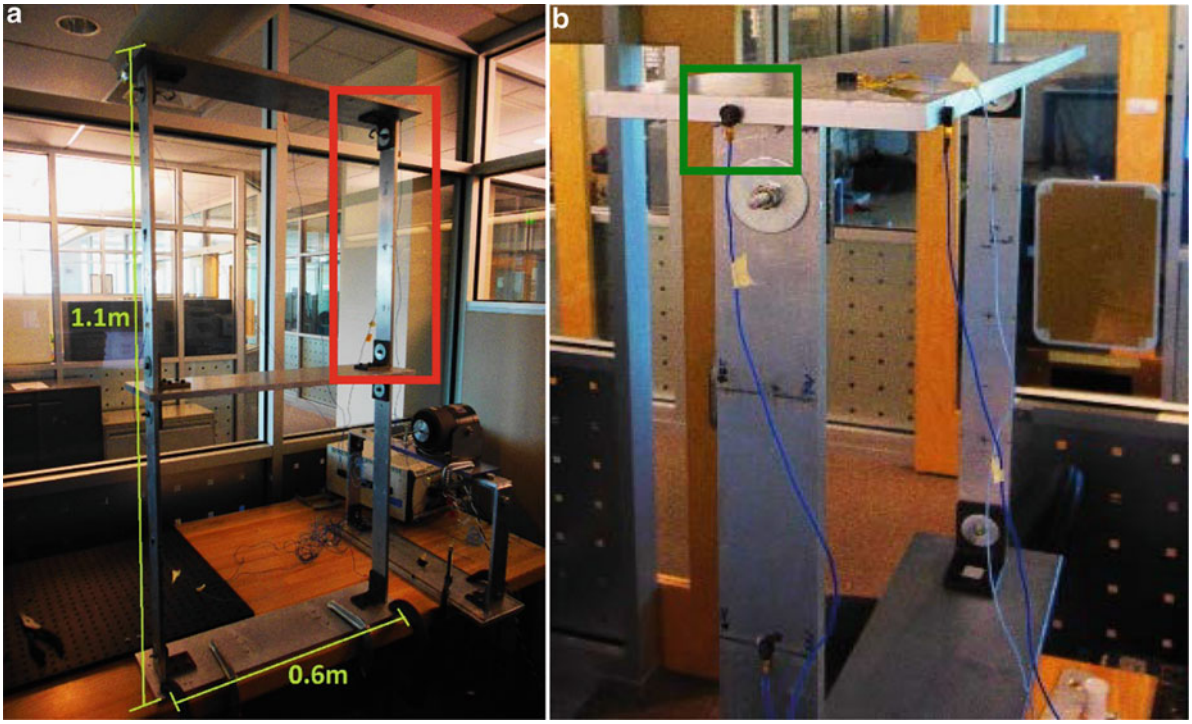

Fig. 13.1 Portal frame structure instrumented to perform the vibration tests. (**a**) *Left*: Test structure. (**b**) *Right*: Sensor placement

Table 13.1 Definition of structural states (pristine, variability, damage) considered

Case	Description	Variability?	Damage?	Replicates
$0^{(I)}$	First set of pristine (before cases I to V)	Yes	No	60
$0^{(II)}$	Second set of pristine (after cases I to V)	Yes	No	20
I	Table kicked during vibration testing	Not sure	Not sure	20
II	One C-clamp added to middle plate	No	Yes	20
III	Two C-clamps added to middle plate	No	Yes	20
IV	Loosening of top-right connection bolt	No	Yes	20
V	Thinner, lighter bottom-right column	No	Yes	20
VI	Removal of three base-plate bolts	No	Yes	20

To capture the response, four accelerometers are attached to the structure, as indicated by the red box in Fig. 13.1a (left). A detail is provided in Fig. 13.1b (right), where the green box shows the location of one of the accelerometers. Two sensors are located such that they can measure acceleration in the same direction as that of shaker input, while the other two are oriented to capture the out-of-plane response. Only the data collected at the location of the green box in Fig. 13.1b (right) are used for the analysis reported herein.

Vibration tests are performed over several days to accumulate sixty sets of pristine response data. Slightly different temperatures and ambient vibrations in the testing environment result from these combinations of days and times. This incorporates further environmental variability in the vibration response of the pristine condition. Our contention is that assessing damage should be made as immune as possible, or robust, to the presence of this environmental variability.

Two independent sets of vibration tests are executed to characterize the pristine condition. The first set is performed before we start to modify the portal frame to introduce different damage scenarios. The second set is performed after testing four of the damage cases. Assessing the statistical consistency of the response provides confidence that the "baseline" (pristine) state of the structure has not significantly shifted due to the various tests performed.

Damage is introduced in the structure in a number of different ways, as summarized in Table 13.1. Firstly, mass is added in the form of one and then two C-clamps attached to the middle plate. These cases are labeled II and III in Table 13.1. A single C-clamp weights about 1 % of the total mass of the portal frame. The mass loading that results is believed to induce a linear change in the vibration response of the structure. Secondly, the bolt located in the top-right connection is loosened (Case-IV). This case potentially generates nonlinear vibrations from the impact between the vertical column, horizontal plate, and

attachment bracket of the portal frame. An advantage of the time series modeling pursued in this work is that it can be used to detect linear and nonlinear changes to the response alike. Thirdly, Case-V replaces the bottom-right vertical column with a thinner (skinnier) and lighter column and Case-VI removes three of the four bolts that connect the vertical column to the horizontal base plate. While its response remains linear, Case-V defines a significant structural change. Case-VI introduces a potential non-linearity in the vibration response because of the higher likelihood for column-to-base-plate impact.

Table 13.1 also includes Case-I that keeps the frame structure in its pristine condition, identical to cases $0^{(I)}$ and $0^{(II)}$, while a member of the team "kicks" the support table during the execution of vibration tests. This unorthodox procedure is meant to define an extreme case of environmental variability where the excitation provided to the portal frame is not even stationary. The table lists the numbers of replicates performed for each case. It can be observed that this experimental campaign results in a significant number of vibration tests ($60 + 7 \times 20 = 200$ tests).

The third and fourth columns of Table 13.1 attempt to categorize the perturbations introduced to the frame structure as either "variability" or "damage." The mass loading cases (II and III) are meant to represent, for example, a heavy piece of equipment that would be installed inside a building. Loosening a connecting bolt defines a clear damage scenario. It is unclear how Case-I, and its extreme form of exciting the structure by kicking the support table, should be categorized. Our main objective is to demonstrate that the damage cases (II, III, IV, V, and VI) can be separated from the pristine cases ($0^{(I)}$ and $0^{(II)}$) in the presence of environmental variability represented by replicate testing of the pristine structure across multiple days. Another success would be to demonstrate that Case-I is not confused for structural damage.

13.3 Diagnosis of Structural Damage in the Presence of Environmental Variability

The procedure being implemented to diagnose the occurrence of structural damage from vibration measurements is to train a time series model using "baseline" data that represent the pristine structural state. Baseline model predictions are compared to actual measurements collected on a potentially damaged structure, and a damage indicator is calculated. This section summarizes the procedure and explains how the experimental variability is handled.

We start by considering three time series models for analysis of the raw acceleration signals: an Auto Regressive (AR) model, an Auto Regressive Moving Average (ARMA) model, and an Auto Regressive Exogenous (ARX) model [7]. Equation 13.1 defines the generic form of these models, which represents the measurements using a linear combination of input and output responses:

$$\widehat{y}_k = \sum_{1 \le j \le N} \beta_j \cdot y_{k-j} + \sum_{1 \le j \le M} \gamma_j \cdot f_{k-j} + e_k \tag{13.1}$$

where f_k denotes the input excitation (force applied by the shaker) at time sample t_k, y_k denotes the output response (acceleration measured by the accelerometer), and e_k is a statistical white-noise term that accounts for model-fitting errors. The symbol $\hat{y}_k$ is the prediction of the model, which can be compared to the actual measurement, y_k, to define the prediction residual, ε_k:

$$\varepsilon_k = y_k - \widehat{y}_k \tag{13.2}$$

In Eq. (13.1), the optimal values of orders (N; M) of AR and MA summations are determined by repeating the training procedure, as discussed in the following. Once the AR and MA model orders are decided, the regression coefficients (β_j; γ_j) are fitted to the "baseline" data.

In contrast to Eq. (13.1), an AR model is restricted to the first summation that defines a linear combination of N past observations (y_{k-1}; y_{k-2}; ... y_{k-N}). An ARMA model is comprised of the AR term to which a contribution that represents an exogenous input is added. In the case of an unknown excitation signal, this additional term can be defined as the residual (13.2) obtained from AR model predictions. These residuals ε_k are then substituted to the input f_k in Eq. (13.1).

An ARMA model is initially selected to model the vibration response of the frame structure. A study is undertaken to determine the optimal orders (N; M) of summations in Eq. (13.1). Both orders are varied to analyze all (N; M) combinations ranging from $1 \le N \le 25$ for the AR term and $1 \le M \le 30$ for the MA term. The mean absolute value of prediction residuals (13.2) is used as a metric for goodness-of-fit between actual measurements (y_k) and predictions ($\hat{y}_k$) of the model.

Figure 13.2 indicates how the mean statistics of residual error vary as a function of orders (N; M). These results are obtained for one of the replicate tests of the pristine structure and it is verified that similar trends are observed with the other replicates. A lower residual mean value describes a model that predicts the measured acceleration response more accurately.

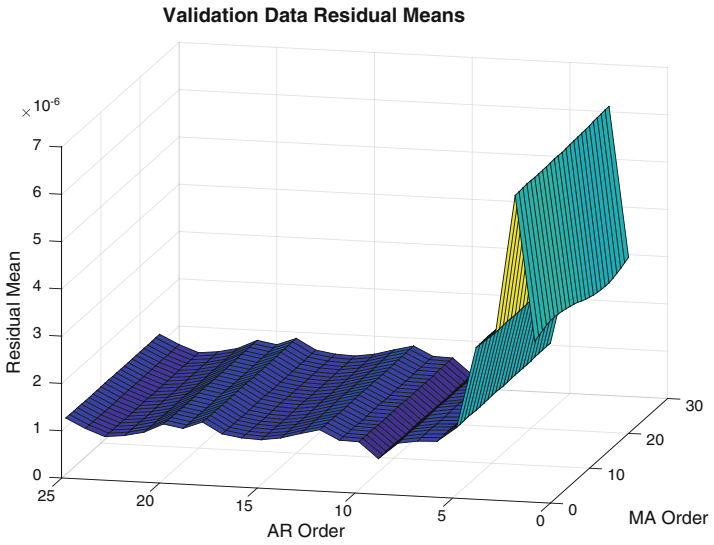

Fig. 13.2 Mean values of ARMA residual errors for varying model orders (N; M)

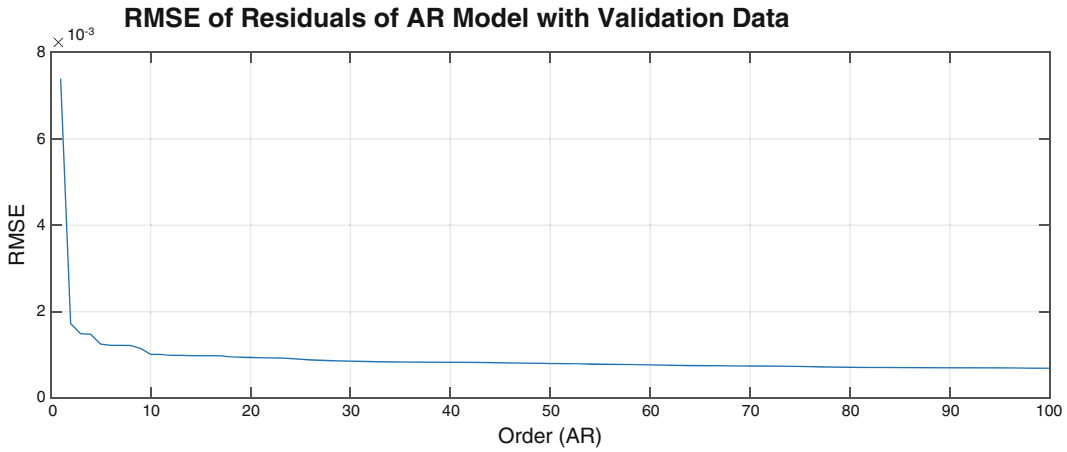

Fig. 13.3 Mean values of AR residual errors for varying model orders, $1 \leq N \leq 100$

From Fig. 13.2, it is clear that, first, an AR order of $N = 10$ suffices to "stabilize" the residual error and, second, the MA term does not seem to have a significant impact on the goodness-of-fit.

In light of the results illustrated in Fig. 13.2, it is decided to conduct our investigation with an AR model. Figure 13.3 shows the Root Mean Square (RMS) value of AR prediction errors (13.2) for model orders that range in $1 \leq N \leq 100$. The figure indicates that a model order of $N = 10$ is sufficient to reach an acceptable level of prediction accuracy while avoiding over-fitting the measurements. For completeness, it is mentioned that ARX models are investigated in a similar manner, with no improvement in accuracy over that of AR models. Results discussed in the remainder of the manuscript are obtained with AR models of order $N = 10$.

After having selected the modeling approach (AR) and model order ($N = 10$), the ten unknown regression coefficients ($\beta_1; \ldots \beta_{10}$) of Eq. (13.1) are best-fitted to acceleration measurements for each replication of Case-$0^{(I)}$, see Table 13.1. The "baseline" AR model of the pristine condition is defined by averaging the regression coefficients across replicate tests:

$$< \beta_j >= \frac{1}{R} \cdot \sum_{1 \leq r \leq R} \beta_j^{(r)} \tag{13.3}$$

where the superscript $(\,)^{(r)}$ identifies one of the replicate tests, that is, $1 \leq r \leq R$, and brackets $< >$ indicate an averaged value. Figure 13.4 illustrates this procedure, which yields the averaged coefficients, $<\beta_1> \ldots <\beta_{10}>$, of the "baseline" AR model.

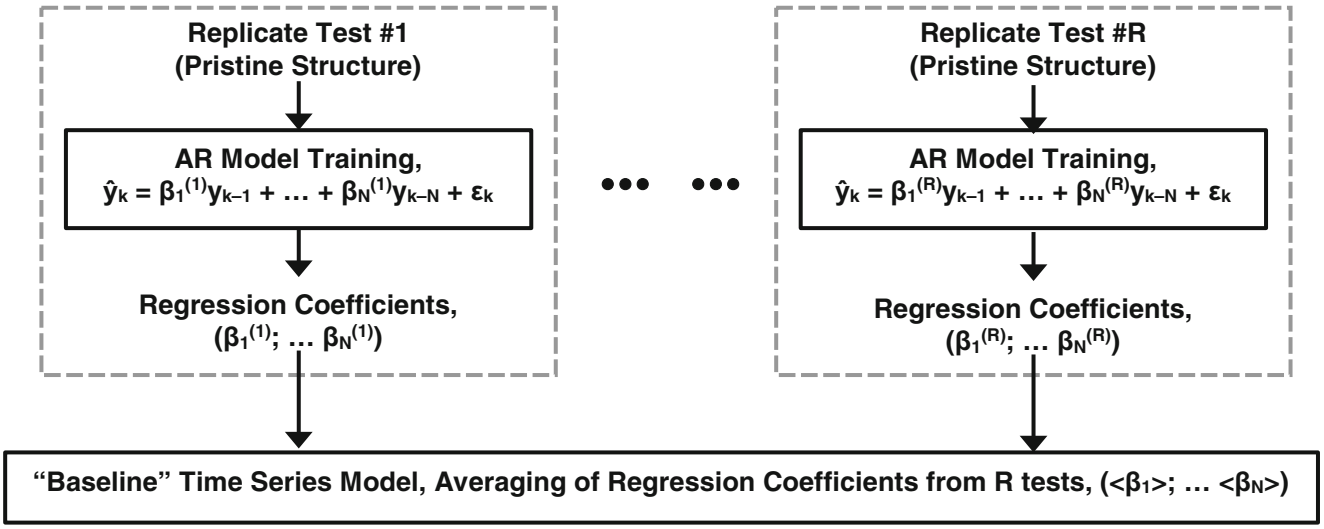

Fig. 13.4 Definition of the "baseline" AR model from tests of the pristine structure

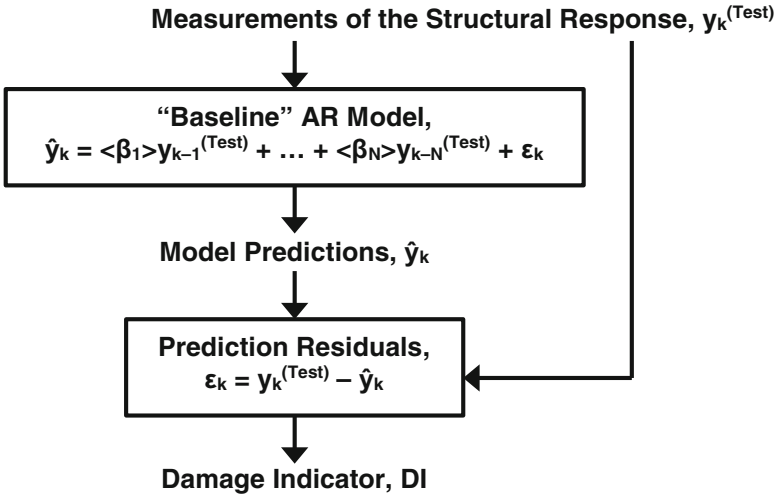

Fig. 13.5 Damage indicator defined from the vibration test of a different structural state

Once the "baseline" AR model is available to characterize the response of the pristine condition, it is analyzed to predict the structural state given a new set of experimental vibration data. The predictions are compared to actual measurements to calculate the residual errors (13.2). The mean value and standard deviation value of prediction residuals are estimated and used to define our Damage Indicator (DI) as a combination of the two statistics:

$$\mathrm{DI} = \left(\frac{\mu}{\mu_0}\right) + \left(\frac{\sigma}{\sigma_0}\right) \tag{13.4}$$

where μ and σ denote the mean and standard deviation values, respectively. In (13.4), the symbols μ_0 and σ_0 are "reference" values used to scale the two contributions to DI. Scaling is needed because the mean statistics are observed to be several orders of magnitude smaller than the standard deviation values. Figure 13.5 illustrates the procedure to calculate DI.

The sixty replicate tests defined for Case-$0^{(I)}$ are divided into training and validation sets. Fifty tests are used for training the "baseline" AR model, that is, R = 50 in Fig. 13.4. The remaining ten tests are utilized to assess how the model performs to predict data that have not been used for training, which is the validation step. The "reference" statistics (μ_0; σ_0) of Eq. (13.4) are estimated from the residual errors of these ten validation tests. Since replicates of the Case-$0^{(I)}$ pristine condition are slightly different because of environmental variability (see Sect. 13.2), this procedure is deemed appropriate to capture its effect on predictions of the "baseline" AR model.

The "baseline" model is defined from multiple replicates of the pristine state. Thus, generating the DI as shown in Fig. 13.5 with a new time series measurement collected from the structure in a pristine condition should result in a low magnitude of residual error. The corresponding value of the DI should be close to 2, which would represent similar statistics as those obtained when analyzing the measurements used for training. Processing a time series measurement that represents a different structural state, on the other hand, should generate prediction residuals whose magnitude exceeds that produced by environmental variability alone. The value of the DI metric should increase. This is how we expect to separate the effect of structural damage from that of environmental variability, irrespective of the vibration dynamics (linear or nonlinear).

After training the "baseline" AR model to represent the pristine condition, the process of Fig. 13.5 is applied to each one of the twenty replicate tests of Case-I, Case-II, Case-III, and Case-IV, see Table 13.1. Within any one of these configurations, the excitation signal applied to the structure differs slightly from test to test due, as mentioned earlier, to the addition of random white noise. It means that the vibration response of the portal frame varies slightly as well for each test. This variability propagates to the prediction residuals, their statistical moments, and the DI metrics.

Figure 13.6 represents the distributions of replicate DI values obtained for the four perturbed states as ranges that extend from the minimum to maximum values. Each color (red, magenta, green, and black) corresponds to one of cases I to IV. The blue interval indicates the range of DI values that results from replicates of the Case-$0^{(I)}$ pristine condition. Black crosses denote the average values of the test replicates.

For each configuration tested, the ranges of DI values capture the effects of the environmental variability. The question is whether the structural perturbations of Cases I to IV produce shifts in DI that can be "separated" from the aforementioned ranges. This is clearly observed for Case-II (magenta interval) and Case-III (green interval), which perturb the nominal configuration of the frame structure through mass loading. The conclusion is similar for Case-IV (black range) where one of the column-to-plate connecting bolts is loosened. The ranges obtained for these three configurations are completely outside the DI bounds obtained for the pristine structure. These cases, therefore, can be confidently classified as damaged. It is interesting to notice that cases II and III register such large DI shifts, even though the mass added is modest (1–3 %).

The red interval, representing the artificial "quake" of Case-I where the support table is kicked during vibration testing, cannot be unambiguously identified as either damaged or undamaged. This is because the interval partially overlaps with the DI bounds of the pristine structure, as indicated in Fig. 13.6. This perturbation represents a case of extreme variability but

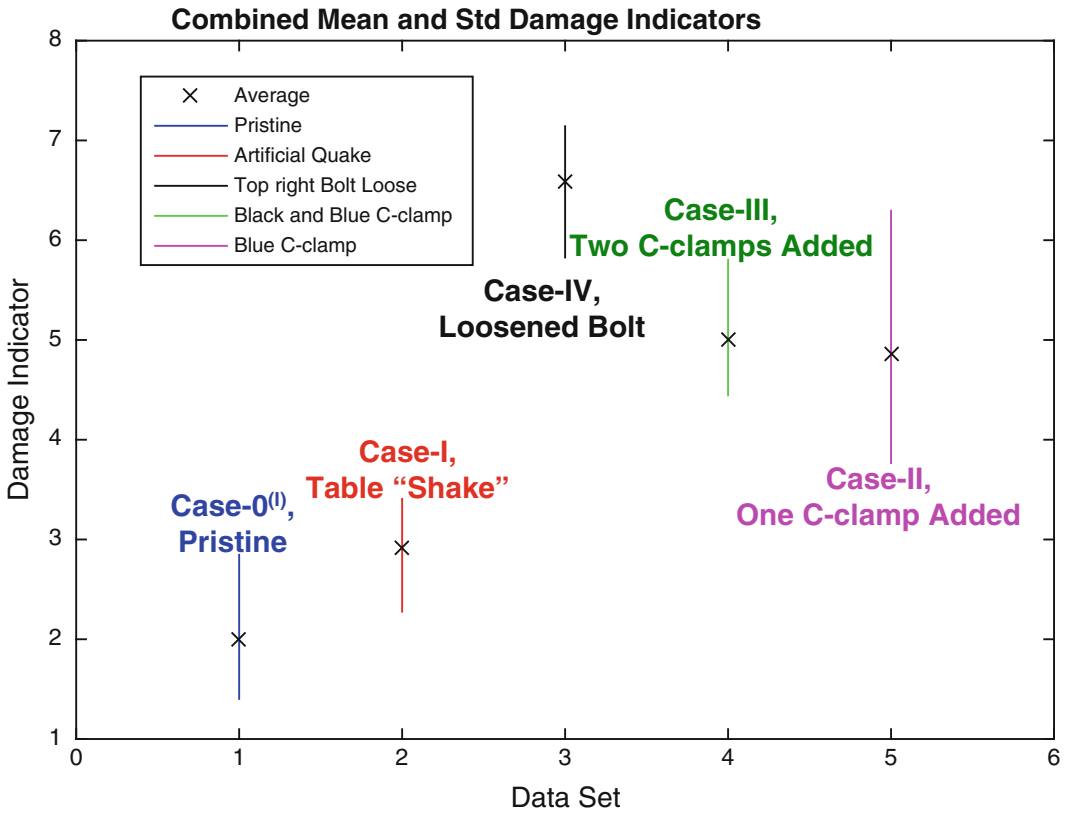

Fig. 13.6 Damage indicators of Case-$0^{(I)}$ (pristine) and cases I to IV (perturbed)

not damage. Because the training data do not encompass such a significant variability, the DI bounds of the pristine state (blue interval) do not fully overlap with DI values obtained for Case-I.

The artificial "quake" of Case-I stands out as a condition that our procedure cannot classify well. The preliminary results obtained nevertheless demonstrate the strong potential that this method offers to classify with accuracy the structural condition despite environmental variability.

13.4 Rendering the Damage Assessment Robust to Modeling Lack-of-Knowledge

In this section, we discuss how to render the assessment of structural condition robust to the inevitable modeling lack-of-knowledge. This modeling uncertainty, here, is represented by the unknown regression coefficients, β_k, of the AR model. Even though it is not discussed here, other sources of modeling uncertainty could easily be included in the proposed methodology. The AR model order, for example, could be considered to be a modeling uncertainty as well as the functional form of the time series representation (ARMA, support vector machine, other?).

The objective of the proposed methodology is to guarantee that the assessment of structural condition (pristine, damaged?) is as robust as possible to the fact that parameters of the time series model are not known precisely. We would not want to find ourselves in a situation where, for example, the assessment of structural condition changes from damaged to undamaged, or vice-versa, simply because the values of model parameters shift slightly due to uncontrolled factors. Establishing robustness provides confidence that the decision reached (*"the structure is damaged"*) is correct despite the fact that model parameters vary from their nominal values.

To establish the robustness of condition monitoring, each regression coefficient of the "baseline" AR model is varied between a lower bound, β_k^{Lower}, and an upper bound, β_k^{Upper}, as:

$$< \beta_k > +\alpha \cdot \left(\beta_k^{\text{Lower}} - < \beta_k >\right) \leq \beta_k \leq < \beta_k > +\alpha \cdot \left(\beta_k^{\text{Upper}} - < \beta_k >\right) \tag{13.5}$$

where α denotes the dimensionless, "horizon-of-uncertainty" parameter greater or equal to zero. The lower and upper bounds are obtained from the population of model regression coefficients ($\beta_k^{(1)}$; $\beta_k^{(2)}$; ... $\beta_k^{(R)}$) calculated in Fig. 13.4 during the training step of the pristine condition.

Equation 13.5 varies each regression coefficient, β_k, between the lower and upper bounds, that is, $\beta_k^{\text{Lower}} \leq \beta_k \leq \beta_k^{\text{Upper}}$, depending on the value of parameter α. With $\alpha = 0$, there is no variation of the regression coefficient that defaults back to its "baseline" value, that is, $\beta_k = <\beta_k>$ as before. With $\alpha = 1$, the regression coefficient can take any value between the lower and upper bounds.

The procedure starts by setting the horizon-of-uncertainty parameter α, then, the assessment of structural condition of Fig. 13.5 is repeated multiple times by varying the values of regression coefficients within the lower and upper bounds of Eq. (13.5). Each calculation of the DI metric is based on predictions of an AR model with coefficients (β_1; ... β_{10}) that deviate from the mean-value coefficients ($<\beta_1>$; ... $<\beta_{10}>$) of the "baseline" AR model. The magnitude of the deviation is controlled by α. The parameter α, therefore, defines the modeling uncertainty embodied, here, by unknown regression coefficients. The goal of the robustness analysis is to demonstrate that the assessment of structural condition can withstand as much modeling uncertainty as possible, that is, an as-high-as-possible value of α.

When performing the robustness analysis, however, the ten model parameters cannot be varied independently from each other. This is because they are statistically correlated. Figure 13.7 depicts the correlation structure for pairs of regression coefficients (β_p; β_q), $p \neq q$. The figure indicates a strong correlation for all pairs of model parameters except combinations (β_7; β_8) and (β_8; β_9).

Figure 13.8 is a notional illustration of what happens when the correlation structure is ignored as the regression coefficients (β_1; ... β_{10}) are generated. The green-dot points remain "true" to the nominal correlation suggested by the ellipsoid shape (blue dashed line). While sampling the model parameters, we wish to avoid generating red-cross points that fall outside the ellipsoid. Independently varying each model parameter according to (13.5) would generate samples that do not accurately map the modeling uncertainty space of the "baseline" AR representation.

To maintain the correlation between regression coefficients of Fig. 13.7, a Principal Component Analysis (PCA) is implemented to transform the coefficients to a generalized coordinate space according to the decomposition:

$$\beta - < \beta >= \mathrm{U} \cdot \Sigma \cdot \mathrm{V}^{\mathrm{T}} \tag{13.6}$$

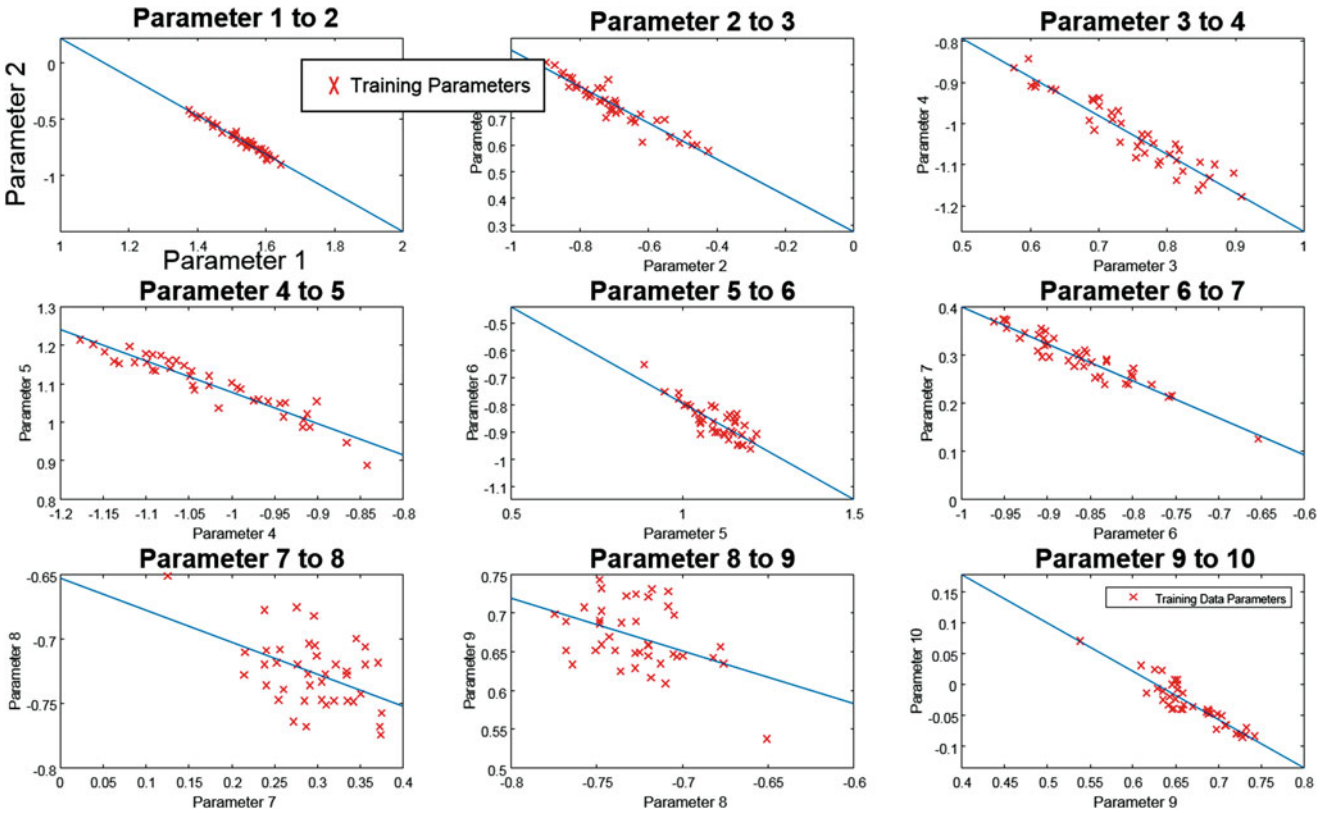

Fig. 13.7 Pairs (β_p; β_q), $p \neq q$, of AR regression coefficients obtained for Case-0(I)

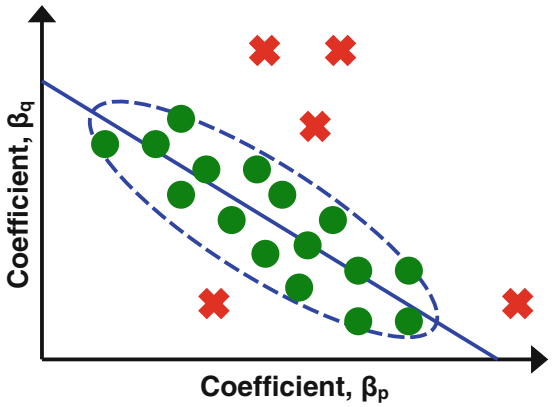

Fig. 13.8 Coefficients sampled inside (green dot) or outside (red cross) the correlation

where the symbol β is the R-by-N matrix of regression coefficients, $<\beta>$ is a matrix of the same size that removes the mean values ($<\beta_1>$; ... $<\beta_{10}>$), and the triplet of matrices (U; Σ; V) in the right-hand side is the PCA decomposition [8]. Equation 13.6 converts the correlated parameters (β_1; ... β_{10}) of the AR model to zero-mean, uncorrelated generalized coordinates (V_1; ... V_{10}).

After calculating the triplet of matrices (U; Σ; V) of the decomposition (13.6), it is used "in reverse" to generate correlated samples of regression coefficients (β_1; ... β_{10}), as illustrated notionally in Fig. 13.9. Because the generalized coordinates (V_1; ... V_{10}) are uncorrelated, a Latin Hypercube Sample (LHS) is implemented to sample their values according to a uniform distribution [9]. The LHS method offers an efficient trade-off between randomness and spreading the samples throughout the 10-dimensional hypercube $([-1; +1])^{10}$ in which the generalized coordinates are defined. Equation 13.6 is used to transform the uniform samples to the correlated space whose principal directions are defined by the left singular vector (U_1; ... U_{10}) of the PCA decomposition. This entire procedure is implemented in Matlab® and only takes a fraction of second to complete when implemented on a single-core desktop processor.

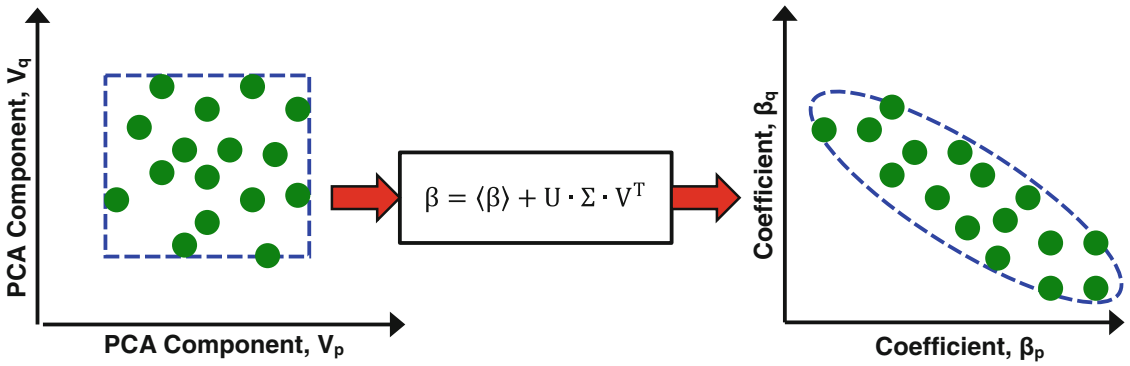

Fig. 13.9 Transform implemented to sample the regression coefficients (β_1; ... β_{10})

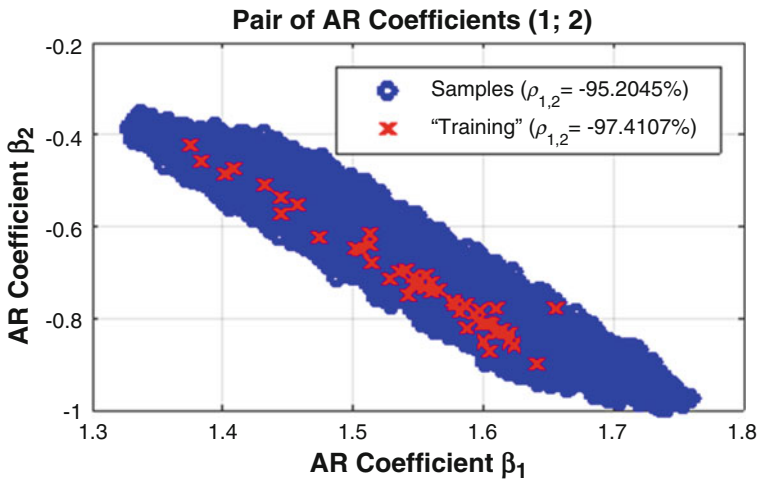

Fig. 13.10 Nominal and new correlation structure for the pair (β_1; β_2) of AR coefficients

A Monte Carlo simulation is analyzed using 10,000 sets of regression coefficients (β_1; ... β_{10}) obtained using the combination of PCA transform and LHS method previously described. The β-values are consistent with the lower and upper bounds of Eq. (13.5) where $\alpha = 1$. A value of the DI is obtained for each Monte Carlo sample, following the flowchart of Fig. 13.5, and with the only difference that samples (β_1; ... β_{10}) are substituted to the mean values ($<\beta_1>$; ... $<\beta_{10}>$).

Figure 13.10 depicts the 10,000 samples obtained for the pair of model parameters (β_1; β_2), which features the strongest correlation of all pairs (β_p; β_q), $p \neq q$. Red crosses represent the training data of the Case-$0^{(I)}$ pristine condition and blue dots are the 10,000 new samples created from Eq. (13.5) at the level of modeling uncertainty of $\alpha = 1$. The figure indicates that the overall correlation is preserved by our sampling algorithm, as suggested by a coefficient of correlation between β_1 and β_2 equal to –97.4 % for the training points and –95.2 % for the new samples.

Figure 13.10 also suggests that the level of modeling uncertainty used, $\alpha = 1$, generates variations of regression coefficients (β_1; ... β_{10}) that exceed those observed when replicating the vibration tests for the Case-$0^{(I)}$ pristine configuration. The perturbations of model parameters generated in this manner account for variability not directly observed during vibration testing and that could manifest itself for that specific structural state at another time. In addition, these perturbations are appropriate to explore the modeling lack-of-knowledge, that is, the fact that adopting a different time series modeling approach or changing the model order(s) could result in a larger-than-currently-observed variation of model parameters. The robustness question is: ***"do these variations of regression coefficients change the assessment of structural condition?"***

The above question is answered by running a Monte Carlo simulation of 10,000 LHS-generated AR models through each case defined in Table 13.1, including the training, support table "quake," and damage cases. Figure 13.11 displays the ranges of DI values obtained from the analysis of each pristine and damage configuration (20 sets of data each) run through these 10,000 AR models. The difference with results shown in Fig. 13.6 is that the uncertainty considered here is much "broader" than the environmental variability investigated in Sect. 13.3.

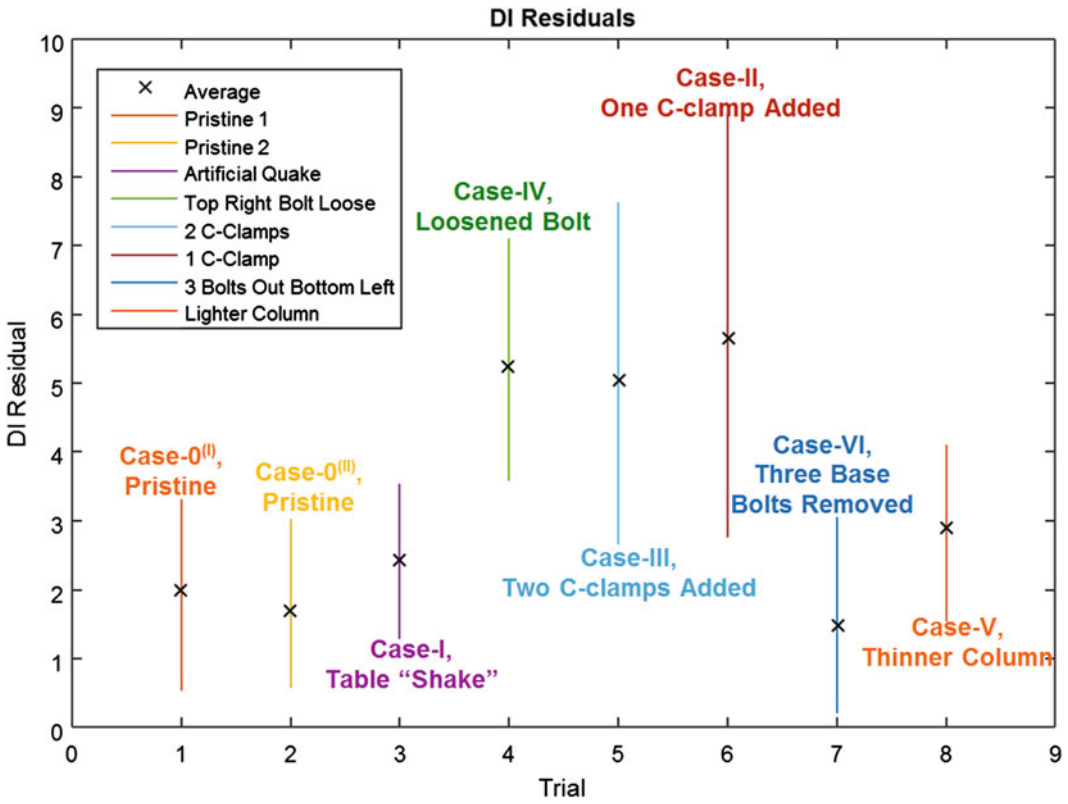

Fig. 13.11 Ranges of damage indicators that account for modeling uncertainty (at $\alpha = 1$)

It can be observed in Fig. 13.11, firstly, that the DI ranges for the two independent tests of the pristine condition, Case-$0^{(I)}$ (orange interval) and Case-$0^{(II)}$ (yellow interval), are remarkably consistent. This gives confidence that our procedure is not adversely affected by small changes to the "baseline" state that might have resulted from modifying the frame structure multiple times and testing it over-and-over. The second observation is that Case-I (purple interval), which represents the artificial "quake" where the support table is kicked during vibration testing, can no longer be separated from the pristine state. This result is welcome since this configuration, while it represents an extreme form of environmental variability, is not, strictly speaking, damaged.

The significance of this observation is emphasized. The consistency of DI bounds for the three sets, Case-$0^{(I)}$ (orange), Case-$0^{(II)}$ (yellow), and Case-I (purple), provides a "calibration" of the horizon-of-uncertainty parameter, α, needed to capture all pristine states of the frame structure. The submersion of the Case-I of extreme variability into the pristine bounds is predicated on a rather large number of trials (20 replicates by 10,000 samples = 200,000 trials), which supports the rigorousness of our exploration of the uncertainty space. The DI bounds predicted for these three states overlap, for the most part, when the modeling lack-of-knowledge represented by (13.5) is explored up to $\alpha = 1$.

Said differently, $\alpha = 1$ is the ***smallest size*** of the uncertainty space that produces consistent DI bounds for the pristine state. It means that the pristine condition of the frame structure can be ***robustly diagnosed***, up to $\alpha = 1$, irrespective of the uncertainty of the vibration testing protocol (nominal testing vs. support table "shake") and environmental variability (test-to-test replication).

The aforementioned adjustment of horizon-of-uncertainty, α, using the different pristine states of the portal frame, leads to a third observation in Fig. 13.11. When analyzed at the level of $\alpha = 1$, the added-mass and loosened bolt configurations are clearly identifiable. Their DI bounds (Case-II, magenta interval, Case-III, light blue interval, and Case-IV, green interval) mostly do not overlap with those of the first three pristine cases, even though the lack-of-knowledge of regression coefficients in Eq. (13.5) is propagated through the analysis.

Repeating the procedure with a larger horizon-of-uncertainty automatically produces larger DI bounds because Eq. (13.5) defines nested intervals of uncertainty as α increases. One could conceive, therefore, increasing the value of α until the DI

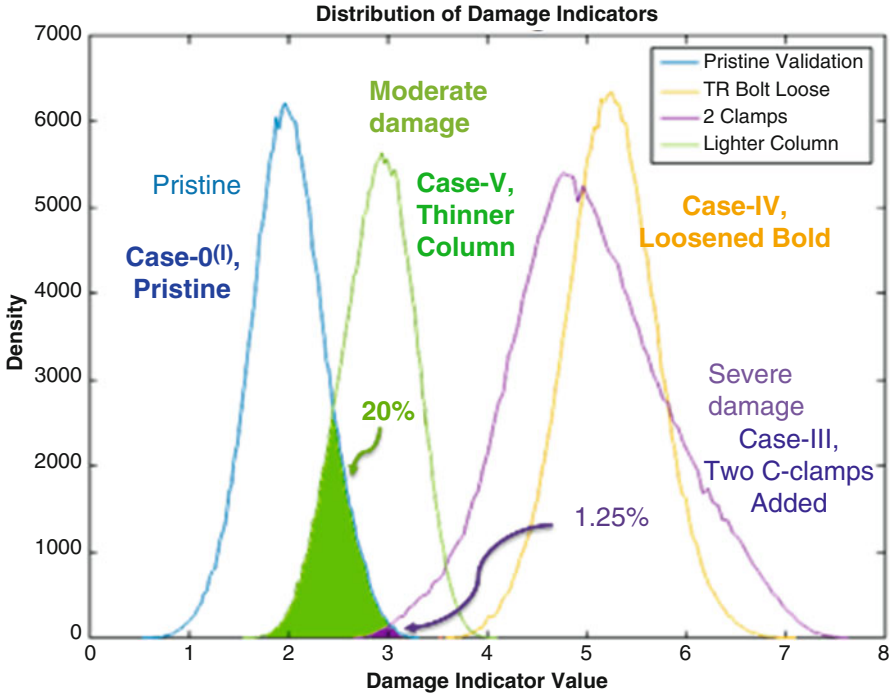

Fig. 13.12 Comparison of empirical histograms of DI values (at $\alpha = 1$)

bounds of the pristine and damaged configurations start to overlap. We estimate that reaching the point where the DI intervals completely overlap requires a horizon-of-uncertainty equal to $\alpha = 3$, approximately.[1]

Because a modeling uncertainty space of size $\alpha \approx 3$ is unambiguously larger than the space of size $\alpha = 1$ inferred from "calibration" to the pristine configurations, it can be concluded with confidence that Case-II, Case-III, and Case-IV are damaged states. These results illustrate the potential offered by our strategy for robust SHM, whereby the "growth" of the uncertainty space (parameter α) is quantified as opposed to simply monitoring the value of a damage indicator.

Lastly, Fig. 13.11 shows that the procedure does not successfully "isolate" the configurations of Case-V (orange interval, thinner column) and Case-VI (dark blue interval, removal of three base bolts) from the pristine condition. These two damage cases represent slightly less severe alterations of the vibration dynamics than those of Case-II/Case-III (mass loading) and Case-IV (loosened bolt). We hypothesize that it is the reason why they remain undetected. In addition, these scenarios introduce structural perturbations at the bottom-left side of the portal frame, while the measurements analyzed are collected from a single sensor located at the top-right. Even though this conjecture has not been verified, sensor data from the other accelerometers, or the addition of more sensors, could have possibly provided a better classification.

For completeness, it is noted that our sampling-based exploration does not just produce the lower and upper bounds of the DI metric at any value of α. An entire population of DI values is available for each damage state, from which statistics can be estimated. Figure 13.12 illustrates the empirical distributions of DI metrics for Case-$0^{(I)}$ (dark blue line, pristine), Case-III (magenta line, two C-clamps added), Case-IV (yellow line, loosened bolt), and Case-V (green line, thinner column).[2] This information is richer than the ranges shown in Figs. 13.6 and 13.11, which could lead to the development of probabilistic-based damage metrics. For example, the probability of falsely classifying a damaged configuration as pristine is defined by the overlap area of the damaged and pristine data. Figure 13.12 shows that these false-positive probabilities are 1.25 % for Case-III (mass loading), 0 % for Case-IV (loosened bolt), and 20 % for Case-V (thinner column).

These statistics do not alter the picture offered in Fig. 13.11 for the mass loading and loosened bolt cases, since the clear separation of their intervals from those of the pristine configurations already classifies them as damaged. The finer

[1] In the interest of full disclosure, it is mentioned that $\alpha \approx 3$ is an estimate based on the assumption that the damage indicator grows linearly with α. While this rule-of-thumb is believed to be conservative, it has not been verified by performing a numerical optimization to search for the minimum and maximum values of DI over the uncertainty space defined in Eq, (13.5). (See References [10, 11] for further details.)

[2] The reader is warned that the color schemes shown in Figs. 13.6, 13.11, and 13.12 are not consistent.

resolution brought by estimating probabilities, however, does alter the conclusion for Case-V (thinner column). While it is indistinguishable from the pristine condition based on comparing DI bounds in Fig. 13.11, the 80 % probability of damage estimated from Fig. 13.12 strongly suggests that Case-V is different from pristine.

13.5 Conclusion

A commonly encountered strategy to deploy Structural Health Monitoring (SHM) solutions is to develop a mathematical or numerical model that represents a given condition, such as the pristine (undamaged) state, and compare predictions to actual data collected on the structure. Discrepancies between the two sets are interpreted as a change in condition and, potentially, structural damage. This strategy generally leaves unaddressed the difficult question of how to handle the sources of uncertainty that can include environmental variability, unknown functional forms of the mathematical models, and non-unique model parameter values.

To meet this challenge, we propose a framework where the assessment of structural condition is made ***robust*** to the aforementioned sources of uncertainty. Instead of monitoring the value of a damage index, we suggest to monitor the "growth" of the uncertainty space that describes the environmental variability and modeling lack-of-knowledge. An increasing level of uncertainty indicates that the structural condition deviates more-and-more from the nominal, "baseline" state and, therefore, is suspected to be evolving towards damage.

This novel concept is illustrated by testing a portal frame structure in different configurations that include pristine, mass-loaded, and damaged states. We demonstrate that the appropriate "size" of the uncertainty space, which describes both environmental variability and unknown values of model parameters, can be "learned" from analyzing replicate measurements of the pristine state. The damage detection procedure is based on developing an auto-regressive time series model, comparing its predictions to measurements, and summarizing the results in the form of a scalar-valued damage indicator. We demonstrate that, when it is embedded within the analysis of robustness, this algorithm is capable of separating the various states of the frame structure. A component essential to the success of this technology is the ability to explore model parameters while preserving their correlation structure. This is achieved by using a correlation-preserving sampling scheme based on the principal component decomposition of the correlation.

Our hypothesis, which is that examining how the uncertainty space changes in time might lead to superior diagnostics of structural damage as compared to only monitoring a damage index, is confirmed by these preliminary results. While this methodology holds promise for robust SHM, future research efforts should consider incorporating more of the statistical information that, while it is generated in our analysis, was not fully exploited. Other potential improvements would be to, first, use or develop more sophisticated indicators of damage and, second, generalize the procedure to multiple-input, multiple-output time series modeling.

Acknowledgments The first three authors acknowledge the support of the Engineering Institute and 2015 Dynamics Summer School at the Los Alamos National Laboratory (LANL). The fourth author acknowledges support from the Advanced Scientific Computing program at LANL. The fifth author is grateful for continued support received from the Advanced Certification Campaign at LANL. LANL is operated by the Los Alamos National Security, L.L.C., for the National Nuclear Security Administration of the U.S. Department of Energy under contract DE-AC52-06NA25396.

References

1. Sigurdardottir, D.H., Glisic, B.: On-site validation of fiber-optic methods for structural health monitoring: streicker bridge. J. Civil Struct. Heal. Monit. **5**(4), 529–549 (2015)
2. Yarnold, M.T., Moon, F.L.: Temperature-based structural health monitoring baseline for long-span bridges. Eng. Struct. **86**, 157–167 (2015)
3. Figueiredo, E., Park, G., Figueiras, J., Farrar, C.R., Worden, K.: Structural health monitoring algorithm comparisons using standard data sets. Technical Report LA-14393, Los Alamos National Laboratory, Los Alamos (2009)
4. Fugate, M., Sohn, H., Farrar, C.R.: Vibration-based damage detection using statistical process control. Mech. Syst. Sign. Process. **15**, 707–721 (2001)
5. Stull, C.J., Hemez, F.M., Farrar, C.R.: On assessing the robustness of structural health monitoring technologies. Int. J. Struct. Heal. Monit. **11**(6), 712–723 (2012)
6. Ben-Haim, Y.: Info-Gap Decision Theory: Decisions Under Severe Uncertainty, 2nd edn. Academic Press, Oxford (2006)
7. Farrar, C.R., Worden, K.: Structural Health Monitoring: A Machine Learning Perspective. Wiley, New York (2012)
8. Worden, K., Manson, G.: Visualisation and dimension reduction of high-dimensional data for damage detection. 17th International Modal Analysis Conference, Orlando (1999)

9. McKay, M.D., Beckman, R.J., Conover, W.J.: A comparison of three methods for selecting values of input variables in the analysis of output from a computer code. Technometrics **21**(2), 239–245 (1979)
10. Van Buren, K.L., Hemez, F.M.: Robust decision-making applied to the NASA multidisciplinary uncertainty quantification challenge problem. AIAA J. Aerospace Inform. Syst. **12**(1), 35–48 (2015)
11. Hemez, F.M., Van Buren, K.L.: Designing a mechanical latch for robust performance. 34th International Modal Analysis Conference, Orlando (2015)

Chapter 14
Experimental Dynamic Characterization of Operating Wind Turbines with Anisotropic Rotor

Dmitri Tcherniak and Matthew S. Allen

Abstract The presented study concerns experimental dynamic identification of (slightly) anisotropic bladed rotors under operating conditions. Since systems with a rotating rotor do not fall into a category of time invariant system, a straightforward application of modal analysis is not valid. Under assumptions of linearity and constant angular speed, a system with rotating rotor can be considered as a linear periodically time variant (LPTV) system; dynamic identification of such systems require dedicated methods. The Harmonic OMA Time Domain (H-OMA-TD) method is one of very few techniques able to deal with anisotropic rotors. This study demonstrates the method on a simple six degrees-of-freedom mechanical system with a three-bladed rotor. It shows that the method is capable of identifying the phenomena specific for anisotropic rotors. The technique is compared with another technique, multiblade coordinate (MBC) transformation, and the advantages of H-OMA-TD become apparent when the rotor is anisotropic. Finally, the method is demonstrated on data measured on a real Vestas V27 wind turbine and data obtain via HAWC2 simulations of the same wind turbine.

Keywords Linear periodic time variant system • LPTV • Dynamic identification • Wind turbine

14.1 Introduction

The presented paper concerns the methods for experimental identification of bladed rotors with slight anisotropy. In industry, such methods are valuable means for investigation of dynamics of operating wind turbines. The current tendency in wind energy can be characterized by bigger wind turbines, greater wind loads (especially for offshore machines), lighter structures and longer lifetime. All these require the detailed understanding of wind turbine dynamic behavior while operating, and demand proper experimental techniques for their dynamic identification.

While a standstill wind turbine can be considered as a linear time-invariant (LTI) system, an operating wind turbine certainly does not fall into this category. It is easy to demonstrate that the mass, stiffness, damping and gyroscopic matrices are dependent on rotor azimuth angle. Still assuming the linearity and constant rotor angular speed, one can categorize such a system as Linear Periodic Time-variant (LPTV, or LTP) system. Then, instead of well-established tools suitable for LTI systems, such as modal analysis and experimental techniques such as EMA and OMA, one needs to employ tools that are more advanced.

In most of the practical cases, the rotor of a wind turbine is not completely isotropic. Despite the efforts of wind turbine manufactures, the rotor blades are never identical; there is some degree of rotor anisotropy even for a newly erected wind turbine. During the lifetime, the degree of anisotropy can increase temporarily or permanently. The former can happen e.g. due to ice formation on one of the blades, the latter—due to damage or loss of structural integrity of one of the blades, failure of the pitch mechanism or blade attachment to the hub. Such rotor anisotropy is considered as an "off-optimum situation" and shall be detected and avoided, if possible. Understanding and being able to characterize the differences in the dynamics between the isotropic and anisotropic rotors can apparently help in the abovementioned scenarios. Thus, one needs a proper tool for experimental dynamic characterization of operating wind turbine whose rotor might be slightly anisotropic.

D. Tcherniak (✉)
Brüel & Kjær Sound & Vibration Measurement, Skodsborgvej 307, Nærum 2850, Denmark
e-mail: dmitri.tcherniak@bksv.com

M.S. Allen
Department of Engineering Physics, University of Wisconsin-Madison, 535 Engineering Research Building, 1500 Eng. Drive, Madison, WI 53706, USA
e-mail: msallen@engr.wisc.edu

S. Pakzad, C. Juan (eds.), *Dynamics of Civil Structures, Volume 2*, Conference Proceedings of the Society for Experimental Mechanics Series, DOI 10.1007/978-3-319-29751-4_14

The tools allowing experimental dynamic characterization of LPTV systems are very limited: one can name MBC transformation adopted to experimental identification [1], the extension of stochastic subspace identification (SSI) to LPTV systems based on angular resampling [2] and harmonic power spectra (HPS) based methods [3]. The MBC transformation method assumes that the rotor is isotropic, it was demonstrated that application of this method to a system with an anisotropic rotor leads to incorrect results [4]. The method based on resampling was designed for systems with fast-rotating rotors such as helicopter, and its application to wind turbine data was not very successful [5]. For today, the HPS-based methods seem to be most suitable for wind turbine applications. Originally implemented in frequency domain (referred as H-OMA-FD) [6], the method was successfully applied to simulated wind turbine data (with isotropic rotor) [3] and to the data measured on real Vestas V27 wind turbine [7]. The time domain implementation of the method (referred as H-OMA-TD) was suggested by the authors in [8], and in [9] it was applied to the data measured on Vestas V27 wind turbine.

Because system identification methods are only now emerging for LPTV systems, there are still very few studies that treat turbines with blade anisotropy, and so it is challenging to understand how the results relate to the turbine's performance. The present study focuses on the effects of rotor anisotropy and investigates how these effects can be identified from experimentally obtained data using H-OMA-TD method. The paper is built as follows: Sect. 14.2 explains what we understand under *dynamic characterization of LPTV systems*; Sect. 14.3 briefs the reader for MBC- and HPS-based methods and explains why MBC transformation is not suitable for anisotropic systems. Section 14.4 demonstrates the H-OMA-TD method in application to systems with anisotropic bladed rotors: first we consider a simple six degree-of-freedom and then demonstrate the method on simulated and measured data from a Vestas V27 wind turbine.

14.2 Theoretical Background

Consider a LTI system governed by equation

$$\mathbf{M}\ddot{\mathbf{y}}(t) + \mathbf{C}\dot{\mathbf{y}}(t) + \mathbf{K}\mathbf{y}(t) = \mathbf{0} \tag{14.1}$$

where $\mathbf{M}, \mathbf{C}, \mathbf{K} \in R^{N\times N}$ are mass, damping and stiffness matrices respectively and vector $\mathbf{y}(t) \in R^N$ is the displacements of system's N degrees of freedom over time t. The solution to (14.1) can be presented as modal decomposition

$$\mathbf{y}(t) = \sum_{r=1}^{N} b_r\, \boldsymbol{\phi}_r e^{\lambda_r t} \tag{14.2}$$

where the mode shape $\boldsymbol{\phi}_r \in \mathbb{C}^N$ and eigenvalue $\lambda_r \in \mathbb{C}$ constitute the modal parameters for the rth mode and $b_r \in \mathbb{C}$ is the mode participation factor, which depends on the system initial conditions. Since one can completely characterize all of the possible dynamic responses of this system in terms of its modal parameters, finding them is often called system's *dynamic characterization*. When the equation of motion is known, modal parameters can be found via eigenvalue analysis, e.g. [10]. In case when the equation of motion is unknown, we use experimental or operational modal analysis (EMA or OMA).

The mass, damping/gyroscopic and stiffness matrices of a system *with rotating rotor* depend on rotor position (azimuth angle θ)

$$\mathbf{M}(\theta(t))\ \ddot{\mathbf{y}}(t) + \mathbf{G}(\theta(t))\,\dot{\mathbf{y}}(t) + \mathbf{K}(\theta(t))\,\mathbf{y}(t) = \mathbf{0}. \tag{14.3}$$

Under the assumption that the rotor angular speed $\Omega = const$, thus $\theta(t) = \Omega t$, the matrices become time-periodic $\mathbf{M}(t+T) = \mathbf{M}(t), \mathbf{G}(t+T) = \mathbf{G}(t), \mathbf{K}(t+T) = \mathbf{K}(t)$ with period $T = 2\pi/\Omega$. We refer to such a system as an LPTV or LTP system.

The main assumption of modal analysis, that the system under test is time invariant, is violated here. It means that generally modal analysis and modal decomposition are not applicable to LPTV systems. However, *Floquet theory* suggests a decomposition, similar to (14.2) but involving T-periodic mode shapes $\mathbf{u}_r(t)$

$$\mathbf{y}(t) = \sum_{r=1}^{N} b_r \mathbf{u}_r(t) e^{\lambda_r t} \tag{14.4}$$

The periodic mode shapes can be expanded using Fourier transform

$$\mathbf{u}_r(t) = \sum_{n=-\infty}^{+\infty} \mathbf{C}_{r,n} e^{jn\Omega t} \tag{14.5}$$

and finally, the solution to (14.3) can be written as a modal superposition of sums of the harmonic components:

$$\mathbf{y}(t) = \sum_{r=1}^{N} b_r \sum_{n=-\infty}^{+\infty} \mathbf{C}_{r,n} e^{(\lambda_r + jn\Omega)t} \tag{14.6}$$

Thus, when saying *dynamic characterization of an LPTV system*, we mean finding its *Floquet exponents* $\lambda_r \in \mathbb{C}$ and the *Fourier coefficients* $\mathbf{C}_{r,n} \in \mathbb{C}^N$. Comparing (14.2) and (14.6), one can see many similarities: in both cases the solution is presented as modal superposition; the Floquet exponents are similar to the eigenvalues of the LTI system; they combine its natural frequency (the imaginary part) and damping (the real part). The Fourier coefficients can be thought as an infinite set of complex vectors, which together represent a periodic mode shape of the LPTV system, and thus they resemble the mode shape of the LTI system $\boldsymbol{\phi}_r$.

If the equation of motion is known, the Floquet exponents and Fourier coefficients can be found via *Floquet analysis* (for small number of DOFs) or *implicit Floquet analysis* (for great DOFs number), see [11], Table 3.1. To *experimentally characterize* an LPTV system, dedicated methods are needed, as will be considered the next section.

14.3 Experimental Techniques for LPTV Systems

There is a very limited set of tools applicable to experimental identification of LPTV systems. Here we briefly introduce multiblade coordinate (MBC) transformation and harmonic power spectra (HPS) based methods.

14.3.1 Multiblade Coordinate (MBC) Transformation

MBC transformation in application to wind turbines was introduced by Hansen, and its detailed description can be found in [12, 13]. The idea of the method lies in special coordinate transformation known as a *multiblade coordinate* or *Coleman* transformation. For a three-bladed rotor, the forward MBC transformation

$$a_{0,k}(t) = \frac{1}{3}\sum_{i=1}^{3} q_{i,k}(t), \quad a_{1,k}(t) = \frac{2}{3}\sum_{i=1}^{3} q_{i,k}(t)\cos(\theta_i(t)), \quad b_{1,k}(t) = \frac{2}{3}\sum_{i=1}^{3} q_{i,k}(t)\sin(\theta_i(t)) \tag{14.7}$$

converts the set of three coordinates $q_{i,k}$ measured at kth DOF of blade no. $i = 1, 2, 3$ into a set of three *multiblade coordinates* $a_{0,k}$, $a_{1,k}$ and $b_{1,k}$. The transformation uses $\theta_i(t)$, which is the azimuth of the ith blade.

Typically, vector $\mathbf{y}(t)$ is a mixture of the coordinates measured on the rotating rotor ($q_{i,k}$) and those measured on not rotating substructures, e.g. on the tower and nacelle (s_l):

$$\mathbf{y}(t) = \{\ldots, q_{1,k}(t), q_{1,k}(t), q_{3,k}(t), \ldots, s_1(t), \ldots, s_L(t)\}^T. \tag{14.8}$$

By substituting the coordinates measured on the rotating frame by the corresponding multiblade coordinates, it can be shown that, under the assumptions outlined below, the LPTV system transforms into an LTI system. Then, the conventional eigenvalue analysis can be performed on the obtained LTI system, resulting in eigenvalues and eigenvectors in multiblade coordinates. Finally, the eigenvectors can be converted back into the physical coordinates using the *backward multiblade coordinate* transformation

$$q_{i,k}(t) = a_{0,k}(t) + a_{1,k}(t)\cos(\theta_i(t)) + b_{1,k}(t)\ \sin(\theta_i(t)). \tag{14.9}$$

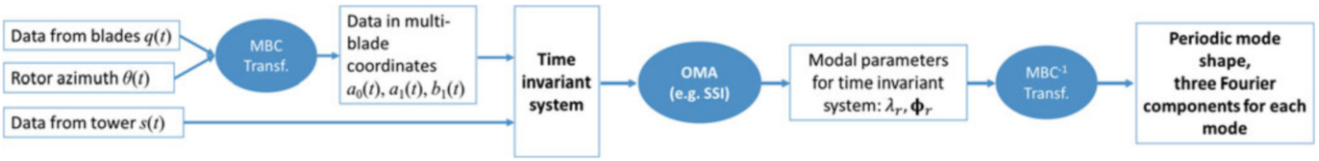

Fig. 14.1 Adaptation of MBC transformation to OMA

It is important to note that MBC transformation converts the LPTV system into the LTI system if the following assumptions fulfill:

1. The rotor is isotropic, i.e. the blades are identical and attached identically to the hub;
2. There is no gravity (for horizontal axis wind turbine, this condition can be relaxed for out-of-plane rotor modes since the out-of-plane blade motion is roughly perpendicular to the vector of gravity).

In [1], the MBC transformation was adopted to experimental system identification, combining the MBC transformation with Operational Modal Analysis (OMA); the flow is shown schematically in Fig. 14.1. The approach was demonstrated on simulated data [1] and on the data measured on operating Vestas V27 wind turbine [4, 7].

Applying the backward MBC transformation (14.9) to the mode shapes of the time invariant system, one can show that in physical coordinates the mode shape becomes periodic

$$\begin{aligned} u_{i,k}(t) = A_{0,k}\sin\left(\omega_r t + \varphi_{0,k}\right) + A_{BW,k}\sin\left(\left(\omega_r + \Omega\right)t + \tfrac{2\pi(i-1)}{3} + \varphi_{BW,k}\right) \\ + A_{FW,k}\ \sin\left(\left(\omega_r - \Omega\right)t - \tfrac{2\pi(i-1)}{3} + \varphi_{FW,k}\right) \end{aligned} \tag{14.10}$$

where $\omega_r = Im\left(\lambda_r\right)$ is the natural frequency of the rth mode of the time invariant system.

Analyzing (14.10), one can note that:

1. The method produces time periodic mode shapes, which always consist of three components.
2. The three components oscillate at frequencies ω_r, $\omega_r + \Omega$ and $\omega_r - \Omega$.
3. All three blades have identical oscillation magnitudes.
4. The phase between the blades is 0 for the first component (thus it is called *collective* component), $-120°$ for the second (*backward whirling* component) and $+120°$ for the third (*forward whirling* component).
   The last two properties can be described as a mode shape *symmetry*. That is, MBC transformation *always* produces modes with symmetric mode shapes.
5. The coordinates measured on the not rotating parts always have only a single component, namely at frequency ω_r.

Drawing the analogy with the Floquet theory, one can notice that (14.10) is a truncated version of (14.5), where $n = -1$, 0, 1; λ_r and $\lambda_r \pm \Omega$ are the three Floquet exponents and the pairs $(A_{X,k}, \varphi_{X,k})$ can be considered as kth element in the Fourier coefficient vector.

It becomes obvious, that application of the MBC transformation to the data measured on anisotropic rotor will lead to erroneous results. The effects of anisotropy, such as modes' asymmetry, will be smeared out by the MBC transformation and cannot be correctly identified. Analysis of such a possible erroneous interpretation can be found in [4].

14.3.2 Harmonic OMA (Frequency Domain) or H-OMA-FD

Allen et al. [3] suggested a framework for experimental identification of LPTV systems. The framework is based on the Floquet theory [14] and on the concept of harmonic transfer functions introduced by Wereley [15]. The method does not assume rotor isotropy, and thus directly suitable for analyzing anisotropic rotors. The detailed description of the approach can be found in [3], below we only present its main steps, which are also outlined in Fig. 14.2.

The core of the method is the *modulation* of the response signals using the phasors rotating with the fundamental circular frequency Ω and its integer multipliers

$$\mathbf{y}_m(t) = \mathbf{y}(t)e^{-jm\Omega t}, \quad m = -M \ldots M, m \in \mathbb{Z}. \tag{14.11}$$

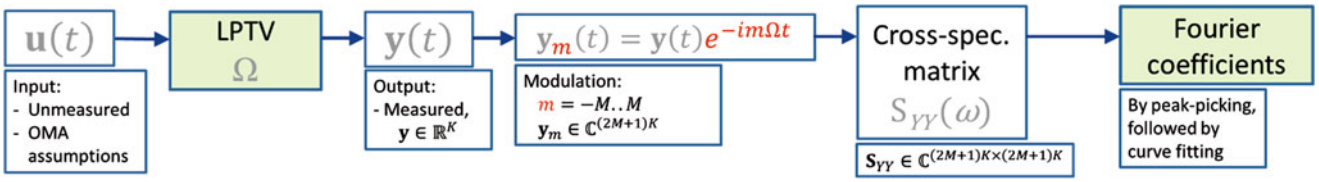

Fig. 14.2 Steps of H-OMA-FD method

Here $\mathbf{y}(t)$ is a vector of measured responses, $\mathbf{y}(t) \in \mathbb{R}^K$, see (14.8). The resulting vector consists of $(2M+1)K$ complex time histories, $\mathbf{y}_m(t) \in \mathbb{C}^{(2M+1)K}$. The next step of the method is the calculation of the harmonic power spectra (HPS) matrix between the modulated signals:

$$\mathbf{S}_{YY}(\omega) = \mathrm{E}\left\langle \mathbf{y}_{\boldsymbol{m}}(\omega)\, \mathbf{y}_{\boldsymbol{m}}(\omega)^H \right\rangle, \tag{14.12}$$

where $\mathrm{E}\langle \ldots \rangle$ is mathematical expectation, $(\ldots)^H$ is Hermitian transpose. Note that the resulting matrix is defined in the frequency domain. The theory in [3] states that the HPS matrix can be presented in terms of modes of the LPTV system. Preserving only dominant terms, [3] proves that the HPS matrix can be decomposed as:

$$\mathbf{S}_{YY}(\omega) \approx \sum_{r=1}^{N} \sum_{n=-\infty}^{\infty} \frac{\mathbf{C}_{n,l} \mathbf{W}(\omega)\, \mathbf{C}_{n,l}^H}{(j\omega - (\lambda_r - jn\Omega))\,(j\omega - (\lambda_r - jn\Omega))^H} \tag{14.13}$$

where λ_r are the Floquet exponents, $\mathbf{C}_{r,n}$ are the Fourier coefficients and N is the number of modes. $\mathbf{W}(\omega)$ describes the input spectrum. Under the standard OMA assumptions regarding the excitation, $\mathbf{W}(\omega)$ becomes an identity matrix.

Finally, the Floquet exponents and Fourier coefficients are extracted from the HPS matrix. This can be done by employing one of the conventional frequency domain methods known from classical modal analysis.

The method operates in frequency domain, and we refer to it as H-OMA-FD method. The method was successfully applied to simulated data from randomly excited Mathieu oscillator and simulated data from an operating wind turbine [3] and to the measured data from an operating Vestas V27 wind turbine [7].

14.3.3 Harmonic OMA (Time Domain) or H-OMA-TD

The recent advances in OMA, especially the improvements of the time domain OMA algorithms such as SSI, make it attractive to replace the curve fitting part of H-OMA-FD by OMA SSI. The adaptation of H-OMA-FD method to OMA SSI was suggested and explained in [8]. In analogy to H-OMA-FD, we refer this extension as Harmonic OMA Time Domain (H-OMA-TD). Below the main steps of the method are presented (and outlined in Fig. 14.3).

The first step of the two algorithms is the same: the measured signals are modulated using the phasor rotating at the rotor speed and its integer multipliers (14.11). In real applications the rotor speed can slightly vary; in this case it is advantageous to measure and use the rotor azimuth angle $\theta(t)$: $\mathbf{y}_m(t) = \mathbf{y}(t)e^{-jm\theta(t)}$. The resulting time histories are complex. To be able utilizing commercial OMA implementations (e.g. SVS ARTeMIS or B&K OMA software Type 7760), one needs to make the time histories real, still conserving the important dynamic information contained in the modulation. Two approaches to convert the modulated signals to real time histories are suggested in [8]; if the OMA implementation allows using complex time histories, this step can be omitted. The "Special data assignment to geometry" step is illustrated in Fig. 14.4, it serves to ease the interpretation of the results. It consists of creating $2M$ "clones" of the original test object geometry and assigning the modulated data to the clones. Finally, the modulated signals are processed by the OMA algorithm, resulting in modal parameters, which can be interpreted as Floquet exponents and the Fourier coefficients; the latter can be animated to visualize each component of the mode shapes. The interpretation of the results is explained in detail in [8].

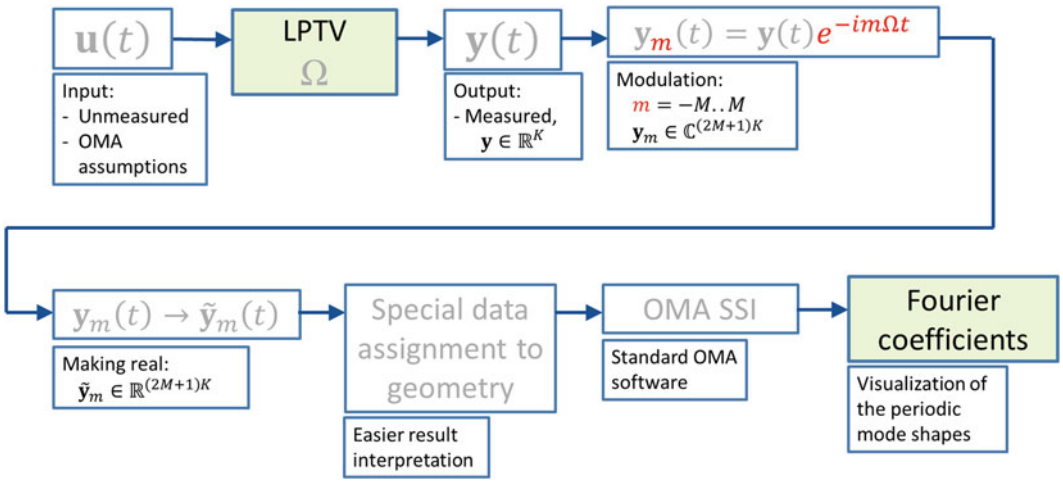

Fig. 14.3 Steps of H-OMA-TD method

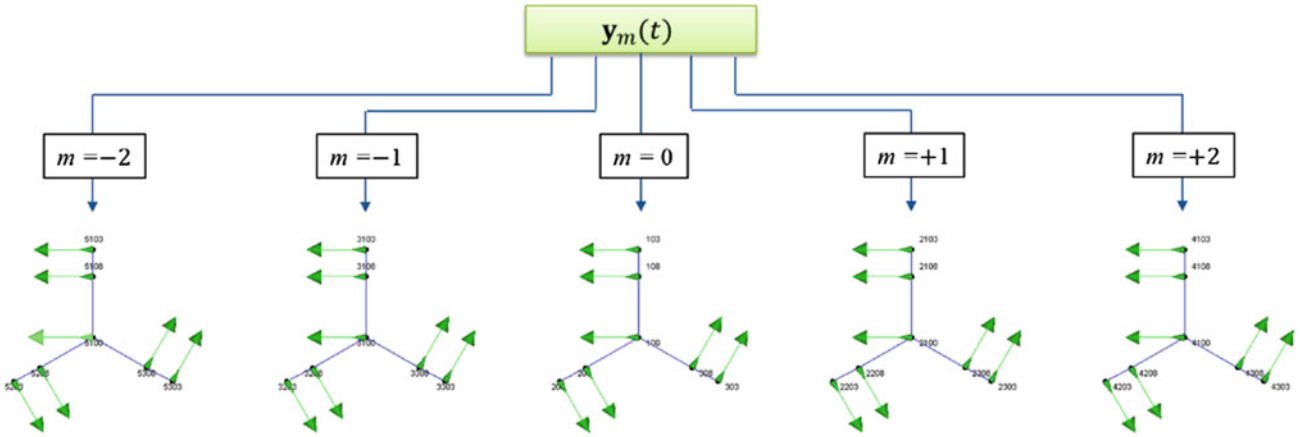

Fig. 14.4 Special data assignment to the geometry

14.3.4 Selection of M

Expression (14.5) expands the periodic mode shape using an infinite number of Fourier components. This is not feasible in practice, and one has to truncate the series:

$$\mathbf{u}_r(t) \approx \sum_{n=-M}^{+M} \mathbf{C}_{r,n} e^{jn\Omega t} \tag{14.14}$$

In the experimental interpretation of the HPS-based method, this corresponds to the selection of M in (14.11). Selecting the value of M, one can take into account the following considerations: As it follows from the MBC transformation (see Sect. 14.3.1), a three bladed isotropic rotor in the absence of gravity requires exactly three Fourier components, thus setting $M = 1$ is sufficient to describe such a rotor. Gravity and anisotropy will require more Fourier components. From authors experience, selecting $M = 2$ or $M = 3$ is sufficient for most wind turbine related cases, when there are three blades and the rotor anisotropy is not too large.

14.4 Application to Anisotropic Rotor

14.4.1 Application to a Simple Six Degree-of-Freedom System

In order to validate the method, let us consider a simple six degree-of-freedom system representing a three-bladed rotor mounted on a supporting structure (Fig. 14.5). The rotor is attached to a mass, which is supported in vertical and horizontal directions by two springs representing the bending and axial stiffness of the tower. Each rotor blade is constructed from two rigid arms, connected by a hinge with an angular spring modelling blade stiffness. The lumped mass at the end of the blade represents blade's mass. The system can model the blade dynamics in the rotor plane and the associated motion of the supporting mass and the "drive train". The same model was considered in [16], where the details are provided. The parameters of the model were selected to represent a 10 MW wind turbine prototype whose rotor rotates at 9.6 rpm (the fundamental frequency is 0.16 Hz).

The system can be fully described by the set of coordinates $\mathbf{y} = \{x_C, y_C, \phi_1, \phi_2, \phi_3, \psi\}^T$, where x_C, y_C are the coordinates of the mass C, angles ϕ_1, ϕ_2, ϕ_3 describe the angular displacements in the hinges and angle ψ is the angular deformation of the flexible "drive train".

Knowing the parameters of the system, the equations of motion can be readily defined, and the Floquet analysis can provide the Floquet exponents and Fourier coefficients for all six modes of the structure. The application of Floquet analysis to the system is straightforward though cumbersome; it is described in details in [16] and omitted here. The results of the Floquet analysis are used as a baseline for the H-OMA-TD method validation.

The validation is conducted via a simulated experiment: the system is subjected to random broadband excitation applied to the supporting mass and to the tips of the blades; and its response is simulated via time domain integration of the equations of motion using fourth order *Runge-Kutta* method. The obtained time histories become an input to the H-OMA-TD algorithm, which identifies the modal parameters (Floquet exponents and Fourier coefficients) of the turbine. These are then compared with the analytically obtained ones for isotropic and anisotropic rotors. The rotor anisotropy is modelled as a 3 % reduction of the stiffness of blade #3: $k_3 = 0.97k_1$.

The focus of the paper is to assess the ability of H-OMA-TD to catch the dynamic features intrinsic to an anisotropic rotor, thus we chose the following validation strategy: First we compare the results of Floquet analysis for an isotropic rotor, with that for anisotropic rotors, with anisotropy due to gravity and due to differing blade stiffness. This reveals features in the Floquet exponents and Fourier coefficients that are indicative of anisotropy. Then, we apply *H-OMA-TD* to the simulated isotropic and anisotropic rotors to see whether one can detect the features characteristic to anisotropic rotor from experimental data.

Figure 14.6 shows three rotor related modes, in industry these modes are traditionally called the backward whirling (BW) mode, forward whirling (FW) mode and collective mode. Three other modes (two tower related and one related to the drive-train) are not shown. Each mode consists of a number of Fourier components, oscillating at frequencies separated by Ω. The component with the biggest magnitude is placed in the center of the plot. One can see that the magnitude of the Fourier coefficients quickly decreases when moving away from the central component, meaning that only a small number of Fourier coefficients is required to describe modes' periodicity. However, one has to be careful when selecting this number since it will increase for rotors with higher degree of anisotropy.

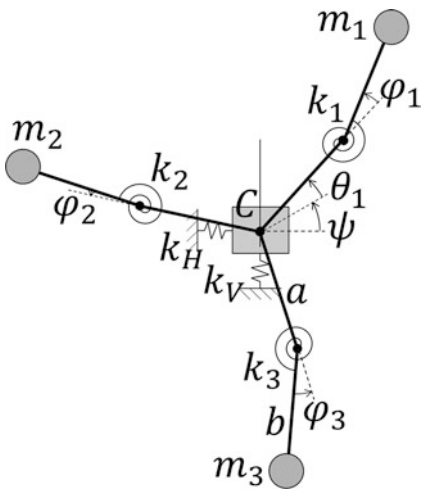

Fig. 14.5 Simplified three-bladed rotor system

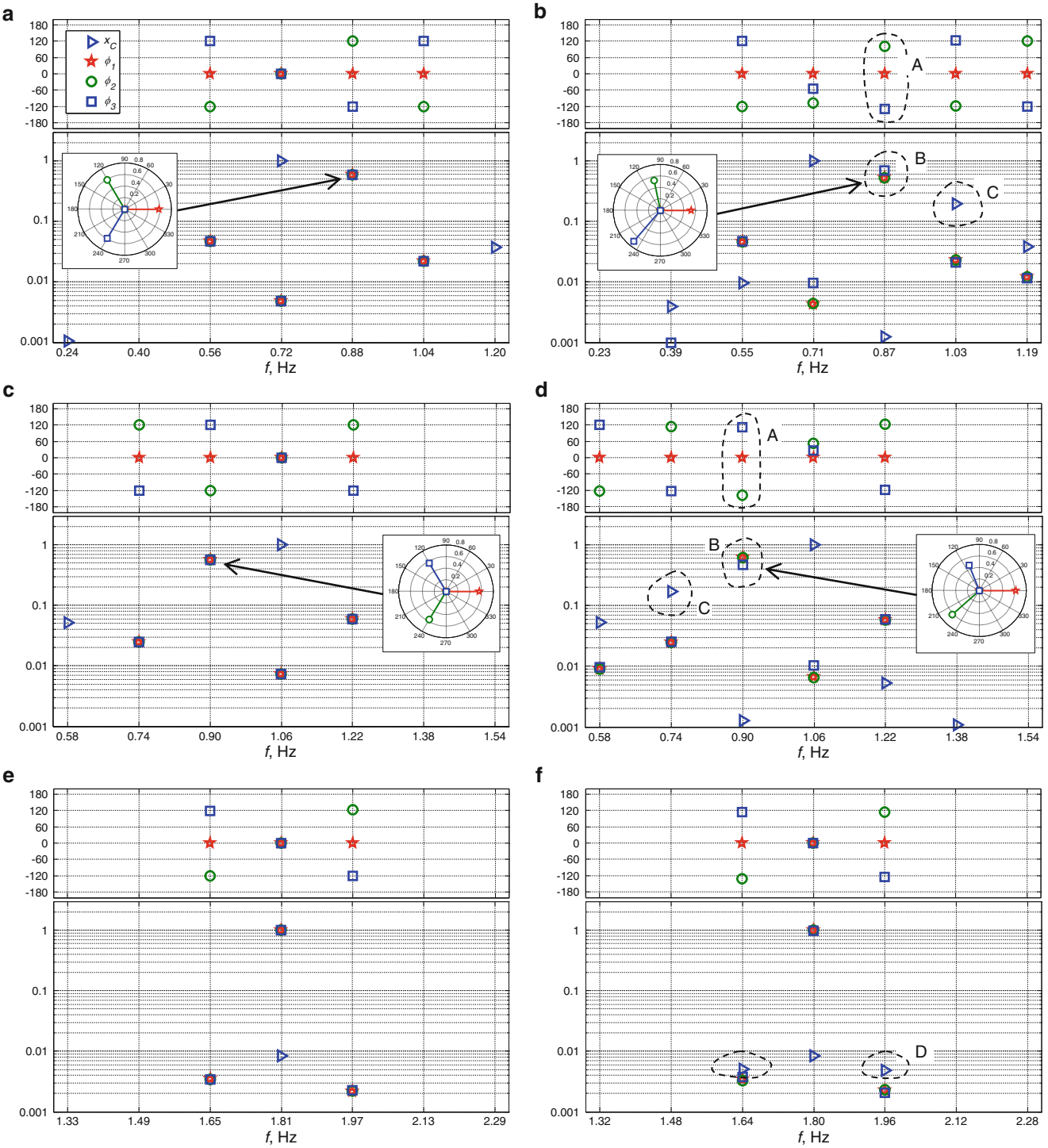

Fig. 14.6 Rotor related modes obtained via Floquet analysis: (**a**, **b**) backward whirling mode, (**c**, **d**) forward whirling mode, (**e**, **f**) collective mode. *Left column*: isotropic rotor in the presence of gravity; *right column*: anisotropic rotor with reduced stiffness of the third blade ($k_c = 0.97k_a$)

The representation of complex Fourier coefficients in Fig. 14.6 may require some explanations. For each mode, the plot shows the magnitude of four DOFs: x_C, ϕ_1, ϕ_2, ϕ_3. The other two DOFs are not shown since their magnitude is much smaller. The magnitude is normalized such a way that the magnitude of the biggest Fourier component is set to unity. The phase subplot shows the phases of the rotor related DOFs ϕ_1, ϕ_2, ϕ_3, which are adjusted such that the phase of ϕ_1 is zero. One has to notice that the plots mix the translational and angular units (for x_C and ϕ_1, ϕ_2, ϕ_3 respectively) thus the direct comparison of the magnitudes corresponding to the different units is not valid.

Comparing the corresponding modes of the isotropic and anisotropic rotors, one can spot some deviations. Naturally, the imaginary parts of the Floquet exponents (namely, the damped natural frequencies, shown by the ticks on the frequency axes) have slightly decreased; this is an obvious result of the reduced rotor stiffness. Secondly, some of the Fourier coefficients describing the mode shapes have changed. One can notice that some Fourier components are affected more than the others. The most evident effects of anisotropy are outlined by a dashed line and labeled by letters A . . . D.

The effects labeled by "A" and "B" represent the significant change of phase and magnitude of blades 1 . . . 3 of the dominant whirling component of the BW and FW modes. This effect is better seen in the complexity plots in the insets. For the BW mode (Fig. 14.6a, b), the magnitude of the blade with the decreased stiffness becomes greater, and the phase between this blade and two other blades becomes greater than 120°. For the FW mode (Fig. 14.6c, d), the effect is opposite: the magnitude of the "damaged" blade becomes smaller and the phase between this blade and two others becomes less than 120°. Generalizing, one can say that the rotor anisotropy causes a *loss of symmetry of the whirling rotor modes*. The idea of using this phenomenon to detect and localize blade damage was introduced and investigated in [16].

The phenomenon labeled by letter C affects both BW and FW modes and appears as a significant increase of side-to-side tower motion at central frequency $\pm 2\Omega$ ("+" for the backward and "−" for the forward mode). Finally, the effect denoted by letter D appears as two sidebands in the tower motion in the collective mode (Fig. 14.6e, f).

Figure 14.7 plots the Fourier coefficients for same three modes, which are now obtained by the H-OMA-TD method applied to the data generated in the simulated experiment. The experiment was repeated five times, every time we generated new random excitation forces; the five datasets containing the simulated dynamic response (each 7200 s long, corresponding to 1150 rotor revolutions) were input to the H-OMA-TD method. The average and confidence intervals of the results are presented in Fig. 14.7. To ease the comparison, we used the same mode normalization and phase rotation scheme as for Fig. 14.6.

As one can see, the abovementioned phenomena due to the rotor anisotropy are caught by the method, though not precisely. The method was able to catch the phase changes due to the anisotropy (the areas denoted by letter A for both backward and forward whirling modes, Fig. 14.7b, d), with quite high confidence. However, the changes in blade magnitudes (areas "B") for these modes are not very evident, though it is present; also, the confidence is lower. The third phenomenon, denoted by letter C is also caught, also with lower confidence. Anyway, it is apparent that the magnitude of the side-to-side component of the whirling modes at the central frequency $\pm 2\Omega$ is about five times higher than for the isotropic rotor. Finally, the method catches the increase of the sidebands magnitudes for the collective mode (areas "D" in Fig. 14.7f), more at 1.64 Hz and less at 1.96 Hz, though again, the confidence is quite low.

It is also clear that the method finds several components that do not exist in the analytical solution (Fig. 14.6). In Fig. 14.7a, they are outlined by the red dashed line and denoted by letter E. These "noise" components all have quite low confidence and can be filtered out. This also points to a challenge in performing this type of identification. The method is prone to identify some component at every line in the spectrum, presumably due to noise or because the input forces are not fully white. Fortunately, the method is most reliable for those response components that contribute most to the motion of the turbine.

It is unclear why the method finds the side-to-side Fourier components at the central frequency $\pm 2\Omega$ in the BW and FW modes for the *isotropic* rotor (outlined by the red dashed line in Fig. 14.7a, c). According to the Floquet analysis, these components should not be present in the modes (see Fig. 14.6a, c). However, the spurious components that were identified in the isotropic case are 5–10× smaller than those in the anisotropic case, so it seems that these components could still be used as a measure of anisotropy.

14.4.2 Application to Data from Simulated Vestas V27 with Introduced Rotor Anisotropy

The simulated experimented conducted on a simple six degree-of-freedom bladed rotor system demonstrated the capabilities of H-OMA-TD to capture the main dynamic effects of rotor anisotropy. However, for the simulations, the rotor was excited by broadband uncorrelated noise, which fulfils OMA assumption regarding the excitation. In reality, the blades of a wind turbine are loaded by aerodynamic forces, which are periodic and partly correlated due to wind turbulence [17]. Wind shear (dependence of the wind speed from the altitude) also causes a strong aerodynamic excitation at 1p. These properties of the excitation can complicate H-OMA-TD, as the loading is not completely fulfil the OMA assumptions.

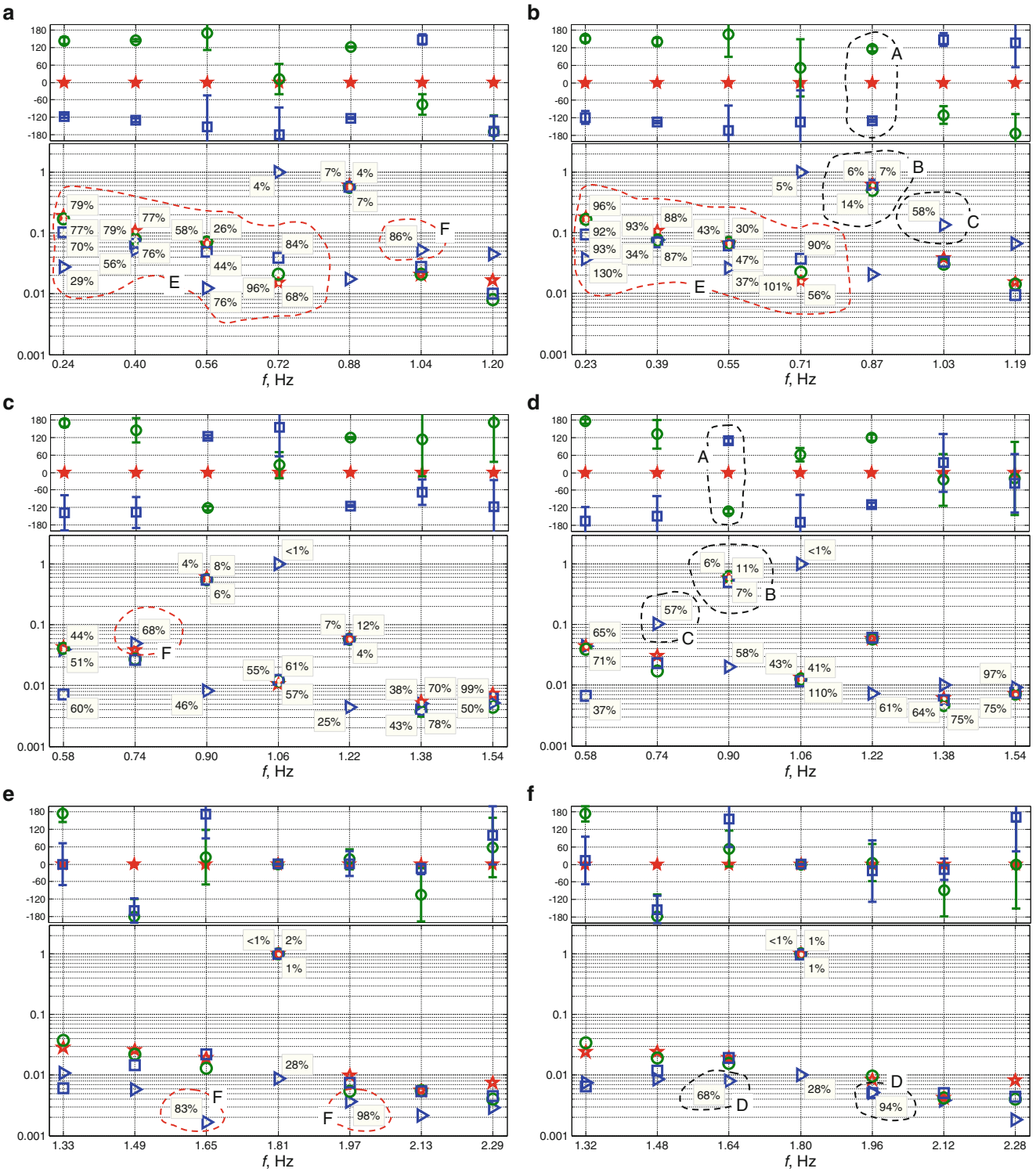

Fig. 14.7 Rotor related modes obtained by H-OMA-TD: (**a**, **b**) backward whirling mode, (**c**, **d**) forward whirling mode, (**e**, **f**) collective mode. *Left column*: isotropic rotor in the presence of gravity; *right column*: anisotropic rotor with reduced stiffness of the third blade ($k_c = 0.97k_a$). The error bars in the phase plots correspond to 95 % confidence; the per-cent values in the magnitude plots denote a half-width 95 % confidence interval as a percentage of the mean magnitude

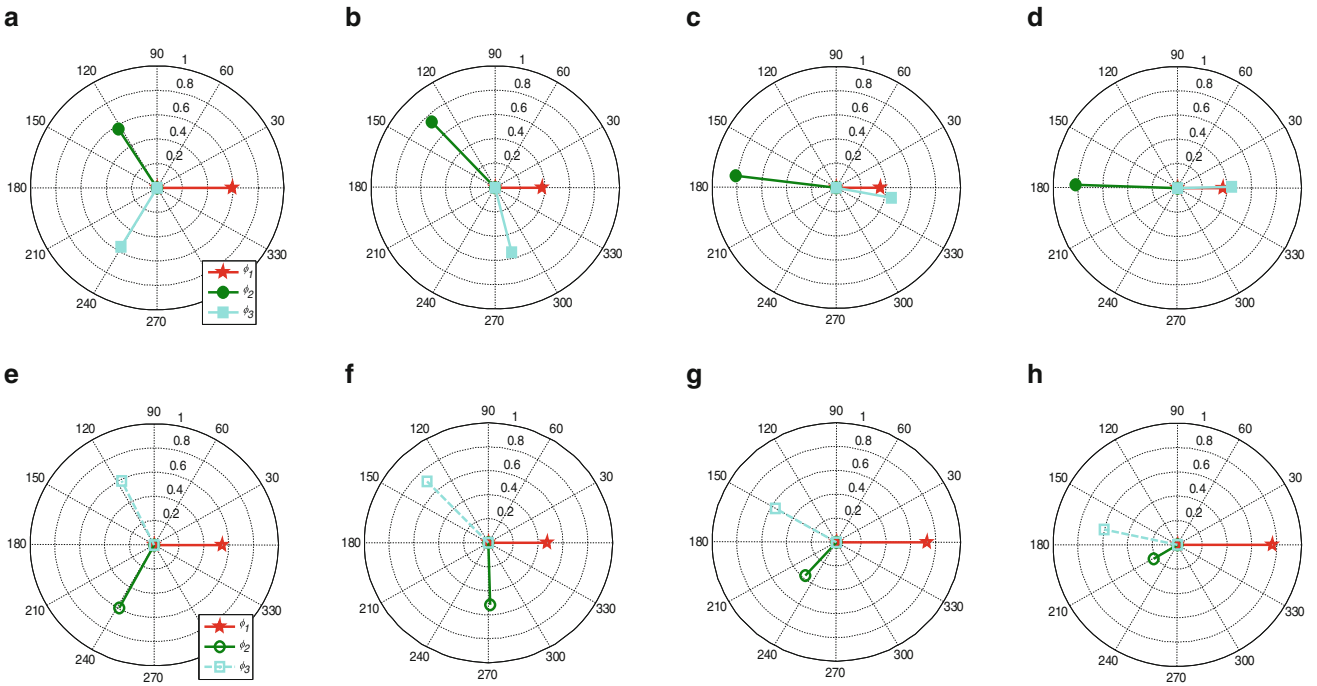

Fig. 14.8 Complexity plots of the dominant components of the whirling modes [16]. *Top*: BW mode: (**a**) isotropic rotor; (**b**) 1 % Young modulus reduction of blade 2; (**c**) 3 % Young modulus reduction of blade 2; (**d**) 5 % Young modulus reduction of blade 2. *Bottom*: FW mode: (**e**) isotropic rotor; (**f**) 1 % Young modulus reduction of blade 2; (**g**) 3 % Young modulus reduction of blade 2; (**h**) 5 % Young modulus reduction of blade 2

In order to check the performance of H-OMA-TD in more realistic scenario, the method was applied to the data generated using *Horizontal Axis Wind turbine Code 2nd generation* (HAWC2). This is a nonlinear aeroelastic code designed for simulation of the wind turbine dynamic response in time domain; the code was developed and maintained by the Wind Energy department of Technical University of Denmark (DTU) [18]. The code models the wind turbulence and calculates the aerodynamic forces acting on the blades. The dynamic response of the blades is simulated employing a multibody formulation, where each blade is represented by an assembly of Timoshenko beam elements.

The vibrations of a Vestas V27 wind turbine were simulated; the same wind turbine type was a test object during the real measurement campaign described later. The detailed description of the modelling, model tuning and setting up a virtual experiment using HAWC2 can be found in [4]. Datasets corresponding to 20 min of wind turbine operating at 32 rpm rotor speed were generated; the rotor anisotropy was modelled by the gradual decrease of Young modulus for blade #2.

Figure 14.8 presents the results of H-OMA-TD applied to the simulated Vestas V27 data. Only the dominant whirling components of the BW and FW modes are shown as complexity plots. Here we see the same tendency as in the insets in Fig. 14.5b, c: for the BW mode, the magnitude of the "damaged" blade becomes greater, while for the FW mode it decreases. The phase between the damaged blade and two others becomes greater than 120° for the BW mode, and oppositely, for the FW mode, it becomes less than 120°. That is, one can see that the H-OMA-TD is able to catch the loss of mode shape symmetry due to the rotor anisotropy but now in more realistic excitation conditions.

14.4.3 Application to Data Measured on Vestas V27 Wind Turbine

This section briefly presents the results of H-OMA-TD applied to the data measured on a real wind turbine (Vestas V27). The details of the measurement setup and the campaign are given in [19].

Starting analyzing data from the real wind turbine, we were not aware about the current rotor state, and we assumed it to be isotropic. In studies [4] and [7], the MBC transformation was applied to the data, and some doubts regarding the rotor isotropy of that particular wind turbine were expressed. Study [9] applied H-OMA-TD to the same data and confirmed the suspected rotor anisotropy. The Fourier coefficients of the BW and FW modes are shown in Fig. 14.9. Both modes are clearly dominated by one component ($m = 0$ corresponds to 3.59 Hz for the BW mode and 3.52 Hz for the FW mode,

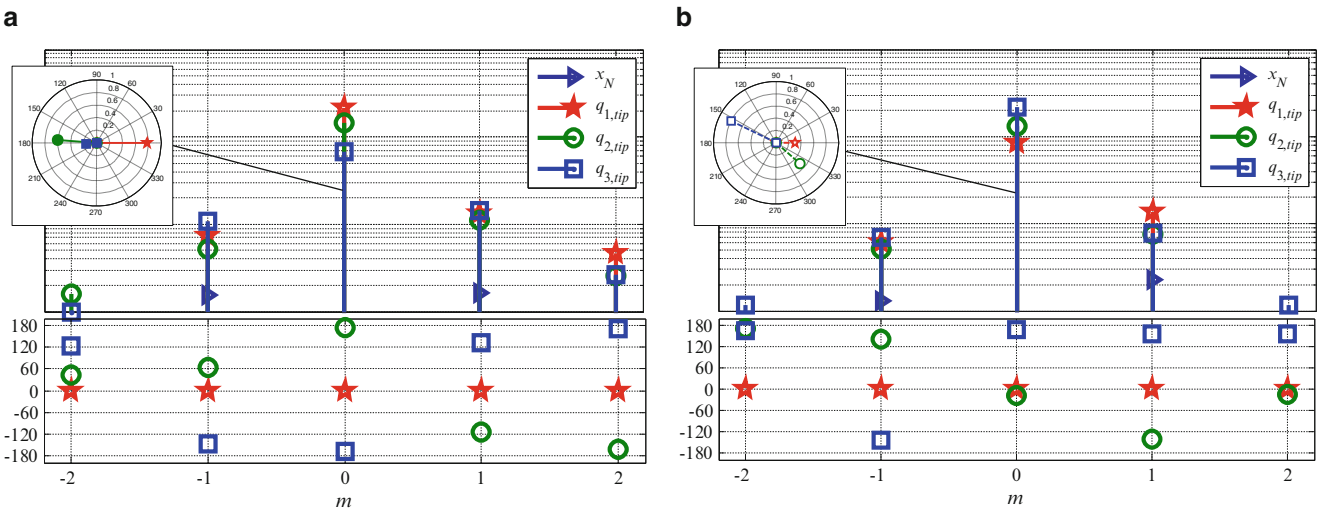

Fig. 14.9 Fourier coefficients: (**a**) BW mode, (**b**) FW mode. *Top*: magnitudes, *bottom*: phase. The *insets* show the complexity plots of the dominant component

for the given case, the rotor speed is 32 rpm).[1] Analyzing the Fourier coefficients of these modes, one can identify some features of the rotor anisotropy, which are listed in Sect. 14.4.1. The mode shapes are not symmetric, all three blades have different magnitudes: the BW mode features the highest magnitude of Blade #1 and lowest of Blade #3, for the FW mode the magnitude order is opposite: Blade #1 is lowest and Blade #3 is highest. The phases do not make a very clear picture; however, one can note almost 180° phase between Blade #1 and two other blades for the BW mode, though the phase distribution of the FW mode does not fit the pattern derived from the analytical model and the simulations.

14.5 Conclusion and Further Research

The paper validates applicability of the time domain implementation of the HPS-based method (referred here as H-OMA-TD) to systems with rotating slightly anisotropic rotor. The validation is based on a simple six DOFs mechanical system resembling a horizontal axis wind turbine and done via comparison with analytic results obtained via Floquet analysis. The method was also applied to data generated via HAWC2 simulations of a Vestas V27 wind turbine and the data measured on a real Vestas V27 machine.

The validation demonstrates that the method can qualitatively catch the important features of rotor anisotropy, such as a loss of symmetry of whirling modes and appearance of the additional side-to-side components in whirling and collective modes. Quantitatively, the method detects some of the effects better than the others, for example, the phase change is detected with good confidence, while the confidence in magnitude change is lower.

Concluding it is important to note that MBC transformation, widely used in wind turbine design, can only produce modes with symmetric mode shapes (see Sect. 14.3.1), thus the MBC-based methods are not capable to catch the abovementioned effects of rotor anisotropy.

Acknowledgement The work was partly supported by EUDP (Danish Energy Technology Development and Demonstration Programme), grant number 64011-0084 “Predictive Structure Health monitoring of Wind Turbines”. The authors wish to acknowledge the great help from Óscar Ramírez Requesón for performing the HAWC2 simulations of the Vestas V27 wind turbine.

[1]Comparing Fig. 14.9 with Figs. 14.6 and 14.7, one has to take into account the scaling between the rotational and translational DOFs: in the analytical and simulation cases, the rotational DOFs are in angular units. In the case of measured data, the rotational DOFs are in translational units (here, the acceleration measured in the tangential direction at the tip of the blades).

References

1. Tcherniak, D., Chauhan, S., Rossetti, M., Font, I., Basurko, J., Salgado, O.: Output-only modal analysis on operating wind turbines: application to simulated data. In: European Wind Energy Conference, Warsaw, Poland (2010)
2. Jhinaoui, A., Mevel, L., Morlier, J.: A new SSI algorithm for LPTV systems: application to a hinged-bladed helicopter. Mech. Syst. Signal Process. **42**(1), 152–166 (2014)
3. Allen, M.S., Sracic, M.W., Chauhan, S., Hansen, M.H.: Output-only modal analysis of linear time-periodic systems with application to wind turbine simulation data. Mech. Syst. Signal Process. **25**, 1174–1191 (2011)
4. Requesón, O.R., Tcherniak, D., Larsen, G.C.: Comparative study of OMA applied to experimental and simulated data from an operating Vestas V27 wind turbine. In: Operational Modal Analysis Conference (IOMAC), Gijón, Spain (2015)
5. Mevel, L., Gueguen, I., Tcherniak, D.: LPTV subspace analysis of wind turbine data. In: European Workshop on Structural Health Monitoring (EWSHM), Nantes, France (2014)
6. Allen, M.S.: Frequency-domain identification of linear time-periodic systems using LTI techniques. J. Comput. Nonlinear Dyn. **4**(4) (2009)
7. Yang, S., Tcherniak, D., Allen, M.S.: Modal analysis of rotating wind turbine using multi-blade coordinate transformation and harmonic power spectrum. In: Int. Modal Analysis Conference (IMAC), Orlando (2014)
8. Tcherniak, D., Yang, S., Allen, M.S.: Experimental characterization of operating bladed rotor using harmonic power spectra and stochastic subspace identification. In: International Conference on Noise and Vibration Engineering (ISMA), Leuven, Belgium (2014)
9. Tcherniak, D., Allen, M.S.: Experimental characterization of an operating Vestas V27 wind turbine using harmonic power spectra and OMA SSI. In: International Operational Modal Analysis Conference (IOMAC), Gijón, Spain (2015)
10. Ewins, D.J.: Modal Testing, Theory, Practice, and Application. Research Study Press, Baldock (2000)
11. Skjoldan, P.F.: Aeroelastic modal dynamics of wind turbines including anisotropic effects. PhD dissertation, Roskilde, Denmark (2011)
12. Hansen, M.H.: Improved modal dynamics of wind turbines to avoid stall-induced vibrations. Wind Energy **6**, 179–195 (2003)
13. Hansen, M.H.: Aeroelastic stability analysis of wind turbines using eigenvalue approach. Wind Energy **7**, 133–143 (2004)
14. Xie, W.-C.: Dynamic Stability of Structures. Cambridge University Press, New York (2006)
15. Wereley, N.M.: Analysis and control of linear periodically time varying systems. PhD dissertation, Department of Aeronautics and Astronautics, Massachusetts Institute of Technology, Cambridge (1991)
16. Tcherniak, D.: Rotor anisotropy as a blade damage indicator for wind turbine structural health monitoring systems. Mech. Syst. Signal Process. (Accepted for publication) (2015)
17. Tcherniak, D., Chauhan, S., Hansen, M.H.: Applicability limits of operational modal analysis to operational wind turbines. In: International Modal Analysis Conference (IMAC), Orlando (2010)
18. Larsen, T.J., Hansen, A.M.: How 2 HAWC2, the User's Manual. Technical University of Denmark, Lyngby (2013)
19. Tcherniak, D., Larsen, G.C.: Application of OMA to an operating wind turbine: now including vibration data from the blade. In: International Operational Modal Analysis Conference (IOMAC), Guimarães, Portugal (2013)

Chapter 15
Exploring Environmental and Operational Variations in SHM Data Using Heteroscedastic Gaussian Processes

N. Dervilis, H. Shi, K. Worden, and E.J. Cross

Abstract The higher levels of Structural Health Monitoring (SHM)—localisation, classification, severity assessment—are only accessible using supervised learning in the data-based approach. Unfortunately, one does not often have data from damaged structures; this forces a dependence on unsupervised learning i.e. novelty detection. This means that detection is sensitive to benign environmental and operational variations (EOVs) in or around the structure. In this paper a two-stage procedure is presented: identify EOVs in training data using a nonlinear manifold approach and remove EOVs by utilising the interesting tool of *heteroscedastic Gaussian processes (GPs)*. In Classical GPs models, the data noise is assumed to have constant variance throughout the input space. This assumption is a drawback most of the time, and a more robust Bayesian regression tool where GP inference is tractable is needed. In this work a combination of data projection and a non-standard heteroscedastic GP is presented as means of visualising and exploring SHM data.

Keywords Environmental and operational variations • Manifold learning • Pattern recognition • Gaussian processes

15.1 Introduction

This current study is a continuation and discussion of a recent paper [1] that investigates nonlinear manifold unfolding for structural health monitoring (SHM) in terms of the influence of environmental variations before choosing and using a reliable feature. It extends to a more robust Bayesian regression algorithm—the variational heteroscedastic GP [2] (compared to the classical GP that was used in [1]) where GP inference is tractable.

Different methods and algorithms have been used in order to investigate the influence of external but benign variations in SHM data such as: principal component analysis, auto-associative neural networks [3] or more recently cointegration [4–11] and robust regression and robust multivariate statistics as a means of characterising and distinguishing the influence of environmental and operational conditions on the structural response [12, 13].

The effect of temperature on structural response affects the dynamic response of the structure, due to its influence on the stiffness of structural parameters and on the boundary conditions of the structure [4, 14–17]. As a result, advanced feature extraction is a critical step in order to derive useful insight from the measured data that can further be post-processed via signal processing techniques.

The layout of this paper is as follows. The discussion in Section Two begins with the description of the Z24 bridge. In Section Three, the strategy that will be followed in this paper is presented. Section Four gives some background analysis regarding the nonlinear manifold learning approach. The study concludes with the presentation of some key results.

15.2 Manifold Learning for Dimensionality Reduction

Methods for feature extraction serve two purposes: a reduction in the feature dimensionality by mapping the data from high-dimensional spaces to lower-dimensional spaces and a revealing of hidden aspects of the data by learning the structure between the variables of interest. For the purposes of this paper, as the main target is the variational heteroscedastic regression, three effective methods of manifold learning: PCA [18–20], locally linear embedding [21, 22] and auto-associative neural networks (AANN) are used [18–20].

N. Dervilis (✉) • H. Shi • K. Worden • E.J. Cross
Dynamics Research Group, Department of Mechanical Engineering, University of Sheffield, Mappin Street, Sheffield, S1 3JD, UK
e-mail: n.dervilis@sheffield.ac.uk

S. Pakzad, C. Juan (eds.), *Dynamics of Civil Structures, Volume 2*, Conference Proceedings of the Society for Experimental Mechanics Series, DOI 10.1007/978-3-319-29751-4_15

Principal Component Analysis is very well established method which takes a multivariate data set and maps it onto a new set of variables called "principal components", which are linear combinations of the old variables. The first principal component will account for the highest amount of the variance in the data set and the second principal component will account for the second highest variance in the data set independent of the first, and so on. The importance of the method arises from the fact that, in terms of mean-squared-error of reconstruction, it is the optimal linear tool for compressing data of high dimension into data of lower dimension. The unknown parameters of the transformation can be computed directly from the raw data set and, once all parameters are derived, compression and decompression are small operations based on matrix algebra [18–20]. One has,

$$[X] = [K][Y] \tag{15.1}$$

Where $[Y]$ represents the original input data with size $p \times n$, with p number of variables and n the number of data sets, $[X]$ is the scores matrix of reduced dimension $q \times n$ where $q < p$ contains the transformed variables and $[K]$ is called the loading matrix. The columns of $[K]$ are the eigenvectors corresponding to the largest eigenvalues of the covariance matrix of $[Y]$. For further details readers are referred to [18–20].

A strong nonlinear method that can be applied in advanced manifold analysis is via auto-associative neural networks (AANN) [3, 19, 23, 24]. This neural network architecture was motivated by Nonlinear Principal Component Analysis (NLPCA) which is a robust and powerful statistical method for feature extraction and dimension reduction. The AANN is a type of multi-layer perceptron MLP whose target outputs are the same as the input. Generally, the auto-associative neural network consists of five layers including the input, mapping, bottleneck, demapping and output layers [23–28]. A restriction of the mentioned topology is that the bottleneck layer must have less neurons than the input and output layers and this is what allows the AANN to perform compression. As the purpose of this study is not an in-depth overview of the AANN an extensive analysis of the algorithm and its optimised architecture for outlier detection can be found in the given references.

Locally linear embedding [21, 22] is also utilised here as a continuation of [1] as an effective method of nonlinear manifold learning. An extensive overview of the algorithm can be found in [21, 22]. Briefly for the purposes of this paper the LLE method is based on simple geometric intuition. If the observations consist of N real-valued vectors $\{x_i\}$ with dimensions D and they are sampled from a smooth underlying nonlinear manifold, then each data point and its neighbours is expected to lie on or close to a locally formed patch of the manifold. The local geometries can be characterised by finding linear coefficients that can reconstruct each data point with respect to each set of neighbours.

15.3 Gaussian Processes for SHM Novelty Detection

The key purpose of this short study is to demonstrate the benefits, if any, of variational heteroscedastic GP in terms of performance when robust novelty detection is the first important step for SHM. Also, the inference between two nonlinear manifolds will be investigated as a further step from [1].

The strategy here concentrates around the regression prediction of the components of the revealed manifold in order to evaluate the influence of benign fluctuations during online monitoring as well as the performance of GPs when the trained feature does not enclose data of these large environmental variations.

Gaussian processes (GPs) are a stochastic nonparametric Bayesian approach to regression and classification problems [29]. These Gaussian processes are computationally very efficient and the nonlinear learning is relatively easy. Gaussian process regression takes into account all possible functions that fit to the training data vector and gives a predictive distribution around a single prediction for a given input vector. A mean prediction and confidence intervals on this prediction can be calculated from the predictive distribution.

The initial and basic step in order to apply Gaussian process regression is to obtain a mean and covariance function. These functions are specified separately, and consist of a specification of a functional form and a set of parameters called hyperparameters. Here, a zero-mean function and a squared-exponential covariance function are applied (see [1, 29]). When the mean and covariance functions are defined, then the inference method specifies the calculation of the exact model and in simple terms describes how to compute hyperparameters by determining the minimisation of the negative log marginal likelihood. The software used for the implementation of GP regression was provided by Rasmussen and Williams [29].

An extension of the classical GPs mentioned before is the variational heteroscedastic GPs and for the brief purposes of this paper a very short description is given as for more detailed information readers are refereed to [2]. The software used for the implementation of GP regression was provided by Titsias and Lázaro-gredilla [2].

In the usual GP regression, the model is given by:

$$y_i = f(\{x\}_i) + \varepsilon_i \tag{15.2}$$

One assumes that ε is an uncorrelated zero-mean Gaussian random variables with constant variance. Something that is called homoscedastic GP regression [2].

In many realistic applications, this global assumption of homoscedastic regression encounters limitations and a consideration of algorithms that can embrace input-dependent variance is desirable. This is refereed as heteroscedastic regression, a model that is useful from neuroscience and engineering to econometrics and meteorology. However, this Bayesian version of heteroscedastic GPs faces some difficult problems as the predictive density and marginal likelihood do not break down to analytic expressions as in classical homoscedastic GPs. In the work of [2], a novel approach is introduced via variational inference tools and is the one used in this work. This variation inference is mapped through variational Bayes and the Gaussian approximation and although the marginal log-likelihood (evidence) looses the analytical calculation it is possible to lower bound it variationally with a continuously tractable approximation.

15.4 The Z24 Bridge Example

The Z24 Bridge (see Fig. 15.1) was a concrete highway structure in Switzerland connecting Koppigen and Utzenstorf, and in the late 1990s, before its demolishment procedure, it was used for SHM purposes under the "SIMCES" project [4, 30]. During a whole year of monitoring of the bridge, a series of sensor systems captured modal parameter measurements, as well as a family of environmental measurements such as air temperature, soil temperature, humidity, wind speed etc. The critical point in this benchmark project was the introduction of different types of real progressive damage scenarios towards the end of the monitoring year.

For the purposes of this study, the four natural frequencies that were extracted over a period of year, including the period of structural failure of the bridge are used. Figures 15.2–15.3 shows the four natural frequencies with values between 0–12 Hz (vertical $y-axis$ is the natural frequencies in Hz). The beginning of the introduced failure occurs at observation 3476.

It was found that the Z24 bridge has a highly nonlinear behaviour. As can be seen, there are some visible fluctuations between observations 1200–1500 (below -5 Celsius degrees). The critical fluctuations are highly related to periods of very cold temperatures (well under zero degrees Celsius) and there is a direct connection with increased stiffness based on the freezing of the asphalt layer of the bridge deck. In turn, these large temperature fluctuations are suitable candidates to introduce nonlinear characteristics. This is the reason that advanced machine learning techniques are utilised as a means of revealing the hidden characteristics of the structural modal data.

The motivation of this paper is to reveal the nonlinear manifold between the natural frequencies and then to try to check how these temperature variations mask presence of the damage. The next section describes the strategy that was followed as well as discusses the results and gives the generated manifolds geometry.

Fig. 15.1 The Z24 bridge

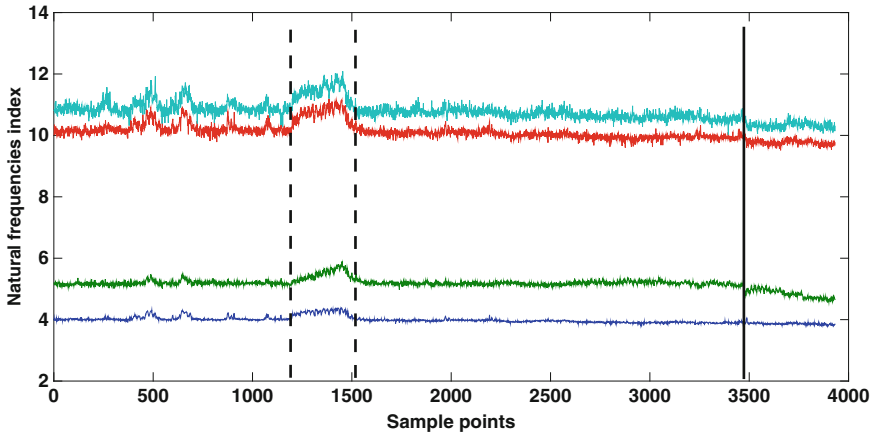

Fig. 15.2 Time history of natural frequencies of the Z24 Bridge (The *dotted lines* represent the very cold temperatures fluctuation and the *black solid line* the introduction of damage)

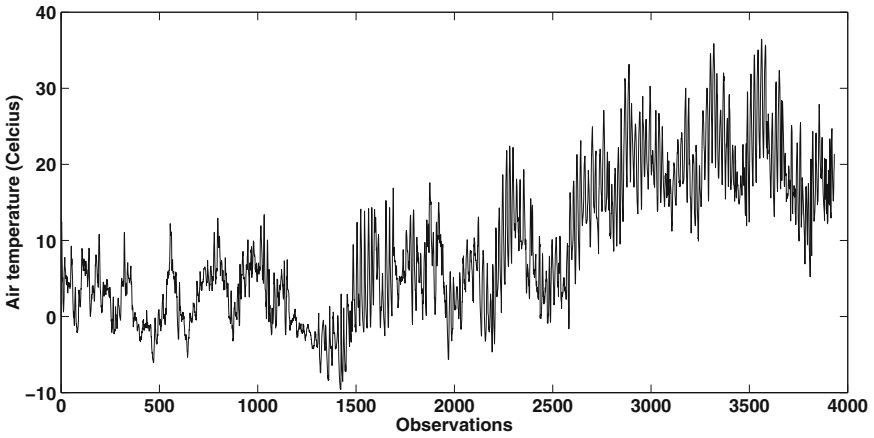

Fig. 15.3 Time history of deck temperature

15.5 Strategy and Results

First, the Z24 natural frequency data is projected into 2-D manifold space using the PCA, LLE and AANN tools and in the Table 15.1 a description of the different data sets in relation to temperature is given. The next step is to use GP regression in order to predict the 1st component based on the 2nd one or vice versa. As a training set for the GPs, only the first 500 points were used and the rest were adopted as a testing set. It has to be pointed out that the training involved the first 500 points, which means no freezing temperatures below −5 Celsius degrees (as between points 1201–1500) are utilised in the training data set. This comment is a vital point in validating that the chain of strategic steps that are followed here can offer a useful tool in the robust investigation of benign variations during a monitoring campaign.

The GP regression model confidence intervals are used as an index of abnormal response. Furthermore, as will be seen later this is a strong visualisation that indicates when faults occur or when benign fluctuations cause increase in the confidence interval uncertainty.

As can be seen from Figs. 15.4 to 15.11, the manifold that is revealed when LLE and AANN are applied is giving two distinctive directions of the data sets, one regarding the cold and very cold temperatures (green) and one regarding the damage observations (black) compared to PCA that gives a flat-linear direction of the different clusters. From Figs. 15.4 to 15.5 it is obvious that the classical GP lacks performance compared to the heteroscedastic GP as it gives very poor damage indication and classifies as outliers more data points coming from the very cold temperatures.

When the LLE manifold is revealed and used as an input for the two different GPs in Figs. 15.6, 15.7 the performance in almost identical. The GPs predict/classify correctly most of temperatures and mainly the very cold temperatures which were found as outliers in Fig. 15.4) and the damaged data exceeds the intervals when damage is present. This kind of

Table 15.1 Description of data sets as they appear in the Figs. 15.4–15.11

Observation	Condition	Colour
1–400	Undamaged	Blue
401–1200	Undamaged (with some cold temperature variations)	Pink
1201–1500	Undamaged (very cold temperature)	Green
1501–3475	Undamaged (with hot temperature variations)	Brown
3476–3932	Damaged	Black

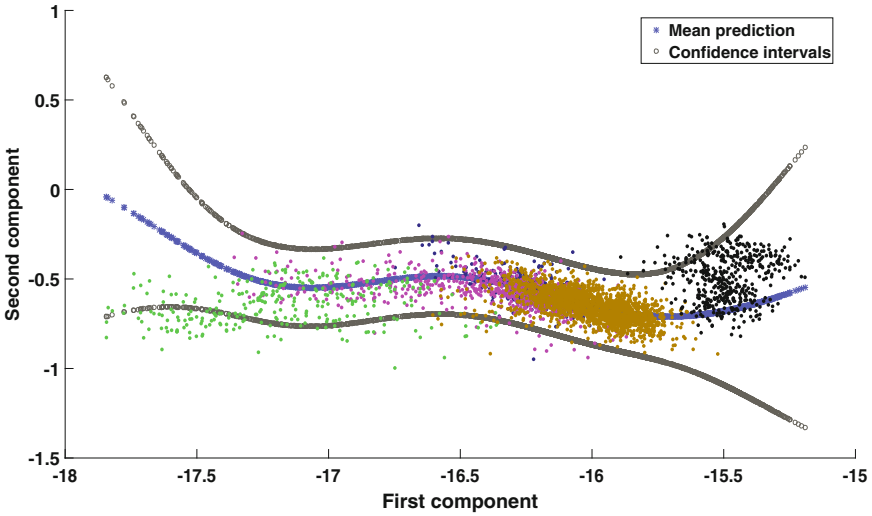

Fig. 15.4 Classical GP prediction of the 2nd component based on 1st component for the PCA manifold

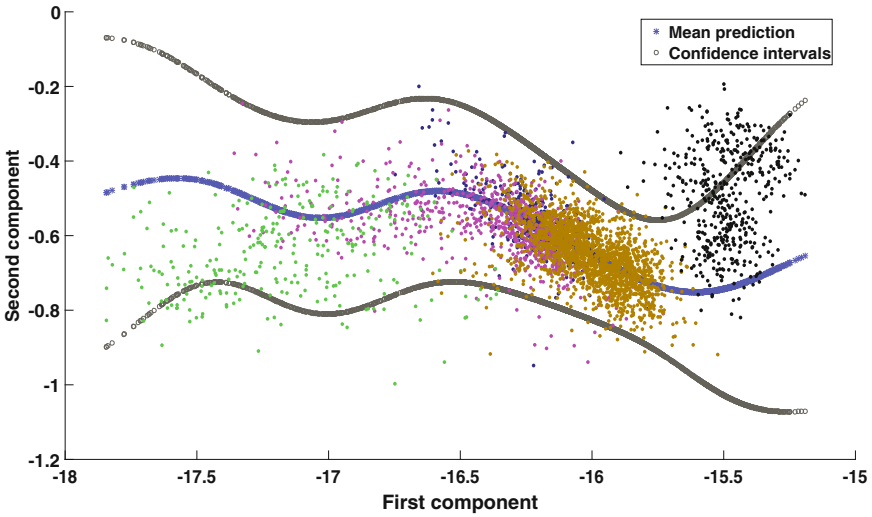

Fig. 15.5 Heteroscedastic GP prediction of the 2nd component based on 1st component for the PCA manifold

behaviour is interesting as the classical GP does perform alright because the manifold structure forces the algorithm to try and learn a multi-valued function. The same analytical manifold is unfolded when AANN in Figs. 15.8, 15.9 is utilised but in this case the performance of the classical GP is very poor compared to heteroscedastic GP as it masks damage indication and classifies the damage outliers within the confidence intervals. This is a strongly encouraging result regarding the usage of the heteroscedastic GP as it manages to a great extent, to minimise the novelty due to temperature variations by learning their nonlinear characteristics and detects novelty that is directly connected with the damaged state of the bridge. The heteroscedastic GP learns the behaviour of very cold temperatures much better and because in the AANN manifold the function is not multivalued, the heteroscedastic GP is essential.

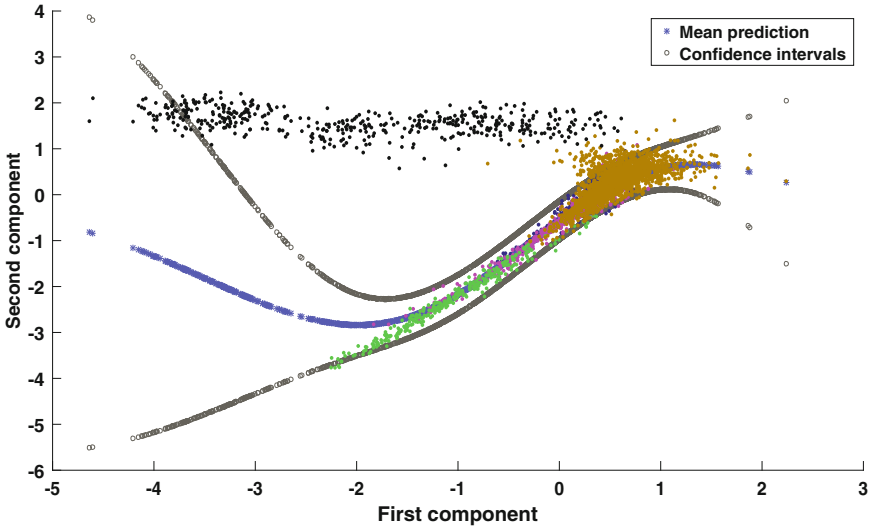

Fig. 15.6 Classical GP prediction of the 2nd component based on 1st component for the LLE manifold

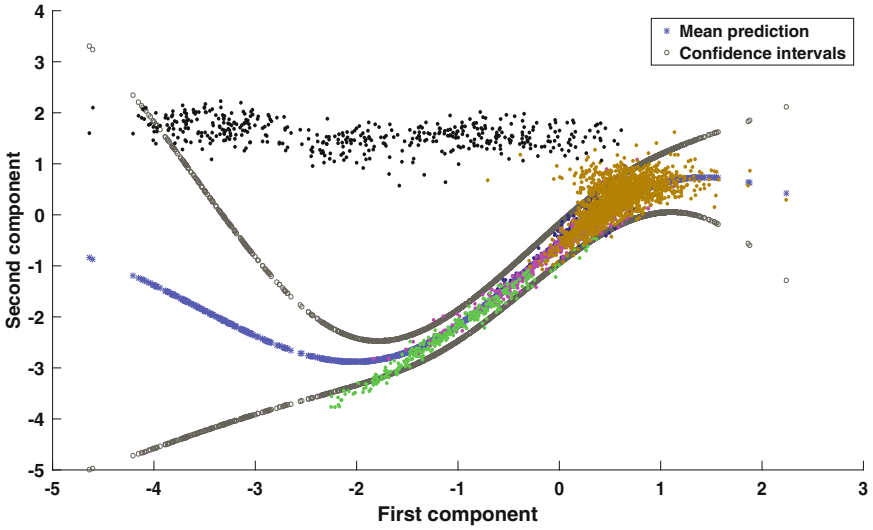

Fig. 15.7 Heteroscedastic GP prediction of the 2nd component based on 1st component for the LLE manifold

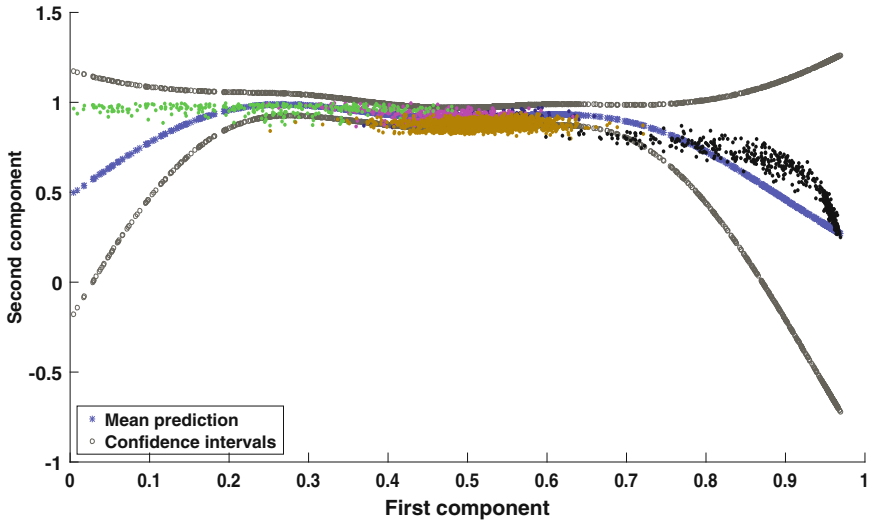

Fig. 15.8 Classical GP prediction of the 2nd component based on 1st component for the AANN manifold

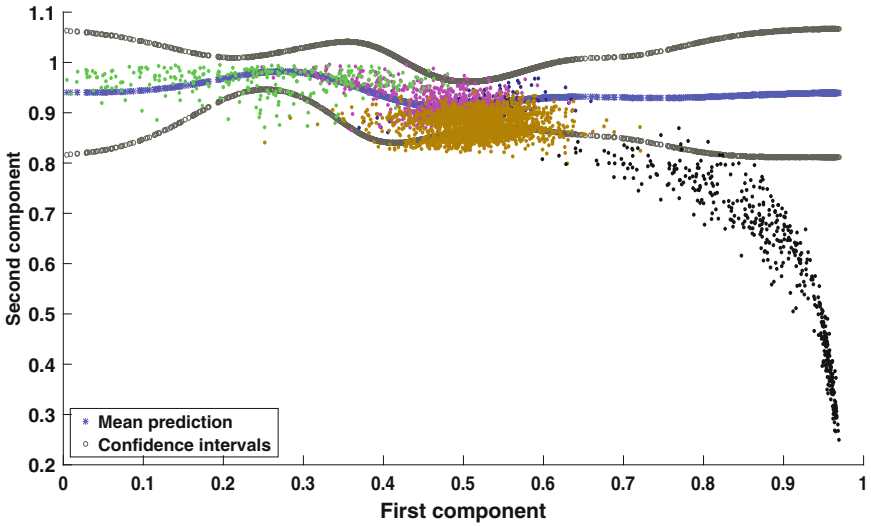

Fig. 15.9 Heteroscedastic GP prediction of the 2nd component based on 1st component for the AANN manifold

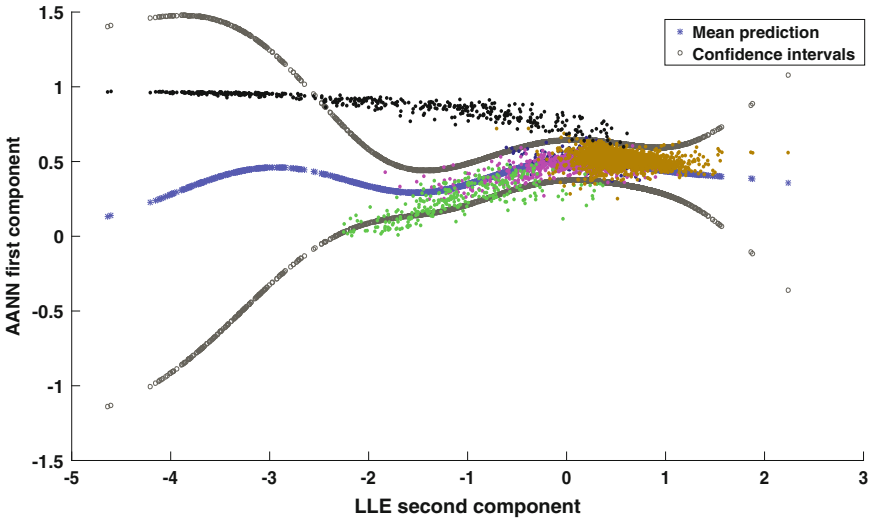

Fig. 15.10 Classical GP prediction of the 1st component for the AANN manifold component based on 2nd component of the LLE manifold

As an extra step one can "play" with several regression combinations, not only between the unfolded manifold branches of the same algorithm but also to make inferences between revealed manifolds of different methodologies as can be in seen in Fig. 15.10, 15.11 where GPs predict components based on components of different manifolds and in this case between LLE and AANN. Here, again the performance of the classical GP is very poor compared to heteroscedastic GP as it masks the fault's indication.

15.6 Conclusion

The purpose of this paper is to highlight the key utility of some specific machine learning methods, not only for novelty detection analysis but also as a method of investigating the uncertainty of the space where data clusters are lying. The main benefit of the heteroscedastic GP approach taken here is that gives more robust determination regarding the presence or absence of novelty when the normal condition set is under the suspicion that it may already include multiple abnormalities due to benign variations.

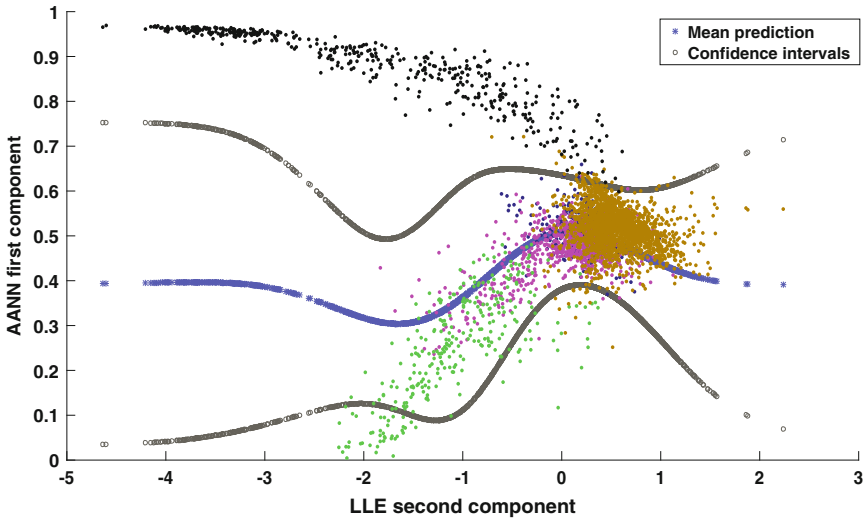

Fig. 15.11 Heteroscedastic GP prediction of the 1st component for the AANN manifold component based on 2nd component of the LLE manifold

Acknowledgements The support of the UK Engineering and Physical Sciences Research Council (EPSRC) through grant reference number EP/J016942/1 and EP/K003836/2 is gratefully acknowledged.

References

1. Dervilis, N., Antoniadou, I., Cross, E.J., Worden, K.: A non-linear manifold strategy for SHM approaches. Strain **51**(4), 324–331 (2015)
2. Titsias, M.K., Lázaro-gredilla, M.: Variational heteroscedastic gaussian process regression. In: Proceedings of the 28th International Conference on Machine Learning (ICML-11), pp. 841–848 (2011)
3. Dervilis, N., Choi, M., Taylor, S.G., Barthorpe, R.J., Park, G., Farrar, C.R., Worden, K.: On damage diagnosis for a wind turbine blade using pattern recognition. J. Sound Vib. **333**(6), 1833–1850 (2014)
4. Cross, E.J.: On structural health monitoring in changing environmental and operational conditions. Ph.D Thesis, University of Sheffield (2012)
5. Cross, E.J., Worden, K., Chen, Q.: Cointegration: a novel approach for the removal of environmental trends in structural health monitoring data. Proc. R. Soc. A Math. Phys. Eng. Sci. **467**(2133), 2712–2732 (2011)
6. Figueiredo, E., Park, G., Farrar, C.R., Worden, K., Figueiras, J.: Machine learning algorithms for damage detection under operational and environmental variability. Struct. Health Monit. **10**(6), 559–572 (2011)
7. Cross, E.J., Manson, G., Worden, K., Pierce, S.G.: Features for damage detection with insensitivity to environmental and operational variations. Proc. R. Soc. A Math. Phys. Eng. Sci. **468**(2148), 4098–4122 (2012)
8. Yi, T.-H., Li, H.-N., Sun, H.-M.: Multi-stage structural damage diagnosis method based on "energy-damage" theory. Smart Struct. Syst. **12**(3–4), 345–361 (2013)
9. Worden, K., Cross, E.J., Antoniadou, I., Kyprianou, A.: A multiresolution approach to cointegration for enhanced SHM of structures under varying conditions–an exploratory study. Mech. Syst. Signal Process. **47**(1), 243–262 (2014)
10. Zheng, W., Yu, W.: Probabilistic approach to assessing scoured bridge performance and associated uncertainties based on vibration measurements. J. Bridg. Eng. **20**(6), 04014089 (2014)
11. Reynders, E., Wursten, G., De Roeck, G.: Output-only structural health monitoring in changing environmental conditions by means of nonlinear system identification. Struct. Health Monit. **13**(1), 82–93 (2014)
12. Dervilis, N., Worden, K., Cross, E.J.: On robust regression analysis as a means of exploring environmental and operational conditions for SHM data. J. Sound Vib. **347**(0), 279–296 (2015)
13. Dervilis, N., Cross, E.J., Barthorpe, R.J., Worden, K.: Robust methods of inclusive outlier analysis for structural health monitoring. J. Sound Vib. **333**(20), 5181–5195 (2014)
14. Cross, E.J., Koo, K.Y., Brownjohn, J.M.W., Worden, K.: Long-term monitoring and data analysis of the Tamar bridge. Mech. Syst. Signal Process. **35**(1), 16–34 (2013)
15. Peeters, B., Maeck, J., De Roeck, G.: Vibration-based damage detection in civil engineering: excitation sources and temperature effects. Smart Mat. Struct. **10**(3), 518 (2001)
16. Alampalli, S.: Effects of testing, analysis, damage, and environment on modal parameters. Mech. Syst. Signal Process. **14**(1), 63–74 (2000)
17. Cornwell, P., Farrar, C.R., Doebling, S.W., Sohn, H.: Environmental variability of modal properties. Exp. Tech. **23**(6), 45–48 (1999)
18. Bishop, C.M.: Pattern Recognition and Machine Learning, vol. 4. Springer, New York (2006)
19. Bishop, C.M.: Neural Networks for Pattern Recognition. Clarendon press, Oxford (1995)
20. Nabney,. I.T.: NETLAB: Algorithms for Pattern Recognition. Springer, New York (2004)

21. Saul, L.K., Roweis, S.T.: An introduction to locally linear embedding. Available at: http://www.cs.toronto.edu/~roweis/lle/publications.html (2000)
22. Roweis, S.T., Saul, L.K.: Nonlinear dimensionality reduction by locally linear embedding. Science **290**(5500), 2323–2326 (2000)
23. Bourlard, H., Kamp, Y.: Auto-association by multilayer perceptrons and singular value decomposition. Biol. Cybern. **59**(4), 291–294 (1988)
24. Scholz, M., Vigário, R.: Nonlinear PCA: a new hierarchical approach. In: Proceedings ESANN, pp. 439–444 (2002)
25. Japkowicz, N., Hanson, S.J., Gluck, M.A.: Nonlinear auto-association is not equivalent to PCA. Neural Comput. **12**(3), 531–545 (2000)
26. Kramer, M.A.: Nonlinear principal component analysis using auto-associative neural networks. AlChE J. **37**(2), 233–243 (1991)
27. Worden, K.: Structural fault detection using a novelty measure. J. Sound Vib. **201**(1), 85–101 (1997)
28. Tarassenko, L., Nairac, A., Townsend, N., Buxton, I., Cowley, P.: Novelty detection for the identification of abnormalities. Int. J. Syst. Sci. **31**(11), 1427–1439 (2000)
29. Rasmussen, C.E., Williams, C.K.I.: Gaussian Processes for Machine Learning.MIT, Cambridge (2006)
30. De Roeck, G.: The state-of-the-art of damage detection by vibration monitoring: the SIMCES experience. J. Struct. Control **10**, 127–134 (2003)

Chapter 16
Ambient Vibration Testing of a Super Tall Building in Shanghai

Yuxin Pan, Carlos E. Ventura, Yu Feng, Xiang Li, Yavuz Kaya, Haibei Xiong, Fengliang Zhang, Jixing Cao, and Minghui Zhou

Abstract The Shanghai Tower is one of the super-tall buildings under construction in the world and will be the tallest structure in China after completion. The building stands approximately 632 m and has 128 stories. It was designed with a double curtain wall system, where a triangular outer facade gradually shrinks and twists clockwise at approximately 120° along the height of the building. On May 8th, 2015, an Ambient Vibration testing was performed on the building in its final stages of construction by a collaborative team from the University of British Columbia and Tongji University. The full-scale test had several purposes that included the evaluation of the current instrumentation techniques and the identification of the dynamic properties of the tower. A set of seven GPS-timed velocity/acceleration recorders was utilized, where two measurements were taken on almost every 15 floors in each setup. This paper presents the signal processing results by using the Frequency Domain Decomposition (FDD) and the Enhanced Frequency Domain Decomposition (EFDD) techniques. The most significant lateral and torsional mode shapes and associated periods of vibration were determined within the frequency range of 0.1–2 Hz. The results will provide useful information for further finite element model update.

Keywords Operational modal analysis • Ambient vibration test • Frequency domain decomposition • Super tall building • Dynamic response

16.1 Introduction

Over the past several decades, a new wave of design and construction of super high-rise buildings has started to meet both economic and social needs, especially in China. Since 2010, there are more than 40 high-rise buildings in China higher than 300 m either completed or under construction. To achieve different design requirements and utility functions, many innovative systems and techniques have been implemented into new building construction. Although both advanced numerical simulation analysis and large scale laboratory experiments were conducted to predict the response of those structures that are beyond the standard design, the complex structural performance and highly nonlinearity are still key issues that have not been studied systematically.

The Shanghai Tower, as one of the most super tall buildings in the world and will be the tallest structure in China after completion, has employed a number of advanced design and construction techniques, such as the double curtain wall system, sustainable energy-saving concept, mega column and core wall resisting system, etc. Considering its importance and complexity, many research teams in China have conducted comprehensive investigations on its response under different load conditions, and predicted its long-term performance. Jiang et al. studied the seismic performance of the Shanghai Tower by conducting a 1:50 scale of shake table test. The results were compared with the numerical finite element model created with ABAQUS and the corresponding dynamic properties of the tower were identified [1]. In 2011, Lu et al. simulated the potential collapse of the Shanghai Tower under strong earthquake hazards and different failure mechanisms were obtained [2]. During the construction of the Shanghai Tower, a sophisticated structural performance monitoring system was incorporated to this building in order to (1) measure the structural performance in different construction stages and (2) investigate its dynamic response under wind loads [3].

As per the invitation of Tongji University and the owner of Shanghai Tower, a joint research team from the University of British Columbia (UBC) and Tongji University carried out an Ambient Vibration (AV) testing of the Shanghai Tower on

Y. Pan (✉) • C.E. Ventura • Y. Feng • X. Li • Y. Kaya
Department of Civil Engineering, The University of British Columbia, 6250 Applied Science Lane, Vancouver, BC, CanadaV6T 1Z4
e-mail: ypan@civil.ubc.ca

H. Xiong • F. Zhang • J. Cao • M. Zhou
State Key Laboratory of Disaster Reduction in Civil Engineering, Tongji University, Shanghai 200092, China

S. Pakzad, C. Juan (eds.), *Dynamics of Civil Structures, Volume 2*, Conference Proceedings of the Society for Experimental Mechanics Series, DOI 10.1007/978-3-319-29751-4_16

May 2015. The collaborative research aims to study the dynamic characteristics of this unique structure at its final stage of construction by performing operational modal analysis. This paper presents the detailed experiment procedures and the subsequent data processing of the ambient vibration test. The acquired results will be used for validating and updating the current numerical models of the Shanghai Tower, and also help to evaluate its response under other loading conditions.

16.2 Description of the Shanghai Tower

The Shanghai Tower is a mega tall skyscraper located in Lujiazui District, Shanghai. Designed by Gensler and owned by a consortium of Chinese state-owned companies, it is the tallest of a group of three adjacent supertall buildings in Pudong: the Jin Mao Tower and the Shanghai World Financial Center, as seen in Fig. 16.1a [4]. The building stands approximately 632 m high and has 128 stories, with a total floor area of 380,000 m^2. The depth of embedment is 31.2 m. The piled raft foundation is in the shape of an octagon. A triangular outer facade encloses the entire structure, which gradually shrinks and twists clockwise at approximately 120° along the height of the building. According to the requirement of building function, the building is divided into nine zones along its height separated by eight independent strengthening floors. Every zone has specific usage function of office, hotel, shopping mall or entertainment, as seen in Fig. 16.1b [3].

For this super tall building, the structural lateral load resisting system utilize a "Core-Outriggers-Mega Frame" system including a central reinforced concrete shear wall core interconnected with the composite mega frame with six two-story high outrigger trusses, super columns and exterior mega frame using double belt trusses, as shown in Fig. 16.2 [3, 5]. This Gravity loads are resisted by steel-concrete composite floor system.

16.3 Description of the Ambient Vibration Testing

Ambient Vibration testing is a non-destructive test aiming to record dynamic response of structure when no severe excitation is applied. Data collected from AV testing could be processed to obtain modal information of tested structure, which is crucial in many research areas including seismic rehabilitation of existing structures and finite element model updating, etc.

Structural vibration sensor called TROMINO is used to carry out the AV testing of Shanghai Tower. TROMINO sensor is widely used by Earthquake Engineering Research Facility (EERF) in UBC to study dynamic characteristics of existing structures. This sensor is a combination of two sets of three orthogonal high-resolution electrodynamic sensors: high gain and low gain velocimeters, and one set of three orthogonal digital accelerometers with frequency range from 0.1 to 300 Hz [6]. Either GPS or Radio could be used to ensure synchronization between sensors. For this test, however, GPS and Radio were not applicable since the signal was blocked within the building floors. Therefore, data synchronization was performed

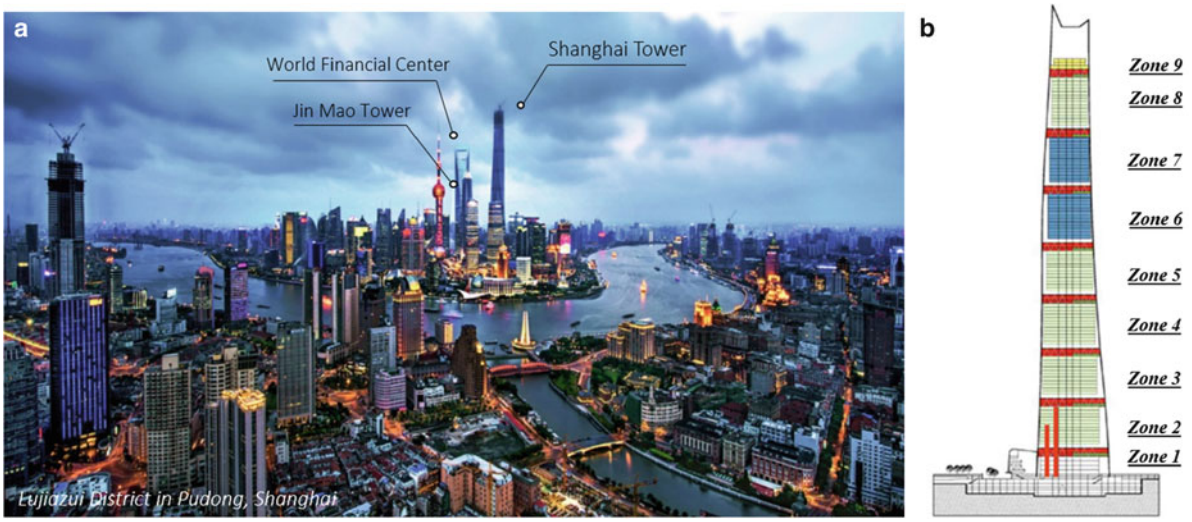

Fig. 16.1 (**a**) Location of the Shanghai Tower (**b**) strengthening floors

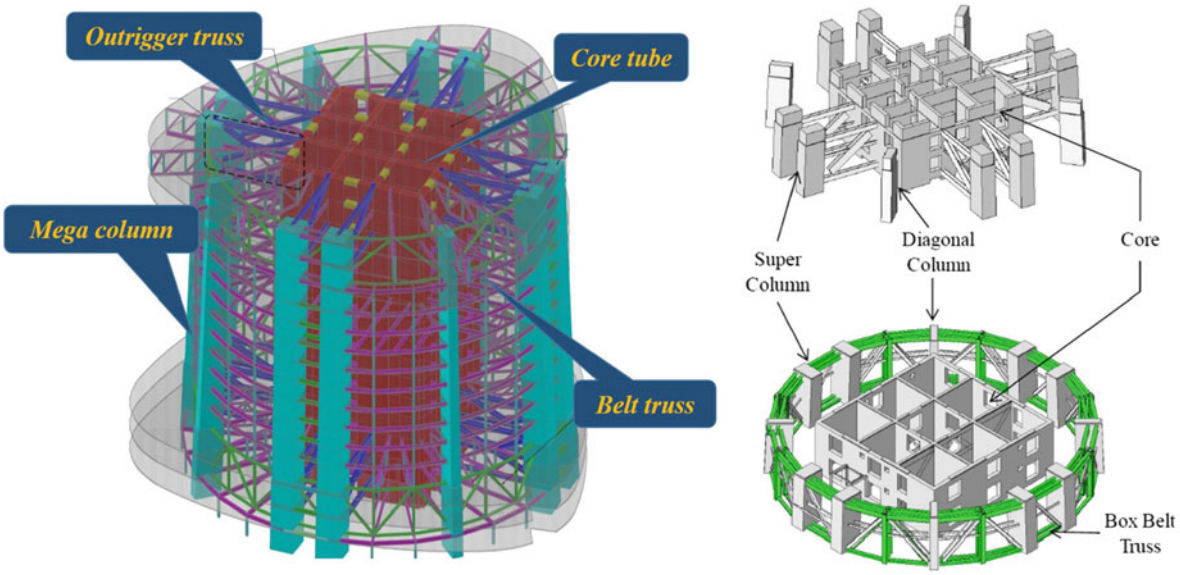

Fig. 16.2 Lateral resisting system of Shanghai Tower

Table 16.1 Start and end time of each setup

	Pre-setup		Main test			
Setup no.	X	Y	A	B	C	D
Start time	8:00	8:40	11:00	12:30	14:00	15:30
End time	8:30	9:00	11:50	13:20	14:50	16:20
Length (minute)	30	20	50	50	50	50

manually afterwards based on internal clocks of the sensors that have been adjusted by two pre-setups. Raw data collected by TROMINO cannot be read directly by modal analysis program. Also, the recorded data need to be synchronized before further data analysis. Grilla software was used to convert the raw data to readable format and synchronize the data when GPS signal is available [6]. For this test, data synchronization was manually performed via MATLAB program and further refined via GEOPSY Software [7].

AV testing took place on Friday, May 8th, 2015 between 8:30 and 16:30 by a joint research team from UBC and Tongji University. The whole test includes two pre-setups (Setup X and Y) and four test setups (Setup A to D). It should be noted that due to the on-going construction of the Shanghai Tower, there was no cellphone signal or interphones available within the structure, and the elevator was controlled by operator manually. Therefore, a specific start time has been set in advance for each main setup. Considering the difficulty of movement and communication among floors, the time gap between each setup was given nearly 40 min for each main setup. In this way, all the testing personnel could coordinate with each other and no significant time delay for each setup could be guaranteed. Table 16.1 lists the start and end time of each setup, notice that all time mentioned in this report is local China Standard Time (CST). All the tests were conducted with a sampling frequency of 512Hz.

As mentioned, to adjust the internal clock of all seven TROMINO devices, two pre-setups with 30-min and 20-min acquisition lengths were conducted by using recording Program 5 (Setup X) and Program 1 (Setup Y), respectively. For more detailed information, please refer to the companion paper "Ambient Vibration Testing of Two Highly Irregular Tall Buildings in Shanghai". Figure 16.3 presented the photo of pre-setup description.

In total, there were seven floors were tested on the testing day within four main setups, as shown in Fig. 16.4. Since the lateral-force-resisting system of Shanghai tower consists of core-tube, outrigger and mega column, all the strengthening stories (where core-tube, outrigger and mega column can be clearly viewed) were tested in order to capture the dynamic behavior of all the three structural systems. Theoretically, instruments should be placed at the very top of the structure to precisely identify the very fundamental mode. However, since the peak floor of the Shanghai Tower (124F) is still in construction and no elevator could access, alternative option was made to 121F. Also, it is of interests to study the dynamic rocking mode of this super tall structure where a 32.8 m of embedment depth was constructed with piles, Setup D was carried out to record the vibration from ground floor and lower ground 5th floor.

Fig. 16.3 Instrument layout for pre-setup

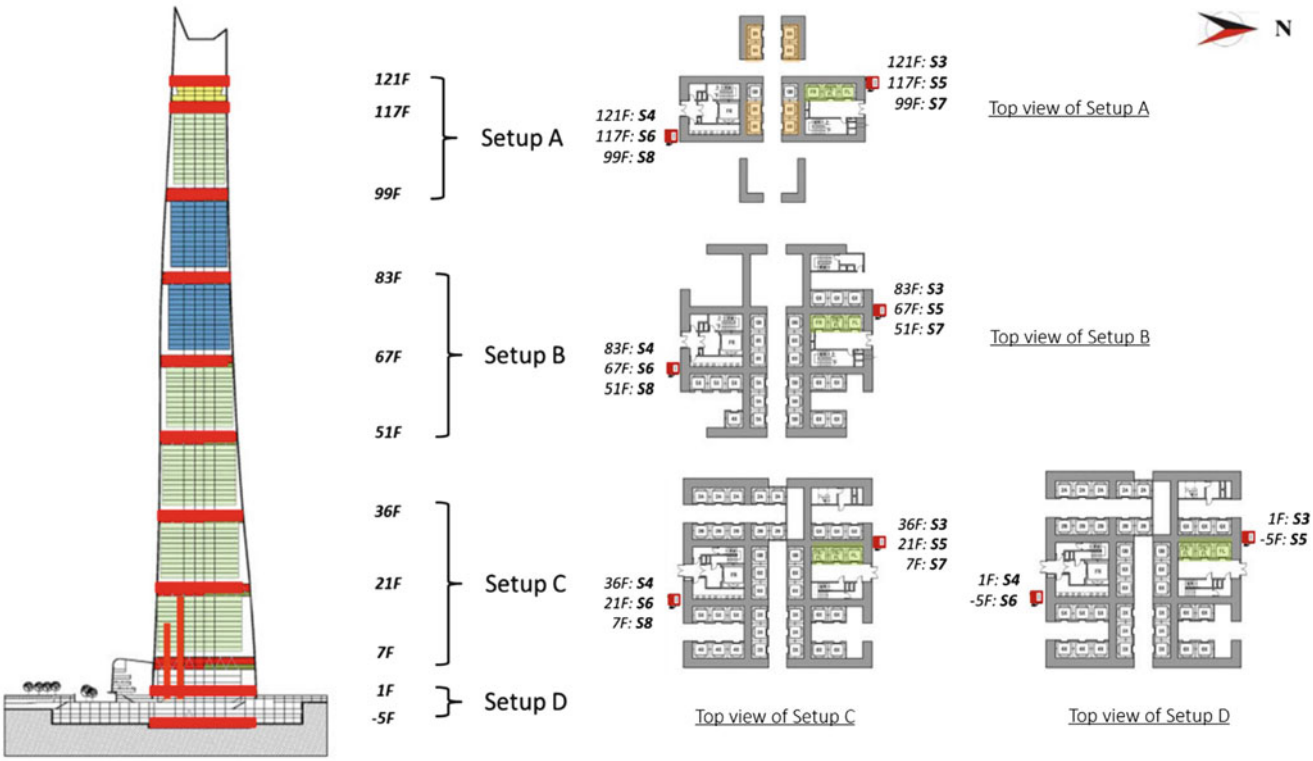

Fig. 16.4 Testing floors and locations of sensors of AV testing

Tested floors are highlighted in red and the sensors were placed around the core-tube on each tested floor. As mentioned in previous section, geometry of the core-tube changes over the height of the building. There are three different types of core-tube geometry within this building. Tested floors in Setup A, B and C have different core-tube geometries from each other. Floors in Setup D have the same core-tube geometry with those in Setup C. However, the sensors were placed at around the same locations on each floor for the convenience of future analysis. It should be noted that due to the complex interior of the structure and construction mechanical conditions, in some certain floors, it was very difficult to identify the shear wall systems. Therefore, in order to get better results, all the sensors were placed around the concrete mega braces that were used to support the shear wall, as seen in Fig. 16.5. There were two braces in each direction of the core-tube system, and the two sensors in each floor were put on North (left) and South (right).

Fig. 16.5 Detailed TROMINO location near the brace

16.4 Natural Frequencies and Mode Shapes

Operational modal analysis was performed using the software ARTeMIS Modal V3.6 [8]. The software is capable to perform high quality modal analysis through various analysis techniques, including the Frequency Domain Decomposition (FDD) technique and several Stochastic Subspace Identification (SSI) approaches. For this project, a simplified spatial representation of the Shanghai Tower shear wall system was established and two methods of modal identification were adopted for analysis: the Frequency Domain Decomposition (FDD) technique and the Enhanced Frequency Domain Decomposition (EFDD) technique.

By incorporating the tested and processed data in the ARTeMIS from the 38 accelerometers, both the lateral and torsional modes were estimated FDD. This method provides an efficient and quick manner for user to obtain the dynamic properties of the structure by peak-picking rules. The power spectral densities (PSD) of the above measurements were averaged to give the Averaged Normalized Power Spectral Density. This technique is based on decomposing the PSD function matrix using Singular Value Decomposition (SVD) where the spectral matrix is decomposed into a set of Single Degree of Freedom (SDOF) system with one corresponding individual mode. As an extension of FDD, EFDD allows users to identify the damping properties of the corresponding modes, which are of significant important to the performance of super tall building. More information could be found in Brincker, et al. [9].

Figure 16.6 presents the picked peak values of the natural frequencies estimations. It should be noted that not all of the peaks in Fig. 16.6 necessarily corresponded to a natural frequency. The mode shapes were generally well consistent in the North–South (N–S) and East–West (E–W) lateral directions. The first three lateral frequencies in each direction were quite close since the Shanghai Tower is a relatively uniform structure. No significant irregular layouts were constructed for structural component except the architectural outer facade with rotational shape.

In total, ten modes have been recognized in the frequency range of 0.1–1 Hz (Period = 1–10 s), including six lateral mode shapes and four torsional mode shapes. The testing results were highly compatible with the finite element (FE) simulation results in other technical publications [2, 10]. As expected, the very fundamental period of the Shanghai Tower is as long as 9.43 s with the corresponding damping ratio of 1.734 %, as seen in Table 16.2. There are also some higher modes have been identified in this study. However, due to the complex geometry and long period characteristics, only the first ten modes were presented and discussed in this paper. In the following section, each mode is shown in a 3-D surface view of the entire structure. For better comparison and understanding, the mode shapes are shown in the order of frequency listed below.

16.5 Discussions

In total, ten modes have been well determined in Fig. 16.7. It should be noticed that some localized coupled torsional modes could also be observed in 2nd and 5th mode shapes. The resolution of higher modes are not as good as lower modes due to the imperfect GPS synchronization where the internal clock of the instruments shifted unexpectedly during the test. As stated previously in the spectral density plot, the first three translational mode shapes in both North–South (1st, 4th and 7th mode shapes) and East–West (2nd, 5th and 8th mode shapes) directions are highly identical due to the uniform structural layout of the Shanghai Tower.

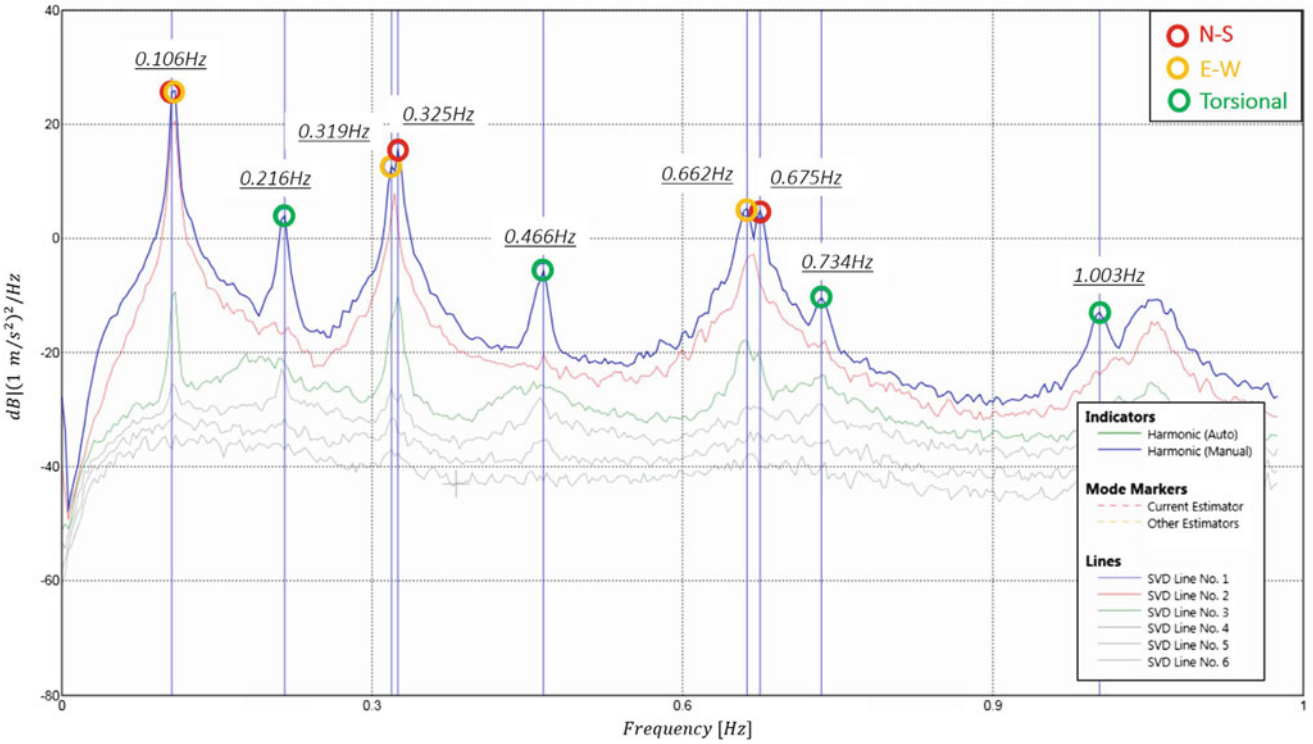

Fig. 16.6 Peak-picking of singular values of spectral densities

Table 16.2 Summary of natural frequencies, damping and mode shapes

	FDD	EFDD		FE model [2]		
Modes	Periods [s]	Periods [s]	Damping (%)	Periods [s]	Difference (%)	Mode shapes
1	9.43	9.26	1.734	9.83	4.24	Fundamental 1st lateral mode (1NS)
2	9.43	9.26	1.688	9.77	3.61	Fundamental 1st lateral mode (1EW)
3	4.63	4.67	0.855	4.09	−11.66	1st torsional mode (1 T)
4	3.13	3.76	0.984	3.57	14.06	2nd lateral mode in East–West (2EW)
5	3.08	3.69	0.912	3.52	14.29	2nd lateral mode in North–South (2NS)
6	2.15	2.15	0.730	1.97	−8.37	2nd torsional mode (2 T)
7	1.51	1.51	0.761	1.67	10.60	3rd lateral mode in East–West (3EW)
8	1.48	1.48	0.679	1.66	12.16	3rd lateral mode in North–South (3NS)
9	1.36	1.37	0.524	1.22	−10.29	3rd torsional mode (3 T)
10	0.98	1.00	0.484	–	–	4th torsional mode (4 T)

The fundamental mode in two directions are lateral-dominated mode shapes with the same natural period of 9.43 s, which are both far greater than the 6 s limit of the design spectra in the Chinese Code for the Seismic Design of Buildings [11]. A smaller fundamental period of 9.26 s is obtained by EFDD technique. The first and second purely torsional mode shapes are determined with the periods of 4.63 s and 2.15 s. Coupled lateral mode shapes are observed in higher torsional modes.

The modal analysis results of the FE model by Lu et al. are compared with the AV testing results, as shown in Table 16.2 [2]. It can be seen that the first and second modes are quite close to the numerical results while a significant different can be found in higher modes. It should also be noticed that numerical model overestimates the natural periods of all the six lateral modes, indicating the actual structure is stiffer than the computational model. However, all the torsional modes have been underestimated in FE analysis. The difference may have various reasons, one explanation is that the numerical model was created in the initial stage of the construction (year of 2011) and all the adopted materials and parameters were based on the design procedure. The AV testing, however, was conducted in year of 2015, the dynamic characteristics may be slightly affected by the actual construction process and material properties.

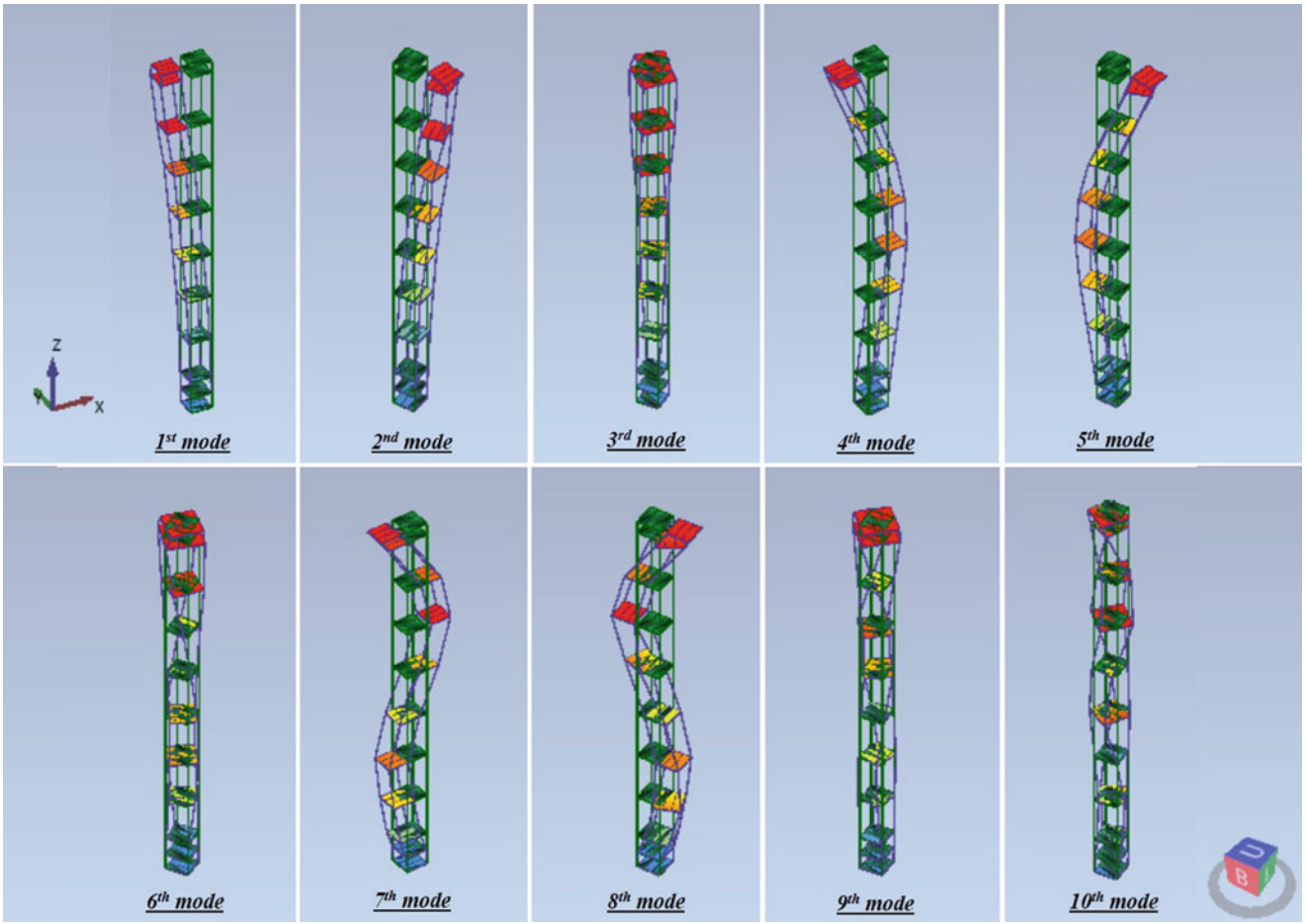

Fig. 16.7 Mode shapes of the identified first ten modes

16.6 Conclusions

The Ambient Vibration testing of the Shanghai Tower was conducted on May 2015, in Lujiazui District, Shanghai, China, by a joint research team from UBC EERF and Tongji University. The testing aimed to investigate the dynamic characteristics of the selected building, and promoted the research collaboration between two academic institutes in the field of earthquake resistance and education.

The processed acquisition data was sufficient to identify 10 modes below 1 Hz. Both The fundamental frequency in North–South (N–S) and East–West (E–W) transverse directions were determined as 0.106 Hz and the corresponding fundamental periods were 9.43 s with the damping ratio of 1.734 %. The fundamental torsional mode was also captured at 0.216 Hz with its period of 4.63 s and 0.855 % damping ratio. Due to the symmetrical layout of the structural system, the first three translational modes in two transverse directions are highly identical to each other, but there was some coupled torsional modes have been identified in the E–W direction. The testing results were also compared with the simulated finite element analysis, and a good agreement has been obtained. Although, due to low levels of the AV testing, the acquired dynamic properties correspond with the elastic response of the Shanghai Tower, the information obtained from the field tests will provide useful and reliable reference for computational model updating of Shanghai Tower under other extreme loading conditions. In turn, it will be used to gain insight into the dynamic performance of the structure. Further, this information will help the tower owner to evaluate its response after construction and during service conditions.

Since this is an on-going collaborative research project, only the FDD and EFDD operational modal analysis techniques were adopted to provide quick and reliable estimation of the natural frequencies and the damping properties of the structure. Other time-domain analysis tools such as the Stochastic Subspace Identification (SSI), will be incorporated later to validate the current results.

Acknowledgements The authors wish to thank the State Key Laboratory of Disaster Reduction in Civil Engineering from Tong University for their interest and support in this study. The assistance and permission to access to the building of the owner of Shanghai Tower is greatly appreciated. The authors would like to acknowledge all the graduate students from Tongji University for assisting the test (in alphabetical order): Hao Fu, Gan Luo, Weiwen Lai, Lu Ouyang, Chengyou Wang, Kangli Wang, Hongsheng Xu, Guiquang Yang and Zhi Yu, their cooperation and enthusiasm is acknowledged with thanks. The technical supports from Mr. Felix Yao at UBC EERF are also well appreciated. The authors would like to acknowledge Ms. Sharlie Huffman of the BC Ministry of Transportation for use of the sensors. A special thank is given to Dr. Palle Andersen of SVS for providing license of ARTeMIS Modal 3.6 for analysis.

References

1. Jiang, H., He, L., Lu, X., Ding, J., Zhao, X.: Analysis of seismic performance and shaking table tests of the Shanghai Tower. Jianzhu Jiegou Xuebao (Journal of Building Structures) **32**(11), 55–63 (2011)
2. Lu, X., Lu, X., Zhang, W., Ye, L.: Collapse simulation of a super high-rise building subjected to extremely strong earthquakes. Sci. China Technol. Sci. **54**(10), 2549–2560 (2011)
3. Su, J.Z., Xia, Y., Chen, L., Zhao, X., Zhang, Q.L., Xu, Y.L., Ding, J.M., Xiong, H.B., Ma, R.J., Lv, X.L., Chen, A.R.: Long-term structural performance monitoring system for the Shanghai tower. J Civil Struct. Health Monit. **3**(1), 49–61 (2013)
4. Li, D.: Reform far form enough for burgeoning economies, News in Brief, CCWE News. Tsinghua University Beijing, China. http://www.ccwe.tsinghua.edu.cn/column/NIB (2015)
5. Poon, D.C., Hsiao, L.E., Zhu, Y., Joseph, L., Zuo, S., Fu, G., Ihtiyar, O.: Non-linear time history analysis for the performance based design of Shanghai Tower. In: ASCE Conference Proceedings, Las Vegas, vol. (401)47 (2011)
6. Micromed, Tromino User's manual, Micromed, 139 pp, 2012.
7. Wathelet, M.: GEOPSY Geophysical Signal Database for Noise Array Processing, Version 2.9.0 2002–2011. Software, LGIT, Grenoble (2005)
8. Structural Vibration Solutions A/S. Artemis Extractor Pro 1999–2015. Version 3.6, NOVI Science Park, Structural Vibration Solutions A/S, Denmark (2015)
9. Brincker, R., Zhang, L., Andersen, P.: Modal identification from ambient responses using frequency domain decomposition. In: Proceedings of the 18th International Modal Analysis Conference (IMAC), San Antonio (2000)
10. Lu, X., Lu, X., Sezen, H., Ye, L.: Development of a simplified model and seismic energy dissipation in a super-tall building. Eng. Struct. **67**, 109–122 (2014)
11. GB50011-2010. Code for Seismic Design of Buildings. Ministry of Construction of the People's Republic of China, Beijing (2010)

Chapter 17
Inelastic Base Shear Reconstruction from Sparse Acceleration Measurements of Buildings

Boya Yin and Henri Gavin

Abstract This paper presents a novel method for recovering base shear forces of building structures with unknown nonlinearities from sparse seismic-response measurements of floor accelerations. The method requires only direct matrix calculations (factorizations and multiplications); no iterative trial-and-error methods are required. The method requires a mass matrix, or at least an estimate of the floor masses. A stiffness matrix may be used, but is not necessary. Essentially, the method operates on a matrix of incomplete measurements of floor accelerations. In the special case of complete floor measurements of systems with linear dynamics and real modes, the principal components of this matrix are the modal responses. In the more general case of partial measurements and nonlinear dynamics, the method extracts a number of linearly-dependent components from Hankel matrices of measured horizontal response accelerations, assembles these components row-wise and extracts principal components from the singular value decomposition of this large matrix of linearly-dependent components. These principal components are then interpolated between floors in a way that minimizes the curvature energy of the interpolation. This interpolation step can make use of a reduced-order stiffness matrix, a backward difference matrix or a central difference matrix. The measured and interpolated floor acceleration components at all floors are then assembled and multiplied by a mass matrix. A sum (or weighted sum) of the resulting vector of inertial forces gives the base shear. The proposed algorithm is suitable for linear and nonlinear hysteretic structural systems.

Keywords Base shear recovery • Nonlinear hysteretic behavior • Seismic isolation • Sparse acceleration measurement • Singular spectrum analysis

17.1 Introduction

Seismic isolation systems have complex nonlinear and hysteretic behavior arising from a number of mechanisms, including plasticity, hyper visco-elasticity, geometric nonlinearities, friction, dynamic contact, and, potentially impact. The identification of a structural model necessarily requires a presumed model form (e.g., linear state-space, bilinear hysteretic, etc.) which may (or may not) represent the behavior of the in-service system. If linear behavior is presumed, analyses may be restricted to low-amplitude behavior [32, 33]. Further, modal analysis methods that rely on high fidelity frequency response function measurements are not well suited to the analysis of measurements from highly transient excitation, such as earthquake ground accelerations [38]. Measurements of the responses of base-isolated structures to earthquake ground motions have been used to investigate their behavior and performance [22]. Quite a few output-only algorithms have been developed, however, they are specialized for linear system. Staszewski [30], Ding et al. [8], and Yang and Nagarajaiah [37].

Celebi [5] and Nagarajaiah, and Xiaohong [26] used the response records of the base-isolated USC hospital from 1994 Northridge Earthquake and linear identified models to conclude that the isolation system provided effective protection [1]. Stewart et al. [31] identified four base-isolated buildings as equivalent, time varying, linear systems and showed the amplitude-dependence of the fundamental mode frequency and damping factors [31]. Chaudhary et al. [6, 7] proposed a two-step system identification approach to identify system parameters from modal parameters using equivalent linear models and to capture the overall behavior [6, 7]. Under the assumption of linear behavior, state-space system identification algorithms such as eigensystem realization algorithm (ERA) [17], subspace system identification (SSID) [28], observer Kalman filter identification (OKID) [18], and complexity pursuit [15] have been used to identify modal parameters. Unfortunately, the true nonlinear behavior can not be assessed by these methods.

B. Yin • H. Gavin (✉)
Department of Civil and Environmental Engineering, Duke University, Durham, NC 27713, USA
e-mail: henri.gavin@duke.edu

S. Pakzad, C. Juan (eds.), *Dynamics of Civil Structures, Volume 2*, Conference Proceedings of the Society for Experimental Mechanics Series, DOI 10.1007/978-3-319-29751-4_17

Energy dissipation mechanisms in many seismic isolation systems involve nonlinear mechanisms (plastic deformation and/or friction) and these nonlinearities play a significant role in the behavior of the isolated structure. In such systems, equivalent linear models may not be able to capture the hysteretic behavior of isolation system in detail [3]. To address this issue a large number of system identification techniques have been developed for nonlinear base-isolated systems. These techniques presume a parameterized model of the nonlinear elements [10, 27] and involve an iterative method such as prediction error minimization (PEM) [13, 21, 35] to converge upon a good model or use time-varying linear models to identify time-varying dynamics from seismic response data of a real structure[29]. Signal processing methods such as the empirical mode decomposition (EMD) [14]; wavelet transform [19, 20], and the Hilbert Huang transform (HHT) [36] have been applied to the analysis of response analyses of base isolated structures. But none of these methods can directly recover the nonlinearities in the isolation system.

In recent years, singular spectrum analysis (SSA), has emerged as a powerful technique for time series analysis and has been developed and applied as a time series analysis and signal processing method [23]. The basic SSA method decomposes a time series into a sum of several interpretable components, such as oscillatory component dominated by a certain frequency, slowly varying trend, and noise [24]. Generally, the SSA method consists of two stages, decomposition and reconstruction. At the first stage, the time series is decomposed and at the second stage, the noise free series is reconstructed by using the individual reconstructed series [12]. SSA methods have not yet been investigated as a means to reconstruct nonlinear behavior from time series measurements.

In this study, an innovative output-only time-domain method for reconstructing base-shear forces is proposed. The method uses floor acceleration measurements at two or more floors, and floor mass information. The method does not involve any mechanistic model of the isolation system, though a stiffness matrix of the super-structure may be used in interpolating floor accelerations. The method is based on direct matrix operations (factorizations and multiplication) and is built from concepts used in singular spectrum analysis (SSA) [4].

17.2 Output-Only Base Shear Recovery

17.2.1 Nonlinear Seismic Isolation System

For a MDOF system with nonlinear hysteretic behavior at isolation level, the equation of motion under earthquake excitation is given by:

$$\mathbf{M}\ddot{\mathbf{x}}(t) + \mathbf{C}\dot{\mathbf{x}}(t) + \mathbf{K}\mathbf{x}(t) + \mathbf{b}f(t) = -\mathbf{M}\mathbf{h}\ddot{u}_g(t) \tag{17.1}$$

where $\ddot{\mathbf{x}}(t), \dot{\mathbf{x}}(t), \mathbf{x}(t)$ are the acceleration, velocity and displacement vectors respectively. $\mathbf{M}, \mathbf{C}, \mathbf{K}$ are the symmetric mass, diagonalizable damping and stiffness matrices. $\mathbf{b} = [1, 0, 0, 0 \ldots]^T$. $\ddot{u}_g(t)$ is the acceleration of base excitation, $\mathbf{h}$ is the matrix describing transfer coefficient between base excitation and input motion into the system, and $f(t)$ is the isolation level internal restoring force.

In the numerical examples shown in the following sections, the nonlinear hysteretic behavior of the system is modeled by a Bouc-Wen model that satisfies the Second Law of Thermodynamics [2, 9, 16]. The restoring force $f(t)$ can be expressed as:

$$f(t) = f_y((1-\kappa)z(t) + \kappa u(t)) \tag{17.2}$$

where f_y is a yield force level, $u(t) = \mathbf{x}(t)/d_y$ is the response displacement normalized by the yield displacement d_y and κ is the ratio of the post yield stiffness to the pre-yield stiffness. $z(t)$ denotes the hysteretic displacement that obeys the following nonlinear differential equation:

$$\dot{z} = (1 - |z|^{\eta}((1-\beta)sgn(\dot{u}z) + \beta))\dot{u} \tag{17.3}$$

in which the exponent η is restricted to be odd.

17.2.2 Base Shear Recovery from Total Accelerations

The objective of the paper is to show a method for recovering $f(t)$ from sparse acceleration measurements, even if $f(t)$is nonlinear in the deformation and velocity across the isolation system. It is straightforward to show that $f(t)$ within the isolation level can be expressed using the total acceleration vector and the mass matrix. Expressing the nonlinear force at the isolation level as f_1, and the interstitial forces between any two adjacent masses as $f_i, i = 2, \ldots, n$, the governing equation can be expressed as the following,

$$\mathbf{M}(\ddot{\mathbf{x}}(t) + \mathbf{h}\ddot{u}_g(t)) + \begin{bmatrix} 1 & -1 & 0 & \cdots & 0 \\ 0 & 1 & -1 & \cdots & 0 \\ \vdots & \vdots & \vdots & \vdots & \vdots \\ 0 & 0 & 0 & \cdots & 1 \end{bmatrix} \begin{bmatrix} f_1 \\ f_2 \\ \vdots \\ f_n \end{bmatrix} = \begin{bmatrix} 0 \\ 0 \\ \vdots \\ 0 \end{bmatrix} \tag{17.4}$$

The summation of all the rows in the above equation gives

$$f_1 = -\sum_{i,j=1}^{n} \mathbf{M}_{ij}(\ddot{\mathbf{x}}_j(t) + \mathbf{h}\ddot{u}_g(t)) \tag{17.5}$$

Therefore, the base shear (nonlinear force at isolation level) is expressed as equation (17.5) which will be easily calculated if floor accelerations are measured at each floor. The problem is that the floor accelerations are typically not measured at each floor. One of the potential solutions is to use a weighted average of the measured floor accelerations. As is shown in Fig. 17.1, the blue line presents the base shear calculated directly using the weighted average of measured floor accelerations. The direct weighed sum doesn't properly capture the higher mode effects. No matter how floor accelerations are interpolated between measured floor accelerations, the summation of total accelerations of each floor is a linear combination of measured floor accelerations. To account for the higher frequency behavior, however, note that the nonlinear systems do not have eigen modes, so we resort to using the principal components of the response.

For linear systems with complete measurements, the principal components are the modes. Rewriting the equation of motion in modal coordinates $\ddot{\mathbf{x}}(t) = \bar{\mathbf{R}}\ddot{\mathbf{q}}(t)$, where $\bar{\mathbf{R}}^T\mathbf{M}\bar{\mathbf{R}} = \mathbf{I}$.

$$\mathbf{M}\bar{\mathbf{R}}\ddot{\mathbf{q}}(t) + \mathbf{C}\bar{\mathbf{R}}\dot{\mathbf{q}}(t) + \mathbf{K}\bar{\mathbf{R}}\mathbf{q}(t) = -\mathbf{M}\mathbf{h}\ddot{u}_g(t) \tag{17.6}$$

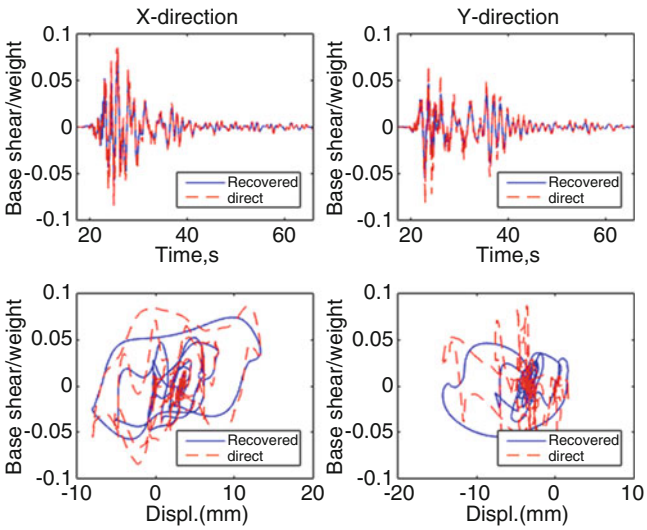

Fig. 17.1 Recovered vs direct weighed sum normalized base shear time histories and hysteresis loop in two dimensions using measurement record set

Including the amount of input excitation $\ddot{u}_g(t)$ in each modal total acceleration,

$$\bar{\mathbf{R}}(\ddot{\mathbf{q}}(t) + \bar{\mathbf{R}}^{-1}\mathbf{h}\ddot{u}_g(t)) = -\mathbf{M}^{-1}(\mathbf{C}\bar{\mathbf{R}}\dot{\mathbf{q}}(t) + \mathbf{K}\bar{\mathbf{R}}\mathbf{q}(t)) \tag{17.7}$$

Setting $\mathbf{p} = \bar{\mathbf{R}}^T\mathbf{M}\mathbf{h}$ and taking the SVD of the complete total acceleration matrix,

$$\ddot{\mathbf{x}}(t) + \mathbf{h}\ddot{u}_g(t) = \bar{\mathbf{R}}((\ddot{\mathbf{q}}(t) + \mathbf{p}\ddot{u}_g(t)) = \mathbf{U}\boldsymbol{\Sigma}\mathbf{V}^T \tag{17.8}$$

Since the modal decomposition and the SVD are both unique, they are equivalent. The left singular vectors are exactly the modal vectors. Singular values are like modal amplification factors. The first n columns of $\mathbf{V}$ give normalized modal response histories.

Unfortunately, the principal components of a matrix of partial measurements have mode mixing. The challenge now is to isolate mode-like principal components from partial acceleration measurements of nonlinear system and then to interpolate those components to the total accelerations of each floor.

17.2.3 Singular Spectrum Analysis

Singular spectrum analysis (SSA) is used to process the measurements [25]. Consider a time series of system response obtained from a specific sensor $\mathbf{y} = (y_1, y_2, \ldots, y_N)$ of length N. In this study, all measurements are of the total horizontal floor accelerations $\mathbf{y}_i = \ddot{\mathbf{x}}_i + \ddot{u}_g$. Let $k(0 < k < N/2 + 1)$ be the window length or the number of rows in the Hankel matrix of signal $\mathbf{y}$ and $l = N - k + 1$, $(l > k)$. Then embed the signal $\mathbf{Y}$ into a Hankel matrix as follows:

$$\mathbf{Y}_H = [\mathbf{Y}_1, \mathbf{Y}_2, \ldots, \mathbf{Y}_l] = (y_{ij})_{i,j=1}^{k,l} = \begin{bmatrix} y_1 & y_2 & y_3 & \cdots & y_l \\ y_2 & y_3 & y_4 & \cdots & y_{l+1} \\ \vdots & \vdots & \vdots & \vdots & \vdots \\ y_k & y_{k+1} & y_{k+2} & \cdots & y_N \end{bmatrix} \tag{17.9}$$

where the Hankel matrix has constant skew-diagonals.

A singular value decomposition (SVD) [34] of the Hankel matrix $\mathbf{Y}_H$ gives

$$\mathbf{Y}_H = \mathbf{U}\boldsymbol{\Sigma}\mathbf{V}^T \tag{17.10}$$

The most significant n components are the first n dyads $\sigma_i\mathbf{u}_i\mathbf{v}_i^T$. A new rank-n matrix $\mathbf{Y}_L$ is built from the first n dyads of the SVD.

$$\mathbf{Y}_L = \sum_{i=1}^{n} \mathbf{Y}_L^{(i)} \tag{17.11}$$

where

$$\mathbf{Y}_L^{(i)} = \sigma_i\mathbf{U}_i\mathbf{V}_i^T \quad (i = 1, 2, \ldots n) \tag{17.12}$$

In the following, a lower rank Hankel matrix $\mathbf{Y}_{LH}$ is made by averaging the skew-diagonal components of matrix $\mathbf{Y}_L$. The reconstructed signal $\tilde{\mathbf{y}}$ can then be extracted from the first column and last row of Hankel matrix $\mathbf{Y}_{LH}$. Furthermore, a set of lower rank Hankel matrix $\mathbf{Y}_{LH}^{(i)}$ are constructed by averaging the skew-diagonal components of matrix $\mathbf{Y}_L^{(i)}$. The most significant n reconstructed subseries $\tilde{\mathbf{y}}^{(i)}$ can be extracted respectively from the first column and last row of Hankel matrices $\mathbf{Y}_{LH}^{(i)}$ mentioned above, which satisfy

$$\tilde{\mathbf{y}} = \sum_{i=1}^{n} \tilde{\mathbf{y}}^{(i)} \tag{17.13}$$

In this way, the initial time series $\mathbf{y} = (y_1, y_2, \ldots, y_N)$ is decomposed into a sum of n extracted subseries.

17.2.3.1 Assemble SSA components

Using the SSA technique, each output measurement from the available sensors can be decomposed into n significantly meaningful reconstructed subseries. Suppose a system has m degree-of-freedom and only the measurement data $\mathbf{y}_1$ and $\mathbf{y}_m$ from sensor 1 and m are available. After conducting SSA, $\mathbf{y}_1$ and $\mathbf{y}_m$ are decomposed into n SSA components respectively,

$$\mathbf{y}_1 = \sum_{i=1}^{n} \tilde{\mathbf{y}}_1^{(i)} \qquad \mathbf{y}_m = \sum_{i=1}^{n} \tilde{\mathbf{y}}_m^{(i)} \tag{17.14}$$

To avoid mode mixing and to enforce each interpretable component dominated by a certain frequency content, it is more practical and helpful to assemble all of the SSA components from each measurement into a big matrix.

$$\mathbf{Y}_R = \begin{bmatrix} \tilde{\mathbf{y}}_1^{(1)} \\ \vdots \\ \tilde{\mathbf{y}}_1^{(n)} \\ \tilde{\mathbf{y}}_m^{(1)} \\ \vdots \\ \tilde{\mathbf{y}}_m^{(n)} \end{bmatrix} \tag{17.15}$$

17.2.3.2 Principal Components from SVD

Conducting a SVD for the assembled matrix $\mathbf{Y}_R$, principal components can be extracted from the first n eigentriples of the SVD.

$$\mathbf{Y}_R = \tilde{\mathbf{U}}\tilde{\mathbf{\Sigma}}\tilde{\mathbf{V}}^T \tag{17.16}$$

where $\tilde{\mathbf{U}} \in \Re^{2n\times 2n}$, $\tilde{\mathbf{V}} \in \Re^{N\times N}$, $\tilde{\mathbf{\Sigma}} \in \Re^{2n\times N}$.

$$\mathbf{Y}_R^{(i)} = \tilde{\sigma}_i \tilde{\mathbf{u}}_i \tilde{\mathbf{v}}_i^T \qquad \mathbf{Y}_R^{(i)} \in \Re^{2n\times N} \tag{17.17}$$

The principal components for $i = 1, 2, \ldots, n$ are expressed as follows:

$$\bar{\mathbf{y}}_1^{(i)} = \sum_{j=1}^{n} \mathbf{Y}_{R,j}^{(i)} \qquad \bar{\mathbf{y}}_m^{(i)} = \sum_{j=n+1}^{2n} \mathbf{Y}_{R,j}^{(i)} \tag{17.18}$$

where j represents the jth row of lower rank matrices $\mathbf{Y}_R^{(i)}$. The principal components extracted are critical to the following targeted base shear recovery.

17.2.3.3 Principal Components Interpolation

For sparse acceleration measurements, only partial measurement data are available. Using the principal components of each available measurement from the above steps is not enough to effectively reflect the system response of locations without measurement under excitation. To address this issue, we interpolate the corresponding principal components by using principal components for locations with measurement. There are several approaches to interpolate the corresponding principal components to the unmeasured coordinates. A simple but powerful approach is to solve a constrained optimization problem with Lagrange multipliers [11], which aims to optimize the interpolation by minimizing an energy norm objective function, such that several linear constraints are satisfied. The linear constraints enforce the interpolated principal components at locations with sensors equal to those obtained above.We can use a stiffness matrix in the optimization if it is available. Otherwise, we can use a second order central difference matrix representing the curvature of principal shape.

For ith($i = 1, 2, \ldots n$) component, the constrained optimization problem is expressed as

$$\min_{\tilde{\mathbf{a}}^{(i)}} J^{(i)} = \frac{1}{2}\tilde{\mathbf{a}}^{(i)T}\mathbf{K}\tilde{\mathbf{a}}^{(i)} \tag{17.19}$$

such that

$$\tilde{\mathbf{a}}_1^{(i)} = \bar{\mathbf{y}}_1^{(i)} \qquad \tilde{\mathbf{a}}_m^{(i)} = \bar{\mathbf{y}}_m^{(i)}$$

where $\tilde{\mathbf{a}}^{(i)} = [\tilde{\mathbf{a}}_1^{(i)}; \tilde{\mathbf{a}}_2^{(i)}; \cdots; \tilde{\mathbf{a}}_m^{(i)}], \mathbf{a}^{(i)} = [\bar{\mathbf{y}}_1^{(i)}; \bar{\mathbf{y}}_m^{(i)}]$. Lagrange multipliers can be applied to modify the objective function through the addition of terms describing the constraints. The augmented objective function is then expressed as,

$$J_A^{(i)} = \frac{1}{2}\tilde{\mathbf{a}}^{(i)T}\mathbf{K}\tilde{\mathbf{a}}^{(i)} + \lambda^{(i)T}(A\tilde{\mathbf{a}}^{(i)} - \mathbf{a}^{(i)}) \tag{17.20}$$

The optimization problem can be written in terms of the augmented objective function as,

$$\max_{\lambda} \min_{\tilde{\mathbf{a}}^{(i)}} J_A^{(i)} \tag{17.21}$$

such that $\lambda_j \geq 0 \ \forall j$.

The following conditions define the optimal design variables such that the constraints are satisfied.

$$\frac{\partial J_A^{(i)}}{\partial \tilde{\mathbf{a}}^{(i)}} = 0 \qquad \frac{\partial J_A^{(i)}}{\partial \lambda^{(i)}} = 0 \tag{17.22}$$

The optimal principal components at every floor $\tilde{\mathbf{a}}^{(i)} = [\tilde{\mathbf{a}}_1^{(i)}; \tilde{\mathbf{a}}_2^{(i)}; \cdots; \tilde{\mathbf{a}}_m^{(i)}], i = (1, 2, \cdots, n)$ obtained from this interpolation are then used to recover the base shear force, which is expressed as follows:

$$f_B = -\sum_{j=1}^{m} \mathbf{M}_{(jj)} \sum_{i=1}^{n} \tilde{\mathbf{a}}_j^{(i)} \tag{17.23}$$

The method presented above is based on one dimensional motion. Several minor changes are necessary if we consider the two orthogonal translational motion and torsional motion. First, output measurements from available sensors are decoupled into x, y translation and θ rotation; then these are decomposed into principal components respectively using SSA method. Second, principal components for different directions are assembled together as coupled. Third, the coupled principal components are directly used for the acceleration interpolation of each floor without other manipulations. In order to numerically verify the proposed algorithm, a series of simple numerical models were constructed in which the nonlinearities resulting from impact or friction were incorporated in the isolation-level. Figure 17.5 shows one of the numerical examples conducted to numerically verify the proposed methodology.

The SSA technique plays the role of an effective filter. In the proposed approach, there is no presumed parametric model to fit measured responses. The prior information of excitation is not necessary. Moreover, the SSA based method accompanied with principal components interpolation is not only able to handle linear system with full sensors and limited sensors, but also nonlinear system with full sensors and limited sensors.

17.3 Numerical Simulations

In this section, a number of numerical simulations are conducted to verify the proposed SSA technique and principal components interpolation on several MDOF mass-spring-damper models with base isolation. A series of earthquake ground accelerations are used as nonstationary random excitation, which are modeled as independent, enveloped, filtered white-noise process. A fixed-step fourth-order Runge-Kutta solver is used to obtain the time series of transient system responses with a sampling frequency of 200 Hz.

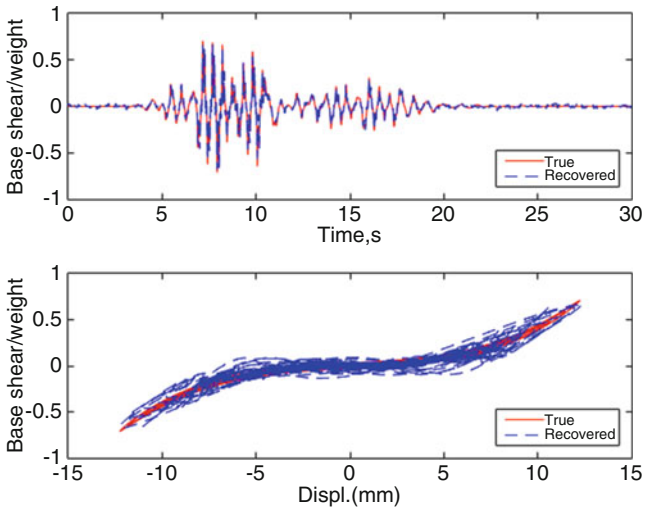

Fig. 17.2 Recovered normalized base shear time history and hysteresis loop using limited sensors for nonlinear seismic isolation system with Duffing oscillator (3 Floor, FF)

17.3.1 Nonlinear Behavior Modeled by Duffing Oscillator

A 3 floor model is set up with the following parameters.

$$\mathbf{M} = m^* \begin{bmatrix} 1 & 0 & 0 \\ 0 & 1 & 0 \\ 0 & 0 & 1 \end{bmatrix} \quad \mathbf{C} = c^* \begin{bmatrix} 2 & -1 & 0 \\ -1 & 2 & -1 \\ 0 & -1 & 1 \end{bmatrix} \quad \mathbf{K} = k^* \begin{bmatrix} 1 & -1 & 0 \\ -1 & 2 & -1 \\ 0 & -1 & 1 \end{bmatrix}$$

where $m^* = 100$, $c^* = 500$. A cubic nonlinear force at the isolation level is modeled as $f(t) = k_d x_1(t)^3$. k_d is an adjustable coefficient. Figure 17.2 shows that the base shear force is recovered with high accuracy.

17.3.2 Nonlinear Impact Force

Changing the nonlinear force to $f(t) = k_i x_1(t)^9$. k_i is an adjustable coefficient. Figure 17.3 shows that the base shear force is recovered with high accuracy.

17.3.3 Hysteretic Behavior

To demonstrate the capability of the SSA method and principal component interpolation for base shear recovery of nonlinear hysteretic seismic isolation system, the parameters used to model the nonlinear hysteretic friction are detailed in Table 17.1. The stiffness of the seismic isolation system is 0.3 times that of the other floors.

In the following, numerical models with more floors are simulated, from which the results are compared. For the sparse measurement case, only measurement data from the first floor and top floor are used. It is worth noting that Fig. 17.4 indicates mode mixing phenomenon in principal components. Despite this, the recovered time history and hysteresis loop of base shear shown in Fig. 17.5 still accurately coincide with those of the known true base shear as is shown in solid line. Figures 17.6 and 17.7 show the base shear recovery of a three floor building system with various earthquake excitation.

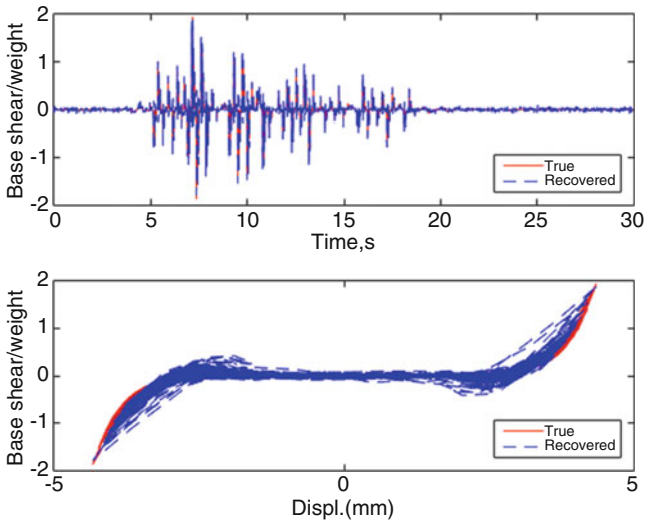

Fig. 17.3 Recovered normalized base shear time history and hysteresis loop using limited sensors for nonlinear seismic isolation system with impact force at isolation level (3 Floor, FF)

Table 17.1 Parameter values for the nonlinear hysteretic friction model

Parameter	Definition	Value	Unit
f_y	Yield force	4×10^5	N
d_y	Yield displacement	0.5	mm
κ	Post-yield stiffness ratio	0.1	–
β	Hysteresis parameter	0.5	–
η	Hysteresis exponent	3	–
m_i	Floor mass	1×10^5	kg
c_i	Floor damping	1×10^3	N s/mm
k_i	Floor stiffness	3×10^4	N/mm

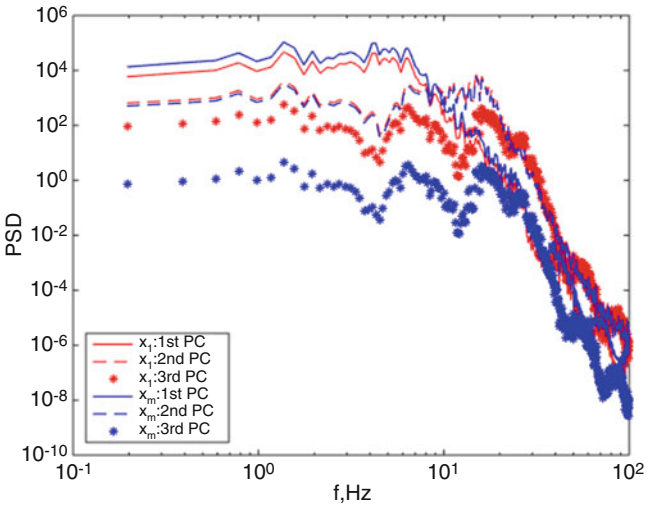

Fig. 17.4 Power spectral density for each principal components using limited sensors for nonlinear hysteretic seismic isolation system under far field shake (3 Floor)

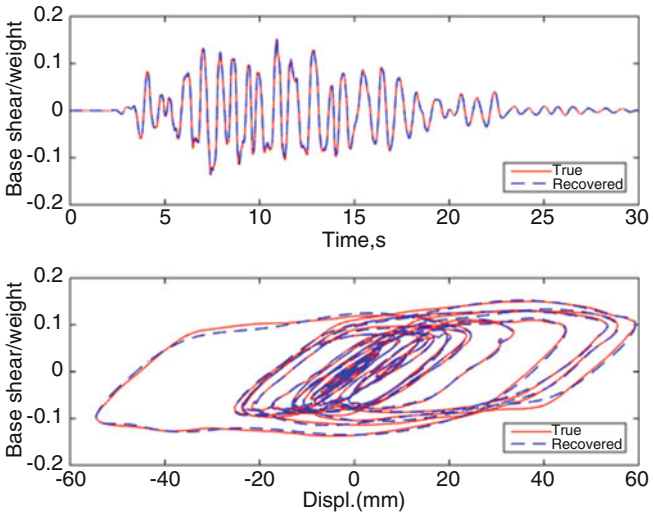

Fig. 17.5 Recovered normalized base shear time history and hysteresis loop using limited sensors for nonlinear hysteretic seismic isolation system under far field shake (3 Floor)

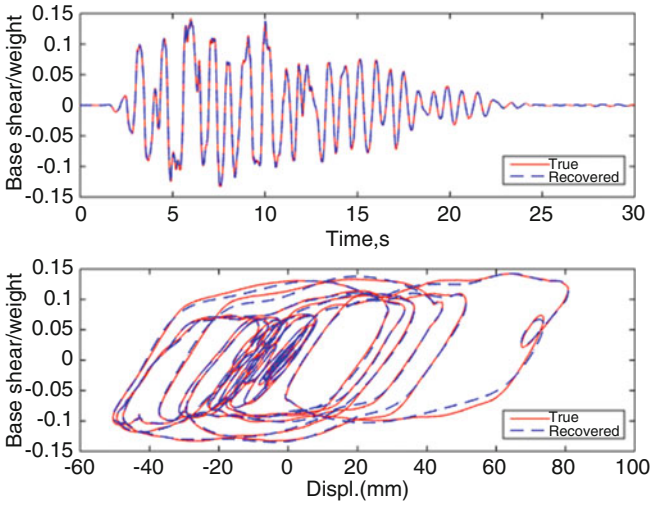

Fig. 17.6 Recovered normalized base shear time history and hysteresis loop using limited sensors for nonlinear hysteretic seismic isolation system under near fault without pulse shake (3 Floor)

17.4 Conclusions

This paper presents a SSA-based time-domain output only algorithm to recover the base shear force within seismic isolation system. Compared to existing output-only identification methods, the proposed SSA algorithm is not only suitable for linear base-isolated systems, but is also capable of recovering the base shear force in nonlinear hysteretic base-isolated systems. Moreover, the developed SSA algorithm recovers base shear force remarkably well when sensors are limited, using an efficient constrained optimization to interpolate principal components for each floor.

The SSA algorithm directly processes the output measurement time series without independent measurement of the input excitation or presuming a stochastic state space model. By putting the time series into a Hankel matrix and conducting SVD, the most pronounced SSA components are extracted from the original time series according to the magnitude distribution of singular values of the Hankel matrix. Even though the mode mixing issue persists in the principal components extracted from SVD of reassembled big matrix consisting of SSA components, the base shear is still recovered with high accuracy using the proposed method.

Results from numerical simulations validate the capability of the SSA algorithm accompanied by principal components interpolation in high-accuracy base shear recovery.

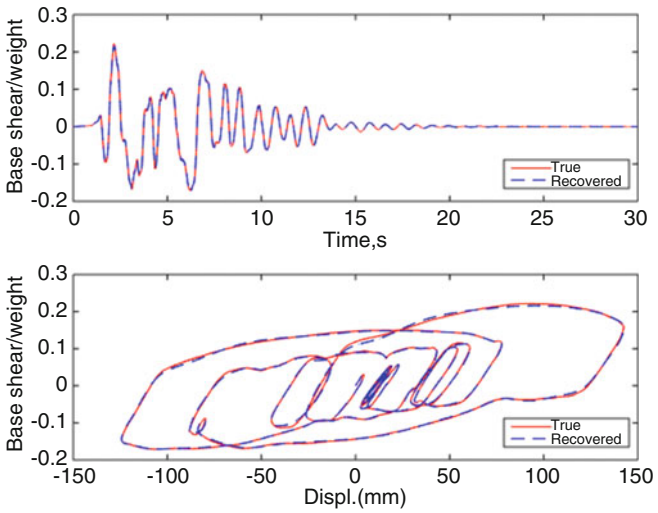

Fig. 17.7 Recovered normalized base shear time history and hysteresis loop using limited sensors for nonlinear hysteretic seismic isolation system under near fault with pulse shake (3 Floor)

Acknowledgements This material is based in part upon work supported by the National Science Foundation under Grant Number CMMI-1258466. Any opinions, findings, and conclusions or recommendations expressed in this material are those of the author(s) and do not necessarily reflect the views of the National Science Foundation.

References

1. Abe, M., Fujino, Y., Yoshida, J.: Dynamic behaviour and seismic performance of base-isolated bridges in observed seismic records. In: Proceedings of 12th World Conference on Earthquake Engineering (2000)
2. Ahmadi, G., Fan, F., Noori, M.: A thermodynamically consistent model for hysteretic materials. Iran. J. Sci. Technol. **21**(3), 257–278 (1997)
3. Alhan, C., Gavin, H.: A parametric study of linear and non-linear passively damped seismic isolation systems for buildings. Eng. Struct. **26**(4), 485–497 (2004)
4. Cadzow, J.A.: Signal enhancement-a composite property mapping algorithm. IEEE Trans. Acoust. Speech Signal Process. **36**(1) , 49–62 (1988)
5. Celebi, M.: Successful performance of a base-isolated hospital building during the 17 January 1994 Northridge earthquake. Struct. Des. Tall Build. **5**, 95–109 (1996)
6. Chaudhary, M., Abe, M., Fujino, Y.: Identification of soil–structure interaction effect in base-isolated bridges from earthquake records. Soil Dyn. Earthq. Eng. **21**(8), 713–725 (2001)
7. Chaudhary, M.T.A., Abe, M., Fujino, Y., Yoshida, J.: System identification of two base-isolated bridges using seismic records. J. Struct. Eng. **126**(10), 1187–1195 (2000)
8. Ding, Y., Law, S., Wu, B., Xu, G., Lin, Q., Jiang, H., Miao, Q.: Average acceleration discrete algorithm for force identification in state space. Eng. Struct. **56**, 1880–1892 (2013)
9. Erlicher, S., Point, N.: Thermodynamic admissibility of Bouc-Wen type hysteresis models. Comptes Rendus Méc. **332**(1), 51–57 (2004)
10. Furukawa, T., Ito, M., Izawa, K., Noori, M.N.: System identification of base-isolated building using seismic response data. J. Eng. Mech. **131**(3), 268–275 (2005)
11. Gavin, H.P., Scruggs, J.T.: Constrained optimization using lagrange multipliers. CEE 201L. Duke University (2012)
12. Golyandina, N., Nekrutkin, V., Zhigljavsky, A.A.: Analysis of Time Series Structure: SSA and Related Techniques. CRC, New York (2001)
13. Huang, M.-C., Wang, Y.-P., Lin, T.-K., Chen, Y.-H.: Development of physical-parameter identification procedure for in-situ buildings with sliding-type isolation system. J. Sound Vib. **332**(13), 3315–3328 (2013)
14. Huang, N.E., Shen, Z., Long, S.R., Wu, M.C., Shih, H.H., Zheng, Q., Yen, N.-C., Tung, C.C., Liu, H.H.: The empirical mode decomposition and the Hilbert spectrum for nonlinear and non-stationary time series analysis. In: Proceedings of the Royal Society of London A: Mathematical, Physical and Engineering Sciences, vol. 454, pp. 903–995. The Royal Society (1998)
15. Hyvärinen, A.: Complexity pursuit: separating interesting components from time series. Neural Comput. **13**(4), 883–898 (2001)
16. Ismail, M., Ikhouane, F., Rodellar, J.: The hysteresis bouc-wen model, a survey. Arch. Comput. Meth. Eng. **16**(2), 161–188 (2009)
17. Juang, J.-N., Pappa, R.S.: An eigensystem realization algorithm for modal parameter identification and model reduction. J. Guid. Control. Dyn. **8**(5), 620–627 (1985)
18. Juang, J.-N., Phan, M., Horta, L.G., Longman, R.W.: Identification of observer/kalman filter Markov parameters-theory and experiments. J. Guid. Control. Dyn. **16**(2), 320–329 (1993)
19. Kampas, G., Makris, N.: Time and frequency domain identification of seismically isolated structures: advantages and limitations. Earthq. Struct. **3**(3–4), 249–270 (2012)

20. Kijewski, T., Kareem, A.: Wavelet transforms for system identification in civil engineering. Comput.-Aided Civ. Infrastruct. Eng. **18**(5), 339–355 (2003)
21. Ljung, L.: Prediction error estimation methods. Circuits Syst. Signal Process. **21**(1), 11–21 (2002)
22. Loh, C.-H., Weng, J.-H., Chen, C.-H., Lu, K.-C.: System identification of mid-story isolation building using both ambient and earthquake response data. Struct. Control. Health Monit. **20**(2), 139–155 (2013)
23. Mahmoudvand, R., Zokaei, M.: On the singular values of the Hankel matrix with application in singular spectrum analysis. Chilean J. Stat. **3**(1), 43–56 (2012)
24. Markovsky, I.: Structured low-rank approximation and its applications. Automatica **44**(4), 891–909 (2008)
25. Markovsky, I.: Low Rank Approximation: Algorithms, Implementation, Applications. Springer Science & Business Media, New York (2011)
26. Nagarajaiah, S., Xiaohong, S.: Response of base-isolated USC hospital building in Northridge earthquake. J. Struct. Eng. **126**(10), 1177–1186 (2000)
27. Oliveto, N.D., Scalia, G., Oliveto, G.: Time domain identification of hybrid base isolation systems using free vibration tests. Earthq. Eng. Struct. Dyn. **39**(9), 1015–1038 (2010)
28. Peeters, B., De Roeck, G.: Reference-based stochastic subspace identification for output-only modal analysis. Mech. Syst. Signal Process. **13**(6), 855–878 (1999)
29. Siringoringo, D.M., Fujino, Y.: Seismic response analyses of an asymmetric base-isolated building during the 2011 great east Japan (Tohoku) earthquake. Struct. Control. Health Monit. **22**(1), 71–90 (2015)
30. Staszewski, W.: Identification of damping in MDOF systems using time-scale decomposition. J. Sound Vib. **203**(2), 283–305 (1997)
31. Stewart, J.P., Conte, J.P., Aiken, I.D.: Observed behavior of seismically isolated buildings. J. Struct. Eng. **125**(9), 955–964 (1999)
32. Takewaki, I., Nakamura, M.: Stiffness-damping simultaneous identification under limited observation. J. Eng. Mech. **131**(10), 1027–1035 (2005)
33. Takewaki, I., Nakamura, M.: Temporal variation in modal properties of a base-isolated building during an earthquake. J. Zhejiang Univ. Sci. A **11**(1), 1–8 (2010)
34. Trefethen, L.N., Bau III, D.: Numerical Linear Algebra, vol. 50. SIAM (1997)
35. Xu, C., Chase, J.G., Rodgers, G.W.: Physical parameter identification of nonlinear base-isolated buildings using seismic response data. Comput. Struct. **145**, 47–57 (2014)
36. Yang, J.N., Lei, Y., Pan, S., et al.: System identification of linear structures based on Hilbert-Huang spectral analysis. part 1: normal modes. Earthq. Eng. Struct. Dyn. **32**(9), 1443–1468 (2003)
37. Yang, Y., Nagarajaiah, S.: Output-only modal identification with limited sensors using sparse component analysis. J. Sound Vib. **332**(19), 4741–4765 (2013)
38. Yoshimoto, R.: Damage detection of base-isolated buildings using multi-inputs multi-outputs subspace identification. Ph.D Thesis, Department of System Design Engineering, Keio University (1776)

Chapter 18
Vibration Testing for Bridge Load Rating

Mohamad Alipour, Devin K. Harris, and Osman E. Ozbulut

Abstract Load rating is the process of determining the safe live-load carrying capacity of a bridge and is thus a major basis in prioritizing maintenance operations and allocation of resources. Traditionally, bridge evaluation standards provide two approaches to load rating, namely the analytical calculations and the empirical static load tests. Analytical load ratings are generally based on simplifying assumptions and may not closely reflect the current physical condition of the bridge. Empirical load tests provide a more realistic picture of live-load capacity of a bridge, but their application has been considerably limited by cost, time, test truck requirement, traffic interruption, and safety. Recently, a new approach named in this paper as "vibration-calibrated model-based load rating" has been investigated by a number of researchers. In this method, a vibration test is performed on the bridge and a refined finite element model is calibrated so as to replicate the observed modal response of the bridge. The calibrated model, which is adjusted to reflect the real in-situ condition and performance of the bridge, will then be used for the purpose of realistic load rating. This paper starts by reviewing the limitations of the current analytical and empirical methods and provides an in-depth explanation of the vibration-based method for load rating. Finally, recent research on this approach is reviewed and a discussion on the advantages, disadvantages and special considerations involved is presented. The areas that require more research and future work are also highlighted.

Keywords Load rating • Modal analysis • Dynamic testing • Vibrations

18.1 Introduction

The national infrastructure system, which includes a diverse series of assets, systems, and networks, is responsible for providing critical social service to the community in support of human quality of life, while serving as a foundation of economic prosperity [1]. Bridges are key components in the transportation infrastructure system and are usually considered to be the weak link in the national highway and railroad network given the increasing average age and number of structurally deficient bridges [2]. Therefore, safety and functionality evaluation and monitoring of bridge structures is a crucial task for the responsible transportation agencies. Load rating is the process of determining the maximum safe load capacity of a bridge and helps the agencies make sure their structures are sufficient for the vehicles that use them. A bridge rated incapable of carrying the specified loads may require to be repaired, posted with weight limitations, or replaced altogether. Accurate and reliable load ratings are thus critical to guarantee public safety and operational functionality while avoiding overly conservative ratings with obvious economic implications. As a recent example highlighting the importance of accurate load ratings, as part of the relief efforts in the aftermath of Hurricane Katrina, state legal truck weights needed to be increased to accommodate the transit of more supply within the crisis-stricken regions. Therefore, accurate maximum safe load ratings of bridges were necessary for the officials to plan aid corridors [3]. In general, overly conservative load ratings may result in unnecessary load postings and detours while unrealistic overestimation of load ratings can lead to bridge collapse with considerable property damage and tragic loss of life [4, 5].

As will be discussed in the following sections, there are analytical and empirical approaches to calculating load ratings. Empirical field load testing methods provide higher accuracy in load ratings than the analytical calculations but they have been limited in application due to the cost and effort involved specifically the need for the deployment of test trucks and traffic interruption. In this paper, possible application of vibration testing in load rating is discussed as a fast and less demanding alternative. This paper starts by reviewing the limitations of the application of current analytical and empirical methods and aims at introducing an emerging hybrid approach for load rating bridges which leverages parts of the strengths of both

M. Alipour • D.K. Harris • O.E. Ozbulut (✉)
Department of Civil and Environmental Engineering, University of Virginia, Charlottesville, VA, USA
e-mail: ozbulut@virginia.edu

S. Pakzad, C. Juan (eds.), *Dynamics of Civil Structures, Volume 2*, Conference Proceedings of the Society for Experimental Mechanics Series, DOI 10.1007/978-3-319-29751-4_18

numerical and empirical approaches. Finally, recent publications focusing on this approach are reviewed and a discussion on the different aspects and considerations involved is presented. In summary, the objectives of this paper can be summarized as:

- Providing an up-to-date review of the literature on load rating via vibration testing-testing calibrated models
- Evaluating the important aspects, advantages, disadvantages, limitations and challenges in the implementation of vibration-based load rating
- Highlighting the areas which require more research and future work

18.1.1 Conventional Methods of Load Rating

Many factors affect the accuracy of a load rating analysis but three prominent yet complicated set of factors with the highest influence are (1) the representation of load transfer mechanism between members, (2) the inclusion of the effect of deterioration mechanisms on load carrying behavior of members, and (3) the consideration of unintended and unforeseen field factors. Load transfer mechanism defines how the applied loads are distributed within the structure and is primarily a function of the properties of the members, supports, connections and their interactions. Therefore, accurate and realistic representation of these properties together with efficient methods of structural analysis are key to accurate load ratings.

Load carrying behavior of a bridge is also a function of the current physical condition of the structure and the level of deteriorations. Different deterioration mechanisms such as material aging, weathering and corrosion, cracking due to excessive loads or fatigue, scour, and vehicle collision negatively affect the behavior and capacity and thus impose uncertainties on the calculated load ratings. Therefore, the results of load ratings must be modified to reflect the current physical condition and deteriorations in the existing structure.

In addition to deteriorations, there are a series of unintended and unforeseen mechanisms that affect the load carrying behavior and thus the result of load ratings. These include but are not limited to unintended composite action between deck and girders due to friction rather than purposefully designed shear studs, unintended continuity/fixity (extra restraints on bearings not accounted for in the design or modeling), participation of nonstructural members such as parapets, and dynamic magnification effects on the vehicle loads. These factors are difficult to quantify and represent in design or modeling and are usually referred to as “field factors” [6]. The presence of field factors and the corresponding uncertainty results in discrepancies between predicted and observed behavior unless properly accounted for in the process of load ratings.

Different load rating methods treat the three above factors differently and the accuracy and reliability of a method greatly depends on the assumptions they make and the evaluation methodology they adopt for characterizing them. The Manual for Bridge Evaluation (referred to as the MBE hereafter) developed by the American Association of State Highway Transportation officials (AASHTO) is the standard document for bridge evaluation and load rating [7]. The MBE considers two types of evaluation methods for load rating: Analytical and Empirical methods.

Analytical methods involve analyzing the structure under loads and calculating the ratio of available capacity for live loads to the existing live load effect for each member. Section 6.A.3 of the MBE then allows the analysis to be done using either simplified analysis methods or refined finite element methods of analysis (FEM) in accordance with Section 4.6.3 of the AASHTO LRFD Design Specifications [8]. The difference between these two approaches is the way they handle load transfer mechanism. Simplified methods provide a useful baseline for estimating the actual load capacity by adopting simplifying and usually conservative assumptions and approximate formulas for load distribution. Refined methods provide a more realistic load transfer analysis by using detailed computer simulations. In both of the analytical approaches, the effect of deteriorations are addressed via standardized visual inspections in which qualified inspectors try to find and measure any signs of deteriorations that can affect structural behavior [9]. However, visual inspection is expensive and labor and time-intensive. Furthermore, many deterioration mechanisms either take place inside the structure and are hidden to the inspector or their effects on structural behavior are hard to characterize [10]. This in addition to the expected level of subjectivity in human judgment will affect the accuracy of the load ratings [11]. As a result, sometimes, non-destructive evaluation (NDE) is employed to provide a better picture of the current condition but those methods are both local, and hard to relate to the behavior of the structure under loads. Therefore, obtaining a realistic global understanding of the deterioration effects on load rating is difficult without the observation of behavior under real loads. Finally, analytical load ratings depend on raters’ assumptions about field factors which are rarely accurate unless confirmed via experiments.

Empirical methods (or load rating by field load testing) provide an efficient means of dealing with different uncertainties in load transfer, field factors, and deterioration effects and provide the highest level of realism by actually observing the response of the structure under external loads. If executed effectively, empirical load testing can provide first-hand information on all the three above-mentioned major factors of load rating accuracy embedded in the observed response of the structure. In other words, hidden or subtle factors affecting load transfer mechanism or deterioration mechanisms will directly affect the response of the bridge without the need for externally accounting for them in the load rating calculations.

The MBE defines field load testing as the process of applying predetermined or controlled loads to a bridge and measuring the response in an effort to assess, monitor or verify the performance or safety of the structure or components or to determine safe load capacity [7]. This manual introduces two empirical load testing methods, namely the diagnostic and proof load tests. Both of these methods are similar in that they involve positioning a truck of a known weight on the bridge and trying to correlate the observed load carrying behavior under the test truck with the load rating of the bridge. Diagnostic load tests are aimed at adjusting analytical estimates of capacity based on observed behavior as the bridge is loaded or to determine characteristics, load distribution behavior, or to validate models [12–17]. In a proof load test the goal is to find the maximum safe load capacity of the bridge by gradually increasing the load on the bridge in small increments until a target load below the ultimate capacity is reached or signs of nonlinear behavior or distress are observed. Diagnostic tests are easier and less expensive and demanding compared with proof test as they are often conducted at a lower load level and do not require the placement of the truck on several locations to find the critical position corresponding to capacity. Also, a challenge in proof tests is to prevent damage to the structure and ensure the safety of personnel. With respect to the interpretation of the results, proof tests directly provide a lower bound load capacity while the diagnostic load tests involve a linear extrapolation of analytical load ratings and are thus an upper bound on the actual nonlinear capacity [6].

As discussed above, empirical methods provide a more accurate and realistic estimate of the load rating of a bridge by consulting the actual response of the bridge. Furthermore, the experience gained in tests and studies by various researchers shows that load ratings obtained by load tests are usually higher than estimated by analytical methods [6] due to the incorporation of reserved capacity, alternative load paths and inherent system redundancy. As a result, bridges diagnosed with insufficient capacity by analytical methods and thus requiring load posting or upgrading may benefit from load tests. Nevertheless, examination of the statistics on the methods currently used in the US to load rate highway bridges shows the dominating popularity of analytical methods. Figure 18.1 shows the method used for inventory load rating of over 610,000 highway bridges longer than 20 ft in the US as recorded in the 2014 National Bridge Inventory (NBI) database [18].

Figure 18.1 shows that over 80 % of the bridges in the NBI are load rated using analytical methods while only 0.6 % are load tested. The reason why empirical methods are not popular in spite of the improved accuracy is in the practical considerations. Load rating using load tests is generally costly, time-consuming and cumbersome and need special vehicles and equipment. In addition, safety is a serious issue particularly in proof load tests. As a result, their practical application has been limited. It is also interesting to note in Fig. 18.1 that about one in five of all NBI bridges are either load rated by engineering judgment or not load rated at all. In many of these cases, sufficient information such as design or construction plans are not available for load ratings to be done using analytical methods. On the other hand, further investigation of the NBI data shows that these bridges are usually short span, local and low-traffic bridges and truck load tests are usually deemed to be too expensive and thus not a viable option considering the importance of the bridge.

In response to these concerns, building upon both the empirical and analytical methods, a third approach to load rating has been recently proposed which takes advantage of the realism of field testing while reducing the cost and resources required for empirical load ratings. In this paper, we refer to this approach as "*vibration-calibrated model-based load rating*". In this approach, a refined FEM model is constructed and calibrated against a simple baseline field test. The model will then be used to replicate the expected behavior of the real bridge. Comprehensive loading scenarios, structural analyses and load ratings can be subsequently performed on the calibrated model. Figure 18.2 summarizes the different approaches discussed for load

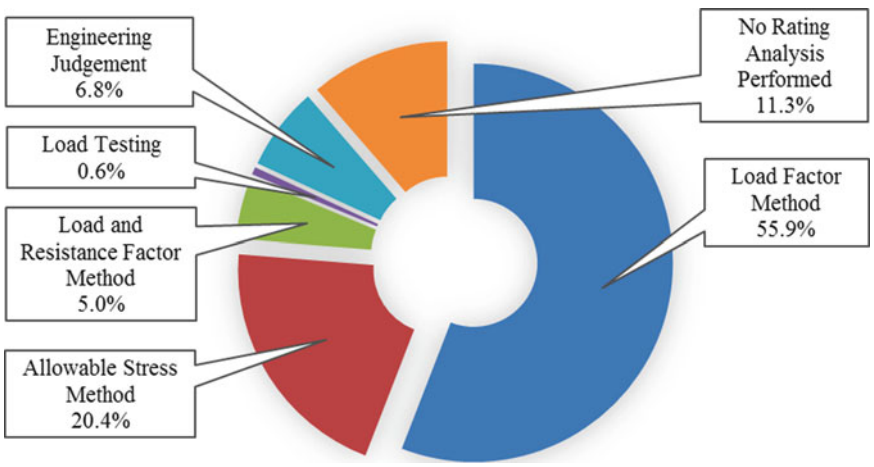

Fig. 18.1 Load ratings methods used for US bridges

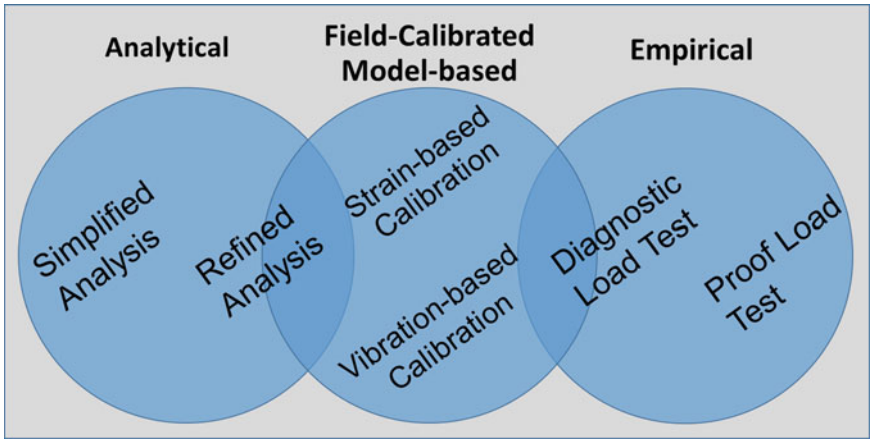

Fig. 18.2 Different approaches to load rating

rating bridges wherein field-calibrated model-based load rating is depicted as an intermediate hybrid method which shares some aspects of analytical and empirical methods and is usually based on strain or vibration measurements.

18.1.2 Vibration Testing of Bridges

The two conventional empirical approaches (diagnostic and proof load rating) are usually static tests because they involve strain or deflection measurements under a stationary truck. However, there are dynamic bridge tests involving transient loads to excite vibrations. Dynamic tests are not directly used for load rating but to determine modes of vibration of the bridge and their frequencies or moving-load impact factors. The MBE enumerates three types of dynamic bridge tests: (1) Weigh-in-motion testing, (2) Dynamic response test, and (3) Vibration tests. Dynamic response tests involve strain measurements under controlled moving truck or normal passing traffic and can be used for estimating impact factors [19]. Vibration tests can be used to evaluate modal parameters of the bridge such as frequencies, mode shapes and damping ratios. In a vibration test, the bridge is dynamically excited at certain points using mechanical shakers, impact hammers, or falling weights (forced or impact testing) and the accelerations are recorded using accelerometers installed on sensitive points on the structure. The test can also be carried out under ambient vibrations from natural sources such as wind and waves (ambient vibration testing) or operational sources such as normal passing traffic (operational vibration test) [20, 21]. Impact testing requires temporary traffic interruption to perform the test but provides a controlled testing input with the desired properties and high signal to noise ratio while the ambient and operational tests do not require special excitation equipment and are thus easier and cheaper to execute. However, special care should be taken with respect to signal quality and duration which sometimes complicates the identification of some vibration modes. More details and information on vibration testing methods are outside the scope of this paper and can be found in [22–24].

Once acceleration data is recorded from the modal test, modal identification is performed by processing the data, usually in frequency domain, to convert raw acceleration data to modal frequencies, mode shapes, and damping coefficients. Modal identification of structures using acceleration data from vibration testing is a well-developed field of research and has been extensively addressed in structural dynamics books and articles. In this paper we are interested in the next step which is updating an FEM model based on those identified modal properties and thus the details of modal identification techniques per se is outside the scope of this paper. Detailed discussion and review of those methods can be found in [24–26].

18.1.3 Vibration-Calibrated Model-Based Load Rating

Vibration-calibrated model-based load rating is built on the concept of model updating. Model updating is the process of matching the predicted response of a numerical model of a structural system with the experimental response obtained from a real-world test in order to characterize the most realistic numerical model parameters [27]. Later on, the calibrated model, which is able to closely replicate an experiment, will be used to conveniently analyze and load rate the bridge under various loading scenarios which would otherwise need multiple time-consuming, expensive and cumbersome truck runs.

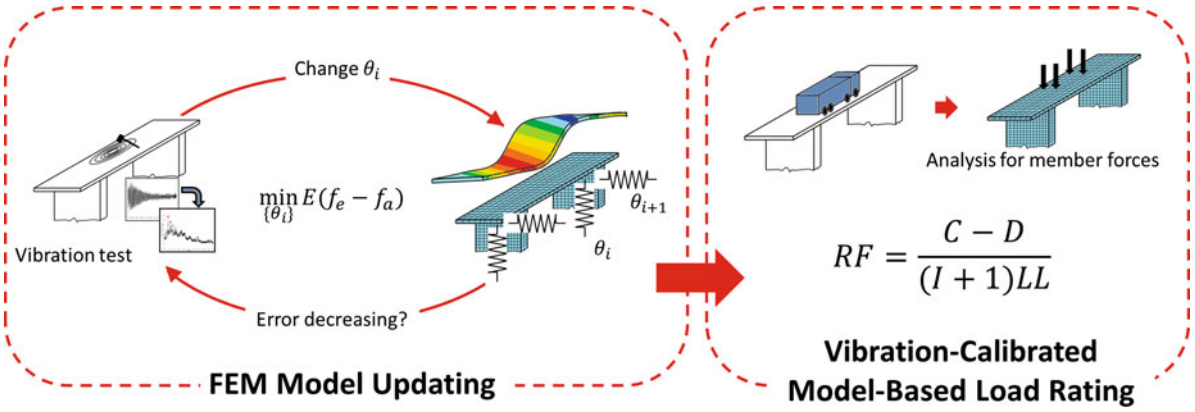

Fig. 18.3 Schematic of vibration-calibrated model-based load rating using static or vibration data

Based on the above definition, the initial step in vibration-calibrated model-based load ratings is to conduct a vibration test. An initial nominal FEM model should also be constructed based on design or as-built drawings and field observations to help design the vibration test. Target response variable (modal frequencies and/or mode shapes or modal assurance criteria) is selected based on the goals of model updating. Then, a number of unknown model parameters (θ_i) are selected to be updated by matching experimental and model-predicted response. Possible options for model parameters are boundary conditions usually in the form of support spring stiffness coefficients, continuity conditions, material properties, and even geometrical member properties such as cross-sectional areas which could inform about possible section losses. The final selection of unknown model parameters is usually achieved by sensitivity analysis usually involving a correlation analysis aimed at finding the parameters with a significant effect on the selected target response. Next, the error between the response predicted by the model and the actual experimental response (usually called the objective function of the optimization problem) is estimated. As the final step, a search in the space of unknown parameters is conducted to find the optimal parameter set which results in the minimum error. This search can either be done using manual trial and errors (manual model updating) or automatically by using an optimization scheme (automatic model updating). Once the FEM model is updated, truck loads are placed on the model in different locations and configurations and structural analysis will be performed to determine member loads which will then be converted to load ratings using the analytical load rating equation. A schematic illustration of vibration-calibrated model-based load rating is depicted in Fig. 18.3 wherein f_e and f_a denote the experimental and analytical modal parameters, θ_i are the unknown model parameters to be updated, E is the error function and C, D, L and I denote the capacity, dead and live load effect and impact factor respectively.

Vibration tests and the identified modal properties have been widely used for FEM model updating especially in aerospace and mechanical and later in bridge engineering [27, 28]. These applications are based on the premise that modal parameters are tightly related to stiffness and mass of the structure and thus to its load carrying behavior and can therefore inform the necessary adjustments to the FEM model so as to be able to replicate structural behavior. Review of the recent applications of vibration-based model updating on bridge structures reveals the widespread popularity of vibration tests and model updating for different bridge types, materials, and purposes. Ribeiro et al. [29] used ambient vibration data from a steel bowstring arch railway bridge in Portugal to perform model updating. They identified 12 global and 12 local (associated with the hangers) vibration modes using the enhanced domain decomposition method and used them in an automatic updating procedure using a genetic algorithm optimization and an objective function consisting of the summation of errors in frequencies and modal assurance criteria. Zivanovic et al. [30] conducted vibration testing and FEM model updating on a lively steel footbridge in Montenegro. The tests included both a forced test using a shaker and an ambient test and seven modes were identified using the canonical variate analysis. An initial manual updating was carried out to facilitate the convergence of the future automatic updating. Sipple and Sanayei [31] used a response variable different from that of most other researches in the area of vibration-based model updating. Instead of merely using frequencies and mode shapes, they employed the frequency response functions which provided more vibration information from the structure to the model. They tested a new concrete deck on steel girder bridge using a shaker and used the difference of experimental and numerical frequency response functions as their objective function to update groups of unknown parameters (deck rigidities, sidewalk rigidity and vertical and transverse rotational support stiffness). Brownjohn et al. [32] conducted ambient and shaker vibration tests on a prestressed concrete bridge in Singapore before and after a structural upgrading program to assess the efficiency of the upgrading.

The researches cited above were solely focused on model-updating based on vibrations. However, there are also a few additional recent cases of vibration tests used by some researchers specifically for the purpose of vibration-calibrated model-based load rating. Uzgider et al. [33] reported dynamic tests and FEM model updating of a 50 m-long, 80-year old reinforced concrete tied-arch railroad bridge in Turkey. A dynamic test was performed using a test train passing the bridge eight times while six longitudinal and three transverse accelerometers recorded accelerations from which frequencies and mode shapes were extracted. A sensitivity analysis using a 3D FEM model resulted in the selection of longitudinal and transverse bearing spring coefficients and joint lumped masses as the unknown model parameters. The model was then manually updated to provide modal assurance values of above 0.99 and the calibrated model was then employed for load ratings using the LRFR load rating equation and to calculate member safety indices.

Ren et al. [34, 35] studied vibration testing, model updating and load capacity evaluation on the historic Roebling suspension bridge built in 1867 over the Ohio River. The bridge had signs of deterioration mostly in the form of corrosion and was posted for loads at the time of the research and in response, the researchers were exploring vibration testing and model updating for realistic condition assessment and planning possible corrective actions. Ambient vibrations under natural excitation sources were recorded using seven accelerometers in either of the longitudinal and transverse directions and were used to identify frequencies of ten modes. It was mentioned that a number of coupled vibration modes could not be detected using the ambient data. A baseline 3D FEM model was constructed and model parameters were manually calibrated by adjusting stiffness parameters so as to replicate the experimental frequencies. As a result of the updating, elastic modulus of stiffening trusses and main cables and also lateral moments of inertia of outer and inner stringers and cross-sectional area of stringers and a few other members were reduced to match the experimental vibration characteristics. The calibrated model was then used for a series of condition assessment studies. Load capacity of the bridge was estimated, and the behavior of the bridge under corrosion and deterioration was studied by reducing the cable areas by 10–40 %. As a notable point, it can be seen that the researchers selected to manipulate and reduce the modulus of elasticity of the cables rather than their cross-sectional area to account for the observed reduction in stiffness in the vibration results. An argument can be made here that in reality, a reduction in cross-section could have been the actual reason behind the observed stiffness decay but the adopted model updating seems to be unable to differentiate between different means of stiffness reduction. In other words, two different calibrated models one with reduced cable cross-sections and the other with reduced elastic modulus can both be the answer to the model updating problems and therefore the uniqueness of the updated model is questionable. Future research is needed to address this concern.

Wang et al. [36] discussed a modal-based condition assessment procedure involving a vibration test used for updating a 3D linear FEM model of a three-span concrete-deck-on-steel-stringer bridge built in 1951. The vibrations were produced using an instrumented hammer and accelerometers installed on the surface of the deck recorded the accelerations while eliminating the need for access to the underside of the superstructure or traffic interruption under the bridge. However, traffic still needed to be restricted over the bridge but the duration of the instrumentation and test could be considerably reduced. Model parameters to be updated were support spring coefficients, weight and elastic modulus of concrete and steel, and the thickness of the deck. Level of composite action was also modeled by changing the flexural stiffness of a series of axially-rigid beam elements that connected the shells representing deck and girders. The abutment and piers were not simulated in the model, therefore, varying nodal masses were applied to nodes above pier locations to account for the pier masses. Frequencies and mode shapes were selected as the target response to be matched. Also, bridge girder condition index (referred to as BGCI [37]), which is the nodal deflection under unit load at each accelerometer point and is calculated by multiplying the flexibility matrix by a unit force vector, was used as a non-modal target response. Strains are also used as target response but details of strain measurements were not reported. The objective function used in the optimization scheme for automatic updating was a function of errors in frequency, modal assurance criteria, strain and BGCIs. The calibrated FEM model was then used to calculate member stresses under different loading scenarios which were then used in the load rating equation to calculate a rating for the structure.

Turer and Shahrooz [38] investigated calibrated model-based load ratings of reinforced concrete deck on steel stringer bridges in which the bridge model was updated based on vibration response and BGCI nodal deflections. In order to match both responses in the updating process, they used an objective function in the form of a weighted sum of errors between analytical and experimental deflections, modal frequencies, modal assurance criteria, and order of modes. They used a staged updating method in which unknown model parameters were grouped into four main groups of element rigidity of longitudinal and transverse members, nodal lumped mass at joints, and support spring coefficients. Automatic model updating was then achieved using a code which ran the model for different parameter groups in an iterative manner while trying to minimize the objective function. The researchers went on to use their framework on data from tests conducted on an existing three-span concrete-deck-on-steel-stringer bridge built in 1968. They did not provide information on the test methods and details, but used 11 modes identified from vibration tests. As a main objective of this research, they studied the effect of the level of modeling by comparing the efficiency of 2D grid models versus full 3D models and concluded that the 2D grid models can

be sufficiently and effectively used for model updating and model-based load rating of the abovementioned bridge type. The writers also argue that the simultaneous consideration of static (BGCI) and dynamic response is important because a model updated solely based on modal properties may converge to an incorrect stiffness state because models with different stiffness and masses may produce the same modal properties.

Kim et al. [39, 40] used operational vibration data to devise a probabilistic model for load rating evaluation. As discussed before, objective functions for the model updating optimization problem are usually formed by a weighted sum of errors in different responses. The authors argue that for different sets of weights, each time a different optimization problem is solved and a different set of calibrated parameters are found resulting in a family of calibrated FEM models. The models were then used to calculate model-based load ratings resulting in a distribution of load ratings which is a tool to account for uncertainties in load ratings. The proposed process was then applied on a steel box-girder bridge with reinforced concrete slab in Korea. Ambient vibration measurement was done to obtain frequencies and mode shapes while a static truck test provided deflection response. 2D grid models incorporating line elements and effective widths for deck were built and over 70 model parameters including bearing stiffness values, elastic moduli, material density and section properties were used in the updating. Five different values for weights resulted in 67 calibrated models. Distribution of load ratings showed considerable variation but resulted in average load rating values close to load ratings performed using a detailed full 3D FEM model previously manually updated to highest precision.

Caglayan et al. [41] conducted static and dynamic tests on a monumental mass concrete arch railroad bridge built in 1912 in Turkey. Frequencies, modal assurance criteria, and damping factors of the first five modes were extracted from the free vibration acceleration data gathered after a test train passed the bridge. They also used tilt meters along the length of the bridge on the deck to measure slopes before and after loading and convert it to deflections. The experimental modal properties and deflection data were used to update a 3D FEM model with elastic material behavior. Sensitivity analyses showed that the stiffness of bearing springs and joint lumped masses were the most influential model parameters in matching the dynamic behavior of the bridge and were thus selected as the unknown model parameters. The model was then used to calculate strains under dead and live loads which were then used for load rating. For this bridge, model updating provided the following benefits: (1) Experimental stress measurements were very difficult to perform because of the lack of access to the underside of the bridge due to the excessive height of the bridge and FEM analysis was the possible option for stress evaluation in different members (2) Proof testing was not an option because the structure was old and monumental (3) The age of the bridge and its unique structural system made it impossible to use regular analytical calculations. They also noted that they had used modal properties to update the model globally and the strain data for local updating.

In this section, published research works on the implementation of vibration-calibrated model-based load ratings were reviewed with a special focus on the case studies, advantages, disadvantages and issues encountered in the application of this approach for load rating of bridges. These topics are further discussed in the next section and the lessons learned and future research needs are emphasized with the aim of encouraging the development and widespread adoption of the vibration-calibrated model-based approach for the load rating and safety assessment of US bridge infrastructure.

18.1.4 Discussion and Future Research

Vibration-calibrated model-based load rating is a new and promising approach aimed at taking advantage of the strengths of both analytical and empirical load ratings while reducing the cost and labor demands compared with empirical load test methods. This method uses a refined FEM model to accurately characterize load transfer. Information on the real material, boundary, and continuity conditions required for accurate load ratings are indirectly accounted for in the model updating process. Likewise, deteriorations and other unintended field factors are accounted for in this method through their effect on the experimental vibration response and thus the calibrated FEM model. The fact that this method essentially involves a refined analytical model, which is adjusted and calibrated to replicate the observed behavior in tests, states why the method is expected to have a significantly more realistic and accurate result than the conventional analytical methods. However, various aspects of the vibration-calibrated model-based load ratings reviewed in this paper revealed three groups of factors as most influential on the quality of load rating results:

- Efficiency of experimental vibration data: quality of collected vibration data, sufficiency of the acceleration sensor network, accuracy of modal identification methods.
- Sufficiency of numerical modeling: simplifying assumptions in modeling such as sufficient representation of structural and non-structural members such as parapets, railings, sidewalks, etc., level of modeling (1D, 2D or 3D), material properties and models employed, numerical discretization and solution.

Table 18.1 Comparison of vibration-based and strain-based tests for load rating

Test feature	Vibration-based	Strain-based
Test truck deployment	Not needed	Needed
Underside accessibility	Not needed	Needed
Traffic interruption	Minimal	Substantial
Time demand	A few hours	A few days
Post-processing	Substantial	Minimal

- Performance of the calibration process: Adequacy of model parameters selected for updating, choice of objective function, and efficiency of the optimization process.

Future research mainly in the form of sensitivity analyses is needed to characterize the effect of these parameters on the results, performance, and robustness of the method.

Vibration-calibrated model-based load rating provides several advantages over the conventional empirical load rating methods. It is less demanding in terms of cost, time and resources. Another significant advantage is that once you have a calibrated model, you can evaluate its behavior under complex moving load scenarios and different types of vehicles (state legal truck, AASHTO trucks, overweight loads etc.). Also, a previously calibrated model can later be used for damage detection and model-based structural health monitoring (SHM) and also for the design of possibly required future retrofit plans [32]. Such models can also be used to investigate the effects of hypothetical damage scenarios [42].

In addition, they do not require test trucks and multiple runs causing full closure of the bridge for a long period of time. As discussed before, vibration excitations can be achieved using an instrumented impact hammer operated by one person or even without the need for intentional excitement in the case of ambient and operational vibration. This makes vibration tests significantly fast and easy to perform and minimizes traffic interruption. Furthermore, vibration tests are more flexible in terms of accessibility. Oftentimes, all the instrumentation can be brought to the top surface of the deck which eliminates the need for traffic obstruction under the bridge (if the bridge crosses another road). It also eliminates the difficulties associated with installing sensing equipment when the bridge crosses a river or when the height of the bridge from the riverbed makes it difficult or impossible to reach the underside. Table 18.1 summarizes the pros and cons of the vibration-based tests versus the conventional strain-based tests using test truck loadings.

When testing a reinforced concrete bridge structure, accelerometers may demonstrate another advantage as cracks are a major factor in these structures and special considerations are needed to accurately measure load effects from surface strain measurements in the presence of cracks. Accelerometers however provide information about the global behavior of the bridge and are thus less sensitive to surface cracks [12].

In spite of the above advantages for vibration-based load ratings, a number of limitations, questions, and challenges can be identified in the application and interpretation of this method. A question about the validity of using vibration tests for load rating is load-dependency of some of the field factors. This means that some unforeseen and unintended mechanisms are only activated at certain load levels [6]. For example, a concrete deck on steel girders without shear studs is considered to have a composite behavior due to friction and adhesion under low load levels, while the deck and girders will act separately at higher design-level loads. The same is true about many of unintended fixity and continuity mechanisms. Vibration testing is conducted usually at very low load levels, thus it is questionable whether the results of such tests are always generalizable to strength limit states where some of those unintended mechanism may be deactivated. Future research is needed to evaluate the significance of such effects.

As discussed before, vibration-calibrated model-based load rating, requires an FEM model to be built and calibrated. However, in some cases, construction of an accurate and reliable model is not easy or possible for a bridge. Examples are bridges where as-built information including structural drawings, details, and material properties are missing or insufficient, bridges with previous repairs or reconstructions or with excessive uncertainties in details and specifications. In such cases, vibration-calibrated model-based methods will be insufficient and only proof tests, which do not need a model, can be used [43, 44].

As discussed in the first section, a major unknown in the behavior and analysis of bridge structures is load transfer or, more specifically, transverse load distribution between superstructure elements. In a strain-based load test, the magnitude of strains in different girders helps determine load distribution factors for the girders. On the other hand, in a vibration test, acceleration data is usually obtained from accelerometers installed on the deck and will then be used to calculate the global modal parameters. Therefore, while vibration tests are efficient in evaluating the global stiffness of the bridge, they are less informative in terms of member distribution behavior. As load ratings are calculated based on the weakest member in the system, they highly rely on distribution behavior and a modal test is expected to provide a less accurate load rating than static strain measurements if significant local phenomena exist in the structure. This issue is more significant in multi-girder bridge

systems where the strength of the superstructure is concentrated in a number of separate girders. However, in continuous superstructure systems such as RC slab bridges (without girders), which are generally used for shorter spans, this won't be a major concern as the continuous deck locally redistributes load in both directions.

A close look at the publications on vibration-calibrated model-based load rating cited in this paper shows that there is a serious shortage of performance evaluations and comparisons between the different load rating approaches referred to in this paper. Future research is needed where one bridge structure is load rated using different analytical, empirical and hybrid approaches and comparisons are conducted on the results. Particularly, comparison of the accuracy of the new vibration-calibrated model-based load rating approach with other load ratings using strain or the conventional diagnostic or proof load tests will shed further light on the performance, possible limitations, and domain of application of the vibration-calibrated model-based load ratings.

18.2 Conclusions

This paper studied a new hybrid analytical-empirical approach to load rating bridge structures through vibration testing and FEM model updating. In response to the highly approximate and oftentimes overly conservative nature of analytical load rating methods, and the inhibiting cost and resource demand associated with empirical load tests, the vibration-calibrated model-based load rating method has been recently introduced in which a vibration test is performed on a bridge and the identified modal characteristics are used to calibrate an FEM model which is later used for load rating. A review of the research on the application of this method reveals several advantages including increased speed, reduced cost, and minimal traffic interruption. Also, both impact tests using instrumented hammers or mechanical shakers, and ambient and operational vibration tests do not require test trucks and the acceleration data can be easily collected using accelerometers installed on the deck, thus eliminating the need to access the underside of the deck. However, the method is not able to address cases where structural drawings or details are insufficient or unreliable to build a model. Furthermore, the load-dependency of some of the unforeseen and unintended field factors is not addressed in this method due to the relatively low level of loads in a vibration test. In addition, vibration-based calibration only accounts for global response while strain-based static load tests can capture local load transfer behavior and transverse distribution factors which may affect the accuracy and efficiency of the results in deck-on-girder type bridges. However, these issues are not currently covered in the existing literature and future research on these topics and comparisons with load ratings using conventional analytical and empirical methods is seriously required.

References

1. Klaesson, J., Johansson, B., Karlsson, C.: Metropolitan Regions: Knowledge Infrastructures of the Global Economy. Springer, New York (2013)
2. Water, D.: Report Card for America's Infrastructure. American Society of Civil Engineers, Reston (2009)
3. Audit of Oversight of Load Ratings and Postings on Structurally Deficient Bridges on the National Highway System, MH-2006-043. U.S. Department of Transportation Inspector General (2006)
4. Wardhana, K., Hadipriono, F.C.: Analysis of recent bridge failures in the United States. J. Perform. Constr. Facil. **17**(3), 144–150 (2003)
5. McLinn, J.: Major bridge collapses in the US, and around the world. IEEE Reliability Society 2009 Annual Technology Report (2009)
6. Cai, C.S., Shahawy, M.: Understanding capacity rating of bridges from load tests. Pract. Period. Struct. Des. Constr. **8**(4), 209–216 (2003)
7. AASHTO, The Manual for Bridge Evaluation. American Association of State Highway and Transportation Officials, Washington, DC (2011)
8. AASHTO, AASHTO LRFD Bridge Design Specifications. Vol. 6. American Association of State Highway and Transportation Officials, Washington, DC (2012)
9. USDOT, National Bridge Inspections Standards Regulation (NBIS). US Department of Transportation, Washington, DC (2004)
10. Alipour, M.G.A., Harris, D.K., Ozbulut, O.E., Barnes, L.E.: A data-driven approach for automated operational safety evaluation of the National Inventory of Reinforced Concrete Slab Bridges. Transportation Research Board (TRB), 95th Annual Meeting, Washington, DC (2016)
11. Graybeal, B.A., et al.: Visual inspection of highway bridges. J. Nondestr. Eval. **21**(3), 67–83 (2002)
12. Chowdhury, M.R., Ray, J.C.: Accelerometers for bridge load testing. NDT & E Int. **36**(4), 237–244 (2003)
13. Son, B.-J., Lee, S.-Y., Ji, H.-S.: Long-term performance of a fiber-reinforced polymer slab bridge superstructure-field load test and ratings. Composites Part B Eng. **45**(1), 644–656 (2013)
14. Gangone, M.V., Whelan, M.J., Janoyan, K.D.: Wireless monitoring of a multispan bridge superstructure for diagnostic load testing and system identification. Comput. Aided Civ. Infrastruct. Eng. **26**(7), 560–579 (2011)
15. Sanayei, M., et al.: Instrumentation, nondestructive testing, and finite-element model updating for bridge evaluation using strain measurements. J. Bridge Eng. **17**(1), 130–138 (2011)
16. Laurendeau, M., et al: Live-load response of a 65-year-old Pratt Truss Bridge. J. Perform. Constr. Facil. p. 04014168 (2014)

17. Sanayei, M., et al.: Load rating of a fully instrumented bridge: comparison of LRFR approaches. J. Perform. Constr. Facil. p. 04015019 (2015)
18. FHWA. National bridge inventory. http://www.fhwa.dot.gov/bridge/nbi.htm (2014)
19. Kwasniewski, L., et al.: Experimental evaluation of dynamic effects for a selected highway bridge. J. Perform. Constr. Facil. **20**(3), 253–260 (2006)
20. Farrar, C.R., et al.: Excitation methods for bridge structures. In: Society for Experimental Mechanics, 17 th International Modal Analysis Conference. Citeseer (1999)
21. Jaishi, B., Ren, W.-X.: Structural finite element model updating using ambient vibration test results. J. Struct. Eng. **131**(4), 617–628 (2005)
22. Green, M.: Modal test methods for bridges: a review. In: Proceedings of the 13th International Modal Analysis Conference (1995)
23. Salawu, O.S., Williams, C.: Review of full-scale dynamic testing of bridge structures. Eng. Struct. **17**(2), 113–121 (1995)
24. Ewins, D.J.: Modal Testing: Theory and Practice, vol. 6. Research Studies Press, Letchworth (1995)
25. Brincker, R., Zhang, L., Andersen, P.: Modal identification from ambient responses using frequency domain decomposition. In: Proceedings of the 18th International Modal Analysis Conference (IMAC), San Antonio (2000)
26. Maia, N.M.M., Silva, J.M.M.: Theoretical and Experimental Modal Analysis. Research Studies Press, Taunton (1997)
27. Mottershead, J., Friswell, M.: Model updating in structural dynamics: a survey. J. Sound Vib. **167**(2), 347–375 (1993)
28. Doebling, S.W., et al.: Damage identification and health monitoring of structural and mechanical systems from changes in their vibration characteristics: a literature review. Los Alamos National Laboratory, New Mexico (1996)
29. Ribeiro, D., et al.: Finite element model updating of a bowstring-arch railway bridge based on experimental modal parameters. Eng. Struct. **40**, 413–435 (2012)
30. Živanović, S., Pavic, A., Reynolds, P.: Modal testing and FE model tuning of a lively footbridge structure. Eng. Struct. **28**(6), 857–868 (2006)
31. Sipple, J.D., Sanayei, M.: Full-scale bridge finite-element model calibration using measured frequency-response functions. J. Bridge Eng. **20**(9): (2014)
32. Brownjohn, J.M.W., et al.: Assessment of highway bridge upgrading by dynamic testing and finite-element model updating. J. Bridge Eng. **8**(3), 162–172 (2003)
33. Uzgider, E., et al.: Performance of a tied-arch reinforced concrete railway bridge: rating, safety assessment, and bond length evaluation. J. Perform. Constr. Facil. **23**(5), 366–371 (2009)
34. Ren, W.-X., Blandford, G.E., Harik, I.E.: Roebling suspension bridge. I: finite-element model and free vibration response. J. Bridge Eng. **9**(2), 110–118 (2004)
35. Ren, W.-X., et al.: Roebling suspension bridge. II: ambient testing and live-load response. J. Bridge Eng. **9**(2), 119–126 (2004)
36. Wang, X., et al.: Overview of a modal-based condition assessment procedure. J. Bridge Eng. **4**, 460–497 (2005)
37. Lenett, M.S.: Global condition assessment using modal analysis and flexibility. In: Proceedings of SPIE—The International Society for Optical Engineering (1999)
38. Turer, A., Shahrooz, B.M.: Load rating of concrete-deck-on-steel-stringer bridges using field-calibrated 2D-grid models. Eng. Struct. **33**(4), 1267–1276 (2011)
39. Kim, H.-J., Kim, H.-K., Park, J.Y.: Reliability-based evaluation of load carrying capacity for a composite box girder bridge. KSCE J. Civil Eng. **17**(3), 575–583 (2013)
40. Kim, H.-J., Park, W., Koh, H.-M.: Probabilistic performance assessment of highway bridges using operational monitoring data. In: IABSE Symposium Report. International Association for Bridge and Structural Engineering (2014)
41. Caglayan, B.O., Ozakgul, K., Tezer, O.: Assessment of a concrete arch bridge using static and dynamic load tests. Struct. Eng. Mech. **41**(1), 83–94 (2012)
42. Bell, E.S., et al.: Objective load rating of a steel-girder bridge using structural modeling and health monitoring. J. Struct. Eng. **139**(10), 1771–1779 (2013)
43. Aguilar, C.V., et al.: Load rating a prestressed concrete double-tee beam bridge without plans by proof testing. In: Transportation Research Board 94th Annual Meeting (2015)
44. Faber, M.H., Val, D.V., Stewart, M.G.: Proof load testing for bridge assessment and upgrading. Eng. Struct. **22**(12), 1677–1689 (2000)

Chapter 19
Finite Element Model Updating of French Creek Bridge

Xiang Li, Yavuz Kaya, and Carlos Ventura

Abstract Built in 1993, the French Creek Bridge is located on highway 19 on Vancouver Island, BC, Canada. The bridge is part of the British Columbia Smart Infrastructure Monitoring System (BCSIMS), funded by the Ministry of Transportation and Infrastructure (MoTI) BC, Canada. The BCSIMS is a real-time seismic monitoring program that continuously assesses the seismic conditions of the selected bridges in BC. As part of this seismic monitoring program, an Ambient Vibration Test (AVT) was conducted in September 2014 to extract to modal properties (modal frequencies, modal damping ratios, and mode shapes) of the bridge. The Finite Element (FE) model of the bridge, developed in SAP2000, is updated using the extracted modal properties. The FE model will then be used to assess the seismic performance of the bridge in accordance with the new Canadian Highway Bridge Design Code, 2015, and this study only presents the results of the first of this assessment: the FE model updating of the bridge.

Keywords Ambient vibration test • Modal analysis • System identification • Finite element model updating • Highway bridge

19.1 Introduction

Launched in 2009 by British Columbia Ministry of Transportation and University of British Columbia, the BCSIMS monitoring program is developed to integrate the Strong Motion Network (consists of 156 Internet Accelerometers stations which maintained by Geologic Survey of Canada) and the Structural Health Monitoring network (consists of fifteen instrumented structures monitored by UBC) in British Columbia [1]. One of the main purposes of the program is to establish a real-time seismic structural response system to provide instant inspection and rapid damage assessment for the Ministry's structures. The French Creek Bridge (FCB), is located on N 49°19.36′ and W 124°24.71′ of geographical coordinates near Parksville, Vancouver Island, British Columbia, Canada. Designed as a disaster-route bridge, the FCB carries the Inland Island Highway 19 over French Creek from south to north. It was designed in 1993 and opened in 1996, in 1997 it was selected by MoTI BC as one of the seismic monitoring sites, the bridge was instrumented with 12 sensors and monitored since then.

In September 2014, an AVT was conducted on the FCB. In this paper the data acquired by AVT was used to extract the dynamic characteristics (natural frequencies, mode shapes, and damping ratio) of the FCB. Commercially available software ARTeMIS® [2] was utilized to carry out the data analysis and modal identification. As an essential part of the structure information, a 3D FE model was developed in CSibridge® [3] and SAP2000® [4], the model was manually updated based on the AVT results, and the updated modal results are presented and discussed in this paper.

19.2 Description of the French Creek Bridge

As shown in Fig. 19.1, the French Creek Bridge is 212 m long with 24.2 m width, and it carries four vehicle lanes and one pedestrian lane at each side of the bridge. Slope of the bridge floor is 1.6 % that makes the elevation descents from south to north. The bridge is composed of five spans and is supported by three piers in the middle, one abutment at each end of the bridge, and one pile bent 10 m away from the south end. The superstructure of the bridge is composed of reinforced concrete

X. Li (✉) • Y. Kaya • C. Ventura
University of British Columbia, Vancouver, BC, Canada
e-mail: lxmichael52@gmail.com

S. Pakzad, C. Juan (eds.), *Dynamics of Civil Structures, Volume 2*, Conference Proceedings of the Society for Experimental Mechanics Series, DOI 10.1007/978-3-319-29751-4_19

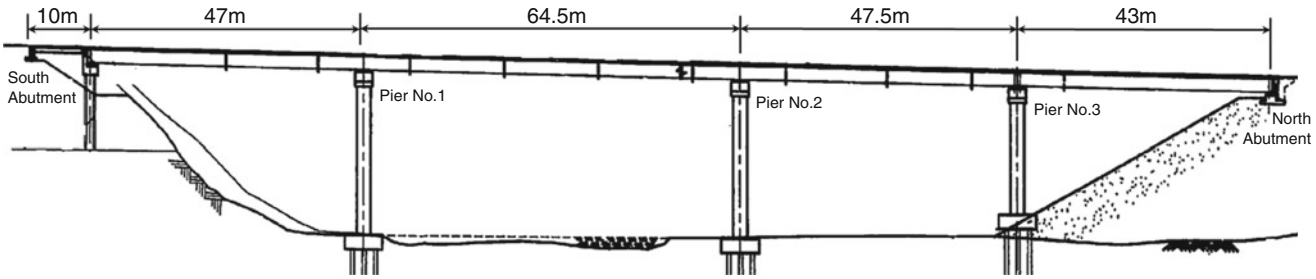

Fig. 19.1 Elevation view of French Creek Bridge

Fig. 19.2 Side view of concrete deck-steel girder system (*left*) and piers in middle spans (*right*)

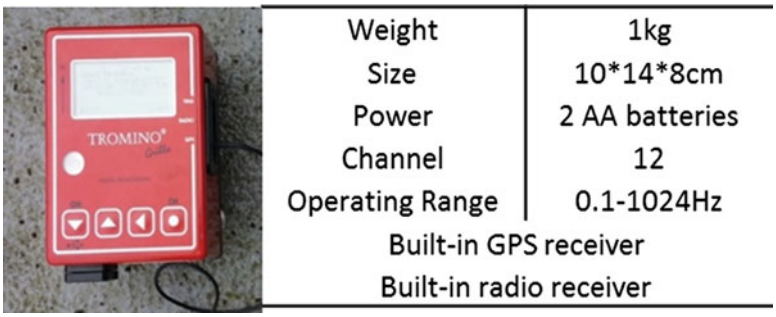

Fig. 19.3 TROMINO® sensor and specification

deck casted on six W-shaped steel girders, which develop throughout the bridge span (shown in Fig. 19.2). All girders are supported by fixed bearings and expansion bearings. The fixed bearings are located at all three piers and the expansion bearings are located at the south pile bent and north abutment. There are two expansion joints that divide the deck slab into three parts: one is located at the south pile bent and another is at the north abutment. Each pier is composed of two identical columns and a cap beam above them, the cap beam is connected to the bottom of steel girders by fix bearings. At each pier, both columns are supported by twenty-odd pipe piles: all piles are driven into the bedrock beneath the foundation soil.

19.3 Ambient Vibration Testing and Results

The AVT was conducted on September 6th 2014, and the TROMINO® [5] sensors are used to capture the dynamic properties of the bridge. Sensor No. 1 act as master sensor that controls rest of the sensors. Configuration and main technical specifications of TROMINO® are shown in Fig. 19.3.

Setup#1		Setup#2		Setup#3		Setup#4		Setup#5		Setup#6		Setup#7	
Sensor#	Location	Sensor#	Location	Sensor#	Location	Sensor#	Location	Sensor#	Location	Sensor#	Location	Sensor#	Location
1	11	1	11	1	11	1	11	1	11	1	11	1	11
2	7	2	8	2	16	2	30	2	31	2	38	2	39
3	6	3	9	3	17	3	29	3	32	3	39	3	45
4	5	4	10	4	18	4	28	4	33	4	40	4	46
5	4	5	12	5	19	5	27	5	34	5	41	5	23
6	3	6	13	6	20	6	26	6	35	6	42	6	47
7	2	7	14	7	21	7	25	7	36	7	43	7	48
8	1	8	15	8	22	8	24	8	37	8	44	8	49

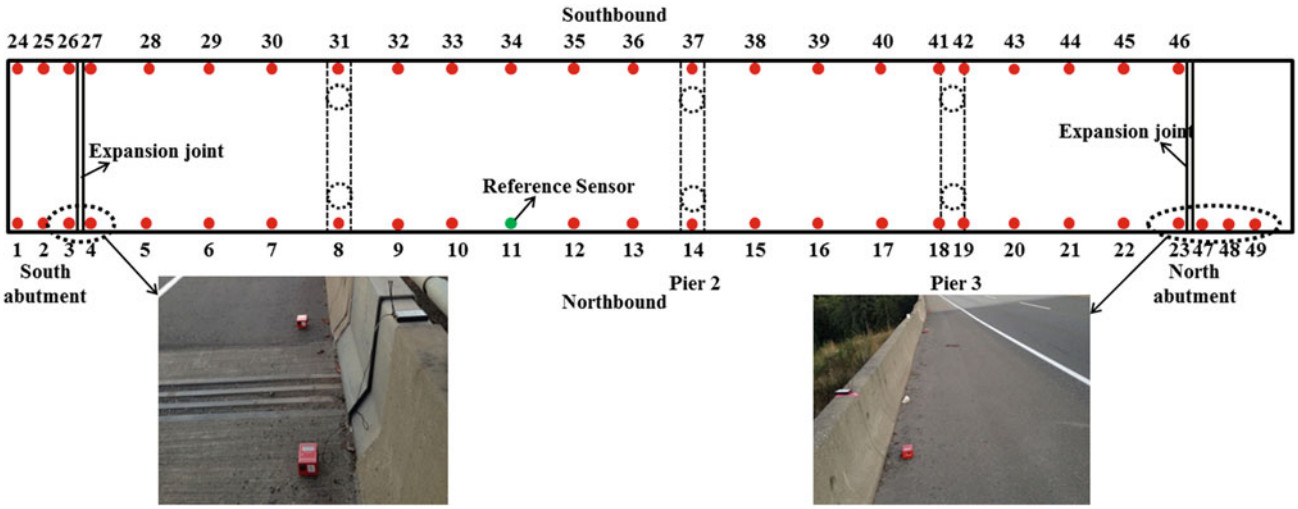

Fig. 19.4 Setup plans and sensor locations of all setups

Totally eight sensors were utilized in every setup of the test. Sensor No. 1 is selected as reference sensor and been placed at the middle span of southbound between pier 1 and 2, the reference sensor's location will remain unchanged throughout the entire test. During each setup, all sensors were placed parallel to the bridge close to the edge of the bridge and face to the north abutment. Figure 19.4 shows the layout details of all setups, as shown in the figure since the vibration characters of both sides of the expansion joint are quite different; two sensors were placed at both sides with approximately 1 m distance in between. The acquisition length of each setup is approximately 30 min with sampling rate of 128 Hz.

After the test, further data processing, filtering and modal identification are done using ARTeMIS Modal Pro® (SVIBS). The inbuilt Frequency Domain Decomposition (FDD) [6] and Enhanced Frequency Domain Decomposition (EFDD) [7] techniques are used to identify the modal properties of the bridge. Figure 19.5 presents the spectral content of the recorded AVT. Totally eight modes are identified, their modal shapes and corresponding frequencies are shown in Fig. 19.6.

19.4 Finite Element Modeling of the Bridge

A FE model of the French Creek Bridge (as shown in Fig. 19.5) is built based on the structural drawings provided by MoT BC. First, the model is developed in integrated 3D bridge analysis and design program called CSibridge® 2015. The major components of the French Creek Bridge including superstructure, bearings, abutments, bents, piers and piles are modeled using frame, shell and link elements created by program. After preliminary modeling of the bridge, the model is converted into program SAP2000® for further refinement (Fig. 19.7).

The structural drawings provide the material properties of concrete and structural steel of the bridge. Concrete materials are divided into two groups: the deck concrete and the foundation concrete. Deck concrete are only used by deck section, foundation concrete are used to build abutments, bents and piers. All steels are sorted into structural steel and reinforcing steel. Summary of material properties used in FE model is listed in Table 19.1.

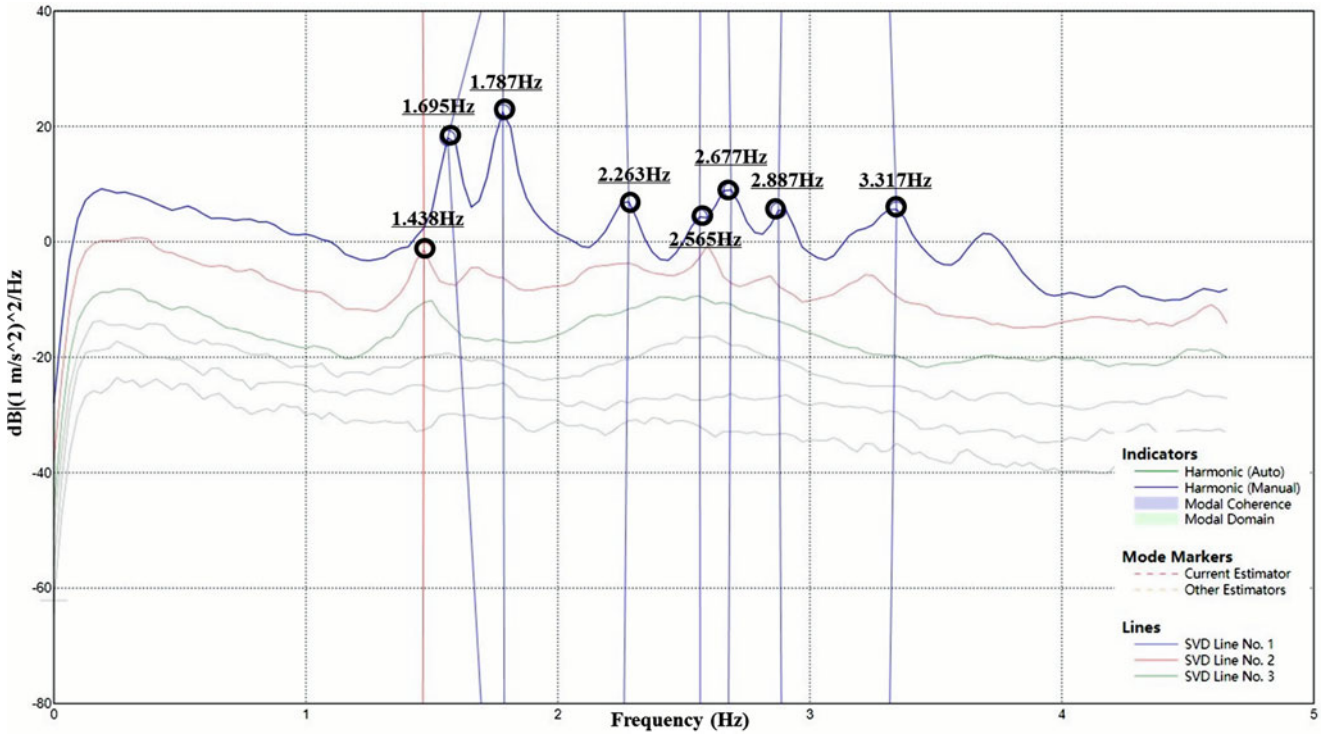

Fig. 19.5 Peak-picking of singular values of spectral densities (ARTeMIS®)

The bridge deck section is combined by reinforced concrete deck with tee beams and six W section steel girders that support underneath throughout the entire span of the bridge. Figure 19.8 compares the sections in drawing and FE model. Section of external and internal girders varies throughout the span while concrete deck section remains the same. Typical intermediate diaphragms are made of steel frames with WT section. All steel girders and diaphragms are modelled by regular 3D frame element and the concrete deck is modelled by thin shell element. Since the connections between the expansion joints are nonstructural, the stiffness of the connections can be ignored. In the FEM, the concrete decking at the expansion joint is divided in two by removing part of the shell element, steel girders are also disconnected where expansion joints is located. Section of bent caps are simplified as rectangular and columns remains as circle section reinforced by longitudinal and spiral rebar, both bent caps and columns are modelled by 3D beam-column elements. Example of column section is shown in Fig. 19.9.

There are two types of bearings used in the FCB, the fixed pot bearings and unidirectional sliding bearings. In FEM, the bearings are modeled by massless rigid link elements, all bearings are assumed to remain elastic. For the fixed bearing, stiffness in all three translational DOFs is considered as rigid, however the elastomer inside allows rotation of the piston [8], the rotational stiffness of the bearing is calculated by equations suggested by Akogul [9]. By adding a unidirectional sliding component on the pot bearing, the fixed bearing becomes a sliding bearing that allows horizontal movement (DOF U2) along the bridge, the stiffness in longitudinal direction along the bridge is merely contributed by the friction between PTFE (Teflon) surfaces. All abutments are simply modelled as infinite rigid since they were disconnected from the main structure by expansion joints and sliding bearings at both ends. To properly model the soil-pile interaction effect, the analytical subgrade reaction model (Winkler Model) [10, 11] is utilized. Piles are modelled as regular frame element and the pile cap is considered as rigid body, the surrounding soil is modeled as an array of soil spring using linear link element, stiffness of the soil spring are calculated following equations given by Das [12].

The natural frequencies and corresponding mode shapes of the French Creek Bridge are evaluated by modal analysis function in SAP2000®. Summary of the initial finite element results are listed as part of the information provided in Table 19.2, corresponding mode shapes are presented in Fig. 19.6.

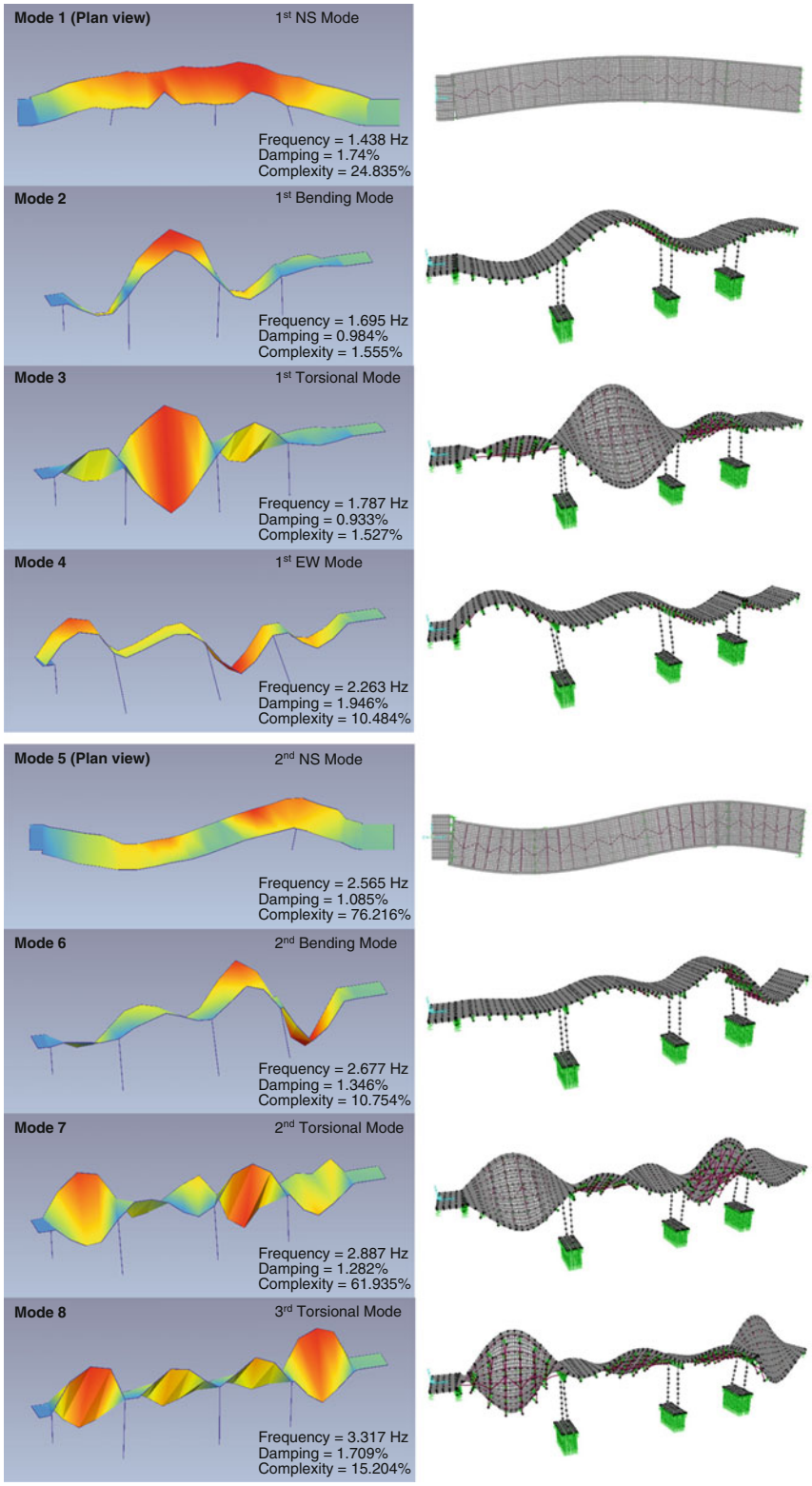

Fig. 19.6 Modal identification results from AVT (ARTeMIS®) (*left*) and FEM (SAP2000) (*right*)

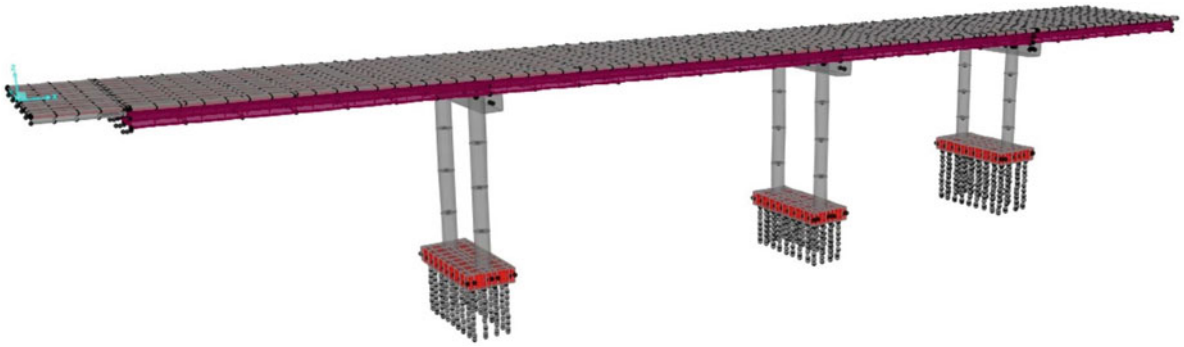

Fig. 19.7 Overview of the FE model of French Creek Bridge

Table 19.1 Material properties of concrete and steel

Material type	F′c (MPa)	Ec (MPa)	Density (kg/m^3)	Poisson ratio
Foundation concrete	30	24,700	2400	0.2
Deck concrete	35	26,600	2400	0.2
Material type	Fy (MPa)	E (MPa)	Density (kg/m^3)	Poisson ratio
Structural steel	350	200,000	7900	0.3
Reinforcing steel	400	200,000	7900	0.3

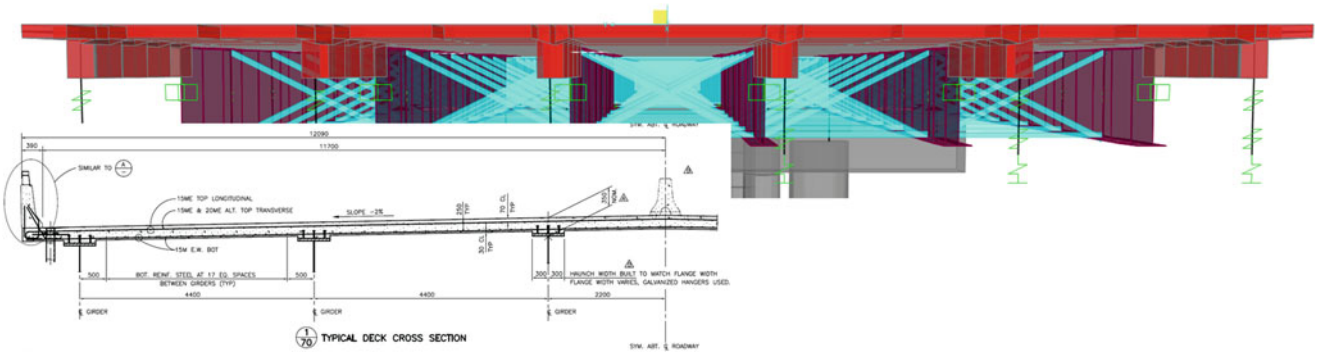

Fig. 19.8 Deck section in structural drawing and FE model

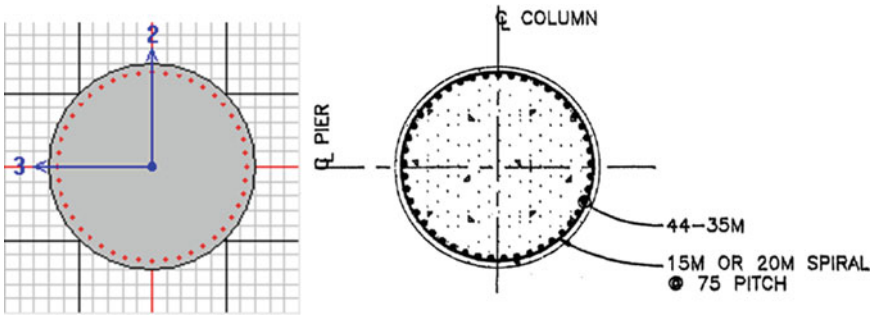

Fig. 19.9 Column section detail in FEM (*left*) and drawing (*right*)

19.5 Manual Model Updating

As described above, the finite element model of the French Creek Bridge is developed based on the structural drawing and series of idealized assumptions, which may not be about to represent the real behavior of the actual structure. As shown in Table 19.2, significant deviation exists between experimental and analytical results. In order to achieve a more accurate prediction of the dynamic response of the bridge, a sensitivity-based manual model updating procedure is conducted on the initial FE model.

Table 19.2 Natural frequencies before and after updating

Mode	Experimental frequency/Hz	f_{FEA} /Hz (before)	Error/%	f_{FEA} /Hz (after)	Error/%	Frequency changed/%
1	1.438	1.176	−22.28	1.413	−1.77	20.15
2	1.695	1.592	−6.47	1.615	−4.95	1.44
3	1.787	1.852	3.51	1.891	5.50	2.11
4	2.263	1.916	−18.11	2.364	4.27	23.38
5	2.565	2.332	−9.99	2.686	4.50	15.18
6	2.677	2.634	−1.63	2.777	3.60	5.43
7	2.887	2.950	2.14	3.172	8.98	7.53
8	3.317	3.219	−3.04	3.718	10.79	15.50

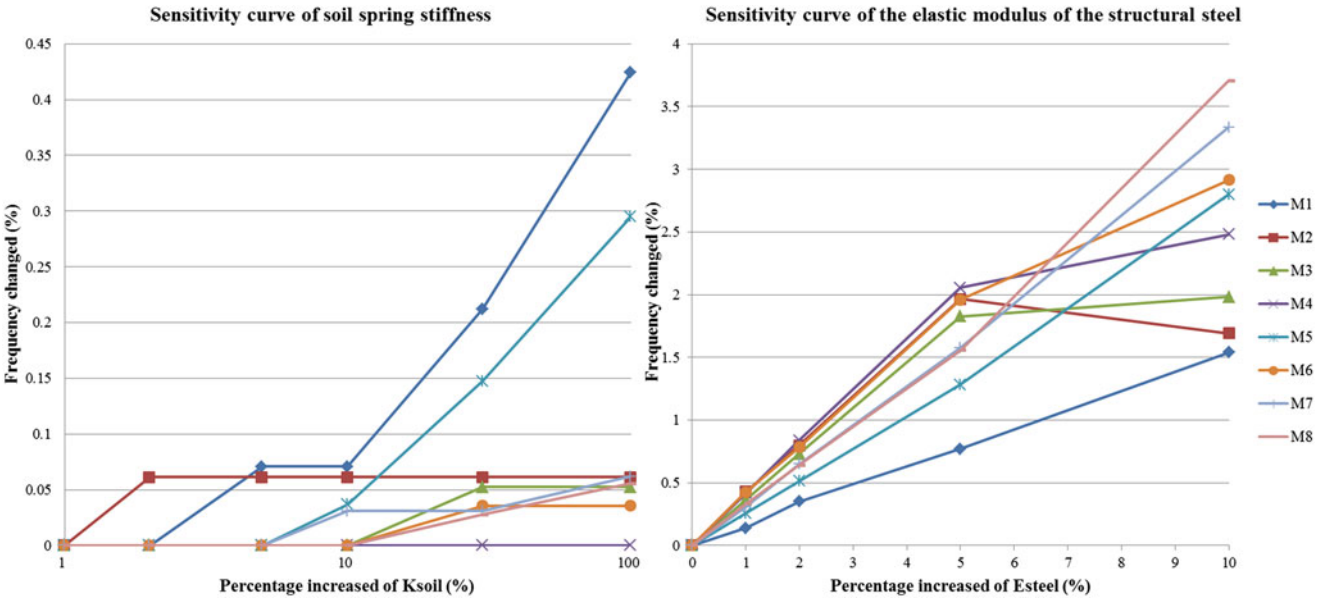

Fig. 19.10 Sensitivity analysis curves of K_{soil} (*left*) and E_{steel} (*right*)

19.5.1 Sensitivity Analysis

In order to select the proper variable and improve the efficiency of optimization and updating, the sensitivity of the modal parameter to the modal frequencies need to be studied first. By inspection, several physical properties are selected for the sensitivity analysis. Four different types of parameters were considered for updating: (i) mass density of the concrete and steel, (ii) elastic modulus of the concrete and steel, (iii) translational and rotation stiffness of bearing link and pile soil spring, (iv) moment of inertial of the girder, decking and column sections.

For each parameter, the original value is altered by 2, 5, 10, 20, 50 and 100 % at each time while other variables remain unchanged, after each alteration, the corresponding modal frequencies are calculated and recorded. Then the influence curves of each parameter on modal frequencies are plotted, as percentage of modal frequency changed against percentage of parameter value changed. Figure 19.10 shows an example of the sensitivity curve of two of the parameters: the elastic modulus of the structural steel E_{steel} and the stiffness of the soil foundation spring K_{soil}. For the E_{steel}, it can be observed that the values of all modal frequencies are quite sensitive to the value of E_{steel}: when the value increased 10 % mode 1 increased about 1.5 % and mode 8 get a more significant 3.7 % increase. On the other hand, there is less than 0.5 % change in all modes even though the K_{soil} value has increased 100 %. Therefore it can be concluded that E_{steel} has significant effect on dynamic characteristic of the structure and it is selected as one of the update parameters while the K_{soil} is ruled out.

Table 19.3 Parameters before and after updating

Parameter	Unit	Initial value	Updated value	Percent changed
E_1	MPa	26,600	31,000	16.54
E_2	MPa	24,700	30,000	21.46
E_3	MPa	200,000	196,000	−2.00
ρ_1	kg/m3	2400	2498	4.08
ρ_2	kg/m3	2400	2396	−0.17
ρ_3	kg/m3	7900	7933	0.42
K_{u2}	kN/mm	110	2500	2172.73
I_{col}	m4	1.74	1.91	9.77

19.5.2 Model Updating

By following the mothed described above, eight parameters (listed in Table 19.3) were chosen for the model optimization because of their influence on the dynamic property of the structure, other parameters such as soil spring stiffness will not be considered in further study, since they have very small effect on the dynamic characteristics of the structure. The eight parameters been considered in model updating are: E_1, E_2 and E_3 for modulus of elasticity of the decking concrete, foundation concrete and structural steel respectively; ρ_1, ρ_2 and ρ_3 for mass density of the three kinds of materials; K_{u2} for translational stiffness of the sliding bearing in bridge longitudinal direction and I_{col} for moment of inertial of the pier column.

In manual updating, the parameters are varied in the way that will improve the match between experimental and analytical results, then the modal results will be evaluated and the parameter will be reassigned with modified value, this "try-and-error" iterative process will repeat until a good match is obtained. For example it can be easily observed that the FE model of the bridge needs to be stiffened, so as the "trial" step, one reasonable way would be increasing the modulus of elasticity of the concrete and steel. During the trial if the result is not satisfactory, other factors could be added into consideration such as increasing the moment of inertial of the column section and the procedure repeats.

19.5.3 Results and Discussion

Table 19.2 shows the summary of the results, the natural frequencies before and after updating are listed and the ambient vibration test results are presented again for comparison purpose. And parameters before and after updating is summarized in Table 19.3.

It can be observed from Table 19.2 that the higher modes from updated model have bigger errors than initial model. The reason is that in order to match the first mode of the initial model, certain parameters are changed to increase the stiffness of the structure. However, when the structure's stiffness is high enough to match the first mode, the higher modal responses become "over stiffened". On the other hand, when the higher modes match the test results the structure become "too soft" and the first mode cannot have a good match. Since matching the first few modes is more important for finite element model to represent the actual structure, the low-error matches of the higher modes are sacrificed.

By comparison, it can be concluded that the stiffness of the concrete is been underestimated, probably because during construction the actual concrete strength is larger than strength grade. Also the decking concrete density is enlarged for 4 % may be due to the extra weight contributed by non-structural component such as asphalt pavement. Variable Ku2 has the most significant change among all factors, the stiffness is now a magnitude greater than the initial value. One reasonable explanation is that the stiffness in U2 direction at sliding bearing is not solely contributed by the friction between sliding surface, probably the assumption about the stiffness of the expansion joint above sliding bearing is incorrect, the non-structural connection joint may have a huge among of contribution to the stiffness value.

19.6 Conclusion

As part of the BCSIMS project, the French Creek Bridge located in Vancouver Island is selected for the seismic monitoring study. This paper presents the study process of the dynamic properties of the French Creek Bridge through both experimental and analytical method. In this study, a 3D finite element model is been developed based on the structural drawing provided,

then the model is been manually updated based on the ambient vibration test results. The first eight modes of the bridge are selected for matching the experimental and analytical results. Totally eight structural parameters are selected for updating based on the sensitivity analysis. During the update, in order to acquire a good match for the primary modes, the accuracy for the higher modes is compromised. But in general, frequencies calculated from the updated model have an overall closer match then initial model, therefore the updated model can reflect the dynamic characteristics of the bridge more accurately, it can be used for further study of nonlinear modeling and dynamic response analysis under seismic excitation.

References

1. Kaya, Y., et al.: British Columbia smart infrastructure monitoring system. EWSHM-7th European Workshop on Structural Health Monitoring (2014)
2. Solutions, Structural Vibration, ARTeMIS Extractor: Ambient Response Testing and Modal Identification Software, User's Manual (2001)
3. Computers and Structures Inc. (CSI), CSIBridge User's Manual-version 15, Berkeley (2011)
4. Computers and Structures Inc. (CSI). SAP2000 User's Manual-version 15, Berkeley (2011)
5. Micromed, Tromino User's manual, Micromed, 139pp (2012)
6. Brincker, R., Zhang, L., Andersen, P.: Modal identification of output-only systems using frequency domain decomposition. Smart Mater. Struct. **10**, 441 (2001)
7. Jacobsen, N.-J., Andersen, P., Brincker, R.: Using enhanced frequency domain decomposition as a robust technique to harmonic excitation in operational modal analysis. International Conference on Noise and Vibration Engineering (ISMA), Leuven (2006)
8. Canam Group Inc., Pot Bearings Introduction Manual (2012)
9. Akogul, C., Celik, O.C.: Effect of elastomeric bearing modeling parameters on the Seismis design of RC highway bridges with precast concrete girders. Proceedings of the 14th World Conference on Earthquake Engineering (2008)
10. Adhikary, S., Singh, Y., Paul, D.K.: Modelling of soil-foundation-structure system. Soil Dyn. Earthquake Eng. **61**, 13–28 (2014)
11. Selvadurai, A.P.S.: Elastic Analysis of Soil-Foundation Interaction. Elsevier, Amsterdam (2013)
12. Das, B.: Principles of Foundation Engineering. Cengage Learning, Boston (2015)

Chapter 20
Damage Detection of a Bridge Model After Simulated Ground Motion

C. Rainieri, D. Gargaro, G. Fabbrocino, L. Di Sarno, and A. Prota

Abstract Vibration-based damage detection techniques offer interesting opportunities for Structural Health Monitoring of strategic structures and infrastructures, such as bridges, and they foster the shift from time-based maintenance to condition-based maintenance. However, effective vibration-based damage detection requires accurate estimates of the modal parameters of the monitored structure automatically obtained from the analysis of the operational response of the structure.

In the present paper, the opportunities and limitations of automated output-only modal identification and modal-based damage detection for bridges are briefly reviewed. The results of an extensive experimental campaign on a scaled bridge model are then illustrated. The objective of the experimental tests was twofold. The dynamic response of the structure has been experimentally characterized for different support conditions (simply supported, with seismic isolation devices). After this first stage of analysis, an input ground motion has been applied by means of a couple of asynchronous shaking tables. As a result of the seismic input, the structure without seismic isolation devices was damaged. The effect of damage on the modal properties and the possibility to detect damage by means of selected damage features are discussed on the basis of the obtained experimental results.

Keywords Vibration based structural health monitoring • Damage detection • Operational modal analysis • Shaking table • Damage features

20.1 Introduction

Over the past decades serious structural damage and collapses have affected bridges in different countries as a result of earthquake shaking. Effective seismic protection is a fundamental requirement for these strategic structures, not only because of the possible consequences of a collapse in terms of life losses, but also because of the primary role in the management of earthquake crisis. Thus, a lot of research efforts have been focused on the evaluation and enhancement of the structural safety of existing bridges against hazardous natural events, such as earthquakes. Nevertheless, there is the need of developing further knowledge about the structural behaviour of structures designed according to obsolete design codes or in the absence of any consideration of seismic action, so that effective design countermeasures resulting in a given decrease of the probability of structural damage can be identified and applied. Traditionally, this task has been accomplished by mixing data and information obtained from laboratory tests and advanced numerical simulations. However, continuous monitoring of modal properties of full-scale structures has been recently recognized as an effective approach to gain knowledge about their dynamic and seismic behavior. As a result, several large research projects have been initiated in the field of civil engineering aimed at assessing the potential of modal-based Structural Health Monitoring (SHM) technologies to evaluate the seismic performance of existing bridges and to identify eventual structural damage. In this perspective, advanced SHM techniques can be addressed as innovative measures of seismic protection and performance assessment. Extensive surveys

C. Rainieri, Ph.D. (✉) • D. Gargaro • G. Fabbrocino
DiBT Department, Structural and Geotechnical Dynamics Laboratory StreGa, University of Molise, Viale Manzoni s.n.c.–86100, Campobasso, Italy
e-mail: carlo.rainieri@unimol.it; danilo.gargaro@unimol.it; giovanni.fabbrocino@unimol.it

L. Di Sarno
Engineering Department, University of Sannio, Corso Giuseppe Garibaldi 107-82100, Benevento, Italy
e-mail: ldisarno@unisannio.it

A. Prota
Department of Structures for Engineering and Architecture, University of Naples "Federico II", Via Claudio 21-80125, Naples
e-mail: andrea.prota@unina.it

S. Pakzad, C. Juan (eds.), *Dynamics of Civil Structures, Volume 2*, Conference Proceedings of the Society for Experimental Mechanics Series, DOI 10.1007/978-3-319-29751-4_20

and dedicated books are available in the literature about vibration-based SHM [1–3]. The monitoring process consists in the observation of the structure over long periods of time. Appropriate sensors and measurement systems continuously acquire records of relevant physical and mechanical parameters; damage sensitive features are then extracted from the collected data and analyzed to assess the health state of the structure.

From a general point of view, damage is defined as any change of the structure that adversely affects its performance [3]. This change can be in the form of stiffness change (for instance, cracking), mass change, connectivity change (for instance, looseness in a bolted joint) or boundary condition change (for instance, bridge scour). An effective SHM system should be able to automatically detect damage at an early stage [1]. Five damage detection levels have been defined [4]:

- Level 1: identification of damage existence;
- Level 2: localization of damage;
- Level 3: identification of the type of damage;
- Level 4: quantification of damage severity;
- Level 5: prediction of the remaining service life of the structure (prognosis).

Modal based damage detection starts by recognizing that the modal parameters depend on physical parameters (mass, stiffness and damping). Assuming that damage yields a change in the physical properties of the structure, this is reflected by a change in the modal properties. Thus, it is theoretically possible to identify damage from the analysis of the variations of the modal parameters, and a number of damage sensitive features have been defined in terms of modal parameters. Damage sensitive features can be defined in terms of natural frequencies and mode shapes. Natural frequency variations provide the easiest way to detect the presence of damage, because they can be accurately estimated even in the presence of a few sensors. However, the information they provide is limited to Level 1 damage detection. Thus, other features have been defined in terms of mode shapes and mode shape curvatures, because mode shapes can provide information also for damage location. However, they are typically estimated with lower accuracy with respect to natural frequencies.

In the present paper, the opportunities and limitations of automated output-only modal identification and modal-based damage detection for bridges are briefly reviewed in view of fast assessment of structures in the early earthquake aftershock. Some results of a recent comprehensive research program, funded by the Italian Ministry of Research through the Project PON-FESR 2007–2013 (PON01_02366, STRIT) "Tools and Technologies for the Management of the Transportation Infrastructures" and focused on the assessment and monitoring of as-built and retrofitted RC bridges, are illustrated. The objective of the experimental tests was twofold. The dynamic response of the structure has been experimentally characterized for different support conditions (simply supported, with seismic isolation devices). After this first stage of analysis, an input ground motion has been applied by means of a couple of asynchronous shaking tables [5]. As a result of the seismic input, the structure without seismic isolation devices was damaged. The effect of damage on the modal properties and the possibility to localize damage by means of selected damage features are discussed on the basis of the obtained experimental results.

20.2 Modal-Based SHM and Application to Bridges

Several applications of modal-based damage detection to bridges are reported in the literature (see, for instance, [3, 6–10]). Even if a comprehensive review is out of the scope of the paper, attention is herein focused on the application to bridges of continuous monitoring of the modal parameters and modal-based damage detection; in particular, advantages and limitations of these techniques are reviewed in view of fast assessment of structures in the early earthquake aftershock. The recent increase in the number of applications of modal based SHM to bridges takes advantage of the recent development of several algorithms for automated identification [11, 12] and tracking [13] of modal parameters based on Operational Modal Analysis (OMA) methods. Damage detection techniques based on changes of the modal parameters of the monitored structure over time are currently well established [14]. Thus, the continuous monitoring of modal parameters has a large potential in performance and health assessment of bridges in the early earthquake aftershock [1, 15, 16]. However, the effectiveness of modal based damage detection techniques depends on the appropriate selection of damage features and metrics [3].

About the selection of damage features, an ideal one is such that it is sensitive to damage and insensitive to the influence of environmental and operational factors. Unfortunately, one of the main drawbacks of modal based damage detection is the sensitivity of modal property estimates to environmental and operational conditions. These can cause changes in the estimates of the same order of magnitude of those induced by damage. As a consequence, the estimates have to be depurated from the effects of environmental factors in order to effectively detect damage. This issue has been addressed in several papers [10, 17, 18], and a number of techniques for compensation of environmental and operational effects on the estimated modal properties have been proposed. Some require measurements of the environmental and operational factors that influence the

estimates. Since the selection of the factors to be measured is typically not straightforward, statistical tools have been used as an alternative to correct the estimates without the need to measure the environmental and operational variables.

Another big issue concerning feature selection is that a given feature is not applicable to all damage scenarios. Thus, when multiple types of damage are possible, the extraction of a set of different damage features from the measured data can enhance the effectiveness of damage detection. Resonance frequencies have been widely used as sensitive feature for damage detection in bridges. However, even if their applicability as damage sensitive features is rather intuitive (the variations of mass, stiffness or boundary conditions induced by damage are reflected by variations of natural frequencies), actual applications pose significant technical challenges, the most important of which is that damage is usually a local phenomenon and as such it does not significantly alter the low-frequency global response of a structure that is measured by ambient vibration tests. Detection of local damage, therefore, requires the selection of damage features that are more sensitive to it than natural frequencies of the fundamental modes.

For a given damage feature, different metrics can provide a different quantification of the degree of modification induced by damage. For instance, when mode shape estimates are used as damage sensitive features and the MAC index [19] is adopted as a metric to quantify the degree of correlation or, alternatively, the variations of a given set of mode shapes after damage, it leads to a significant data compression, since it reduces the comparison of two vectors to a scalar. However, if the damage has not completely altered the mode shapes, the percentage changes in the MAC values are usually much smaller than the individual change of the mode shape components that are affected the most by the presence of damage [3]. This is because the MAC index is sensitive to large differences between the corresponding components of the vectors under comparison, but it is basically insensitive to small changes and small magnitudes of the modal displacements [20].

After the selection of damage sensitive features and the removal of environmental and operational effects, a number of tools can be applied for feature discrimination. Machine learning approaches are becoming very popular to this aim. They can be broadly classified as supervised and unsupervised learning approaches [3]. The former are applied when data are available for both the undamaged and damaged structure, while the latter are applied when reference data are available only for the structure in healthy state.

Whatever damage feature and metric are selected, accuracy of modal parameter estimates plays a fundamental role to ensure the success of damage detection [3]. Most of the available automated OMA algorithms suffer common drawbacks [11] that affect their accuracy. They are mainly related to the adoption of statically set thresholds and parameters that have to be tuned at startup [11]. Thus, an automated modal parameter identification procedure able to tackle the following challenges:

1. provide accurate and precise modal parameter estimates, including damping,
2. not rely on application-dependent parameters that have to be tuned by the user,
3. be characterized by a high success rate (robustness with respect to problems of false and missed identification),
4. allow the control of computational efforts,

is highly desirable. In the present application, an innovative automated modal identification algorithm able to fulfill the above mentioned requirements has been adopted [12]. Its effectiveness and accuracy have been proved by a large number of tests based on simulated as well as real datasets. It ensures a success rate larger than 99 % even in the presence of data characterized by low signal-to-noise ratio. Moreover, it is able to provide very accurate estimates, including damping. In fact, the error in the estimation of damping is typically much lower than 20 % [12].

20.3 Experimental Tests on a Scaled Bridge Model

A number of dynamic tests have been carried out on a scaled bridge model in order to assess the opportunities of modal based SHM for post-earthquake health assessment and performance monitoring of existing bridges. The structure under test (Fig. 20.1) was a scaled model (1:3) of a reinforced concrete single span bridge representative of the stock built in Italy in the Seventies in terms of material properties and structural details (more details can be found elsewhere [21]); it was tested under different configurations. It was first equipped with seismic isolation devices, and then it was tested in the simply supported reference configuration. Details of the supports in the reference configuration are shown in Fig. 20.2. Input ground motions of increasing amplitude have been applied to one of the piers by means of a shaking table and the response of the structure has been measured by a set of force balance accelerometers. A 221 kN preload was applied to the columns before testing in order to replicate the typical stress level in the columns under operational conditions.

The sensor layout is schematically reported in Fig. 20.3. Sixteen sensors have been installed: twelve were located on the superstructure in order to observe the fundamental bending and torsional modes, while the remaining two couples were located at the base of the column and on the shaking table applying the input. The ambient vibration response of the bridge

Fig. 20.1 The testing configuration of the bridge model

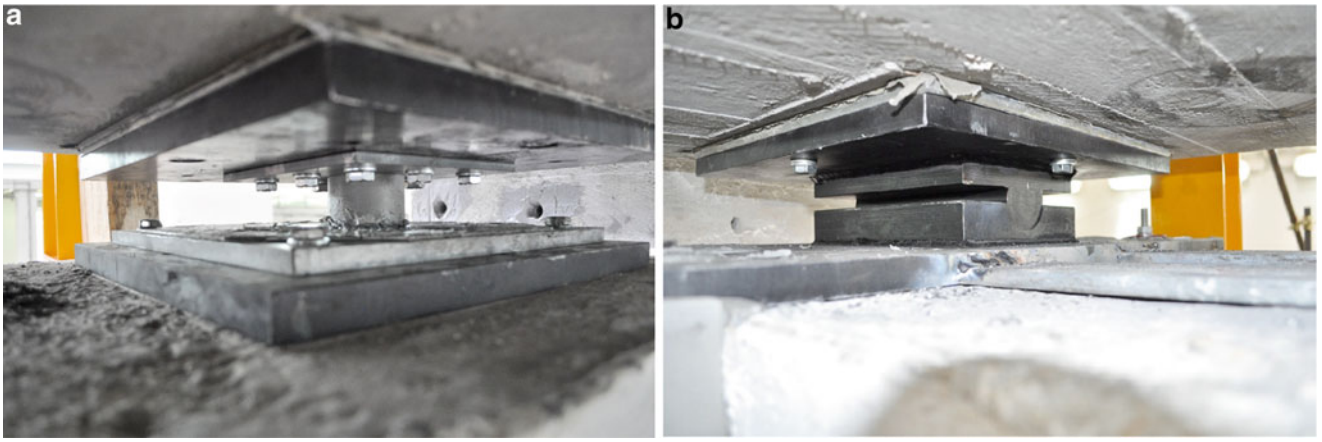

Fig. 20.2 Supports on top of the *left* (**a**) and *right* (**b**) column

was recorded by the twelve accelerometers installed on the superstructure before and after the application of the input ground motions. The accelerometers had the following specifications: 0.25 g full scale range, 40 V/g sensitivity, 140 dB dynamic range. A measurement device with 16 bit resolution and on-board anti-aliasing filter was used for data acquisition. A sampling frequency of 100 Hz has been adopted.

The ambient vibration response of the structure in the reference configuration has been processed in order to evaluate the variations of the modal properties induced by damage. Manual as well as automated modal identification procedures have been applied, in order to check the effectiveness of the latter. In particular, the manual identification has been carried out according to the Frequency Domain Decomposition (FDD) [20, 22] and the Covariance Driven Stochastic Subspace Identification (Cov-SSI) [20, 23] methods, while the adopted automated modal identification procedure was ARES® [12].

The recorded time series have been pre-processed in order to remove the offset and eventual spurious trends before the estimation of the modal parameters. Moreover, they have been inspected in order to identify eventual measurement anomalies (clipping, noise spikes, and so on) [20, 24]. Finally, data have been filtered and decimated by a factor of 2. When the FDD method was applied, power spectra were computed according to the Welch procedure by applying the Hanning window and considering a 66 % overlap. When the Cov-SSI method was applied, a maximum model order of 50 was considered in the construction of the stabilization diagram; the number of block rows was set after a sensitivity analysis in a way able to enhance the quality of the stabilization diagram [25, 26].

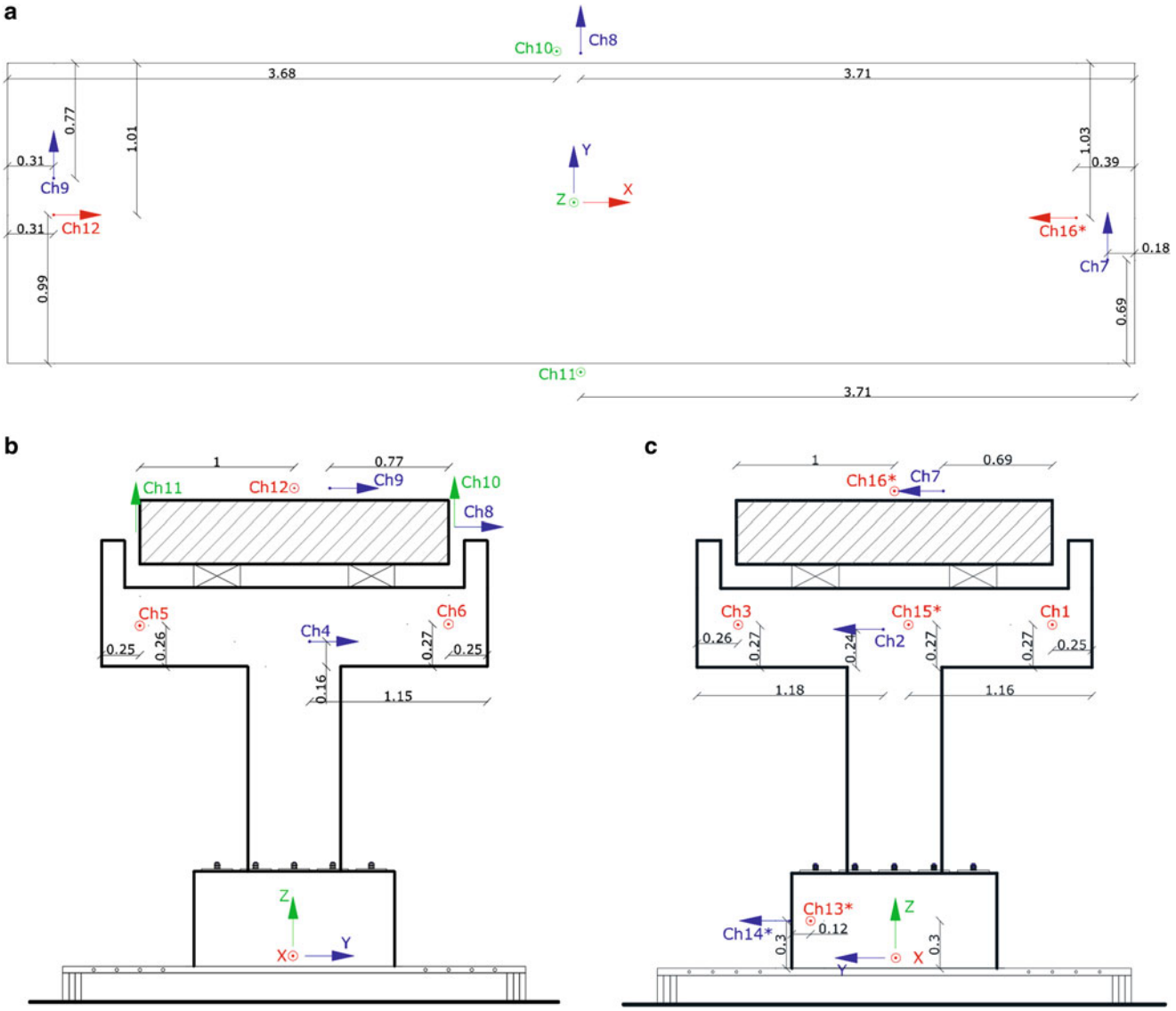

Fig. 20.3 Sensor layout: *top view* (**a**), *left column* (**b**), *right column* (c)

Table 20.1 Comparison of the estimated modal properties before (be) and after (ae) the ground motion (simply supported)

Mode No.	f_{be} [Hz]	f_{ae} [Hz]	Δf_{be-ae} [%]	ξ_{be} [%]	ξ_{ae} [%]	$\Delta\xi_{be-ae}$ [%]	MAC_{be-ae}
1	9.49	7.81	−17.66	0.89	0.72	−19.30	0.956
2	11.45	9.59	−16.21	0.89	0.77	−13.50	0.984
3	13.43	12.91	−3.87	0.39	0.33	−15.90	0.996
4	18.04	15.96	−11.50	0.88	1.08	23.49	0.972

The ground motions damaged the column to whose base the input was applied (the right column in Fig. 20.1). Table 20.1 shows the modal identification results of the structure under test before and after damage as provided by ARES. Crosschecks with the results of manual identification confirmed the reliability, effectiveness and accuracy of ARES in estimating the modal properties of the structure from its ambient vibration response.

Both natural frequencies and mode shapes were affected by damage (Table 20.1). In particular, the first, the second and the fourth mode experienced significant variations of the corresponding natural frequencies. Also the mode shapes were influenced by damage, as pointed out by the MAC values computed between the corresponding mode shapes before and after damage (Table 20.1). On the contrary, the third mode showed poor sensitivity to the damage affecting the right column.

Table 20.2 Comparison of the estimated modal properties before (be) and after (ae) the ground motion (isolated)

Mode No.	f_{be} [Hz]	f_{ae} [Hz]	Δf_{be-ae} [%]	ξ_{be} [%]	ξ_{ae} [%]	$\Delta\xi_{be-ae}$ [%]	MAC_{be-ae}
1	9.55	9.54	−0.09	1.08	0.90	−16.81	1.000
2	11.25	11.31	0.46	1.06	1.03	−3.30	0.999
3	14.16	14.15	−0.10	0.52	0.47	−9.69	0.999
4	17.45	17.37	−0.47	1.48	1.13	−23.39	0.997

Fig. 20.4 Seismic isolation device

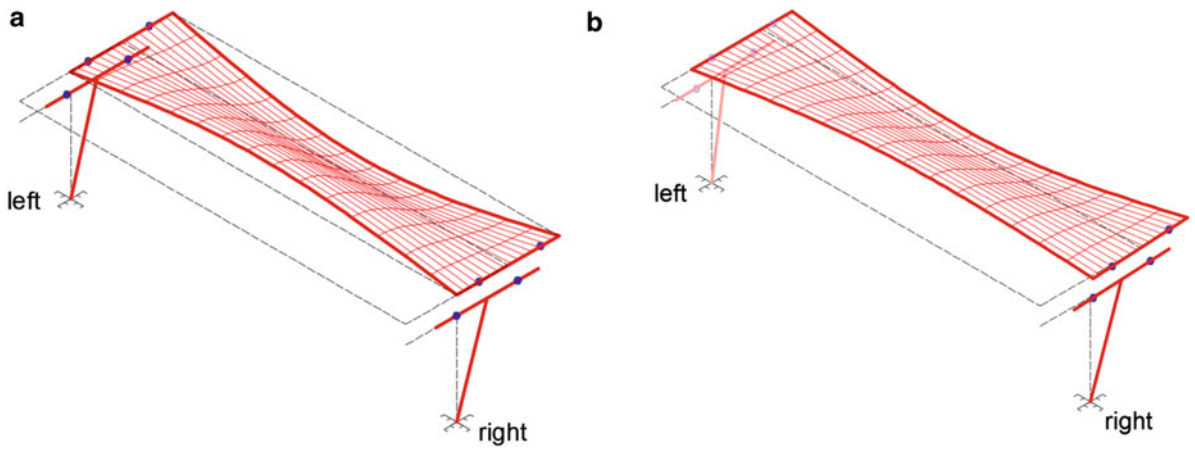

Fig. 20.5 Graphical representation of the first mode shape before (**a**) and after (**b**) damage

The fairly large variations of natural frequencies, in the absence of significant changes in the environmental and operational conditions, were clear symptoms of the presence of damage. In fact, when the structure under test was equipped with seismic isolation devices, no damage occurred and this was confirmed by the negligible variations of the modal properties after the application of the input ground motion. Table 20.2 reports the modal property estimates for the bridge model equipped with seismic isolation devices of the FPS type (Fig. 20.4) made by FIP Industriale. The very small magnitude of modal property changes with respect to the bridge model without isolation devices can be easily recognized. Such variations were basically due to the influence of environmental and operational factors.

In order to figure out how the damage affected the mode shapes of the bridge, they are qualitatively represented in Figs. 20.5, 20.6, 20.7 and 20.8, which show a direct comparison of the mode shapes of the fundamental modes before and after damage. Even if it does not affect the monitored elements but only the base of one of the columns, the modifications of the mode shapes it yields are quite evident. The visual comparison of the mode shapes also provides a qualitative indication of the portion of the bridge interested by the major modifications and, therefore, by damage (Fig. 20.5).

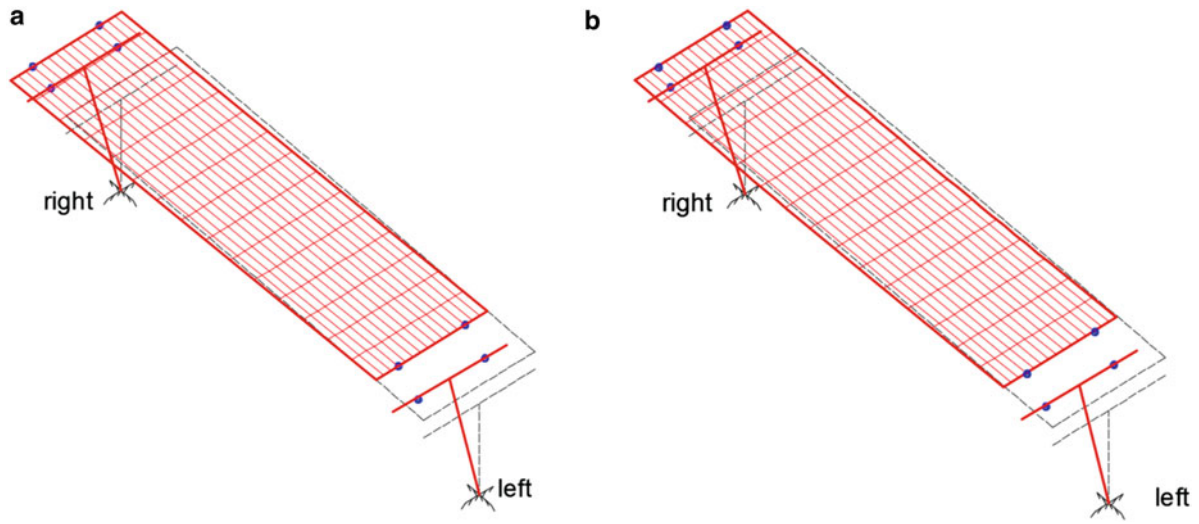

Fig. 20.6 Graphical representation of the second mode shape before (**a**) and after (**b**) damage

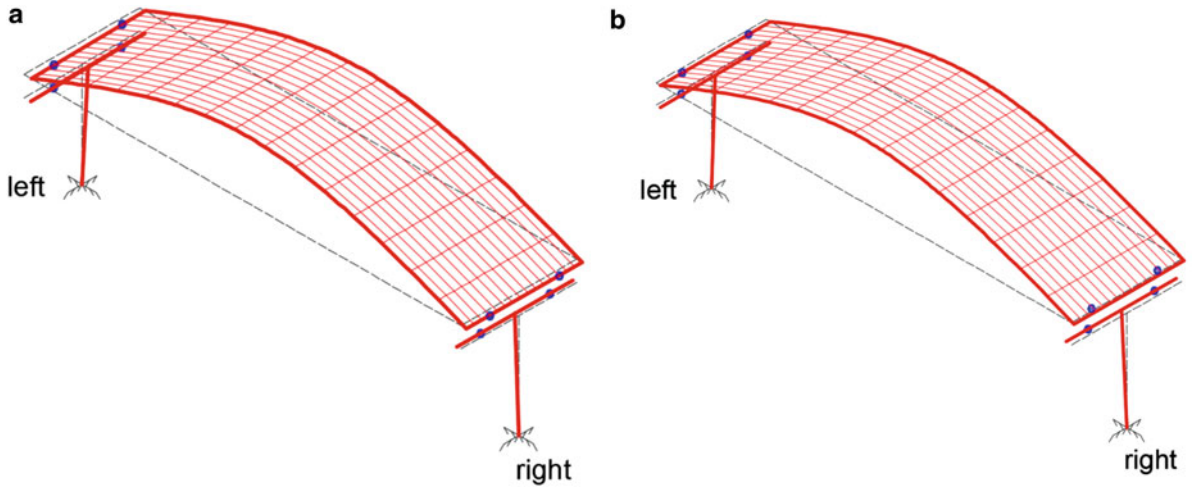

Fig. 20.7 Graphical representation of the third mode shape before (**a**) and after (**b**) damage

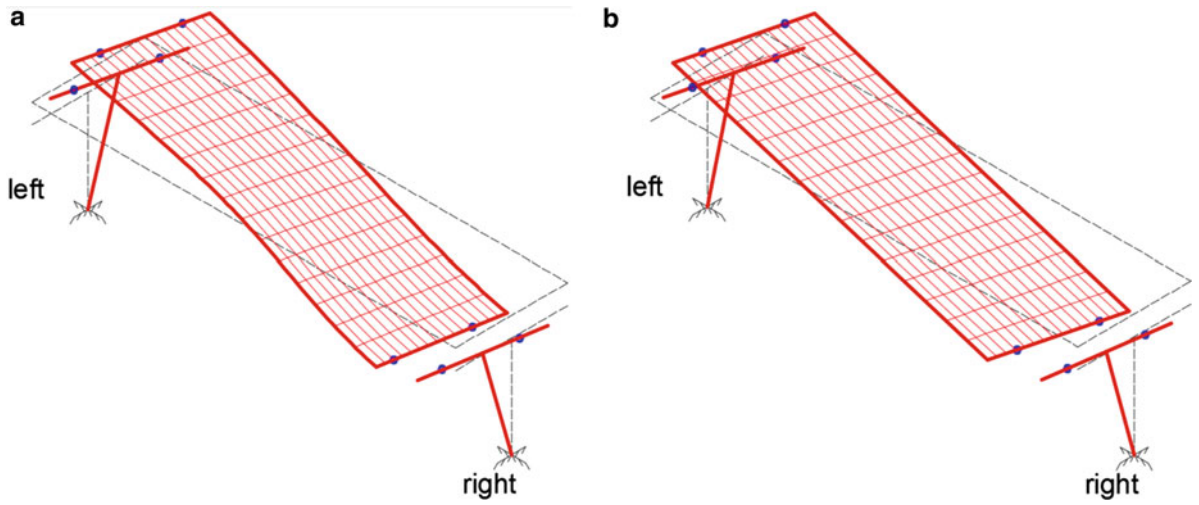

Fig. 20.8 Graphical representation of the fourth mode shape before (**a**) and after (**b**) damage

20.4 Conclusions

The opportunities and limitations of automated output-only modal identification and modal-based damage detection for bridges have been discussed in light of the results of an extensive experimental campaign on a scaled bridge model. The dynamic response of the structure has been experimentally characterized for different support conditions (simply supported, with seismic isolation devices). Shaking table tests have been then carried out. As a result of the seismic input, the structure without isolation devices was damaged. The effect of damage on the modal properties of the bridge has been presented, pointing out the possibility to detect damage by means of selected damage features. The obtained results remark the promising applicative perspectives of modal based damage detection for SHM of bridges in seismically prone areas.

Acknowledgments The present work was part of the Project PON-FESR 2007–2013 (PON01_02366, STRIT) "Tools and Technologies for the Management of the Transportation Infrastructures"—OR3 'Monitoring'—coordinated by STRESS s.c.a.r.l., whose activity is gratefully acknowledged. The authors are also grateful to Dr. D. Zurlo and Eng. Jr. Michele Pepe for their contribution in the installation and management of the monitoring system.

References

1. Rainieri, C., Fabbrocino, G., Cosenza, E.: Integrated systems for structural health monitoring: worldwide applications and perspectives. In: Proceedings of The Fourth European Workshop on Structural Health Monitoring, Cracow (2008)
2. Sohn, H., Farrar, C.R., Hemez, F.M., Shunk, D.D., Stinemates, D.W., Nadler, B.R.: A review of structural health monitoring literature: 1996–2001. Technical Report LA-13976-MS, UC-900, Los Alamos National Laboratory, New Mexico (2003)
3. Farrar, C.R., Worden, K.: Structural Health Monitoring: A Machine Learning Perspective, p. 631. Wiley, Chichester (2012)
4. Rytter, A.: Vibrational Based Inspection of Civil Engineering Structures. Ph.D. Thesis, Aalborg University, Aalborg (1993)
5. Fabbrocino, G., Cosenza, E.: Shaking tables for seismic simulation, overview of the CRdC-AMRA Project. In: The many facets of the seismic risk—Proceedings of the Workshop on Multidisciplinary Approach to Seismic Risk Problems. Doppiavoce Ed., Sant'Angelo dei Lombardi (Avellino) (2003)
6. Hu, W.-H., Caetano, E., Cunha, A.: Structural health monitoring of a stress-ribbon footbridge. Eng. Struct. **57**, 578–593 (2013)
7. Magalhães, F., Cunha, A., Caetano, E.: Vibration based structural health monitoring of an arch bridge: From automated OMA to damage detection. Mech. Syst. Signal Process. **28**, 212–228 (2012)
8. Cross, E.J., Koo, K.Y., Brownjohn, J.M.W., Worden, K.: Long-term monitoring and data analysis of the Tamar Bridge. Mech. Syst. Signal Process. **35**, 16–34 (2013)
9. Maeck, J., De Roeck, G.: Damage assessment using vibration analysis on the Z24-bridge. Mech. Syst. Signal Process. **17**(1), 133–142 (2003)
10. Peeters, B., De Roeck, G.: One-year monitoring of the Z24-Bridge: environmental effects versus damage events. Earthquake Eng. Struct. Dyn. **30**, 149–171 (2001)
11. Rainieri, C., Fabbrocino, G.: Automated output-only dynamic identification of civil engineering structures. Mech. Syst. Signal Process. **24**(3), 678–695 (2010)
12. Rainieri, C., Fabbrocino, G.: Development and validation of an automated operational modal analysis algorithm for vibration-based monitoring and tensile load estimation. Mech. Syst. Signal Process. **60–61**, 512–534 (2015)
13. Rainieri, C., Fabbrocino, G., Cosenza, E.: Near real-time tracking of dynamic properties for standalone structural health monitoring systems. Mech. Syst. Signal Process. **25**(8), 3010–3026 (2011)
14. Doebling, S.W., Farrar, C.R., Prime, M.B., Shevitz, D.W.: Damage identification and health monitoring of structural and mechanical systems from changes in their vibration characteristics: a literature review. Technical Report LA-13070-MS, UC-900, Los Alamos National Laboratory, New Mexico (1996)
15. Rainieri, C., Fabbrocino, G., Manfredi, G., Dolce, M.: Robust output-only modal identification and monitoring of buildings in the presence of dynamic interactions for rapid post-earthquake emergency management. Eng. Struct. **34**, 436–446 (2012)
16. Rainieri, C., Fabbrocino, G., Cosenza, E.: Integrated seismic early warning and structural health monitoring of critical civil infrastructures in seismically prone areas. Struct. Heal. Monit. **10**(3), 291–308 (2010)
17. Deraemaeker, A., Reynders, E., De Roeck, G., Kullaa, J.: Vibration-based structural health monitoring using output-only measurements under changing environment. Mech. Syst. Signal Process. **22**, 34–56 (2008)
18. Rainieri, C., Gargaro, D., Fabbrocino, G.: Statistical tools for the characterization of environmental and operational factors in vibration-based SHM. In: Proceedings of IMAC XXXIII, International Modal Analysis Conference, Orlando (2015)
19. Allemang, R.J., Brown, D.L.: A correlation coefficient for modal vector analysis. In: Proceedings of The 1st International Modal Analysis Conference, pp. 110–116. Orlando (1982)
20. Rainieri, C., Fabbrocino, G.: Operational Modal Analysis of Civil Engineering Structures: An Introduction and Guide for Applications, p. 322. Springer, New York (2014)
21. Cosenza E., Manfredi G., Prota A., Fiorillo A., Campanella G., Del Vecchio C., Di Sarno L., Maddaloni G.: Seismic assessment of typical existing Italian bridge. In: Proceedings of ANIDIS 2015, L'Aquila (2015)
22. Brincker, R., Zhang, L., Andersen, P.: Modal identification of output-only systems using frequency domain decomposition. Smart Mater. Struct. **10**, 441–445 (2001)
23. Peeters, B.: System Identification and Damage Detection in Civil Engineering. Ph.D. Thesis, Katholieke Universiteit Leuven, Leuven (2000)

24. Bendat, J.S., Piersol, A.G.: Random Data: Analysis and Measurement Procedures, 3rd edn. Wiley, New York (2000)
25. Rainieri, C., Fabbrocino, G., Cosenza, E.: Some remarks on experimental estimation of damping for seismic design of civil constructions. Shock Vib. **17**, 383–395 (2010)
26. Rainieri, C., Fabbrocino, G.: Influence of model order and number of block rows on accuracy and precision of modal parameter estimates in stochastic subspace identification. Int. J. Lifecycle Performance Eng. **1**, 317–334 (2014)

Chapter 21
Bridge Assessment Using Weigh-in-Motion and Acoustic Emission Methods

L. Dieng, C. Girardeau, L. Gaillet, Y. Falaise, A. Žnidarič, and M. Ralbovsky

Abstract Most of civil engineering structures are subjected to potential damages mainly due to dynamic oscillations induced by wind, rain or traffic. The aim of this paper is to combined Bridge Weigh-In-Motion (B-WIM) technic and Acoustic Emission (AE) monitoring in order to evaluate the health state of bridge structures. AE technique is able to determine location of active damage zones, if sufficient density of sensors is used. Within TRIMM European project, this technique was for the first time combined with Bridge-Weigh-In-Motion (BWIM) technique to correlate real traffic load level with registered cracking activity. Combination of AE and B-WIM techniques enables determining of load level at which nonlinearities start to develop. The technique provides an indication of progressing structural damage under operating traffic loads.

Keywords Bridge • Weigh-in-motion • Acoustic emission • Cracks

21.1 Introduction

This paper refers to the accomplished work in TRIMM Work-Package 3: Advanced Bridge Monitoring Techniques.

Measurement techniques have been applied on bridges since the need for accurate data in assessment arose. The techniques developed from determination of crack width to measurements of settlement, inclination, strain and vibration. Bridge monitoring has evolved from these techniques, driven by the need of continuous data acquisition. Monitoring data offered the engineers an opportunity to compare actual with assumed bridge behaviour, further to detect structural changes in time, and ultimately use this information to improve maintenance management. Continuous monitoring systems are nowadays used on a number of bridges worldwide so that these measurement systems became well established. Recent improvements in availability of mobile data transmission as well as computer hardware further accelerated spread of continuous bridge monitoring applications. The aim of TRIMM WP3 is to provide managers of road infrastructure assets more developed tools for assessment of bridges. The primary goal of the advanced tools is to deliver more accurate information about bridge condition. This information is essential for efficient, sustainable and cost-effective decision making, at both the network and project level.

Two main aspects of the advanced monitoring methods are early detection of developing damages and accurate determination of damage type and extent. This information can be used in planning of maintenance measured. Bridge management and maintenance is currently considered as a reactive process without consideration of future developments. Road operators rely mostly on periodic visual inspections that are carried in interval of several years. Sometimes additional investigations are performed if it is considered necessary to obtain more detail information. This widespread inspection methodology assumes that relevant damages are visible in a stage that is sufficient to implement proper maintenance measures.

L. Dieng (✉) • C. Girardeau • L. Gaillet • Y. Falaise
Ifsttar, MAST, Centre de Nantes, Route de Bouaye - BP 4129, 44341 Bouguenais, France
e-mail: lamine.dieng@ifsttar.fr

A. Žnidarič
ZAG, Srednje Gameljne, Ljubljana, Slovenia
e-mail: ales.znidaric@zag.si

M. Ralbovsky
AIT, Seibersdorf, Austria
e-mail: marian.ralbovsky@ait.ac.at

S. Pakzad, C. Juan (eds.), *Dynamics of Civil Structures, Volume 2*, Conference Proceedings of the Society for Experimental Mechanics Series, DOI 10.1007/978-3-319-29751-4_21

Within TRIMM, the work on Advanced Bridge Monitoring Techniques was devoted to further develop the bridge assessment methods for capturing the visual condition, the chemical degradation, as well as mechanical condition of the structure. The work was organized in 5 tasks, which are listed below :

- Image Based Bridge Inspection technique
- Traffic loading and acoustic monitoring techniques
- Corrosion monitoring techniques
- Monitoring of joints and bearings
- Integrated Bridge Monitoring Method

This paper is focused on the use of traffic loading and acoustic monitoring techniques. This non destructive monitoring method is devoted to detection of acoustic emission activities that originate in formation of microcracks in the structure. The method is intended to provide information about the amount of nonlinear activities inside the material. This information is useful primarily for reinforced (or prestressed) concrete, bridges that show heavy deterioration, are under designed in terms of present traffic loading requirements, or bridges without documentation on design and construction. The technique was tested on several concrete bridges and one steel bridge.

21.2 Traffic Loading and Acoustics Monitoring

21.2.1 Introduction to Combined BWIM AE Monitoring

It is expected that a combined B-WIM-AE monitoring would give more reliable information about the structure (bridge) integrity/safety, in comparison to the real traffic load alone, as it would likely provide information about consequences of traffic loading on the structure. This information shall allow for more accurate prediction of the lifetime of obsolete reinforced (or prestressed) concrete bridges, primarily in the case of:

- Deteriorated bridges, to the extent that carrying capacity is reduced (e.g. cracks, corroded reinforcement) ,
- Under designed bridges, for present traffic loading as they were built according to older design codes,
- Bridges of which no information about design and construction procedures exist.

Traditionally, to keep such bridges in service (or to repair them optimally) a proof load test would be needed, which applies increasing loads on a bridge to prove the resistance. Proof load tests are expensive and can even damage the bridge, and are hence understandably unpopular among stake holders and users. Yet, the ARCHES project [5] demonstrated that combining proof load testing with acoustic emission can stop increasing load in time when acoustic activities start to build up, that is when additional damage is caused by testing. To avoid expensive and time consuming proof load tests which require closing the traffic, TRIMM project is applying the same principles on the running traffic by combining AE with B-WIM measurements. The assessment of bridges based on B-WIM determined real traffic loads and on AE method measured material responses is possible due to the so called Kaiser Effect [19]. It was assumed that AE events occur only after the previously applied load/deflection is exceeded.

On the other hand, when AE activity is measured at lower load level, decrease of load bearing capacity is likely caused by material degradation due to corrosion of reinforcement, freeze-thaw degradation, alkali-aggregate reaction or other causes. Possible explanations for AE activities at lower loads can also be found in other causes, i.e. settlement of foundations or failure of dilations or bearings. Furthermore, sufficient number of AE sensors also allows locating the damage in the bridge.

21.2.2 Bridge Weigh-in-Motion

Weigh-in-motion (WIM) systems have been traditionally used to collect freight traffic data to support transportation planning and decision making activities. As high axle loads are responsible for road and bridge damage, the aim of any WIM system is to obtain accurate axle load and gross weight information. Despite the dynamic interaction between the vehicles and the pavement which affects accuracy of WIM results, weighing in motion is well recognized as the only weighing method which can measure the entire population of vehicles on a road section, including the overloaded vehicles which successfully avoid other modes of weighing. There are two major groups of WIM systems on the market, the ones that weigh with sensors built into the pavement, with numerous varieties and quality of sensors, and the bridge WIM systems. After moderate success of

its first generation products from 1980s [10], Bridge WIM (BWIM) started to regain momentum 20 years ago in Europe, when its development was reinitiated in a European Commission COST action [7]. The main research work was then funded at the end of the last century through the European Commission 4th Framework, WAVE project (WAVE 2002). New and improved algorithms were being developed to enhance its accuracy, especially of the individual axle loads, and to extend its applicability to different types of road bridges, the SiWIM bridge-WIM prototype was born. In an independent test performed within the WAVE project, the B-WIM systems at that time were shown to have accuracy comparable to other technologies such as bending plate and piezo quartz. WAVE project also generated the idea of a Free-of-Axle Detector system (FAD) that does not require any sensors (axle detectors) on the pavement. This results in no traffic congestions during installation and maintenance of the system. After conclusion of the WAVE developments of the bridge-WIM technology continued, both in Europe and in Asia [12]. In Europe, the main theoretical developments are taking place in Ireland and Slovenia, where the main focus is optimization of measurements and measuring parameters.

Bridge weigh-in-motion (B-WIM) systems are applied on existing bridges or culverts from the road network which are transformed into undetectable weighing scales (WAVE 2001). For this purpose the structures are typically instrumented with the strain measuring gauges and, when necessary, with the axle detectors. Traditionally, strains are measured on the main longitudinal members of the bridge to provide response records of the structure under the moving vehicle load, but other locations can be used to improve the results. Measurements during the entire vehicle pass over the structure provide redundant data, which facilitates evaluation of axle loads. This is an advantage over the pavement WIM systems where an axle measurement generally lasts only a few milliseconds. Bridge WIM is particularly appropriate for:

- Shorter term measurements as it can be easily installed and detached from the bridge. Unlike other WIM system, its accuracy of results is not affected due to portability of installation.
- Measurements on sites, where cutting into the pavement is not allowed, is not feasible due to the heavy traffic or if permissions for road blocks are difficult to obtain.
- Bridge assessments, as it provides supplementary structural data: the dynamic (impact) factors [3], the load distribution factor and the strain records.

B-WIM is today an established WIM technology used in approximately 20 countries. Its main features are complete portability (without losing its accuracy as with portable pavement installations), accuracy, especially on smooth pavements and shorter bridges (below 20-m span), ease of installation and interventions, connectivity and price efficiency. SiWIM bridge WIM system efficiently deals with presence of several vehicles on the bridge (Znidaric et al. 2012). Still, bridges with influence lines longer than 30–40 m will likely provide less accurate results because number of multiple-presence vehicles can increase beyond reasonable amount.

Collected data is used in various applications, from traffic studies, design and reconstruction of pavements, pre-selection of overloaded vehicles and bridge applications. There, the main advantages compared to the pavement WIM systems are the measured influence lines and load distribution factors of the structure being measured, as well as Dynamic Amplification Factors (DAF) of all loading events on the bridge. Details about decoupling the static and dynamic components of measured strain signals in the SiWIM software are given in [3] and (Znidaric & Lavric 2010). SiWIM can be also equipped with a number of additional sensors (accelerometers, displacement gauges, strain gauges. . .) that provide correlated results between the traffic loading and the reactions at the points of measurements.

21.2.3 Acoustic Emission (AE)

The acoustic technique is one of the most promising non-destructive techniques that can be used to monitor development of defects in the structural elements. Acoustic emission (AE) is a phenomenon of creating transient elastic waves resulting from local internal micro-material movements [11]. The main principle of this method consists in detecting fast discharge of elastic energy caused by micro-scale deformations or defects inside the loaded material. These waves can be detected by piezoelectric sensors (Fig. 21.1). AE method can be applied to different materials, processes and structures. An active crack can be detected much earlier by AE methods than with the unaided eye of an inspector. AE methods can be used for detecting active cracks, corrosion, leaking, etc. The location of the event can also be identified, using an array of sensors.

The AE approach has been used for monitoring of bridges [5], but never in combination with soft load testing and WIM techniques. To date, no standards have been set for field monitoring using acoustic emission techniques on structures like bridges, but recommendations were issued by the RILEM (International Union of Laboratories and Experts in Construction Materials, Systems and Structures) technical committee TC212-ACD [13]. All on site AE measurements were as far as

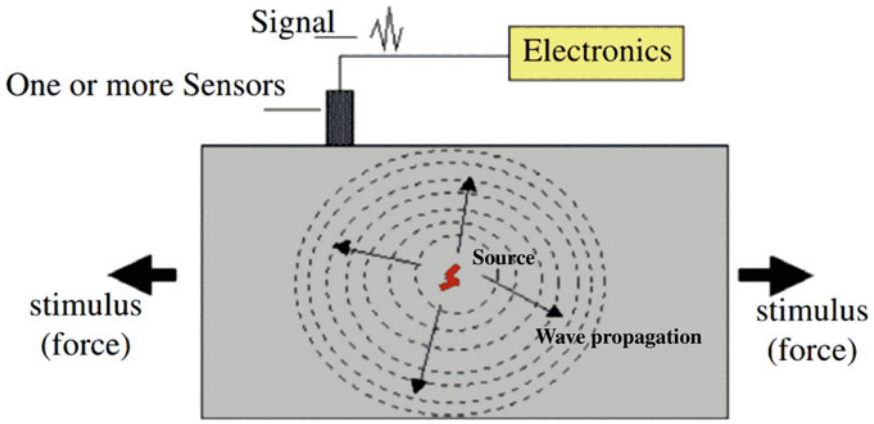

Fig. 21.1 The principle of acoustic emission methods

Table 21.1 Basic parameters used in AE methods

Name	Unit	Description
Threshold level	[dB, ref 1 μV]	Parameter to detect AE signals. The threshold is set such as that the unwanted noise is minimized. In this project, the threshold is set to 45 dB
Hits	[−]	Number of AE burst signals
Counts	[−]	Number of threshold crossings within one discriminated burst signal
Amplitude	[dB, ref 1 μV]	Amplitude of AE signal
Peak amplitude	[dB, ref 1 μV]	It is the greatest measured voltage of signal. Signals with amplitudes above the threshold correspond to an event, if the amplitude is below the threshold, isn't recorded
Energy	[J]	Signal strength, approximation
Rise time	μs	Time between 1st threshold crossing and maximum amplitude (A_{max})
Duration	μs	Signal length/time between 1st and last threshold crossing
Background noise level	μV	Background noise level at pre-amplifier input prior to a hit

Fig. 21.2 Example of AE signal

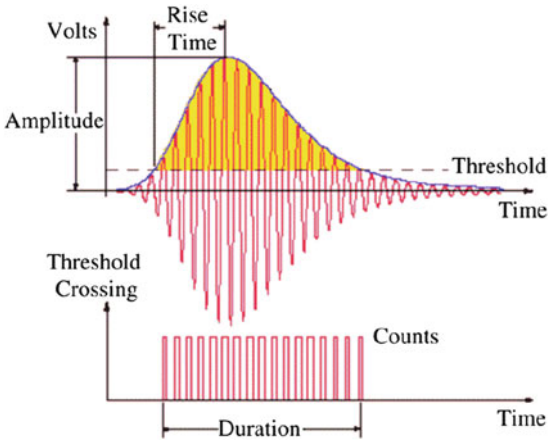

possible performed in accordance with ARCHES recommendations [4]. The main technical terms can be found in EN 1330-9:2009 Non-destructive testing—Terminology—Part 9: Terms used in acoustic emission testing (EN 1330-9:2009), recommendations of RIELM TC 212-ACD [13] and elsewhere [8]:

The basic parameters of AE signals being usually measured are listed in Table 21.1 and presented in Fig. 21.2.

21.2.3.1 Interpretation of Acoustic Emission Data

Acoustic emission is an effective NDT method to detect and monitor the cracking process of civil engineering materials and structures, which cannot be done by other testing methods. Identified AE events provide further information on fracturing processes in material based on the energy-related AE signals, slope of the waveforms as well as their frequency characteristics. Based on experimental findings, several promising AE based methods can be applied for the assessment of actual infrastructures. The assessment of real structures involves not only monitoring the progress of any detected defects, but also considering the impact of these defects on overall structural condition. Therefore, the AE activity, induced by friction among existent cracks or damage dealing with in-situ assessment shall primarily refer to as secondary AE activity, while crack-induced AE is defined as primary AE activity (Shiotani 2012). Recently novel findings to apply in-situ AE methods for assessment of large concrete structures for their current status have been published [14], [21], (Kobayashi et al. 2014), (Behnia et al. 2014), and [16]. Basic ideas of both established and novel approaches are presented hereafter. Some of them were utilised in TRIMM project.

Primary AE Activity

Crack-induced AE is defined as primary AE activity. When load increases, the failure processes and thus AE activity increase exponentially, as schematically presented in Fig. 21.3. These phenomena can be successfully used, in combination with proof-load testing, to abort the loading process before a substantial damage is induced on the tested bridge. Examples of such applications can be found elsewhere [4, 17, 18].

AE Waveforms Characteristics Based Evaluation

The AE waveforms change with fracture processes. These phenomena can be used for the evaluation of damage level. In the process of developing damage, tensile type of cracks is more common in early stage, followed by mixed mode (tensile and shear) type and by shear type of cracks [22]. Corresponding to the change of crack types as the damage progress, it is expected that fracture velocity becomes smaller. This suggests two important particulars of AE waveforms:

- Gradients of ascending parts of waveforms become smaller with the progress of fracture; and
- Low-frequency components become dominant with damage progress (Fig. 21.4).

A "grade" was introduced by Shiotani et al. [20] defined as the peak amplitude divided by the rise time (Rise Angle factor). The large values imply the early stage of fracture where cracks of tensile type are dominant, while smaller ones indicate the approach to the final stage where cracks of shear type (Fig. 21.5). Aggelis et al. [1].

That applicability of the grade has been studied on the process of concrete materials [9] or on classification of crack types in combination with average frequency [15]. It has been shown undoubtedly both in-lab and on-site that the peak frequencies of AE events decrease with damage progress, and that the peak frequency of measured AE signals could be a clue to provide the degree of fatigue damage. Therefore a new approach, a Q-value, was introduced by Shiotani et al. (2013).

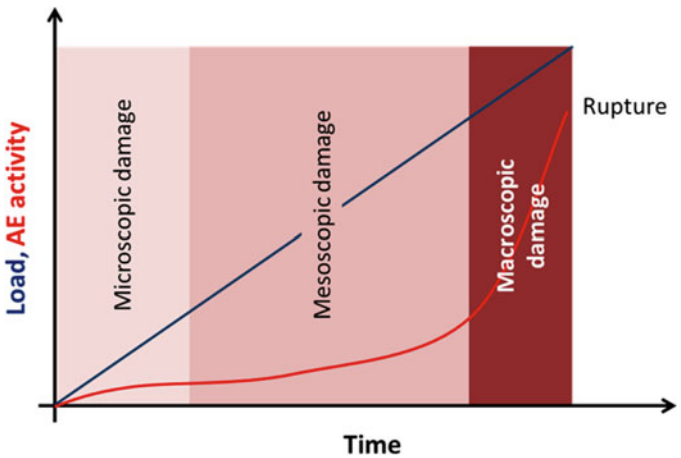

Fig. 21.3 Typical exponential increase of AE activity before rupture

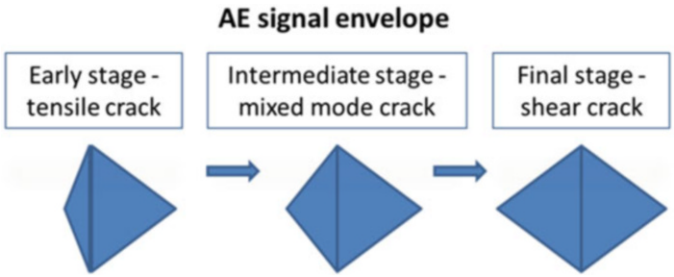

Fig. 21.4 Typical change in AE signal shape during increased damage

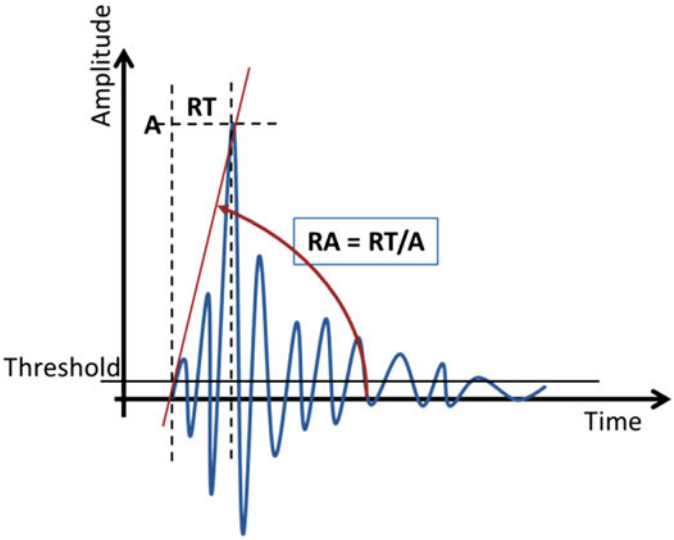

Fig. 21.5 RA-Value

b-Value Analysis

The b-value analysis is presented and proposed as a method to study the development of the fracture process [6]. Different types of cracks generate different types of AE signals with varying frequency ranges and amplitudes. Microcracks generate a large number of events of small amplitude while macrocracks generate fewer events with large amplitude. The b-value analysis can take all these factors into account and it could then be used as an alternative way to process and interpret data recorded during local AE monitoring (Fig. 21.6).

$$log_{10}N = a - bM_L \tag{21.1}$$

with

- M_L : Amplitude of the events—one event represents a group of AE hits corresponding to a single source
- N : Number of events with amplitude in range of $\pm M/2$
- a, b : Empirical constants

In Equation (21.1), the b-value is the negative gradient of the log-linear AE Hit/amplitude plot; it represents the slope of the amplitude distribution. The b-value changes systematically with the different stages of fracture growth. The minimum b-value trend suggests macrocracks have formed, while the maximum b-value trend implies microcrack growth. Quantitative considerations in the case of reinforced Concrete Beam were drawn by S. Colombo, and are summarized in Table 21.1.

Although the analysis of the b-value is well-known in the field of seismology, very little work has been done on its use in the assessment of civil engineering structures (Table 21.2).

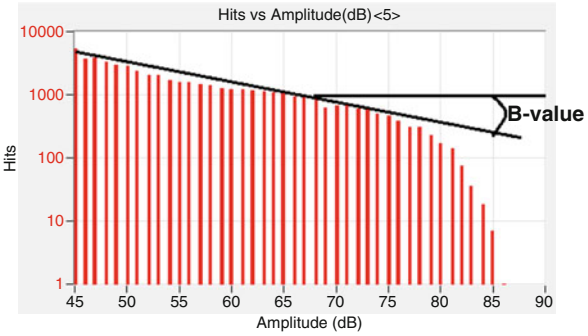

Fig. 21.6 b-value

Table 21.2 b-value quantitative results for concrete beam—[6] [S. Colombo, et al. 2003]

$1.0 < b - value < 1.2$	Macrocracks forming
$1.2 < b - value < 1.7$	Macrocracks are constant
$b - value > 1.7$	Microcracks are dominant or macrocracks are opening

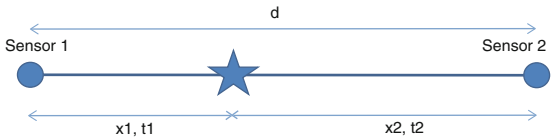

Fig. 21.7 Principle of location in 1D

AE Event Location Determination

An AE measuring system can be used to determine the location of the AE event. Depending on the type of the structure, a minimum of 2 (for linear structures) or 3 (for planar problems) sensors are needed. Based on the differences of the signal arrival times and assumed or known (measured) AE wave velocity the location of the AE event can be calculated.

The following example shows the calculation of the AE event location in a scenario with 2 sensors (Fig. 21.7):

The time difference between 2 sensors is evaluated as shown:

$$\Delta t = t_2 - t_1 = \frac{1}{v}(x_2 - x_1) \tag{21.2}$$

with v the speed of sound in the material. By replacing in the equation with $d = x_1 + x_2$, one obtain

$$\Delta t = \frac{1}{v}(d - 2x_1) \tag{21.3}$$

Reversing the equation, the distance between the event and the sensor 1 are evaluated by.

$$x_1 = \frac{1}{2}(d - v\Delta t) \tag{21.4}$$

21.3 Field Tests and Results

Within the TRIMM project, combined B-WIM and AE monitoring has been applied on 3 bridges:

1. Bridge PT0343: A 6.4-m long slab bridge on a local road in Slovenia, just prior to the replacement of the bridge in 2012
2. Underpass VA0028: A 6-m long integral slab bridge on the motorway A2 Ljubljana Klagenfurt (Austria), where measurements have been performed since August 2012
3. Bridge Cheviré, a prestressed bridge with a central metallic span located near Nantes (France). (France).

Only results obtained for Bridge Cheviré are presented in this paper.

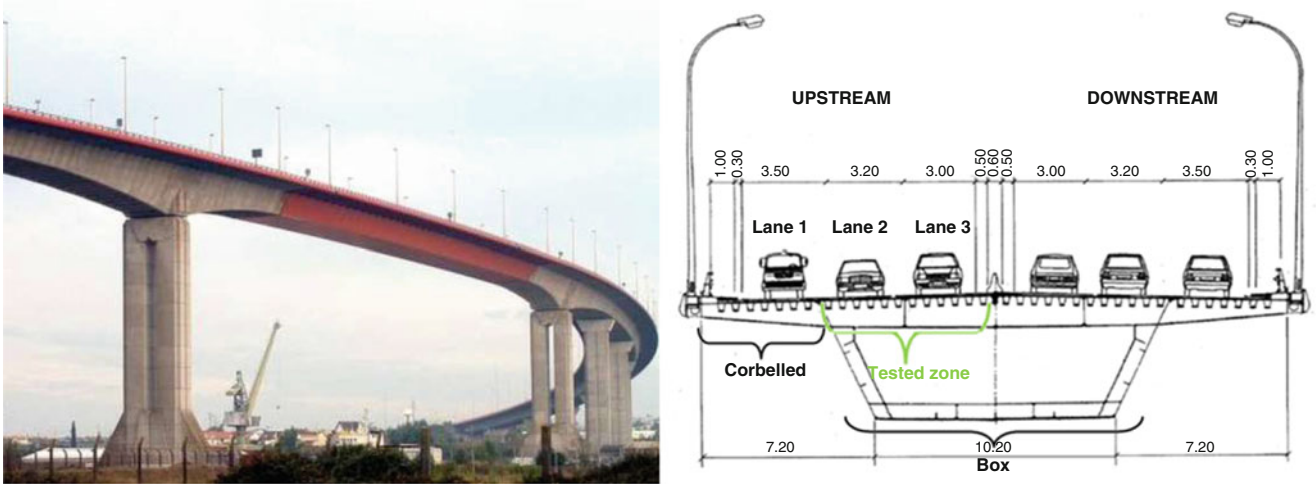

Fig. 21.8 Cheviré bridge & cross section

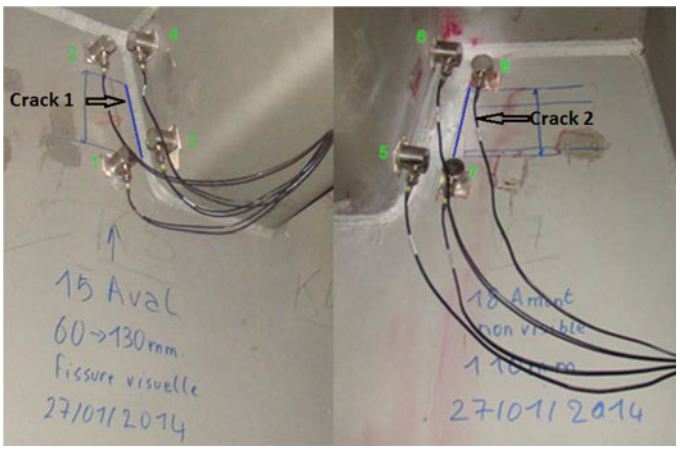

Fig. 21.9 Installation and displays cracks

21.3.1 About the Bridge

The Cheviré Bridge (Fig. 21.8) is located in the west of Nantes in France. It is a road bridge crossing the "Loire River". It was built in 1986 and is an important part of Nantes ring road. The bridge is 52 m high and 1563 m long. It consists of concrete and steel sections. The steel sections are located on the mid-length of the bridge and is an orthotropic bridge deck. During the visual inspection cracks were spotted between the deck and concrete viaducts, on the north side. Cracks are under the fast lane (line 2) on the upstream side (see Fig. 21.8). The project's goal was to correlate measurements recorded by the Weigh-in-motion (WIM) and Acoustic Emission measurements in order to detect any evolution of two cracks located under the metallic deck at the junction between crossbeam and longitudinal stiffeners. The position of the 2 cracks and the location of AE sensors are presented in Fig. 21.9. Cracks are delimited by blue lines and are located at the welding.

21.3.2 Tests Performed

A SiWIM monitoring system, provided by Cestel (Slovenia), was used to measure the traffic load. B-win sensors was placed under the deck in two rows : a row of 4 sensors located at a distance of 14 m and another row of 12 sensors at a distance of 10 m of cracks across the bridge section. All sensors are connected to a data logger which allows saving daily data. Vehicle speed, gross vehicle weight, axle number and spacing and load distribution were determined. A four sensor Acoustic Emission system, provided by Physical Acoustics, USA, was used to monitor the AE activities around the each crack.

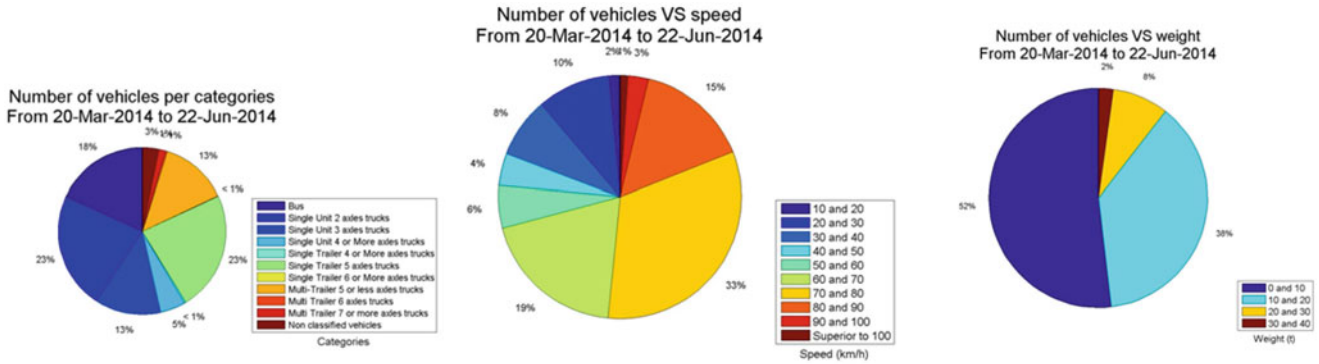

Fig. 21.10 Distribution in terms of category, speed and weight

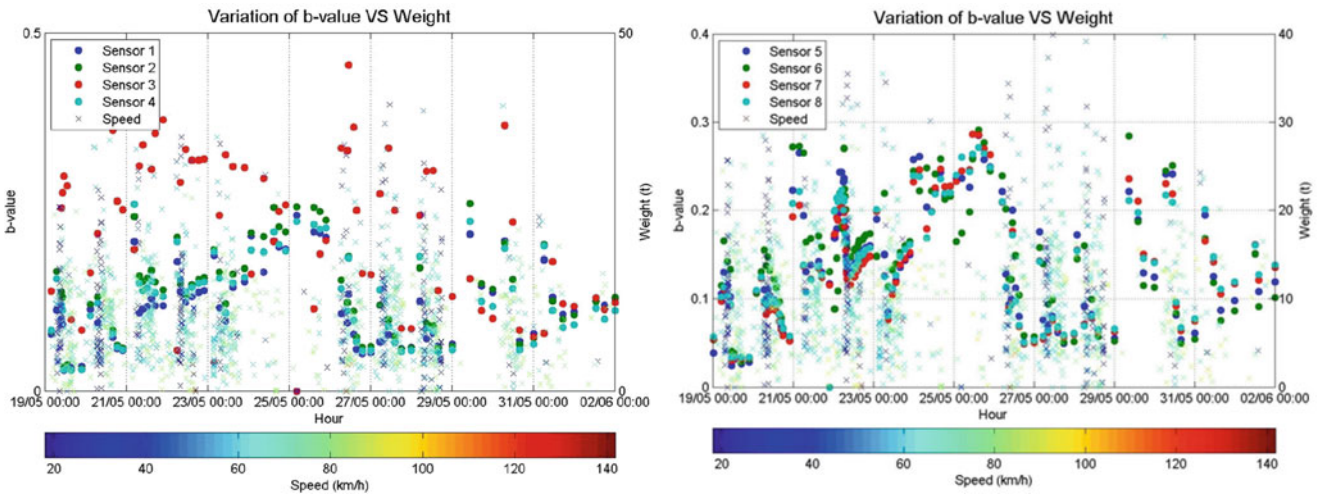

Fig. 21.11 Variation of b-Value Vs. Truck weight and Speed

21.3.3 Test Results

Traffic analysis shows that cheviré Bridge are submitted to important traffic with heavy trucks. The average value is around 160 trucks with peaks around 450 vehicles for several days. Repartition in terms of category, speed and weight are represented on Fig. 21.10.

Regarding the vehicle categories, we note a predominance of buses, single unit 2 axle trucks and single trailer 5 axle trucks. While the grouping of multi trailer class represent 15 % of traffic. The average speed is at around 65 km/h, corresponding to about limited speed of 70 km/h. About 20 % of users exceed this limited speed. The majority of trucks (90 %) has a weight between 0 and 20 tonnes. Lanes 2 and 3 still support 10 % of the heavy traffic (over 20 tonnes). Although, trucks are supposed drive on the slow lane (Lane 1), this could have consequences on cracks evolution.

The trend of the b-value was then calculated and plotted for each vehicle passage and for each channel. By comparing the numerical values obtained for all four sensors with the location of the sensors themselves b-value is less than 0.5 (see Fig. 21.11). This might imply that the analysis of the b-value is meaningful on good structures as it provides information between the micro-cracking beginning up to the stage where macro-fractures occur by localization i.e., the number of micro-cracks is high and they join creating a localized macro-crack. Quantitatives values reported by Colombo et al. [6] were determined for concrete beam and are not suitable for steel beam.

Truck speed and gross vehicle weight are compared to AE signal given by sensor located around cracks. For example Fig. 21.12 shows the variation of the b-value (acoustic emission parameter) calculated for sensor 2 compared to the truck speed. This figures suggests a linear relationship between truck speed and b-value. In presence of cumulative damage the relationship between traffic load and AE parameters are expected to be nonlinear. This non-linear relationship could be a good indicator of damage.

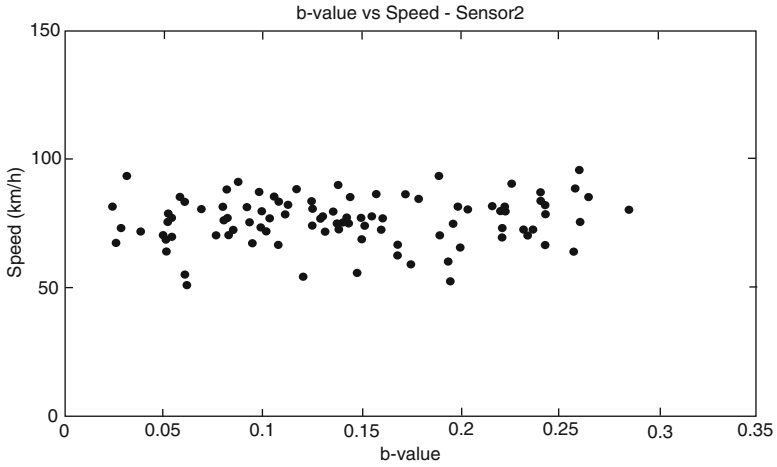

Fig. 21.12 Variation of b-Value vs. Truck speed

21.4 Concluding and Remarks

The goal of this work was to make a link between crack acoustic and traffic activities in order to monitor the health state of bridge structures. In the first part, traffic analysis was performed, which provided such information as number of trucks/day, weight/truck, and velocity. Traffic measurements combined with acoustic activities around the crack show an excellent correlation between WIM analysis output and acoustic parameters. Results also show that the traffic is an important factor of acoustic activity. RA-value and b-value (acoustic emission parameters), seem to be good indicators to study the evolution of a crack. However, these parameters are usually used for concrete and less for steel structures. In order to make statements about damage progress in the monitored area, reference values for AE activity in steel structures are needed. Such reference values are not available nowadays and should be a subject of future research. The needed reference values could be obtained by carrying out fatigue tests on pre-cracked specimen and following the evolution of the crack and the changing of AE.

Acknowledgements The research leading to these results has received funding from the European Community's Seventh Framework Programme (FP7/2007/2013) under grant agreement n285119. Thanks to Bajko Kulauzovic from Cestel Company.

References

1. Aggelis, D., Blom, J., El Kadi, M., Wastiels, J.: Influence of geometry on the fracturing behavior of textile reinforced cement monitored by acoustic emission. In: Proceeding of SPIE, vol. 9063. Nondestructive Characterization for Composite Materials, Aerospace Engineering, Civil Infrastructure, and Homeland Security, vol. 90630E (2014). ISBN-ISSN: 978-0-8194-9989-9
2. ARCHES D08: Recommendations on bridge traffic load monitoring, Brussels: European Commission (2009). http://arches.fehrl.org
3. ARCHES D10: Recommendations on dynamic amplification allowance, Brussels: European Commission (2009) http://arches.fehrl.org
4. ARCHES D15: Recommendation for the Acoustic Emissions Method Based Monitoring of Reinforced Concrete Bridges (2009) http://arches.fehrl.org
5. ARCHES D16: Recommendations on the use of soft, diagnostic and proof load testing. Brussels: European Commission (2009) http://arches.fehrl.org
6. Colombo, I., Main, I., Forde, M.: assessing damage of reinforced concrete beam using "b-value" analysis of acoustic emission signals. J. Mater. Civ. Eng. 280–286 (2003)
7. COST 323: In: Jacob, B., OBrien, E.J., Jehaes, S. (eds.) Weigh-in-Motion of Road Vehicles: Final Report of the COST 323 Action. LCPC, Paris (2002)
8. Grosse, C.U., Ohtsu, M.: Acoustic Emission Testing, DMRB vol. 3, sect. 1, part 4. Inspection of Highway Structures, BD 63/07. Highways Agency, London (2007/2008)
9. Iwanami, M., Kamada, T., Nagataki, S.: Application of AE technique for crack monitoring in RC beams. JCI Proceedings of Cement and Concrete, vol. 51 (1997)
10. Moses, F.: Weigh-In-Motion system using instrumented bridges. ASCE Transp. Eng. J. **105**, 233–249 (1979)
11. Nair, A.: Acoustic emission monitoring of bridges: review and case studies (2010)
12. O'Brien, E.J., Žnidarič, A., Ojio, T.: Bridge Weigh-in-Motion Latest Developments and Applications World Wide, pp. 39–56. LCPC, Paris (2008)

13. Ohtsu, M.: RILEM TC 212-ACD: Final report on acoustic emission and related non-destructive evaluation techniques for crack detection and damage evaluation, s.l.: s.n. (2010)
14. Ohtsu, M.: Towards the Establishment of Infra-Dock for Concrete Structures. Structural Faults and Repair 2014. London (2014)
15. RILEM TC-212-ACD: Recommendation of RILEM TC-212-ACD: acoustic emission and related NDE techniques for crack detection and damage evaluation in concrete. The method for classification of active cracks in concrete structures by acoustic emission. Mater. Struct. **43**, 1187–1189 (2010)
16. RILEM TC239-MCM: On-site measurement of concrete and masonry structures by visualized NDT, 7th TC Meeting. London (2014)
17. Šajna, A., Bremec, T.: Use of the acoustic technique on reinforced concrete bending loaded specimens, s.n., pp. 211–220. Varenna (2008)
18. Šajna, A., Kovač, J., Bajt, Ž.: Acoustic emission monitoring of cracking in reinforced concrete specimens, s.n., pp. 207–224. Quebec City (2006)
19. Seto, M., Utagawa, M., Katsuyama, K.: The estimation of pre-stress from AE in cyclic loading of prestressed rock. Progress in Acoustic Emission VII, pp. 159–166 (1992)
20. Shiotani, T., Ohtsu, M., Ikeda, K.: Detection and evaluation of AE waves due to rock deformation. Constr. Build. Mater. **15**, 235–246 (2001)
21. Shiotani, T., Takada, Y., Ishitusuka, K.: Damage assessment of concrete structures by using ultrasonic Q-value. Structural Faults and Repair. London (2014)
22. Yuyama, S., Okamoto, T., Shigeishi, M., Ohtsu, M.: Quantitative evaluation and visualisation of cracking process in reinforced concrete specimens by moment tensor analysis of acoustic emission (1994)
23. Žnidarič, A., Lavrič, I.: Applications of B-WIM technology to bridge assessment. In: Nidari, A., Lavri, I., Kalin, J., Kreslin, M. (eds.) Using Strips to Mitigate the Multiple-Presence Problem of BWIM Systems, pp. 89–98. ISTE/Wiley, Philadelphia/Dallas/London/Hoboken (2010/2012)

Chapter 22
Model-Based Estimation of Hydrodynamic Forces on the Bergsoysund Bridge

Øyvind Wiig Petersen, Ole Øiseth, Torodd S. Nord, and Eliz-Mari Lourens

Abstract Knowledge of excitation loads on bridges are important for reliable design. Load models are however prone to uncertainties. Force identification using dynamic response measured on full-scale structures can be used to reduce the uncertainty. In this contribution, numerical simulations are performed to examine the feasibility of force identification on the floating pontoon Bergsoysund Bridge. We present a practical case study in which wave excitation forces and motion induced forces are estimated using only acceleration output. The sensor network considered represents the monitoring system currently installed on the bridge. A reduced order model with 26 modes is used to represent the structure in the identification. Wave force time series are generated by Monte Carlo simulations, and the acceleration response is obtained from a frequency domain solution of the equations of motion. The generated acceleration data is polluted with noise and subsequently used for identification. The results show that a joint input-state estimation algorithm is able to adequately identify a subset of hydrodynamic forces acting on the pontoons in the presence of both measurement and model errors. The translational forces are identified with a larger accuracy than the moments. Lastly, considerations and improvements for an analysis with experimental field data are presented.

Keywords Force identification • Floating bridge • Sensor network • Fluid-structure interaction • Wave loading

22.1 Introduction

Dynamic behaviour plays an important role in the design of long-span bridges. In this regard the dynamic forces and resulting structural response are the most interesting variables. The process of finding the forces and response is usually based on established models of the loading and the dynamic system. However, the dynamic analysis is prone to uncertainties inherited from the uncertainties in the load models as well as the modelling of the relevant dynamic phenomena. In the development of novel structural concepts it is desired to reduce this uncertainty. For example, Norway is currently reviewing solutions to crossings of wide fjords (1–3 km): suspension bridges with floating towers, floating bridges and submerged tunnels are among the concepts considered. Dynamic effects not very pronounced in existing structures might play a critical role in these novel structures. Accurate knowledge of the critical features in design is vital for the new structures not to be restricted by the current engineering norms or codes [1]. Reducing the uncertainty related to the excitation forces is important for reliable design. By studying existing structures the state of the art understanding can be extended. This is especially true for civil engineering concepts which are still largely unexplored, such as floating bridges. A case study of the floating Bergsoysund Bridge is carried out in this paper. An overview of large floating bridges, including the Bergsoysund Bridge, can be found in [2]. The interesting dynamics of the bridge has also attracted other studies, amongst them theoretical inquiries into the response in the frequency domain [3, 4].

Analysing field data from a large floating bridge is motivated by the possibility to learn more about the in-situ dynamic loading and response conditions. For most practical cases encountered in civil engineering it is impossible to measure the external forces at full-scale, while the response is typically easier to obtain. This has led to the development of system inversion techniques, where the input forces are estimated from a limited set of response measurements. Several methods for force identification have been suggested, of which many time domain approaches are based on Kalman filter variants (see e.g. [5–12]) or least square schemes [13–15]. Frequency domain approaches can also be found [16, 17]. Probabilistic

Ø.W. Petersen (✉) • O. Øiseth • T.S. Nord
Norwegian University of Science and Technology, 7491 Trondheim, Norway
e-mail: oyvind.w.petersen@ntnu.no

E.-M. Lourens
Delft University of Technology, 2628 CN Delft, The Netherlands

S. Pakzad, C. Juan (eds.), *Dynamics of Civil Structures, Volume 2*, Conference Proceedings of the Society for Experimental Mechanics Series, DOI 10.1007/978-3-319-29751-4_22

methods for determining wave excitation moments have been applied on scale models studying ship rolling [18]. Gillijns and Moor [19] developed a joint input-state estimation algorithm, where no prior knowledge of the input forces is needed. Later the algorithm was adapted to structural dynamics and in particular to reduced order models [20], which is the kind used in this study. The framework was expanded by Maes et al. [21, 22], who looked at general conditions to ensure identifiability of the dynamic forces and response for instantaneous inversion methods. The method was also tested experimentally identifying drop-weight impact forces on a footbridge using acceleration data only [20]. Nord et al. [23] applied the same algorithm on a scale model to study ice-induced vibrations when both acceleration and strain data were available. Acquiring displacement or strain data at the Bergsoysund Bridge is very challenging, but acceleration data can be collected relatively easy. For this reason this paper focuses on simulations of force estimation using acceleration output only. Although this paper presents only numerical simulations, the aim is to demonstrate and design a realistic scenario in which field data is used. The sensor network considered in this paper reflects the current instrumentation at the bridge.

22.2 Theory

When modelling the dynamic behaviour of floating bridges, fluid-structure interaction needs to be included in addition to the structural vibrations. Consider a system with n_{DOF} degrees of freedom (DOF). The governing equations of motion can be formulated in the frequency domain as follows:

$$-\omega^2\mathbf{M}(\omega)\mathbf{u}(\omega) + i\omega\mathbf{C}(\omega)\mathbf{u}(\omega) + \mathbf{K}(\omega)\mathbf{u}(\omega) = \mathbf{S}_{ph}\mathbf{p}_w(\omega) \tag{22.1}$$

where $\mathbf{u}(\omega)$ and $\mathbf{p}_w(\omega)$ are the Fourier transforms of the displacement vector $\mathbf{u}(t) \in \mathbb{R}^{n_{DOF}}$ and wave excitation force vector $\mathbf{p}_w(t) \in \mathbb{R}^{n_p}$, respectively. Since only a part of the structure has direct fluid contact, the wave excitation forces are only active in a DOF subset, assigned by the selection matrix $\mathbf{S}_{ph} \in \mathbb{R}^{n_{DOF}\times n_p}$. Mass, damping and stiffness matrices are split into two parts [24]:

$$\mathbf{M}(\omega) = \mathbf{M}_s + \mathbf{M}_h(\omega) \tag{22.2}$$

$$\mathbf{C}(\omega) = \mathbf{C}_s + \mathbf{C}_h(\omega) \tag{22.3}$$

$$\mathbf{K} = \mathbf{K}_s + \mathbf{K}_h \tag{22.4}$$

where $\mathbf{M}_s, \mathbf{C}_s$ and $\mathbf{K}_s$ are the mass, damping and stiffness matrices related to the structure only. The frequency dependent terms $\mathbf{M}_h(\omega)$ and $\mathbf{C}_h(\omega)$, representing the hydrodynamic mass and damping, originate from the fluid-structure interaction. $\mathbf{K}_h$ is hydrodynamic restoring stiffness, which is assumed not to vary with frequency. For the purpose of force identification a time domain formulation is sought. When applying the inverse Fourier transform and rearranging, Eq. (22.1) becomes:

$$(\mathbf{M}_s + \mathbf{M}_{h0})\ddot{\mathbf{u}}(t) + \mathbf{C}_s\dot{\mathbf{u}}(t) + (\mathbf{K}_s + \mathbf{K}_h)\mathbf{u}(t) = \mathbf{S}_{ph}\mathbf{p}_w(t) + \mathbf{S}_{ph}\mathbf{p}_{mi}(t) = \mathbf{S}_{ph}\mathbf{p}_h(t) \tag{22.5}$$

where we define motion induced forces $\mathbf{p}_{mi}(t) \in \mathbb{R}^{n_p}$ by the following expression:

$$\mathbf{S}_{ph}\mathbf{p}_{mi}(t) = -\int_{-\infty}^{\infty} \dot{\mathbf{u}}(t-\tau)\tilde{\mathbf{k}}(\tau)\,\mathrm{d}\tau \tag{22.6}$$

It also follows from the Fourier convulsion theorem that the kernel $\tilde{\mathbf{k}}$ has the definition:

$$\tilde{\mathbf{k}}(t) = \frac{1}{2\pi}\int_{-\infty}^{\infty} (i\omega(\mathbf{M}_h(\omega) - \mathbf{M}_{h0}) + \mathbf{C}_h(\omega))\, e^{i\omega t}\,\mathrm{d}\omega \tag{22.7}$$

Here, the constant terms $\mathbf{M}_{h0}$ (the pontoon mass) as well as $\mathbf{K}_h$ have been included in the left hand side of Eq. (22.5). A choice is made to interpret these time invariant matrices as part of a linear system, while the effects of the frequency dependent terms, i.e. the added mass and damping, are interpreted as motion induced forces felt by the time-invariant system. The n_p unknown forces which are to be identified, are therefore collected in the hydrodynamic force vector $\mathbf{p}_h(t) = \mathbf{p}_w(t) + \mathbf{p}_{mi}(t)$. Thus the force identification does not directly distinguish between the wave excitation forces and the motion induced forces.

It is often convenient to introduce a reduced order model based on n_m selected modes through $\mathbf{u}(t) = \mathbf{\Phi}\mathbf{z}(t)$, where $\mathbf{z}(t) \in \mathbb{R}^{n_m}$ is the modal coordinate vector and $\mathbf{\Phi} \in \mathbb{R}^{n_{DOF} \times n_m}$ contains the mass normalized mode shapes. In the case of proportional damping, the modal transform of Eq. (22.5) then becomes:

$$\ddot{\mathbf{z}}(t) + \mathbf{\Gamma}\dot{\mathbf{z}}(t) + \mathbf{\Omega}^2\mathbf{z}(t) = \mathbf{\Phi}^T\mathbf{S}_{ph}\mathbf{p}_h(t) \tag{22.8}$$

where $\mathbf{\Gamma} \in \mathbb{R}^{n_m \times n_m}$ and $\mathbf{\Omega} \in \mathbb{R}^{n_m \times n_m}$ are both diagonally populated with natural frequencies ω_j and modal damping ratios ξ_j:

$$\mathbf{\Omega} = \text{diag}(\omega_1, \omega_2, \ldots, \omega_{n_m}), \quad \mathbf{\Gamma} = \text{diag}(2\omega_1\xi_1, 2\omega_2\xi_2, \ldots, 2\omega_{n_m}\xi_{n_m}) \tag{22.9}$$

Note that the modal transformation here is acquired from the far left side of Eq. (22.5); the modal properties are inherited from the structural system matrices ($\mathbf{M}_s$, $\mathbf{C}_s$, $\mathbf{K}_s$) together with $\mathbf{M}_{h0}$ and $\mathbf{K}_h$. In other words, the modal quantities does not correspond to solving a complex eigenvalue problem including $\mathbf{M}_h(\omega)$ and $\mathbf{C}_h(\omega)$. The modal properties and transformation do however accurately reflect the linear system formulation as chosen in Eq. (22.5). Furthermore, when a sampling rate of $1/\Delta t$ and a zero order hold on the force is assumed, the discrete time state-space representation of Eq. (22.8) can be formulated as:

$$\mathbf{x}_{k+1} = \mathbf{A}\mathbf{x}_k + \mathbf{B}\mathbf{p}_{h,k} \tag{22.10}$$

where $\mathbf{x}_k$ and $\mathbf{p}_{h,k}$ are the state and force vector at time $t_k = k\Delta t$ ($k \in \mathbb{N}$):

$$\mathbf{x}_k = \begin{pmatrix} \mathbf{z}(t_k) \\ \dot{\mathbf{z}}(t_k) \end{pmatrix}, \quad \mathbf{p}_{h,k} = \mathbf{p}_h(t_k) \tag{22.11}$$

The state transition matrix $\mathbf{A} \in \mathbb{R}^{2n_m \times 2n_m}$ and input matrix $\mathbf{B} \in \mathbb{R}^{2n_m \times n_p}$ are given as:

$$\mathbf{A} = e^{\mathbf{A}_c \Delta t}, \quad \mathbf{B} = (\mathbf{A} - \mathbf{I})\mathbf{A}_c^{-1}\mathbf{B}_c, \quad \mathbf{A}_c = \begin{bmatrix} \mathbf{0} & \mathbf{I} \\ -\mathbf{\Omega}^2 & -\mathbf{\Gamma} \end{bmatrix}, \quad \mathbf{B}_c = \begin{bmatrix} \mathbf{0} \\ \mathbf{\Phi}^T\mathbf{S}_{ph} \end{bmatrix} \tag{22.12}$$

Furthermore, we consider an output vector $\mathbf{y} \in \mathbb{R}^{n_{d,a}}$ containing $n_{d,a}$ response measurements. The vector $\mathbf{y}$ can, when only acceleration output is considered, be written as:

$$\mathbf{y}_k = \mathbf{S}_a\ddot{\mathbf{u}}(t_k) = \mathbf{G}\mathbf{x}_k + \mathbf{J}\mathbf{p}_{h,k} \tag{22.13}$$

where $\mathbf{S}_a \in \mathbb{R}^{n_{d,a} \times n_{DOF}}$ is a selection matrix describing the linear relationship between the output and the physical DOFs. $\mathbf{G} \in \mathbb{R}^{n_{d,a} \times n_m}$ and $\mathbf{J} \in \mathbb{R}^{n_{d,a} \times n_p}$ symbolizes the output influence matrix and direct transmission matrix, respectively:

$$\mathbf{G} = -\mathbf{S}_a\mathbf{\Phi}\begin{bmatrix}\mathbf{\Omega}^2 & \mathbf{\Gamma}\end{bmatrix}, \quad \mathbf{J} = \begin{bmatrix}\mathbf{S}_a\mathbf{\Phi}\mathbf{\Phi}^T\mathbf{S}_p\end{bmatrix} \tag{22.14}$$

In the presence of noise, zero mean white noise vectors are added to Eqs. (22.10) and (22.13), which completes the stochastic state-space representation:

$$\mathbf{x}_{k+1} = \mathbf{A}\mathbf{x}_k + \mathbf{B}\mathbf{p}_{h,k} + \mathbf{w}_k \tag{22.15}$$

$$\mathbf{y}_k = \mathbf{G}\mathbf{x}_k + \mathbf{J}\mathbf{p}_{h,k} + \mathbf{v}_k \tag{22.16}$$

The model error $\mathbf{w}_k$ and measurement error $\mathbf{v}_k$ have covariance $\mathbb{E}[\mathbf{w}_k\mathbf{w}_k^T] = \mathbf{Q}$ and $\mathbb{E}[\mathbf{v}_k\mathbf{v}_k^T] = \mathbf{R}$. While not strictly necessary, the two noise vectors are in addition assumed mutually uncorrelated. A formulation taking into account correlation can be found in [25]. The error covariance is important since the joint input-state estimation, which is used to identify forces in this paper, is based on a minimum variance unbiased criterion. The algorithm is recursive and can be divided into three steps:

Input estimation:

$$\tilde{\mathbf{R}}_k = \mathbf{G}\mathbf{P}_{k|k-1}\mathbf{G}^T + \mathbf{R} \tag{22.17}$$

$$\mathbf{M}_k = (\mathbf{J}^T\tilde{\mathbf{R}}_k^{-1}\mathbf{J})^{-1}\mathbf{J}^T\tilde{\mathbf{R}}_k^{-1} \tag{22.18}$$

$$\hat{\mathbf{p}}_{k|k} = \mathbf{M}_k(\mathbf{y}_k - \mathbf{G}\hat{\mathbf{x}}_{k|k-1}) \tag{22.19}$$

$$\mathbf{P}_{\mathbf{p}[k|k]} = (\mathbf{J}^T\tilde{\mathbf{R}}_k^{-1}\mathbf{J})^{-1} \tag{22.20}$$

Measurement update:

$$\mathbf{L}_k = \mathbf{P}_{k|k-1}\mathbf{G}^{\mathrm{T}}\tilde{\mathbf{R}}_k^{-1} \tag{22.21}$$

$$\hat{\mathbf{x}}_{k|k} = \hat{\mathbf{x}}_{k|k-1} + \mathbf{L}_k(\mathbf{y}_k - \mathbf{G}\hat{\mathbf{x}}_{k|k-1} - \mathbf{J}\hat{\mathbf{p}}_{k|k}) \tag{22.22}$$

$$\mathbf{P}_{k|k} = \mathbf{P}_{k|k-1} - \mathbf{L}_k(\tilde{\mathbf{R}}_k - \mathbf{J}\mathbf{P}_{\mathbf{p}[k|k]}\mathbf{J}^{\mathrm{T}})\mathbf{L}_k^T \tag{22.23}$$

$$\mathbf{P}_{\mathbf{xp}[k|k]} = \mathbf{P}_{\mathbf{px}[k|k]}^{\mathrm{T}} = -\mathbf{L}_k\mathbf{J}\mathbf{P}_{\mathbf{p}[k|k]} \tag{22.24}$$

Time update:

$$\hat{\mathbf{x}}_{k+1|k} = \mathbf{A}\hat{\mathbf{x}}_{k|k} + \mathbf{B}\hat{\mathbf{p}}_{k|k} \tag{22.25}$$

$$\mathbf{P}_{k+1|k} = \begin{bmatrix}\mathbf{A} & \mathbf{B}\end{bmatrix}\begin{bmatrix}\mathbf{P}_{k|k} & \mathbf{P}_{\mathbf{xp}[k|k]} \\ \mathbf{P}_{\mathbf{px}[k|k]} & \mathbf{P}_{\mathbf{p}[k|k]}\end{bmatrix}\begin{bmatrix}\mathbf{A}^{\mathrm{T}} \\ \mathbf{B}^{\mathrm{T}}\end{bmatrix} + \mathbf{Q} \tag{22.26}$$

$\hat{\mathbf{p}}_{k|k}$ and $\hat{\mathbf{x}}_{k|k}$ are the filter estimates of the input forces and states, respectively. For more information on the assumptions behind the algorithm, we refer to the original works [19] and the extension to structural dynamics [20].

22.3 Case Study: The Bergsoysund Bridge

22.3.1 Structure and Sensor Network

The Bergsoysund Bridge, depicted in Fig. 22.1, is a 931 m long floating bridge located in the mid-western part of Norway. It is one the worlds very few long-span floating bridges with end-support only. This feature makes the bridge susceptible to dynamic excitations induced by wave loads. The bridge rests on seven pontoons dividing the bridge into eight spans of 105 m each, see Fig. 22.2. The steel superstructure is a trusswork of circular tubes, while the air-filled pontoons (approximate size 34 m×20 m×7 m) are made from lightweight concrete. Half the pontoon is submerged at rest conditions.

Fig. 22.1 Panorama view of the Bergsoysund bridge

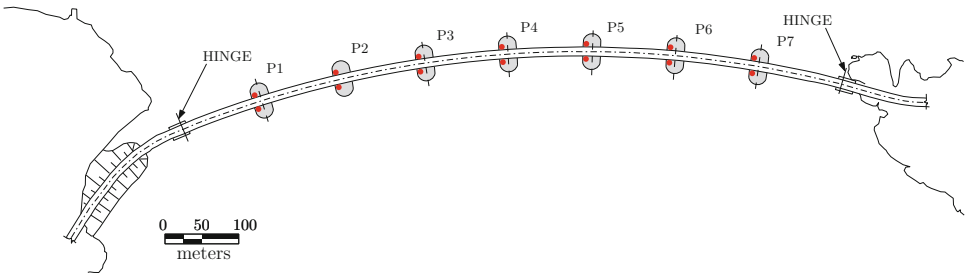

Fig. 22.2 Overhead view of the Bergsoysund bridge with the locations of the 14 triaxial accelerometers marked in *red*

Fig. 22.3 Accelerometer clamped to the steel truss

A finite element model was constructed in the software Abaqus using 3-node Timoshenko beam elements for the steel truss and 8-node shell elements for the upper deck. Structural damping is assumed stiffness and mass proportional with coefficients $\alpha = \beta = 5{\times}10^{-3}$:

$$\mathbf{C}_\mathrm{s} = \alpha(\mathbf{M}_\mathrm{s} + \mathbf{M}_\mathrm{h0}) + \beta(\mathbf{K}_\mathrm{s} + \mathbf{K}_\mathrm{h}) \tag{22.27}$$

Hydrodynamic mass, damping and stiffness matrices related to the pontoon-water interface were obtained in the software DNV HydroD WADAM (see [4] for details). Although the hydrodynamic forces in reality are spatially distributed, the forces are presumed to have six equivalent force resultants working in a single node located in the centre of each pontoon. At the bridge there are one pair of accelerometers mounted on the steel truss at each pontoon, see Figs. 22.2 and 22.3. $\mathrm{n_{d,a}} = 42$ acceleration signals are available from the sensor network consisting of 14 triaxial accelerometers. The sampling rate is set to 41.72 Hz.

22.3.2 Simulation Model

Obtaining measurement data and the process of estimating forces are in general two independent exercises. A clear distinction is therefore made between the model used to simulate the forces and measurement data, and the model which is used to identify the forces. The purpose of the simulation model is to closely mimic the real behaviour of the bridge and thereby generate realistic data sets (i.e. response and forces). The identification model, described in the next section, can have simplifications while still being able to represent structure and its dynamic behaviour relevant for processing the measurement data in a force identification case. Here, generating artificial force and response data are done by means of Monte Carlo simulations using a wave load spectrum $\mathbf{\Lambda}_\mathrm{pw}(\omega) \in \mathbb{R}^{\mathrm{n_p}\times\mathrm{n_p}}$. The wave load spectrum is obtained from an assumed sea state defined by a range of parameters such as significant wave height (H_s), mean wave angle (θ_0) and crest length spreading constant (s). A one-dimensional generalized Pierson-Moskowitz [26] distribution was chosen for the wave elevation spectral density. For the directional distribution of the waves, a cos-2s [27] distribution with $\theta_0 = 90°$ and $s = 29$ was utilized. The first parameter means the wave density is distributed symmetrically about the mid pontoon, while the second parameter signifies a rather small spatial correlation of wave elevation. H_s, defined as the upper $1/3$-fraction of wave elevations, was taken as 0.9 m, a value which is expected to occur annually. Figure 22.4 shows the resulting wave force spectrum for the middle pontoon. For more details on the loading conditions and the transfer function relating wave elevation and wave induced forces the reader is referred to [3].

A total of $\mathrm{n_m} = 65$ modes are included in the simulation, the highest of which has a natural frequency of 5.9 Hz. The number of simulated forces at the seven pontoons is $\mathrm{n_p} = 6{\times}7 = 42$. The wave excitation load $\mathbf{p}_\mathrm{w}(t)$ is sampled elementwise (denoted $p_{\mathrm{w},m}(t)$) from the spectrum $\mathbf{\Lambda}_\mathrm{pw}(\omega)$, which is discretized with $\Delta\omega = 0.001$ rad/s:

$$p_{\mathrm{w},m}(t) = \sqrt{2\Delta\omega}\,\mathrm{Re}\left(\sum_{l=1}^{m}\sum_{k=1}^{N} L_{ml}(\omega_k)e^{i(\omega_k t+\alpha_{lk})}\right) \quad (m = 1\ldots\mathrm{n_p}) \tag{22.28}$$

where α_{lk} is a phase angle uniformly random in $[0, 2\pi]$ and L_{ml} are the elements of the decomposition matrix $\mathbf{L}(\omega)$:

$$\mathbf{\Lambda}_\mathrm{pw}(\omega) = \mathbf{L}(\omega)\mathbf{L}^*(\omega) \tag{22.29}$$

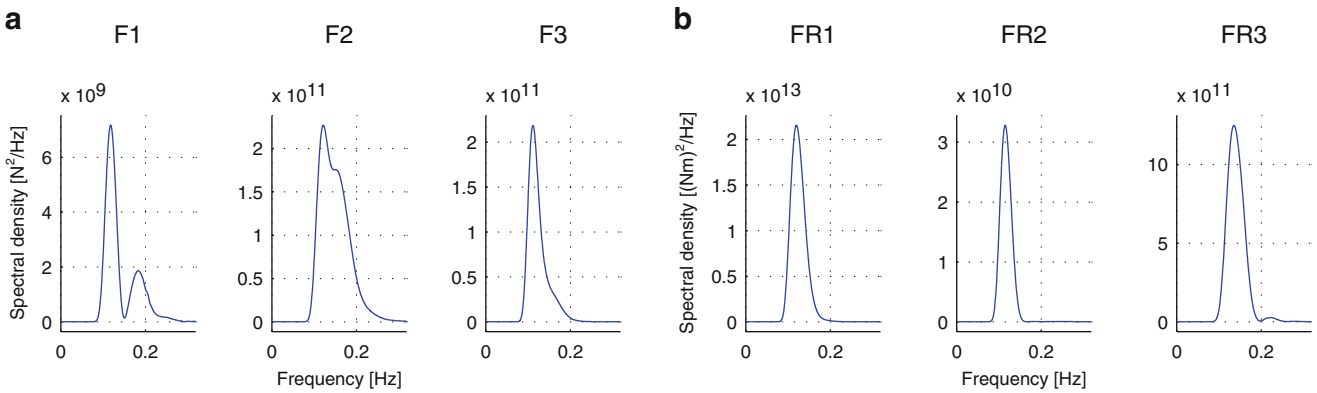

Fig. 22.4 Diagonal elements of $\mathbf{\Lambda}_{\mathrm{pw}}(\omega)$ for (**a**) the wave excitation forces (axial, lateral and vertical) and (**b**) wave excitation moments (torsion, vertical bending and lateral bending) at the middle pontoon

The response of the structure to the simulated forces is obtained in the frequency domain. First, the generalized wave load $\mathbf{p}_{\mathrm{w},g}(t) \in \mathbb{R}^{\mathrm{n_m}}$ is defined as:

$$\mathbf{p}_{\mathrm{w},g}(t) = \mathbf{\Phi}^{\mathrm{T}}\mathbf{S}_{\mathrm{ph}}\mathbf{p}_{\mathrm{w}}(t) \tag{22.30}$$

The load is then transformed into the frequency domain using the Fast Fourier Transform (FFT):

$$\mathbf{p}_{\mathrm{w},g}(\omega) = \mathrm{FFT}\left(\mathbf{p}_{\mathrm{w},g}(t)\right) \tag{22.31}$$

The modal response $\mathbf{z}(\omega)$ is then obtained using the generalized transfer function $\mathbf{H}_g(\omega)$:

$$\mathbf{H}_g(\omega) = \left[-\omega^2\left(\mathbf{I} + \mathbf{\Phi}^{\mathrm{T}}(\mathbf{M}_{\mathrm{h}}(\omega) - \mathbf{M}_{\mathrm{h0}})\mathbf{\Phi}\right) + i\omega\left(\mathbf{\Gamma} + \mathbf{\Phi}^{\mathrm{T}}\mathbf{C}_{\mathrm{h}}(\omega)\mathbf{\Phi}\right) + \mathbf{\Omega}^2\right]^{-1} \tag{22.32}$$

$$\mathbf{z}(\omega) = \mathbf{H}_g(\omega)\mathbf{p}_{\mathrm{w},g}(\omega) \tag{22.33}$$

It is emphasized that $\mathbf{H}_g(\omega)$ is the force-to-motion transfer function and includes the hydrodynamic mass and damping [28], and is thus not the transfer function of the time-invariant system in Eq. (22.8). $\ddot{\mathbf{z}}(t)$ is found using the inverse FFT:

$$\ddot{\mathbf{z}}(t) = \mathrm{IFFT}\left(-\omega^2\mathbf{z}(\omega)\right) \tag{22.34}$$

Finally, the modal acceleration output is transformed back to physical coordinates:

$$\mathbf{y}(t) = \mathbf{S}_{\mathrm{a}}\ddot{\mathbf{u}}(t) = \mathbf{S}_{\mathrm{a}}\mathbf{\Phi}\ddot{\mathbf{z}}(t) \tag{22.35}$$

22.3.3 Identification Model

As mentioned, the model used for force identification can differ from the simulation model. A choice is made to only identify a subset of the 42 forces, namely the vertical and horizontal forces as well as the torsional moment, see Fig. 22.5. Thus $\mathrm{n_p} = 3 \times 7 = 21$. The other force components are discarded mainly because their influence on the output is negligible and they are therefore considered too difficult to identify. From a practical standpoint, the neglected forces are also significantly smaller than those included in the identification. Nevertheless, by adding this error to the force terms in Eqs. (22.15) and (22.16), an additional modelling error is introduced. Also, the assumption that the measurement and modelling errors are uncorrelated is violated. The former effect can be accommodated for by means of the error covariance matrix $\mathbf{Q}$, while there is no straightforward remedy to the violation of the correlation assumption. As will be shown later, though, the effect hereof seems negligible.

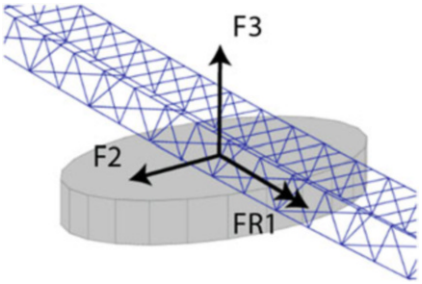

Fig. 22.5 Force components identified: vertical (F3), horizontal (F2) forces and torsional moment (FR1)

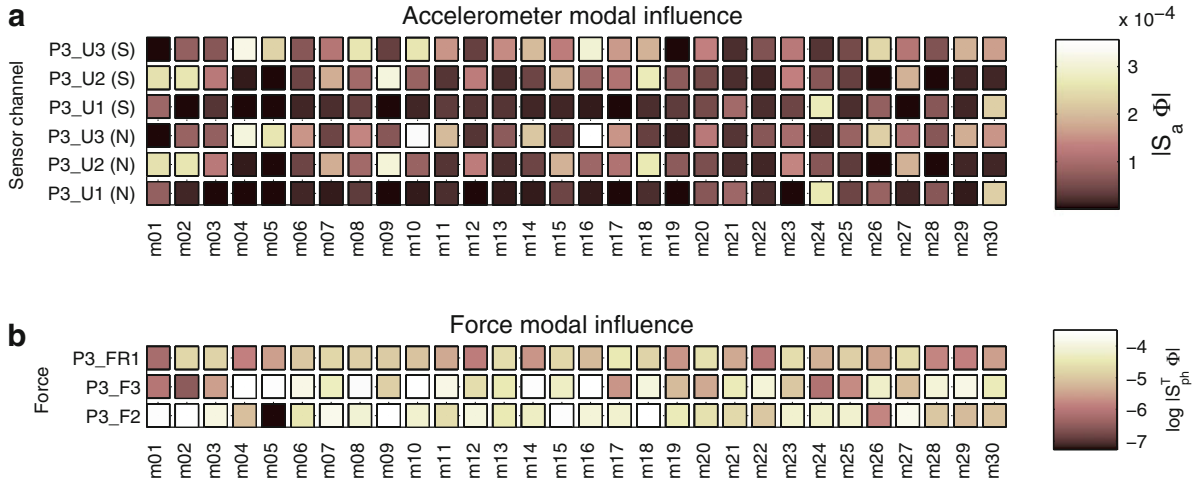

Fig. 22.6 (**a**): modal influence for sensors located at pontoon 3 (N=north side, S=south side); (**b**): modal influence for forces at pontoon 3

The modes which are included in the identification model are selected on the basis of a set of charts mapping the quantities $\mathbf{S}_a\boldsymbol{\Phi}$ and $\mathbf{S}_{ph}^T\boldsymbol{\Phi}$, which is seen as modal projections of the forces and sensors. It is mentioned that the same approach can also be used to determine sensor positions [22]. Figure 22.6 shows a subset of $\mathbf{S}_a\boldsymbol{\Phi}$ and $\mathbf{S}_{ph}^T\boldsymbol{\Phi}$ for sensors and forces at pontoon 3 for the 30 lowermost modes. It is desired to exclude modes having very little influence on the output or modes which the forces cannot control [29]. By reviewing similar charts for all forces and all sensors, mode number 21, 22, 29 and 30 are removed from the model. A reduced order model with the remaining $n_m = 26$ modes is used in the identification. If the modes are not removed, the system can suffer from ill-conditioning, giving rise to inaccurate estimates when noise is present. It is mentioned that the maps shown primarily serve as an indicator of improper modal candidates, and judging the results for several system configurations is necessary to gauge how the estimates conditions to the reduced order model.

State-space systems are widely studied and the fundamental conditions for system inversion are in general well established. For the special case of reduced order models in structural dynamics a set of necessary requirements can be found in [22]. We emphasize that the requirements must in general be considered necessary, but not sufficient for a successful estimation. They do not guarantee good results; they are only meant to reflect the estimation feasibility from an algorithmic point of view. Whether or not the requirements are met depends on the identification model as well as the sensor network. The two most important requirements in relation to input estimation can be summarized as follows:

Direct invertibility: This criterion establishes whether the system can be inverted without delay. This is fulfilled if and only if the matrix $\mathbf{J}$ in Eq. (22.16) has rank equal to n_p. Since $\mathbf{J} = [\mathbf{S}_a\boldsymbol{\Phi}\boldsymbol{\Phi}^T\mathbf{S}_{ph}]$, it implies that the number of acceleration measurements ($n_{d,a}$) must be equal or greater than the number of unknown forces (n_p). In addition, the reduced model order must be such that $n_m \geq n_p$.
Criterion evaluation: We directly observe that $n_p = 21 < n_{d,a} = 42$. It is found that $\text{rank}(\mathbf{J}) = 21$.
Stability: The stability in inversion of the state-space system depends on the transmission zeros $\lambda_j \in \mathbb{C}$, which satisfies the relation:

$$\begin{bmatrix} \mathbf{A} - \lambda_j\mathbf{I} & \mathbf{B} \\ \mathbf{G} & \mathbf{J} \end{bmatrix} \begin{bmatrix} \mathbf{x}_0 \\ \mathbf{p}_{h,0} \end{bmatrix} = \begin{bmatrix} \mathbf{0} \\ \mathbf{0} \end{bmatrix} \tag{22.36}$$

Transmission zeros could present a problem since a force $\mathbf{p}_{\mathrm{h},k} = \mathbf{p}_{\mathrm{h},0}\lambda_j^k$ ($k = 0, 1, \ldots N$) will not be distinguishable from the output, thereby making a unique system inversion impossible. Any $|\lambda_j| > 1$ is called an unstable transmission zero, while any $|\lambda_j| < 1$ is called stable since the undetectable force component converges towards zero when k increases. When only acceleration output is available, a so-called marginal transmission zero ($\lambda_j = 1$) will always be present, signifying that static components cannot be distinguished from the data.
Criterion evaluation: The only transmission zero present is $\lambda_j = 1$. The system inversion is marginally stable. It should be noted that all transmission zeros can hypothetically be eliminated if at least $\mathrm{n_p}$ displacement measurements are included in the output. However, as mentioned in the introduction, this is practically infeasible.

In addition, two other criteria which are less relevant are mentioned for the sake of informative purposes. *Controllability* is fulfilled since the matrix $\mathbf{S}_{\mathrm{ph}}^{\mathrm{T}}\boldsymbol{\Phi}$ contains no zero columns. This means that the hydrodynamic forces used in the identification are theoretically able to excite all modes that could be present in the measurement data. *Observability* is also fulfilled since $\mathbf{S}_{\mathrm{a}}\boldsymbol{\Phi}$ has no zero columns. The accelerometers this captures all modes in the identification model, and state estimation is feasible.

It is important to keep in mind, that from a practical perspective the actual force-mode transfer is highly dependent on the frequency content of the force as well as the structural transfer function. The wave force spectrum for instance, is practically zero above 0.5 Hz. It is mainly the lower modes that will be excited and thus will contribute to the output. It should be noted that the motion induced force frequency content will also depend on the modes themselves. The number of modes included is for this reason partly chosen on an algorithmic basis and partly on realistic evaluations of the expected dynamic behaviour.

22.4 Force Estimation

An initial state estimate $\hat{\mathbf{x}}_{0|-1}$ and error covariance $\mathbf{P}_{0|-1}$ must be supplied to initiate the joint input-state estimation. Here, $\mathbf{P}_{0|-1} = \mathbf{I}\times 10^2$ is chosen, while $\hat{\mathbf{x}}_{0|-1}$ is set to zero since the initial state is unknown. Uncorrelated white noise is added to the acceleration data, scaled by the standard deviation σ_{y}:

$$\tilde{\mathbf{y}} = \mathbf{y} + \epsilon_{\mathrm{y}}\boldsymbol{\Sigma}_{\mathrm{y}}\mathbf{r} \quad , \quad \boldsymbol{\Sigma}_{\mathrm{y}} = \mathrm{diag}(\sigma_{y_1}, \sigma_{y_2}, \ldots, \sigma_{y_{n_{d,a}}}) \tag{22.37}$$

where $\mathbf{r}$ is a vector of normally distributed numbers and the scale factor ϵ_{y} is chosen as 5 %. The measurement noise covariance is accordingly set to $\mathbf{R} = (\epsilon_{\mathrm{y}}\boldsymbol{\Sigma}_{\mathrm{y}})^2$. In a similar fashion the model noise covariance is established:

$$\mathbf{Q} = (\epsilon_{\mathrm{x}}\boldsymbol{\Sigma}_{\mathrm{x}})^2 \quad , \quad \boldsymbol{\Sigma}_{\mathrm{x}} = \mathrm{diag}(\sigma_{x_1}, \sigma_{x_2}, \ldots, \sigma_{\dot{x}_{nm}}) \tag{22.38}$$

The factor $\epsilon_{\mathrm{x}} = 0.1\,\%$ is selected to account for the modelling errors. In the present case the modal influence from the discarded forces is small, so the associated error contribution will also be limited.

A time series with length $T = 480$ s is considered and run through the algorithm formed by Eqs. (22.17)–(22.26). In the case of acceleration output only, a so-called drift in the estimates is often observed [5, 6, 20, 25] which can be explained by the lack of displacement data needed to stabilize the estimation process. This phenomenon is clearly displayed in Fig. 22.7, which shows raw (unfiltered) force estimates. To eliminate this unwanted effect the estimated forces are therefore high-pass filtered (6th order Butterworth filter) with a cutoff at 0.2 Hz. Choosing the cutoff values is an exercise done with care; the

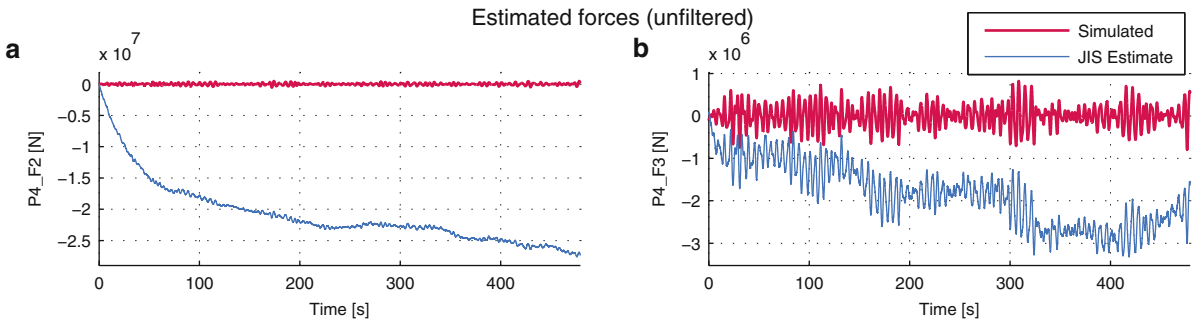

Fig. 22.7 Identified (**a**) horizontal and (**b**) vertical forces at pontoon 4 before high-pass filtering vs. the reference (simulated) forces

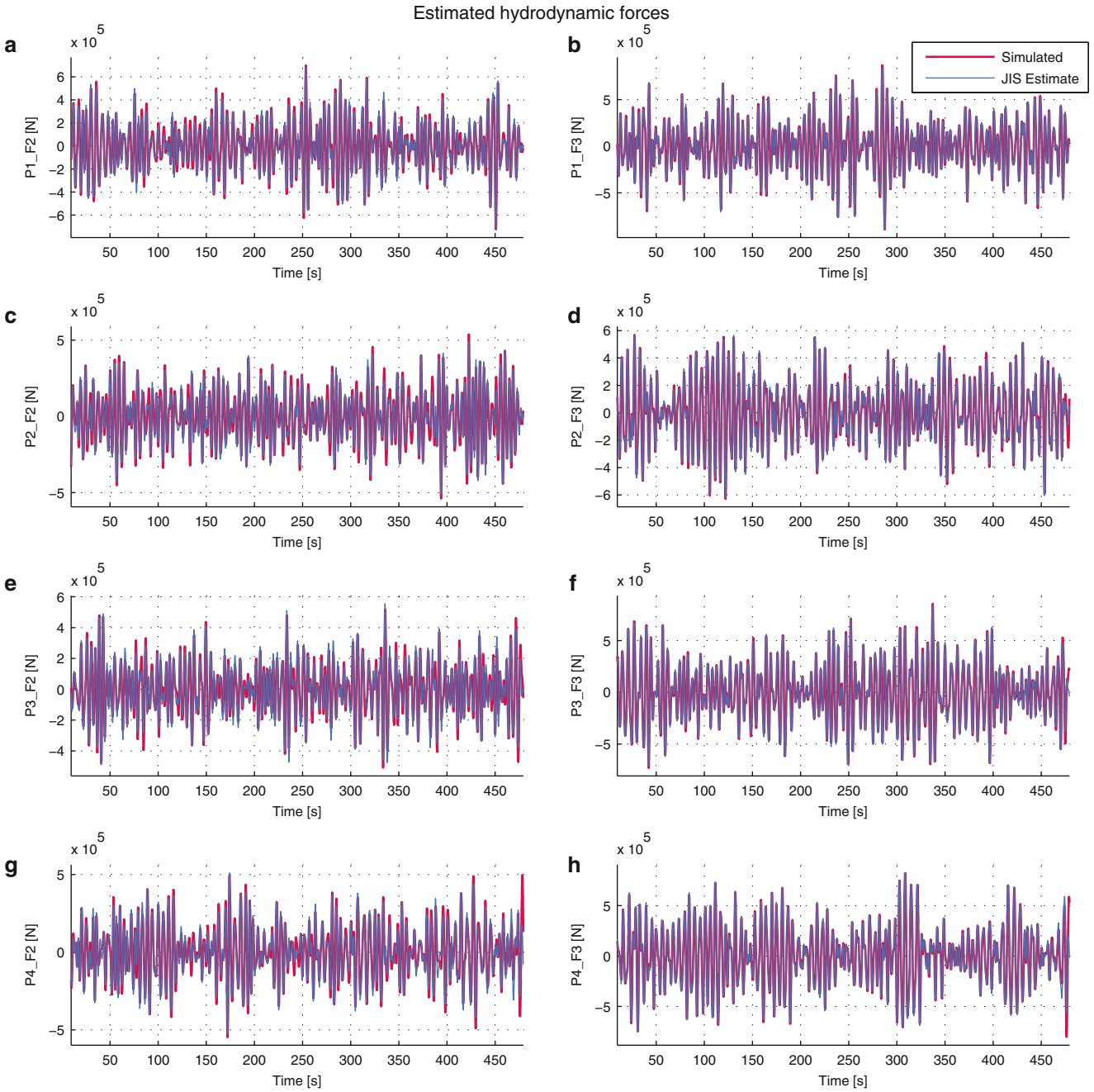

Fig. 22.8 Identified horizontal and vertical forces at pontoon 1 (**a**,**b**), pontoon 2 (**c**,**d**), pontoon 3 (**e**,**f**) and pontoon 4 (**g**,**h**)

frequency range at which the drift manifests is close to the range of the true forces. A low-pass filter (6th order Butterworth, 5 Hz cutoff) is also applied to remove unwanted high frequency content originating mainly from the added white noise in Eq. (22.37).

From Fig. 22.8 the identified forces are seen to agree well with the reference solution. For the identified moments in Fig. 22.9, larger errors are seen. The explanation lies partly in the fact that the moments generally have a weaker connection to the output than the forces, which is clear by examining the columns of the direct transmission matrix $\mathbf{J}$. An increased sensitivity to the measurement noise is therefore seen for the moments. Yet the estimated moments can, judged from a practical perspective, be considered to have satisfactory accuracy. While not shown here, the quality of the results at pontoon 5–7 are similar to pontoon 1–3 because of the structural symmetry. It is also evident that neglecting the force components F1, FR2 and FR3 is not particularly detrimental to the final results, nor is the assumption that the measurement and modelling

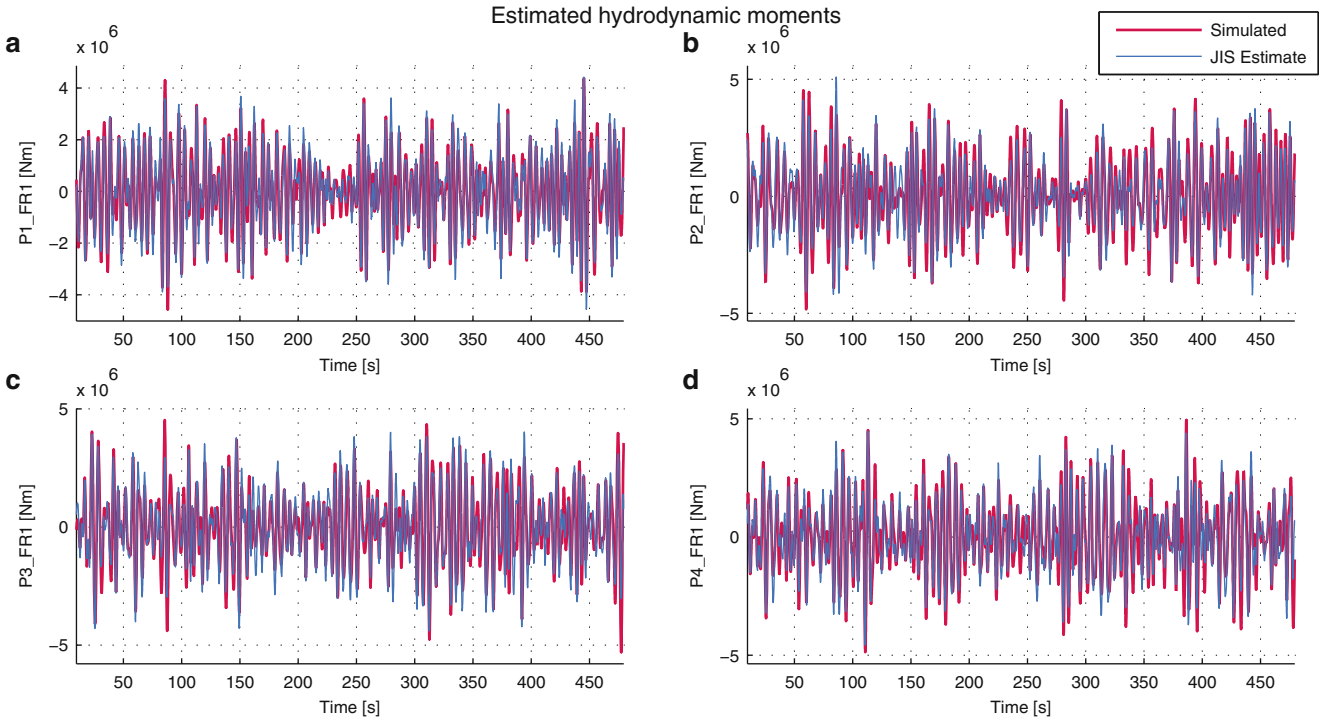

Fig. 22.9 Identified moments at pontoon 1 (**a**), pontoon 2 (**b**), pontoon 3 (**c**) and pontoon 4 (**d**)

errors are uncorrelated. The identified forces are expected to somewhat compensate for the unmodelled forces, and the small difference seen is reasonable considering the simplifications and assumptions which are made on the identification model.

A frequency domain comparison is shown in Fig. 22.10 for the forces estimated at pontoon 4. There are no frequencies in particular which display a noticeable domination of disturbance. However for the moment some of the peaks seem to be undervalued. The results at pontoon 4 are representative; a frequency domain comparison for six other pontoons displays similar traits.

22.5 Concluding Remarks

Knowledge of the hydrodynamic forces on large marine structures such as floating bridges are important for reliably design. Reducing load model uncertainties is motivated by an increase in the structural safety, which is valuable in the development of novel structures. It is desired to reduce these uncertainties by studying the dynamics of existing structures. The approach applied in this contribution is model-based force identification using measured dynamic response. This study has performed numerical simulations of the response to wave forces of the floating Bergsoysund Bridge. A reduced order model consisting of 26 modes was used in the identification process. A joint-input state estimation algorithm was applied for estimating the hydrodynamic forces on the Bergsoysund Bridge pontoons from acceleration output only. The results indicate that identification of a subset of the pontoon forces is feasible. The horizontal and vertical forces as well as the torsional moment on the seven pontoons are estimated accurately when the estimates are filtered to remove the low frequency drift encountered in acceleration output only estimation.

In the case of analysing field data from the Bergsoysund Bridge, several new challenges arise. Ambient excitation from traffic and wind will often be present in the measurement data. The former largely manifests at high frequencies and can be filtered out, whereas the latter has components in the same frequency range as the wave forces. Fortunately the wind forces are significantly smaller than the hydrodynamic ones. Further numerical case studies with both wind and wave forces could determine the significance of wind in the measurement data. Another problem encountered is establishing the error covariance matrices when the actual errors present are known to a much lesser extent. Correlation in the errors may be needed considered as well.

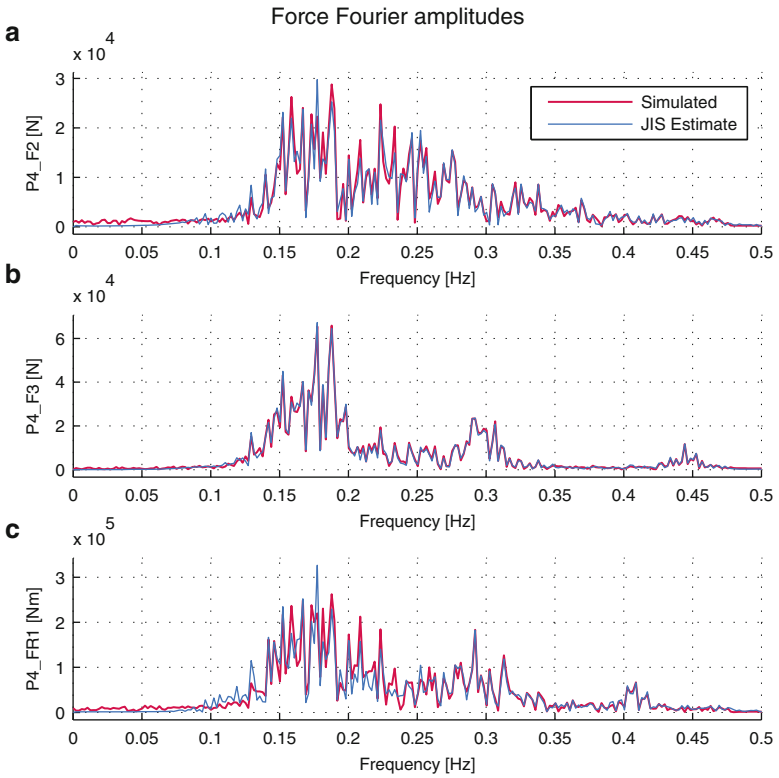

Fig. 22.10 Frequency content of identified vertical forces (**a**), horizontal forces (**b**) and moments (**c**) at pontoon 4

It is also possible to reformulate the problem to exclude $\mathbf{M}_{h0}$ and $\mathbf{K}_h$ from the linear system in Eq. (22.5) and consequently include their effects in the definition of the motion induced forces (Eqs. (22.6) and (22.7)). This changes the fundamental properties of the linear system. It is not straightforward to show how this would affect the results, seeing that the natural frequencies and mode shapes would differ significantly, thus altering e.g. the input identification requirements and the maps in Fig. 22.6. The formulation applied in this paper also does not distinguish between the motion induced and wave forces. An interesting problem is to separate the estimated hydrodynamic forces into the two contributions. Also, while it was possible to filter out the estimation drift for the presented case, a study of the drift evolution and drift removal methods will be useful to extend the research. The authors also aim to present results from full-scale identifications using field data soon.

References

1. Moe, G.: Design philosophy of floating bridges with emphasis on ways to ensure long life. J. Mar. Sci. Technol. **2**(3), 182–189 (1997)
2. Watanabe, E., Utsunomiya, T.: Analysis and design of floating bridges. Prog. Struct. Eng. Mater. **5**(3), 127–144 (2003)
3. Kvåle, K.A., Øiseth, O., Sigbjörnsson, R.: Modelling of the stochastic dynamic behaviour of the Bergsoysund bridge: an application of the power spectral density method. In: Proceedings of the 9th International Conference on Structural Dynamics, EURODYN (2014)
4. Kvåle, K.A., Øiseth, O., Rønnquist, A., Sigbjörnsson, R.: Modal analysis of a floating bridge without side-mooring. In: Dynamics of Civil Structures, vol. 2, pp. 127–136. Springer, Berlin (2015)
5. Lourens, E., Reynders, E., De Roeck, G., Degrande, G., Lombaert, G.: An augmented Kalman filter for force identification in structural dynamics. Mech. Syst. Signal Process. **27**, 446–460 (2012)
6. Azam, S.E., Chatzi, E., Papadimitriou, C.: A dual Kalman filter approach for state estimation via output-only acceleration measurements. Mech. Syst. Signal Process. **60**, 866–886 (2015)
7. Naets, F., Croes, J., Desmet, W.: An online coupled state/input/parameter estimation approach for structural dynamics. Comput. Methods Appl. Mech. Eng. **283**, 1167–1188 (2015)
8. Hwang, J., Kareem, A., Kim, W.: Estimation of modal loads using structural response. J. Sound Vib. **326**(3), 522–539 (2009)
9. Hwang, J.-S., Lee, S.-G., Ji-hoon, P., Eun-Jong, Y.: Force identification from structural responses using Kalman filter. In: Institute of Materials Engineering, Volume 33, pp. 257–266, Melbourne, Australia (2009)
10. Ma, C.-K., Lin, D.-C.: Input forces estimation of a cantilever beam. Inverse Prob. Eng. **8**(6), 511–528 (2000)
11. Ma, C.K., Chang, J.M., Lin, D.C.: Input forces estimation of beam structures by an inverse method. J. Sound Vib. **259**(2), 387–407 (2003)

12. Hwang, J.-S., Kareem, A., Kim, H.: Wind load identification using wind tunnel test data by inverse analysis. J. Wind Eng. Ind. Aerodyn. **99**(1), 18–26 (2011)
13. Adams, R., Doyle, J.F.: Multiple force identification for complex structures. Exp. Mech. **42**(1), 25–36 (2002)
14. Liu, J.-J., Ma, C.-K., Kung, I.-C., Lin, D.-C.: Input force estimation of a cantilever plate by using a system identification technique. Comput. Methods Appl. Mech. Eng. **190**(11), 1309–1322 (2000)
15. Mao, Y., Zhang, W., Ouyang, H., Lin, J.: Input force estimation accounting for modeling errors and noise in responses. Arch. Appl. Mech. **85**(7), 909–919 (2015)
16. Liu, Y., Shepard, W.S. Jr.: Dynamic force identification based on enhanced least squares and total least-squares schemes in the frequency domain. J. Sound Vib. **282**(1), 37–60 (2005)
17. Parloo, E., Verboven, P., Guillaume, P., Van Overmeire, M.: Force identification by means of in-operation modal models. J. Sound Vib. **262**(1), 161–173 (2003)
18. Han, S.L., Kinoshita, T.: Investigation of a stochastic inverse method to estimate an external force: applications to a wave-structure interaction. Math. Probl. Eng. **175036**, 25 (2012)
19. Gillijns, S., De Moor, B.: Unbiased minimum-variance input and state estimation for linear discrete-time systems with direct feedthrough. Automatica **43**(5), 934–937 (2007)
20. Lourens, E., Papadimitriou, C., Gillijns, S., Reynders, E., De Roeck, G., Lombaert, G.: Joint input-response estimation for structural systems based on reduced-order models and vibration data from a limited number of sensors. Mech. Syst. Signal Process. **29**, 310–327 (2012)
21. Maes, K., Lourens, E., De Roeck, G., Lombaert, G.: General conditions for instantaneous system inversion in structural dynamics. In: Proceedings of the 5th International Conference on Structural Engineering, Mechanics and Computation, SEMC, pp. 43–48 (2013)
22. Maes, K., Lourens, E., Van Nimmen, K., Reynders, E., De Roeck, G., Lombaert, G.: Design of sensor networks for instantaneous inversion of modally reduced order models in structural dynamics. Mech. Syst. Signal Process. **52**, 628–644 (2014)
23. Nord, T.S., Lourens, E., Øiseth, O., Metrikine, A.: Model-based force and state estimation in experimental ice-induced vibrations by means of Kalman filtering. Cold Reg. Sci. Technol. **111**, 13–26 (2015)
24. Taghipour, R., Perez, T., Moan, T.: Time-domain hydroelastic analysis of a flexible marine structure using state-space models. J. Offshore Mech. Arct. Eng. **131**(1), 011603 (2009)
25. Maes, K., Lourens, E., Van Nimmen, K., Reynders, E., Van den Broeck, P., Guillaume, P., De Roeck, G., Lombaert, G.: Verification of joint input-state estimation by in situ measurements on a footbridge. In: Proceedings of the 9th International Workshop on Structural Health Monitoring, vol. 1, pp. 343–350 (2013)
26. Pierson, W.J. Jr., Moskowitz, L.: A proposed spectral form for fully developed wind seas based on the similarity theory of S. A. Kitaigorodskii. J. Geophys. Res. **69**, 5181–5190 (1964)
27. National Academy of Sciences: Ocean Wave Spectra: Proceedings of a Conference, Easton, Maryland May 1961. Prentice Hall (1963)
28. Taghipour, R., Perez, T., Moan, T.: Hybrid frequency–time domain models for dynamic response analysis of marine structures. Ocean Eng. **35**(7), 685–705 (2008)
29. van der Male, P., Lourens, E.: Operational vibration-based response estimation for offshore wind lattice structures. In: Proceedings of IMAC XXXIII International Modal Analysis Conference, pp. 83–96 (2015)

Chapter 23
Operational Modal Analysis and Model Updating of Riveted Steel Bridge

Gunnstein T. Frøseth, Anders Rönnquist, and Ole Øiseth

Abstract Riveted steel bridges are common in the Norwegian and European railway network. Assessment of the current state is important to ensure continuous and safe operation of the railway. Furthermore, the prediction of remaining service life of these bridges is essential to allocate limited funds and resources to the most critical points in the infrastructure. Reliable and accurate numerical models are necessary tools to assess the current state and predict the remaining service life of these bridges.

This paper presents work carried out in obtaining a validated finite element model of the Lerelva railway bridge. System identification was carried out with data driven stochastic subspace identification using data with both initial conditions from train passage and ambient excitation. The modal data from the system identification procedure was utilized in updating the finite element model.

Keywords Operational modal analysis • Railway bridge • Field measurements • Model updating • System identification

23.1 Introduction and Background

The Norwegian railway network was built during the last century and largely completed by 1960. There are about 1000 steel bridges in the railway network, half of which were built before 1930. Older steel bridges were typically constructed with built up riveted members and an unballasted open deck trusswork to carry the railway. These bridges were not designed for fatigue failure, and during the last decades considerable research has been conducted to determine the fatigue resistance of riveted steel members [1], adapting numerical methods to assess stresses in these members [2, 3], develop and adapt methodology from the reliability framework to assess remaining service life of riveted steel bridges [4–7]. The reliability framework is a probabilistic methodology which allows inclusion of uncertainties in load, resistance and model, the consequence is that more realistic estimates of remaining service life may be obtained. Sensitivity analysis on the reliability of a railway bridge carried out in previous work by the authors [8] indicated that the estimated reliability is highly sensitive to the model uncertainty. The same indication was found from parametric studies carried out by Imam et al. [6]. The degree of sensitivity is obviously dependent on the bias and spread of the basic variable, but the fundamental reason for the sensitivity is due to the limit state function for fatigue failure being dependent on model uncertainty to a power, typically in the range between 3 to 5. Reducing the model uncertainty will therefore significantly improve the estimate on remaining service life for any bridge with respect to fatigue.

Model uncertainty can be chosen based on structural understanding and experience of the practitioner [9]. In practice this often means that the model uncertainty is based on general guidelines, e.g. [10], with larger spread and conservative bias as consequence to cover the entire scope of the source document. In fatigue evaluation of existing steel bridges, the model uncertainty is defined as the ratio between real stresses in the bridge and calculated stresses from the numerical model of the bridge. The model uncertainty may therefore be effectively determined by field measurements on the existing bridge and reduced by performing updating and validation of the numerical model.

Extending the service life of riveted steel bridges by field measurements and validation of numerical models has a significant economic and environmental benefit due to the volume of bridges in the Norwegian railway network. In addition, maintenance and operational breakdowns of railway bridges are extra costly since the traffic can not be easily rerouted within the railway infrastructure. Developing recommended practice for field measurements and validation of numerical models to extend service life of railway bridges is important because it increases the efficiency and reliability of the approach.

G.T. Frøseth (✉) • A. Rönnquist • O. Øiseth
Department of Structural Engineering, Norwegian University of Science and Technology, Richard Birkelandsveg 1a, 7491 Trondheim, Norway
e-mail: gunnstein.t.froseth@ntnu.no

S. Pakzad, C. Juan (eds.), *Dynamics of Civil Structures, Volume 2*, Conference Proceedings of the Society for Experimental Mechanics Series, DOI 10.1007/978-3-319-29751-4_23

Fig. 23.1 Overview of Lerelva railway bridge

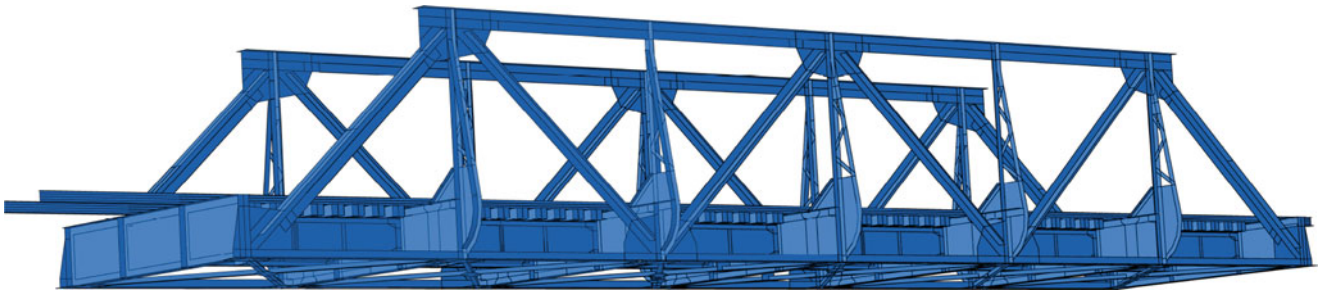

Fig. 23.2 The finite element model of Lerelva railway bridge

This paper presents the work carried out so far in establishing recommended practice in validation of numerical models of riveted steel railway bridges. Acceleration measurements on Lerelva railway bridge and operational modal analysis (OMA) is used to extract modal data. Model updating with the sensitivity method is utilized to update the numerical model, and to identify error sources in the finite element model.

Lerelva railway bridge lies on Dovrebanen between Trondheim and Heimdal station. Construction of the bridge was finished in 1917, it is an open deck riveted structure with a main span of 25 m and a width of 5.1 m. The bridge does not have upper lateral bracing and all lateral deflection is therefore taken by the bracing system below the open deck. The bridge lies in a curve with radius 300 m and it has a single track mounted on the supports with cant (Figs. 23.1 and 23.2).

23.2 Finite Element Model

The finite element model is built with shell elements in the general purpose finite element program Abaqus 6.14.

The geometry of the bridge is determined from drawings and inspection at the site. All plates and profiles was included in the modeling, but rivets were not modeled. Instead the profiles were merged into structural components by constraining adjacent surfaces together by ties. This will introduce additional stiffness to the component, since the actual continuity of the member is dependent on several factors, such as clamping force of rivets, friction coefficient on adjacent surfaces and type of load applied [2]. The railway track was included in the model to ensure proper mass distribution of the track and to study the influence of this substructure on the bridge. The track consists of two rails and a series of sleepers. In the real structure, the track is attached to the bridge by hooks going through the sleepers and onto the flange of the stringer. The hooks ensure that the track stays on the bridge, and may even contribute to structural stiffness by constraining the bridge

through interaction at the interface between the two systems. In the finite element model, the rails were constrained to the sleepers with tie constraints. The connection between the railway track and bridge was modeled by constraining the lateral and vertical translational DOFs at a single node on each side of the sleeper to the nearest node on the stringer. The DOF in the longitudinal direction of the bridge was kept free. This is obviously a simplification in comparison to the complex interaction between track and bridge which should be investigated further in another study. Inspection at the site discovered that the real supports are close to idealized pinned and roller bearing. The bridge is modeled as simply supported with pinned boundary conditions towards Trondheim. The nominal material parameters used in the finite element model are $E_{\text{steel}} = 210\,000\,\text{MPa}$, $\nu_{\text{steel}} = 0.3$, $\rho_{\text{steel}} = 7850\,\text{kg/m}^3$ for steel and $E_{\text{wood}} = 10\,000\,\text{MPa}$, $\nu_{\text{wood}} = 0.25$, $\rho_{\text{wood}} = 720\,\text{kg/m}^3$.

23.3 System Identification

Measurements were carried out with 9 wireless tri-axial accelerometers, mounted on separate axes along the bridge, see Fig. 23.3. The acquisition rate was set to 200 Hz, the data was preprocessed by high pass filtering with cutoff 1 Hz, then low pass filtered at 40 Hz and finally resampled at 100 Hz before the data was used further in the analysis.

OMA was performed on data series acquired just after a train left the bridge. The data series then contained initial conditions from the train passing the bridge in addition to ambient excitation. Quin et al. [11] showed that the accuracy of the detected mode parameters and the number of modes identified increased when the data series contains combined initial conditions and ambient excitation. They also showed that the length of the data series could be lowered under these conditions. The length of the acquired data series was set to 60 s based on the finding in the paper by Quin et al. [11] and an expected fundamental frequency 5 Hz for the bridge.

System identification was performed with data driven stochastic subspace identification (SSI) using the implementation in MATLAB toolbox MACEC 3.2 [12]. In the identification, half the number of block rows was 120 and the model order was chosen 250 after considering several different values for the model order. Figure 23.4 shows stabilization diagram from the system identification.

The stabilization diagram shows that the system identification gives very clear indication of stable poles. The fundamental mode has a frequency 5.18 Hz, also note that there are six modes in the range 8–10 Hz. The system identification showed that the bridge was lightly damped, with all identified modes below 1 % damping ratio.

Four modes identified from the experimental data were chosen as reference modes for model updating. Based on a pairing with the initial finite element model, the modes can be qualitatively described as the first global bending mode about vertical and lateral axis, bending of the side walls and roll mode, see Fig. 23.5.

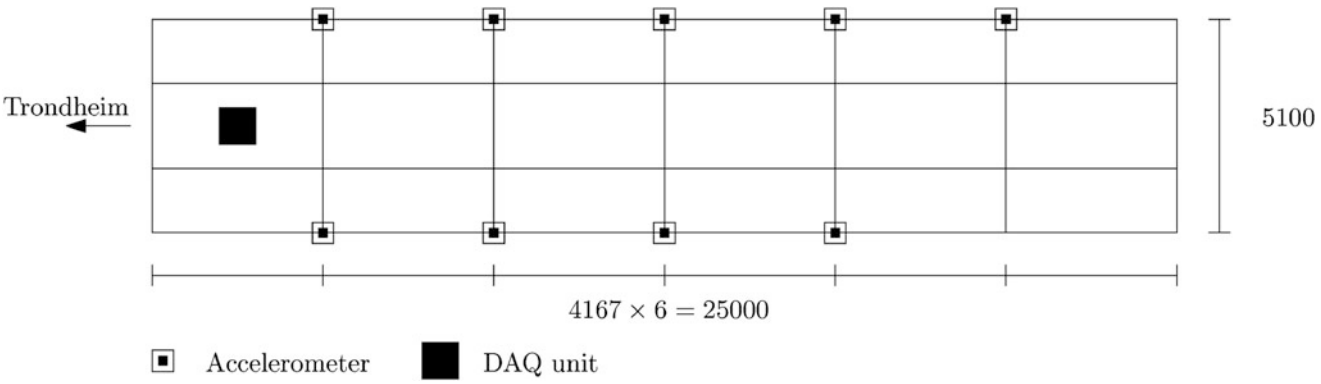

Fig. 23.3 Distribution of sensors network on the bridge

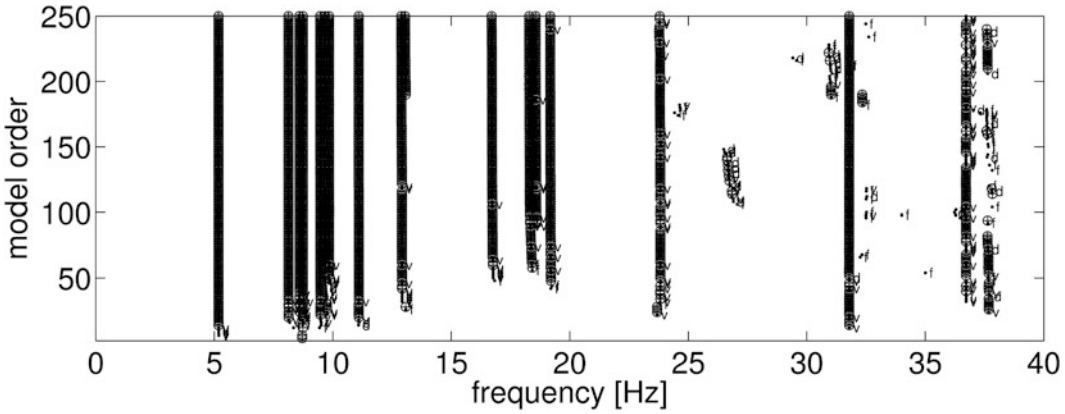

Fig. 23.4 Stabilization diagram showing the identified modes; ⊕ denotes a stable pole, *v* stable vector and frequency; *d* stable damping and frequency; and *f* stable frequency. The stabilization criteria used in the diagram were *frequency*: 1 %, *damping ratio*: 5 %, *mode shapes*: 1 % and *MPC* 0.50

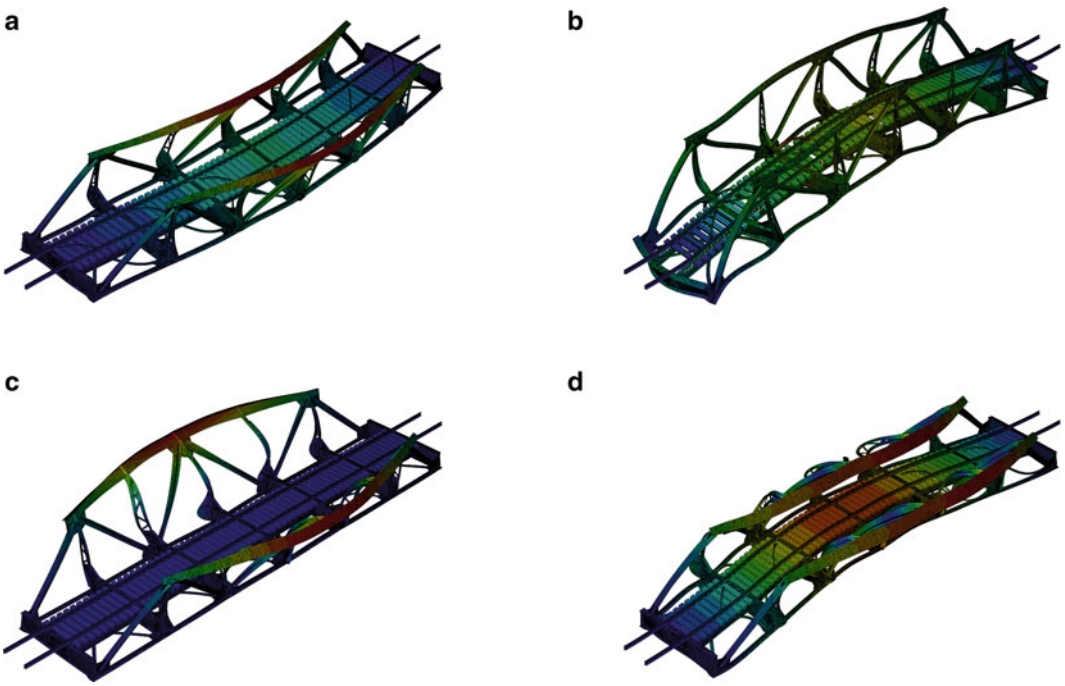

Fig. 23.5 The figure shows the modes chosen as reference modes in the model updating procedure. (**a**) 1st Lateral bending, 5.18 Hz. (**b**) 1st Vertical bending, 9.47 Hz. (**c**) Side wall bending, 9.84 Hz. (**d**) Roll, 11.09 Hz

23.4 Model Updating

23.4.1 Updating Algorithm

Sensitivity method was applied in the model updating step by utilizing the eigenvalue residual. The sensitivity matrix $\mathbf{G}_n$ was obtained by perturbing the updating parameters at the linearization point $\mathbf{z}_n = \mathbf{z}(\mathbf{x}_n)$, where $\mathbf{z}(\mathbf{x})$ is the predicted response vector and $\mathbf{x}$ are the updating parameters. The response vector obtained from finite element analysis was matched with the reference response vector by mode correlation utilizing the modal assurance criterion (MAC). The sensitivity method is based on first order Taylor series expansion around the linearization point

$$\mathbf{e}_z = \mathbf{z}_m - \mathbf{z}(\mathbf{x}) \approx \mathbf{r}_n - \mathbf{G}_n \Delta \mathbf{x}_n \tag{23.1}$$

where $\mathbf{z}_m$ is the measured response vector and $\mathbf{r}_n = \mathbf{z}_m - \mathbf{z}_n$ is the residual response vector. The objective function $J(\mathbf{x})$ to be minimized becomes

$$J(\mathbf{x}) = \mathbf{e}_z^T \mathbf{W}_e \mathbf{e}_z \tag{23.2}$$

where $\mathbf{W}_e = \text{diag}\,\{\mathbf{z}_m\}^{-2}$ is the weighing matrix. The weighing matrix was chosen to emphasize the lowest modes in the updating procedure. The condition number $\kappa(\mathbf{G}_n^T \mathbf{W}_e \mathbf{G}_n)$ was around 10^2 during the updating procedure and confirmed that the system in the study was well conditioned, regularization was therefore not necessary. The parameter increment was determined by the following relation

$$\Delta \mathbf{x}_n = \left(\mathbf{G}_n^T \mathbf{W}_e \mathbf{G}_n\right)^{-1} \mathbf{G}_n^T \mathbf{W}_e \mathbf{r}_n \tag{23.3}$$

and the updated parameter $\mathbf{x}_{n+1}$ is then found by

$$\mathbf{x}_{n+1} = \mathbf{x}_n + \Delta \mathbf{x}_n \tag{23.4}$$

See Mottershead et al. [13] for more details.

23.4.2 Updating Parameters

Updating parameters were chosen based on engineering judgment, considerations on uncertainties related to modeling and geometry of the model. The objective function of the updating procedure is defined by the difference between the measured and predicted eigenfrequencies of the system. The updating procedure is therefore dependent on (1) material properties of the bridge and track, (2) the geometry of the different parts and (3) constraints introduced in the modeling.

The continuity and coherence of built up structural members for riveted bridges is a challenging topic as mentioned in Sect. 23.2. The verticals in Lerelva railway bridge have relatively complex geometry and multiple critical joints, i.e joints with a single rivet, which makes them sensitive to geometric errors and damage. The stiffness of each vertical may therefore have considerable variability, but the general stiffness of the verticals may also be in error due to the geometric aspects mentioned above. The focus here will be on investigating the general error in stiffness when modeling the verticals. The uncertainty related to modeling of verticals are parametrized by the elastic modulus E_{vert} assigned to this group of members. Forces in the lateral direction of the bridge are mainly taken up by the bracing below the secondary load carrying system. The structural stiffness of the bridge in the horizontal direction is therefore largely dependent on proper modeling of this subsystem. The elastic modulus of the bracing system E_{brace} is introduced in the updating procedure to further investigate the sensitivity of the structural system to modeling of the lateral bracing and the overall stiffness of the system in the lateral direction.

The track is built up of wooden sleepers and a two steel UIC60 rails. The material parameters and geometry of the rails are well known and not suitable candidates for updating. The geometry of the wooden sleepers is also well defined, but the material parameters show considerable spread [14]. Gryc et al. [15] reports densities ranging from 664 kg/m^3 to 912 kg/m^3 in European beech, which is typically used in railway sleepers. Density of the wooden sleepers, ρ_{wood}, is therefore introduced as a updating parameter to account for the uncertainty in this parameter.

23.5 Results and Discussion

This section presents preliminary results obtained in the model updating step. A stable solution was found and is shown in Table 23.1. Several sets of initial conditions were chosen for the updating procedure to ensure that the converged solution was the one closest to the nominal parameters. Table 23.1 shows that the initial finite element model has high frequencies in the lateral bending mode and in the roll mode compared to the measured data, while the frequencies for the side wall mode is too low. The vertical bending mode obtained from the initial finite element model is in good agreement with the frequencies identified from the measured data. The table also shows that MAC, which expresses the correlation between the predicted and measured mode shapes, are above 0.75 for all choses modes in the initial step.

Table 23.1 The table shows the measured frequencies for the chosen modes for updating as well as frequencies and MAC numbers before and after updating

Mode	Measured	Initial		Updated		Error in frequency	
		Frequency	MAC	Frequency	MAC	Initial (%)	Updated (%)
1st lateral bending	5.18	5.77	0.99	5.18	0.98	11	0
1st vertical bending	9.47	9.68	0.92	9.48	0.91	2	0
Side wall bending	9.84	9.33	0.75	9.85	0.75	−5	0
Roll motion	11.09	12.25	0.85	11.01	0.96	10	−1

Frequencies are given Hertz [Hz]

Table 23.2 Initial and updated parameters

Parameter	Initial	Updated	Difference (%)
E_{brace} [GPa]	210	71	−66
E_{vert} [GPa]	210	242	15
ρ_{wood} [kg/m^3]	720	802	11

The frequencies in the updated model are in agreement with the measured frequencies. The MAC number between the updated and measured mode is unchanged for lateral, vertical and side wall bending, while it has increased for the roll mode.

Table 23.2 shows that the density of wood has increased by 11 % in the updating procedure. This is well within the bounds presented by Gryc et al. [15], and may from an isolated point of view be taken as a plausible physical value. The lateral bracing system represented by E_{brace} has attained considerable reduction in stiffness after the model updating step. If the reduction is to be explained in the lateral bracing system alone, there are several possible reasons which may lead to reduction of stiffness. Firstly, the actual elastic modulus might be lower, but the uncertainty related to this parameter for steel is negligible and therefore not responsible for the severe reduction. Secondly, the loss of cross sectional area will affect stiffness. Corrosion will reduce cross sectional area, but the stiffness is not affected significantly until severe reduction occurs due to redistribution of strains within the cross section. Inspection at the site revealed corrosion at some points on the bracing system, but not systematically nor to the degree of severity that implies corrosion to be the reason for the reduced stiffness in E_{brace}. The riveting technique introduces holes in members of the bracing system which reduces the cross sectional area of members in the actual system, and may partially explain the observed stiffness change in the bracing system. Lastly, the large reduction in E_{brace} may be a result of lateral stiffness introduced in other parts of the structure through the modeling process. In particular increased stiffness in joints due to the tie constraints. This means a large reduction in E_{brace}, since it is the main parameter to compensate for such errors.

23.6 Conclusion and Further Work

This paper presented system identification and model updating of a riveted steel bridge. The use of data driven SSI in system identification gave a clear indication of identified modes in the structure. The model updating step indicated that the finite element model used in the study was to stiff in the lateral direction. This extra stiffness could not be attributed to a physical reason related to the updating parameter, but indicated that other parts in the structure and modeling choices added stiffness to the structure. In future work, a sensitivity study should be carried out to identify the components and modeling choices which are the reason for the added stiffness in the finite element model.

Acknowledgements The funding for the research has been provided by the Norwegian National Rail Administration (Jernbaneverket) and is gratefully acknowledged. Bartosz Siedziako has contributed to building the finite element model and Petter R. Nåvik has contributed to the present work by mounting and operating the wireless sensor network.

References

1. Taras, A., Greiner, R.: Development and application of a fatigue class catalogue for riveted bridge components. Struct. Eng. Int. **20**(1), 91–103 (2010)
2. Al-Emrani, M., Kliger, R.: FE analysis of stringer-to-floor-beam connections in riveted railway bridges. J. Constr. Steel Res. **59**(7), 803–818 (2003)

3. Imam, B.M., Righiniotis, T.D., Chryssanthopoulos, M.K.: Numerical modelling of riveted railway bridge connections for fatigue evaluation. Eng. Struct. **29**(11), 3071–3081 (2007)
4. Kunz, P., Hirt, M.A.: Reliability analysis of steel railway bridges under fatigue loading. In: IABSE Colloquium(Copenhagen): Remaining Strucutral Capacity (1993)
5. Tobias, D.H., Foutch, D.A.: Reliability-based method for fatigue evaluation of railway bridges. J. Bridg. Eng. **2**(2), 53–60 (1997)
6. Imam, B.M., Righiniotis, T.D., Chryssanthopoulos, M.K.: Probabilistic fatigue evaluation of riveted railway bridges. J. Bridg. Eng. **13**(3), 237–244 (2008)
7. Imam, B.M., Chryssanthopoulos, M.K., Frangopol, D.M.: Fatigue system reliability analysis of riveted railway bridge connections. Struct. Infrastruct. Eng. **8**(10), 967–984 (2012)
8. Frøseth, G., Rönnquist, A.: System reliability analysis of steel railway bridge based on historic rolling stock records. In: 13th Nordic Steel Construction Conference (2015)
9. Ditlevsen, O.: Model uncertainty in structural reliability. Struct. Saf. **1**(1), 73–86 (1982)
10. Joint Commitee on Structural Safety: Probabilistic Model Code (2013)
11. Quin, S., Reynders, E., He, L., Bui, T.T., De Roeck, G.: Effects of initial conditions on operational modal analysis. Struct. Control. Health Monit. **21**, 557–573 (2014)
12. Reynders, E., Schevenels, M., De Roeck, G.: MACEC 3.2 A Matlab Toolbox for Experimental and Operational Modal Analysis. Leuven University, Belgium (2014)
13. Mottershead, J.E., Link, M., Friswell, M.I.: The sensitivity method in finite element model updating: a tutorial. Mech. Syst. Signal Process. **25**(7), 2275–2296 (2011)
14. Ozyhar, T., Hering, S., Niemz, P.: Moisture-dependent elastic and strength anisotropy of European beech wood in tension. J. Mater. Sci. **47**(16), 6141–6150 (2012)
15. Gryc, V., Vavrčík, H., Gomola, S.: Selected properties of European beech (Fagus sylvatica L.). J. For. Sci. **2008**(9), 418–425 (2008)

Chapter 24
Full-Scale Measurements on the Hardanger Bridge During Strong Winds

Aksel Fenerci and Ole Øiseth

Abstract Completed in 2013, the Hardanger Bridge is now the longest suspension bridge in Norway and it is among the most slender suspension bridges in the world. In the context of an extensive research project initiated by the Norwegian Public Roads Administration, the bridge was installed with a comprehensive monitoring system to investigate the wind characteristics at the site along with the dynamic response of the bridge. Wind velocities are measured using nine anemometers installed on different locations at the bridge span. A representative 10 min recording with high mean wind velocity and perpendicular wind direction is selected to present the preliminary results. Time series of turbulence components and one-point spectra are presented. Spatial properties of the wind field are studied by examining the coherences of turbulence components for several separation distances. Dynamic response of the bridge is measured using 20 accelerometers distributed along the main span. Time histories of the accelerations as well as the response spectra are presented. The relationship between bridge vibrations and wind measurements is discussed.

Keywords Wind field characterization • Full-scale measurement • Suspension bridge • Power spectral density • Coherence function

24.1 Introduction

The E39 Coastal Highway is located at the west coast of Norway, connecting Trondheim to Kristiansand. Along the highway, currently there exist several ferry dependent fjord crossings which increase the travel time significantly. In order to decrease the travel time, Norwegian Public Roads Administration (NPRA) has initiated an extensive research project to investigate the possibility and feasibility of replacing the existing ferries with road transportation. However, the landscape at the western coast of Norway, famous for its high mountains and deep fjords makes this a very challenging task. Among many options which are being considered, cable-supported bridges constitute the most effective solution for many of the cases. Therefore, accurate prediction of wind-induced dynamic response of such structures becomes a matter of crucial importance.

Prediction of wind-induced dynamic response of cable-supported bridges requires knowledge and understanding of the wind field and turbulence characteristics of the site. Since the terrain of the fjords influences the wind flow, the turbulence characteristics will be more complex than usual and will perhaps require special attention in design. In order to investigate the wind field characteristics and the validity of the state-of-the-art models for response prediction, a monitoring system was installed on the Hardanger Bridge to measure the wind velocities and accelerations along the bridge span.

Hardanger Bridge is spanning across the Hardangerfjord (Fig. 24.1) in Hordaland country of Norway. It is currently the longest suspension bridge in Norway with a main span of 1310 m and towers reaching up to 186 m. The bridge consists of only two traffic lanes, one in each direction and a pedestrian lane, and therefore constitute a very slender structure. After its completion in 2013, a monitoring system consisting of nine triaxial sonic anemometers and 20 triaxial accelerometers was installed on the bridge. The layout of the measurement system is shown in Fig. 24.2. The anemometers were installed on the hangers (except one anemometer installed on a light pole) at a height of 8 m from the bridge deck and the accelerometers were installed inside the bridge deck. Accelerometers were installed as pairs, one in each side of the bridge deck to monitor torsional deflections. Time synchronization was ensured by means of GPS antennas and the communication through the data loggers was established by wireless antennas. The data is transferred from several data loggers along the bridge to a main logger unit at the top of the north tower and then transferred to storage units at NTNU by an internet connection. An overview of the data transfer scheme is also given in Fig. 24.2.

A. Fenerci (✉) • O. Øiseth
Department of Structural Engineering, Norwegian University of Science and Technology, Richard Birkelands vei 1A, Trondheim 7491, Norway
e-mail: aksel.fenerci@ntnu.no

S. Pakzad, C. Juan (eds.), *Dynamics of Civil Structures, Volume 2*, Conference Proceedings of the Society for Experimental Mechanics Series, DOI 10.1007/978-3-319-29751-4_24

Fig. 24.1 The Hardanger Bridge (map image from © Kartverket)

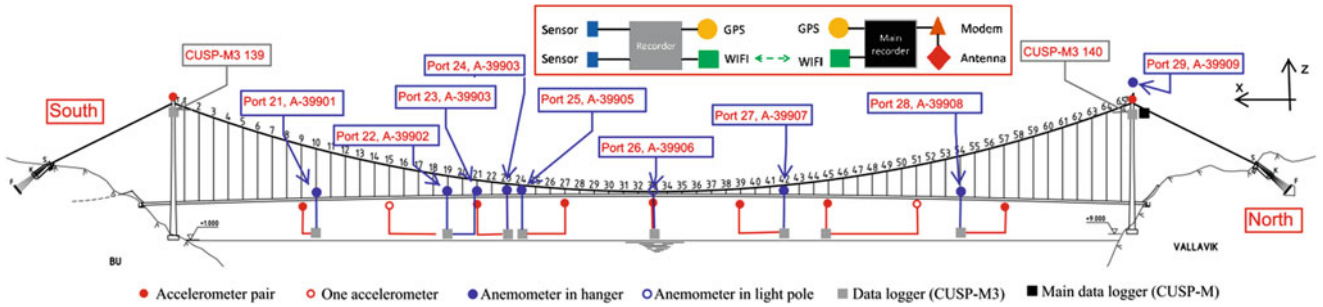

Fig. 24.2 The measurement system

24.2 Characteristics of the Wind Field

24.2.1 General

The wind velocities at the Hardanger Bridge site were measured from February 2015 to October 2015. The wind roses of 10-min mean wind velocity (U) and turbulence intensities (I_u, I_v and I_w) for the along-wind (u), horizontal cross-wind (v) and vertical (w) turbulence components are displayed (Fig. 24.3). A threshold value of 8 m/s was set to show only the recordings with high wind speeds. The results for sensor A6 are displayed in the figure, which is the anemometer located at the midspan of the bridge (Fig. 24.2). The bridge alignment is shown by a red line, meaning that winds with approaching angles of 90° and 270° are perpendicular to bridge direction.

The plots indicate that the dominant wind direction is almost perpendicular to the bridge, with a slight tilt in agreement with the topography. For the winds coming from the east, the approaching angle was between 90° and 120°, whereas for the winds coming from the west, it was between 240° and 330°. The highest recorded mean wind velocity during the considered time was 24.2 m/s and the corresponding mean wind direction was 100°. The winds with highest mean wind velocities appear to be concentrated around 100° for the easterly winds and 320° for the westerly winds. The winds perpendicular to the bridge, on the other hand, had mean wind velocities not more than 15 m/s. The turbulence intensities of the along-wind and cross-wind components were higher for the westerly winds, where the highest turbulence intensities for the vertical turbulence were measured during easterly winds from the direction of 130°. Plots of turbulence intensity against mean wind velocity are shown in Fig. 24.4 for the 10-min recordings. A threshold value of 3 m/s was used for the mean wind velocity. It is observed that the turbulence intensities for all turbulence components tend to decrease with high values of mean wind velocity. The most turbulent winds were measured between mean wind velocity values of 5–10 m/s. For winds with high mean speeds (>15 m/s), the along-wind turbulence intensity (I_u) was bounded between 0.1 and 0.2.

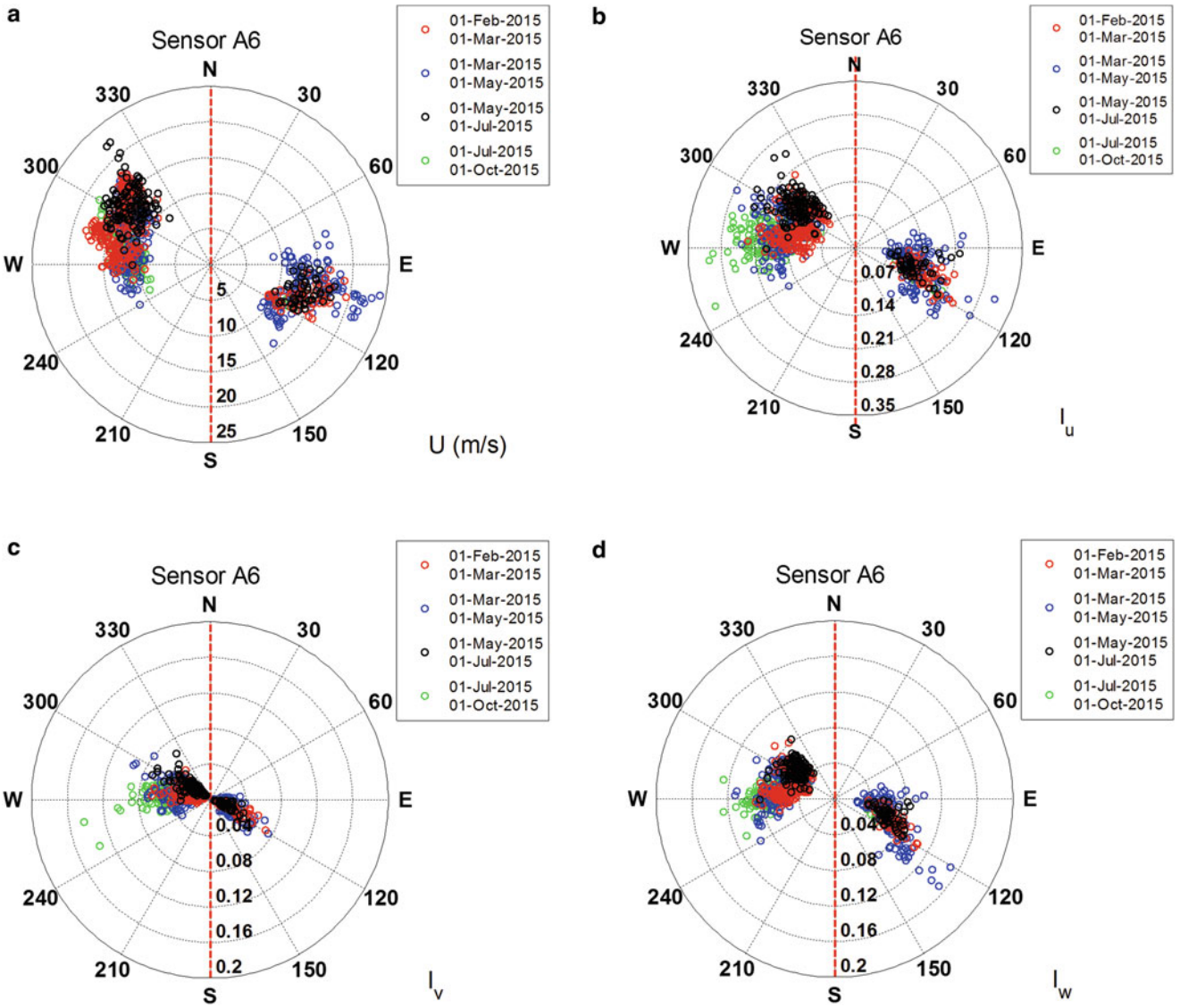

Fig. 24.3 Wind roses of mean wind velocity and turbulence intensities. (**a**) Mean wind velocity. (**b**) Along-wind turbulence. (**c**) Cross-wind turbulence. (**d**) Vertical turbulence

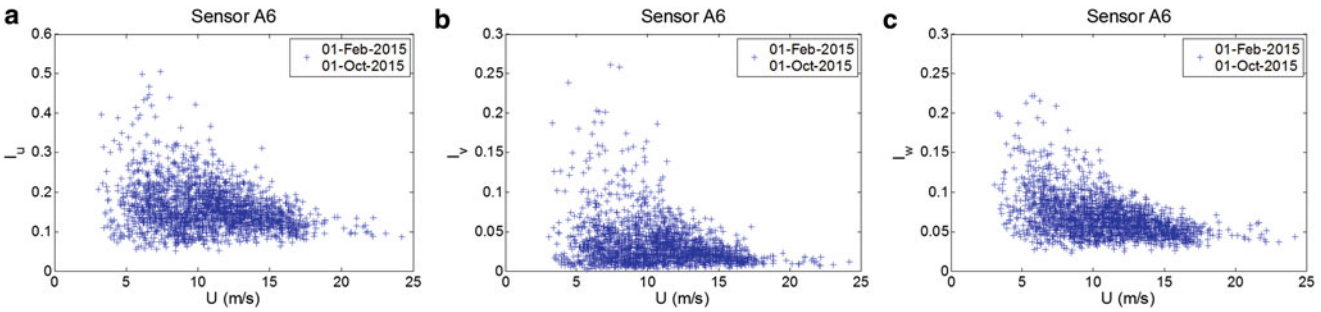

Fig. 24.4 Turbulence intensities vs. mean wind velocity (10 min). (**a**) Along-wind turbulence. (**b**) Horizontal cross-wind turbulence. (**c**) Vertical turbulence

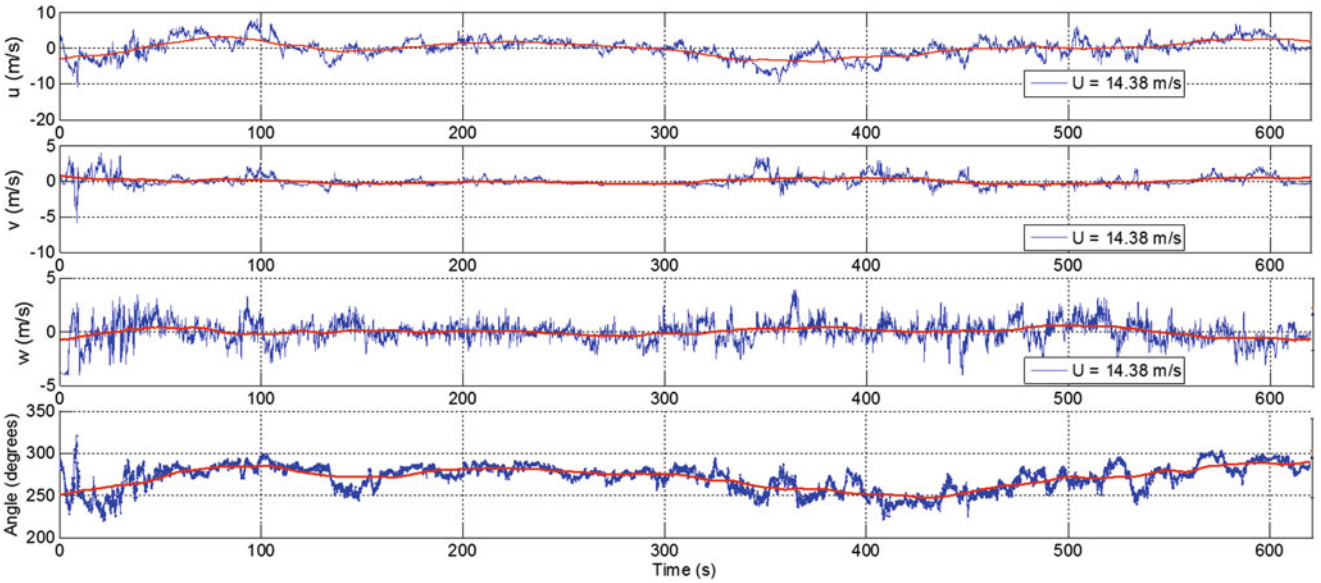

Fig. 24.5 Time series of turbulence components and wind direction

24.2.2 One-Point Spectra of Turbulence

Wind-induced dynamic analysis of civil engineering structures requires analytical models of spectral densities of the atmospheric turbulence. Several expressions based on theoretical, semi-empirical or empirical models have been suggested by wind engineers over the last 70 years [1–5]. Although the wind field is usually represented well using these models, field measurement data is often used to calibrate existing models to consider the site-specific properties of the wind field [6, 7].

To study the properties of atmospheric turbulence on the Hardanger Bridge site, a 10-min recording was selected among the vast data that has been recorded. The time series of the three orthogonal turbulence components as well as the wind direction are shown in Fig. 24.5. The selection of this particular recording was based on the criteria that the time series exhibited fairly stationary behavior, the mean wind velocity was high and the wind was blowing perpendicular to the bridge direction. The time series were recorded on 14.09.2015 during day time. The mean wind velocity was 14.4 m/s and the mean wind direction was 270.8°, meaning that the wind was blowing from the west, almost perfectly perpendicular to the bridge deck. The data were sampled with 32 Hz and then resampled to 20 Hz after applying a low-pass filter.

The power spectral densities (PSDs) of the along-wind, cross-wind and vertical turbulence components were estimated using Welch's averaged periodogram method [8]. The time series of each component were divided into eight segments with 50 % overlap. The PSDs were then calculated for each segment using the fast Fourier transform (FFT) method and averaged after applying a Hanning window to each segment. The normalized auto and cross spectral densities of the three turbulence components for the midspan of the bridge are presented in Fig. 24.6. The auto-spectra exhibited expected shapes, with peaks around 0.01 Hz for the along-wind component and 0.02 Hz for the cross-wind and vertical components, implying anisotropic turbulence. The cross-spectra shows significant amplitudes, especially for the u and w components where the peaks of the spectra are more clear. However, the variance is generally too high to see the distinct shapes of spectra for the other components.

Models for the turbulence spectra frequently used in wind engineering have been fitted to the measured data. The expressions given by von Kármán [1], Kaimal et al. [2] and Simiu and Scanlan [5] are presented in Table 24.1. Here, $L_n, n \in \{u,v,w\}$ denote the length scales, $f_z = f.z/U$ denotes the reduced frequency, z the height above the ground, f the frequency while U is the mean wind velocity. The ratio $\beta n = \sigma_n/u^*$, $n \in \{u,v,w\}$ was used in the expressions where u^* is the shear velocity and σ_n is the standard deviation of the turbulence component. The parameters of the models were estimated by fitting the expressions to the measured data by utilizing a least squares algorithm. The auto-spectra obtained by the three models are plotted along with the measured data (Fig. 24.7).

It is important to have some knowledge of which frequency range that is of high importance when evaluating the performance of the expressions fitted to the data. Operational modal analysis (OMA) of the Hardanger Bridge was conducted by Øiseth et al. [9]. The study revealed that the first symmetrical horizontal and vertical natural frequencies of the bridge were 0.05 Hz and 0.14 Hz respectively, while the second symmetrical vertical natural frequency was 0.2 Hz. The natural

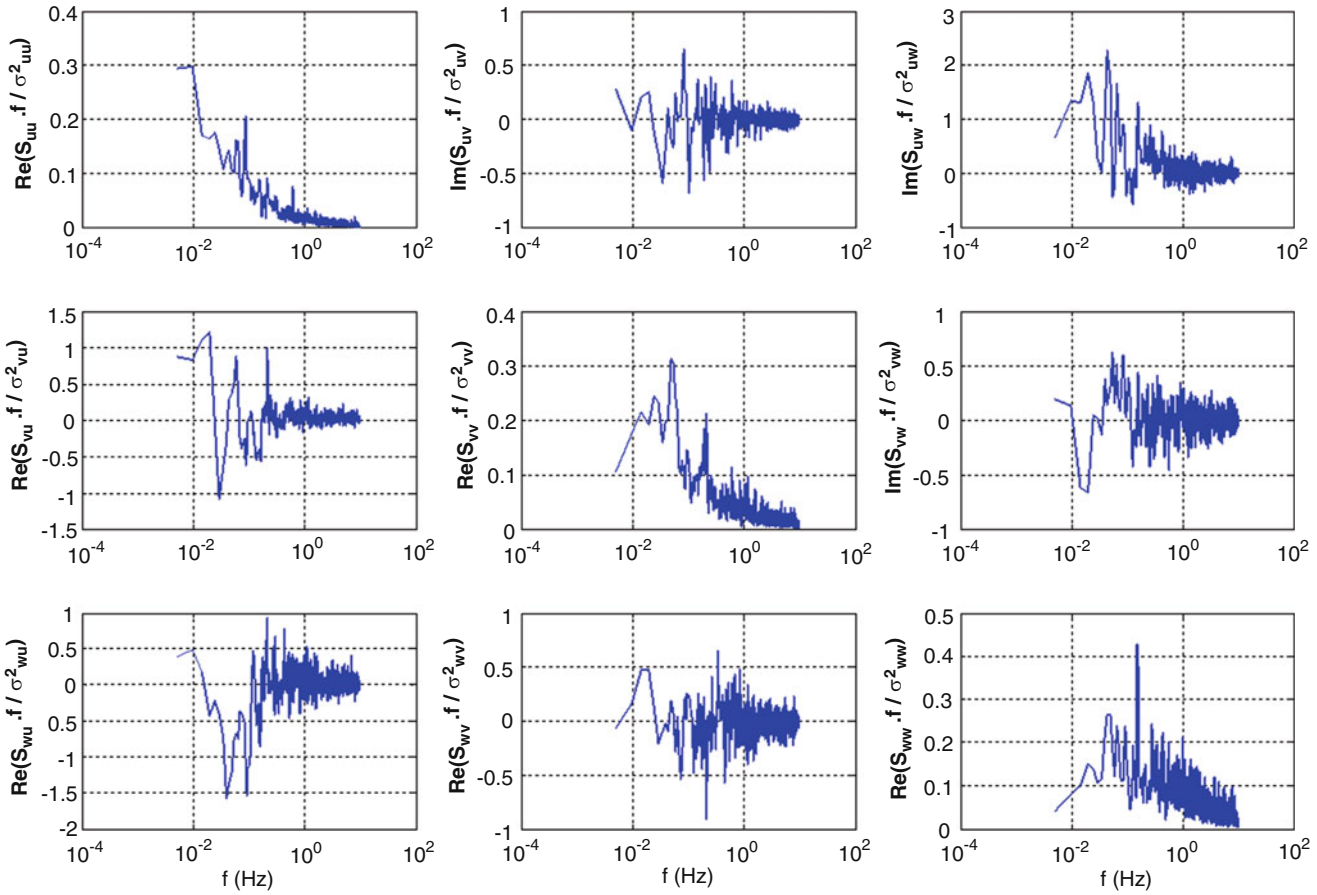

Fig. 24.6 One-point spectra of turbulence for midspan

Table 24.1 Expressions for models of atmospheric turbulence from literature

	Von Kármán [1]	Kaimal et al. [2]	Simiu and Scanlan [5]
$\frac{f.S_u(f)}{\sigma_u^2}$	$\frac{4.\frac{L_u.f}{U}}{\left[1+70.8\left(\frac{L_u.f}{U}\right)^2\right]^{5/6}}$	$\frac{105f_z}{\left(1+33f_z\right)^{5/3}.\beta_u^2}$	$\frac{200f_z}{\left(1+50f_z\right)^{5/3}.\beta_u^2}$
$\frac{f.S_v(f)}{\sigma_v^2}$	$\frac{4.\frac{L_v.f}{U}\left[1+755\left(\frac{L_v.f}{U}\right)^2\right]}{\left[1+283\left(\frac{L_v.f}{U}\right)^2\right]^{11/6}}$	$\frac{17f_z}{\left(1+9.5f_z\right)^{5/3}.\beta_v^2}$	$\frac{15f_z}{\left(1+9.5f_z\right)^{5/3}.\beta_v^2}$
$\frac{f.S_w(f)}{\sigma_w^2}$	$\frac{4.\frac{L_w.f}{U}\left[1+755\left(\frac{L_w.f}{U}\right)^2\right]}{\left[1+283\left(\frac{L_w.f}{U}\right)^2\right]^{11/6}}$	$\frac{2f_z}{\left(1+5.3f_z^{5/3}\right).\beta_w^2}$	$\frac{3.36f_z}{\left(1+10f_z^{5/3}\right).\beta_w^2}$

frequencies are shown on the spectral plots (Fig. 24.7) to stress the important frequency range. Although the spectral estimations of the three models gave reasonable results at the high frequency range, the spectra were underestimated by Kaimal and Simiu models in the range where the natural frequencies lie. The Von Kármán model seems to represent the wind field with good accuracy. However, it should be noted that the turbulence length scales used in the estimations were obtained by a least squares fit. In most cases where the length scales are not known, estimation of these parameters will be the deciding factor on the accuracy of the model.

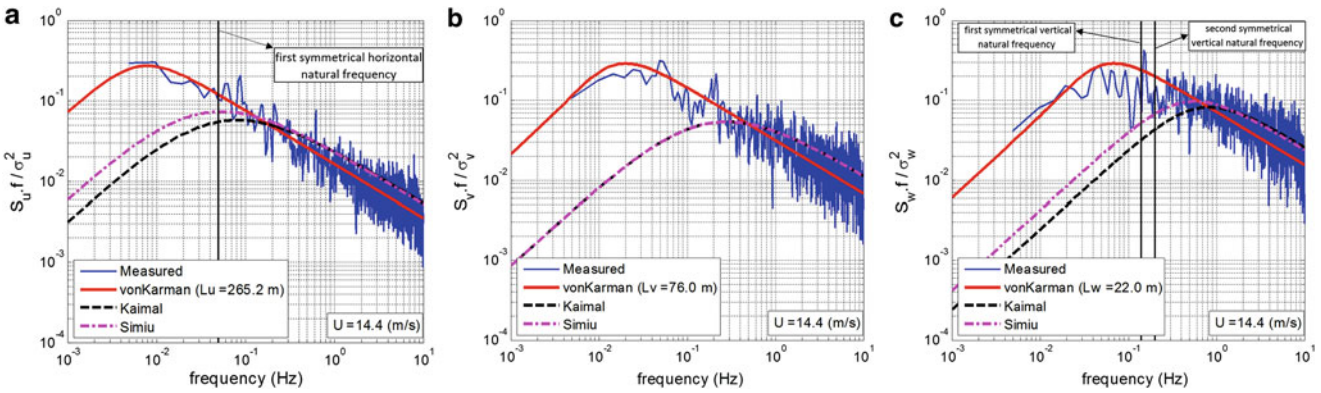

Fig. 24.7 Comparison of measured one-point spectra with spectral models from literature. (**a**) Along-wind turbulence. (**b**) Cross-wind turbulence. (**c**) Vertical turbulence

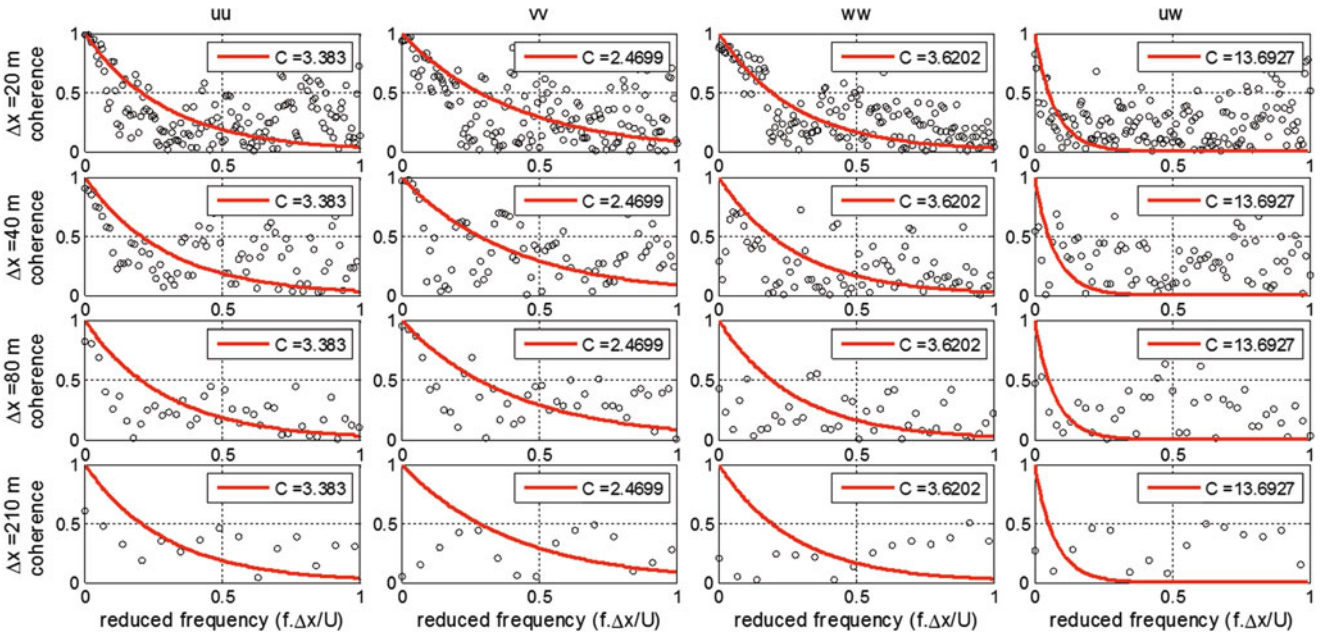

Fig. 24.8 Root coherence functions of turbulence components for different separation distances

24.2.3 Spatial Properties of Turbulence

The spatial properties of the wind field are of crucial importance when designing long span bridges. A detailed characterization of the spatial structure of the atmospheric turbulence is therefore necessary. Frequency dependent correlation of turbulence components are usually represented using the coherence function. Coherence can be written as [10]:

$$Coh\,(f,\,\Delta x) = \frac{|S_{nm}(f)|^2}{S_n(f)S_m(f)} \tag{24.1}$$

Here, S_{nm} $n \in \{u,v,w\}$, $m \in \{u,v,w\}$ denotes the cross-spectral density while S_n $n \in \{u,v,w\}$ and S_m $m \in \{u,v,w\}$, denote the auto-spectral densities. The square root of the coherence function, namely the root coherence function, can be interpreted as a frequency dependent correlation coefficient. Root coherences for several separation distances are displayed in Fig. 24.8. In calculation of the root coherences, the spectral estimation method described in Sect. 24.2.2 was used and only the real part of the cross-spectral density (co-spectrum) was considered. The imaginary part of the cross-spectral density, namely the quad-spectrum contains the phase information. In atmospheric turbulence, the quad-spectrum is small compared to the co-spectrum [5] and usually neglected in response calculations.

Davenport [11] proposed a simple empirical relation for the root coherence which reads:

$$\sqrt{Coh\,(f,\Delta x)} = \exp\left(-C\frac{f.\Delta x}{U}\right) \tag{24.2}$$

where C is a decay coefficient. Davenport's equation was fitted to the measured data in least squares sense and C coefficients were obtained. The least squares fit and the obtained C coefficients are also shown in Fig. 24.8. The coherence estimations yielded significant scatter, which can be attributed to the high variance in the spectral estimations. It should also be noted that the exponential coherence model implies large coherence in the low frequency range even for large separation distances, which is unrealistic. For low values of frequency and small separations, root coherences of all components indicate significant correlation, including the coherence of u and w components. For separations larger than 40 m, correlations of w-w and u-w components seem to disappear. However, u-u and v-v components continue to display correlated behavior even for higher separation distances, implying higher length scales (larger eddies) in those directions.

24.3 Dynamic Response

The dynamic response of the Hardanger Bridge was measured using 20 accelerometers distributed along the bridge. The same 10-min long recording was used to deduce the response characteristics. The acceleration time histories recorded at the midspan of the bridge are given in Fig. 24.9. The vertical and horizontal accelerations were calculated as the average value of the two sensor located at each side of the bridge deck. The torsional acceleration (denoted as a_θ) of the deck is calculated as the difference of the vertical acceleration readings divided by the separation distance. Frequency domain properties of the response are also presented in the form of spectral density estimates (Fig. 24.10). The power spectral densities of acceleration components were estimated using the same methodology described earlier. The first peaks of both spectra occurred at the fundamental frequencies, which are 0.05 Hz for the first horizontal and 0.14 Hz for the first vertical mode.

To further elaborate on the relationship between bridge vibrations and wind speeds, root mean square (RMS) values of acceleration time series are plotted against 10-min mean wind velocity in Fig. 24.11. The points on the plot was obtained for 10-min recordings made on September 14th and a threshold value of 8 m/s was applied. It is seen that the RMS values of both components increase with higher wind speeds with significant scatter. The results were divided into three groups with different vertical turbulence intensity intervals to demonstrate the effect of vertical turbulence on both response parameters. Although some amount of inherent randomness is still present (due to wind direction, horizontal turbulence), it is seen that the RMS acceleration response tends to increase with increased values of vertical turbulence intensity.

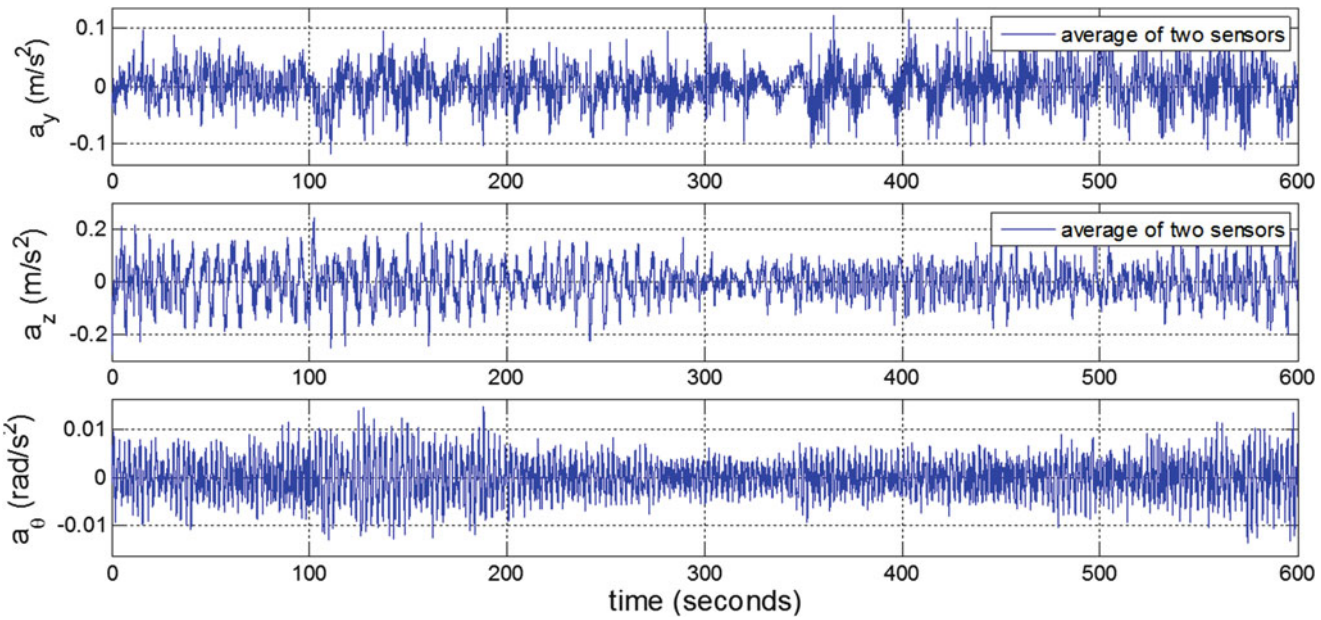

Fig. 24.9 Acceleration time histories for the midspan of the bridge

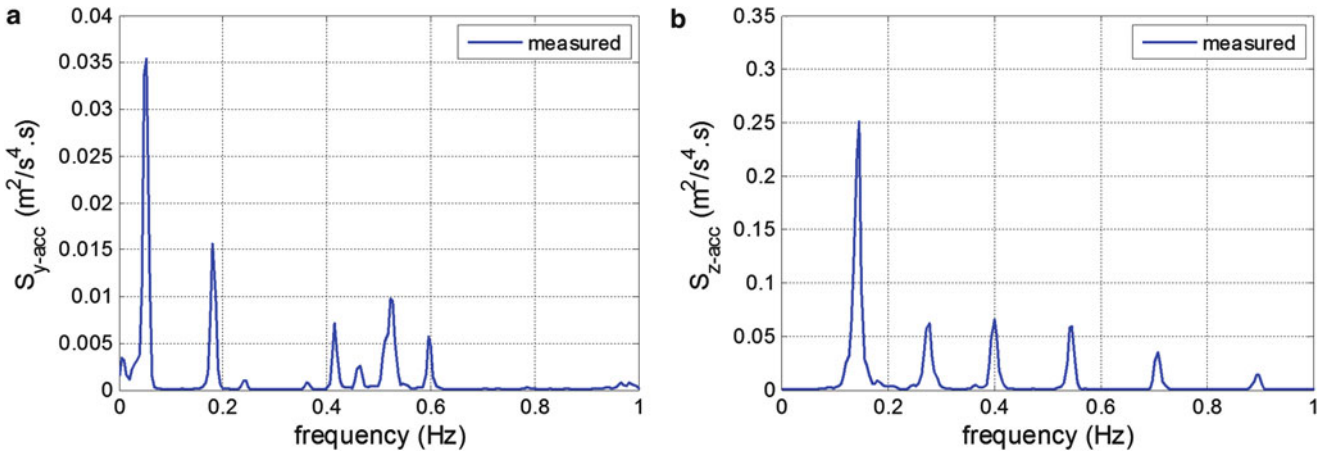

Fig. 24.10 Acceleration response spectra. (**a**) Horizontal acceleration. (**b**) Vertical acceleration

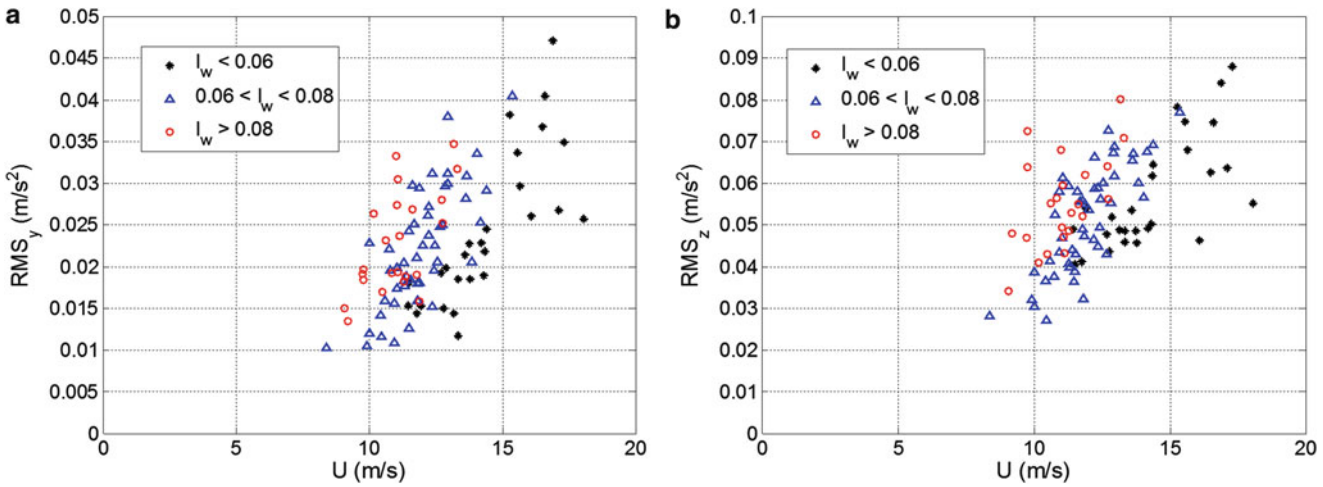

Fig. 24.11 RMS acceleration response vs. 10-min mean wind velocity. (**a**) Horizontal acceleration. (**b**) Vertical acceleration

24.4 Conclusion

Wind field characteristics as well as the dynamic response of the Hardanger Bridge were studied in light of the field measurements taken during strong winds. The wind measurements revealed two main wind directions with deviations up to 45° from the perpendicular bridge direction. A fairly stationary, perpendicular and strong wind recording was selected to study the frequency domain properties. The cross-spectral density estimates indicated significant correlation for u and w components. Von Kármán's spectral turbulence model is found to be best suited to the site, given that the length scales are estimated by fitting the model to measured data. Root coherence plots revealed significant correlation of u and w components for small separations. The response of the bridge was assessed using acceleration measurements. The acceleration response spectra yielded clear peaks at the locations of fundamental natural frequencies. RMS values of vertical and horizontal accelerations are found to increase with higher mean wind velocities based on measurements taken in a duration of 1 day. It is also found that the vertical turbulence intensity has considerable influence on both horizontal and vertical RMS acceleration responses.

References

1. von Kármán, T.: Progress in the statistical theory of turbulence. Proc. Natl. Acad. Sci. U. S. A. **34**, 530–539 (1948)
2. Kaimal, J.C., Izumi, Y., Wyngaard, J.C., Cote, R.: Spectral characteristics of surface-layer turbulence. Q. J. Roy. Meteorol. Soc. **98**, 563–589 (1972)
3. Solari, G.: Turbulence modeling for gust loading. J. Struct. Eng. ASCE **117**(7), 1550–1569 (1987)
4. Harris, R.I.: Some further thoughts on the spectrum of gustiness in strong winds. J. Wind Eng. Ind. Aerodyn. **33**, 461–477 (1990)
5. Simiu, E., Scanlan, R.H.: Wind Effects on Structures Fundamentals and Applications to Design, 3rd edn. Wiley, New York (1996)
6. Hui, M.C.H., Larsen, A., Xiang, H.F.: Wind turbulence characteristics study at the Stonecutters Bridge site: part II: wind power spectra, integral length scales and coherences. J. Wind Eng. Ind. Aerodyn. **97**, 48–59 (2009)
7. Øiseth, O., Rönnquist, A., Sigbjörnsson, R.: Effects of co-spectral densities of atmospheric turbulence on the dynamic response of cable-supported bridges: a case study. J. Wind Eng. Ind. Aerodyn. **116**, 83–93 (2011)
8. Welch, P.D.: The use of the fast Fourier transform for the estimation of power spectra: a method based on time averaging over short, modified periodograms. IEEE Trans. Audio Electroacoust. **15**, 70–73 (1967)
9. Øiseth, O., Rönnquist, A., Kvåle, K.A., Sigbjörnsson, R.: Monitoring wind velocities and dynamic response of the Hardanger Bridge. In: Dynamics of Civil Structures. Proceedings of the 33rd IMAC, A Conference and Exposition on Structural Dynamics, vol. 2 (2015)
10. Tamura, Y., Kareem, A.: Advanced Structural Wind Engineering. Springer, Tokyo (2013)
11. Davenport, A.G.: The spectrum of horizontal gustiness near the ground in high winds. Q. J. Roy. Meteorol. Soc. **87**, 194–211 (1961)

Chapter 25
Finite Element Model Updating of Portage Creek Bridge

Yu Feng, Yavuz Kaya, and Carlos Ventura

Abstract Constructed in 1983, the Portage Creek Bridge is a three span highway bridge located in Victoria, British Columbia (BC), Canada. This bridge is a part of a smart seismic monitoring program, British Columbia Smart Infrastructure Monitoring System (BCSIMS), which funded by the British Columbia Ministry of Transportation and Infrastructure (MoTI), Canada. The BCSIMS aims to continuously monitors the seismic conditions of the selected bridges on lifeline highways in British Columbia, and as part of this goal, an ambient vibration test was carried out on the bridge in September 2014 in order to update/calibrate the finite element model of the bridge in SAP2000. The updated model will then used to assess the seismic performance of the bridge in accordance with the Canadian Highway Bridge Design Code, 2015. This paper presents the first phase of the seismic performance assessment, which includes finite element model updating using the results of the ambient vibration test.

Keywords Ambient vibration test • Highway bridge • Modal analysis • Finite element model updating • Structural health monitoring

25.1 Introduction

The BCSIMS is comprehensive seismic monitoring program that integrates the Strong Motion Network (SMN) and the seismic Structural Health Monitoring (SHM) network in British Columbia (BC). The program was initiated in 2009 and involves 15 structures (14 bridges and one tunnel) that are currently being monitored in real-time. One of the main intentions of the SHM network is to mitigate the seismic risk in bridges in BC by continuously assessing the seismic condition of the bridges, and it is done using the tools and techniques that have been developed over the last 6 years.

The Portage Bridge is located in Victoria on the Vancouver Island, BC, Canada at 48°27′53″N and 123°23′55″W geographic coordinates and is part of the BCSIMS project. The bridge was built in 1983 and was undergone a seismic retrofit by ISIS Canada in 2003 that included the implementation of Fiber Reinforce Polymer (FRP) wraps to strengthen the short columns. As part of the BCSIMS project, the seismic assessment of the bridge is being carried out. This paper presents the dynamic characteristics (modal frequency, damping ratio, and mode shape) of Portage Creek Bridge located in Victoria, BC, Canada through an Ambient Vibration Test (AVT) carried out in September, 2014, and compares the AVT results with those obtained from Finite Element (FE) model of the bridge created in SAP2000 [1]. The FE model of the bridge is updated using the extracted modal properties from the AVT. The updating is done both manually and automatically using the commercially available software, FEMTools [2].

25.2 Description and the Finite Element Model of the Bridge

The Portage Creek Bridge is a disaster-route bridge in Victoria, BC, Canada. It crosses the Interurban Road at McKenzie Avenue as shown in Fig. 25.1. The bridge is 125 m long and has three spans with concrete deck. The steel girders are supported using two reinforced concrete piers as can be seen in Fig. 25.2. The deck has a roadway width of 16 m (52 ft) with two 1.78 m (6′6″) sidewalks and an aluminum railing on either side of the bridge. The bridge was designed in 1982,

Y. Feng (✉) • Y. Kaya • C. Ventura
Department of Civil Engineering, Earthquake Engineering Research Facility, University of British Columbia,
6250 Applied Science Lane, Vancouver, BC, Canada
e-mail: yuvon1990@gmail.com

S. Pakzad, C. Juan (eds.), *Dynamics of Civil Structures, Volume 2*, Conference Proceedings of the Society
for Experimental Mechanics Series, DOI 10.1007/978-3-319-29751-4_25

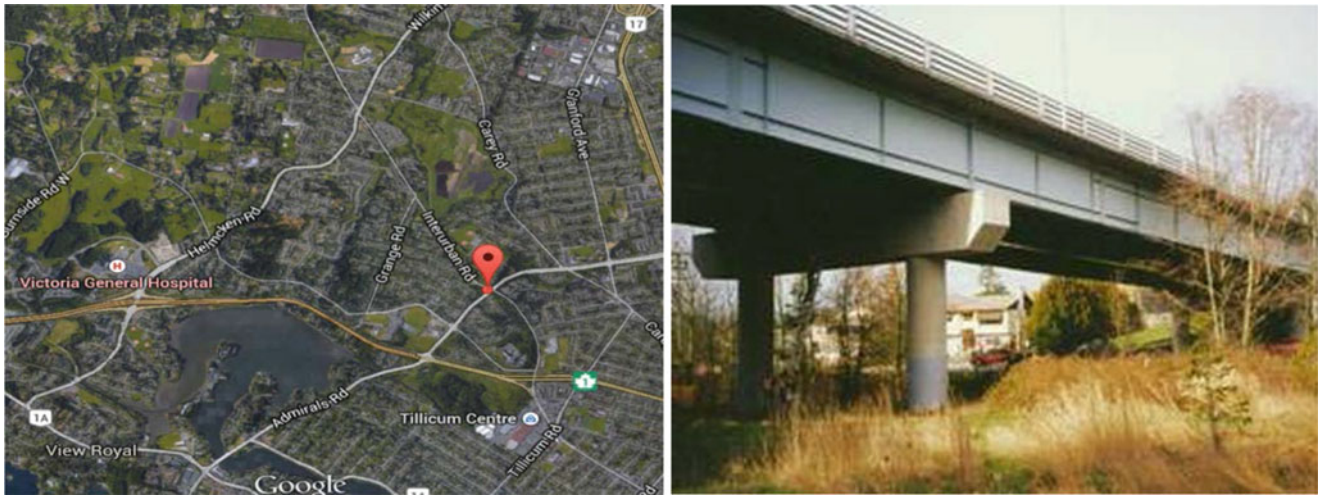

Fig. 25.1 Location and view of Portage Creek Bridge

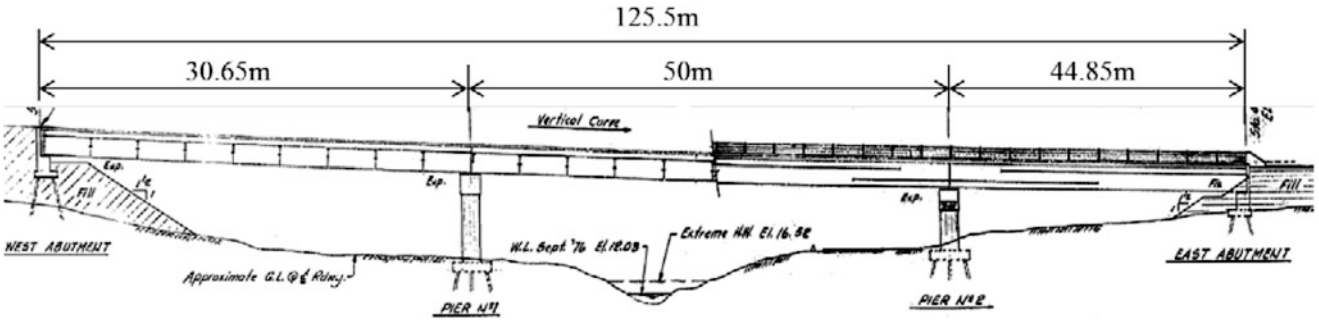

Fig. 25.2 Elevation of Portage Creek Bridge

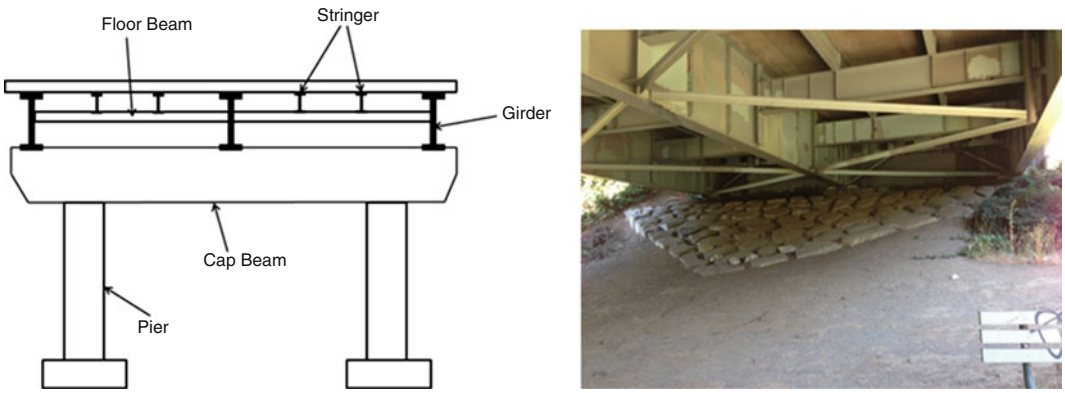

Fig. 25.3 Cross-section of Portage Creek Bridge and location of bracing

which is long before the introduction of current seismic design standards. As part of a seismic retrofit project, the seismic analysis of the bridge was performed by ISIS Canada, and seismic retrofit was carried out in 2003 in order for the bridge to meet the seismic design requirement at that time. An innovative retrofit technique-Fiber Reinforce Polymer Wraps (FRPs) was applied to strengthen the short column for shear [3]. With the structural aging and introduction of new seismic design provisions in 2015, the bridge is in need of a re-assessment of seismic performance in accordance with the new Canadian Highway Bridge Design Code, 2015 (Fig. 25.3).

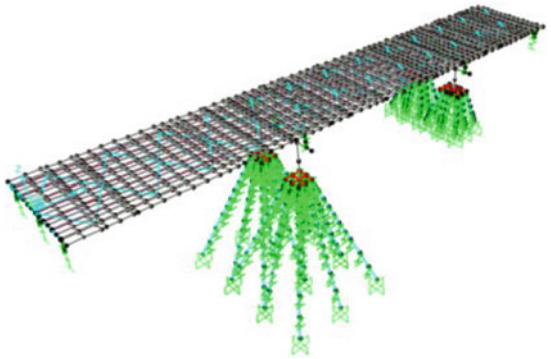

Fig. 25.4 Finite element model of Portage Creek Bridge

Table 25.1 Material properties

	Modulus of elasticity (MPa)	Density (kN/m^3)
Concrete for deck	27,805	23.5
Concrete for bent & column	24,421	23.5
Structural steel	200,000	76.9
Rebar steel	200,000	76.9

The FE model of the bridge was built in Sap2000 as seen in Fig. 25.4. The Geometry and the material properties of the structure were obtained from the original structural drawings and the retrofit project in 2003. Table 25.1 summarizes the material properties used in the FE model of the bridge.

Structural members were modeled in different ways in Sap2000. Shell area elements were used for concrete slab. The cross section of the concrete slab is uniform within each span but differs between spans. Three steel girders and four small steel stringers support concrete slabs. Steel beams connect the girders and stringers. The girder section is changing over the span while stringer and beam section remain unchanged. Girder, stringer, and beam are all made of H-shape steel and were modeled as frame elements. Concrete bents and piles that support the superstructure were simply modeled as frame elements. There are sliding bearings between concrete bents and steel girders to dissipate energy during earthquake. The bearings were modeled as link elements, which is free to slide in translational directions and fixed in other DOFs. Due to lack of detailed material properties, the stiffness of the link element was estimated by equations proposed by Akogul [4]. Link element was used to model the soil conditions: the soil-spring model is referred as Winkler model [5]. Stiffness of these soil springs was estimated following the instruction of Das [6].

25.3 Ambient Vibration Test and Modal Analysis

The AVT is a non-destructive test aiming to record dynamic response of structure when no severe excitation is present. Data collected from the AVT are used to extract the modal information of tested structure (modal frequency, modal damping ratio, and mode shape). This information is crucial in many research areas including seismic rehabilitation of existing structures and finite element model updating.

Structural vibration sensors, TROMINO sensors as seen in Fig. 25.5, were used to carry out the AVT of the Portage Creek Bridge. These sensors are widely used by researchers around the world to study the dynamic characteristics of existing structures, and they are a combination of two sets of three orthogonal high-resolution electrodynamic sensors: high gain and low gain velocimeters, and one set of three orthogonal digital accelerometers with frequency range from 0.1 to 300 Hz [7]. Each TROMINO sensor is powered by two 1.5 V alkaline batteries and could keep working for 80 h at sampling rate of 128 Hz. Either the GPS or the Radio signals could be used to ensure synchronization between sensors in a network. For this AVT, the radio synchronization was used.

All of the TROMINO sensors were placed on the sidewalk of the bridge, and one radio amplifier was connected to each sensor as shown in Fig. 25.5. In order to capture the higher modes with good accuracy, 32 testing points are selected at different locations of the bridge. The test was divided into five setups, and eight sensors were used for each setup (Fig. 25.6).

Fig. 25.5 TROMINO sensor with radio

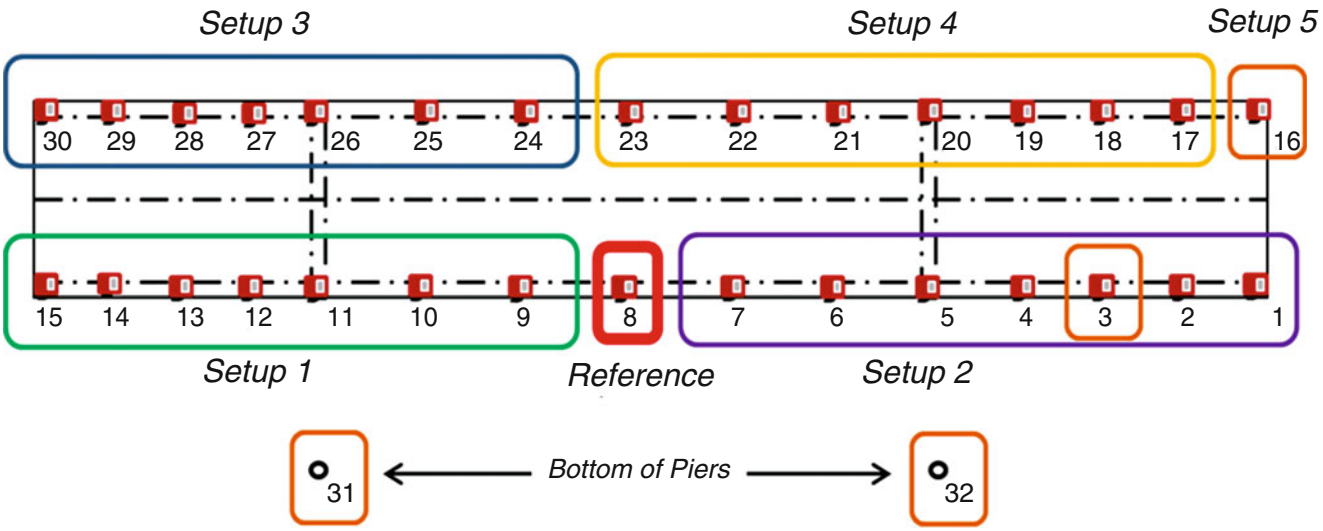

Fig. 25.6 Locations for all test setups

One sensor located at the mid-span of the bridge was used as reference sensor for all setups. The length of the recording for each setup is 30 min with a sampling frequency of 128 Hz. Sensor locations for five setups are highlighted in Fig. 25.6. The AVT test was started at 14:25 pm and was finished at 17:34 pm. The recorded data from all setups were synchronized using the Grilla software [7]. Only the high gain velocity records were used in the modal analysis because of the limitations of Grilla software in the data synchronization.

A commercial software ARTeMIS [8] was used for data processing, modal identification and the visualization of mode shapes. The raw data from each setup was first baseline corrected and low-pass filtered with a cutoff frequency of 20 Hz. Enhanced Frequency Domain Decomposition (EFDD) techniques was used to extract the modal properties of the bridge. Modal frequencies, mode shapes and damping were estimated though peak-picking spectral densities, as shown in Fig. 25.7, and the extracted modes are listed in Table 25.2.

25.4 Finite Element Model Updating

Due to the uncertainties in the material properties, bearings, soil condition, and boundary conditions, the FE model of the bridge does not represent the current condition of the bridge; therefore, the FE model of the bridge is updated (calibrated) using the AVT. The model updating can be done either automatically or manually. Many researchers around the world have long used FEMtools (a model updating software) for this purpose. The user inputs the experimental modal properties and

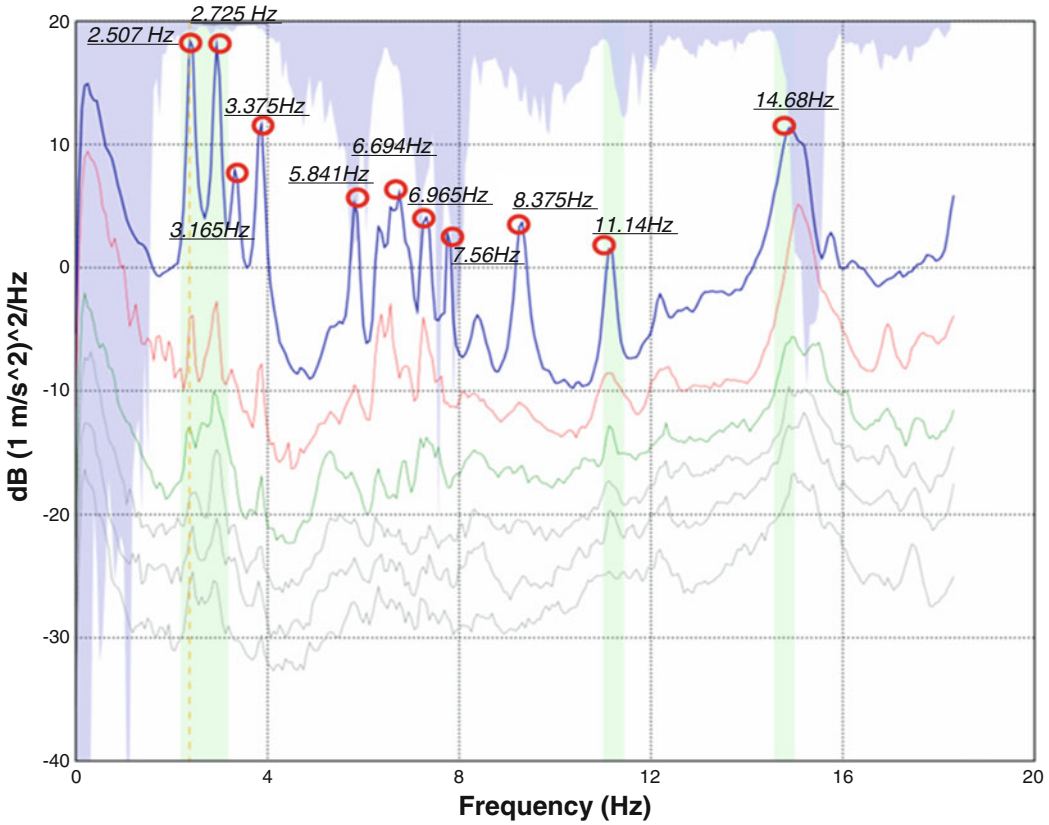

Fig. 25.7 Singular values of the spectral densities calculated by EFDD technique in ARTeMIS

Table 25.2 Parameters chosen for FE model updating of the bridge

Element	Deck		Girder		Column		Foundation	Expansion bearing
Type	E	ρ	E	ρ	E	ρ	k	k

selects the parameters of the FE model to be updated, and the FEMtools automatically updates those parameters. However, FEMtool has some limitation on the user selectable parameters: it can update the parameters of a frame element (i.e., cross sectional area, Young Modulus, rigidity, etc.), but cannot deal with the link elements in the FE model. Since the link elements are expected to be of great significance in the FE model of this bridge, a manual FE model updating approach is adopted to calibrate the FE model.

The key to success in model updating is the choice of parameters. The parameters should be selected where uncertainties are likely to arise. Table 25.2 summarizes the selected parameters for model updating. E, ρ , and k represents the modulus of elasticity of the materials, the material density, and the stiffness for link element, respectively.

Updating the FE model manually is basically a trial and error approach, but it is very time consuming. The process is expedited by running a sensitivity analysis on the selected parameters of the FEM model. Eight sets of sensitivity analysis were performed for all the parameters listed in Table 25.1. Figure 25.8 shows typical results from sensitivity analysis. It is found that the sensitivity analysis results show different characteristics for material properties and link properties, as shown in Fig. 25.8. For material properties, all the modes have similar sensitivities to certain material parameter, so it do not help a lot when I want to adjust the frequencies of some modes and leave those of other modes unchanged. For instance, if the first mode from FE model matches the test results perfectly while the third mode does not, it is impossible to achieve a good match for both modes through adjusting the material parameters. However, different modes show a variety of sensitivities towards link properties, which makes it possible to calibrate the model when encountering the situation mentioned above.

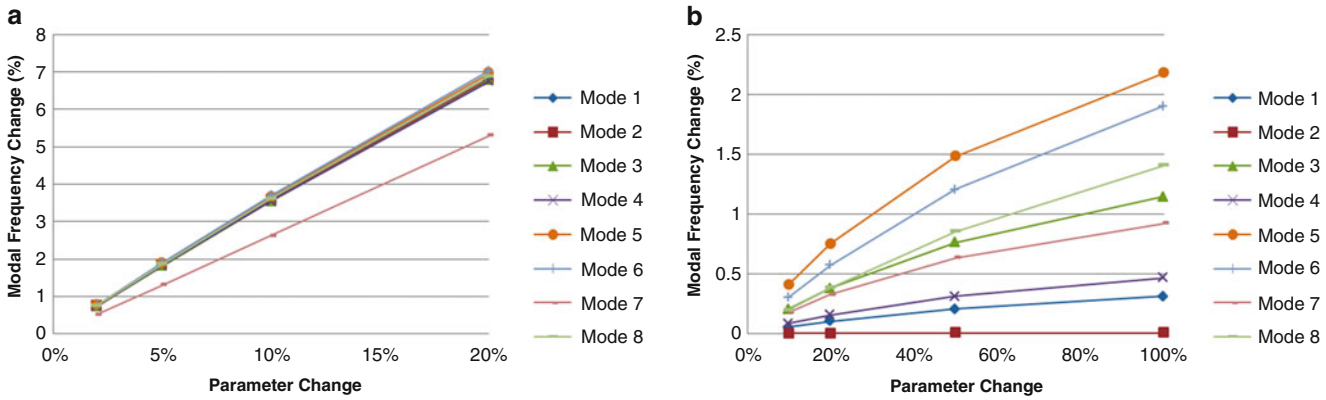

Fig. 25.8 Typical results from sensitivity analysis of (**a**) material property and (**b**) link property

Table 25.3 Modal properties of the Portage Bridge before and after FE model calibration

Mode no.	FEM (Hz)	ARTeMIS (Hz)	Damping (%)	Updated FEM (Hz)	Diff (%)	Mode description
1	2.416	2.507	3.19	2.442	2.59	Fist vertical direction
2	2.664	2.725	3.189	2.763	1.39	Fist torsional
3	3.275	3.165	3.15	3.258	2.94	Second vertical direction
4	3.308	3.375	3.154	3.356	0.56	Second torsional
5	7.031	6.96	1.175	7.09	1.87	Third torsional
6	7.897	7.56	2.404	7.969	5.41	Third vertical direction
7	8.377	8.375	2.862	8.499	1.48	Fourth vertical direction
8	11.235	11.14	0.881	11.368	2.05	Fifth vertical direction

Based on the findings from the sensitivity analysis, the FE model of the bridge was updated manually. For example, the sensitivity analysis shows the second mode is most sensitive to the bearing stiffness in translational directions, so the frequency of second mode was calibrated by adjusting bearing stiffness manually. The final results are tabulated in Table 25.3. The comparisons of mode shapes between numerical and experimental results are shown in Fig. 25.9.

25.5 Summary, Discussion and Future Work

This study presents the FE model updating of the Potage Creek Bridge in Victoria, BC, Canada using the ambient vibration test data collected in September 2014. ARTeMIS Modal was used for extracting the modal properties of the bridge, and the FE model was calibrated manually using the extracted modal information from the AVT. An acceptable match between numerical and experimental results was achieved with a maximum difference of 5.41 % in the sixth mode. After model updating, the material properties of the model were slightly changed by no more than 10 %. Stiffness of the bearings, on the other hand, was significantly increased by more than 100 %, which indicates that the equations proposed by Akogul [4] were not applicable to the bearings in Portage Creek Bridge.

Future works includes the development of the nonlinear FE model of the bridge to carry out a nonlinear static analysis (pushover analysis) and nonlinear time-history analysis in order to assess the seismic performance of the bridge in accordance with the Canadian Highway Bridge Design Code, 2015.

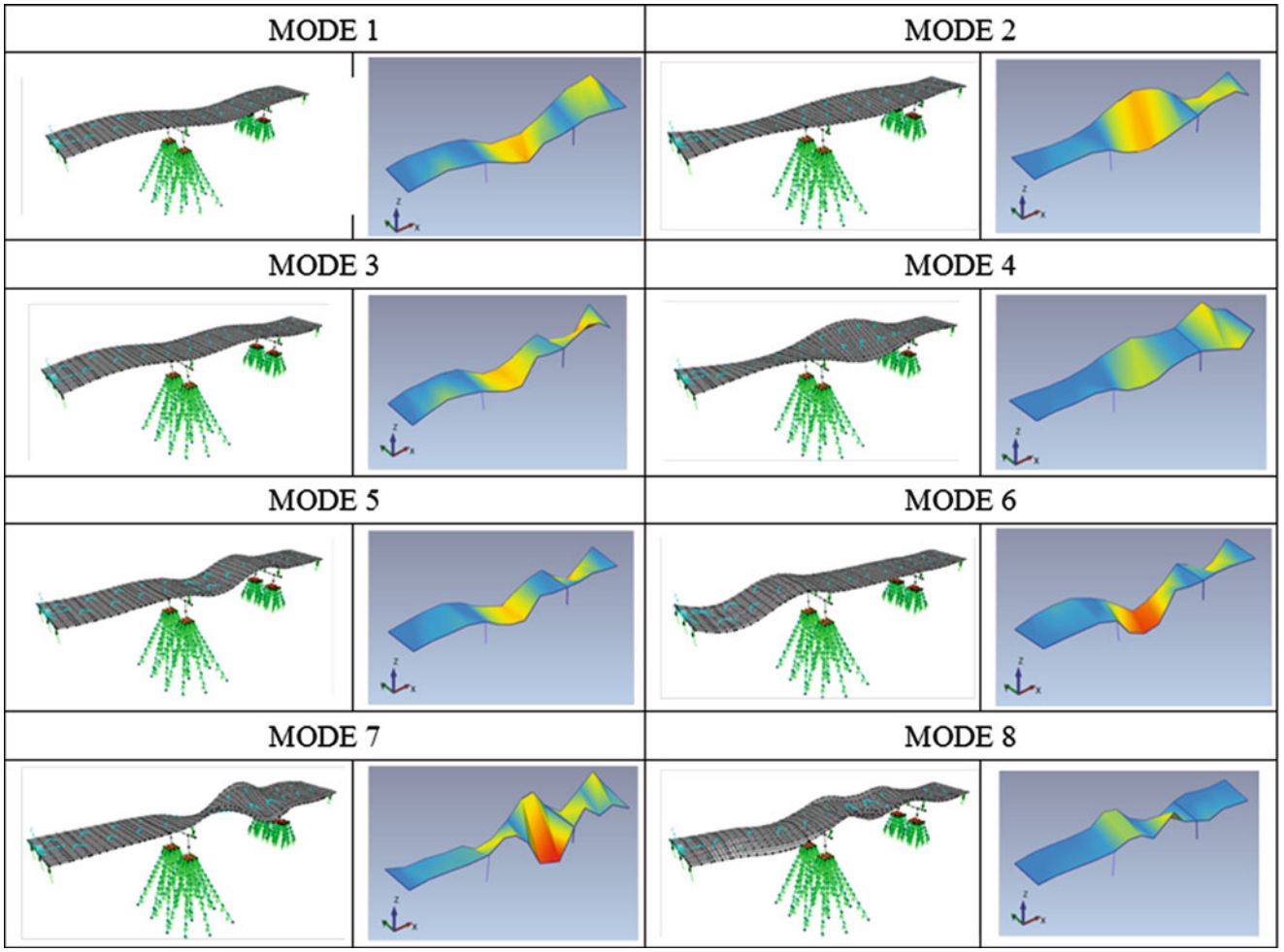

Fig. 25.9 Comparison of mode shapes between numerical and experimental results

References

1. Habibullah, A., Wilson, E.L.: SAP2000 user's manual. Computers & Structures, Inc, Berkeley, CA (1996)
2. Lord, J.-F., Ventura, C.E., Dascotte, E.: Automated model updating using ambient vibration data from a 48-storey building in Vancouver. In: Proceedings of the 22nd International Modal Analysis Conference (2004)
3. Huffman, S., Bagchi, A., Mufti, A., et al.: GFRP seismic strengthening and structural heath monitoring of Portage Creek Bridge concrete columns. Arab. J. Sci. Eng. **31**, 25–42 (2006)
4. Akogul, C., Celik, O.C.: Effect of elastomeric bearing modeling parameters on the Seismis design of RC highway bridges with precast concrete girders. In: Proceedings of the 14th World Conference on Earthquake Engineering (2008)
5. The calculation of modulus of subgrade reaction for a "Winkler Spring" model. Finite Element Analysis Ltd (2013)
6. Das, B.: Principles of Foundation Engineering. Cengage Learning, Boston (2015)
7. TROMINO user's manual. http://www.tromino.eu
8. Structural Vibration Solutions: ARTeMIS extractor: ambient response testing and modal identification software, user's manual (2001)
9. Lamarche, C.P., et al.: Assessment of the frequency domain decomposition technique by forced-vibration tests of a full-scale structure. Earthq. Eng. Struct. Dyn. **37**(3), 487 (2008)

Chapter 26
Seismic Behavior of Partially Prestressed Concrete Structures

Milad Hafezolghorani Esfahani, Farzad Hejazi, Keyhan Karimzadeh, and Tan Kok Siang

Abstract The demand for buildings and bridge structures with long spans and light weight which are able to sustain against dynamic loads are increasing in recent years. To overcome natural weakness of concrete in tension, prestressed concrete method is one of the best ways. Partially prestressed concrete structures fill the gap between fully prestressed concrete structures and conventional reinforced concrete (RC) structures which are now accepted and applied by many engineers. Although considerable effort has been made for evaluation of seismic-resistant of RC structures, little information is available on the behavior of monolithic partially prestressed concrete (PPC) and prefabricated partially prestressed concrete (IBS) structures against earthquake. In the present paper, seismic response of PPC and IBS frames are evaluated and damage plasticity theory is implemented in order to investigate the behavior of concrete in tension and compression. For this purpose, finite element model of the PPC and IBS frames is developed and pushover, cyclic and time history analysis are conducted to simulate the seismic response. Comparison of the obtained results from PPC and IBS frames with the conventional RC frames shows significant improvement for PPC and IBS structures subjected to both severe gravity and dynamic loads simultaneously.

Keywords Monolithic and prefabricated partially prestressed concrete • Seismic response • Damage plasticity • Finite element model • Dynamic load

26.1 Introduction

Partially prestressed concrete technique has been widely used for long span bridges and buildings carrying gravity loads. The other advantages of prestressing are its structural efficiency, superior structural performance, cost-reduction, and aesthetics. Partially prestressing method has been widely accepted as a beneficial integration of prestress process into conventional reinforced concrete. However the acceptance level of extensive application of prestressed structures in highly seismic areas is obstructed by the uncertainties about the responses of prestressed construction elements to seismic loading. Therefore, more research is required in this field.

Park and Thompson [1] conducted cyclic load tests on prestressed and partially prestressed beam-column of frame to simulate the effect of sever earthquake loading. The results from the tests show that the ductility of prestressed beams was enhanced by the presence of non-prestressed reinforcing in the compression zones of members. Hawkins [2] reviewed the results of analysis and experiments on the seismic resistance of prestressed and precast concrete structures and their sub-assemblages. Researchers Su and Zhu [3] presented a finite element algorithm for hysteresis analysis of prestressed concrete frames subjected to arbitrary loading history. Morgen and Kurama [4] developed a new type of friction damper for unbonded post-tensioned precast concrete building moment frame structures in seismic region. It is found that damper placed at beam-to-column joint provides energy dissipation to the frame, at the same time preserves the self-centering capability of the structure. Furthermore installation of damper reduces beam deterioration under cyclic lateral loading. Xue et al. [5] performed a study on the seismic performance of high-performance concrete (HPC) frames under low reversed cyclic loading to provide guidance to support the design of HPC structures in seismic regions. According to study done by Yee and Adnan [6], seismic performance of precast concrete structure depended on the ductility capacity of the connectors jointing each precast components, especially the beam-to-column connection. Han et al. [7] studied the crack development characteristics, failure pattern, hysteresis curve and displacement ductility of new prestressed precast reinforced concrete intelligent structure by analyzing it under low reversed cyclic load test. Li [8] carried out a pseudo-dynamic test on bonded and unbonded

M.H. Esfahani • F. Hejazi (✉) • K. Karimzadeh • T.K. Siang
Civil Engineering Department, University of Putra Malaysia, Serdang 43300, Malaysia
e-mail: fhejazi@upm.edu.my

S. Pakzad, C. Juan (eds.), *Dynamics of Civil Structures, Volume 2*, Conference Proceedings of the Society for Experimental Mechanics Series, DOI 10.1007/978-3-319-29751-4_26

prestressed concrete flat beam. It is found that whether prestressed tendon is bonded or unbonded has little influence on the overall seismic performance of the structure. Vidjeapriya and Jaya [9] compared the performance of precast and monolithic beam-column joints subjected to cyclic loading. The researchers found out that precast structure is more versatile, and offers high structural efficiency. The results of a study done by Hamid et al. [10] shows that damage mostly occurred at the corbel in-plane with the loading direction and also at the cast-in-place area of concrete. In the research they revealed that hysteresis loop from experimental results can be modeled by Ruaumoko Hysteresis Programming and Wayne Stewart Hysteresis Rule gives the closest pattern. Marsono et al. [11] presented a standard test to check the design and strength of IBS components via experimental flexural test and verify with FEM analysis in ABAQUS.

In spite of appreciable effort in research on seismic response of reinforced concrete (RC) structure, there is inadequate research done on the behaviour of monolithic partially prestressed concrete (PPC) and prefabricated partially prestressed concrete (IBS) structures under seismic loading. This paper presents an evaluation of the seismic response of RC, monolithic and prefabricated PPC structures with consideration to the concrete damaged plasticity theory. For this purpose, finite element model of the PPC frame is developed pushover, cyclic and time history analysis are conducted to simulate the seismic response.

26.2 Numerical Analysis

In the current paper, effect of prestressing tendon on the behavior of monolithic and prefabricated partially prestressed concrete frames under self-weight and different super imposed dead loads is investigated and compared with conventional RC frames. For this aim, a three dimensional (3D) nonlinear finite element program, ABAQUS 6.11 is utilized to analyze all models under nonlinear-static (push-over and cyclic) and pseudo-dynamic (time history) loading. . The detail of geometry; properties of the samples; prestressing force and loading procedure; and failure criteria are explained below.

26.2.1 Sample Description

Three specimens of one-bay, one-story reinforced concrete (RC), monolithic partially prestressed concrete (PPC) and prefabricated partially prestressed concrete (IBS) frames were modeled. The details of all frames are illustrated in Fig. 26.1. The first sample was denoted as conventional RC frame, and second specimen was denoted as monolithic PPC frame with prestressed beam. RC and PPC frames are monolithic . The third sample was indicated as IBS frame, with bonded prestressed beam. Interaction between beam and column is surface to surface with friction factor of 0.5.

The models consist of one beam and two columns. The clear length of beam is 1800 mm and height of the column is 2000 mm. Both beam and column have 200 mm $\times$ 200 mm cross sections. The diameter of longitudinal steel reinforcements of columns and beam are 20 mm and 10 mm respectively. The diameter of steel link is 8 mm (column:D8@80 mm;beam:D8@100 mm). 3*7 wire strands (D15.2 mm) with 420 mm^2 in area are placed in a hollow duct with 40 mm eccentricity from the center of the beam. The cover of 25 mm and 20 mm for column and beam are provided to fulfill the requirement of fire, durability and corrosion protection as shown in Fig. 26.1a–e. The detail of corbel is shown in Fig. 26.1f.

The material properties of concrete; longitudinal and link reinforcement; and PT strands are shown in Table 26.1.

26.2.2 Loading Procedure

Five types of loading are imposed during this study at the five stages outline below. The columns are fixed at the bottom in all stages.

1. Post-tensioning of prestressed strands with 40 mm eccentricity from the center of beam. A 210 kN equivalent of 30 % of the tension yielding capacity of three prestressing strands, 15.2 mm diameter, are applied during this stage.
2. During this simulation, three different gravity loads (self-weight and two superimposed dead loads) are applied above the reinforced and prestressed concrete frame structures as:

   - Case 1: self-weight, 4.8 kN/m^2

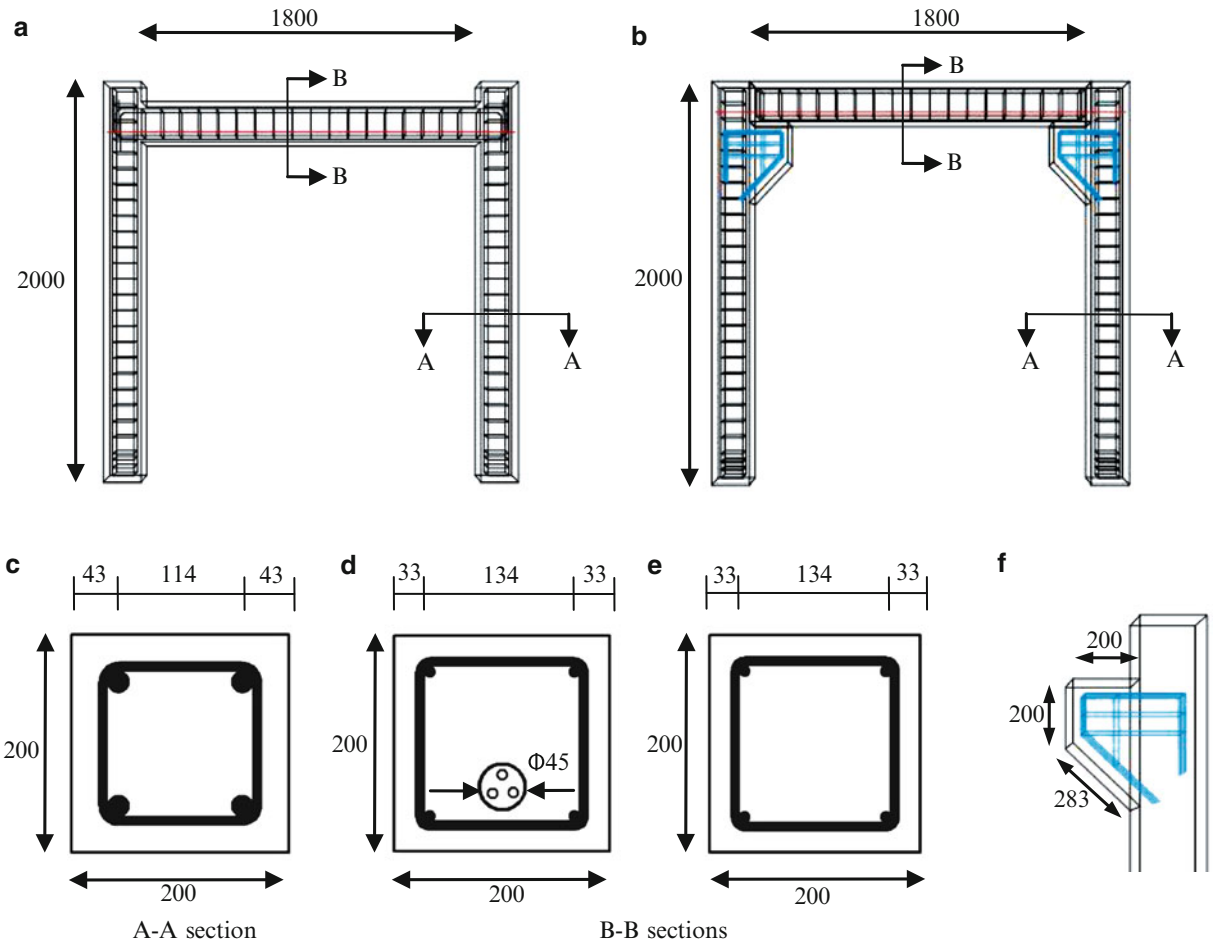

Fig. 26.1 Dimensional and reinforcement details (**a**) RC and monolithic PPC frames (**b**) IBS frame (**c**) cross section of column (**d**) cross section of prestressed beam (**e**) cross section of RC beam and (**f**) corbel details

Table 26.1 Mechanical properties of specimens

	Steel bar			Tendon		Concrete
Mechanical property	Φ8	Φ10	Φ20	3Φ15.2	Mechanical property	
Yield strength, fy (MPa)	270	413	413	1690	Strength of concrete f_c (MPa)	40
Ultimate strength, fu (MPa)	310	460	460	1861	Modulus of elasticity E_c (GPa)	30
Modulus of elasticity Es (GPa)	200	200	200	196.5	Poisson's ratio ν	0.2
Poisson's ratio, ν	0.3	0.3	0.3	0.3		

- Case 2: self-weight + superimposed dead load, 204.8 kN/m^2
- Case 3: self-weight + superimposed dead load, 404 8 kN/m^2.

3. Nonlinear static analysis of the reinforced and partially prestressed concrete frames under monotonically increasing lateral loads (push-over analysis) is presented during this paper.
4. Lateral cyclic loading applied at the top of the frames. The cyclic loading history is shown in Fig. 26.2. The loading is imposed with arithmetic progression of P = 5 (0, 5, 10, 15, . . . ,100 mm). Three cycles of loading are repeated for each increment of displacement. Damage plasticity criteria (Damage in tension and compression) and the occurrence of a 1 % residual drift are considered as failure criteria of the FE models.
5. Nonlinear dynamic analysis (Time-history) is performed for the RC, PPC and IBS frames. The frames were analyzed under North–south component of El-Centro, 1940 earthquake record as shown in Fig. 26.3.

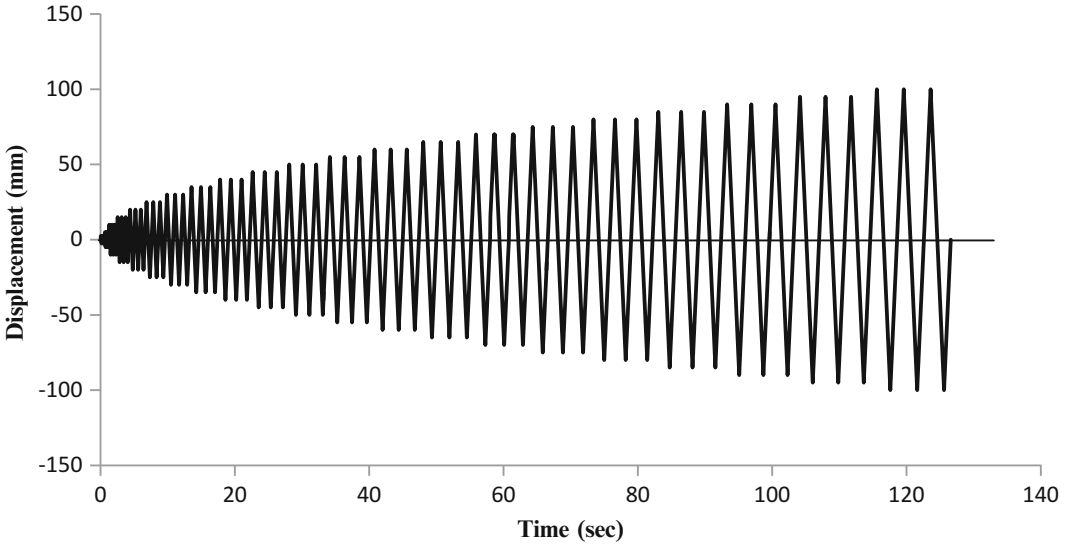

Fig. 26.2 Cyclic loading history of the FE models

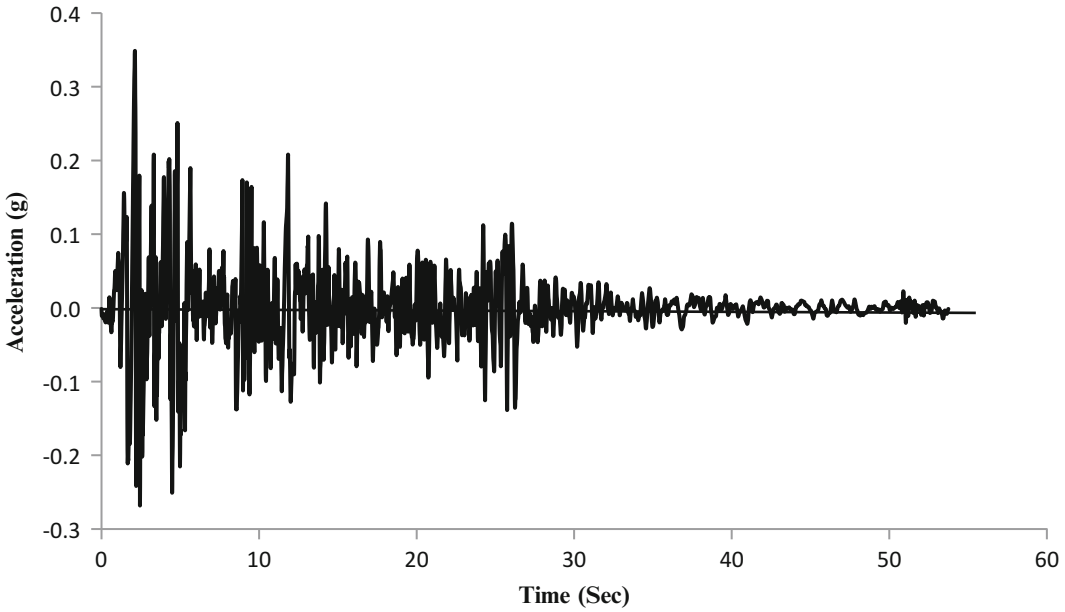

Fig. 26.3 Earthquake record of North–south component of El-centro (1940-USA)

26.2.3 Type of Elements

Finite element software, ABAQUS was used to simulate the elements for the modeling of materials, such as concrete, steel reinforcement and prestressing tendon that must be selected accordingly to derive precise results concerning stiffness, yielding displacement and residual displacement under reverse cyclic and seismic loading.

The reinforcing bar elements and prestressing tendon element modeled as 2-node linear 3-D truss elements (T3D2). These elements were embedded among the concrete. A three dimensional 8-node linear brick, reduced integration element (C3D8R) was used simulate concrete parts.

Figure 26.4a, b show the meshing configuration of reinforced concrete, monolithic partially prestressed concrete and prefabricated partially prestressed concrete frames. The elements and meshing applied for longitudinal and links steel reinforcement, prestressing tendon are shown in Fig. 26.4c.

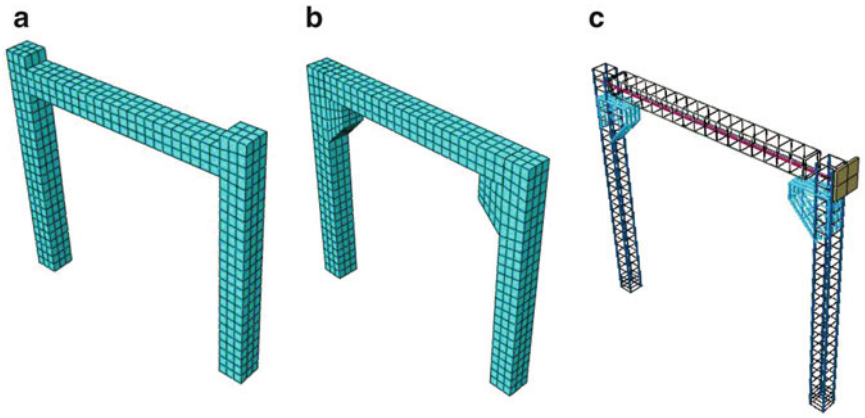

Fig. 26.4 FE meshes of (**a**) RC and monolithic PPC frames (**b**) IBS frame (**c**) reinforcement and strand

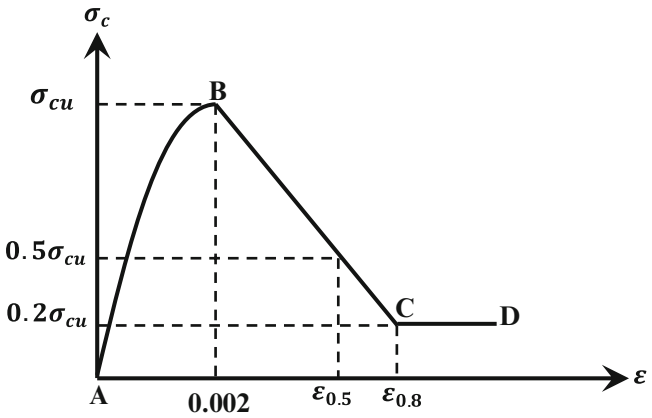

Fig. 26.5 Kent and Park model for compressive behavior of concrete [13]

26.2.4 Failure Criteria of Concrete

In this paper a Concrete Damaged Plasticity (CDP) model was used. The CDP model is suitable to show the nonlinear behavior of concrete in compression and tension. As shown in Fig. 26.5, Kent and Park parabolic model is utilized to simulate the compressive behavior of unconfined and confined concrete, which is expressed by the following equation:

$$\sigma_c = \sigma_{cu}\left[2\left(\frac{\varepsilon_c}{\varepsilon'_c}\right) - \left(\frac{\varepsilon_c}{\varepsilon'_c}\right)^2\right] \tag{26.1}$$

where σ_c and ε_c are nominal compressive stress and strain, and σ_{cu} and ε'_c are ultimate compressive strength of cylinder specimen and it's strain, respectively. The amount of ε'_c is considered as 0.002 as reported by Park [12].

Generally, 7–10 % of maximum compressive strength, σ_{cu} is chosen as a tensile strength, σ_{t0} and in this study the maximum value has been taken as follows:

$$\sigma_{t0} = 0.1\sigma_{cu} \tag{26.2}$$

Besides, in CDP model, damage in compression (d_c) and damage in tension (d_t) are effective parameters to represent the cyclic behavior of concrete and can be defined as follows:

$$d_c = 1 - \frac{\sigma_c}{\sigma_{cu}} \tag{26.3}$$

$$d_t = 1 - \frac{\sigma_t}{\sigma_{t0}} \tag{26.4}$$

where σ_c and σ_t are nominal compressive and tensile stresses respectively.

26.3 Parametric Study

In this section, a parametric study is performed to investigate the effects of gravity loads on the seismic behavior of RC, PPC and IBS finite element models. These models are subjected to self-weight (4.8 kN/m^2) and various superimposed dead loads (204.8 and 404.8 kN/m^2) and then analyzed under quasi-static push-over, cyclic analysis and pseudo-dynamic analysis (time-history). The results are compared as follows.

26.3.1 Nonlinear Static Push-Over Analysis

The monotonic force-displacement curves are obtained in service stage subjected to self-weight and different super imposed loads. Also a prestressing force of 210 kN is applied to the both monolithic PPC and IBS frames. Figure 26.6a–c show the force versus displacement curves under gravity loads of 4.8 kN/m^2, 204.8 kN/m^2 and 404.8 kN/m^2 respectively. The results are analyzed up to 150 mm lateral displacement (7.5 % of drift).

As shown in Fig. 26.6a, the capacity of conventional RC model is 7.437 kN m whereas the capacities of PPC and IBS models indicate 22.5 % and 31.3 % increase respectively. Similarly, under gravity load of 204.8 kN/m^2 (see Fig. 26.6b), the capacity of PPC and IBS frames are increased up to 44 % and 65.4 % of capacity of RC frame. It can be seen from Fig. 26.6c, the capacity of RC frame under the 404.8 kN/m^2 is decreased to 1.864 kN m, while the capacity of PPC and IBS frames are 9.8 kN m and 8.2 kN m respectively.

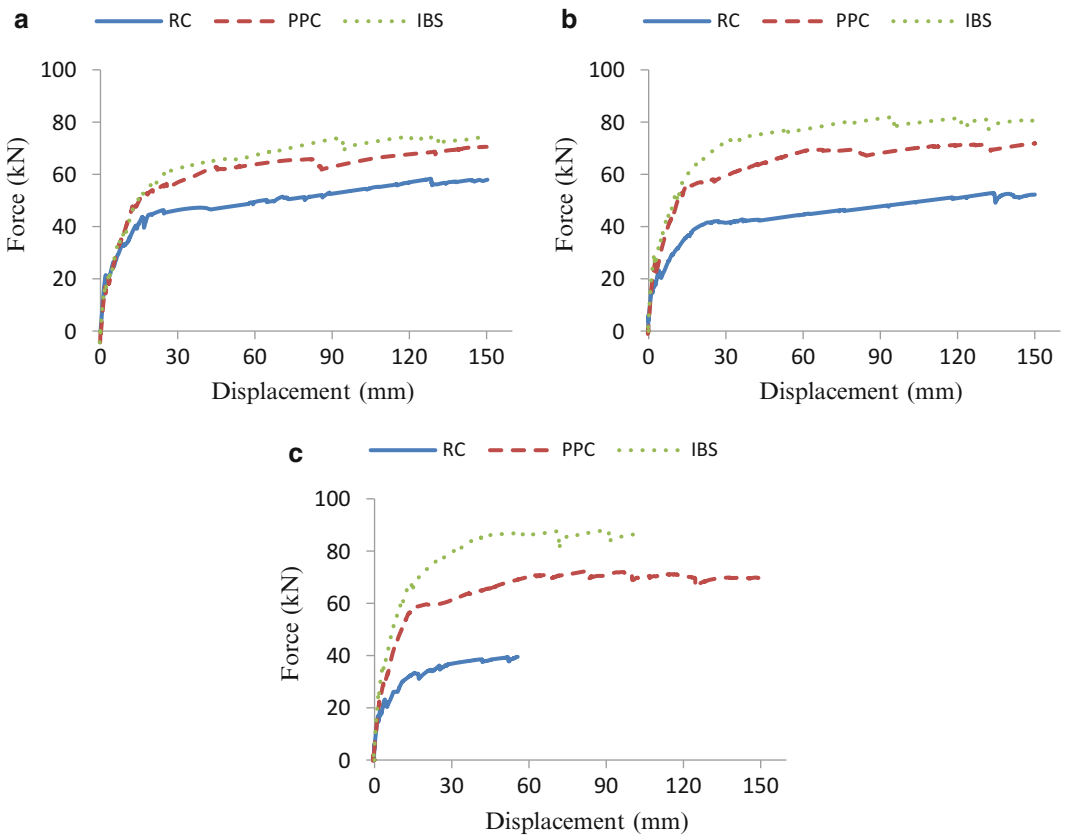

Fig. 26.6 Reaction force-displacement curves under gravity loads (**a**) 4.8 kN/m^2 (**b**) 204.8 kN/m^2 and (**c**) 404.8 kN/m^2

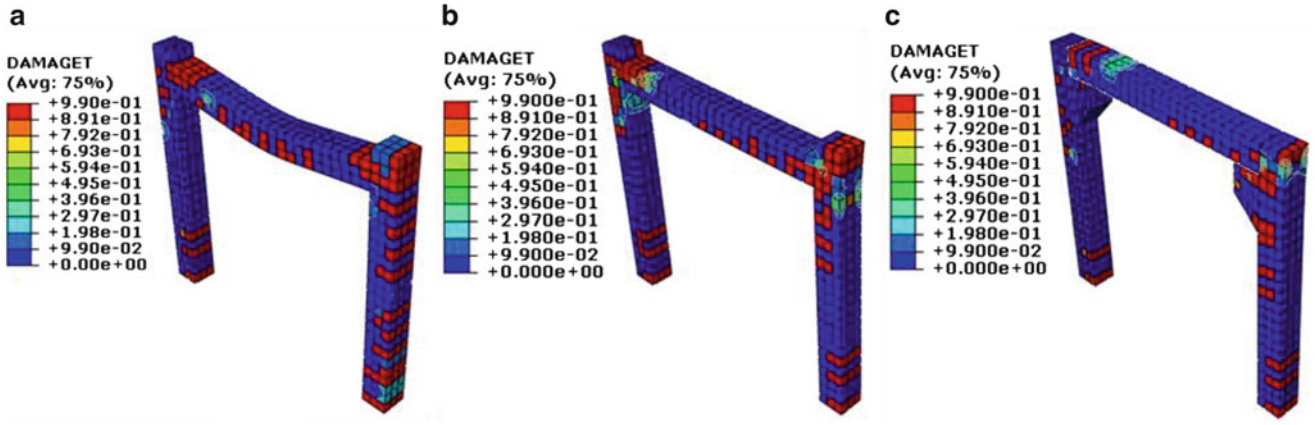

Fig. 26.7 Damage due to tension in concrete under 404.8 kN/m^2 gravity load for (**a**) RC frame (**b**) PPC frame and (**c**) IBS frame

As the reaction force-displacement curves in Fig. 26.6c indicate, strength of the partially prestressed monolithic and prefabricated frames is considerably increased, while the strength of conventional RC frame is reduce to 38 kN. It should be noted that the monolithic PPC frame is more ductile than RC and IBS frames under severe gravity load.

Damage in tension is shown in Fig. 26.7 for RC, PPC and IBS models subjected to 404.8 kN/m^2 of gravity load. FE models fail when damage in tension reach 0.99 or lateral displacement reaches up to 150 mm.

26.3.2 Nonlinear Static Cyclic Analysis

The results of the lateral cyclic loading-displacement of the conventional reinforced concrete (RC), monolithic partially prestressed concrete (PPC) and prefabricated partially prestressed concrete (IBS) frames under self-weight and super imposed dead loads (4.8 kN/m^2, 204.8 kN/m^2 and 404.8 kN/m^2) are compared in Fig. 26.8.

As shown in Fig. 26.8a, the FE models are analyzed up to 75 mm lateral displacement (3.7 % drift). As the figure indicates, the strength of RC, PPC and IBS frames reach 76.4 kN, 72.1 kN and 79.6 kN respectively under 4.8 kN/m^2 self-weight. In contrast with the RC and IBS frames, PPC frame exhibits high hysteretic energy dissipation capacity (shown in Fig. 26.9) and more lateral displacement (about 75 mm).

In Fig. 26.8b, the maximum strength and lateral displacement of the PPC frame is close to the IBS frame under 204.8 kN/m^2 of super imposed dead load. Besides, as the gravity load increases, the strength, ductility and hysteretic energy dissipation capacity of the RC frames decrease dramatically.

As shown in Fig. 26.8c, maximum lateral cyclic loads in RC, PPC and IBS frames under 404 kN/m^2 are 65.6 kN, 72.2 kN and 91.3 kN respectively. Accordingly, the maximum lateral displacement at the end of full cycles of the RC, PPC and IBS models are 24.98 mm, 34.3 mm and 64.75 mm respectively. Energy dissipation in full cycles of RC frame is about 32.6 kN m whereas the energy dissipations of the PPC and IBS models indicate 124.53 % and 743 % increase respectively (Fig. 26.9).

26.3.3 Nonlinear Dynamic Time-History Analysis

A non-linear time-history analysis is crucial to evaluate the effect of prestressing tendon on the dynamic behavior of monolithic partially prestressed (PPC) and precast partially prestressed concrete (IBS) framed structures. This study compares the performance of the conventional RC frame with the PPC and IBS frames. El-Centro earthquake record (North–south component; USA-1940) with peak ground acceleration of 0.348 (g) is utilized to examine the seismic response of the RC, PPC and IBS FE frames.

Figures 26.10, 26.11 and 26.12 compare the lateral peak displacement and acceleration magnitude of RC, PPC and IBS frames under gravity loads of 4.8 kN/m^2, 204.8 kN/m^2 and 404.8 kN/m^2 at 13th second of El-Centro record. Time-history analyses in Fig. 26.10a indicate that the peak lateral displacement in RC, PPC and IBS are 118.29 mm, 121.44 mm and

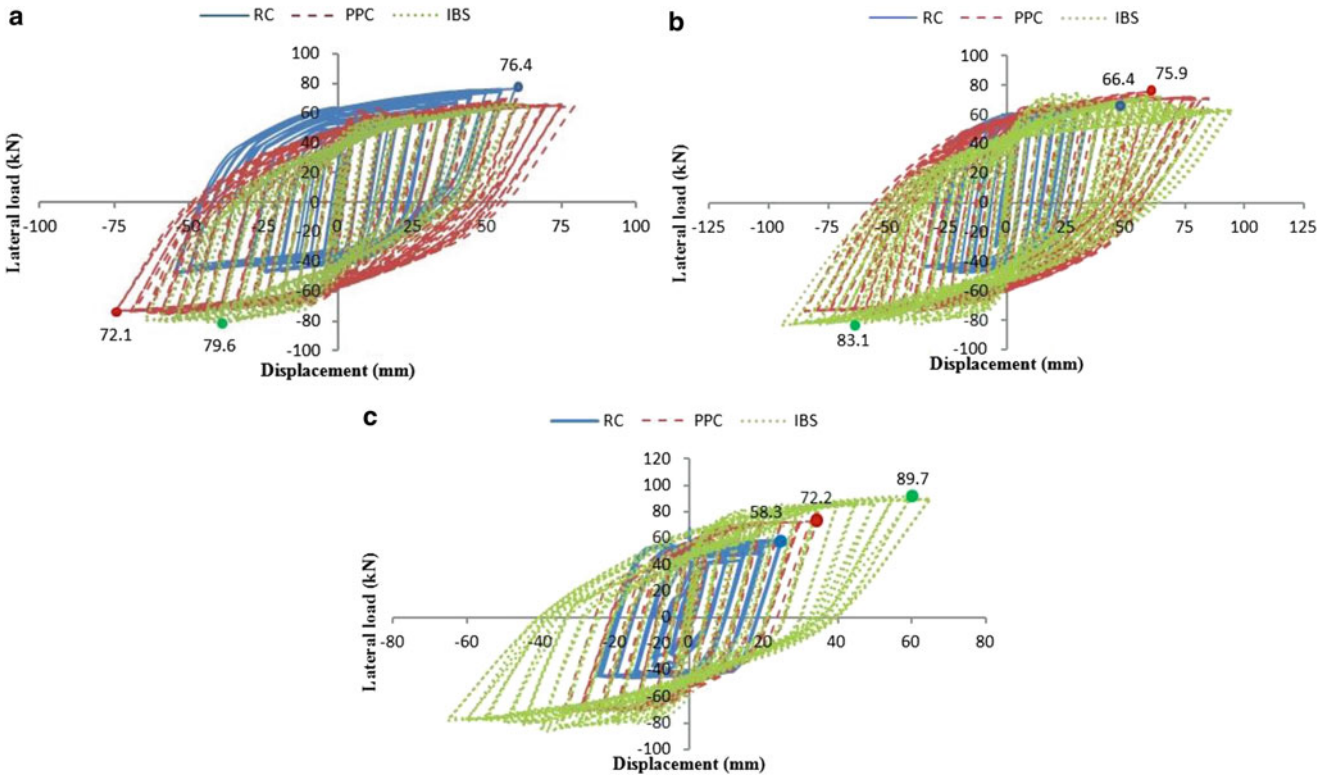

Fig. 26.8 Lateral cyclic load–displacement curves under gravity loads (**a**) 4.8 kN/m^2 (**b**) 204.8 kN/m^2 and (**c**) 404.8 kN/m^2

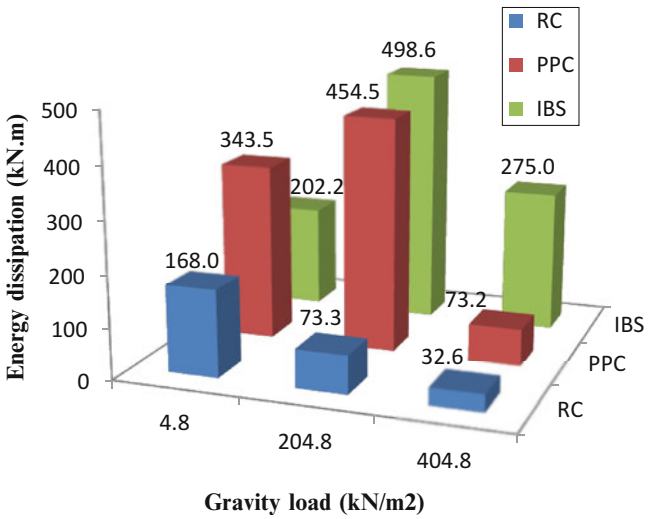

Fig. 26.9 Energy dissipation for full cycles of RC, PPC and IBS FE models

119.82 mm respectively (at times 3.058 s, 2.997 s and 3.076 s respectively). Therefore, PPC has more lateral displacement at the top due to less amount of damage and high amount of energy dissipation capacity (Fig. 26.8). Also acceleration versus time is shown in Fig. 26.10b.

Figure 26.11a, b shows that IBS frame has higher magnitude of peak displacement and acceleration compared to the RC and PPC frames under 204.8 kN/m^2 gravity load. The maximum top deflection in IBS is 133.94 mm at 5.896 s. While, 132.68 mm and 119.69 mm displacement for RC and PPC occurred at 12.41 s and 5.81 s respectively.

The maximum deflection and acceleration of the RC, PPC and IBS frames occurred at times 5.47 s, 4.07 s and 5.26 s as shown in Fig. 26.12. It can be observed that the IBS frame has more lateral displacement due to high amount of strength and energy dissipation under huge gravity load (Figs. 26.6c and 26.9). To clarify more RC, PPC and IBS show 92.27 mm, 88.35 mm, 118.08 mm respectively.

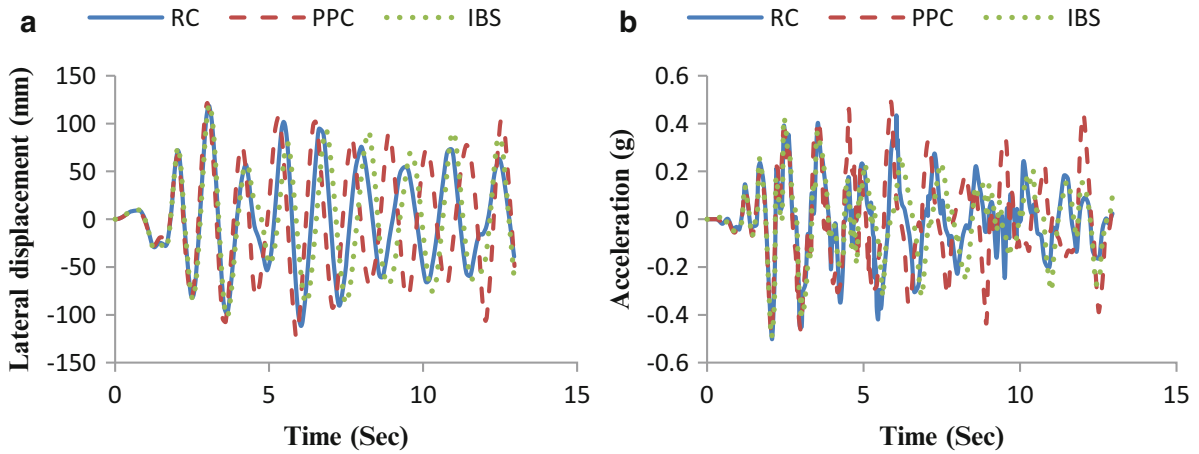

Fig. 26.10 Comparison of seismic response of RC, PPC and IBS frames under gravity load of 4.8 kN/m^2 (**a**) lateral top displacement (**b**) acceleration

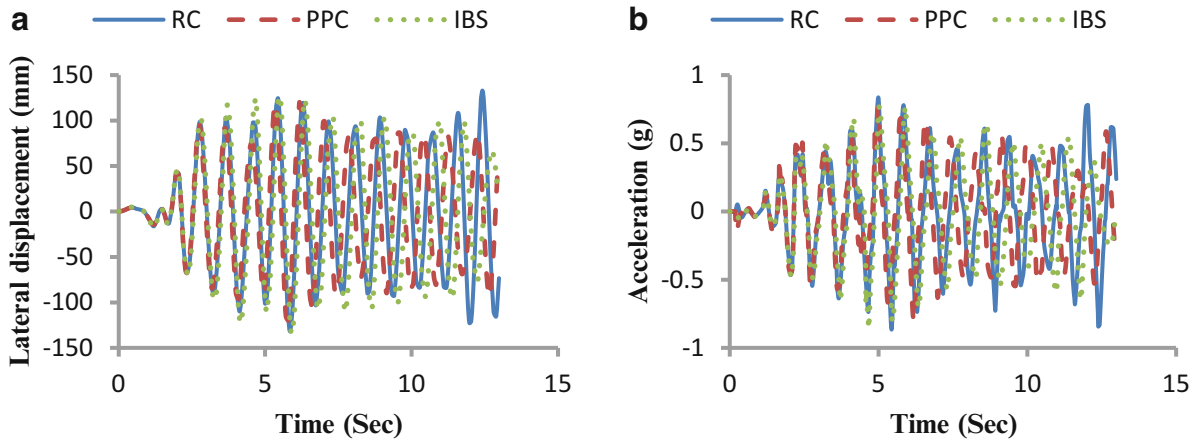

Fig. 26.11 Comparison of seismic response of RC, PPC and IBS frames under gravity load of 204.8 kN/m^2 (**a**) lateral top displacement (**b**) acceleration

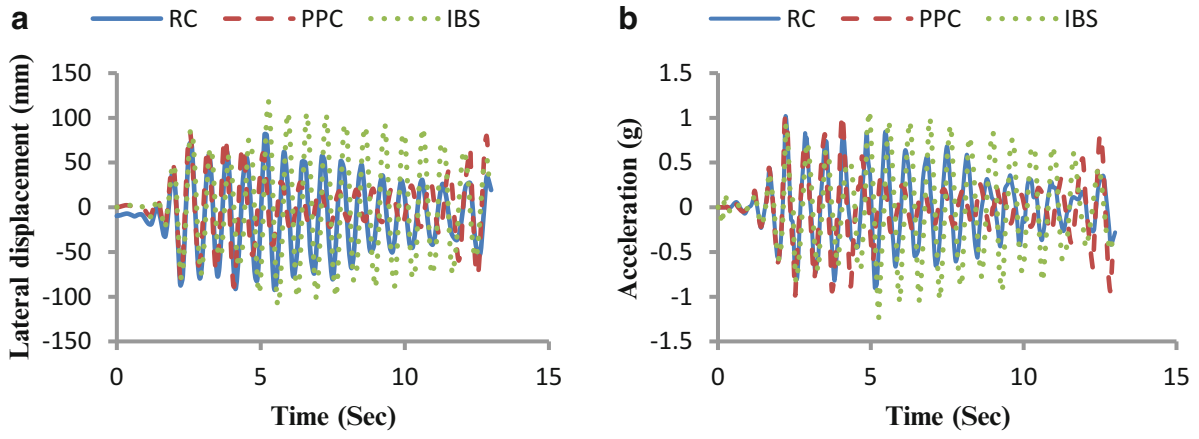

Fig. 26.12 Comparison of seismic response of RC, PPC and IBS frames under gravity load of 404.8 kN/m^2 (**a**) lateral top displacement (**b**) acceleration

26.4 Conclusion

In this study, push-over, cyclic and time-history analysis are implemented to investigate the seismic performance of the conventional reinforced concrete, monolithic partially prestressed concrete and prefabricated partially prestressed concrete FE frames subjected to various gravity loads.

- In push-over analysis, the lateral loads are monotonically applied to account the capacity of RC, PPC and IBS models. The results show that the capacity of RC frames is significantly decreased with increasing the gravity loading. While the results verified incredible improvement in strength and capacity of the PPC and IBS frames under severe gravity loads in comparison to the conventional reinforced concrete technique.
- Nonlinear cyclic analysis indicates that as the gravity load increases, the lateral cyclic load, ductility and hysteretic energy dissipation capacity of the RC frame decrease. However effect of prestressing leads to improve the behavior of the PPC and IBS frames against lateral cyclic loads. Although, the ultimate strength of the IBS is more than the PPC frame, PPC shows more lateral displacement in comparison to IBS.
- As mention before, PPC and IBS frames have high amount of capacity and energy dissipation compared to the RC frame that lead to a delay in the failure process of concrete frames subjected to both gravity and dynamic load. Therefore, the results from time-history analysis indicated that PPC and IBS frames have higher seismic performance in comparison to the conventional RC frame.

References

1. Park, R., Thompson, K.: Cyclic load tests on prestressed and partially prestressed beam-column joints. PCI J **22**(5), 84–110 (1977)
2. Hawkins, N.M.: Seismic resistance of prestressed and precast concrete structures. PCI J **22**(6), 80–110 (1977)
3. Su, X., Zhu, B.: Algorithm for hysteresis analysis of prestressed-concrete frames. J. Struct. Eng. **120**(6), 1732–1744 (1994)
4. Morgen, B., Kurama, Y.: A friction damper for post-tensioned precast concrete beam-to-column joints. PCI J **49**(4), 112–133 (2004)
5. Xue, W., Cheng, B., Zheng, R., Li, L., Li, J.: Seismic performance of Non-prestressed and prestressed HPC frames under low reversed cyclic loading. J. Struct. Eng. **137**(11), 1254–1262 (2010)
6. Yee, P., Adnan, A.: Performance of IBS precast concrete beam-column connections under earthquake effects: a literature review. Am. J. Eng. Appl. Sci. **4**(1), 93–101 (2011)
7. Han, J.Q., Li, B.Z., Song, S.X.: Research on seismic performance of prestressed precast reinforced concrete intelligent structure. Appl. Mech. Mater. **50**, 1003–1007 (2011)
8. Li, F.: The research on seismic response of prestressed concrete flat beam in pseudo-dynamic test. 2nd International Conference on Electronic & Mechanical Engineering and Information Technology, pp. 806–809 (2012).
9. Vidjeapriya, R., Jaya, K.: Behaviour of precast beam-column mechanical connections under cyclic loading. AJCE **13**(2), 233–245 (2012)
10. Hamid, A., Hamzah, H., Ghani, A.: Seismic performance of beam-column corbel connections (IBS) in the existing precast reinforced concrete frame under reversible lateral cyclic loading. pp. 1–53. UiTM University (2013)
11. Marsono, A., Ying, W., Tap, M., Chieh, Y., Haddadi, A.: Standard verification test for Industrialised Building System (IBS) repetitive manufacturing. Procedia CIRP **26**, 252–257 (2015)
12. Park, R.: Reinforced Concrete Structures. John Wiley & Sons, New York (1975)
13. Kent, D., Park, R.: Flexural members with confined concrete. J. Struct. Div. **97**(7), 1969–1990 (1971)

Chapter 27
Estimating Effective Viscous Damping and Restoring Force in Reinforced Concrete Buildings

P. Hesam, A. Irfanoglu, and T.J. Hacker

Abstract In seismic design, buildings are designed to respond to strong earthquake ground motions inelastically. The engineering norm followed in design and analysis is to use constant modal viscous damping ratios to account for all energy dissipation aside from that arising from material nonlinearity. In general, equivalent linear models, which aim to capture primarily the peak response with typically 2–5 % of critical damping are employed. In this paper, we show that the effective viscous damping ratio can be estimated from the dynamic response of actual building structural systems without linearization of the load-deformation characteristics. The empirical method we present, which estimates the effective viscous damping ratios of buildings, has been applied to several laboratory specimens and actual buildings. We show that the effective viscous damping ratio in a low to mid-rise reinforced concrete (RC) building responding at its dominant mode (equivalent of fundamental mode in linear elastic systems) varies linearly with the effective period of its dominant mode. The practical use of the method is demonstrated using acceleration records obtained in two 9-story small-scale RC laboratory test specimens during a series of strong base motions. Fundamental mode envelopes of hysteretic responses, that is, the backbone curves for both structures are estimated by excluding higher mode effects from the measured responses.

Keywords Effective viscous damping ratio • Viscous damping coefficient • Reinforced concrete buildings

27.1 Introduction

The response of buildings to earthquake ground shaking is a complex process. During strong shaking, the structural system of the building may be forced to behave inelastically. In addition to the hysteretic energy dissipation due to inelastic behavior, the structure will dissipate energy through means currently not well understood. In the simplest of approaches, linear viscous damped models with constant modal damping ratios are used. More elaborate models may use Rayleigh damping or Caughey damping [1] but not necessarily always with justification [2]. Compared with assuming a constant value for the viscous damping ratios, say, 2 % or 5 % of the critical damping, using effective damping ratios estimated from the dynamic response of actual building structural systems would be more realistic. Such an empirical approach may also help identify the structural system and response parameters that are well-correlated with the damping ratio. An empirical method based on the procedure proposed by Dowgala [3] is presented here. The method is applied to two 9-story reinforced concrete laboratory specimens tested on a shaketable at the University of Illinois at Urbana-Champaign.

27.2 Background

Based on tests by Eberhard [4] and Schultz [5], Algan [6] observed that the peak inelastic displacement of a reinforced concrete (RC) structure subjected to a strong ground motion (GM) correlates with its elastic fundamental period. Different methods have been proposed to estimate the maximum inelastic deformation using equivalent periods and damping ratios (for example, Lepage [7] or displacement modification factors Newmark [8] and Miranda [9]). The key parameters

P. Hesam (✉) • A. Irfanoglu
Lyles School of Civil Engineering, Purdue University, West Lafayette, IN 47907, USA
e-mail: pedramhesam@purdue.edu; ayhan@purdue.edu

T.J. Hacker
Department of Computer and Information Technology, Purdue University, West Lafayette, IN 47907, USA
e-mail: tjhacker@purdue.edu

S. Pakzad, C. Juan (eds.), *Dynamics of Civil Structures, Volume 2*, Conference Proceedings of the Society for Experimental Mechanics Series, DOI 10.1007/978-3-319-29751-4_27

(equivalent period, damping ratio, displacement modification factors) are expressed as functions of displacement ductility ratio (Rosenblueth [10]; Gulkan [11]; Iwan [12]; Kowalsky [13]; Priestley [14]). Assuming velocity proportional linear viscous damping, the motion of a structure responding to ground acceleration can be written as the equation

$$M\left[\ddot{x}(t) + \ddot{x}_g(t)\right] + C\dot{x}(t) + Fs(t) = 0 \tag{27.1}$$

where,

M: Mass of the structure

C: Effective viscous damping coefficient of the structure

$Fs(t)$: Restoring force provided by the structural system; if the structure remains linear-elastic, $Fs(t) = Kx(t)$ with K being the stiffness of the structure

$x(t)$: Displacement relative to the ground

$\dot{x}(t)$: Velocity relative to the ground

$\ddot{x}(t)$: Acceleration relative to the ground

$\ddot{x}_g(t)$: Ground acceleration

Taking a mass-normalized formulation approach, the acceleration measured on the structure becomes the mass-normalized inertial force. The equation for the mass-normalized damping force is then:

$$C_m\dot{x}(t) = -\left[\ddot{x}(t) + \ddot{x}_g(t)\right] - F_{sm}(t) \tag{27.2}$$

where,

C_m: Mass-normalized effective viscous damping coefficient

$C_m\dot{x}(t)$: Mass-normalized viscous damping force

$\ddot{x}(t) + \ddot{x}_g(t)$: Mass-normalized inertial force

$F_{sm}(t)$: Mass-normalized restoring force

The procedure proposed by Dowgala [3, 15, 16] is used herein to estimate the mass-normalized damping coefficient. The procedure is based on the principle that peaks in the restoring force should occur at instances of zero relative velocity. Enforcing this principle yields the mass-normalized damping coefficient. After fitting a probability distribution to the extracted values, one can obtain a single effective damping coefficient for the length of time of the ground motion. The velocity proportional effective viscous damping ratio can be written in terms of the mass-normalized damping coefficient and the natural period of a sub-critically structure as

$$\beta = \frac{C_m}{4\pi}T_n \tag{27.3}$$

where,

β: effective viscous damping ratio of the structure

C_m: mass-normalized effective viscous damping coefficient

T_n: natural period of the structure (i.e., the period of the dominant mode of response)

The proposed method of estimating the damping ratios of buildings [3] has so far been applied to two 10-story 3-bay MDOF RC small-scale frames with yielding girders tested by Cecen [17], two 9-story 3-bay MDOF soft-story RC frames with yielding columns tested by Schultz [5] and 15 SDOF RC test structures with different stiffness and mass tested by Bonacci [18]. The details of the experiments and summary of observations are given in the next section.

27.3 Overview of Studied Laboratory Experiments and Observations

We applied the proposed empirical method of estimating the change in the damping ratio of softening structural systems to two 9-story 3-bay RC test structures ES1 and ES2 tested by Eberhard [4]. Each structure was composed of two 9-story frame structures acting in parallel. Both specimens had identical geometry but different strength. The girders were stronger than columns in flexure. Frames had three columns and one interior slender wall (Fig. 27.1). The dimensions of girders and columns were, respectively, 38×57 mm and 38×38 mm. The slender walls were 38 mm by 114 mm. Both specimens had the same girder reinforcement ratios of 2.6 % and 1.8 %, respectively, for levels 1–3 and 4–9. Both specimens had the same longitudinal reinforcement ratio of 1.5 % throughout the height of their slender walls. The ES2 columns had

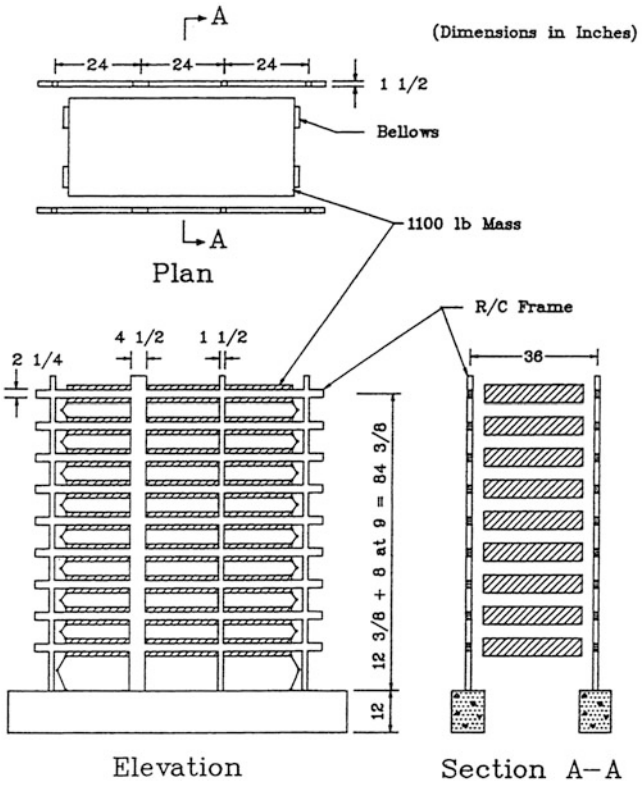

Fig. 27.1 Dimensions of the Eberhard test specimen [4] (Figure used by permission)

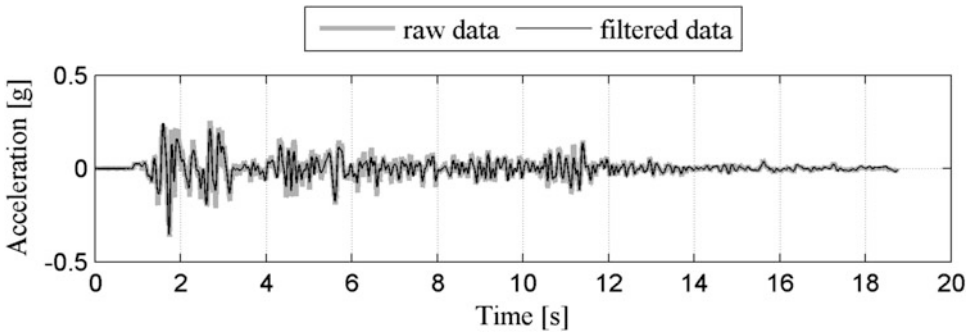

Fig. 27.2 Scaled and compressed 1940 El Centro earthquake motion

lighter reinforcement compared with the corresponding columns of ES1. In the exterior columns of ES2 the longitudinal reinforcement ratio was 1.2 % while the ES1 columns had, respectively, 1.8 % and 1.2 % longitudinal reinforcement ratios at level 1 and levels 2 through 9. In the interior columns ES2 had 1.2 % longitudinal reinforcement ratio throughout the height, and ES1 had, respectively 3.5 %, 2.3 %, and 1.2 % at level 1, levels 2–8, and level 9. ES1 had the fundamental elastic frequency measured at 5.5 Hz while ES2 had it at 6.2 Hz. Eberhard obtained these frequencies from free vibration (mass-pulley) tests on the uncracked structures [4].

Eberhard applied sequential earthquake ground motions to each structure. Both ES1 and ES2 were subjected to three sequential ground motions (GMs) with increasing peak ground acceleration (PGA). The 1940 El Centro N–S GM (Fig. 27.2) was scaled and used as the base excitation. After three sequential GM tests, both structures, now damaged, were subjected to cyclic accelerations for about 5.5 s. Figure 27.3 shows the base acceleration Eberhard applied in the cyclic tests.

Figures 27.4 and 27.5 show the peak ground accelerations (PGAs) and peak ground velocities (PGVs) from the test runs.

Figure 27.6 shows the first story absolute acceleration response for the first run of ES1.

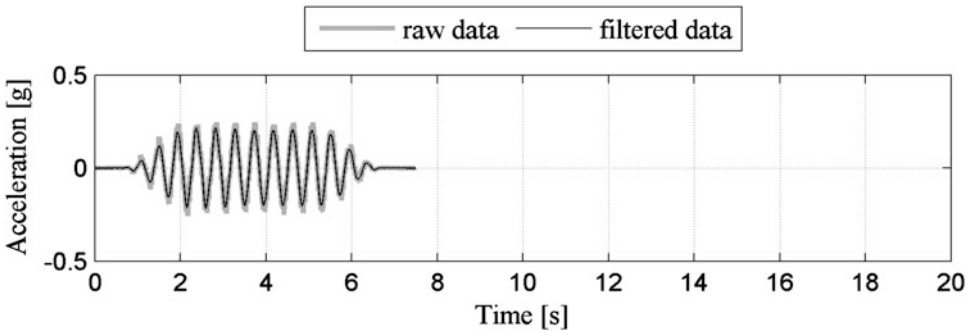

Fig. 27.3 Base cyclic motion for the fourth test runs

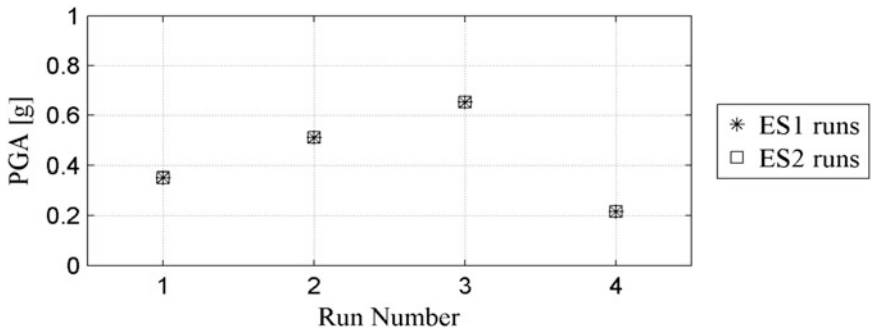

Fig. 27.4 Peak ground accelerations (PGAs) in the Eberhard test runs

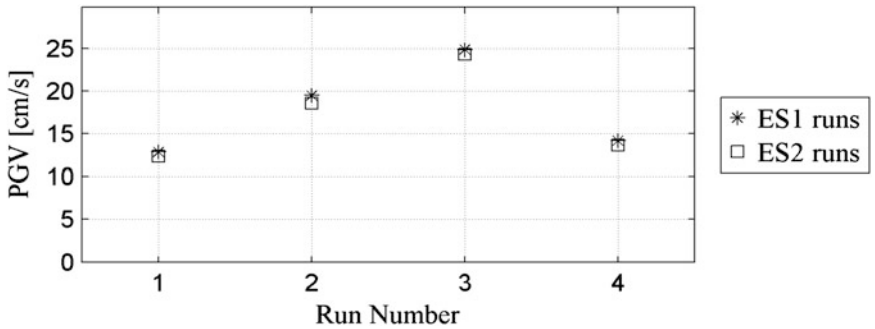

Fig. 27.5 Peak ground velocities (PGVs) in the Eberhard test runs

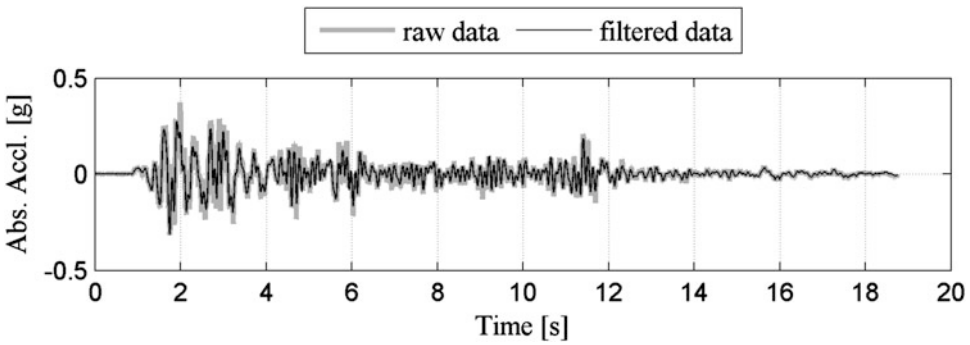

Fig. 27.6 First story acceleration response from run#1 of Eberhard test structure ES1

The absolute velocity and displacement responses can be estimated from the acceleration response. Velocity and displacement relative to the ground for the first run of ES1 are shown in Figs. 27.7 and 27.8, respectively. Figure 27.9 shows the mass-normalized inertial force.

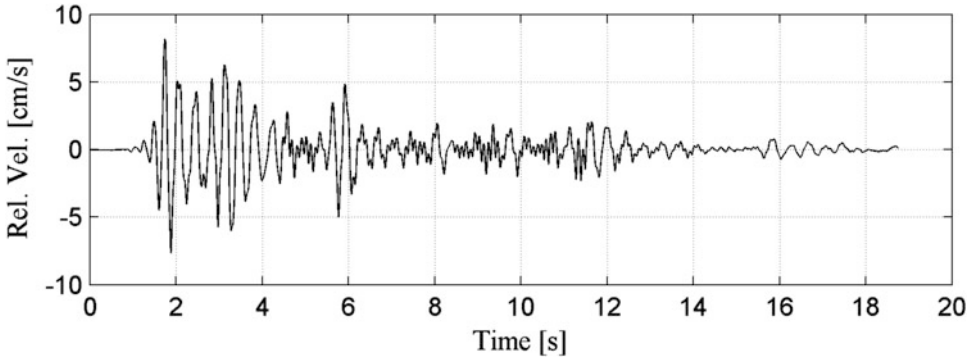

Fig. 27.7 First story relative velocity response from run #1 of the Eberhard test structure ES1

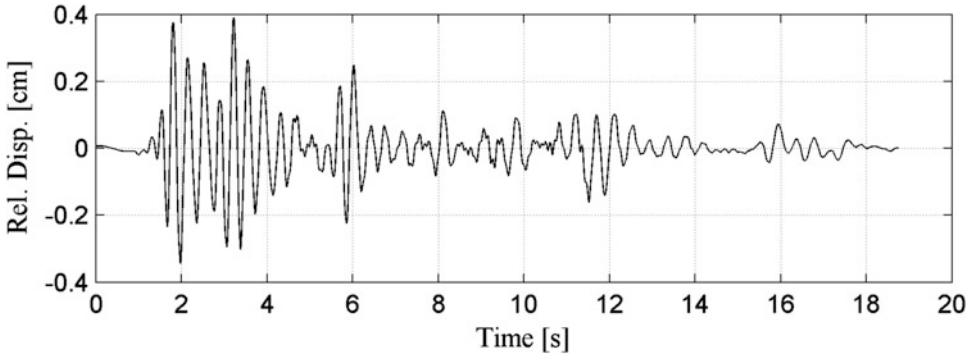

Fig. 27.8 First story displacement response from run #1 of the Eberhard test structure ES1

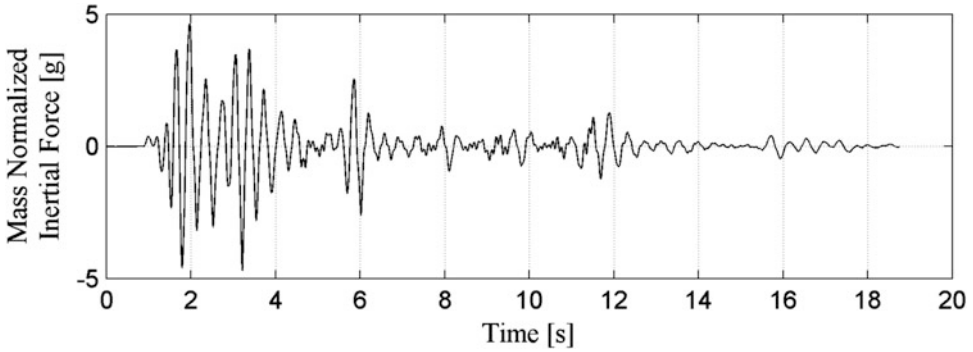

Fig. 27.9 Mass-normalized inertial force from run #1 of the Eberhard test structure ES1

The mass-normalized viscous damping coefficient we extracted from the ES1 first run is shown in Fig. 27.10. After fitting a log-normal probability distribution to the data, we estimated the median mass-normalized viscous damping coefficient and used it as the effective mass-normalized viscous damping coefficient for the structure during this event.

The same approach was followed for ES2. We found that during the entire sequential test runs, the mass-normalized damping coefficient remained nearly constant for both structures (see Fig. 27.11).

Based on Eq. (27.3), there is a linear relationship between the damping ratio and the period of the ES1 and ES2 test specimens. Figure 27.12 shows the linear relationship between the effective period and damping ratio of the dominant mode in these specimens.

We carried out similar analyses on data from tests by Cecen [17], Schultz [5] and Bonacci [18]. The results [19] are similar to what we present here from our study of Eberhard tests [4]: the effective viscous damping coefficient remained nearly constant for a given test structure throughout the GM series in Cecen, Schultz and Bonacci tests [19].

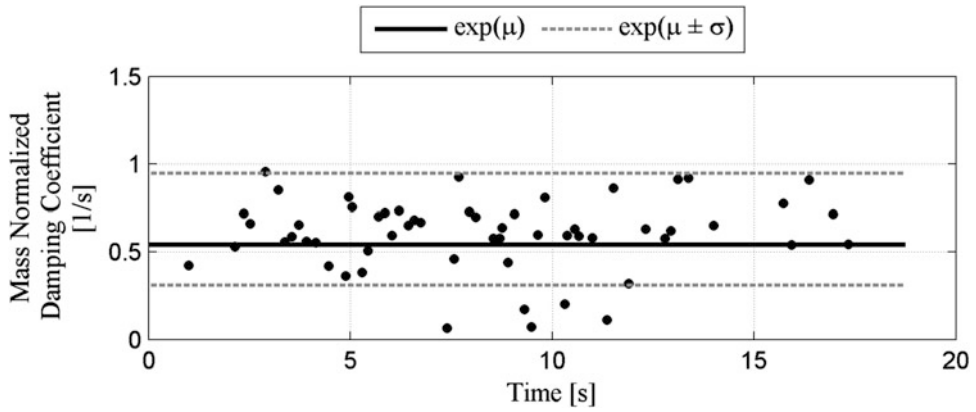

Fig. 27.10 Mass-normalized damping coefficient from run #1 of the Eberhard test structure ES1. The mean and (mean ± one standard deviation) of the fitted log-normal distribution are indicated

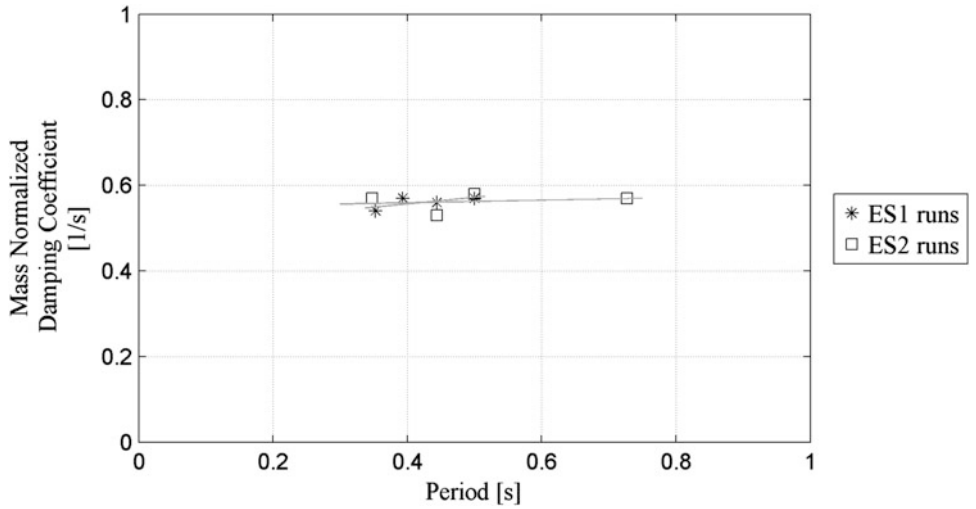

Fig. 27.11 Mass-normalized damping coefficient vs. period for the Eberhard test structures

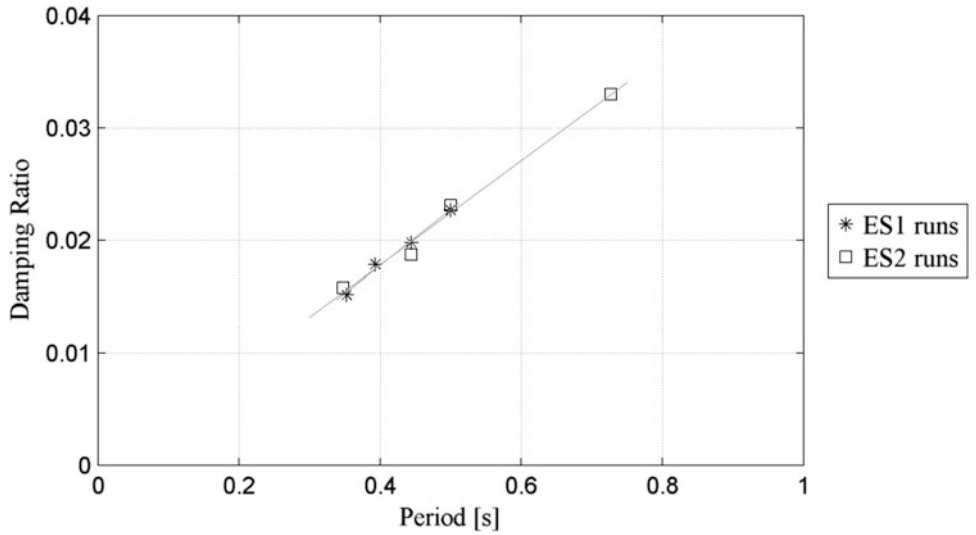

Fig. 27.12 Effective viscous damping ratio vs. period for the Eberhard test structures

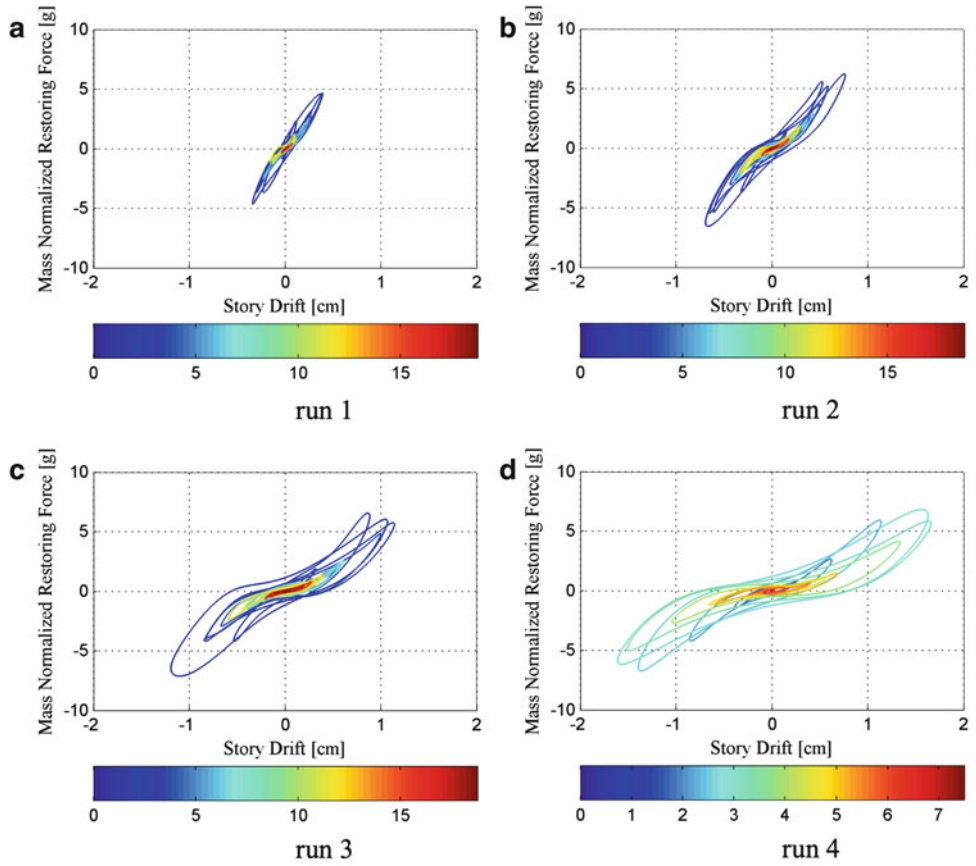

Fig. 27.13 Mass-normalized restoring force vs. first story drift for ES1 test runs

27.4 Estimating the Hysteretic Behaviour of the Test Structures

The mass-normalized restoring force in the structure can be calculated at any time as the difference between the mass-normalized inertial force and the mass-normalized damping force. Figure 27.13 shows the mass-normalized restoring force versus first story displacement relative to the base, i.e. first story drift, we found for the ES1 runs. Figure 27.14 shows the absolute values of the mass-normalized restoring force versus the first story drift. Figure 27.15 shows the envelope of the hysteretic responses of the ES1 and ES2 test specimens for the entire run series.

27.5 Conclusions

Our study of data from laboratory test structures indicates that the effective viscous damping coefficient for a low to mid-rise RC building structural system responding at its dominant mode may be assumed to be nearly constant during its response to base excitations. The corollary is that the corresponding effective viscous damping ratio varies linearly with the effective period of the dominant mode. If this observation is shown to hold true for a wide range of RC building structural systems, more realistic dominant mode (fundamental mode) damping ratios can be identified to estimate the internal forces in components of RC structural systems with less uncertainty. In short, proper modelling of damping ratio would allow better estimation of the seismic response of RC buildings.

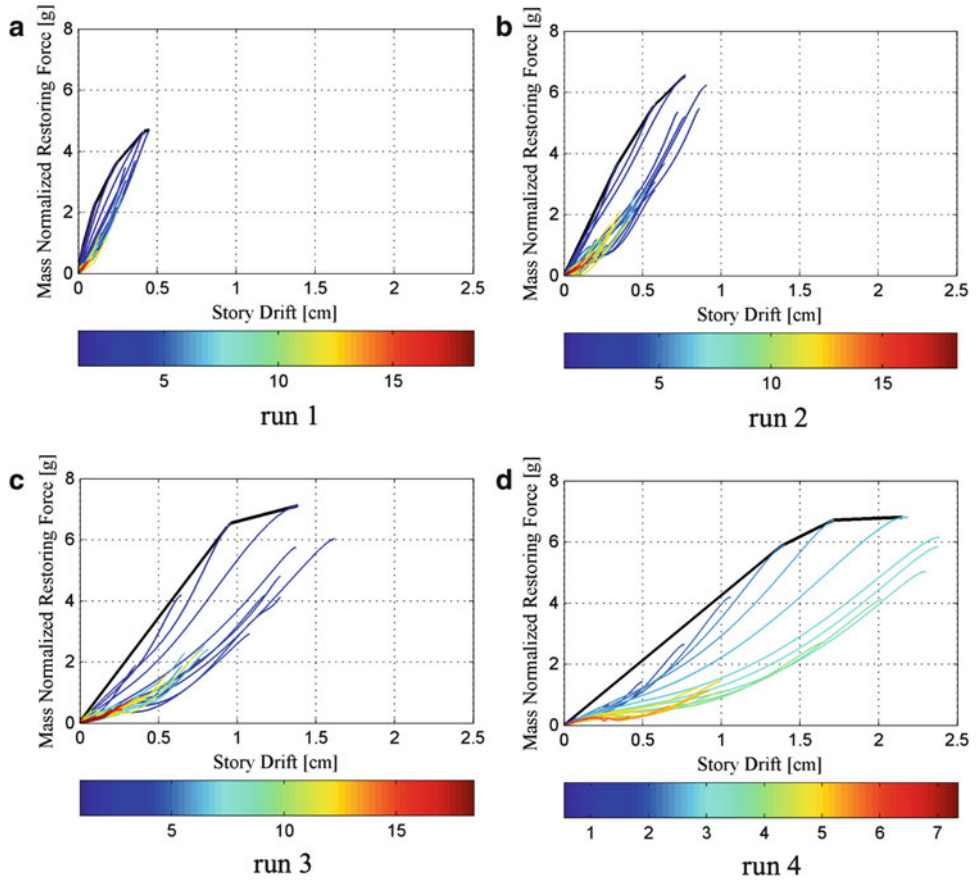

Fig. 27.14 Mass-normalized restoring force vs. first story drift for ES1 test runs. Note that absolute values are shown, i.e. no differentiation in direction of motion is made

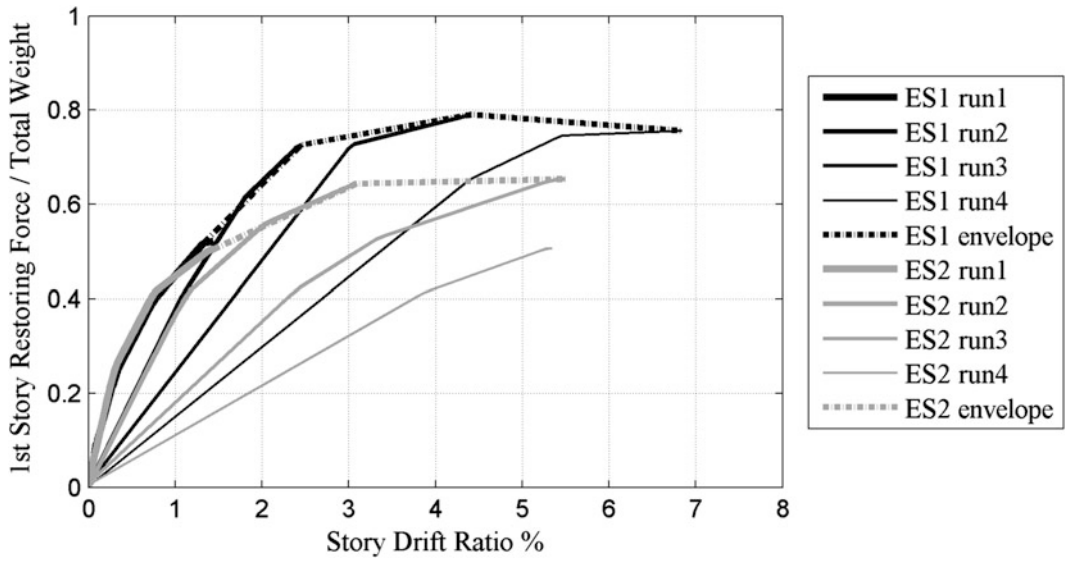

Fig. 27.15 Envelope of first story shear coefficient vs. deformation curves for the entire runs of ES1 and ES2

References

1. Caughey, T.K.: Classical normal modes in damped linear dynamic systems. J. Appl. Mech. **27**, 269 (1960)
2. Wilson, E.L.: Static and Dynamic Analysis of Structure. Computers and Structures, Inc., Berkeley (2010)
3. Dowgala, J.D.: Detecting and quantifying damage in buildings using earthquake response data and capacity curves. PhD Dissertation, Purdue University, West Lafayette (2013)
4. Eberhard, M.O., Sozen, M.A.: Experiments and analysis to study the seismic response of reinforced concrete frame-wall structures with yielding columns. Structural Research Series Report No. 548, University of Illinois, Urbana-Champaign (1989)
5. Schultz, A.: An experimental and analytical study of the earthquake response of R/C frames with yielding columns. PhD Dissertation, University of Illinois, Urbana-Champaign (1986)
6. Algan, B.: Drift and damage considerations in earthquake-resistant design of reinforced concrete buildings. PhD Dissertation, University of Illinois, Urbana-Champaign (1982)
7. Lepage, A.: Seismic drift estimates for RC structures. 11th World Conference on Earthquake Engineering (11WCEE). Mexico (1996).
8. Newmark, N.M.: Earthquake Spectra and Design. Earthquake Engineering Research Institute, Berkeley (1982)
9. Miranda, E.: Inelastic displacement ratios for structures on firm sites. J. Struct. Eng. **126**(10), 1150–1159 (2000)
10. Rosenblueth, E.H.: On a kind of hysteretic damping. J. Eng. Mech. **90**(4), 37–48 (1964)
11. Gulkan, P., Sozen, M.A.: Inelastic response of reinforced concrete structures to earthquake motions. ACI J **71**(12), 604–610 (1974)
12. Iwan, W.D.: Estimating inelastic spectra from elastic spectra. Earthq. Eng. Struct. Dyn. **8**(4), 375–388 (1980)
13. Kowalsky, M.P.: Displacement-Based Design, a Methodology for Seismic Design Applied to Single Degree of Freedom Reinforced Concrete Structures. University of California, San Diego, La Jolla (1994)
14. Priestley, M.K.: Preliminary development of direct displacement-based design for multi- degree of freedom systems. In: Proceedings of the 65th Annual Convention. SEAOC, Maui (1996)
15. Dowgala, J.D., Irfanoglu, A.: Detecting and quantifying damage in buildings using earthquake response data and capacity curves. Second Conference on Smart Monitoring, Assessment and Rehabilitation of Civil Structures, 9–11 Sept 2013, Istanbul (2013)
16. Dowgala, J.D., Irfanoglu, A.: Extracting empirical capacity curves from building earthquake response data. 10th National Conference on Earthquake Engineering (10NCEE), Anchorage, Alaska, Earthquake Engineering Research Institute, Oakland (2014)
17. Cecen, H.: Response of ten story, reinforced concrete model frames to simulated earthquakes. PhD Dissertation, University of Illinois, Urbana-Champaign (1979)
18. Bonacci, J.F.: Experiments to study seismic drift of RC structures. PhD Dissertation, University of Illinois, Urbana-Champaign (1989)
19. Khajeh Hesameddin P., Irfanoglu A., Hacker T.J.: Effective viscous damping ratio in seismic response of reinforced concrete structures. 6th ANCRiSST, 11AESE, Urbana-Champaign, Illinois (2015)

Chapter 28
Design of Metamaterials for Seismic Isolation

P.-R. Wagner, V.K. Dertimanis, E.N. Chatzi, and I.A. Antoniadis

Abstract This study assesses the implementation of locally resonant metamaterials in seismic isolation applications, by investigating their potential feasibility in low frequency bands. To this end, via adoption of both Blochs Theorem and classical vibration analysis, both one-dimensional and two-dimensional mass-in-mass lattices are analyzed in overlapping subbands and corresponding relations for the structural parameters are derived. The lattices are first examined in an infinite setup, for determining the arrangement of the resulting band gaps. Subsequently finite lattice configurations are investigated in the frequency and time domain. In this work, previous results are corroborated and additionally expanded to the 2D case. The parametric study that was carried out reveals interesting properties, particularly for low external-to-internal stiffness ratios of the unit cells comprising the lattices. Further investigation is required for confirming the feasibility of application of the resulting setups in full scale.

Keywords Seismic isolation • Metamaterials • Bloch's theory • Mass-in-mass unit cell

Nomenclature

DOF	Degrees-of-freedom	External stiffness	k_1 (1D) and k_1, k_2, k_3, k_4 (2D)
FRF	Frequency Response Function	Internal stiffness	k_2 (1D) and k_5 and k_6 (2D)
n	Number of DOFs	$\imath$, $\jmath$	Unit cell coordinates
γ	Wavenumber	N,M	Number of unit cells in specific dimension

28.1 Introduction

Earthquakes are in general reported as relatively rare events in most parts of the world. Nevertheless large earthquakes do occur, oftentimes resulting in severe destruction in earthquake prone zones involving material but also human toll [1]. The random nature of these events interlinked with extreme intensities, leads into difficulties in their effective mitigation. The earthquake loads may be carried either via foundation, which is fixed to the ground, or by allowing the structure to move on the ground. The former approach comes at a lower cost but often leads to damage requiring repairs and may threaten lives, whilst, the latter necessitates special response modification devices, i.e., isolators which, if designed properly, may more effectively mitigate damage [2–4].

Despite the development of various types of isolation systems in the past years, their implementation is non-trivial, and their effective design is not straightforward (often interlinked to reduced resistance to vertical deformation, possible large horizontal displacements during earthquake [5]). Therefore, the development of a base-isolation system that is freed of these shortcomings would be of the essence in ensuring resilience. Within such a context, the idea of exploiting the property of metadamping, for devising antiseismic foundations, has recently surfaced [6, 7].

P.-R. Wagner • V.K. Dertimanis (✉) • E.N. Chatzi
Institute of Structural Engineering, ETH Zürich, Stefano-Franscini-Platz 5, CH-8093 Zürich, Switzerland
e-mail: v.derti@ibk.baug.ethz.ch

I.A. Antoniadis
Department of Mechanical Engineering, National Technical University of Athens, Zografos Campus, 15780 Zografou, Athens, Greece

S. Pakzad, C. Juan (eds.), *Dynamics of Civil Structures, Volume 2*, Conference Proceedings of the Society for Experimental Mechanics Series, DOI 10.1007/978-3-319-29751-4_28

Metadamping occurs in periodically arranged unit cells, comprising varying mass and stiffness properties, leading to the emergence of frequency band gaps. These band gaps may be interpreted as blind spots for waves traveling at certain frequencies. As earthquakes typically propagate at low frequency ranges, a targeted engineering of these band gaps could be a feasible alternative to other seismic mitigation procedures.

The aim of this paper is to examine whether metamaterials are applicable to low frequency ranges, which are characteristic of strong ground motions. To this end, a mass-in-mass unit cell configuration is adopted and Bloch's Theorem is applied for delivering the dispersion relations of both 1D and 2D infinite lattices. It is deduced that the frequency limits of these bands are directly controlled by the structural parameters. Correspondingly, a parametric study on the effects of the most important quantities, including the external-to-internal stiffness ratio and the adopted damping, is presented in both time and frequency domains. The results indicate that metamaterial-based seismic isolation is indeed feasible, giving rise to the engineering design of physically realisable unit cells.

28.2 Theoretical Background

In this section, fundamental theoretical information is provided on general periodic mechanical systems under harmonic excitation. A 1D lattice is examined herein, nonetheless results are extendible to higher dimensions as well [8]. The system under investigation may comprise any type of repeating unit, made up of an assembly of masses, dampers and springs. The system's periodicity is a necessary trait, as it allows for great simplification in the mathematical description.

When an elastic wave is propagating in a mechanical system, there is always a direct relation between its temporal frequency f and its spatial frequency, or wavenumber γ. For certain infinite periodic systems frequencies without a corresponding wavenumber may exist. These blind spots in the dispersion plot, defined as the evolution graph of f vs. γ, comprise the so-called band gaps, implying that waves of these frequencies can not travel through the system. The dispersion plot and thus the band gaps' locations depend on the system parameters.

28.2.1 Infinitely Periodic Mechanical System: Dispersion Relation

In order to obtain the dispersion relation of a mechanical system that consists of infinite unit cells, one first needs to determine the mass (**M**), damping (**C**) and stiffness (**K**) matrices. The governing equation of such a system is generally of the form:

$$\mathbf{M}\ddot{\mathbf{u}} + \mathbf{C}\dot{\mathbf{u}} + \mathbf{K}\mathbf{u} = \mathbf{F}. \tag{28.1}$$

The vector **u** and its derivatives contain the system's DOF and **F** is the excitation force. In a first step, harmonic excitations are investigated; therefore F may be written as

$$\mathbf{F} = \{A_1, A_2, \ldots, A_n\} \cdot e^{i\omega t} \tag{28.2}$$

where ω and A_n denote the excitation frequency and amplitude, respectively.

Since $n = \infty$, Bloch's Theorem is used to facilitate the solution of the Eq. (28.1). Accordingly, waves traveling in an infinite periodic lattice will be of the form [9]

$$u_\iota = B_\alpha e^{i x_{\iota,\alpha}\gamma + \lambda t} = B_\alpha e^{i x_{\iota,\alpha}\gamma} e^{\lambda t} \tag{28.3}$$

where B_α is the wave amplitude in a certain unit cell's DOF α, γ is the wavenumber in the medium, subscript ι represents the unit cell in question and $x_{\iota,\alpha}$ stands for the location of the ιth unit cell's DOF α. The complex frequency function λ allows for temporal propagation in the medium. Since the system is (infinitely) periodic, it is sufficient to focus on a single unit cell and the DOFs connected to this unit cell alone (subindex R) for studying the wave propagation

$$\mathbf{M_R}\ddot{\mathbf{u}}_\mathbf{R} + \mathbf{C_R}\dot{\mathbf{u}}_\mathbf{R} + \mathbf{K_R}\mathbf{u_R} = \mathbf{F_R}, \qquad \text{where} \quad \mathbf{F_R} = \mathbf{0}. \tag{28.4}$$

$$\mathbf{u_R} = [u_{\iota-1,1}, u_{\iota-1,2}, \ldots, u_{\iota-1,F}, u_{\iota,1}, u_{\iota,2}, \ldots, u_{\iota,F}, u_{\iota+1,1}, u_{\iota+1,2}, \ldots, u_{\iota+1,F}]^T$$

$\mathbf{F_R}$ is assumed equal to $\mathbf{0}$ since there is no force acting directly on the elements within the infinite lattice. The subindices of $u_{\iota,\alpha}$ describe the unit cell ι and this cell's DOFs α. The subscript F stands for the last DOF of unit cell α. The waves traveling through this infinite system comprise the same amplitude for any unit cell's DOF α. This further implies, when referring to Eq. (28.3), that B_α is the same for all unit cells ι and their repeating DOFs α ($B_{\iota-1,\alpha} = B_{\iota,\alpha} = B_{\iota+1,\alpha}$).

Plugging in Eq. (28.3) and its derivatives into Eq. (28.4) renders the quadratic eigenvalue problem

$$[\mathbf{M}^*\lambda^2 + \mathbf{C}^*\lambda + \mathbf{K}^*]\mathbf{B} = \mathbf{0} \tag{28.5}$$

where $\mathbf{B}$ is the vector of wave amplitudes B_α of the unit cell. The eigenvalue problem of Eq. (28.5) may be solved for extracting the eigenvalues λ_u, which are of the form

$$\lambda_u(\gamma) = -\xi_u(\gamma)\omega_u(\gamma) \pm i\omega_{d,u}(\gamma) \tag{28.6}$$

The frequencies and the damping ratios may then be determined as $\omega_{d,u}(\gamma) = \Im[\lambda_u(\gamma)]$ and $\xi_u(\gamma) = -\Re[\lambda_u(\gamma)]/|\lambda_u(\gamma)|$, respectively. The graphical representations of these latter expressions for $\omega_{d,u}$ and $\xi_u(\gamma)$ as functions of the wavenumber γ, formulate the dispersion plots [10].

28.2.2 Finitely Periodic Mechanical System: FRFs

In the case of a finite lattice, Eq. (28.1) is still valid, but n is now a finite number. Furthermore, the excitation vector (Eq. (28.2)) takes on a more specific form. Indeed, the assumed ground excitation is applied in the form of base acceleration, $\ddot{x}_g(t)$, translated in the following force vector [11]

$$\mathbf{F} = -\mathbf{M}\boldsymbol{\iota}\ddot{x}_g(t) \tag{28.7}$$

where $\boldsymbol{\iota} = [1\ 1\ \ldots\ 1]^T$ is the influence vector, which comprises unit entries in the DOFs lying along the direction of the earthquake excitation and zeros otherwise [11]. Notice further that in this case the vector $\mathbf{u}$ corresponds to the relative (to the base) displacement of each DOF. Assuming a harmonic ground excitation, $\ddot{x}_g(t)$ is expressed by $\ddot{x}_{g0}e^{i\omega t}$ with a peak ground acceleration $\ddot{x}_{g0}$. The steady state solution to the constitutive equation for any harmonic excitation is always of the form $\mathbf{u}(t) = \mathbf{d}(\omega)e^{i\omega t}$ which can be readily derived and inserted into Eq. (28.1), thus yielding

$$[-\omega^2\mathbf{M} + i\omega\mathbf{C} + \mathbf{K}]\mathbf{d}(\omega) = -\mathbf{M}\boldsymbol{\iota}\ddot{x}_{g0}, \qquad \mathbf{d}(\omega) \in \mathbb{C} \tag{28.8}$$

which, for any excitation frequency ω, is a system of linear equations that can be solved for $\mathbf{d}(\omega)$. The vector $\mathbf{d}(\omega)$ now contains the complex displacement amplitude of all DOFs and the relative accelerations can be expressed as:

$$\ddot{\mathbf{u}}(t) = -\omega^2\mathbf{d}(\omega)e^{i\omega t}, \qquad \ddot{\mathbf{u}}(t) \in \mathbb{C} \tag{28.9}$$

$$\ddot{\mathbf{u}}_\mathbf{0} = |-\omega^2\mathbf{d}(\omega)|, \qquad \ddot{\mathbf{u}}_\mathbf{0} \in \mathbb{R} \tag{28.10}$$

where $\ddot{\mathbf{u}}_\mathbf{0}$ is the vector of maximum relative acceleration amplitudes. Absolute accelerations are then derived by the relation $\ddot{\mathbf{x}}(t) = \ddot{\mathbf{u}}(t) + \boldsymbol{\iota}\ddot{x}_g(t)$. This eventually yields [12]:

$$\ddot{\mathbf{x}}_\mathbf{0} = |-\omega^2\mathbf{d}(\omega) + \boldsymbol{\iota}\ddot{x}_g|, \qquad \ddot{\mathbf{x}}_\mathbf{0} \in \mathbb{R} \tag{28.11}$$

for the vector of absolute acceleration amplitudes $\ddot{\mathbf{x}}_\mathbf{0}$. It is thus now possible to plot the FRFs for any DOF. The quantity of interest within the context of a seismic study is the absolute acceleration and is the one plotted in what follows.

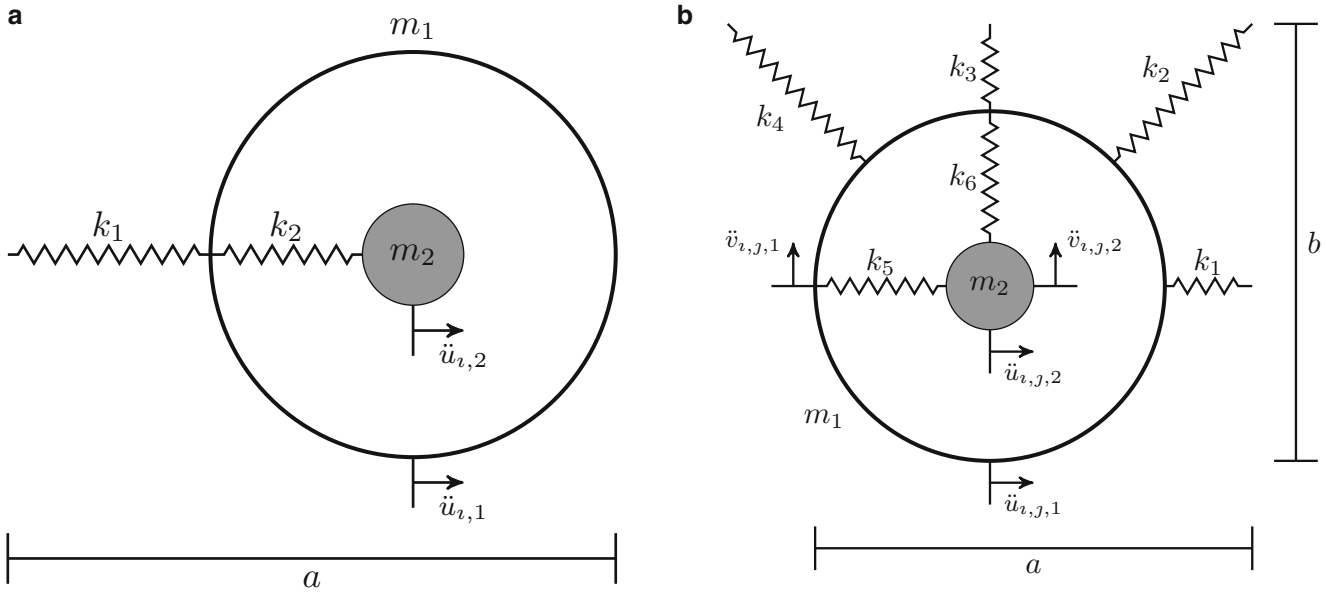

Fig. 28.1 The mass-in-mass unit cells used in the proposed model. The variable parameters of the unit cells include the masses m_r and the stiffnesses k_r. Throughout this paper the internal and external stiffnesses will be referred to as $k_{ex} = k_1$ (1D) and $k_{ex} = k_1 = k_2 = k_3 = k_4$ (2D) or $k_{int} = k_2$ (1D) and $k_{int} = k_5 = k_6$ (2D). In (**a**) the $\imath$th cell of the 1D infinite lattice is shown, whereas in (**b**) the unit cell at the lattice position ($\imath$th, $\jmath$th) is illustrated. The variables a and b designate the spacing of the unit cells in horizontal and vertical direction respectively. (**a**) 1D, (**b**) 2D

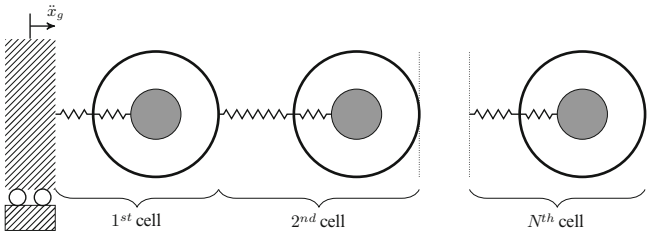

Fig. 28.2 1D finite chain. The ground excitation is applied on the far left unit cell

28.2.3 Implementation

The theoretical background of the previous section needs to now assume concrete form. In this work, a the mass-in-mass unit cell is implemented, though other cells have also been considered in exiting literature [8, 9]. A distinction is made between the 1D and 2D setup, to firstly compare the results to [9], where a 1D analysis was performed, and to subsequently extend the model to the 2D case. The unit cell configuration is demonstrated in Fig. 28.1. These unit cells are subsequently arranged as depicted in Figs. 28.2 and 28.3. There the excitation origin is visible as an applied ground motion $\ddot{x}_g$ at the boundaries.

28.3 Parametric Analysis

A parametric study is presented in this section. After listing the unit cell parameters, the dispersion relations of the infinite lattice are computed, while the results are then verified via investigation of finite lattices. The results are firstly reported in the frequency domain, in order to examine the mitigation effects' dependency on the number of used unit cells. Subsequently, the time domain structural response is investigated in order to study the actual response of the finite lattice in time and the resulting mitigation.

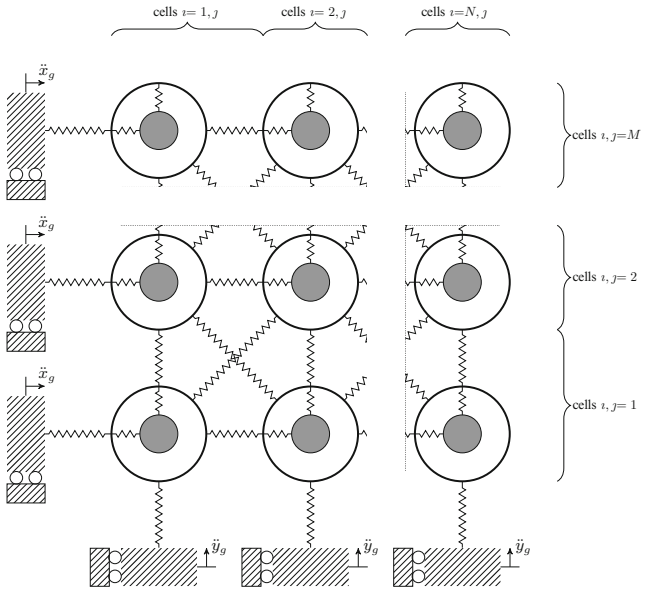

Fig. 28.3 2D finite lattice. The ground excitation is applied on the *left* and *bottom* border. This is performed differently to [13], where only one border was excited, while the other was connected to viscous springs

Table 28.1 Parameters used in the 1D and 2D analysis that produce a band gap between [0.5 . . . 1.5][Hz]

	a	b	m_1	m_2	k_{ex}	k_{int}
Unit	m	m	kg	kg	N/m	N/m
1D case	1.2	–	378	3021	298176	29818
2D case	1.2	1.2	378	3021	298176	29818

28.3.1 Parameters Used in the Simulations

The parameters used in this section are taken from [12], where a feasibility analysis of 1D cells was performed. These parameters were used as a starting point for the analysis carried out herein and are repeated in Table 28.1, in accordance with the notation used in Fig. 28.1. It is noted that the effects of damping are treated in a specific section below. In all other individual analyses, damping is considered zero.

28.3.1.1 1D Case

In [12] an estimate for the band gap location given certain unit cell parameters is proposed. This formula yields results for both the lower (f_L) and upper (f_H) band gap limits and is repeated here:

$$f_L \approx \frac{1}{2\pi}\sqrt{\frac{k_2}{m_2}}, \quad f_H \approx f_L\sqrt{\frac{m_1+m_2}{m_1}} \tag{28.12}$$

It can be straightforwardly verified that the band gaps in Fig. 28.4 appear at the predicted locations when adopting the parameters provided in Table 28.1. It has to be noted however that the above formulas seem to hold true only for stiffness ratios $k1/k2 > 1$, which is examined in more detail below.

28.3.1.2 2D Case

Since homogeneous external and internal stiffness are assumed, only parameter k_2 needs to be exchanged for $k_{int} = k_5 = k_6$. As observed via the emerging band gaps in Fig. 28.5 it can be seen that the estimation formulas and the relevant observations from the previous section prove in fact also valid for the 2D case.

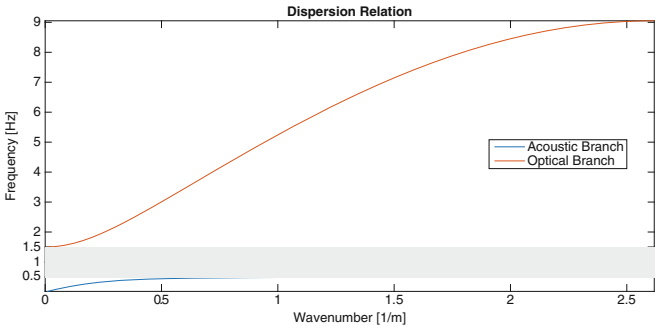

Fig. 28.4 1D dispersion relations in the 1st Brillouin zone from $0 < \gamma < \frac{\pi}{a}$

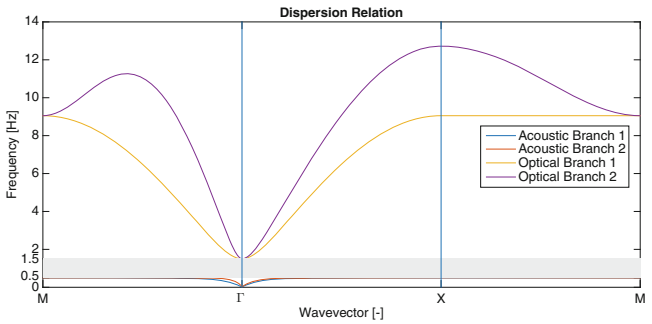

Fig. 28.5 2D dispersion relations in the 1st Brillouin zone as seen in [10] from $\boldsymbol{\gamma} = M \ldots \Gamma \ldots X \ldots M$

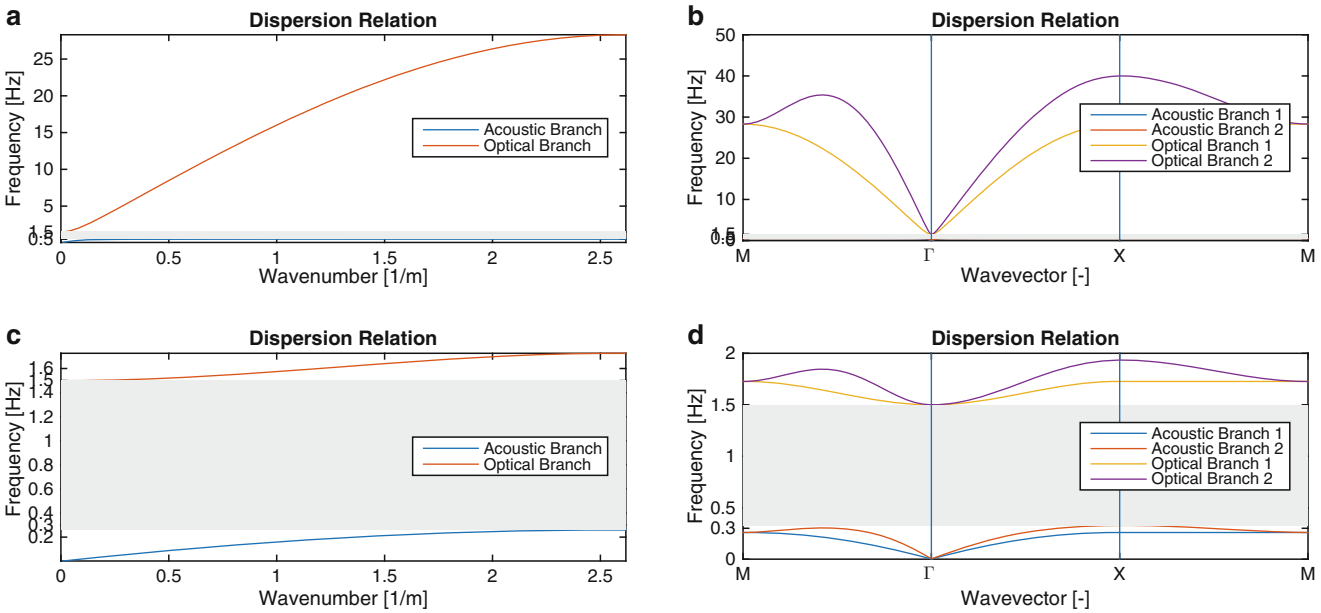

Fig. 28.6 1D and 2D dispersion relations using the 1st band gap properties for two different stiffness ratios k_{ex}/k_{in}. (**a**) $k_{ex}/k_{int} = 100$ Gap: [0.5 . . . 1.5]. (**b**) $k_{ex}/k_{int} = 100$ Gap: [0.5 . . . 1.5]. (**c**) $k_{ex}/k_{int} = 0.1$ Gap: [0.26 . . . 1.5]. (**d**) $k_{ex}/k_{int} = 0.1$ Gap: [0.33 . . . 1.5]

28.3.1.3 Influence of the External Stiffness on the Dispersion Relation

As mentioned before the external stiffness parameters $k_{ex} = k_1$ (1D) or $k_{ex} = k_1, k_2, k_3, k_4$ (2D) do significantly influence the band gap locations. This is examined in this section in greater detail, via adoption of stiffness ratios k_{ex}/k_{int}. As observed in Fig. 28.6, a decrease of this stiffness ratio results in significant decrease of the lower band gap border f_L. This implies that Eq. (28.12) has to be appropriately modified so as to account for these observations.

In coming up with an improved representation, it helps to examine the branches of the dispersion relations individually and observe at the locations that define the frequency band gap limits. For the 1D case the upper gap border f_H is always located in the optical branch at the lowest wavenumber ($\gamma = 0$). When evaluating the eigenvalues of Eq. (28.5) the following is obtained

$$f_{H,1D}(m_1, m_2, k_{int}) = \sqrt{\frac{k_{int}(m_1 + m_2)}{m_1 m_2}} \frac{1}{2\pi} \tag{28.13}$$

which is identical to Eq. (28.12) for f_H. The lower band gap on the other hand, can be obtained by looking at the acoustic branch with a maximum wavenumber in the 1st Brillouin zone of $\gamma = \frac{\pi}{a}$. Again evaluating Eq. (28.5) yields

$$f_{L,1D}(m_1, m_2, k_{ex}, k_{int}) = \sqrt{\frac{4k_{ex}m_2 + k_{int}(m_1 + m_2) - \sqrt{(4k_{ex}m_2 + k_{int}m_2)^2 - 8k_{ex}k_{int}m_1m_2 + k_{int}^2m_1^2 + 2k_{ex}^2m_1m_2}}{2m_1m_2}} \frac{1}{2\pi} \tag{28.14}$$

Equation (28.14) is obviously not very compact but contrary to Eq. (28.12) the external stiffness $k_{ex} = k_1$ does influence the band gap location. This procedure can be extended to the 2D case as well and since only homogeneous external and internal stiffness is considered, the relations can be simplified. The upper band gap limit f_H is always located at the point Γ, i.e. $\gamma_x = \gamma_y = 0$ in the optical branch 1 or 2. When solving the eigenvalue problem of Eq. (28.5) the same relation as for the 1D case is obtained (Eq. (28.13)):

$$f_{H,2D} = f_{H,1D} \tag{28.15}$$

The lower border, however, is not the same as in the 1D case. It always lies at point X, i.e., at the point where $\gamma_x = \frac{\pi}{a}$, $\gamma_y = 0$ in the acoustic branch 2. By solving the eigenvalue problem once more, the following is obtained

$$f_{L,2D}(m_1, m_2, k_{ex}, k_{int}) = \sqrt{\frac{8k_{ex}m_2 + k_{int}(m_1 + m_2) - \sqrt{(8k_{ex}m_2 + k_{int}m_2)^2 - 16k_{ex}k_{int}m_1m_2 + k_{int}^2m_1^2 + 2k_{ex}^2m_1m_2}}{2m_1m_2}} \frac{1}{2\pi} \tag{28.16}$$

which again delivers a function of the external stiffness k_{ex}.

28.3.2 FRFs of Finitely Periodic Unit Cells

The pattern of these frequency band gaps is now examined for a finite lattice in the frequency domain. The results are obtained by subjecting the model to a range of excitation frequencies and directions (the latter applies only to the 2D case).

28.3.2.1 1D Case

The model under investigation can be seen in Fig. 28.2. The DOF of interest is $u_{N,1}$, i.e., the one located on the far most end with respect to the excitation source. The spatial mitigation effect is examined by plotting the displacement and acceleration FRFs values for each DOF at certain frequencies.

The first observation deduced from the FRFs in Fig. 28.7 is that the unit cell lattice responds in a differently for displacement and acceleration; in the former case the amplitude of the FRF inside the band gap approaches asymptotically the high limit, whereas in the acceleration FRF the opposite happens. Vibration attenuation is already observed for $N = 2$ and becomes significant from $N = 5$, implying that a small number of unit cells maybe sufficient for seismic isolation.

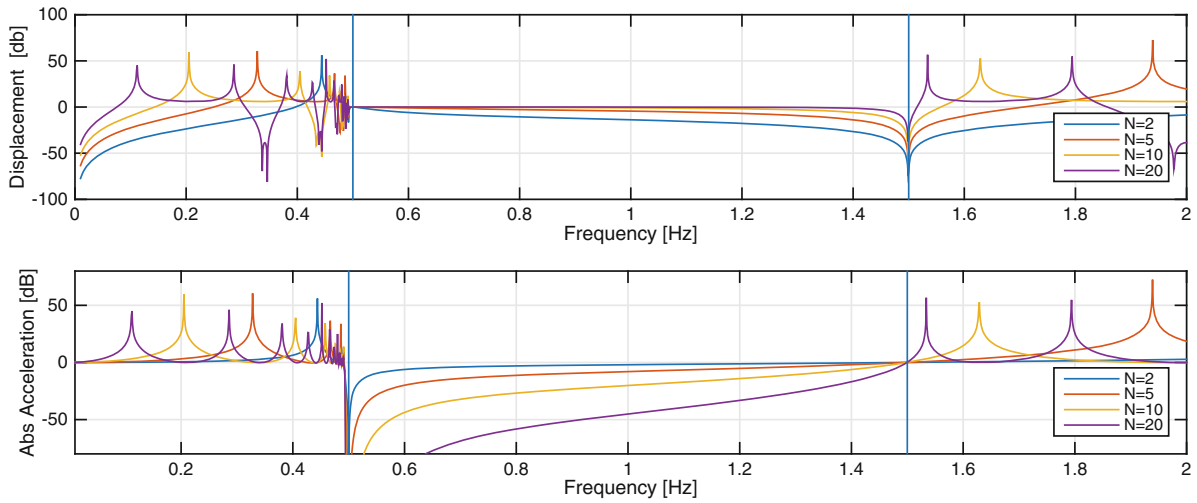

Fig. 28.7 1D FRFs in the frequency domain for the 1st band gap. The values in the axis of ordinate are scaled in [dB] versus the excitation amplitude: $10log(\frac{u_2^2}{u_g^2})$

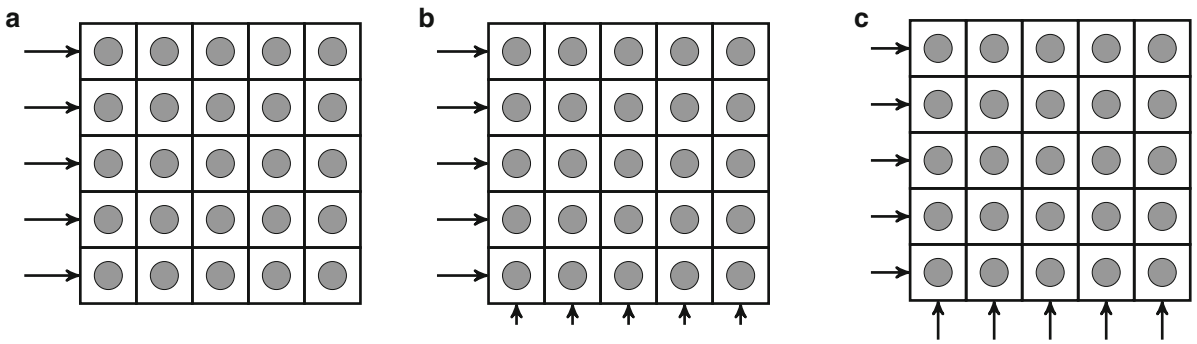

Fig. 28.8 Different incident angles α for the 2D lattice. The number of unit cells is indicative only. The arrow length corresponds to the applied acceleration amplitude. (**a**) $\alpha = 0°$. (**b**) $\alpha = 22.5°$. (**c**) $\alpha = 45°$

28.3.2.2 2D Case

An important difference between the 1D and the 2D case lies in the possibility to account for different incident angles at which the seismic waves may hit the unit cell assembly (see Fig. 28.8). Herein, an angle $\alpha = 22.5°$ is considered. The DOFs of interest are once again the ones located furthest away from the excitation source. In the 2D case these are $u_{N,M,1}$ and $v_{N,M,1}$. As observed in the FRF plots of Fig. 28.9, the vibration attenuation performance of the system inside the band gap is similar to the 1D case; the difference in response amplitude is mostly due to the increased external spring stiffness. The spatial mitigation can be better observed by looking at Fig. 28.10.

28.3.2.3 The Effect of Damping on the FRFs

Caughey damping is now included in order to more realistically model the energy dissipation in actual unit cells. The damping ratios in commonly do not exceed values of $\zeta_i = 0.1$. So the parametric study will focus on damping ratios lying lower than this threshold value.

From the plots in Fig. 28.11 it can be deduced that damping reduces the number of peaks in the FRFs outside the frequency band gap. This has positive effects concerning the response outside the gaps, in that the peak accelerations and displacements are reduced or removed entirely. A drawback of high damping ratios is the slight response increase inside the band gaps. Mitigation of the seismic ground motion however still takes place inside the band gaps.

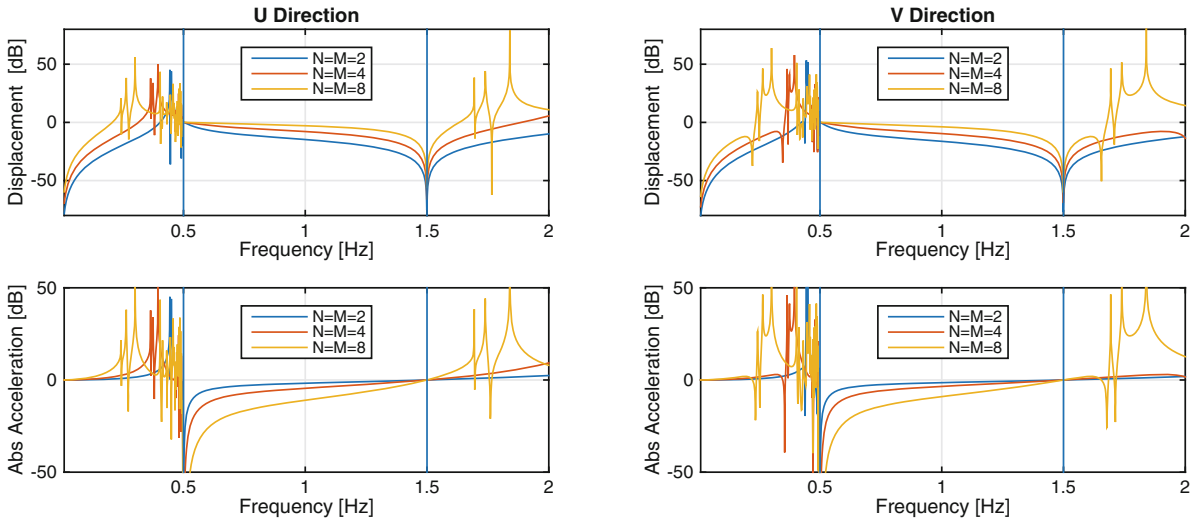

Fig. 28.9 2D FRFs in the frequency domain for the 1st band gap for the incident angles $\alpha = 22.5°$. The values in the axis of ordinate are scaled in [dB] versus the excitation amplitude: $10log(\frac{u^2}{u_g^2})$. The ground motion in direction u was used to scale the output in the direction u, whereas in v direction the ground motion in v direction was employed

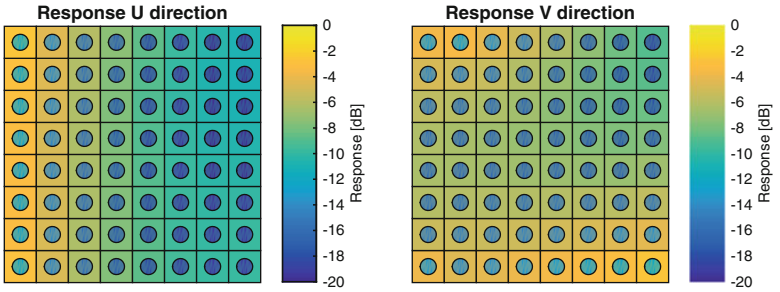

Fig. 28.10 2D spatial distribution of the absolute acceleration FRF values for the 1st band gap setup in the $N = M = 8$ lattice with an incident angle of $\alpha = 22.5°$. The excitation frequency is chosen at 1[Hz] again. The color in the circles represents DOF $u_{i,2}$ whereas the one in the *rectangle* stands for DOF $u_{i,1}$. The values are scaled in [dB] versus the excitation amplitude in the corresponding direction (u or v): $10log(\frac{u^2}{u_g^2})$

28.3.2.4 Influence of the External Stiffness on the FRFs

The observed width increase of the frequency band gap previously reported is now investigated in the frequency domain. To this end, an incident angle of $\alpha = 22.5°$ is once again examined. The frequency domain performance can be seen in Fig. 28.12 and confirms the findings previously reported based on the dispersion relation. Indeed, high stiffness ratios facilitate vibration displacement attenuation but not acceleration one, while low stiffness ratios have the inverse effects.

28.3.3 Structural Response of Finitely Periodic Unit Cells

In this section the results obtained from the frequency domain analysis of the previous section are verified in the time domain. This allows additionally observing the transient response in combination with the steady state response.

28.3.3.1 1D Case

The parameters assumed herein may once again be retrieved from Table 28.1. Contrary to the frequency domain analysis, a damping ratio of $\zeta_i = 0.01$ was included from the beginning. The response plots in Fig. 28.13 demonstrate effective attenuation of the band gap specific excitation (upper plot), however the response actually increases for the El Centro excitation (lower plot).

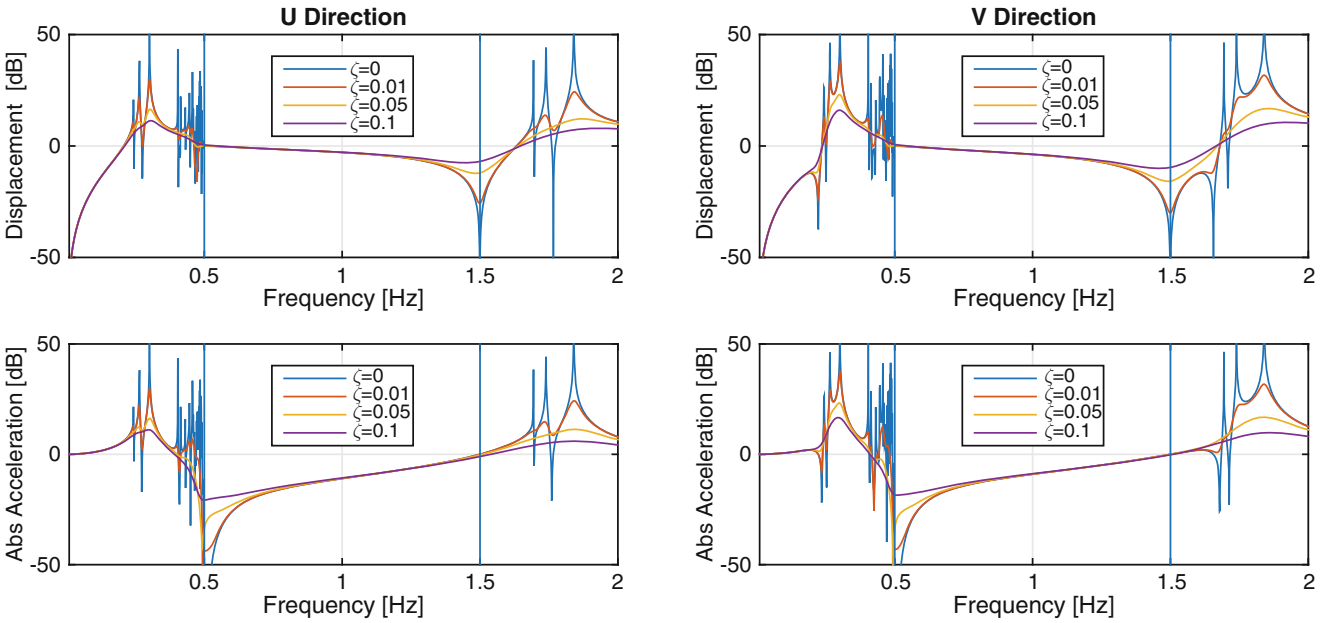

Fig. 28.11 Damping effects on the 2D FRFs of the *upper right* external mass for $N = M = 8$ unit cells. The acceleration was applied with an incident angle of $\alpha = 22.5°$ and the assigned damping ratios are $\zeta_i = 0.01, 0.05, 0.1$

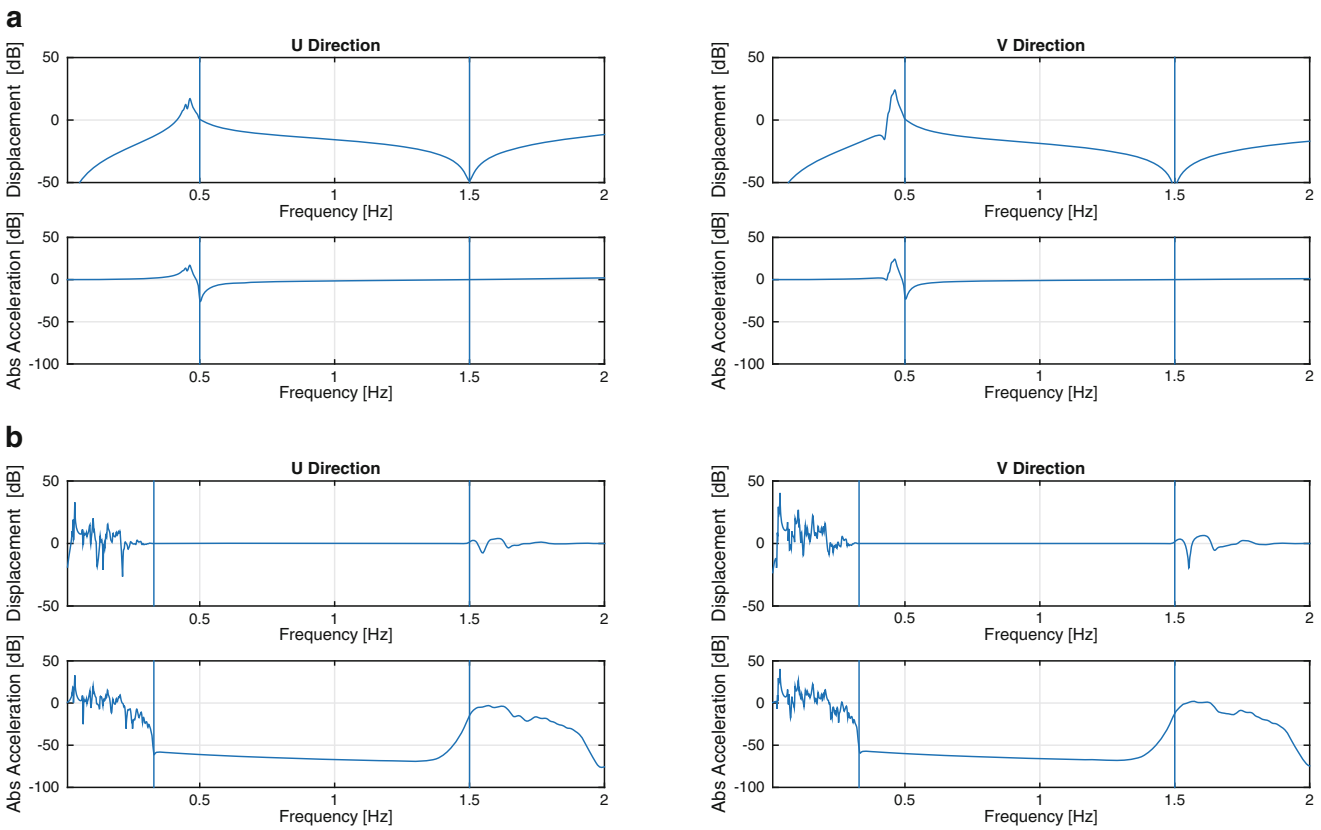

Fig. 28.12 FRFs for different stiffness ratios of the *upper right* unit cell's external mass in a 2D lattice. A minimal damping ratio of $\zeta_i = 0.01$ is used. The system under investigation comprises $N = M = 8$ unit cells with the parameters configured as listed in Table 28.1. (**a**) $k_{ex}/k_{int} = 100$. (**b**) $k_{ex}/k_{int} = 0.1$

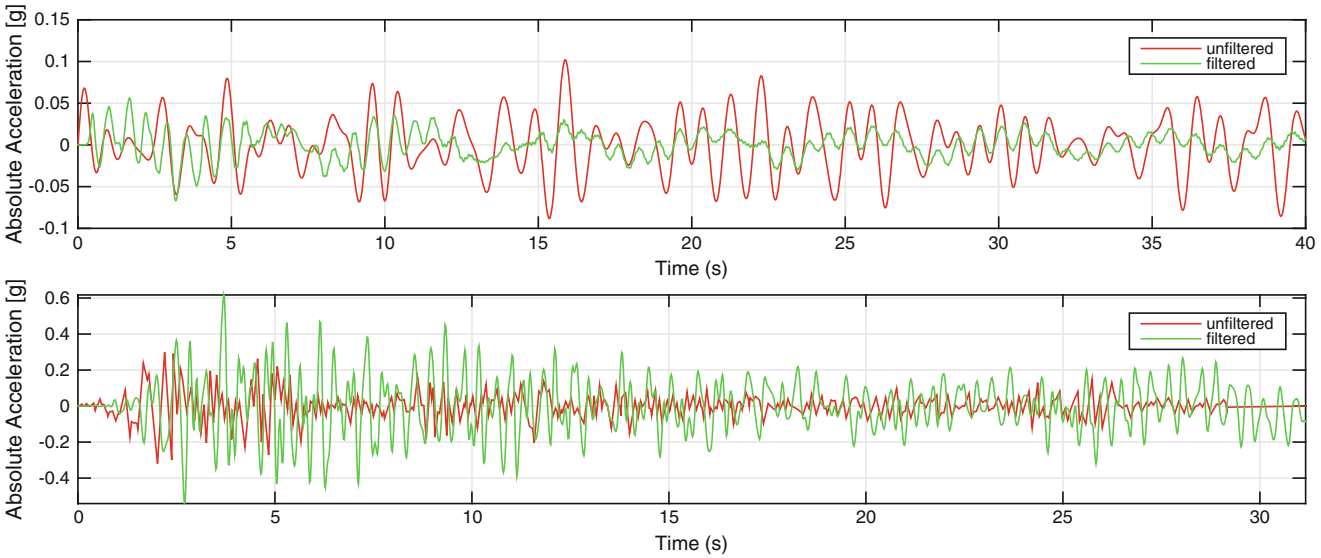

Fig. 28.13 Response of the 1D system in the time domain. A chain of $N = 10$ unit cells is employed with a damping ratio of $\zeta_i = 0.01$. The plots show the rightmost external DOF. Each subplot illustrates the response to a band gap specific excitation (*upper*) and the El Centro excitation (*lower*)

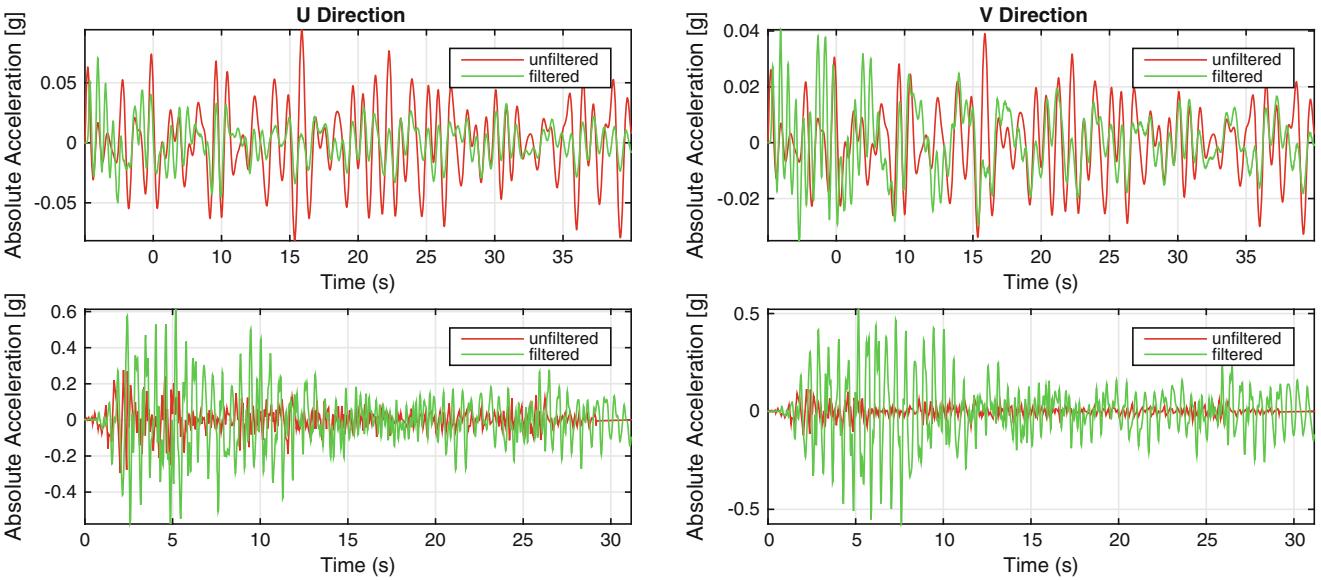

Fig. 28.14 Response of the 2D system in the time domain with an incident angle of $\alpha = 22.5°$. A lattice of $N = M = 8$ unit cells was used with a damping ratio of $\zeta_i = 0.01$. The plots show the response of the upper right external DOF. Each subplot shows the response to a band gap specific excitation (*upper*) and the El Centro excitation (*lower*)

28.3.3.2 2D case

The parameters for the 2D analysis can be taken from Table 28.1 and a damping ratio of $\zeta_i = 0.01$ is once again employed. The structural response is depicted in Fig. 28.14, where again a good attenuation effect is demonstrated when the excitation signal contains only frequencies which lie within the specified band gap, whereas for more general excitations (El Centro) the structural response is conversely amplified.

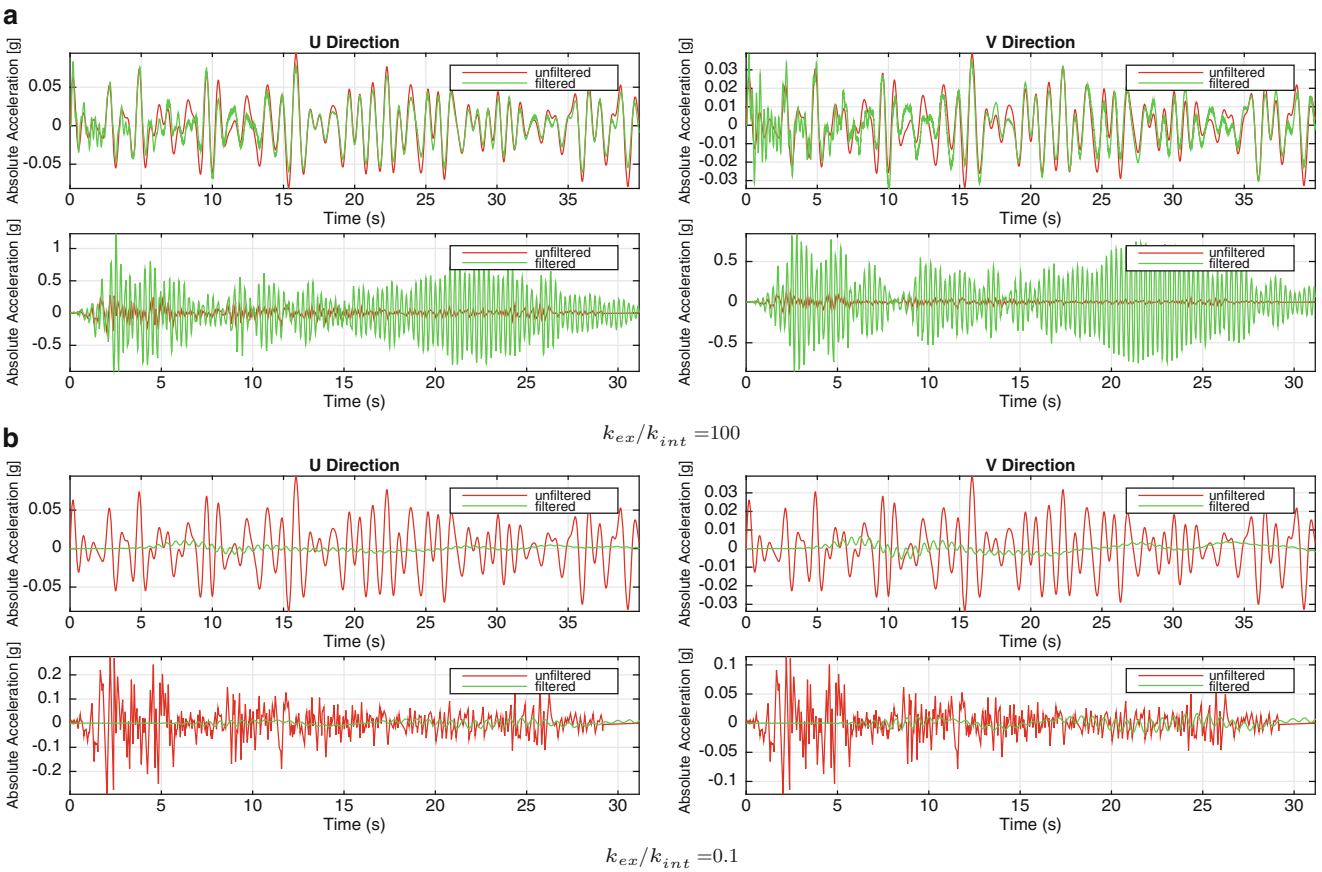

Fig. 28.15 Response in the time domain for different stiffness ratios of the upper right unit cell's external mass in a 2D lattice. A minimal damping ratio of $\zeta_i = 0.01$ was used. The system under investigation was comprised of $N = M = 8$ unit cells with the parameters (except for the changing k_{ex}) from Table 28.1. The incident angle was $\alpha = 22.5°$. Each subplot shows the response to a band gap specific excitation (*upper*) and the El Centro excitation (*lower*). (**a**) $k_{ex}/k_{int} = 100$. (**b**) $k_{ex}/k_{int} = 0.1$

28.3.3.3 Influence of the External Stiffness on the Structural Response

This section studies the influence of stiffness ratio on the structural response. The observations formerly noted in the frequency domain are further verified in the time domain as confirmed in Fig. 28.15. The response appears clearly linked to the stiffness ratio and increases for a corresponding increase of this parameter.

28.4 Conclusion

The goal of this paper was to determine the possible use of periodically arranged unit cells for mitigating seismic ground motions. In a first, fundamental exploration, the so called metadamping phenomenon is quantified for the 1D and 2D case. It was shown that, depending on the chosen unit cell parameters, significant excitation mitigation can be achieved, depending however on the frequency content of the acting excitation signal. A crucial parameter of the unit cell configuration, which was identified to play an important role in the damping effectivity is the external stiffness ratio k_{ex}/k_{int}.

One negative side effect of metadamping is the response increase outside the frequency band gaps. Via use of appropriate damping mechanisms, these peak responses can however be reduced. To this end, future work will include designing a physically realisable engineering model of the proposed unit cells. A configuration, which allows fashioning unit cells of low stiffness ratios (k_{ex}/k_{int}) in conjunction with fairly high masses has to be defined. The suitable dimensions and scalability of the proposed scheme may only be verified via testing, which is the primary research direction to be undertaken next.

References

1. Stein, S., Wysession, M.: An Introduction to Seismology, Earthquakes, and Earth Structure. Wiley, New York (2009)
2. Mao, L., Li, A: The simplified models and their precision for analysis of multi-story sliding isolated Structures. J. Build. Struct. **26**(2), 117–123 (2005)
3. Ordonez, D., Foti, D., Bozzo, L.: Comparative study of the inelastic response of base isolated buildings. Earthq. Eng. Struct. Dyn. **32**(1), 151–164 (2003)
4. Kelly, J.M.: Base isolation: linear theory and design. Earthq. Spectra **6**(2), 223–244 (1990)
5. Providakis, C.: Effect of supplemental damping on LRB and FPS seismic isolators under near-fault ground motions. Soil Dyn. Earthq. Eng. **29**(1), 80–90 (2009)
6. Jia, G.F., Shi, Z.F.: A new seismic isolation method and its feasibility study. Earthq. Eng. Eng. Vib. **9**(1), 75–82 (2010)
7. Bao, J., Shi, Z., Xiang, H.: Dynamic Responses of a Structure with Periodic Foundations. J. Eng. Mech. **138**(7), 761–769 (2012)
8. Jensen, J.: Phononic band gaps and vibrations in one- and two-dimensional mass–spring structures. J. Sound Vib. **266**(5), 1053–1078 (2003)
9. Hussein, M.I., Frazier, M.J.: Metadamping: an emergent phenomenon in dissipative metamaterials. J. Sound Vib. **332**(20), 4767–4774 (2013)
10. Cheng, Z., Shi, Z.: Novel composite periodic structures with attenuation zones. Eng. Struct. **56**, 1271–1282 (2013)
11. Chopra, A.K.: Dynamics of Structures. Prentice-Hall International Series in Civil Engineering and Engineering Mechanics, 3rd edn. Pearson Education, Upper Saddle River, USA (2007)
12. Dertimanis, V.K., Antoniadis, I.A., Chatzi, E.N.: Feasibility analysis on the attenuation of strong ground motions using finite periodic lattices of mass-in-mass barriers. J. Eng. Mech. accepted for publication, Under Review
13. Huang, J., Shi, Z.: Application of periodic theory to rows of piles for horizontal vibration attenuation. Int. J. Geomech. **13**(2), 132–142 (2013)

Chapter 29
Genetic Algorithm use for Internally Resonating Lattice Optimization: Case of a Beam-Like Metastructure

Osama Abdeljaber, Onur Avci, and Daniel J. Inman

Abstract Metamaterial inspired structures, or metastructures, are structural members that incorporate periodic or non-periodic inserts. Recently, a new class of metastructures has been introduced which feature chiral lattice inserts. It was found that this type of inserts has frequency bandgaps which can be tuned by altering the geometry of the chiral lattice. Previous studies have shown that inserting non-periodic chiral lattices inside a beam-like structure results in efficient vibration attenuation at low frequencies. In the study presented in this paper, a genetic algorithm based optimization technique is developed to automatically generate chiral lattices which are tuned to suppress vibration in a flexible beam-like structure. Several parameters are incorporated in the optimization process such as the radius of circular nodes and characteristic angle as well as the spacing and distribution of circular inserts. The efficiency of the proposed optimization technique is verified analytically by numerical simulations.

Keywords Metastructures • Genetic algorithm • Internally resonating lattice • Optimization • Metamaterials

29.1 Introduction

Metamaterials have been widely used in research and practice for applications related to control of electromagnetic waves. The exceptional electromagnetic characteristics exhibited by metamaterials can be attributed to the fact that these artificial materials contain microscopic periodic impurities that change waves propagation through the material [1]. Later, studies have been conducted in an attempt to utilize the idea of metamaterials to reduce mechanical vibrations, noise, and sound transmission. As a result, a new class of metamaterials called acoustic metamaterials has been introduced. Basically, acoustic metamaterials are manufactured by injecting periodic inhomogeneities into a particular material. It was found that the resonance of the local material phases within an acoustic metamaterial creates frequency bandgaps around the resonance frequencies. Mechanical waves passing through an acoustic metamaterial are significantly attenuated within the range of these bandgaps [2].

The concept of acoustic metamaterials has been recently employed in order to manufacture a new class of structural members called metamaterial inspired structures, or simply, metastructures. Similar to metamaterials, a metastructure is manufactured by inserting a number of periodically-distributed small inserts within a primary structure. These periodic inserts are designed to resonate locally with the mechanical wave propagating through the primary structure. The out-of-phase motion of the primary structure with respect to the locally resonating inserts induces a vibration attenuation band over a certain frequency range which is directly related to the resonance frequencies of the inserts.

Several types of inserts have been used in the literature to create beam-like metastructure. These inserts include periodically distributed 1-DOF spring-mass-damper resonators [3, 4] and 2-DOF two-mass spring-mass-damper resonators [5]. Recently, the efficiency of a new type of resonators called chiral lattice inserts has been investigated [6]. As shown in Fig. 29.1, chiral lattices incorporate a number of circular masses interconnected by ligaments. The parameters governing the topology of chiral lattices can be easily varied in order to alter the locations and the bandwidths of the frequency bandgaps of the metastructure. Experimental studies have suggested that periodic chiral lattices exhibit superior damping characteristics and low-frequency bandgaps [7].

O. Abdeljaber • O. Avci (✉)
Department of Civil and Architectural Engineering, College of Engineering, Qatar University, P.O. Box 2713, Doha, Qatar
e-mail: onur.avci@qu.edu.qa

D.J. Inman
Department of Aerospace Engineering, University of Michigan, Ann Arbor, MI 48109-2140, USA

S. Pakzad, C. Juan (eds.), *Dynamics of Civil Structures, Volume 2*, Conference Proceedings of the Society for Experimental Mechanics Series, DOI 10.1007/978-3-319-29751-4_29

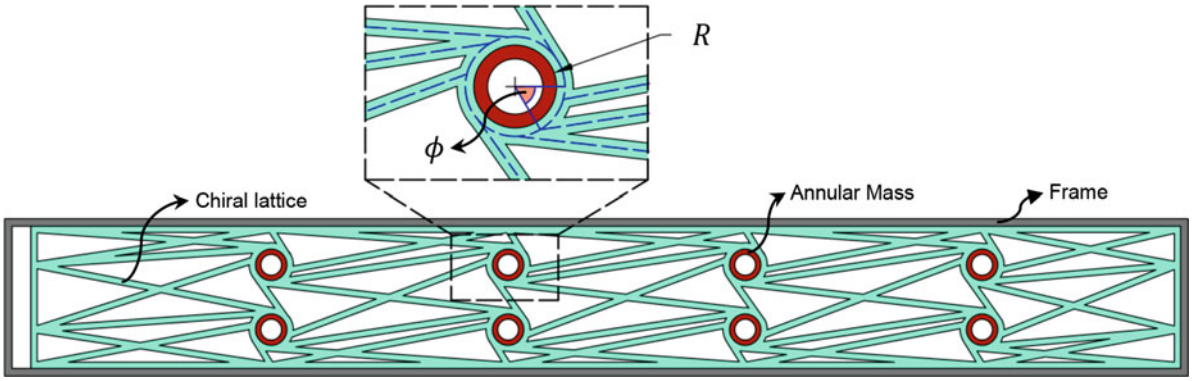

Fig. 29.1 Description of the chiral lattice inserts adopted in this study

In another experimental study, Baravelli and Ruzzene (2013) [8] utilized chiral inserts for low-frequency vibration attenuation of a flexible aluminum frame. The chiral lattices examined in this study consisted of annular steel masses connected by rubber-like ligaments as shown in Fig. 29.1. First, they studied the behavior of periodic chiral lattices in which the annular masses have constant radii and are uniformly distributed along the flexible frame. It was found that this type of inserts results in vibration attenuation at relatively high frequencies. In an attempt to move the frequency bandgaps toward lower frequencies, they introduced another type of inserts referred to as non-periodic chiral inserts. In this type of chiral lattices, the radii of the mass inclusions as well as the spacing between them vary along the primary structure. They found that the location and bandwidth of the attenuation bandgaps can be tuned by adjusting the parameters such as the number, location, size, and distribution of the annular elements. A trial-and-error approach have been successfully applied to obtain the chiral parameters that will result in lower frequency bandgaps. However, it was suggested that automated optimization techniques can be used instead of trial-and-error to obtain optimal chiral topologies.

Therefore, in the study presented in this paper, an automated chiral optimization algorithm based on genetic algorithms (GA) is introduced. This algorithm is designed to search for optimal periodic and non-periodic chiral designs that will maximize vibration suppression in a flexible beam-like member. First, the chiral parameters considered in this optimization study are explained. New parameters are introduced to enable the algorithm to explore non-periodic chiral designs. Secondly, the study discusses the development of an automated routine which is fully parametrized in terms of the chiral parameters. This routine takes the aforementioned chiral parameters as an input and generate a finite element model of the beam-like structure incorporating the chiral topology described by these premiers. Third, this routine is incorporated in a genetic algorithm based optimization algorithm for chiral optimization. Lastly, the efficiency of this algorithm is demonstrated analytically by a numerical simulation.

29.2 Genetic Algorithms

Analytical modeling of chiral lattices, especially non-periodic ones, can be extremely challenging due to the geometrical complexity of such inserts. Therefore, finite element modeling is used instead of closed-form methods in order to estimate the response of chiral inserts. Nevertheless, FE modeling does not allow obtaining a closed-form representation of the cost function which is necessary in conventional optimization techniques. On the other hand, non-conventional optimization methods such as genetic algorithms do not require explicitly-defined cost functions. Therefore, it was decided to utilize GAs to carry out the chiral optimization process.

Basically, GAs randomly generate an initial population consisting of a number of solutions (i.e. individuals) [9]. Each individual in the population is evaluated by a cost function (i.e. fitness function). After that, a number of genetic operators, which are inspired by the natural evolution process, are applied in an iterative manner until the population evolves toward the global optima. The main genetic operators incorporated in a GA are *evaluation*, *selection*, *crossover*, and *mutation* [10]. The interested reader is referred to [11] for more details on genetic algorithms and genetic parameters.

29.3 The Parameters Governing Chiral Lattice Inserts

As mentioned in the introduction, the first step toward the development of the chiral optimization algorithm is to define the parameters governing periodic and non-periodic chiral lattices. Previous studies on periodic chiral lattices have concluded that periodic chiral inserts are governed by the following parameters:

1. The number of circular nodes in the long direction, n_x.
2. The number of circular nodes in the short direction, n_y.
3. The characteristic angle ϕ that determines the degree of asymmetry of the lattice.
4. The thickness of the ligaments, t.

In addition to the aforementioned parameters, this study introduces new parameters referred to as grading and distribution parameters. These parameters enable the optimization technique to explore non-periodic in addition to the periodic designs. The grading and distribution parameters are:

1. Three parameters to determine how the radii of the circular nodes are graded in the long direction. These parameters are listed below and illustrated in Fig. 29.2.
   (a) The radius of the leftmost node, R_s.
   (b) The radius of the rightmost node, R_f.
   (c) The radius of middlemost node, R_m.

   The radii of the nodes between the abovementioned nodes are interpolated according to a 2nd order polynomial as illustrated in Fig. 29.2.
2. Two parameters to determine locations of the circular nodes in the long direction. These parameters are listed below and explained in Fig. 29.3.
   (a) The distance between the center of the leftmost node and the inner face of the lattice frame, x_s.
   (b) The distance between the center of the rightmost node and the edge of the lattice, x_f.

   As shown in Fig. 29.3, the distances between x_s and x_f are interpolated linearly. By altering the parameters described in this section, many parametric and non-parametric chiral designs can be generated and tested. This fact is demonstrated by the three examples shown in Fig. 29.4.

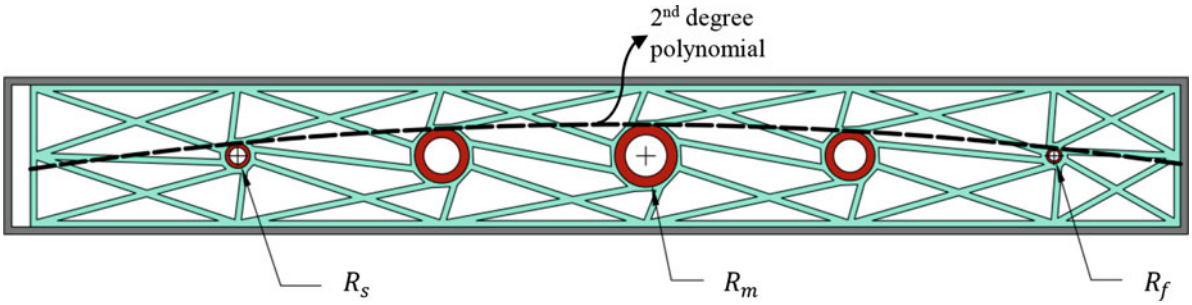

Fig. 29.2 The parameters governing the size grading of the circular nodes along the frame

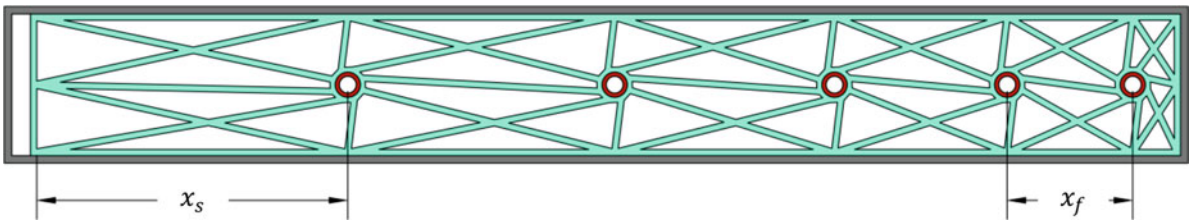

Fig. 29.3 The parameters governing the distribution of circular nodes along the frame

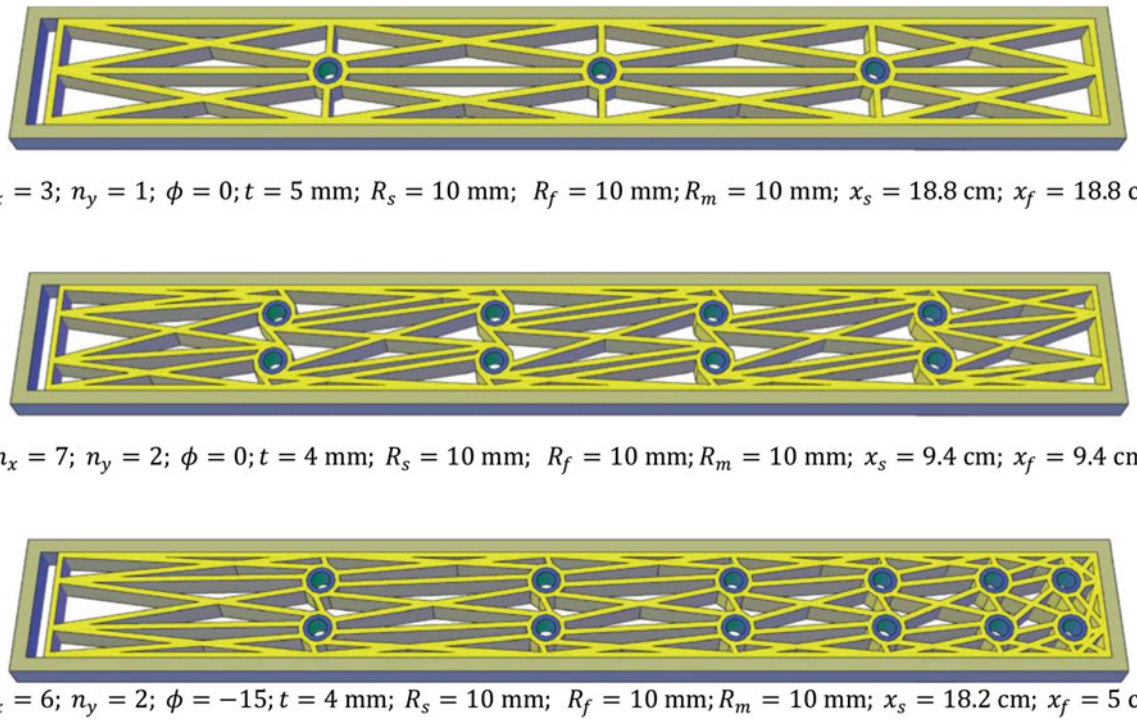

Fig. 29.4 Various chiral lattice designs

29.4 The Optimization Process

As mentioned before, this study implements genetic algorithms for seeking optimal chiral lattice topologies for a particular case. As in any other optimization method, genetic algorithm requires the definition of the variables to be optimized, the range of each variable, the linear and nonlinear constraints, and the fitness function that determines the optimality of individuals.

This section briefly describes the chiral optimization process developed in this study. As explained in Sect. 26.3, the optimization process incorporates a total of nine optimization parameters. For each parameter, an upper and lower bound should be defined to ensure that the optimization process would result in feasible chiral lattice topologies. Also, linear and nonlinear constraints should be imposed in order to force the GA based process to generate chiral inserts that fit inside the primary host structure. In this study, a nonlinear constraint was applied to restrict the annular masses to lay within the width of the beam-like structure. Additionally, a linear and a nonlinear constraints were imposed to ensure sufficient spacing between the annular nodes in the long direction. The constraints are not provided here for brevity.

A Matlab [12] routine was written to carry out the GA based chiral optimization process. This routine utilizes the genetic algorithm solver available in Matlab Genetic Algorithm Toolbox. The GA solver requires the user to define the optimization fitness function, bounds, and constraints. Also, it requires specifying the genetic algorithm options including population creation, selection, crossover, and mutation options. The initial population consists of a number of feasible solutions (i.e. individuals) that satisfy the bounds and constraints. Each individual is simply a vector containing certain values of the nine chiral parameters.

As previously explained, the fitness function in a GA serves as a cost function in conventional optimization technique. In other words, the fitness function is responsible for evaluating the optimality of each individual in the current population. Another Matlab routine has been written to serve as a cost function for the chiral optimization process. This routine takes the parameters values corresponding to each individual and automatically creates an Abaqus [13] FE model of the flexible frame featuring the chiral insert described by the values of the parameters. 2D solid elements (4-node bilinear plain stress quadrilateral elements) are used for the FE mesh. Next, the Matlab routine initiates an Abaqus dynamic simulation to estimate the response of the metastructure corresponding to a particular individual under a band-limited white noise base excitation in the vertical direction. The frequency content of the excitation signal should be selected according to the desired attenuation range. For instance, if the optimization goal is to maximize vibration attenuation within the range 0–200 Hz, a white noise base acceleration signal with a bandwidth of 0–200 Hz is used. After that, the RMS value of the acceleration response of the

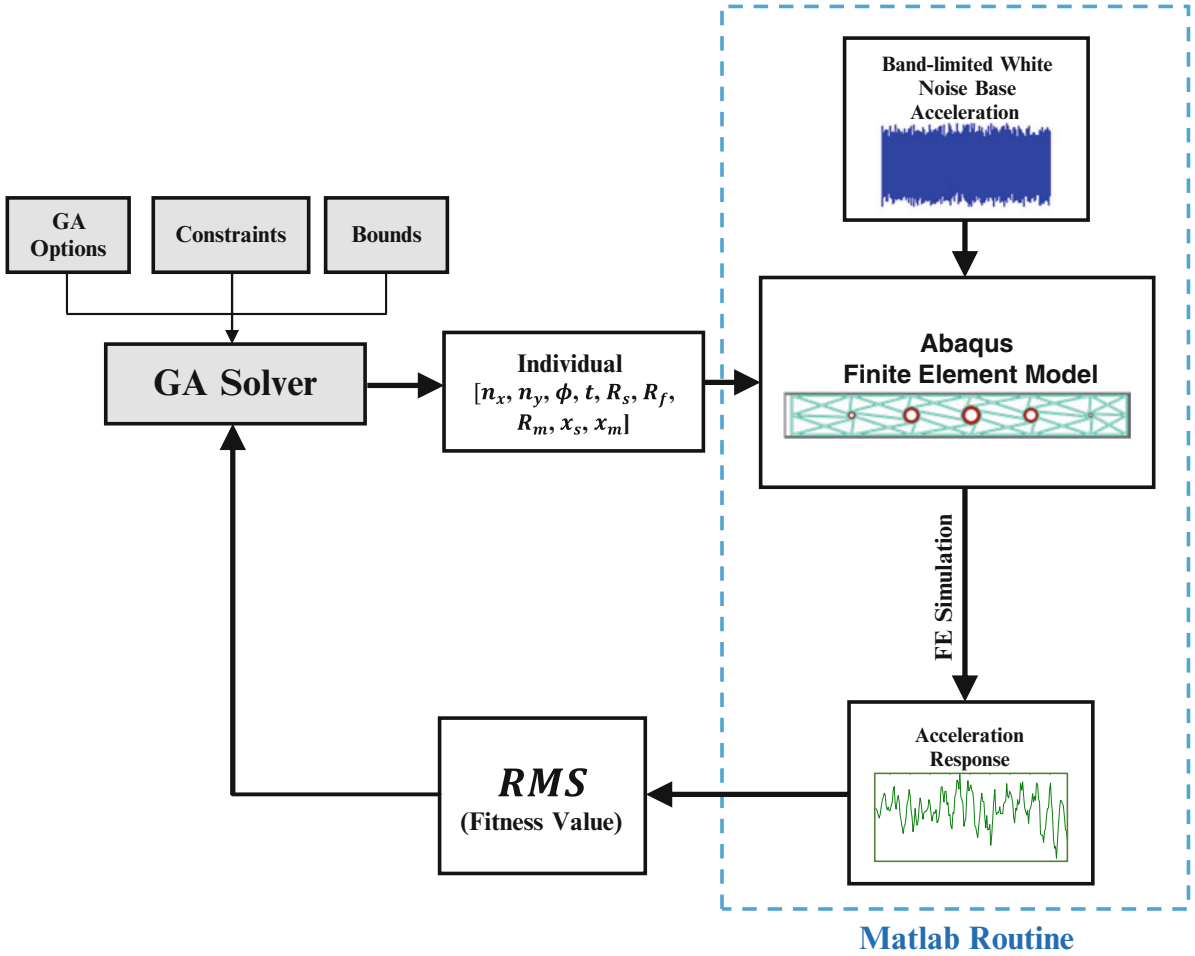

Fig. 29.5 The optimization algorithm process

metastructure is computed and used as an index that represents the optimality of the individual. The optimization process searches for chiral topology that will result in the minimum RMS value over the simulation time. The optimization algorithm explained in this section is illustrated in Fig. 29.5.

29.5 Numerical Demonstration

In this section, a numerical example is provided to test the efficiency of the GA based chiral optimization algorithm. In this example, the algorithm is applied to obtain an optimal chiral design for the simply-supported beam-like structure defined in Fig. 29.6. The material properties of the primary structure as well as the chiral inserts are given in Table 29.1. A mass-proportional model was used to introduce damping to the chiral lattice rubber-like material (liquid two-phase silicone rubber). The parameters of this damping model (α and β) are also provided in Table 29.1. The upper and lower bounds of the optimization process are given in Table 29.2. The frequency range of interest in this study is 0–200 Hz. Therefore, a white noise base acceleration signal with a bandwidth of 0–200 Hz was used to excite the flexible frame when evaluating each individual.

The genetic algorithm based optimization process was conducted for a sufficient amount of iterations (i.e. generations). The process has converged to the solution given in Table 29.3 and Fig. 29.7. It can be noticed from the optimal chiral solution (Fig. 29.7) that the optimization process has resulted in a non-periodic chiral topology. This result supports Baravelli and Ruzzene's [8] observation which indicates that graded chiral topologies result in better vibration suppression and energy dissipation characteristics than periodic ones.

Fig. 29.6 Dimensions of the flexible frame

Table 29.1 Material properties

Component	Material	Properties	
Frame	Aluminum	E	69 GPa
		ρ	2713 kg/m^3
Annular masses	Steel	E	193 GPa
		ρ	8027 kg/m^3
Chiral Lattice	Silicon	E	1.37 MPa
		ρ	1240 kg/m^3
		α	5
		β	0.0002

Table 29.2 Upper and lower bounds for the optimization process

Parameter	n_x	n_y	ϕ	t (mm)	R_s (mm)	R_f (mm)	R_m (mm)	x_s (cm)	x_f (cm)
Lower bound	1	1	−70	3	1	1	1	2	2
Upper bound	10	3	70	5	20	20	20	25	25

Table 29.3 The parameters of the optimal chiral insert

n_x	n_y	ϕ	t (mm)	R_s (mm)	R_f (mm)	R_m (mm)	x_s (cm)	x_f (cm)
4	3	55	3.78	3.54	7.79	9.61	10.1	14.7

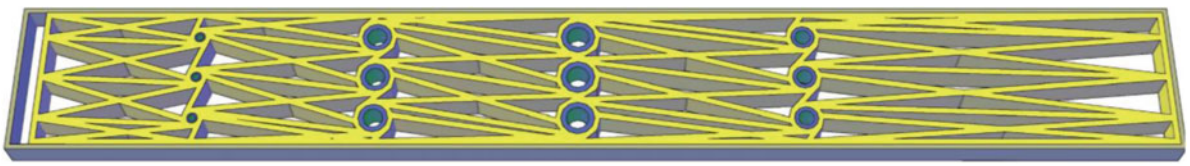

Fig. 29.7 Optimal chiral lattice topology obtained using the chiral optimization algorithm

In order to demonstrate the performance of the optimization algorithm, Fig. 29.8 displays a comparison between the FRF of the acceleration response of the plain frame and the FRF of the response of the frame with the optimal chiral lattice obtained using the proposed algorithm. In both cases, the FRF was computed for the vertical acceleration response at the mid-span with respect to the base acceleration excitation.

This comparison clearly shows the significant reduction in vibration amplitudes over the entire frequency range after inserting the optimal chiral lattice inside the flexible frame. Therefore, it can be concluded that the algorithm is efficient for chiral optimization. Additionally, it is noticed that the optimization process has converged to a chiral lattice with $n_y = 3$ which is the maximum value allowed by the limits given in Table 29.2. Maximizing n_y (i.e. maximizing the number of circular nodes in the short direction), generates lattices with larger number of ligaments. Increasing the number of ligaments resonating at a particular frequency results in better vibration suppression characteristics around this frequency.

29.6 Conclusions

In this study, an automated genetic algorithm based process has been developed for optimization of chiral lattice inserts. This process seeks optimal periodic and non-periodic chiral designs with broadband vibration attenuation capabilities. The optimization algorithm incorporates nine parameters which govern the chiral topology. Numerical simulations were carried

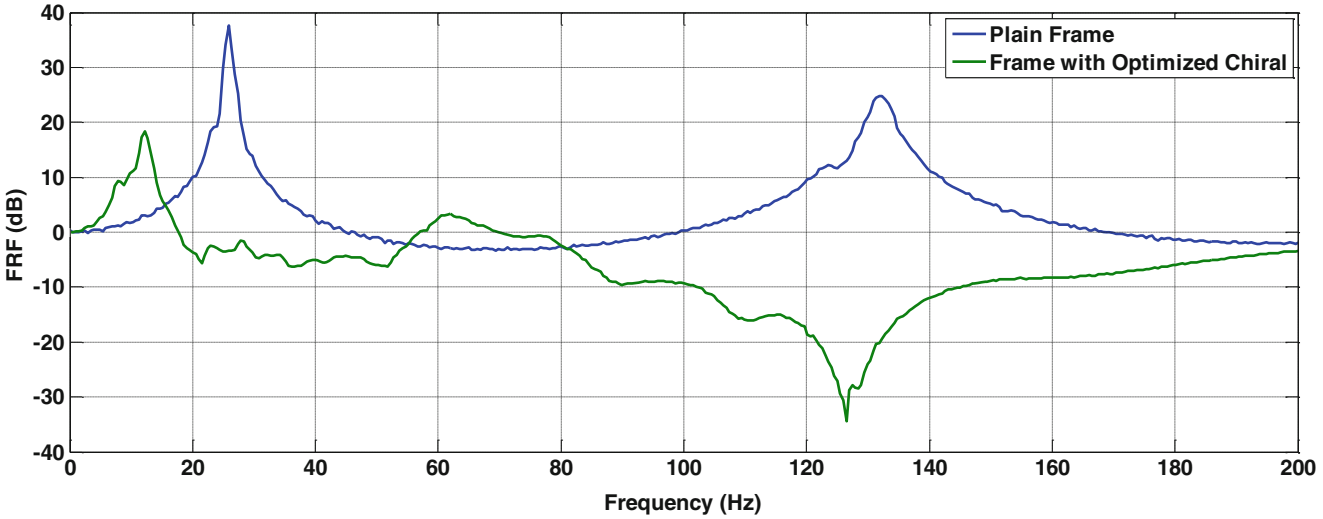

Fig. 29.8 FRF comparisons for the plain frame and frame with the optimal chiral design

out to verify the efficiency of the proposed algorithm. The results have shown clearly that the algorithm was able to generate non-periodic chiral lattice with exceptional vibration suppression characteristics. Further research should be conducted in order to test the ability of the proposed algorithm to obtain optimal chiral designs for other types of structural members. Also, it is crucial to verify the outcomes of the optimization process experimentally. The authors have already started working on this task.

Acknowledgements The financial support for this research was provided by Qatar National Research Fund, QNRF (a member of Qatar Foundation) via the National Priorities Research Program (NPRP), Project Number: NPRP 6-526-2-218. The statements made herein are solely the responsibility of the authors.

References

1. Pendry, J.B., Schurig, D., Smith, D.R.: Controlling electromagnetic fields. Science **312**, 1780–1782 (2006)
2. Hussein, M.I., Hamza, K., Hulbert, G.M., Saitou, K.: Optimal synthesis of 2D phonotic crystals for broadband frequency isolation. Wave Random Complex Media **17**, 491–510 (2007)
3. Pai, P.F.: Metamaterial-based broadband elastic wave absorber. J. Intell. Mater. Syst. Struct. **21**, 517–528 (2010)
4. Sun, H., Du, X., Pai, P.F.: Theory of metamaterial beams for broadband vibration absorption. J. Intell. Mater. Syst. Struct. **21**, 1085–1101 (2010)
5. Pai, P.F., Peng, H., Jiang, S.: Acoustic metamaterial beams based on multi-frequency vibration absorbers. Int. J. Mech. Sci. **79**, 195–205 (2014)
6. Liu, X.N., Hu, G.K., Sun, C.T., Huang, G.L.: Wave propagation characterization and design of two-dimensional elastic chiral metacomposite. J. Sound Vib. **330**, 2536–2553 (2011)
7. Zhu, R., Liu, X.N., Hu, G.K., Sun, C.T., Huang, G.L.: A chiral elastic metamaterial beam for broadband vibration suppression. J. Sound Vib. **333**, 2759–2773 (2014)
8. Baravelli, E., Ruzzene, M.: Internally resonating lattices for bandgap generation and low-frequency vibration control. J. Sound Vib. **332**, 6562–6579 (2013)
9. Qdais, H.A., Bani-Hani, K., Shatnawi, N.: Modeling and optimization of biogas production from a waste digester using artificial neural network and genetic algorithm. Resour. Conserv. Recycl. **54**, 359–363 (2010)
10. Inman, D.J., Farrar, C.R., Lopes, V., Steffen, V.: Damage Prognosis: For Aerospace, Civil and Mechanical Systems. Wiley, Chichester (2005)
11. Sivanandam, S.N., Deepa, S.N.: Introduction to Genetic Algorithms. Springer, Berlin (2007)
12. Matlab version 8.1.0.604. Natick, Massachusetts: The MathWorks Inc. (2013)
13. Abaqus/CAE version 6.12-1. Providence, Rhode Island, Dassault Systèmes (2012)

Chapter 30
Vibration Transmission Through Non-Structural Partitions Between Building Floor Levels

P. J. Fanning and A. Devin

Abstract An assessment of the extent of vibration transmission, attributable to non-structural partitions, was made using experimental tests and numerical simulations, for a recently constructed multi-storey reinforced concrete building. Mechanical excitation was provided to one floor. The extent of vibration on the floor above was found to be as high as 65 % of that recorded on the excited floor. A numerical model was also used to simulate the response to a person walking along a corridor. The extent of transmission was 9 % with partitions and 1.8 % without them. These findings imply that the vibration level on any given floor level will be due to excitation on that particular floor and also the not insignificant level of vibration that may be transmitted through structural and non-structural components due to concurrent activity from floors above and below. This issue of vibration transmission between floor levels is not addressed in any current guidance of floor vibration serviceability assessment and requires further detailed investigation.

Keywords Vibration serviceability • Floor vibrations • Non-structural partitions

30.1 Introduction

Vibration serviceability of floor systems can be a significant issue in buildings. Traditional reinforced concrete floor systems, with their high stiffness and damping ratios, have had an excellent track record in this regard [1]. Recently there is a trend towards increased floor spans and slenderness, caused by a demand for faster construction times and open-plan floor layouts, which are more likely to exhibit vibration serviceability issues due to their slenderness and lower energy dissipation capability [2–4].

It has also been illustrated that non-structural elements can have significant effects on the dynamic response of floor systems of buildings; evidence of such effects was observed in determining the dynamic parameters of both slender floor systems [5, 6] and traditional concrete floor systems [7]. Exclusion of non-structural elements has been shown to result in discrepancies between a numerical model of a building and its actual structural response. Miskovic et al. [6] analysed the effect of full-height partitions using forced vibration testing. Ventura et al. [8] used ambient vibration results to update a finite element (FE) model of a building including non-structural elements. Li et al. [9] highlighted that measured natural frequencies of a 79 storey building were higher than those calculated from the FE model, concluding that this difference was due to the presence of non-structural elements. No significant research, to the authors' knowledge, has been undertaken to date on the extent of vibration transmission from one floor level to the next due to these non-structural partitions.

This paper describes a combined experimental and numerical investigation in to the extent of vibration transmission between one floor and the next. In a series of experimental tests mechanical excitation was provided on one floor level of a recently constructed reinforced concrete building, a traditional column and slab system, with non-structural partitions forming corridors and various working spaces on each floor level. Responses were recorded on the excited floor level and the one above to measure the extent of vibration transmission during these tests. It was not possible to repeat these tests without partitions in situ and hence a validated numerical model [7] was used to compare the response on two floors, using models with and without partitions, due to a person walking along a corridor length in the bulding. The aim of the simulation was to attempt to determine the contribution, if any, of the partitions to vibration transmission between floors.

P.J. Fanning (✉)
University College Dublin, School of Civil Engineering, Dublin, Ireland
e-mail: paul.fanning@ucd.ie

A. Devin
Skidmore, Owings & Merrill Inc., The Broadgate Tower, London EC2A 2EW, UK

S. Pakzad, C. Juan (eds.), *Dynamics of Civil Structures, Volume 2*, Conference Proceedings of the Society for Experimental Mechanics Series, DOI 10.1007/978-3-319-29751-4_30

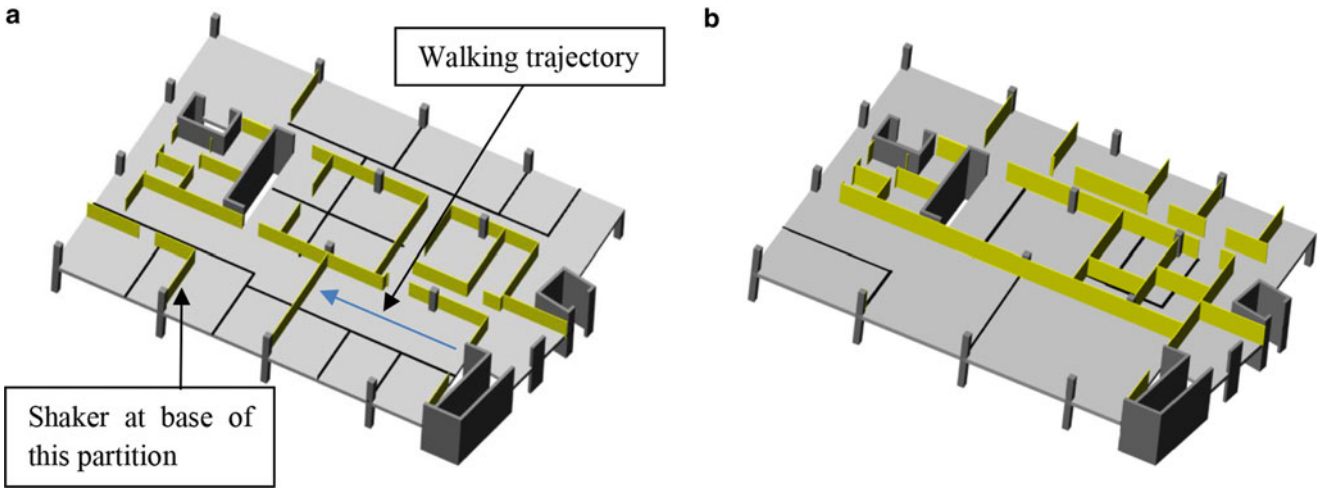

Fig. 30.1 (**a**) First floor internal partition layout. (**b**) Second floor internal partition layout

30.2 Test Structure: The Charles Institute at University College Dublin

The Charles Institute on the University College Dublin (UCD) campus in Ireland is a four storey reinforced concrete frame office building. Structurally, the frame consists of two-way spanning flat slabs, 0.3 m thick, supported by 0.4 m^2 columns with a maximum bay size of 7.5 × 6.6 m. The lateral load resisting system is made up of a number of reinforced concrete stairwells, lift cores and service ducts with wall thicknesses of 0.2 m. Each floor level is divided into state-of-the-art laboratories and office accommodation using lightweight non-structural partitions. These partitions consist of two layers of gypsum boards, 25 mm total thickness, attached to both sides of lightweight metal studs at 400 mm centres which house an insulation material. Exterior wall cladding consists of large polished Chinese black basalt panels 40 mm thick supported on galvanised steel rectangular sections fixed to the concrete slab above and below at 400 mm centres. The structure of each floor is identical with only the layout of internal partitions varying from floor to floor. The layouts of partitions, for the two floor levels considered, are shown in Fig. 30.1a, b. In both cases the solid black lines indicate the partition layout on the floors below.

30.3 Vibration Transmission Due to Mechanical Excitation

The objective of the mechanical excitation tests was to determine the vibration response on floor level 2 due to excitation on floor level one. An APS Dynamics electrodynamic shaker, with a capacity of 500 N, was used to provide vertical excitation on floor level 1, while Endevco 7754-1000 piezoelectric accelerometers (at quarter points and mid-way along the partition at its' base and immediately above it on floor level above) were used for response measurements. A sweeping 'chirp' force was applied to Floor Level 1 at the base of, and mid-way along, an internal partition ('A' in Fig. 30.1a). The frequency range for the force was 5–40 Hz, sweeping a rate of 0.63 Hz per second; the maximum applied force was 480 N, reducing to 100 N over the length of the 'chirp'. The resulting vibration response of Floor Levels 1 and 2 mid-way along the partition are shown in Fig. 30.2. As expected the highest response is recorded on the excited floor level but the level of transmission to floor level 2 is not insignificant. The acceleration time histories were used to calculate a percentage of vibration transmission; the percentage of vibration transmission being defined as the ratio of the instantaneous vibration level at Floor Level 2 to that at Floor Level 1. This percentage of vibration transmission is plotted against time in Fig. 30.3 for each of the three sensor pairs along the length of the partition. The extent of vibration transmission varied between approximately 10 % and 65 % over the variation of the chirp test—the average level of transmission was of the order of 32 %.

Ideally the mechanical excitation tests would have been repeated on the bare frame system in the absence of partitions but it was not feasible to remove all partitions. Thus while it is obvious from the test data that there is transmission of vibrations from one floor level to the next it cannot be confirmed categorically whether, and to what extent, the partitions contribute to this transmission. Thus, the response of validated numerical models, discussed subsequently, in which partitions are included and also removed, were also studied.

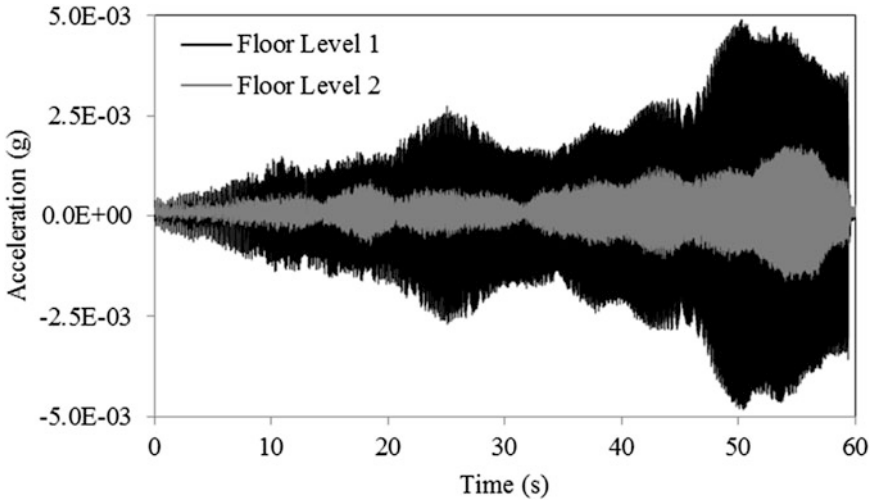

Fig. 30.2 Acceleration time histories mid-way along partition on floor levels 1 & 2

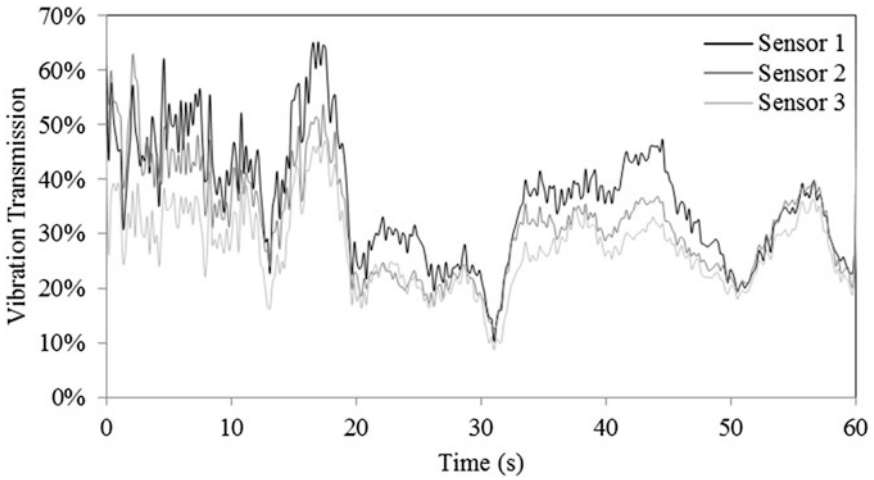

Fig. 30.3 Extent of vibration transmission for 3 sensor locations

30.4 Vibration Transmission Due to Simulated Walking

During the process of quantifying the effect of non-structural partitions on the modal characteristics of the Charles Institute building [7, 10, 11] validated finite element models of both the bare frame (columns, slabs and shear walls only) and completed structure (additional inclusion of non-structural partitions and external façade cladding units, both modelled using equivalent vertical springs) were developed. These models thus provide the opportunity to evaluate, numerically, the contribution of partitions to the vibration transmission from one floor level. The finite element meshes, where the nominal element size on each floor level is of the order of 0.4×0.4 m, are shown in Fig. 30.4. The only difference is the inclusion of spring type elements to account for the partitions in one of the models.

For the purposes of this numerical evaluation the responses, at two points, one on floor level 1 and the other on floor level 2, due to a person walking along a section of floor way (indicated as 'walking trajectory' with an arrow in Fig. 30.1a) on floor level one are evaluated. The pedestrian load applied, as a function of time in Newtons, after [12] is given by Eq. (30.1). It describes the temporal variation in load due to a pedestrian of mass 80 kg walking at a pacing rate of 1.8 Hz with a first harmonic factor of 0.4.

$$F(t) = 784.8 + 0.4\,(784.8)\sin 2\,\pi(1.8)t \tag{30.1}$$

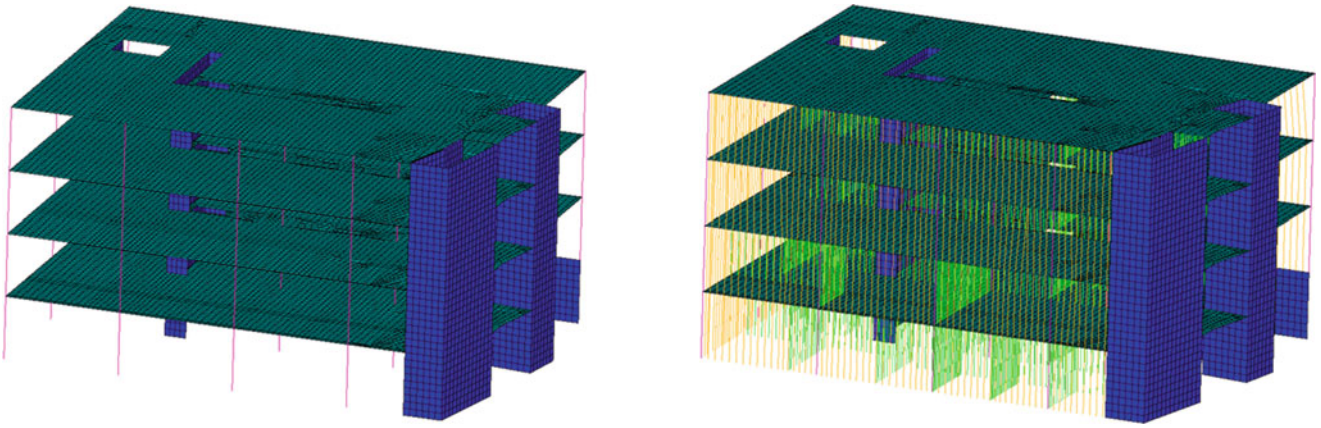

Fig. 30.4 Finite element meshes without (on left) and with (on right) partitions

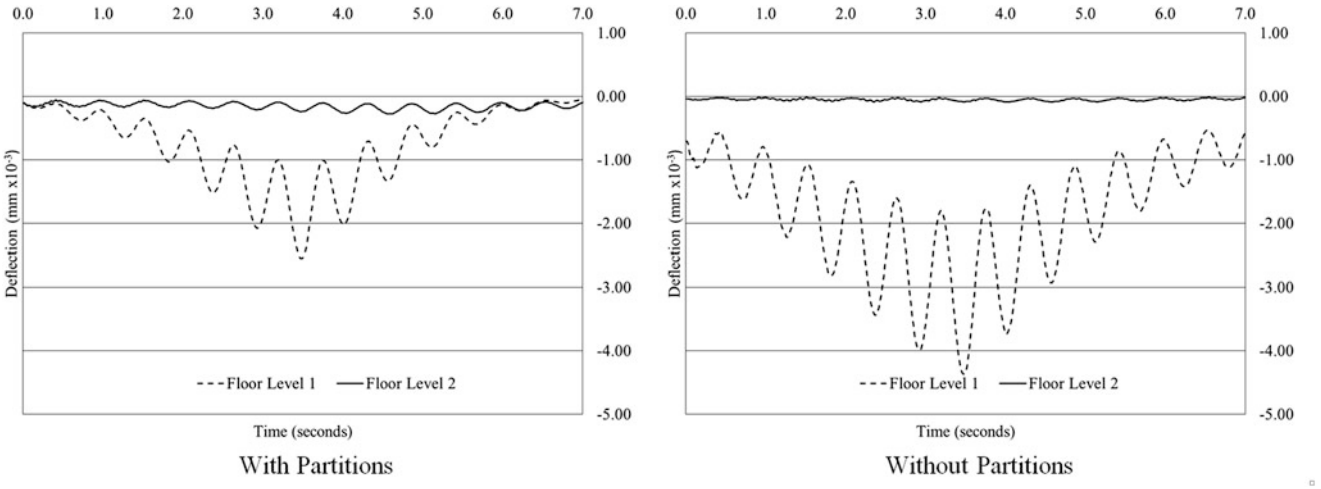

Fig. 30.5 Displacement responses on levels 1 and 2 due to pedestrian walking

Table 30.1 Peak floor level accelerations due to walking

Model	Floor level 1 (mm × 10^3/s^2)	Floor level 2 (mm × 10^3/s^2)	Transmission ratio (%)
With partitions	99.1	8.9	9.0
Without partitions	163.7	3.0	1.8

For the purposes of considering vibration transmission the responses at a point mid-way along the walking trajectory and at a point located immediately above this, on floor level two, were considered. A transient dynamic analysis was performed using a time step of approximately 0.015 s so as to adequately capture the load dependency on the pacing frequency of 1.8 Hz. The analysis duration was 7 s. For each time step the force exerted and position along the walking path was determined. The load was then shared pro-rata to the two closest node points along the path and ramped from prior values. Because of the un-even nature of the mesh (node to node distances were nominally 0.4 m but not exactly 0.4 m) this led to a unsteady high frequency content in the acceleration response which made direct comparison of effects difficult using acceleration responses—displacement responses, at the two reference points, were thus employed for evaluating comparative accelerations. These displacement (in the vertical direction) responses are plotted in Fig. 30.5.

The response at each reference point is an oscillatory response at 1.8 Hz due to the walking load model pacing frequency applied. The peak acceleration at the reference point occurs when the load is at the reference point and is determined from the maximum peak to peak deflection divided by two and multiplied by the response frequency squared in radians per second. The peak accelerations, so calculated, are listed in Table 30.1.

The model without partitions is characterised by higher accelerations on the load floor level but relatively little transmission of vibration (ratio of peak floor level 2 acceleration to floor level 1 acceleration) to the floor above. In the absence of partitions the level of transmission is 1.8 % compared to 9 % when partitions are included.

30.5 Discussion of Results

The experimental and numerical investigations into vibration transmission between floor levels discussed above seek to explore the contribution of non-structural partitions to such transmission. Both sets of investigations show that excitation on a given floor level can be expected to produce a vibration response on the floor above.

In the case of the numerical simulations the presence of the partitions results in a stiffer system which is consistent with prior experimental modal studies [7] which showed that nominally identical floors in the absence of partitions had increased frequencies and altered modes of vibration once the partitions were added. Hence with partitions included although the vibration levels (Fig. 30.5 and Table 30.1) identified on the floor along which walking was simulated are lower the extent of transmission to the floor above is higher—the upper floor vibration level is predicted to be of the order of 9 % of those on the excited floor compared to only 1.8 % in the absence of the partitions. This constitutes a fivefold increase in transmission from one floor to the next due to the presence of partitions.

While it was not possible to undertake the experimental test programme with and without partitions the extent of transmission was at least as pronounced, being in the range of 10–65 % over the duration of the test. Vibration transmission of the order of 10 % is considered significant and implies that the actual vibration response on a given floor level is likely to be due to the activity on that floor level itself and also to some not insignificant level of transmission from the floors below. This is currently not acknowledged in any code of practice for floor vibration serviceability assessment and is in the authors' opinions an area of research that requires further investigation.

30.6 Conclusions

Experimental and numerical studies have shown that there is transmission of vibration from one floor to the next. The extent of transmission along a partition line was measured to be in the range of 10–65 % for a recently constructed reinforced concrete building with different partition layouts on each floor level.

Numerical models of the test structure indicate that the extent of transmission is increased, a fivefold increase in this case, due to the presence of partitions. It follows that building floor vibration serviceability assessment should account for this transmission. Currently this in not the case and further research work, preferably experimentally based, on full scale structures with and without internal partitions, is required.

Acknowledgements The authors wish to express their gratitude to (1) the Irish Research Council for Science, Engineering & Technology for their financial support, (2) the Vibration Engineering Research Section of Sheffield University for use of their equipment at the time the testing was undertaken, and (3) the Buildings Office at University College Dublin (UCD) for access to the Charles Institute at UCD.

References

1. Pavic, A., et al.: Critical review of guidelines for checking vibration serviceability of post-tensioned concrete floors. Cem. Concr. Compos. **23**(1), 21–31 (2001)
2. Pavic, A., Miskovic, Z., Reynolds, P.: Modal testing and finite element model updating of a lively open-plan composite building floor. J. Struct. Eng. **133**(4), 550–558 (2007)
3. Pavic, A., Widjaja, T., Reynolds, P.: The use of modal testing and FE model updating to investigate vibration transmission between two nominally identical building floors. In: Proceedings of the International Conference on Structural Dynamics Modeling-Test, Analysis, Correlation and Validation. pp. 347–355. Instituto Superior Tecnico Lisbon, Lisbon (2002)
4. Nyawako, D., Reynolds, P., Hudson, M.: Findings with AVC design for mitigation of human induced vibrations in office floors. In: Catbas, F.N., Pakzad, S., Racic, V., Pavic, A., Reynolds, P. (eds.) Topics of Dynamics in Civil Structures, vol. 4, pp. 37–44. Springer, New York (2013)
5. Reynolds, P.: The effects of raised access flooring on the vibrational performance of long-span concrete floors. PhD Thesis, University of Sheffield (2000)
6. Miskovic, Z., Pavic, A., Reynolds, P.: Effects of full-height nonstructural partitions on modal properties of two nominally identical building floors. Can. J. Civil Eng. **36**(7), 1121–1132 (2009)

7. Devin, A., Fanning, P.J., Pavic, A.: Modelling effect of non-structural partitions on floor modal properties. Eng. Struct. **91**, 58–69 (2015)
8. Ventura, C.E., Lord, J.-F., Simpson, R.D.: Effective use of ambient vibration measurements for modal updating of a 48 storey building in Vancouver, Canada. In: International Conference on Structural Dynamics Modeling—Test, Analysis, Correlation and Validation. Madeira Island (2002)
9. Li, Q.S., et al.: Field measurements of amplitude-dependent damping in a 79-storey tall building and its effects on the structural dynamic responses. Struct. Des. Tall Build. **11**(2), 129–153 (2002)
10. Devin, A., Fanning, P.J.: The evolving dynamic response of a four storey reinforced concrete structure during construction. Shock Vib. **19**(5), 1051–1059 (2012)
11. Devin, A.: The effect of non-structural elements on the vertical dynamic response of floors. PhD Thesis, School of Civil, Structural and Environmental Engineering, University College Dublin (2013)
12. Bachmann, H., & Ammann, W.: Vibrations in structures induced by man and machines. International Association for Bridge and Structural Engineering, Structural Engineering Document, Zurich (1987)

Chapter 31
Hybrid Time/Frequency Domain Identification of Real Base-Isolated Structure

Patrick Brewick, Wael M. Elhaddad, Erik A. Johnson, Thomas Abrahamsson, Eiji Sato, and Tomohiro Sasaki

Abstract This paper presents a case study using hybrid time- and frequency-domain identifications in a synergistic manner to develop models of a full-scale experimental base-isolated structure. This four-story reinforced-concrete building on an isolation layer (of rubber bearings, elastic sliding bearings, passive metallic yielding dampers, and controllable oil dampers) was designed and constructed at the large-scale Japanese NIED E-Defense earthquake engineering laboratory. A variety of sensors, including accelerometers, were mounted within the structure to measure building response to shake table excitations. While the building was ultimately subjected to historical and synthetic ground motions, the recorded table and building accelerations during a number of random excitation tests are used to identify the structure's natural frequencies, damping ratios and mode shapes. The substantial damping provided by the isolation layer necessitates adopting a hybrid time- and frequency-domain approach for identification. The modes of the structure are separated by frequency content wherein lower frequency modes are identified using time domain approaches from the subspace identification family of methods and higher frequency modes are identified using frequency response functions. Individually, neither approach is able to successfully identify all of the desired modes but, through their combination, the modal properties of the structure are successfully characterized.

Keywords Full-scale testing • Base-isolation • State-space models • Frequency response functions • Modal analysis

31.1 Introduction

While often costly, conducting full-scale tests for large building specimens offers researchers valuable information about the building's dynamics and mechanical behavior. These tests become all the more necessary when innovative seismic protection systems, such as base-isolation and passive damping devices, are included in the building's design. Recently, the construction and inclusion of base-isolation systems within structures has increased, especially after the strong earthquakes that have struck the United States and Japan [1]. The increasing popularity of these devices has motivated efforts to better model the systems and structures in which they have been integrated so that responses to excitations outside of the testing regime may be better predicted. Further, the behavior of base-isolation devices may be dependent on various input characteristics, such as frequency and amplitude, meaning that the linearity, or nonlinearity, of a response will directly depend on the excitation.

The researchers at E-Defense (a part of the Japan's *National Research Institute for Earth Science and Disaster Prevention*, NIED), a unique facility capable of testing full-scale structures, designed and constructed an asymmetric base-isolated building to test and study, in part, the performance of the isolation layer when subjected to strong impulsive and long period excitations [2]. The isolation layer upon which this four-story reinforced-concrete structure rests is composed of several different damping and energy dissipation devices, namely: conventional rubber bearings, elastic sliding bearings, passive metallic (steel) yielding dampers, and controllable oil dampers (with solenoids to provide several discrete damping levels). The performance of the building, as measured by the response of the structure, was monitored through extensive

P. Brewick (✉) • W.M. Elhaddad • E.A. Johnson
Sonny Astani Department of Civil and Environmental Engineering, University of Southern California, 3620 South Vermont Avenue, KAP 210, Los Angeles, California 90089, USA
e-mail: brewick@usc.edu

T. Abrahamsson
Department of Applied Mechanics, Chalmers University of Technology, Gothenburg 412 96, Sweden

E. Sato • T. Sasaki
National Research Institute for Earth Science and Disaster Prevention, 1501-21 Nishikameya, Mitsuta, Shijimi-cho Miki, Hyogo 673-0515, Japan

S. Pakzad, C. Juan (eds.), *Dynamics of Civil Structures, Volume 2*, Conference Proceedings of the Society for Experimental Mechanics Series, DOI 10.1007/978-3-319-29751-4_31

instrumentation that included several accelerometers placed on each floor of the building specimen as well as on the table itself. To anticipate and facilitate possible future analyses of this specimen at E-Defense, this paper proposes a nominal model of the linear system that characterizes its modal properties using the measured responses (subsequent studies will then refine it to a fully nonlinear model).

The process of creating a dynamical model from observed input and output signals is commonly called system identification [3]. While system identification encompasses a great many methods and algorithms, one of the more popular methods when performing system identification on input–output systems is subspace identification [4]. Within subspace identification, the advanced numerical algorithm for subspace state-space system identification (N4SID) offers numerically reliable state-space models for complex multivariable dynamical systems that are computed directly from the measured data [5]. One of the strengths of the N4SID algorithm is its flexibility with measurement data, as it may be applied to either frequency domain or time domain measurements [6, 7]. A more comprehensive review of subspace identification, including information on other algorithms, may be found in [8]. Subspace identification methods offer further advantages, as they may be utilized for model reduction purposes that allow potentially large or complex systems to be solved on a more manageable scale [4].

This study will focus on using the measurement data from the first day of testing to create a nominal reduced-order model that will represent the response of the full-scale system in the linear range. This will be accomplished through application of the N4SID algorithm to both time domain and frequency domain measurement data in order to identify the nominal modal properties. The experimental testing set-up and identification methodology are presented first, followed by a discussion of the identification results. Conclusions and proposed avenues for future research are presented at the end.

31.2 Experimental Measurement Data

The base-isolated test structure at E-Defense was constructed in late 2012 and early 2013, and underwent initial testing in March 2013. The test structure was mounted on E-Defense's shake table, which is capable of six degree-of-freedom seismic simulations [2]. The structure consists of a four story, asymmetric, reinforced concrete, moment frame with a setback and coupled transverse-torsional motion (Fig. 31.1a). The 690-t superstructure has dimensions of approximately 14 m by 10 m by 15 m and was built to satisfy Japanese design code. As previously detailed, the building sits on a passive base-isolation layer composed of rubber bearings, sliding bearings, passive steel dampers and oil dampers (with solenoids). Tests conducted during a 3-week span in August 2013, on which this study is based, featured the controllable oil dampers acting in a purely passive mode and included both random base motions and historical and synthetic ground motions.

The shake table and structure were extensively instrumented, with numerous quantities and types of sensors that included a substantial number of accelerometers. Accelerometers were placed at 14 locations on the structure, with 3 channels per location, *i.e.*, channels recording in the x, y, and z directions, creating a total of 42 acceleration channels. Fig. 31.1b presents a general floor plan for the sensor locations on floors 1–4, showing the locations of 9 acceleration channels (three tri-directional accelerometers) per floor; there were only 6 acceleration channels on the roof, with sensors at the 1A and 3C locations. In addition, accelerometers were placed on the shake table at 4 locations, with 3 channels at each location, for a total of 12 acceleration channels. All sensors featured a sampling rate of 1 kHz; the signals were passed through a low-pass filter with a cutoff frequency of 35 Hz.

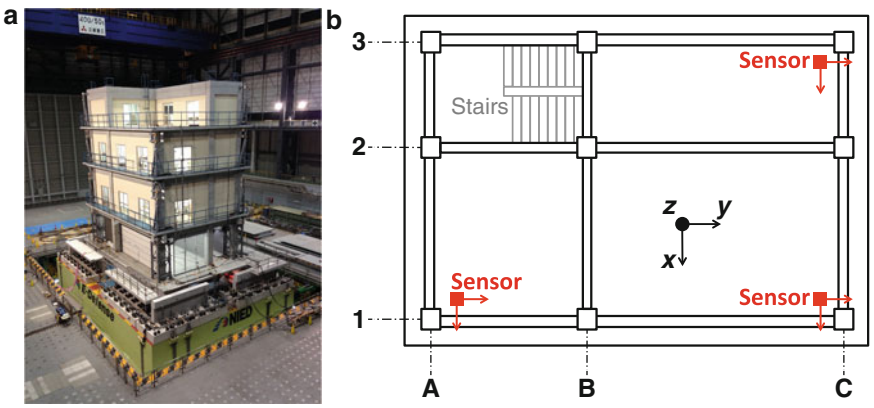

Fig. 31.1 (**a**) Elevation view of E-Defense building used for testing and (**b**) typical floor plan

Table 31.1 Description of tests conducted on 08/08/2013

Test no.	Description
003	Random excitation along *x*-axis
004	Random excitation along *y*-axis
005	Random excitation along *z*-axis
009	Random excitation in Yaw (*xy*-plane)
010	Random excitation in all table DOFs

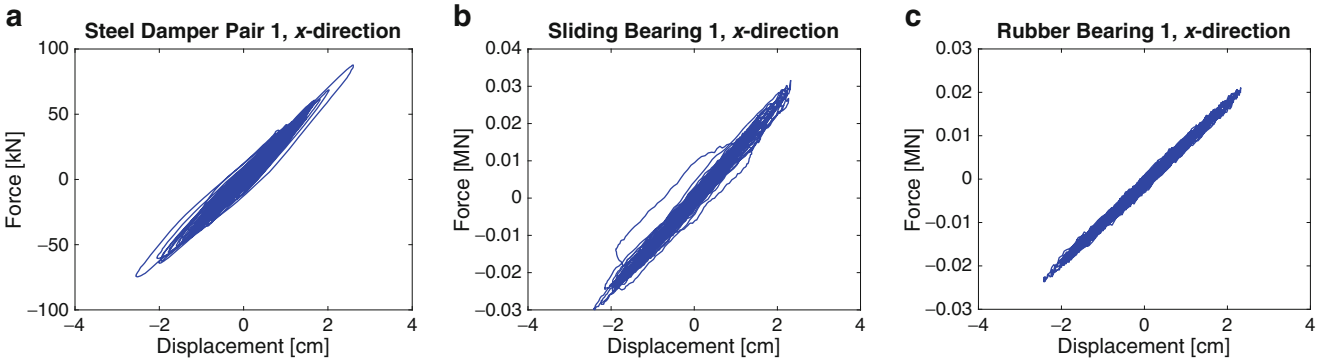

Fig. 31.2 Measured restoring forces in the *x*-direction for (**a**) Steel Damper Pair 1, (**b**) Sliding Bearing 1, and (**c**) Rubber Bearing 1 during random excitation Test 010

Numerous tests were conducted over that 3-week span, but this study focuses exclusively on the first day of testing (8/8/2013). During these tests, the base-isolation layer was configured with two or more of each type of damper, for a total of eight damping devices, *i.e.*, two rubber bearings, two sliding bearings, and two pairs of passive yielding dampers (in each pair, one steel damper is oriented along each horizontal axis); the oil dampers were excluded from these initial tests. The first several tests (Tests 001–012) subjected the building to random excitation along different axes and planes of the shake table's translational and rotational degrees-of-freedom (DOFs). Brief descriptions for tests within the subset considered for this study are shown in Table 31.1. Each test had a duration of 165–170 s.

The instrumentation on the table also included sensors to measure the forces exerted by each isolation device and the displacements across the isolation layer. Measurements taken from the different damping devices showed that the relationships between their restoring forces and displacements remained generally linear throughout the tests with randomized excitations. Sample restoring force–displacement plots are given in Fig. 31.2 for the first (of two) steel damper pair, the first sliding bearing and the first rubber bearing.

31.3 Modeling Approach

The dynamic response of the building was modeled as a multi-input/multi-output (MIMO) system. Since the acceleration responses of the table were recorded, they serve as the inputs for the dynamic system. As mentioned previously, the instrumentation on the table included 12 acceleration channels. The table was assumed to behave in a rigid manner and, as such, could then be modeled using a set of generalized coordinates, namely: 3 translational degrees-of-freedom and 3 rotational degrees-of-freedom. For a test in which each sensor has recorded n samples in time, the relationship between the measured acceleration responses of the table, denoted by $12 \times n$ matrix $\ddot{\mathbf{x}}_{\mathrm{T}}$, and the generalized table acceleration responses $\ddot{\mathbf{q}}_{\mathrm{T}}$ $(6 \times n)$ is shown in Eq. (31.1)

$$\mathbf{T}\ddot{\mathbf{q}}_{\mathrm{T}} = \ddot{\mathbf{x}}_{\mathrm{T}} \tag{31.1}$$

where $\mathbf{T}$ is the 12×6 transformation matrix relating the measured accelerations from the table to their generalized responses. Since this is an overdetermined system, the matrix of generalized table accelerations may be determined in a least-squares sense using the pseudo-inverse of matrix $\mathbf{T}$. The reduction from 12 to 6 inputs was further substantiated by performing a singular value decomposition that revealed six dominant singular values for the original 12 accelerations. The outputs for the dynamic system were the acceleration responses recorded on the structure; all 42 acceleration channels were used.

The outputs could be similarly transformed into generalized accelerations for each floor; however, it was found that, using an approximate transformation, the generalized accelerations did not produce significantly different results during identification.

The superstructure was assumed to behave linearly as a shear structure; combined with the linear behavior exhibited in Fig. 31.2 by the dampers in the isolation layer, this means that the principle of superposition would apply to the dynamic responses. Therefore, the inputs and outputs for the model were created through a superposition of the measurement data from Tests 003, 004, 005 and 009. These tests, and specifically a linear combination thereof, generally covered the expected range of motion for the table and structure. Additionally, the random nature of these inputs helped ensure that all relevant modes of the structure would be excited during identification.

Using the input and output measurements, N4SID seeks to build a state-space model for the system, where Eq. (31.2) shows the typical state-space formulation for a dynamical system

$$\begin{aligned} \dot{\mathbf{X}}(t) &= \mathbf{A}\mathbf{X}(t) + \mathbf{B}\mathbf{U}(t) \\ \mathbf{Y}(t) &= \mathbf{C}\mathbf{X}(t) + \mathbf{D}\mathbf{U}(t) \end{aligned} \tag{31.2}$$

where $\mathbf{X}(t)$ is a vector of the states and $\mathbf{U}(t)$ is a vector of the inputs. Additionally, $\mathbf{A}$ is the state or system matrix, $\mathbf{B}$ is the input or forcing influence matrix, $\mathbf{C}$ is the output matrix, and $\mathbf{D}$ is the feedthrough matrix; together these constitute the state-space matrices. The vector $\mathbf{Y}(t)$ represents the observed or measured response quantities. In this case, the input $\mathbf{U}(t)$ will be the measured table accelerations and the outputs $\mathbf{Y}(t)$ will be the measured structure accelerations. The N4SID algorithm will estimate the state-space matrices that provide the best fit for the given the input and output information.

When estimating these matrices, a model order must be assumed, where the model order is associated with the expected number of states and, therefore, determines the dimensions of the square matrix $\mathbf{A}$, as well as the row and column dimensions of $\mathbf{B}$ and $\mathbf{C}$, respectively. The structure was modeled as a second-order system, meaning that for m degrees-of-freedom the dimension of $\mathbf{A}$ would be $2m \times 2m$. Modal parameters, such as frequencies and damping ratios, are extracted from the complex eigenvalues of the system matrix $\mathbf{A}$, where m modal frequencies and damping ratios would be expected from a matrix $\mathbf{A}$ of dimension $2m$.

31.3.1 Frequency Domain Identification

A model of the dynamical system was created using the estimated transfer functions between the inputs and outputs, as shown in Eq. (31.3), where $j = \sqrt{-1}$ and * signifies a complex conjugate (Hermitian) transpose.

$$H_{ij}(j\omega) = \frac{Y_i(j\omega) \cdot U_j^*(j\omega)}{U_j(j\omega) \cdot U_j^*(j\omega)} \tag{31.3}$$

where $H_{ij}(j\omega)$ is the frequency response function of the jth input and ith output, and $U_j(j\omega)$ and $Y_i(j\omega)$ are the respective Fourier transforms of $U_j(t)$ and $Y_i(t)$ that have been averaged via Hamming windows. In this case, the inputs and outputs were the matrices of inputs $\mathbf{U}_{\text{sup}}(t)$ and outputs $\mathbf{Y}_{\text{sup}}(t)$ created through superposition of the measurement data from aforementioned tests. Using Eq. (31.3), the frequency response functions, or FRFs, were estimated for the 6 generalized inputs and 42 outputs in $\mathbf{U}_{\text{sup}}(t)$ and $\mathbf{Y}_{\text{sup}}(t)$, respectively. These estimated FRFs were used as the model inputs for the chosen identification method, N4SID.

Prior to being input into the N4SID algorithm, the FRFs were further divided by frequency content based on the presence of a few dominant modes with frequencies very close to zero and other dominant modes at frequencies greater than 10 Hz. Given the order of magnitude difference between dominant frequencies, separating the FRFs would allow for the appropriate frequency resolutions to be utilized in each range. The FRFs were divided such that identification would be performed in two parts: on the FRFs from 0 to 9 Hz and on the FRFs from 9 to 35 Hz.

In order to take advantage of the model reduction capabilities of subspace identification, a low-order model was assumed for the structure. For each FRF segment a model order of 12 was assumed, which would provide 6 sets of modal parameters, *i.e.*, modal frequencies and damping ratios, based on the assumption of a second-order system. When the FRF-based model was considered in total, this led to a model order of 24 with a prediction of 12 sets of modal parameters, representing a significant reduction from the original 42 recorded accelerations.

31.3.2 Time Domain Identification

The identification of the structure using time domain information was fairly straightforward as the matrices of inputs $\mathbf{U}_{sup}(t)$ and outputs $\mathbf{Y}_{sup}(t)$ were directly incorporated into the N4SID algorithm. Unlike the frequency-domain data, no transformations or portioning of the data was necessary for identification; however, prior to implementation of N4SID, the accelerations were de-trended, low-pass filtered, and decimated to a reduced sampling rate of 70 Hz. For consistency, a model order of 24 was also assumed.

31.4 Results and Discussion

31.4.1 Identification

It was found during the course of this study that, of the six generalized inputs, only the three translational DOFs were needed for the frequency response models; the inclusion of the three rotational DOFs had a negative impact and led to a larger number of spurious (false) modes and fewer true (structural) modes. However, the amplitudes of motion for the rotational DOFs were quite small and their contribution to the overall motion was likely negligible. As expected, the choice of a model order of 24 produced 12 sets of modal parameters, which are given in Table 31.2.

Sample comparisons of the transfer functions produced by the measurement data and the FRFs produced by the frequency domain model are shown in Fig. 31.3. The plots in Fig. 31.3 show the transfer functions of the generalized inputs in the *x*, *y*, and *z* directions with corresponding outputs from a sensor on the roof in the same general directions, *e.g.*, the transfer function of *x*-directional input to *x*-directional output. The difference in the frequency resolutions used for the two FRF components can be clearly observed in Fig. 31.3, as there is a pronounced change around 9 Hz. The transfer functions in the *x* and *y* directions show large modal peaks just below 1 Hz whose magnitudes are an order of magnitude larger than the other peaks along their frequency ranges. Similarly, the transfer function in the *z* direction shows a few modal peaks between 10 and 25 Hz with a nearly smooth spectrum for frequencies below 10 Hz. This disparity in modal information motivated the decision to divide the FRF into two parts for identification. However, neither component of the FRF managed to find a proper fit for the modal peaks around 5 Hz, which may be clearly seen in the *x*- and *y*-directional plots.

Table 31.2 Modal parameters estimated through frequency domain and time domain identification

Frequency domain identification			Time domain identification		
Mode no.	Frequency (Hz)	Damping ratio (%)	Mode no.	Frequency (Hz)	Damping ratio (%)
1	0.6837	7.095	1	0.6929	9.7469
2	0.7073	8.092	2	0.7256	5.8925
3	0.7544	0.492	–	–	–
–	–	–	3	1.1158	83.2490
4	3.8363	0.963	–	–	–
5	5.1560	1.064	4	5.4167	7.1307
6	7.2162	0.666	–	–	–
–	–	–	5	7.6883	86.4963
7	10.8280	5.895	–	–	–
–	–	–	6	12.0222	26.5799
8	16.8484	3.447	7	15.9520	8.4555
9	17.9120	1.687	8	17.5373	3.6009
–	–	–	9	19.7861	23.8426
10	23.2145	3.654	10	22.7595	4.5942
11	25.1972	1.560	11	24.2137	3.8124
–	–	–	12	26.1671	6.0617
12	28.8780	3.598	13	28.4660	2.4013
–	–	–	14	29.7945	9.6166
–	–	–	15	30.1683	4.7095

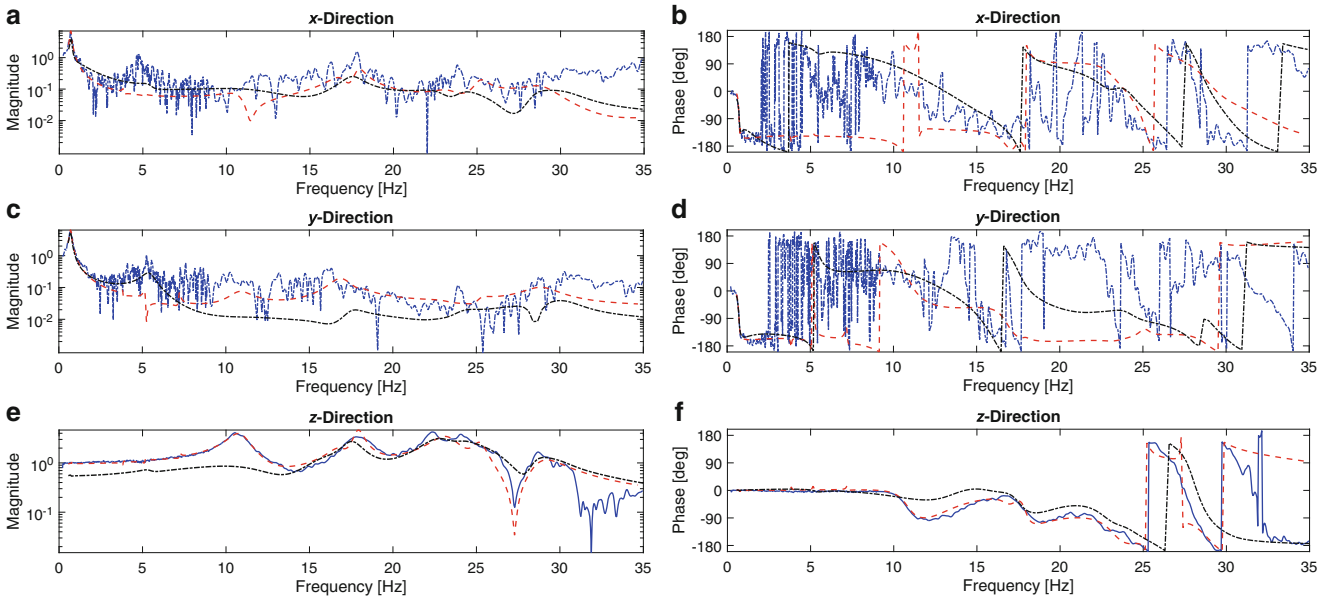

Fig. 31.3 Comparison of measured and model transfer functions between the input and a roof sensor in the (**a**–**b**) *x*-direction, (**c**–**d**) *y*-direction, and (**e**–**f**) *z*-direction (magnitude plots on the left, phase plots on the right). The sold blue lines denote measurement data, dashed red lines the frequency model and black dash-dot lines the time model

Unlike the frequency domain identification, all six generalized inputs were used for the time domain model; the inclusion of the rotational DOFs was found to have a small but net positive effect on the identification results. While a model order of 24 was originally assumed, it was found that the resulting modal parameters included a few false modes. Therefore, the model order was slightly increased to 32, which resulted in 15 sets of modal parameters that still included a few false modes (in addition, 2 of the eigenvalues of **A** were excluded because they were real-valued and, therefore, overly damped). The modal parameters estimated via time domain identification are shown in the columns to the right in Table 31.2; the modes that are likely false can be easily identified by their unreasonably large damping ratios. Excluding the false modes, there is generally good agreement between the frequencies of the frequency-domain and time-domain models. The damping ratios for the first two modes are also comparable, but the time-domain model seems to estimate much larger damping ratios for the remaining modes.

The FRFs from the time-domain model were included in the plots in Fig. 31.3 and comparing these FRFs to those produced by the frequency domain model exposes some of the strengths and weaknesses of each. The time domain model better estimates the intermediate frequencies between 3 and 10 Hz; this may be most clearly seen in the plots for the *y*-directional FRF where the time domain model captures the modal peak around 5 Hz. However, the *z*-directional plot exposes the time domain model's inability to capture some of the higher frequency modes, as it misses the mode at 10 Hz. The FRFs from the frequency-domain model also seem to better capture the higher frequency modes present in the *x*- and *y*-directional FRFs.

Both models were also used to recreate the time histories of the same roof sensors from Fig. 31.3. The responses predicted by the models were compared to the original superposition of measurements and plotted in Fig. 31.4, which shows a 10-second time window for the *x*- and *y*-directional responses and a 2-second window for the *z*-directional response. (Different time windows were chosen owing to the different dominant frequencies present in each response.) These figures show that both models provide reasonably accurate predictions of the responses, sufficiently approximating the dominant frequency components with proper phase. The time-domain model offers a better estimate of the *y*-directional response, but the plot of the *z*-directional response further demonstrates that the time domain model underestimates some of the higher frequencies. The *x*-directional plot appears fairly comparable.

31.4.2 Validation

After demonstrating an ability to provide strong qualitative estimates of the structural responses, the models were validated using the measured table accelerations from Test 010 as inputs. Test 010 involved excitation from all DOFs of the shaker and, thus, represented a strong candidate for validation because the original input, the aggregate result of the superposition of the first few tests, was similarly multi-directional. Additionally, it was expected that the random nature of the input from Test 010 would result in similar modes being excited as during identification.

The validation test data was entered into both models and the structural responses were then estimated; a few of these predicted responses are shown in Fig. 31.5. The responses in Fig. 31.5 are for the same roof sensors shown in Fig. 31.4 and, as was observed during identification, both models present reasonable approximations of the structural behavior. The amplitudes, frequencies, and phases generally match, with the time domain model exhibiting a closer fit to the measured data in the time windows shown for the *x*- and *y*-directional responses. As before, the time domain model demonstrates a rather persistent underestimation of the amplitudes for the response in the *z* direction. These plots demonstrate that either model could be used to predict the structural responses for an unknown random input, but that the choice of either model should be influenced by the targeted modal frequency range.

It is likely that a portion of the inaccuracy in the predicted responses is due to the model reduction. Table 31.2 demonstrated that some of the identified modes from the time-domain model were not truly structural modes, and Fig. 31.3 showed that the frequency-domain model did not fully capture each and every mode. However, the effect of model reduction does not seem to greatly diminish the qualitative results of the model.

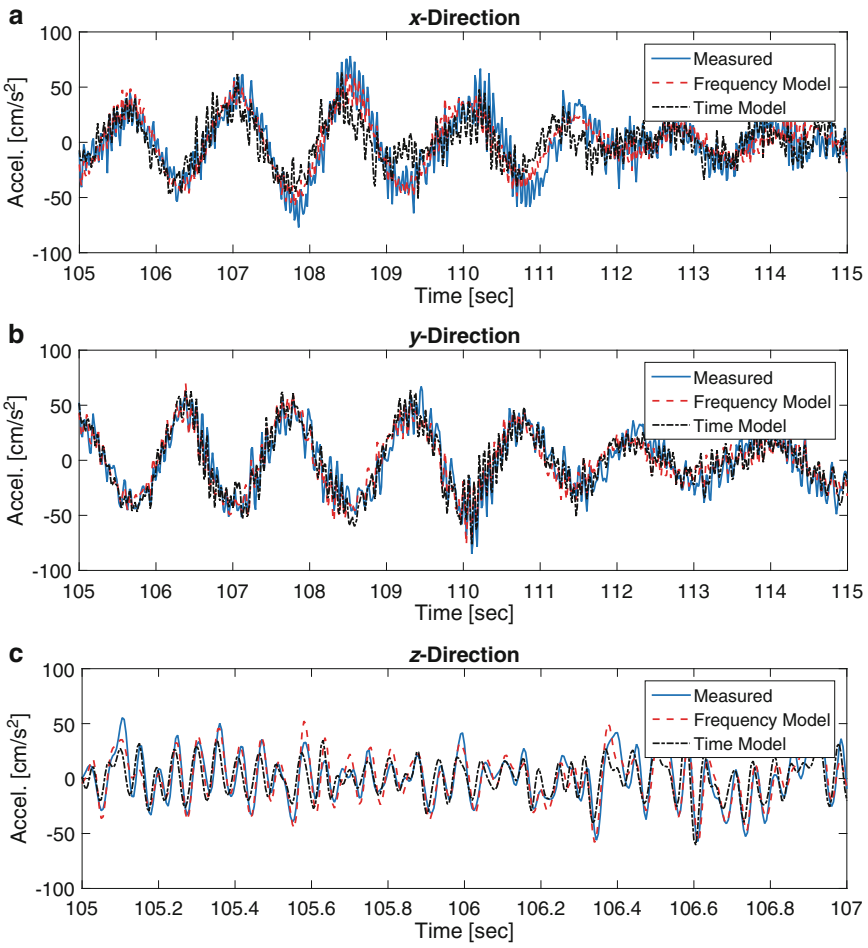

Fig. 31.4 Comparison of measured and model-predicted responses for roof sensors in the (**a**) *x*-direction, (**b**) *y*-direction, and (**c**) *z*-direction using the test data created through superposition

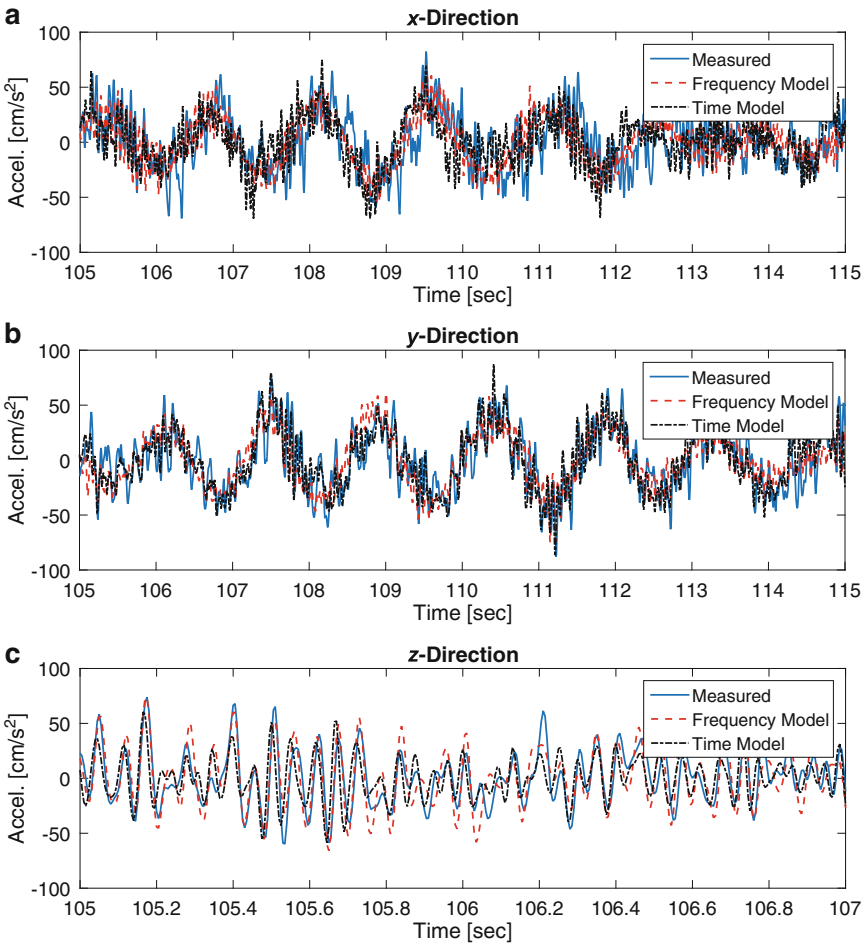

Fig. 31.5 Comparison of measured and model-predicted responses for roof sensors in the (**a**) *x*-direction, (**b**) *y*-direction, and (**c**) *z*-direction using validation measurement data from Test 010

31.5 Conclusions

Reduced-order models were created using time-domain and frequency-domain experimental measurement data. The data used for identification was produced through superposition of a series of tests that subjected the test structure to random excitation along different axes and planes of the shake table. The resulting frequency-domain model displayed an ability to capture the major features of the structure, such as the dominant modal peaks below 1 Hz and the numerous modes above 10 Hz, but failed to properly include the modal information in the 3–9 Hz range. The time-domain model provided better results for the lower frequency modes (those below 10 Hz) but did not fully incorporate the higher frequency modes. Considering the relative strengths, and weaknesses, of each, both models produced reasonable response approximations when validated using a random input from a test not included during identification.

These results, while preliminary, imply that reduced-order modeling for a full-scale base-isolated structure is possible, given that the behavior and responses are confined to the linear range. While the reductions in model order likely influenced the model's accuracy, the qualitative predictions of the structural responses were high enough in quality to gauge the general behavior of the structure, proving the usefulness of the reduced-order model. Subsequent studies will focus on the performance of these models as the restoring forces in the isolation layer of this structure begin to enter the nonlinear range. This study also demonstrates that both time domain and frequency domain identification may be necessary for capturing the full complement of structural modes. It is suggested that future studies look into further developing a more seamless fusion of the time-frequency data.

Acknowledgments This material is based upon work supported by the National Science Foundation under Grant CMMI 13-44937; any opinions, findings, and conclusions or recommendations expressed in this material are those of the authors and do not necessarily reflect the views of the National Science Foundation. The first author gratefully acknowledges the support of the Viterbi Postdoctoral Fellowship from the University of Southern California.

References

1. Furukawa, T., Ito, M., Izawa, K., Noori, M.N.: System identification of base-isolated building using seismic response data. ASCE J. Eng. Mech. **131**, 268–275 (2005)
2. Sato, E., Sasaki, T., Fukuyama, K., Tahara, K., and Kajiwara, K.: Development of Innovative Base-Isolation System Based on E-Defense Full-Scale Shake Table Experiments Part I: Outline of Project Research, pp. 751–752. AIJ Annual Meeting, Hokkaido, Japan (2013) (in Japanese)
3. Ljung, L.: System Identification: Theory for the User. Prentice Hall, Upper Saddle River (1999)
4. Van Overschee, P., De Moor, B.: Subspace Identification for Linear Systems: Theory, Implementation, Application. Kluwer, Dordrecht (1996)
5. Van Overschee, P., De Moor, B.: N4SID: Subspace algorithms for the identification of combined deterministic-stochastic systems. Automatica **30**, 75–93 (1994)
6. McKelvey, T., Akçay, H., Ljung, L.: Subspace-based multivariable system identification from frequency response data. IEEE Trans. Autom. Control **41**(7), 960–979 (1996)
7. Van Overschee, P., De Moor, B.: Continuous-time frequency domain subspace system identification. Signal Process. **52**, 179–194 (1996)
8. Qin, S.J.: An overview of subspace identification. Comput. Chem. Eng. **30**, 1502–1513 (2006)

Chapter 32
The Use of OMA for the Validation of the Design of the Allianz Tower in Milan

Elena Mola, Franco Mola, Georgios Stefopoulos, Carlo Segato, and Chiara Pozzuoli

Abstract Future headquarter of an insurance company, the Allianz Tower is a 202 m high, 52-storey building currently topped out and belonging to the large CityLife development in Milan, Italy. The architectural design concept, by Arata Isozaki, is that of a slender, streamlined machine-building, with exposed structural and functional systems. The very significant slenderness and the intrinsic damping properties of the Tower make lateral and torsional response due to wind actions not negligible for structural analysis and occupant comfort. To mitigate these effects eight external viscous dampers were designed, and located at the base of four steel "struts", stemming out of the surrounding plaza and podium at the base of the tower and connected to its main cores at the 11th floor. The design of the dampers and of the struts required refined analyses to be carried out. At the end of construction, two sets of Operational Modal Analysis (OMA) tests were carried out on the building, with and without dampers, to validate the design and construction process. Moreover, given the importance of the building, the Tower was equipped with a state-of-the-art continuous monitoring system acquiring data on all of the relevant structural and functional parts, including the dampers. The present paper will present the main structural features of the Tower, the main features of the design of the damping devices for wind comfort, the test set up for the dynamic OMA tests, followed by a discussion of their results.

Keywords Operational modal analysis • Tall building • External dampers • Model tuning

32.1 Introduction

In Italy, dynamic tests on buildings are not explicitly required by the current Building Code, i.e. NTC 2008, [1]: the Code only states that for 'strategically relevant' bridges and flyovers, some kind of dynamic testing is required in addition to traditional static load tests. Nevertheless, for important buildings, and tall buildings in particular, it is widely accepted by practitioners and contractors alike that dynamic tests are a very valuable source of information that cannot be derived from any other kind of test. In fact, by means of experimental or operational modal analysis, experimental evidence of the global behavior of the structure is obtained, in particular as for seismic and wind excitation response, the dynamic properties of the building are measured, in terms of frequencies and mode shapes, and compared to those derived from numerical analysis. Through this process, numerical models are validated and a benchmark for continuous monitoring activity is obtained, so that maintenance operations can be planned and decisions about the operability of the building can be quickly made in the aftermaths of exceptional events. Because dynamic tests provide such valuable information, in the case of tall buildings, which are important and expensive structures, in Italy they are normally prescribed by the Owner or by the project Validator so that they become a necessary pre-requisite in order for the design and construction process to be validated, even if they are not mandatory according to the Italian Building Code.

E. Mola (✉) • G. Stefopoulos
ECSD Srl, Via Carlo Goldoni, 22, Milan 20129, Italy
e-mail: elena.mola@ecsd.it

F. Mola
Politecnico di Milano, Piazza Leonardo da Vinci, 32, Milan 20133, Italy

C. Segato
P. Structural Engineer, Milan, Italy

C. Pozzuoli
Unit 1 Tilers Road, Milton Keynes, Buckinghamshire MK11 3LH, UK

S. Pakzad, C. Juan (eds.), *Dynamics of Civil Structures, Volume 2*, Conference Proceedings of the Society for Experimental Mechanics Series, DOI 10.1007/978-3-319-29751-4_32

This was the case for the Allianz Tower: both the project Validator and the Owner agreed on the opportunity of carrying out dynamic tests at the end of construction: it was decided to use the Operational Modal Analysis method, so that only the environmental excitation would be exploited to derive the modal properties, with no need to move and install large tools at the top of the building to provide additional forcing, which would have been required for Experimental Modal Analysis, [2].

The results of the dynamic tests were used to validate the finite element model of the building that had been implemented in the structural analysis software MidasGen. Moreover, since a peculiar architectural and functional feature of the Allianz Tower remains in the external viscous dampers at the base of the struts, which are designed to provide additional damping under wind loads, i.e. in service life conditions, for very low levels of vibration, the OMA tests in this case also provided insight on the actual efficiency of those devices: the tests were carried out before and after the installation of the dampers, so that it was possible to experimentally derive the modal damping in service life conditions with and without the contribution of the dampers, thus obtaining important data for the validation of their design and installation process.

32.2 Description of the Structure

The Allianz Tower occupies the center of the redevelopment site of the former exhibition center in Milan, called CityLife, in front of the building that housed the old Sports Palace, which overlooks Viale Boezio. The building, which is going to be used as the headquarters offices of Allianz in Italy, has a height of 202 m above the ground level of the main plaza and 207 m above the street level. Below the ground level, one underground level connects the tower with the underground shopping area as well as the metro station, and two other underground levels are devoted to mechanical use (Fig 32.1).

Fig. 32.1 (**a**) Masterplan of the CityLife Development; (**b**) Architectural rendering of the three CityLife Towers (Allianz Tower is on the right), (**c**). The topped-out Allianz Tower

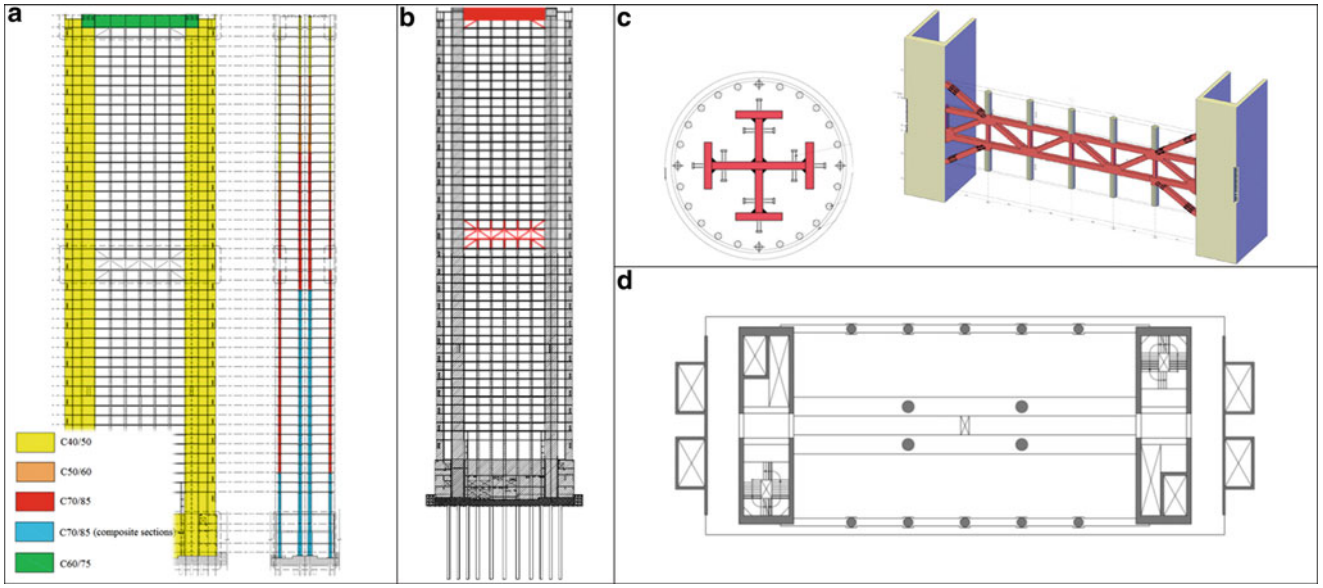

Fig. 32.2 (**a**) Scheme of the concrete classes used for the structural elements of the Allianz Tower, (**b**) FE model highlighting the belt trusses (**c**) Typical cross-section of the composite columns at the lower levels and view of the steel belt-truss, (**d**) Typical plan of the Allianz Tower

The structural system is composed of two main reinforced concrete cores, with a wall thickness varying from 120 to 40 cm, located on the North and South sides of the tower; two outrigger structures, called belt-trusses, connect the two cores. The first belt truss is a two-storey high steel truss structure placed mid-height, i.e. between Levels 23 and 26, whereas the second one is a prestressed reinforced concrete wall beam, placed at the top of the building, i.e. between Levels 49 and 50. Finally, four external steel struts, covered in golden paint, jutting out of the building at mid-height, connect it to the ground, at the top of the podium: at the base of each strut, two two-way viscous dampers are installed, which help to mitigate the effects of the resonant component of the wind excitation, thus improving the comfort of the building.

The columns have circular sections, with diameters ranging from 170 to 65 cm. Up to Level 4 for the external columns, and up to Level 21 for the internal ones, the vertical elements are composite steel-concrete columns, having a circular reinforced concrete section with a composed cross-shaped steel section inside. The decks are 20 cm thick, cast-in-situ reinforced concrete slabs supported by T-beams, having a depth of 45–50 cm. In Fig. 32.2, some details of the structural design of the building are provided: a typical floor plan, the scheme of the concrete classes used for the structural elements and a view of the composite cross section of the columns at the lower levels.

32.3 Modeling and Analysis

32.3.1 Modeling Assumptions

The dynamic properties of Allianz Tower were numerically analyzed by means of a finite element (FE) model which was developed using the commercial software for structural analysis MidasGen 2012 V3. Since the main purpose of this model is to provide a numerical counterpart for the experimental results of the operational modal analysis, great care was taken in accurately replicating the actual longitudinal and transverse geometry of the structure and its loads and boundary conditions at the time of the dynamic tests.

The FE model itself is made of 12,000 linear elements, which are mostly used to represent the columns, the belt trusses and some secondary elements, and 105,000 plate elements, which were used to model not only the decks and the concrete cores, but the T-beams of the decks as well.

This modeling choice for the beams proved to yield more accurate results with respect to more simplified models that had been implemented as a benchmark: due to the fact that the depth of the beams is only 0.5 m, i.e. not far from the depth of the slabs, which is 0.2 m, and because the spans are significant, in the range of 6–8 m, the global behavior of a single floor is very close to that of a bending membrane plate, which is better approximated with the use of plate elements for both the

beams and the slab. Due to the slenderness of the structure and of the slabs, no floor diaphragm constraint was applied for the floors, which can freely bend and deform out of plane.

As for the eigenvalue analysis itself, the calculation of eigenvectors was carried out by the method of Lanczos and, for all the elements of the structure, the geometry of the gross cross section was considered, since the structure is expected to behave elastically under the low dynamic loads provided by the environmental excitation. The composite sections of the columns of the first floors was represented in the model with homogenized sections with respect to their bending moment stiffness (EI). Finally, an eigenvalue analysis was carried out for both the building with and without the struts and the dampers. . Due to the negligible effect of the struts on global stiffness and mass of the building, the results of the eigenvalue analysis, in terms of frequencies and mode shapes, were identical for both cases, as expected.

The same model was used to carry out a dynamic response spectrum analysis (Fig. 32.4a). The spectra used for the analysis are specifically derived for slender building, i.e. for periods larger than 4 s, Fig. 32.4b and the damping values used were those compatible with a very streamlined tall building, i.e. 1 % for all the modes, instead of 5 %. The expected low values of inherent damping were then increased by introducing the additional damping contribution that the dampers were designed to provide, i.e. a nominal additional damping of 9 % on the first and on the third mode. As further detailed in the following, one of the results of the dynamic tests was to confirm the estimation both of the inherent and of the additional damping, thus validating the design and installation of the dampers themselves.

32.3.2 Eigenvalue Analysis Results

In the following, the frequencies and mode shapes obtained from the numerical model are reported. In Fig. 32.3, the first 12 mode shapes are represented, whereas in Table 32.1, the modal masses, frequencies and periods are summarized. Only the results pertaining to the configuration without struts and dampers are reported, since, as discussed before, the results of the analysis on the final configurations are not affected by the presence of the struts and dampers, which provide only negligible contributions in terms of additional mass and stiffness. From Fig. 32.3 and Table 32.1, it can be noted that the first mode is mostly flexural along the weak axis of the building, the second mode is mostly flexural along the strong axis, whereas the third mode is mostly torsional. Since the building is very slender in the weak direction, it is particularly sensitive to the across-wind effects when the wind blows along the long side of the building; also, the sensitivity to wind loads along the weak axis is enhanced by torsional effects, which are evident already in the third mode.

32.4 Experimental Analysis

32.4.1 Description of the Tests

The experimental tests were carried out according to the Operational Modal Analysis method, both before and after the installation of the viscous dampers. In both cases, the accelerations due to environmental excitation were continuously acquired for 3.5 days, with a sampling frequency of 20 Hz, and averaged over 3-h windows.

The test set-up consisted of 30 horizontal accelerometers, measuring X- and Y-direction acceleration, according to the reference system in Fig. 32.5 vertical accelerometers, measuring Z-direction accelerations. The location of the sensors is reported in Fig. 32.5, represented the plan configuration of the typical instrumented floor. The same configuration was replicated for all the instrumented floors, i.s. Levels 12, 24, 33, 42, 49.

The accelerometers used for the tests were PCP Piezotronics sensors having high sensitivity (10 V/g) and antialiasing filters. The wind speed was also measured by means of an anemometer directed along the X direction, according to the reference of Fig. 32.5.

The data were analyzed by means of the Polymax algorithm, [3], implemented into an in-house software owned by the Company who carried out the tests, which automatically chooses the best averaging windows to minimize bias to the data due to the presence of workers or other accidental forcing sources.

The PSD (Power Spectral Density) plots for some of the sensors are reported in Fig. 32.6a.

In order to increase the reliability of the estimated modal properties, cross-correlation was checked between all the computed modes up to 5 Hz, by calculating the values of the AutoMAC index, as exemplified in Fig. 32.6b, showing the results for Mode 1.

Fig. 32.3 Mode shapes of the first 12 vibration modes of the Allian Tower, as derived by eigenvalue analysis

Table 32.1 Frequencies, periods and modal mass values for the first 20 vibration modes of the Allianz Tower

	Frequency		Period	TRAN-X		TRAN-Y		TRAN-Z	
Mode no	(rad/s)	(cycle/s)	(sec)	MASS (%)	SUM (%)	MASS (%)	SUM (%)	MASS (%)	SUM (%)
1	1.26	0.20	5.00	66.28	66.28	0.01	0.01	0.00	0.00
2	1.39	0.22	4.51	0.01	66.29	57.85	57.86	0.00	0.00
3	2.79	0.44	2.25	0.00	66.29	0.00	57.86	0.00	0.00
4	4.39	0.70	1.43	10.21	76.49	0.00	57.86	0.00	0.00
5	7.00	1.11	0.90	0.00	76.49	19.03	76.89	0.00	0.00
6	9.86	1.57	0.64	5.26	81.76	0.00	76.89	0.00	0.00
7	9.96	1.58	0.63	0.00	81.76	0.00	76.89	0.00	0.00
8	15.90	2.53	0.40	2.53	84.29	0.02	76.91	0.00	0.00
9	16.47	2.61	0.38	0.01	84.30	6.59	83.50	0.00	0.00
10	17.67	2.81	0.36	0.00	84.30	0.00	83.50	58.53	58.54
11	21.32	3.39	0.29	0.00	84.30	0.00	83.51	0.00	58.54
12	21.52	3.43	0.29	0.37	84.67	0.00	83.51	0.00	58.54
13	23.77	3.78	0.26	1.93	86.60	0.00	83.51	0.01	58.54
14	24.38	3.88	0.26	0.00	86.60	0.00	83.51	15.49	74.03
15	26.03	4.14	0.24	0.00	86.60	0.00	83.51	0.02	74.05
16	27.01	4.30	0.23	0.00	86.60	3.18	86.69	0.00	74.05
17	27.49	4.38	0.23	0.00	86.60	0.01	86.70	0.01	74.06
18	29.99	4.77	0.21	0.66	87.26	0.00	86.70	0.00	74.06
19	31.19	4.96	0.20	0.00	87.26	0.00	86.70	0.00	74.06
20	31.25	4.97	0.20	0.00	87.26	0.00	86.70	0.00	74.06

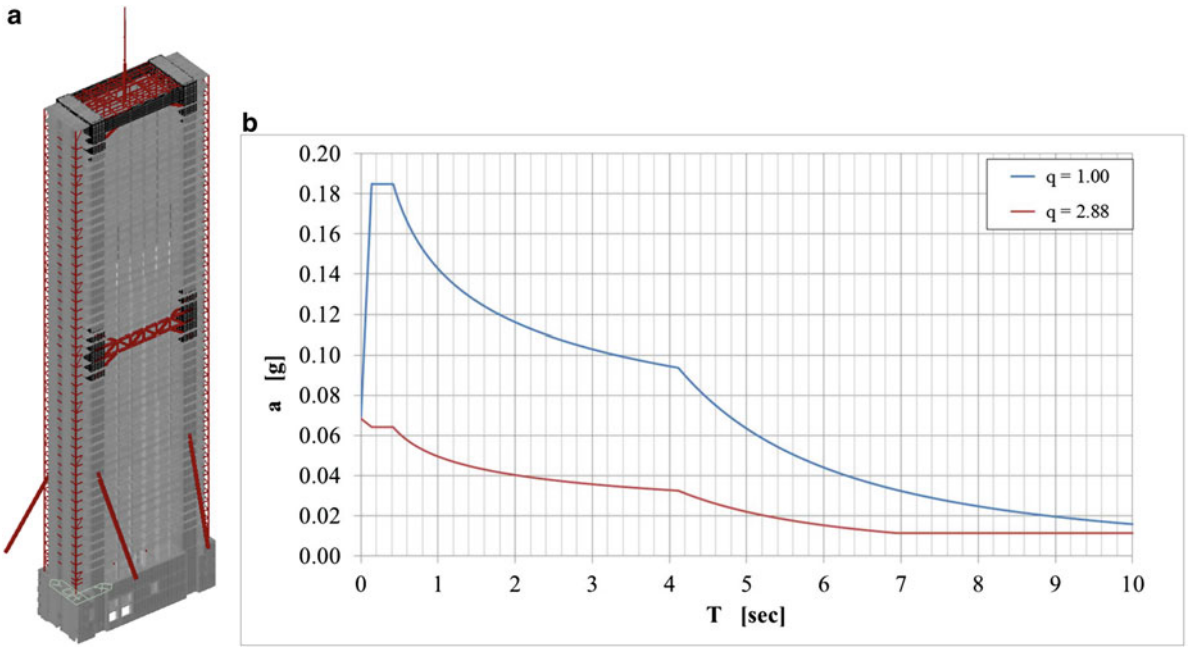

Fig. 32.4 **(a)** Finite element model of the Allianz Tower for eigenvalue and response spectrum analysis; **(b)** Site-specific, long-period response spectrum used for the analysis

32.4.2 Test Results and Comparison with Numerical Analysis

The experimentally derived frequencies and modal damping values are reported in Table 32.2, together with the frequencies derived from the numerical model, for the modes that were identified: the numbering of the mode sequence is that of the experimental measures, but in brackets the numbering corresponding to the sequence of the eigenvalue analysis is also provided. In Figs. 32.7, 32.8 and 32.9, the experimental mode shapes of the identified modes are plotted together with the

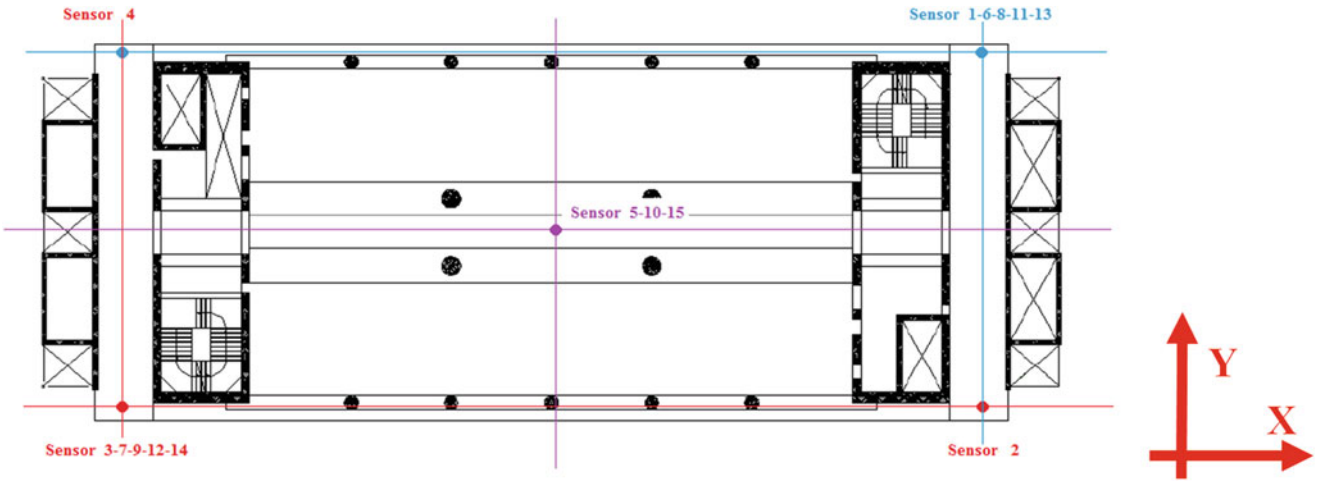

Fig. 32.5 Test set-up: location of the sensors on the typical instrumented floor

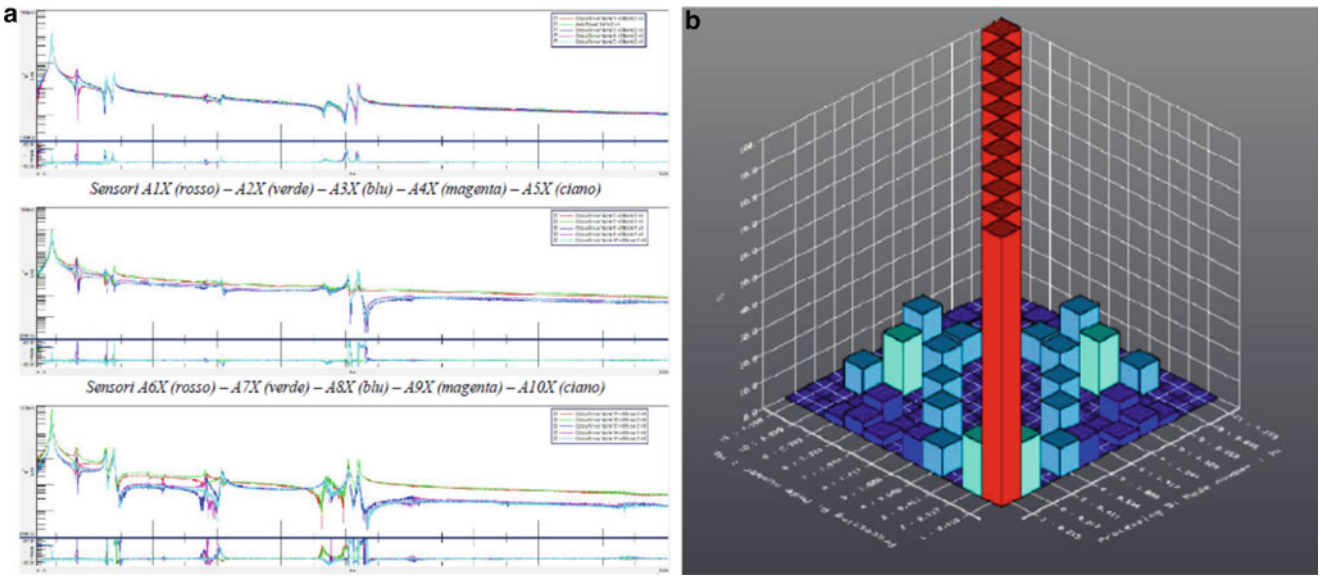

Fig. 32.6 (**a**) PSDs for sample channels; (**b**) AutoMAC matrix

Table 32.2 Experimental and numerical frequencies and experimental damping estimates for the identified modes

Experimental mode # (numerical mode #.)	Frequency [Hz] (Exp.)	Frequency [Hz] (Num.)	Num. Freq./Exp. Freq.	Damping [%] (Exp.)
Mode N.1 (N.1)	0.215	0.20	0.93	0.50
Mode N.2 (N.2)	0.217	0.22	1.01	0.48
Mode N.3 (N.3)	0.411	0.44	1.07	0.35
Mode N.4 (N.4)	0.696	0.70	1.005	0.30
Mode N.5 (N.5)	1.006	1.11	1.10	0.52
Mode N.6 (N.7)	1.417	1.58	1.11	0.30
Mode N.7 (N6)	1.544	1.57	1.02	0.34
Mode N.8 (N.9)	2.329	2.61	1.12	0.60
Mode N.9 (N.8)	2.353	2.53	1.07	0.24
Mode N.10 (N.11)	3.035	3.39	1.1	0.29

mode shapes derived from the numerical analyses for the first 9 identified modes. In order to meaningfully compare the mode shapes and to plot the values, the values of the eigenvectors from the numerical model were computed at the exact locations were the accelerometers were installed.

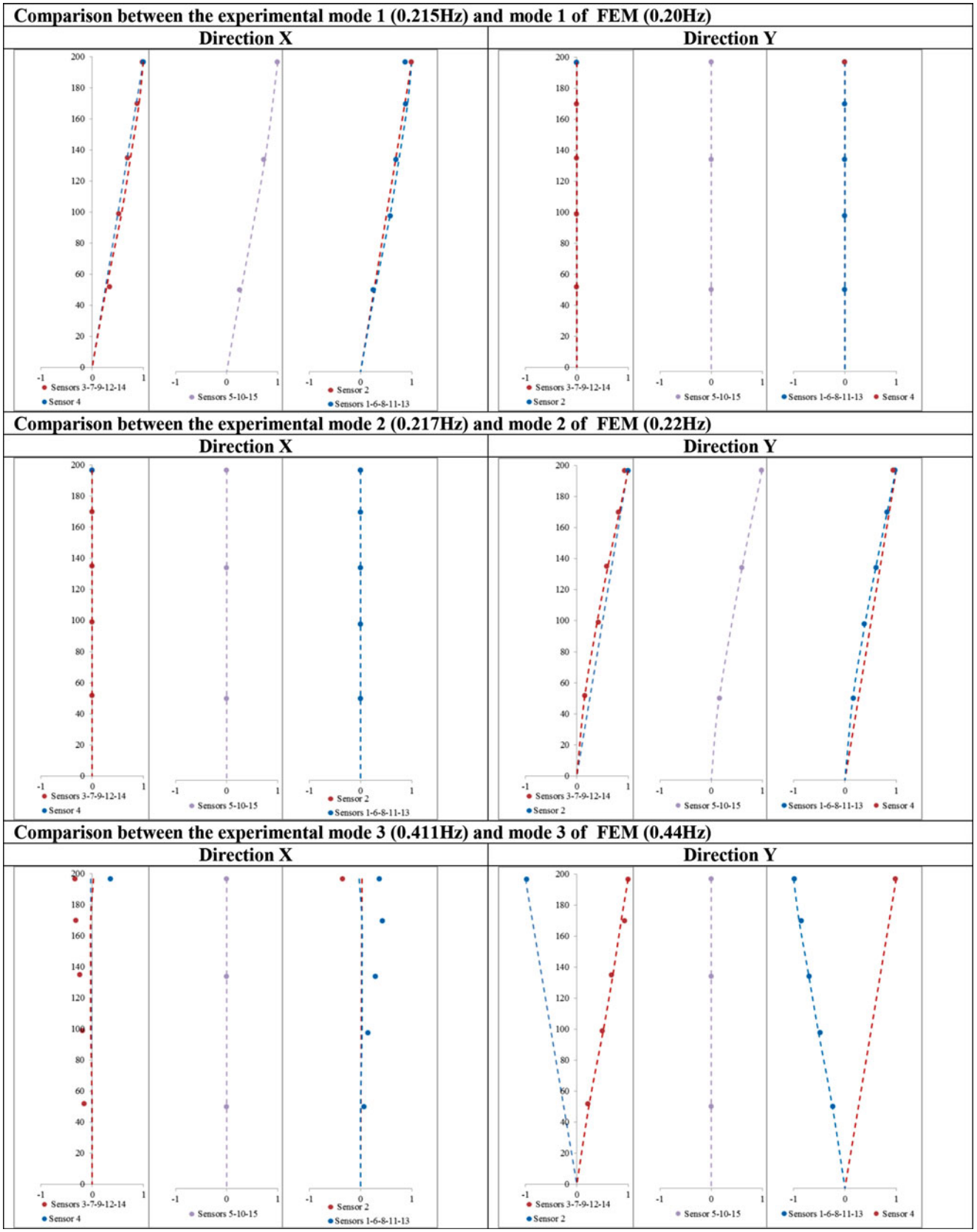

Fig. 32.7 Plots of the experimental mode shapes compared to the numerical ones for Mode N.1., Mode N.2, Mode N.3

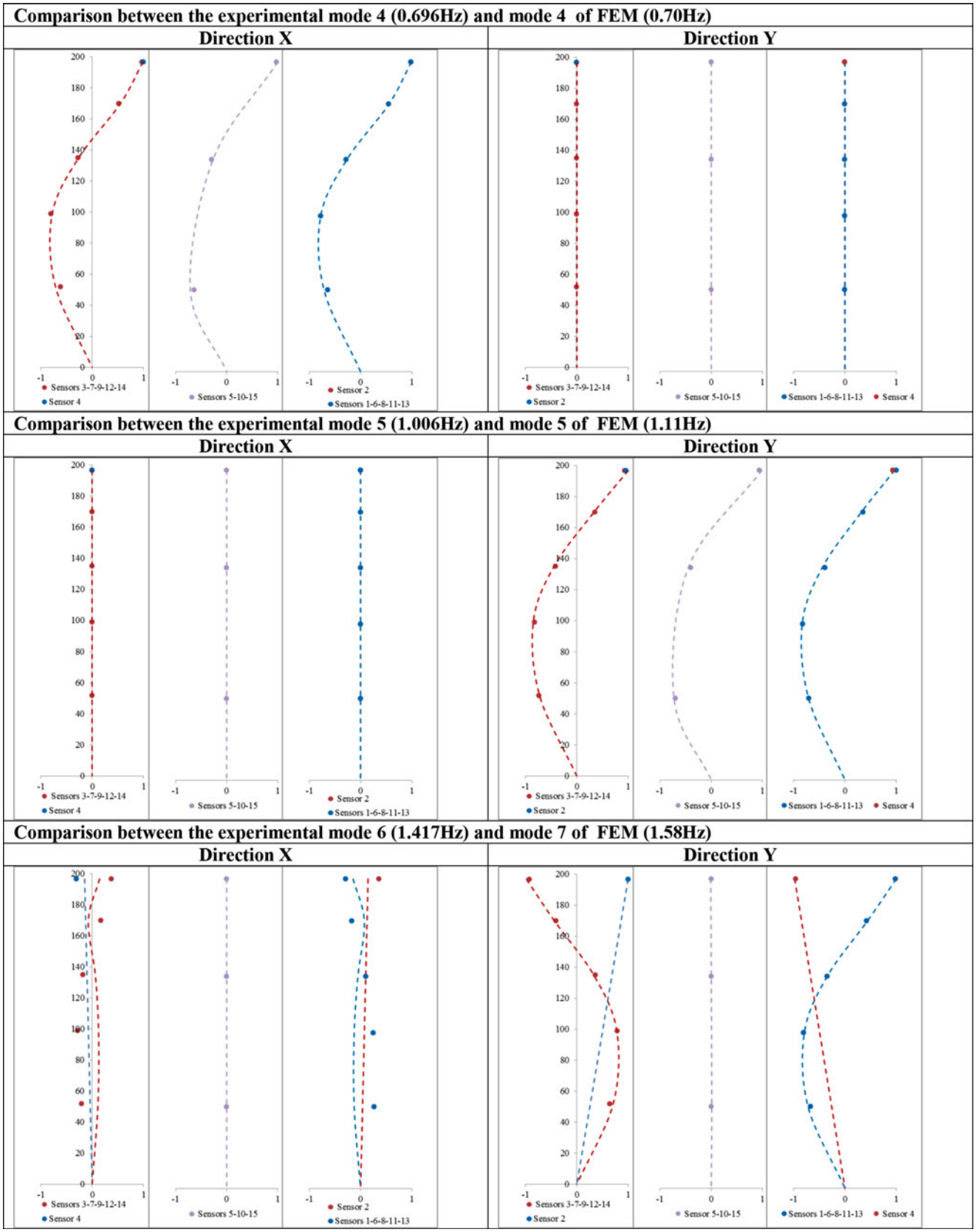

Fig. 32.8 Plots of the experimental mode shapes compared to the numerical ones for Mode N.4., Mode N.5, Mode N.6

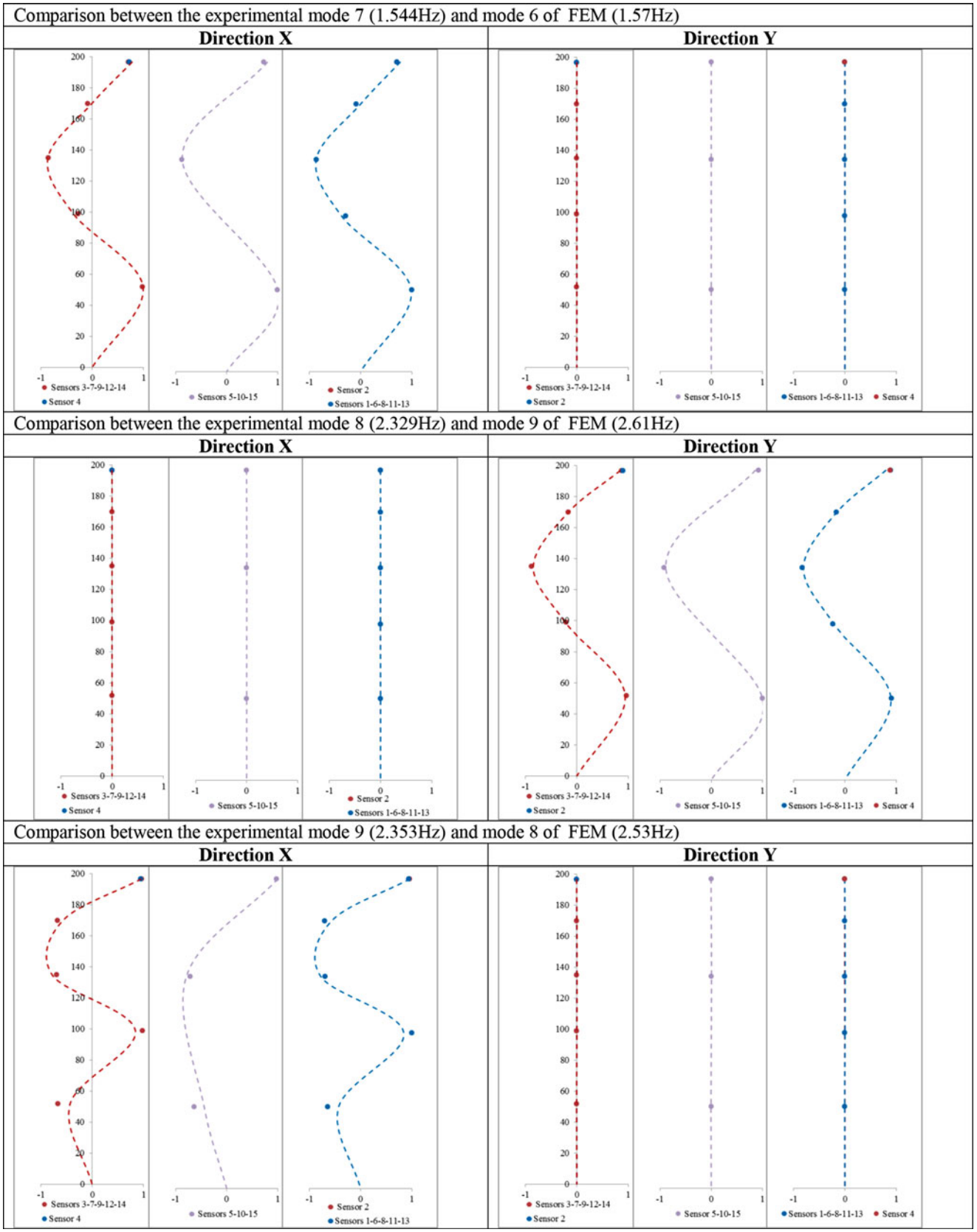

Fig. 32.9 Plots of the experimental mode shapes compared to the numerical ones for Mode N.7., Mode N.8, Mode N.9

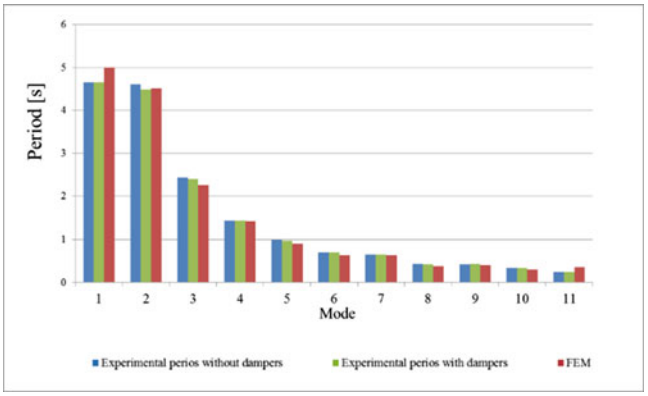

Fig. 32.10 Synoptic comparison of periods for the identified modes: OMA tests without dampers (*blue plot*), OMA test with dampers (*green plot*), numerical analysis (*red plot*)

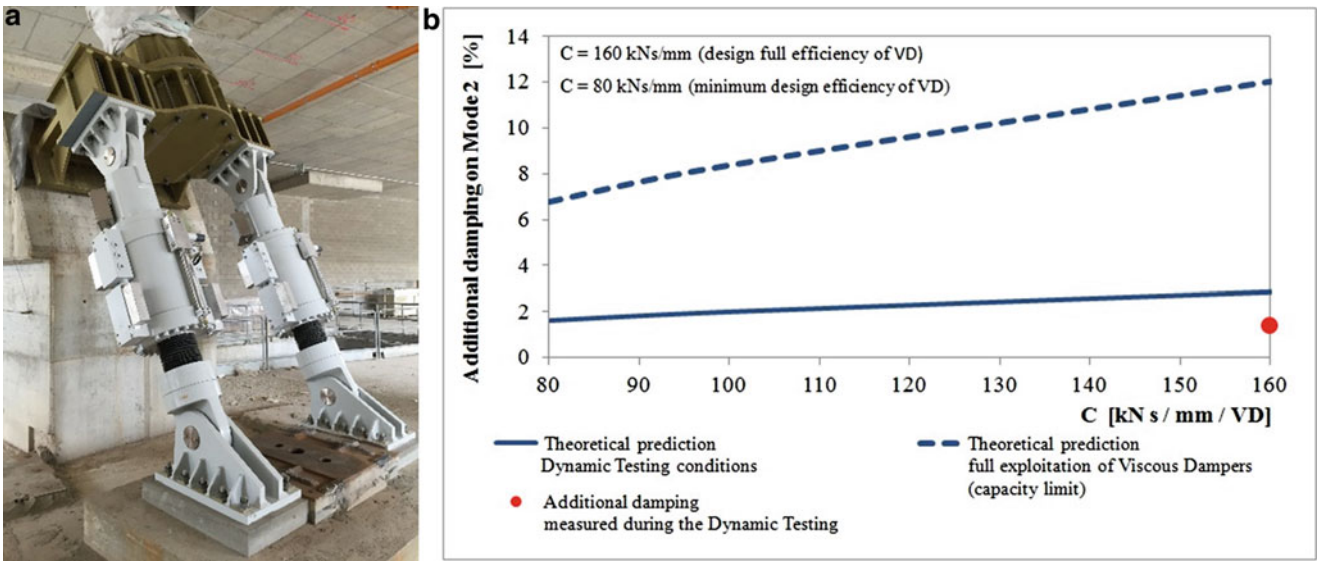

Fig. 32.11 (**a**) Dampers installed at the base of the struts of the Allianz Tower; (**b**) Plots of the theoretical expected behavior of the dampers

In Fig. 32.10, the values of frequencies identified during the tests without dampers are plotted again and compared to those derived from numerical analysis and those identified during the tests with dampers: it can be noted that the presence of the dampers does not significantly affect the frequencies, as expected and as predicted by the numerical analyses.

From Table 32.2 and Figs. 32.7, 32.8 and 32.9, a very good agreement between the prediction of the numerical model and the experimental results can be observed: the maximum difference between the frequencies is 12 % for Mode N.8. For all the modes but Mode N.1, the numerical frequencies are slightly higher than the experimental ones, since the model was implemented using un-cracked gross sections for all the elements. The numerically derived eigenvectors are highly coherent with the values derived from the experiments, at the locations of the sensors, and for all the identified modes.

32.4.3 Damping Estimation with and Without Additional Dampers

As discussed above, the OMA tests in the two configurations were useful to validate the design and installation process of the dampers, represented in Fig. 32.11a, and to gauge their efficiency in service life conditions, for very low levels of vibration.

The modal damping estimations provided by the tests with the dampers are reported in Table 32.3 and compared to those obtained in the configuration without dampers, which had already been reported in Table 32.2. It can be observed that the dampers increase the modal damping for Mode N.2 and Mode N.3 by 3.1 times and 2.9 times respectively. These

Table 32.3 Experimental modal damping estimates in the configuration with and without dampers

Exp. mode #	Damping [%] (No dampers)	Damping [%] (with dampers)
Mode N.1	0.50	0.58
Mode N.2	0.48	1.50
Mode N.3	0.35	1.03
Mode N.4	0.30	0.40
Mode N.5	0.52	0.77

estimations proved that the design pre-requirements, i.e. for the dampers to contribute to the damping of selected modes only, i.e. Mode N.2 and Mode N.3, were achieved. Also, in Fig. 32.11b, the plots representing the theoretical behavior curves for the dampers are reported. On the vertical axis, the theoretical additional damping on Mode N.2 is plotted vs the values of the C constant defining the different operational conditions of the dampers: the dotted line refers to the prediction of the additional damping for the dampers in test conditions; from the latter, it can be noted that the theoretical predicted value for $C = 160$ [kNs/mm/VD] is very close to the actual measured performance point in tests conditions, represented by the red dot.

By means of these remarks, an additional validation of the damping device was achieved: the devices had already undergone extensive laboratory tests according to the requirements of European Standards for fatigue and cyclic loading, but the OMA tests offered the unique opportunity to have an insight on their operational behavior, once installed on site.

32.5 Conclusions

The Operational Modal Analysis carried out on the recently topped-out Allianz Tower in Milan proved to be an effective tool to validate the design and construction process.

Experimental tests were carried out in two different configurations, with and without external viscous dampers, which have been designed to mitigate wind effects in service life conditions, thus allowing a better insight on the operational behavior of the devices to be achieved.

The experimentally derived modal properties are in very good agreement with the ones derived by numerical analysis, both in terms of frequency, mode shapes and sequence of modes, with the largest frequency difference being well under the 10 % threshold for most of the identified modes. These results allowed a validation of the finite element model to be achieved and a reliable benchmark to be obtained for the actual continuous monitoring activity, which will allow to efficiently schedule ordinary maintenance activities and to promptly decide on the operability of the building in the aftermath of unexpected events.

References

1. Consiglio Superiore dei Lavori Pubblici, Nuove Norme Tecniche per le Costruzioni, D.M. 14-01-2008, Roma, Italy, 2008 *(in Italian)*
2. Cigada, A., Mola, E., Mola, F., Stella, G., Vanali, M.: Dynamic behavior of the palazzo Lombardia tower: comparison of numerical models and experimental results. J. Perform Constr. Fac. **28**(3), 491–501 (2014)
3. Peeters, B., Van Der Auwerarer, H., Guillaume, P., Leuridan, J.: The Polymax frequency-domain method: a new standard for modal parameter estimation? Shock Vib. **11**(3–4), 395–409 (2004)

Chapter 33
Transfer Length Probabilistic Model Updating in High Performance Concrete

Albert R. Ortiz, Ramin Madarshahian, Juan M. Caicedo, and Dimitris Rizos

Abstract A High Strength Reduced Modulus High Performance Concrete (HSRM-HPC) is being developed for the construction of railroad ties. This new material has the potential to produce ties with a longer life span than those built from traditional concrete because the reduced Young's modulus could avoid stress concentrations. Railroad ties are commonly fabricated as prestressed concrete elements. The transfer length is an important parameter on these structural elements because the rail is placed toward the ends of the element. This paper uses Bayesian model updating to infer the transfer length with limited experimental data from a test performed in one prestressed beam. The material characteristics, experimental setup, and transfer length model are described in detail. Results show histograms of the transfer length obtained from the models considered.

Keywords Railroad ties • Prestressed concrete • Model updating • Transfer length

33.1 Introduction

The transfer length is a parameter that strongly affects the performance of railroad ties. Many train derailing have occurred because of tie failures. Famous cases are Home Valley, WA on April 3 of 2005 and Sprague, WA on January 28 of 2006 [1]. Common problems of railroad ties are a decreased strength of the concrete, a larger transfer length than specified, and corrosion affecting steel and concrete [2, 3]. Although the modeling of transfer length in prestressed concrete has been widely studied, there has been not much research conducted focusing on railroad ties, where this is a critical condition given the reduced span length [4].

This paper applies a probabilistic approach for comparing models of the transfer length. The probabilistic method is based on Bayesian model updating which is a technique currently being applied in the field of structural engineering for model updating [5–8]. In this paper, two models are updated and predictions on the transfer length are performed. One model is the ACI 318-11 code [9] which estimates the transfer length as a function of the nominal diameter of the strand and the stress applied after all prestress losses. The other model is proposed by Mitchel et al. [10]. Mitchel's model establishes a more complicated relation involving the strength of concrete as an additional parameter.

This paper is divided into four sections. The background section explains the models which will be updated and offers an introduction to Bayesian Model Updating. The section on experimental setup describes tests performed and how the data was read. The last two sections, results and conclusions, present the performance of updated models and the distributions of the parameters.

A.R. Ortiz (✉) • R. Madarshahian • J.M. Caicedo • D. Rizos
Department of Civil and Environmental Engineering, University of South Carolina, 300 Main St., Columbia, SC 29208, USA
e-mail: aro@email.sc.edu; alrortiz@gmail.com; mdrshhn@email.sc.edu; caicedo@cec.sc.edu; rizos@cec.sc.edu

S. Pakzad, C. Juan (eds.), *Dynamics of Civil Structures, Volume 2*, Conference Proceedings of the Society for Experimental Mechanics Series, DOI 10.1007/978-3-319-29751-4_33

33.2 Background

33.2.1 Transfer Length Models

The prestress applied in a steel strand is transferred to the concrete through bond stresses. Bonds need a distance to fully transmit stresses. In a prestressed concrete beam, this distance starts from the ends, where the stress in the concrete is zero, and ends where the strands and concrete are totally bonded. This distance is called transmission or transfer length [11].

The ACI 318-11 code [9] determines the transfer length as expressed by (33.1). In this equation, the transfer length is only dependent on the diameter of the strand and the prestress applied.

$$L_t = \frac{\sigma_{pcs}\phi}{20.7} \tag{33.1}$$

In this equation, σ_{pcs} is the effective stress in the prestressed strand after all prestress losses (in MPa) and ϕ is the nominal diameter of the strand (mm).

Mitchell et al. [10] proposed an equation where strength of the concrete, f_{ci}, affects the transfer length. In their model, they also consider that the transfer length should be a function of the stress in the steel just after the prestress is released. Therefore, the term σ_{pi} should be used instead of σ_{pcs}. The equation proposed by Mitchell et al. [10] is:

$$L_t = \frac{\sigma_{pi}\phi}{20.7}\sqrt{\frac{20.7}{f_{ci}}} \tag{33.2}$$

33.2.2 Model Updating

Parameters of both models were updated using Bayesian inference. Bayesian inference uses rules of the conditional probability for updating models in a probabilistic sense [12, 13]. Through Bayesian inference, the Probability Density Function (PDF) of the parameters of a model can be obtained based on observed experimental data and a prior knowledge [14]. The Bayesian inference is governed by (33.3).

$$P(\Theta|D) \propto P(D|\Theta)P(\Theta) \tag{33.3}$$

In this equation, the term $P(D|\Theta)$ is called the likelihood. The role of the likelihood is to join experimental and analytical values of the model given a set of parameters. Term $P(\Theta)$ is called the prior, and it refers to the prior knowledge of the parameters Θ before updating.

For updating models shown in equations Eqs. (33.1) and (33.2), the constant parameters were replaced for other variables. Therefore, equations Eqs. (33.1) and (33.2) were updated as follows by Eqs. (33.4) and (33.5) for both models.

$$L_t = \frac{\sigma_{pcs}\phi}{K} \tag{33.4}$$

$$L_t = \frac{\sigma_{pi}\phi}{K}\sqrt{\frac{K}{f_{ci}}} = \sigma_{pi}\phi\sqrt{\frac{1}{Kf_{ci}}} \tag{33.5}$$

33.3 Experimental Test Description

Experimental data was collected from a 11 in. × 11in. × 8ft beam. The beam was built using 4 strands of 0.5 in. of nominal diameter. The beam was made of high performance concrete composed of coarse aggregates with smaller modulus of elasticity. Strands were released when concrete strength reached 28.5MPa. The tension in the wires was measured using 350Ohm strain gages located at the middle of each strand and 12 in. from the ends. Figure 33.1 shows a diagram of the beam with the location of strain gages.

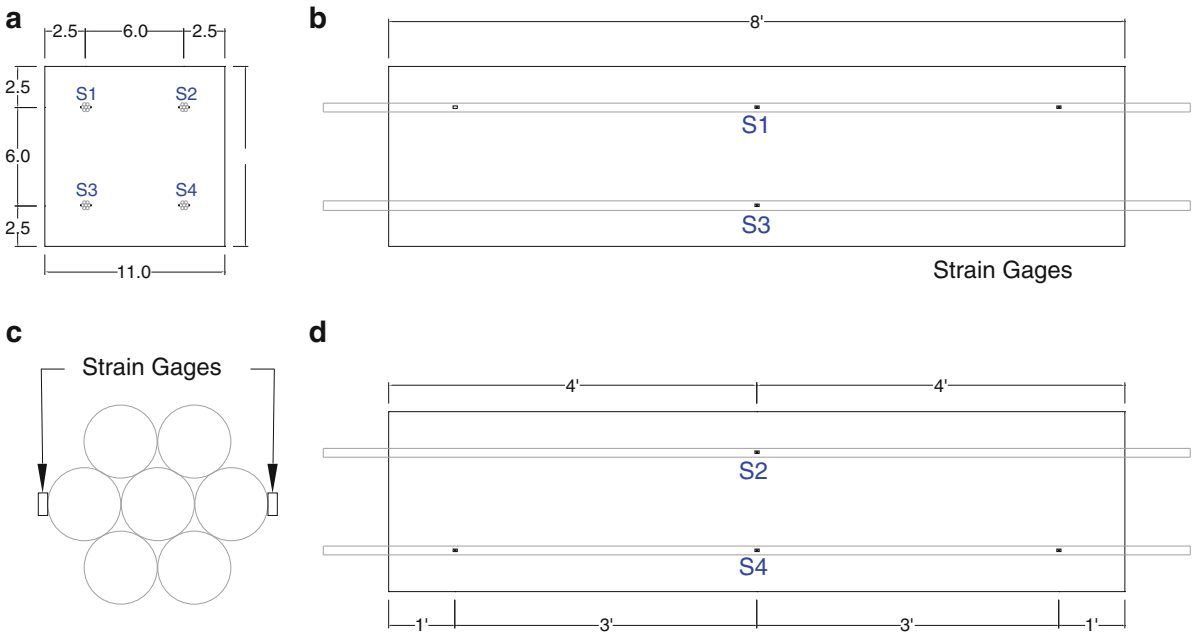

Fig. 33.1 Sketch of the instrumented beam. (**a**) Cross section of the beam, (**b**) Strands 1 and 3 and strain gages, (**c**) Cross section of a typical strand, and (**d**) Strands 2 and 4 and strain gages

Fig. 33.2 Prestress beam after all strands were released

Table 33.1 Prior knowledge of the parameters

Parameter	Units	Distribution
ϕ	mm	$N(12.7, \frac{12.7}{1000})$
f_{ci}	MPa	$N(28.0, 1.5)$
Position	mm	$N(304.8, 10)$

A sudden release of the strands was performed by cutting the strands on the left end. Strain gages were able to track the initial tension of the beam, as well as immediate and short time losses. Unfortunately sensors located in strand 4 were damaged during curing, and only the sensors at strand 1 were available to calculate the transfer length. Figure 33.2 shows a picture of the beam after the strands were released.

The prior knowledge used for parameters ϕ, f_{ci} and the position of the sensor were the same for both models. Table 33.1 presents the distributions used.

The prior for the parameter K was defined as a normal distribution with mean 20.7 and standard deviation of 10.4. An additional constraint was added to the models in order to guarantee that the transfer length is between 100 and 1400 mm (half length of the beam).

33.4 Results

The three and four parameters models were updated using the measurements of the two strain gage located 12in from the ends of the beam. The strain recorded at the middle of the beam were used to calculate the strain after the releasing of the strands. The stress change on the strand was assumed to be linear according to references [11, 15, 16]. The posterior PDF was sampled using the Metropolis Hastings algorithm [17]. Histograms of the parameters for the ACI 318-11 model are shown in Fig. 33.3. Figure 33.3a shows the marginal histograms of the samples in the diagonal. Correlations between variables can be studied using the figures above the diagonal.

The posterior PDF of the parameters for Mitchel's model are presented in Fig. 33.4. Figure 33.4a shows no signs of correlation between f_{ci} and other parameters. Figure 33.4b shows the predicted stresses at the strand. The dot indicates the average of the two strain gauges at 12in from the ends.

The histogram of the Transfer length produced by the samples for each model is presented in Fig. 33.5. The ACI model shows a wider range than the model proposed by Mitchell et al. [10]. Table 33.2 shows a statistical summary for the Transfer length samples for both models.

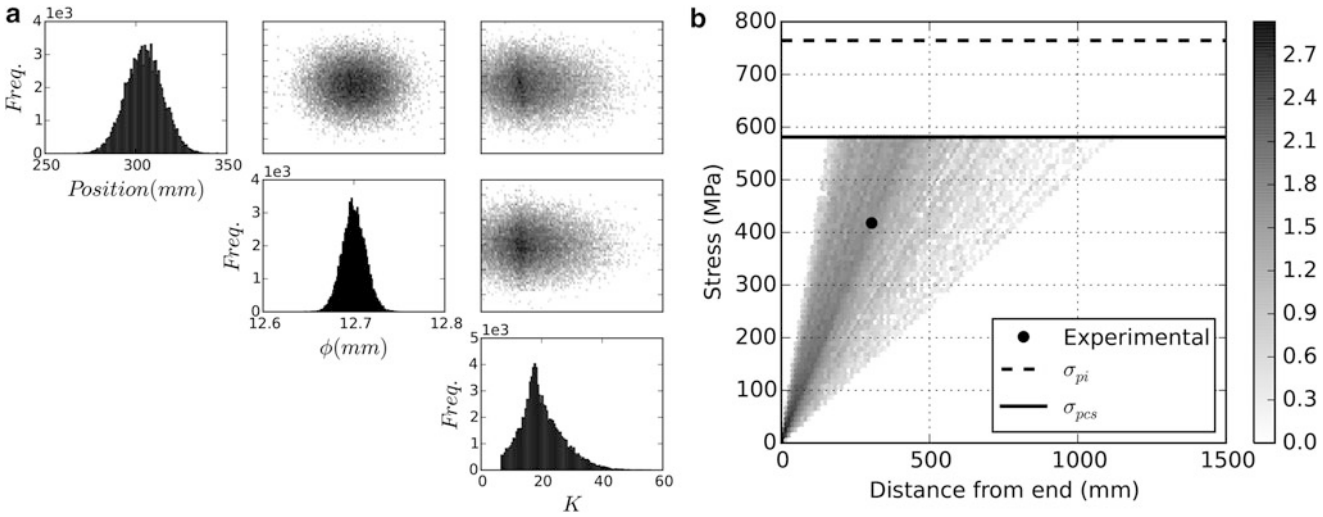

Fig. 33.3 Results of updating the model established in the ACI 318 code. (**a**) Marginal histograms for parameters involved in the model proposed by ACI. (**b**) Samples obtained from updating ACI model vs experimental data

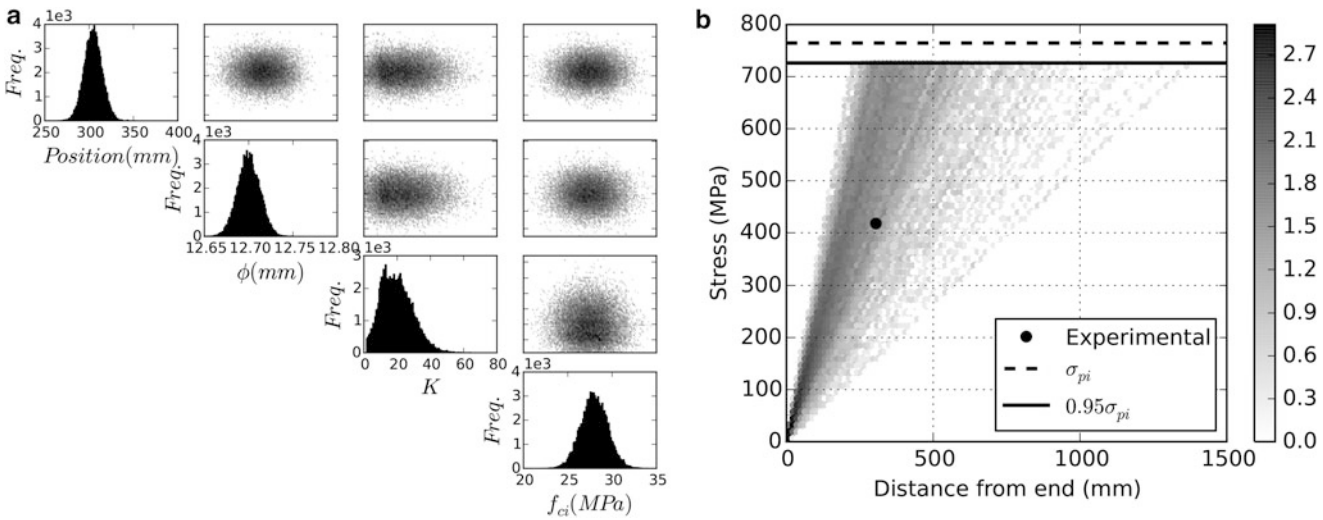

Fig. 33.4 Results of updating the model proposed by Mitchell et al. (**a**) Marginal histograms for parameters involved in the model proposed by Mitchell (**b**) Samples obtained from updating Mitchell's model vs experimental data

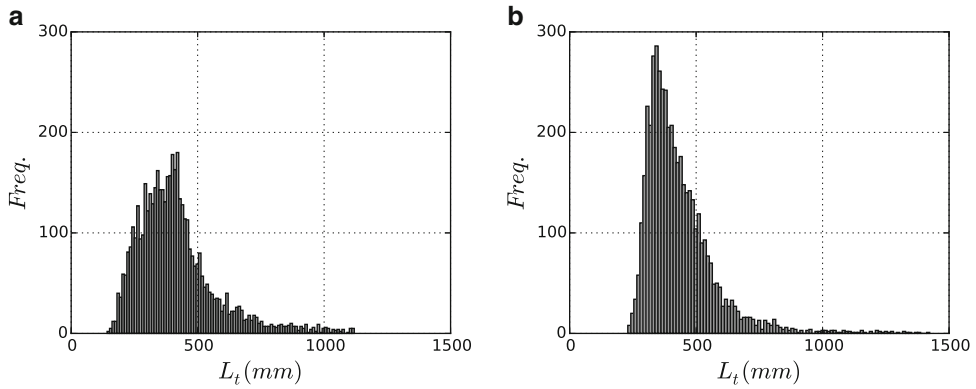

Fig. 33.5 Analytical transfer length histograms. (**a**) Histogram of the Transfer Length obtained from samples using ACI 318-11 [9] model. (**b**) Histogram of the Transfer Length obtained from samples using Mitchell et al. [10] model

Table 33.2 Statistics of transfer length estimation

	ACI	Mitchell
Mean	413	432.7
Std	157.4	138.8
Median	389.2	399.3

33.5 Conclusions

The goal of this paper was to update two prestress concrete transfer length models in a probabilistic fashion using limited experimental data (one strain gauge). The models updated are the ACI 318-11 code [9] and Mitchell's model [10]. The transfer length in the ACI 318-11 model is proportional to both the diameter and the stress applied to the strand. Mitchel's model uses the concrete strength as an additional parameter.

Results indicate no dependency between the model parameters in either model. The mean of the Transfer length obtained with the ACI model is shorter than that obtained with Mitchel's model. The standard deviation of the transfer length was smaller in Mitchel's model. Future work will focus on comparing these models in a probabilistic sense to determine if one model is more probable when limited experimental data is available.

Acknowledgements This material is based upon work supported by Federal Railroad Administration BAA-2014, CSX Transportation, KSA-Koppers Concrete Tie Division Inc. under the project entitled "High Strength Reduced Modulus High Performance Concrete for Prestressed Concrete Tie Applications"

References

1. Jeong, D.: Concrete ties, fasteners and critical failure modes. In: FRA Research and Development Research Review (2012)
2. Zeman, J.C., Edwards, J.R., Barkan, C.P., Lange, D.A.: Failure mode and effect analysis of concrete ties in north America. In: Proceedings of the 9th International Heavy Haul Conference, pp. 270–278 (2009)
3. Kaewunruen, S., Remennikov, A.M.: Dynamic crack propagations in prestressed concrete sleepers in railway track systems subjected to severe impact loads. J. Struct. Eng. **136**(6), 749–754 (2009)
4. Yu, H., Jeong, D.: Finite element bond models for seven-wire prestressing strands in concrete crossties. In: Proceeding of 2015 Joint Rail Conference (JRC) (2015)
5. Beck, J., Katafygiotis, L.S.: Updating models and their uncertainties i: Bayesian statistical framework. J. Eng. Mech. **124**, 455–461 (2009)
6. Cheung, S.H., Beck, J.: Bayesian model updating using hybrid monte carlo simulation with application to structural dynamic models with uncertain parameters. J. Eng. Mech. **135**, 243–225 (2009)
7. Zárate, B.A., Caicedo, J.M.: Finite element model updating: multiple alternatives. Eng. Struct. 30(12), 3724–3730 (2008)
8. Madarshahian, R., Caicedo, J.M.: Reducing MCMC computational cost with a two layered Bayesian approach. In: Model Validation and Uncertainty Quantification, vol. 3, pp. 291–297. Springer, New York (2015)
9. Committee, A., et al.: Building Code Requirements for Structural Concrete (318-11) and Commentary-(318r-11). American Concrete Institute, Detroit (2011)
10. Mitchell, D., Cook, W.D., Khan, A.A., Tham, T.: Influence of high strength concrete on transfer and development length of pretensioning strand. Precast/prestress. Concr. Inst. J. **38**(3), 52–66 (1993)

11. Martí-Vargas, J.R., Serna, P., Navarro-Gregori, J., Pallarés, L.: Bond of 13 mm prestressing steel strands in pretensioned concrete members. Eng. Struct. **41**, 403–412 (2012)
12. Gelman, A., Carlin, J.B., Stern, H.S., Rubin, D.B.: Bayesian Data Analysis, vol. 2. Taylor & Francis (2014)
13. Zárate, B.A., Caicedo, J.M., Yu, J., Ziehl, P.: Bayesian model updating and prognosis of fatigue crack growth. Eng. Struct. **45**, 53–61 (2012)
14. Jaynes, E.T.: Probability Theory: The Logic of Science. Cambridge university press, Cambridge (2003)
15. Martin, L.D., Scott, N.L.: Development of prestressing strand in pretensioned members. ACI J. **73**(8), 453–456 (1976)
16. Buckner, C.D.: A review of strand development length for pretensioned concrete members. PCI J. **40**(2), 84–99 (1995)
17. Hitchcock, D.B.: A history of the metropolis–hastings algorithm. Am. Stat. **57**(4), 254–257 (2003)

Chapter 34
Multi-Shaker Modal Testing and Modal Identification of Hollow-Core Floor System

Atheer F. Hameed and Aleksandar Pavic

Abstract The approach used to estimate dynamic properties of civil engineering structures normally comprise numerical modelling and much less frequently—experimental modal analysis. Hence, the work presented in this paper focuses on the later approach. The multi-input multi-output (MIMO) modal test for civil engineering structures is not commonly used and is rarely presented in the literature due to its cost and practical difficulties. This paper aims to show the advantages of adapting this exercise in the identification of the modal properties of a full-scale floor system. The floor is located on the first level of a building undergoing major refurbishment. The results presented in this paper are for a test conducted on the bare floor where no modifications were done to the as-built structural layout. A forced vibration test was undertaken with three electrodynamic shakers and 14 accelerometers. To excite the floor, the shakers were driven by statistically uncorrelated random excitation signals with frequency spans of 0–50 Hz. The testing demonstrated that the floor has closely spaced modes of vibration. The procedure for identifying the estimated modal properties from this experimental modal analysis exercise will be discussed.

Keywords Precast hollow-core planks • Modal testing • MIMO • Modal properties • Vibration serviceability

34.1 Introduction

This paper describes the procedure of a modal test conducted to evaluate the dynamic properties (natural frequencies, mode shapes, modal masses and modal damping ratios) of a building floor undergoing significant refurbishment. The floor comprises hollow-core precast planks supported by a reinforced concrete frame. This type of construction has been in use for more than five decades. However, research papers describing its dynamic behaviour are rare [1, 2]. The main difficulty with understanding this behaviour is modelling of boundary conditions and lateral stiffness considering connection specifics between the hollow core elements. Since the desire for high-speed construction is increasing, it is expected that more precast floors will be constructed in the future. The ability to predict modal properties is an essential step in assessing the vibration serviceability of any floor type, including this type, when following the current state-of-the-art design guidelines [3–5]. Current state-of-the-art is such that numerical FE models cannot be used always with confidence to estimate the modal properties of floors. This is basically due to the difficulties of modelling various floor features. For instance, the presence of non-structural elements, structural non-linarites such as cracking, and boundary conditions are quite difficult to model with confidence when checking floor serviceability. Therefore, a modal test of a full-scale floor structure is often required for detailed dynamic performance investigation and for recovering reliable set of modal properties for an existing structure or for future similar structures.

The main advantages of a precast hollow core slab system could be summarised in two main points. Firstly, it has a higher speed of construction than a conventional reinforced concrete floor as the precast planks are cast off site, and can be constructed in any weather conditions. The other point is that it has a lower cost of construction, as there is a significant

A.F. Hameed (✉)
Vibration Engineering Section, College of Engineering, Mathematics, and Physical Sciences, University of Exeter, Kay Building, North Park Road, Exeter EX4 4QF, UK

Civil Engineering Department, University of Anbar, Ramadi, Anbar, Iraq 31001
e-mail: afhh201@exeter.ac.uk

A. Pavic
Vibration Engineering Section, College of Engineering, Mathematics, and Physical Sciences, University of Exeter, Kay Building, North Park Road, Exeter EX4 4QF, UK

Full Scale Dynamics Ltd., 40 Leavygreave Road, Sheffield, South Yorkshire S3 7RD, UK
e-mail: a.pavic@exeter.ac.uk

S. Pakzad, C. Juan (eds.), *Dynamics of Civil Structures, Volume 2*, Conference Proceedings of the Society for Experimental Mechanics Series, DOI 10.1007/978-3-319-29751-4_34

reduction in the required formwork and access scaffolding. Other benefits of this slab system that could be considered by designers and surveyors are fire resistance, good sound insulation and high thermal mass. All these factors could decrease the cost of building operation and maintenance. However, the issue of dynamic performance needs investigation due to uncertain effects of monolithisation of pre-cast planks.

In this paper, firstly the structure of the floor tested is described in detail. Then, the modal testing procedure is explained, along with the data acquired from the test. Finally, the results of analysing these data are shown as a set of modal properties and mode shapes of the as-built floor.

34.2 Background

In general, a floor slab comprising hollow-core precast planks usually has a high level of stiffness in its main direction. Consequently, this slab falls into the category of high-frequency floors. Vibration responses of high frequency floors in buildings under human-induced dynamic loading are not predominantly resonant. However, this will not assure that this floor will have the desired vibration serviceability level for every floor usage [1, 3]. As previously mentioned, only a few studies describing the dynamic performance of this type of floors are available in the public domain [1, 2]. Moreover, there is no specific guidance in the aforementioned design guidelines [3–5] about this particular type of floor. The closest guidance could be found in [6], where only precast concrete units supported by steel frames are considered (not specifically hollow-core precast planks).

Hollow-core floors are considered to be easy and fast to build concrete structures. Once the building frame is up, the precast planks are placed next to each other, according to a layout provided by the designer. Then, typically, a non-structural cast *in situ* concrete screed (with or without thermal reinforcement mesh) is placed on top of the planks to finish the floor. Considering the monolithic way of construction, the floor will have higher stiffness in one direction (transverse to the beam) than the other direction (parallel to the beam). The estimation of these stiffness values is not a straightforward process and requires experimental data to verify and validate them [2, 7]. Moreover, there is a possibility that cracking of cast *in-situ* concrete could produce a lack of connection between the planks. This would make the planks work separately and prevent the engagement of the whole floor area. In such case, local modes of the planks could develop yielding much higher dynamic response of the floor [6].

Hence, there is a need to check the applicability of the current state-of-the-art design guidelines on this type of floor structure. This could only be done by combining modal testing and numerical modelling of a full-scale structure.

34.3 Structural Description

The floor was built in the mid-1970s and it had been used as an open plan shopping area. The floor has undergone massive refurbishment since early 2015, and the ultimate goal of these works is to use the floor as a dining/dancing floor. The test was conducted when the bare floor structure was exposed after stripping all partitions and other non-structural elements form the main area of the floor. Figure 34.1 shows an overview of the floor during testing. The floor comprises 250 mm precast hollow-core planks supported by 600 mm × 450 mm reinforced concrete (RC) beams. Both precast planks and supporting beams have a span of 6.4 m. The whole slab system is supported by 725 mm × 300 mm RC beams on the edges, with a span of 4.8 m. On top of the precast planks, a non-structural *in situ* 50 mm thick screed with A98 steel reinforcement mesh was placed. The floor area is about 600 m^2 with 520 kg/m^2 estimated mass per unit area, making the total estimated mass of the floor level tested of about 310,000 kg. The floor is located on the first level of a two-storey building with the storey height of 3.7 m. At the time of testing, a concrete-block wall was partitioning the northern bay of the slab. Figure 34.2 shows the as-built floor plan, building elevation and the location of the concrete-block wall.

The floor has two openings with the largest one shown in Fig. 34.1. For the multi-input multi-output (MIMO) measurements of frequency response functions (FRFs) of the floor, a test grid comprising 77 test points (TPs) covering the whole floor area was used. Figure 34.3 shows the test grid where red points represent column locations, dark-blue lines represent beams, and light-blue, pink, and green points are shakers positions.

Fig. 34.1 View of the floor

34.4 Modal Testing

This section contains a detailed description of the procedure used for modal testing.

34.4.1 Instrumentation and Data Acquisition

Multi-input multi-output (MIMO) modal test was conducted using three electrodynamic shakers (one small shaker APS113 and two large shakers APS400 [8, 9]) to excite the floor. The small shaker was positioned at TP16 and the two large shakers were positioned at TP22 and TP38, respectively. A typical setup of the three shakers is shown in Fig. 34.1. The purpose of using three shakers (as opposed to a single shaker) is to increase the excitation energy and improve the signal to noise ratio [7]. Floor responses were acquired using 14 Honeywell QA750 [10] force balance accelerometers fixed to Perspex plates, as shown in Fig. 34.4. These accelerometers were distributed using the test grid shown in Fig. 34.3. Endevco 7754–1000 piezoelectric accelerometers [11] were used to quantify each shaker force by measuring its moving mass acceleration. Figure 34.5 shows the data acquisition station setup during the test.

34.4.2 Measurements

The shakers were set to operate simultaneously and excite the structure with three uncorrelated random forces in the frequency range 0–50 Hz. A data acquisition block size of 64 s was used, with a sampling frequency of 128 samples per second. A stable averaging method was adopted with a 75 % overlap and approximately 8 min of data acquisition time per set of measurements.

The data were collected as three sets of FRFs, each set corresponding to one of the shaker references (input forces). Therefore, the measured data represent three rows of the FRF matrix [12]. The measurements contain all the information required to describe the dynamic performance of the floor tested (i.e., natural frequencies, mode shapes, modal masses and modal damping ratios).

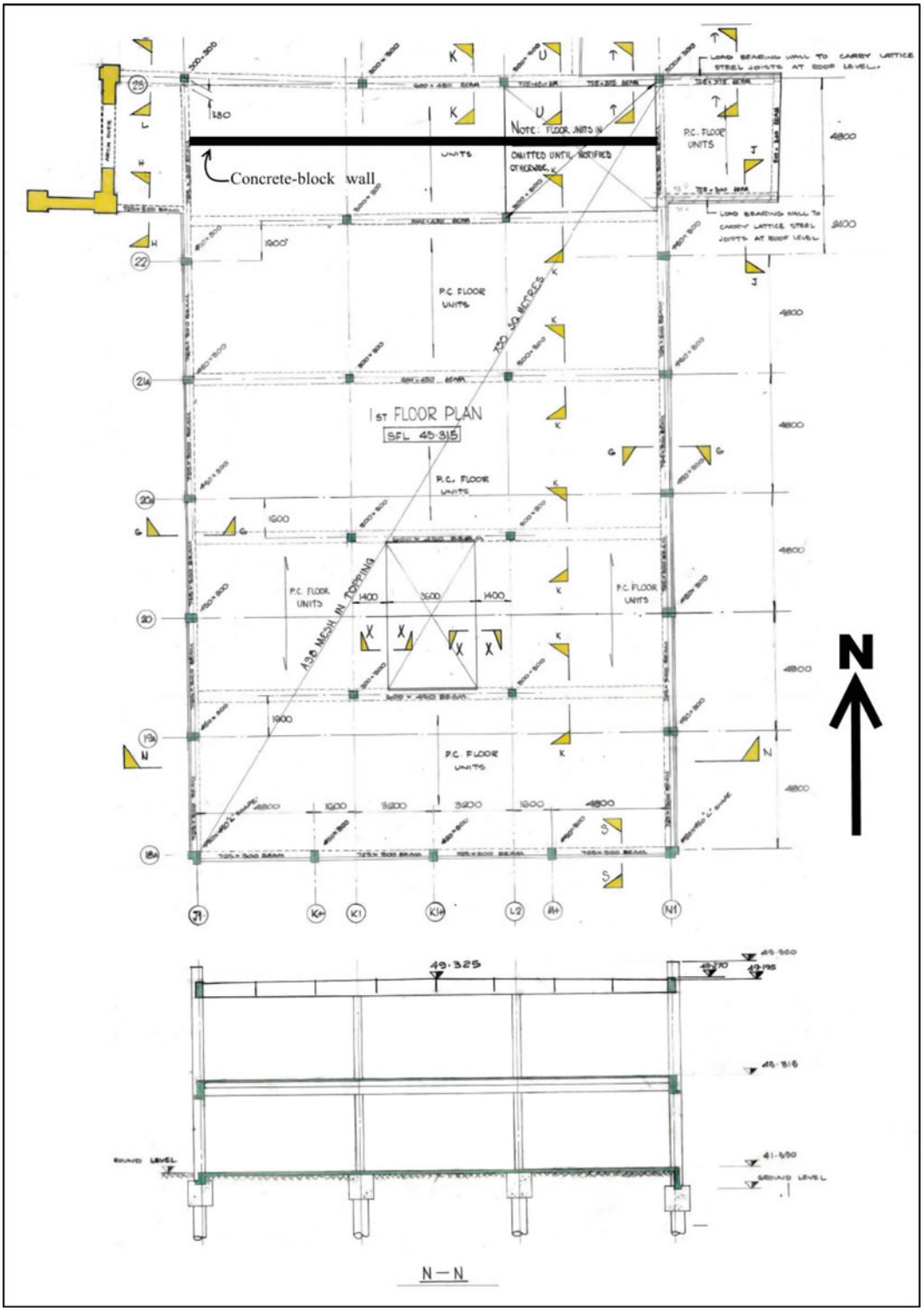

Fig. 34.2 As-built floor plan and building elevation

Point accelerance FRF is the measurement taken when the excitation and response correspond to the same degree of freedom (DOF). Figure 34.6 illustrates the point accelerance FRFs corresponding to each shaker. The visual examination of the acquired FRFs indicates that strong peaks corresponding to natural frequencies of modes excited at shaker TPs are all above 14 Hz. In addition, it is clear that the floor has closely spaced modes of vibration.

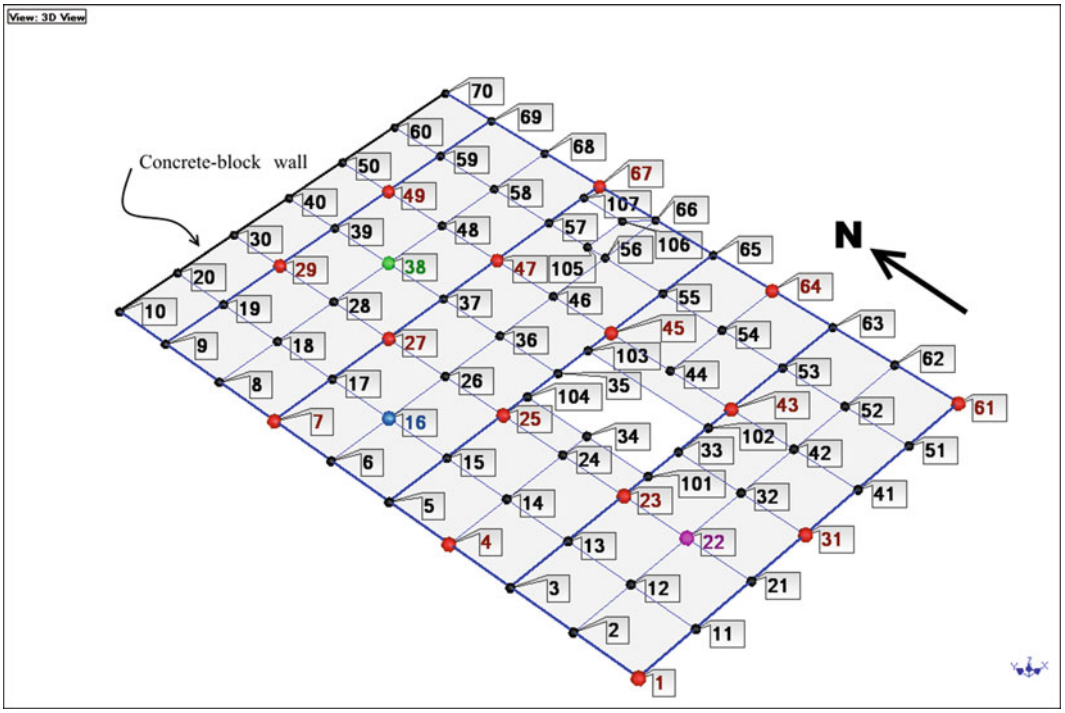

Fig. 34.3 Test Grid featuring 77 TPs—Shakers positioned at TP16 (*light-blue*), TP22 (*pink*), and TP38 (*green*); *red* points represent column locations; *dark-blue lines* represent beams

Fig. 34.4 Point accelerance measurements

34.4.3 Reciprocity Check

Reciprocity check is one of the measured FRFs quality assurance checks [12]. This check is done by plotting two FRFs: $H(f)_{i,j}$ (excitation at TP j, response at TP i) and FRFs: $H(f)_{j,i}$ (excitation at TP i, response at TP j). For an ideal linear structure in a noiseless environment, these two FRFs should be identical due to Maxwell's reciprocity theorem [12]. The checks for the tested floor are presented in Figs. 34.7, 34.8 and 34.9. Each figure corresponds to a pair of test points.

Although they are not perfectly identical, there is a very good level of correlation between each pair. The miss-matching indicates that measured FRFs are noisy to some extent due to low signal-to-noise ratio. For a full-scale floor structure the low signal-to noise ratio could be caused by a number of reasons, such as:

Fig. 34.5 Data acquisition station

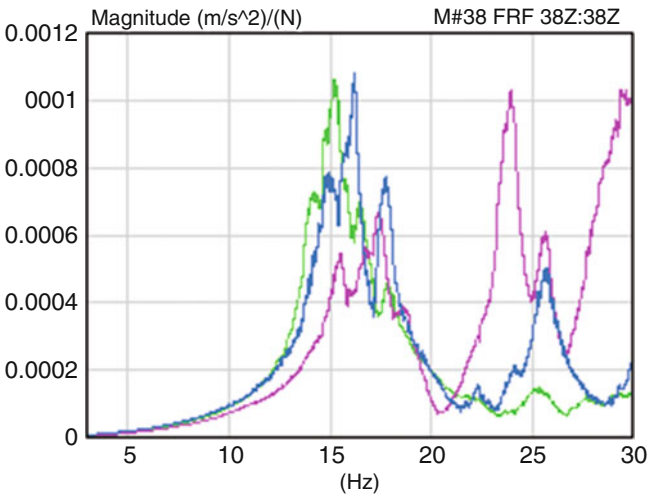

Fig. 34.6 Point accelerance FRFs—3–30 Hz. (Light-blue: TP16, Pink: TP22; *green*: TP38)

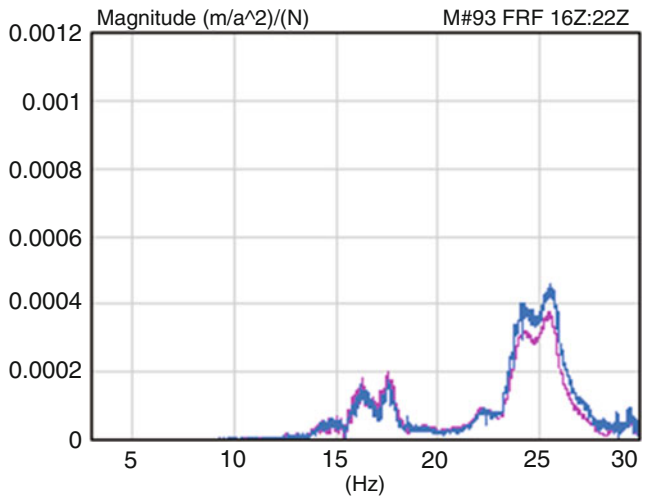

Fig. 34.7 Reciprocity plot TP16 (*light-blue*)-TP22 (*pink*)

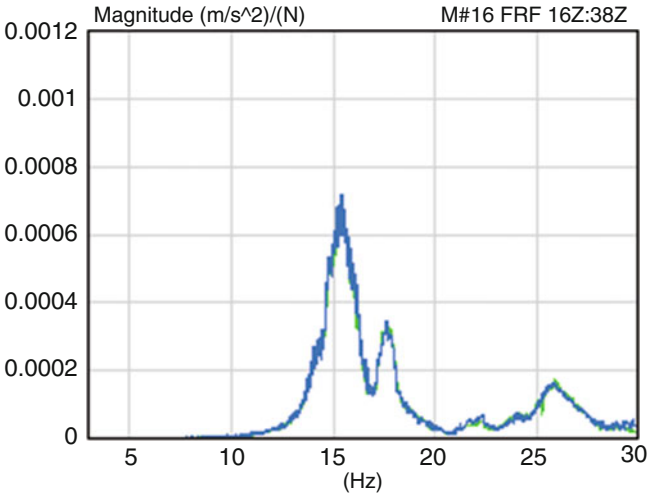

Fig. 34.8 Reciprocity plot TP16 (*light-blue*)-TP38 (*green*)

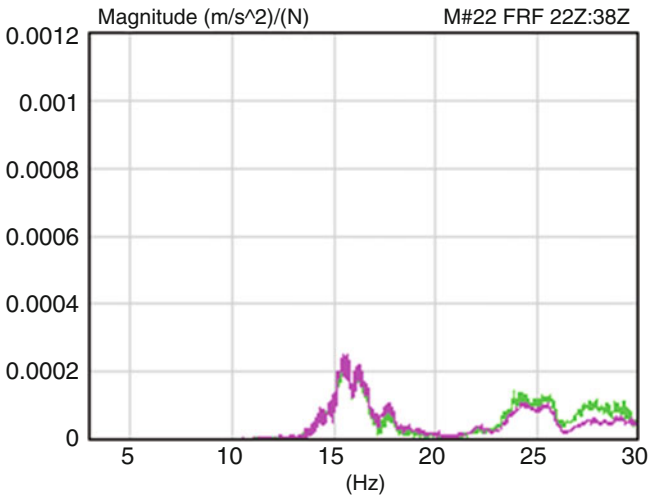

Fig. 34.9 Reciprocity plot TP22 (*pink*)-TP38 (*green*)

- the building resides in an open-space noisy environment,
- the floor level was not completely empty and that people (testing personnel) were moving around occasionally,
- other floor levels were occupied and excited and vibrations from them got transferred though the columns,
- the sheer size and mass of the whole floor, which had to be excited to have a measurable dynamic response across a range of frequencies and widely separated locations,
- the effects of structural (e.g., columns connected to foundations) and non-structural elements connected to the floor, which were dissipating excitation energy away from the floor and
- the effects of various other nonlinearities, such as rattling, which invariably exist in real life full-scale civil engineering structures.

All these plots indicate that, in the context of a large floor structure, meaningful results were gathered by the MIMO setup, but that the acquired FRF data were noisy.

34.5 Modal Analysis

To identify the modal properties of the floor tested, ME'Scope software was used [13]. The multi-reference Complex Mode Indicator Function (CMIF) was adopted for the curve fitting process. The curve fitting process is an attempt to produce a mathematical model that describes the tested structure as closely as possible [12]. This mathematical model resulting from the curve fitting process is a linear approximation of the complex and more or less non-linear real-life structure. A typical curve fit for the tested floor structure is shown in Fig. 34.10. This process usually results in complex (as opposed to real) mode shapes as a description of the dynamic behaviour of the floor [14]. The first four modes of vibration, along with modal complexity plots, are shown in Fig. 34.11. All modes shown are engaging most of the floor area (global modes), which indicates that the joints between planks are efficient enough to engage the adjacent areas of the floor and provide reasonable level of lateral stiffness. However, the closeness of the measured peaks indicate closely spaced modes of vibration which may be caused either by repetitive geometry or large differences between the main and lateral stiffnesses of the floor.

Interestingly, some of the columns (red points) are engaged in those vertical mode shapes as well, indicating less than rigid support conditions. This is not surprising considering that the columns went all the way to the foundations (3.7 m) and that the foundations were piled on 6 m long piles. Theoretically speaking, modes which have all mode shapes amplitudes either in phase (0°) or out of phase (180°) (real modes) usually result from easy to excite full-scale structures with proportional damping. In the case of the floor tested in this study, all modes have a certain degree of complexity. This indicates that the structure could have non-proportional damping resulting in genuine complex mode shapes [14]. Also, the structure is potentially non-linear, but nonlinearity is not the only reason behind the emergence of complex mode shapes in full-scale structures. Sizeable signal-to-noise ratio could also be a reason [14] in particular for this structure and considering the less than ideal quality of FRFs gathered (Figs. 34.7, 34.8 and 34.9). This noise could originate from any of the sources discussed in the previous section and lead to a miss-match in the reciprocity plots.

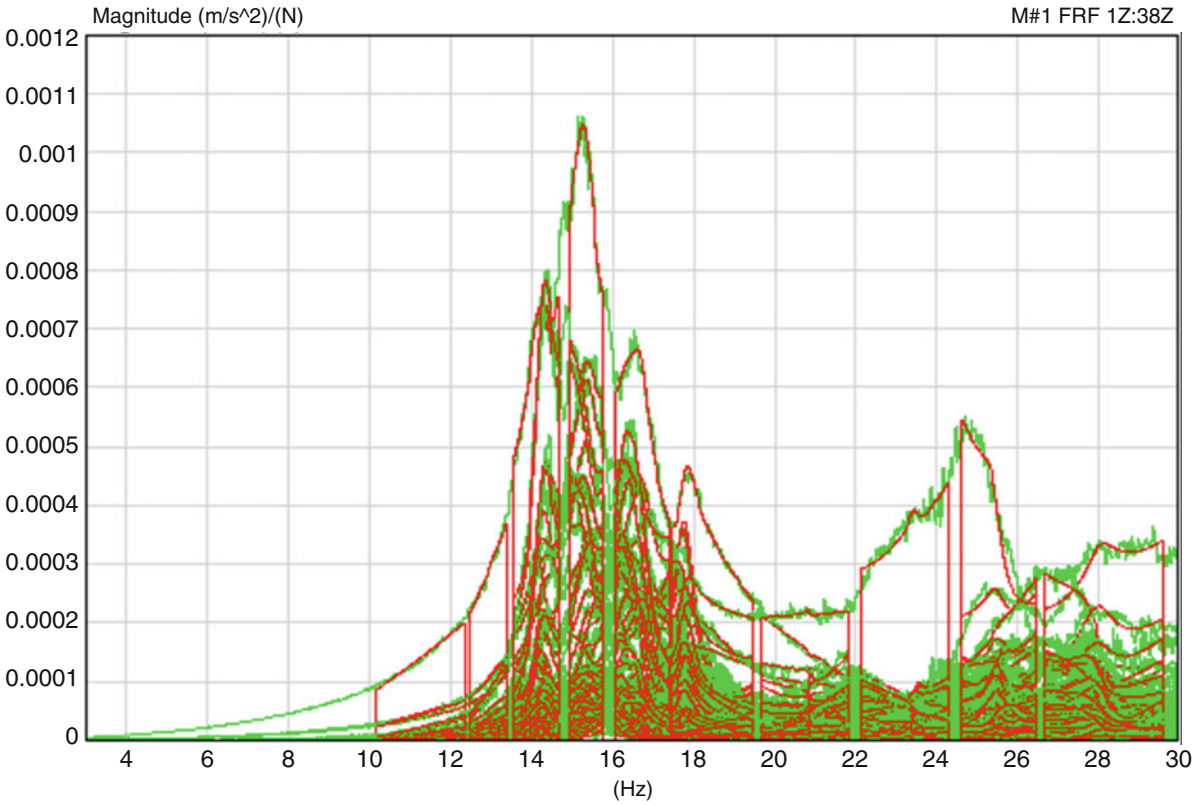

Fig. 34.10 Typical curve fitting

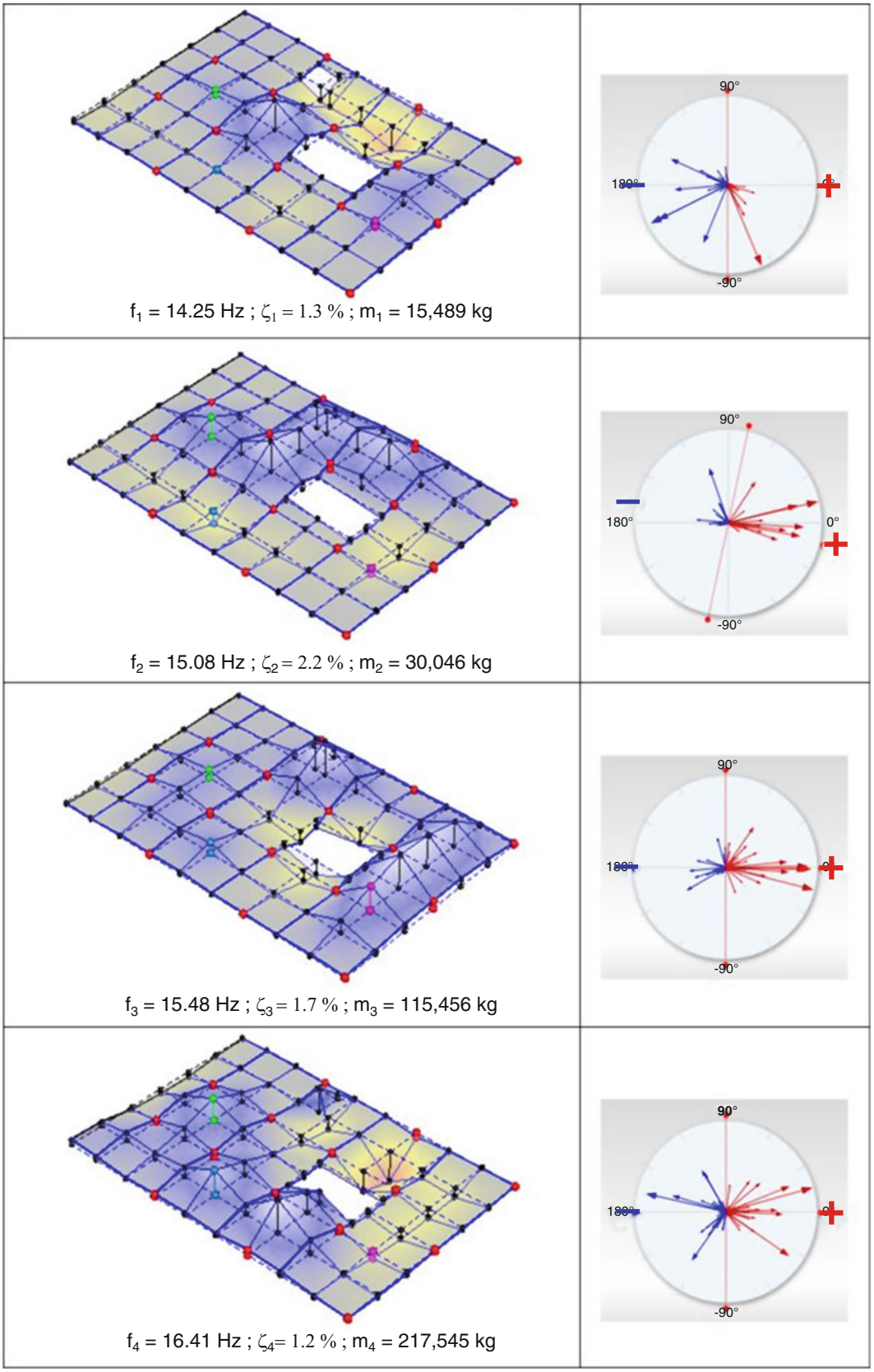

Fig. 34.11 Predicted vertical mode shapes and modal complexity plots

34.6 Conclusions

The dynamic properties of a floor comprising hollow-core precast planks and undergoing a massive refurbishment process have been identified using MIMO modal testing. The measured FRFs have certain level of noise which has not affected the measurement significantly. This is clearly shown by checking the reciprocity plots where there is a good level of match between corresponding references. The FRF-estimated vertical modes are showing a noticeable degree of complexity. These complex mode shapes were to be expected due to the possibility of the floor featuring non-proportional damping, low signal-to-noise ratio and noisy measured FRFs. The test, which is the first in a series, will be used as a platform to assess different vibration serviceability related issues and will published in due course.

Acknowledgements The paper was prepared with the financial and technical support of the University of Exeter and Engineering and Physical Sciences Research Council (EPSRC) grant reference EP/K03877X/1 for which the writers are grateful. The financial support of The Higher Committee for Education Development in Iraq (HCED IRAQ scholarship reference GD-13-5) is highly appreciated as well. WSP-Parsons| Brinckerhoff, and ISG plc are acknowledged for allowing access to the site during construction.

References

1. Brownjohn, J.M.W., Pan, T.-C., Middleton, C.J., Tan, S.C., Yang, G.: Floor vibration serviceability in a multistory factory building. J. Perform. Constr. Facil. 04014203-1-14 (2014)
2. Pavic, A., Reynolds, P., Prichard, S., Lovell, M.: Evaluation of mathematical models for predicting walking-induced vibrations of high-frequency floors. Int. J. Struct. Stab. Dyn. **3**, 107–130 (2003)
3. Pavic, A., Willford, M.R.: Vibration serviceability of post-tensioned concrete floors - CSTR43 App G, Appendix G in Post-Tensioned Concrete Floors Design Handbook. Technical Report 43, pp. 99–107 (2005)
4. Willford, M.R., Young, P.: A design guide for footfall induced vibration of structures - CCIP-016. The Concrete Centre, Slough (2006)
5. Murray, T.M., Allen, D.E., Ungar, E.E.: Floor vibrations due to human activity - AISC DG11 (2003)
6. Smith, A.L., Hicks, S.J., Devine, P.J.: Design of floors for vibration - a new approach SCI P354, revised Ed. The Steel Construction Institute, Ascot (2009)
7. Pavic, A., Miskovic, Z., Živanović, S., Zivanovic, S.: Modal properties of beam-and-block pre-cast floors. IES J. A Civ. Struct. Eng. **1**, 171–185 (2008)
8. Instruction manual, Electro-seis, Model 113 Shaker (1996)
9. Instruction manual, Electro-seis, Model 400 Shaker (2013)
10. I. Honeywell International, QA-750 Accelerometer Datasheet (2005)
11. E. Corporation, endevco model 7754A-1000 Datasheet
12. Ewins, D.J.: Modal testing: theory, practice and application. Research Studies Press, Baldock (2000)
13. Vibrant Technology Inc., ME'Scope VES 6.0 (2015)
14. Imregun M, Ewins DJ.: Complex modes: origins and limits. In: Proceedings of the 13th International Modal Analysis Conference, pp. 496–506. Society for Experimental Mechanics, Inc., Nashville (1995)